2nd International Workshop on Reacting Particle-Gas Systems

Supported by the Collaborative Centre/ Transregio 287
"BULK-REACTION – Reacting and moving granular assemblies with gas flows"

June, 16th – 18th, 2025

Otto von Guericke University Magdeburg

Modelling and Experimental Characterization of Reactive Particle-Gas Systems

Imprint

Editors:

Dominique Thévenin
Otto von Guericke University Magdeburg
thevenin@ovgu.de

Viktor Scherer
Ruhr University Bochum
scherer@leat.ruhr-uni-bochum.de

The CRC/TRR 287 BULK REACTION is funded by the Deutsche Forschungsgemeinschaft (DFG, German Research Foundation) – Project-ID 422037413-TRR 287. The organisation of this event was partly supported by the DFG.

Website: https://bulk-reaction.de/

DOI: http://dx.doi.org/10.25673/118928

Program

June 17th, 9:00 am – Sessions:

Session I	DEM & CFD Chairperson: B. van Wachem	Page
10:00-10:20	**Simulation of hydrogen combustion in a gas-fired lime shaft kiln** S. Meschede[1], S. Haep[1], D. Bathen[1,2] [1]Institut für Umwelt und Energie, Technik und Analytik (IUTA), Germany [2]Thermal Process Engineering, University of Duisburg-Essen, Germany	1
10:20-10:40	**Advanced heat exchange and radiation sub-models in coarse-grained CFD-DEM simulations** M. Mitterlindner, M. Niemann[2], D. Louw[2], P. Kieckhefen[3], C. Goniva[2], M. Salehi[1,4], S. Radl[1] [1]Graz University of Technology, Austria [2]DCS Computing GmbH, Austria [3]BASF SE, Germany [4]Virtual Vehicle GmbH, Austria	4
11:10-11:30	**Consistent Euler-Lagrange point-particle modeling using the volume-filtering framework** M. Hausmann, B. van Wachem Chair of Mechanical Process Engineering, Otto von Guericke University Magdeburg, Germany	7
11:30-11:50	**Experimental study on sludge drying characteristics and optimized design of dryer based on CFD-DEM simulation** G. Li[1,2], H. Zhang[3], Z. Zhou[4], R. Zou[1], A. Yu[1,2] [1]ARC Research Hub for Smart Process Design and Control, Department of Chemical and Biological Engineering, Monash University, Clayton VIC 3800, Australia [2]School of Energy and Environment, Southeast University, China [3]School of Metallurgy, Northeastern University, China [4]Jiangxi University of Science and Technology, China	10
11:50-12:10	**Locally resolved DEM/CFD simulations of a generic oxy-fuel kiln for lime production** M. Brömmer, E. Illana, V. Scherer Institute of Energy Plant Technology, Ruhr-University Bochum, Germany	13
12:10-12:30	**Mean flow properties in a packed bed with varying geometry** W. Sadowski, H. Demir, F. di Mare Lehrstuhl für Thermische Turbomaschinen und Flugtriebwerke, Ruhr-Universität Bochum, Bochum, Germany	16

Session II	Advanced experimental techniques Chairperson: O. Speck	Page
10:00-10:20	**Using AI, positron imaging, and insider knowledge to digitally optimise industrial fluid- and particle-handling systems** K. Windows-Yule School of Chemial Engineering, the University of Birmingham, Edgbaston, Birmingham, B15 2TT	19

10:20-10:40	**State of the art of three selected techniques for advanced solids flow diagnostics: MPT, MST and high frequency radar** D. C. Guío-Pérez, D. Pallarès Division of Energy Technology, Chalmers University of Technology, Göteborg, Sweden	22
11:10-11:30	**Development of a PET-like system for particle tracking** Y. Hartych, N. Böhle, M. Fink, M. Fritsch, M. F. H. Heinsius, T. Held, T. Holtmann, M. Huckestein, J. Oppotsch, M. Steinke, C. Wais, U. Wiedner Institute of Experimental Hadron Physics, Ruhr University Bochum, Germany	25
11:30-11:50	**A configurable real-time data acquisition system for PEPT in particle-gas flow measurement** D. Passaretti[1], E. Antonecchia[2], N. D'Ascenzo[2,3] [1]Forschungscampus STIMULATE, Otto von Guericke University of Magdeburg, Magdeburg, Germany [2]Department of Life Science, BF Research, Jolanda di Savoja, Italy [3]School of Information Science and Technology, University of Science and Technology of China, Hefei, China	28
11:50-12:10	**Unveiling the power and limitations in X-Ray imaging of organic materials** S. Gruber[1], N. Vorhauer-Huget[2], E. Tsotsas[2], P. Först[1] [1]Technical University of Munich, School of Life Sciences, Food Process Engineering, Weihenstephaner Berg 1, Freising, Germany [2]Otto von Guericke University Magdeburg, Institute of Process Engineering, Thermal Process Engineering, Germany	31
12:10-12:30	**High-spatial-resolution Raman distributed temperature sensing system** J. M. López Bonilla, F. Beyrau Institute of Fluid Dynamics and Thermodynamics, Otto von Guericke University Magdeburg, Germany	35

June 17th, 14:30 pm – Sessions:

Session III	**Iron & metal particles** Chairperson: M. Schiemann	Page
14:30-14:50	**The role of hydrogen flow rates in the direct reduction of iron ore pellets: Investigating external mass transfer limitations** M. L. Ali, S. Fong, Q. Fradet, U. Riedel German Aerospace Center (DLR), Institute of Low-Carbon Industrial Processes, Germany	38
14:50-15:10	**CFD-DEM investigation of agglomeration effects in iron powder reduction** J. G. Ramírez[1], Y. Tang[2,3], M. Van Sint Annaland[1,3], N. Deen[2,3], I. Roghair[1,3] [1]Chemical Process Intensification, Department of Chemical Engineering & Chemistry, Eindhoven University of Technology, Eindhoven, Netherlands [2]Power and Flow Group, Department of Mechanical Engineering, Eindhoven University of Technology, Eindhoven, Netherlands [3]Eindhoven Institute for Renewable Energy Systems (EIRES), Eindhoven University of Technology, Eindhoven, Netherlands	41

June 18th, 9:00 am – Sessions:

Session VI	**Nanoparticles, dust & powders** Chairperson: R. Kneer	Page
9:30-9:50	**Continuum model and benchmarking experiment of powder mixing in a cylindrical bladed mixer** A. M. Baecke, A. P. Ganesh Ruthraruba, U. Hampel, G. Lecrivain Helmholtz-Zentrum Dresden-Rossendorf e.V., Germany	107
9:50-10:10	**Ignition and flame propagation in mixtures of combustible dusts with hydrogen** P. Zhao, D. Gabel, U. Krause Otto von Guericke University Magdeburg, Germany	110
11:40-12:00	**Comparison of 1D and 3D models for the thermochemical conversion of carbonaceous pulverized particles** M. Kiss, T. Nanz, M. Bösenhofer TU Wien, Austria	113
12:00-12:20	**Scalable production of nanostructured materials for energy and health applications using gas phase deposition** J. R. van Ommen Delft University of Technology, Netherlands	117
12:40-13:00	**Investigation of the hetero-aggregation mechanisms of nano particles by desublimation in the supersonic flow** M. Nestriepke, M. Weirich, D. Misiulia, S. Antonyuk RPTU Kaiserslautern-Landau, Germany	120

June 18th, 15:00 pm – Sessions:

Session VII	**Heat transfer & electric heating** Chairperson: A. Bück	Page
15:00-15:20	**Simulation of methanol steam reforming in packed bed reactors – comparison of wall-heated and induction-heated configurations** M. Dal Belo Takehara, K. Umeki Luleå University of Technology, Sweden	123
15:20-15:40	**Dynamic microwave freeze-drying with in-situ neutron imaging: Insights in the drying of particle bulk** M. Hilmer, Z. Kis, M. Schulz, P. Först Technical University of Munich, Germany	126
15:40-16:00	**Modelling a lab-scale microwave dryer for thermally thick materials** A. Ujjani Narasimhaiah, A. Schmidt, L. Briest, A. Tretau, R. Wagner, E. Tsotsas, N. Vorhauer-Huget Otto von Guericke University Magdeburg, Germany	128
16:00-16:20	**Regenerative absorption and desorption between CO_2 and dolomite particles for CCS processes** A. Kropman, W. Aliyu, E. Specht, F. Beyrau Otto von Guericke University Magdeburg, Germany	131

June, 18th, 10:10 am - Postersession:

Table of contents

Simulation of hydrogen combustion in a gas-fired lime shaft kiln

S. Meschede[1*], S. Haep[1] and D. Bathen[1,2]

*E-Mail: meschede@iuta.de

[1] *Institut für Umwelt & Energie, Technik & Analytik e.V. (IUTA), Bliersheimer Straße 58-60, 47229 Duisburg, Germany*

[2] *Thermal Process Engineering, University of Duisburg-Essen, Lotharstraße 1, 47057 Duisburg, Germany*

Introduction

In the production of limestone, significant amounts of the greenhouse gas CO_2 are emitted. The identification and realization of both techno-economic and sustainable technologies to reduce the environmental impact is therefore an important goal in order to reduce the carbon footprint of the sector, in line with political guidelines and climate targets. The European Lime Association (EuLA) envisions multiple pathways to achieve this [1], including carbon capture, utilization, and storage (CCU/CCS) as well as the integration of alternative carbon-free fuels.

Hydrogen is expected to play a key role as an energy carrier and fuel in future energy systems. However, its impact on lime kiln operations remains largely unexplored. Compared to natural gas, hydrogen exhibits fundamentally different properties, affecting combustion characteristics, heat transfer, and process stability.

Experimental investigations of the impact of hydrogen combustion in lime kilns are highly challenging due to extreme process temperatures, dense particle beds, and inertial process behaviour. Additionally, pilot-scale testing is difficult to operate and cost-intensive. As a result, oven simulations offer a viable approach to gaining locally and temporally resolved insights into gas-solid interactions within the entire kiln system. However, the computational effort required to simulate full-scale lime kilns strongly depends on the complexity of the underlying physical models. Achieving a balance between computational efficiency and model accuracy is crucial for advancing hydrogen-based decarbonisation strategies in the lime industry.

Modeling and simulation procedure

To reduce computational costs in the initial simulation phase, one-eighth of the kiln was modeled, corresponding to a radius of 1 m and a bed height of approximately 10 m.

Different approaches exist for modeling the solid phase within the kiln. In this study, a Discrete Element Method (DEM) model was employed to describe the multi-disperse discrete particle movement. The bulk material moves at an approximate velocity of 2 m/h, and the system accounts for around 16,000 particles. To maintain a constant particle count and a continuously filled bed with a random packing structure, particles exiting the domain are refilled at the top section of the kiln.

For the CFD (Computational Fluid Dynamics) side, a porous media approach was adopted. Resolving the detailed flow through individual void spaces between particles would be computationally prohibitive, as it would drastically increase the simulation time, especially for the entire kiln. Instead, the Ergun equation, a widely used empirical model for gas flow in packed beds, was implemented to describe the resistance terms within the Navier-Stokes equations. The semi-empirical model uses the porosity and the sauter diameter of the packed bed, which is calculated by the DEM model.

The kiln is gas-fired, with fuel supplied through side lances that do not penetrate the bed. The combustion process was assumed to reach chemical equilibrium and was governed primarily by the mixing of fuel and oxidizer. Due to this assumption, the Eddy Dissipation Model (EDM) was chosen to describe the turbulent combustion process, as it provides a computationally efficient approach for diffusion-limited reactions.

Heat and mass transfer between gas and particles was modeled using Nusselt and Sherwood correlations. A DEM-CFD overlay scheme ensured accurate transfer of mass and energy source terms to the corresponding CFD cells [2]. Additionally, radiative heat transfer between particles was considered.

The porous carbonate particles (5–9 cm in diameter) create significant temperature, pressure, and concentration gradients across their size. To capture these effects, a particle shell model [3] was additionally implemented, resolving the calcination process. The model includes heat conduction, gas diffusion, Darcy flow, and calcination kinetics, enabling a more accurate representation of the internal gradients and the reaction dynamics within the particles.

Particle model validation

Due to scarce real kiln data, experimental validation of simulation results is challenging but essential. Single-particle calcination experiments, such as those by Cheng & Specht [4], provide valuable reference data. They calcined carbonate specimens in a 1000 °C oven, measuring core temperature and calcination degree over time.

As shown in Figure 1, calcination occurs in four phases: pre-heating, where the core temperature rises to 875 °C; reaction, where endothermic calcination proceeds isothermally; post-heating, where the temperature increases further; and finally, the equilibrium phase, where the core and gas phase reach thermal balance. The particle calcination is completed after around 3 hours.

The particle shell model closely matches these experimental results, confirming its accuracy and applicability for simulating calcination dynamics.

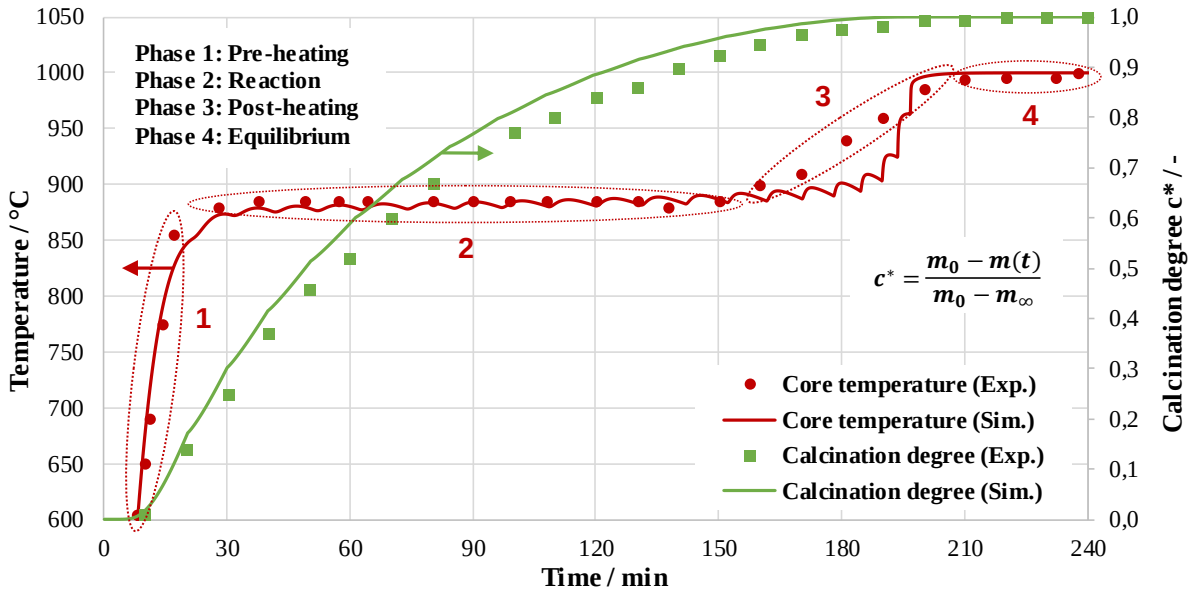

Figure 1. Calcination procedure of a calcium carbonate sample (d = 4.7 cm).

The thermophysical properties of CaO and $CaCO_3$ were carefully selected based on available literature data [5]. However, material properties can vary significantly depending on the geological origin of the raw material. Therefore, it is essential to reassess these values for specific kiln locations to ensure model accuracy.

Simulation of a lime shaft kiln

The coupled DEM-CFD simulation was performed using ANSYS Fluent to model the normal shaft kiln, which has a production capacity of around 130 t_{CaO}/d. This corresponds to a thermal input of 6 MW and a hydrogen flow rate of 2000 Nm^3/h.

Due to its high computational cost, the DEM simulation is the most demanding part of the model. However, since particle inertia is high and shape and size remain nearly constant, the gas phase has minimal influence on particle movement. Therefore, the bed movement is computed independently and only once. To ensure accurate coupling, the DEM-CFD overlay is updated every 10 seconds, assigning CFD cells to the corresponding particles. The results of the coupled approach are presented in Figure 2.

Fuel and combustion air enter the kiln at high velocity through the gas nozzles, maintaining the same thermal input and fuel-air ratio (1.3) as in the natural gas case. Due to the high bed resistance, the flame barely penetrates the particle bed.

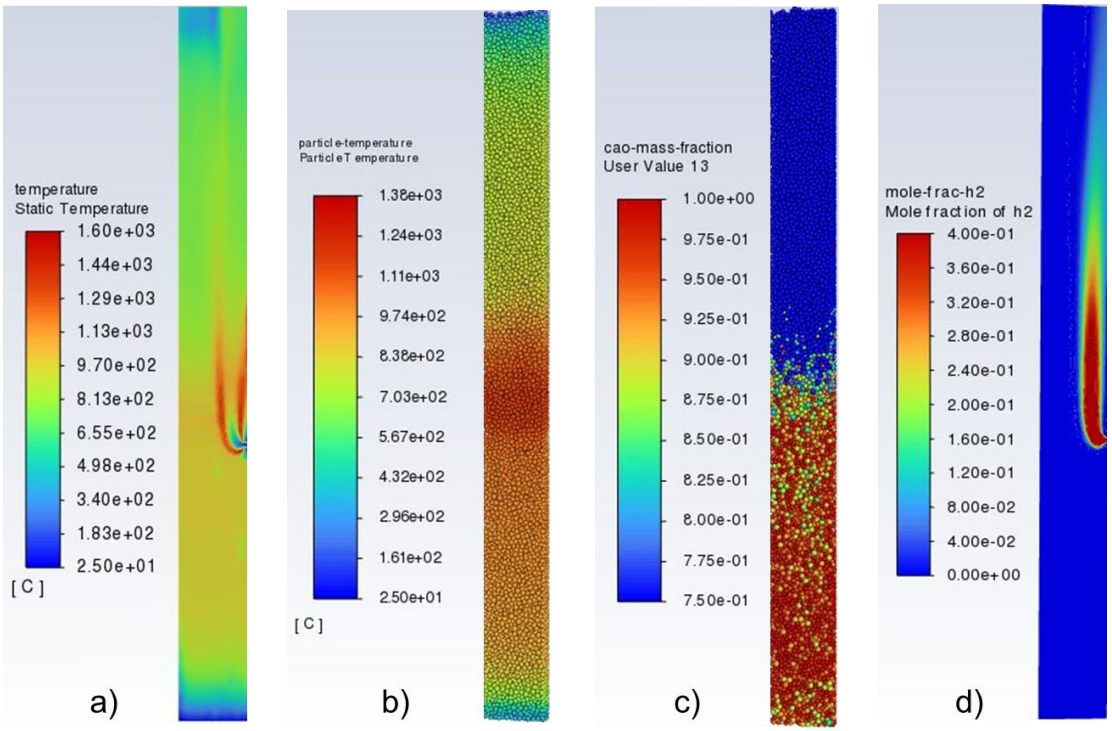

Figure 2. Coupled DEM-CFD simulation of a normal shaft kiln. Gas temperature (a), particle surface temperature (b), calcination degree (c) and hydrogen mole fraction (d)

Maximum gas temperatures reach 1600 °C near the nozzles, slightly exceeding those of natural gas firing (1500 °C). A similar trend is observed for particle surface temperatures (1380 °C vs. 1300 °C). Complete calcination is achieved for smaller particles (5–6 cm), while larger particles (8–9 cm) remain partially uncalcined due to higher thermal resistance.

The hydrogen mole fraction indicates incomplete combustion, likely caused by oxygen diffusion limitations. Adjusting the airflow and burner design could potentially resolve this issue.

Conclusion and outlook

The simulation results provide valuable insights into the impact of hydrogen combustion in lime shaft kilns, but further investigations are needed to refine the model and validate it under real operating conditions. Future research will focus on industrial-scale kilns, considering the integration of additional pure oxygen, which will become increasingly available in energy systems based on large-scale hydrogen production via electrolysis.

In this context, oxyfuel combustion will be explored to produce an off-gas with a high CO_2 concentration, facilitating downstream CCU/CCS processes. This is essential, as a significant portion of CO_2 emissions still originates from the calcination reaction itself.

References

[1] European Lime Association: *A pathway to negative CO_2 emissions by 2050: The contribution of the lime industry to a carbon-neutral Europe*, EuLA, 2025, Available: https://www.eula.eu.

[2] Krause B., Liedmann B., Wiese J., Wirtz S., Scherer V.: *Coupled three dimensional DEM–CFD simulation of a lime shaft kiln—Calcination, particle movement and gas phase flow field*, Chemical Engineering Science, 134, 834-849, 2015.

[3] Takkinen S., Saastamoinen J., Hyppänen T.: *Heat and Mass Transfer in Calcination of Limestone Particles*, AIChE Journal, 58(8), 2563–2572, 2012.

[4] Cheng C., Specht E.: *Reaction rate coefficients in decomposition of lumpy limestone of different origin*, Thermochimica Acta, 449 (1-2), 8–15, 2006.

[5] Sandaka G.: *Calcination behaviour of lumpy limestones from different origins*, Ph.D. Thesis, Univ. of Magdeburg "Otto von Guericke", 2015.

Advanced Heat Exchange and Radiation Sub-Models in Coarse-Grained CFD-DEM Simulations

M. Mitterlindner[1], M. Niemann,[2] D. Louw,[2] P. Kieckhefen,[3] C. Goniva[2], M. Salehi[1,4] and S. Radl[1*]

*E-Mail: radl@tugraz.at

[1] Institute of Process and Particle Engineering, Graz University of Technology, Inffeldgasse 13/III, 8010 Graz, Austria
[2] DCS Computing GmbH, Industriezeile 35, 4020 Linz, Austria
[3] BASF SE, Carl-Bosch-Str. 38, 67063 Ludwigshafen am Rhein, Germany
[4] Virtual Vehicle GmbH, Inffeldgasse 21a, 8010 Graz

Introduction

Coupled computational fluid dynamics and discrete element method (CFD-DEM) [1] simulations are critical for understanding complex interactions in particulate systems, including fluid flow, heat transfer, and chemical reactions. They play a critical role in industrial process optimization, although challenges remain in computational efficiency and modelling accuracy, particularly for coarse-grained simulations. This work introduces three key improvements: a heat exchange limiter to stabilize energy transfer, view factor corrections for radiative heat transfer, and mesh refinement guidelines for the P1 radiation model. Together, these enhancements allow for more accurate and efficient simulations of particle-fluid systems.

Methods

Heat Exchange Limiter for Coarse-Grained CFD-DEM Simulations

In coarse-grained simulations, particle-fluid interactions must be approximated based on assumption of individual particle temperatures. This may introduce potential errors in heat transfer calculations due to this non-existing sub-parcel resolution. To address this issue, a heat exchange limiter has been developed, which relies on an explicit-explicit coupling scheme. This limiter works by limiting the heat exchanged in case the equilibrium temperature of a defined virtual volume is reached. Also, our limiter ensures energy conservation. The limiter works as follows: first, the equilibrium temperature of the virtual control volume is calculated using Equation (1):

$$T_{eq,i} = \frac{m_p C_{p,p} T_{p,i}^n + m_f C_{p,f} T_{f,i}^n}{m_p C_{p,p} + m_f C_{p,f}} \quad (1)$$

Next, the maximum initial amount of heat that can be exchanged during a CFD time step is calculated using Equation (2):

$$Q_{ex,max} = m_p C_{p,p} \left(T_{eq,i} - T_{p,i}^n\right) \quad (2)$$

Finally, in each DEM timestep the exchanged heat is calculated and integrated. In case $Q_{ex,max}$ is reached, no more heat exchange is allowed (adiabatic limiter). Also, additional parcel heat sources (e.g., due to reaction, conduction, or radiation) may be considered in Eqn. 1 to allow heating of the surrounding fluid even though the CFD timestep is larger. This limiter is especially important when the fluid quickly relaxes to the parcel temperature, or large heat sources are present.

View Factor Improvements for Coarse-Grained Radiative Heat Exchange

In radiative heat transfer, view factors determine the amount of energy exchanged between surfaces or particles. Coarse-graining introduces significant errors in these factors because parcels represent large groups of individual particles. We have developed corrections to ensure that the radiative heat exchange rates between parcels (and between parcels and walls) in coarse-grained simulations are consistent with classical (i.e., non-coarsened) results. Specifically, approaches for view factor correction for parcel-parcel, and parcel-wall interactions have been investigated: for parcel-parcel radiative exchange, we modify the effective surface area of the parcels to account for sub-parcel energy transfer. Thereby, we match the effective conductivity of the bed. The corresponding equation is shown in Equation (3), and illustrated in **Figure 2**. Since this equation contains highly nonlinear terms, the correction should be

applied in the direction of the temperature gradient. This is important to ensure energy conservation. Parcel-wall interactions can be derived in a similar manner.

$$\frac{\dot{q}_{prim}^{rad}}{\dot{q}_{CG}^{rad}} = \frac{T_1^4 - \left(\frac{T_1 \cdot (\alpha_{CG}-1) + T_{2,CG}}{\alpha_{CG}}\right)^4}{\alpha_{CG} \cdot (T_1^4 - T_{2,CG}^4)} \tag{3}$$

Addressing P1 Model Limitations

A second possibility of radiation modeling, the P1 radiation model with coarse-grained DEM particles, is investigated. This is a continuation of the study in [2]. The model can be widely used due to its simplicity and computational efficiency. However, it requires extremely fine spatial grid resolution in regions with high absorption, i.e., where small, highly absorbing particles are located. Along this way of thoughts, our study analyzed the sensitivity of the P1 model with respect to grid resolution. We identified the necessary CFD grid resolution (i.e., Δz_{CFD}) to the mean free radiation path (l_m) as the main indicator for maintaining accurate radiation flux predictions. The mean free radiation path can be calculated using Equation (4), where S_V is the specific surface area, and θ_{ext} is the extinction coefficient:

$$l_m = \frac{1}{\beta_p} = \frac{1-\varphi_p}{S_V\, \theta_{ext}} \tag{4}$$

In order to enhance the model's reliability for large coarse graining ratios, it is necessary to employ particle smoothing after mapping particle properties to the CFD grid. We recommend a smoothing radius of approximately two times the parcel diameter for this sub-step of the algorithm.

Results

The improvements for the heat exchange limiter were tested in a simple "Pearl Chain" setup (without radiation) consisting of four parcels and four CFD cells. A temperature difference between the parcels and the fluid results in a heat exchange during the first timestep. The original case has a small timestep, in the range of the fluid's heat relaxation time (i.e., approximately $\Delta t_{CFD,orig} = 10^{-4}[s]$). For the two cases with our limiter, the timestep was set to $\Delta t_{CFD} = 10^{0}[s]$ with a DEM-CFD coupling interval of 10. As illustrated in **Figure 1c**, the application of a limiter that incorporates additional heat fluxes to the parcel (in this case, a heat source and heat conduction) enables the attainment of the same temperature as the original case within the original timestep $\Delta t_{CFD,orig}$. In contrast, the conventional limiter exhibits a delay of one CFD timestep. The implementation of the adiabatic limiter in the software CFDEM® (which utilizes Aspherix® [formerly LIGGGHTS®] and OpenFOAM®) ensures perfect energy conservation during the coupling process (i.e., energy errors below 10^{-14}). In summary, our limiter allows significantly larger timesteps (factor 10^4!) by moving constraints related to fluid's heat relaxation time scale.

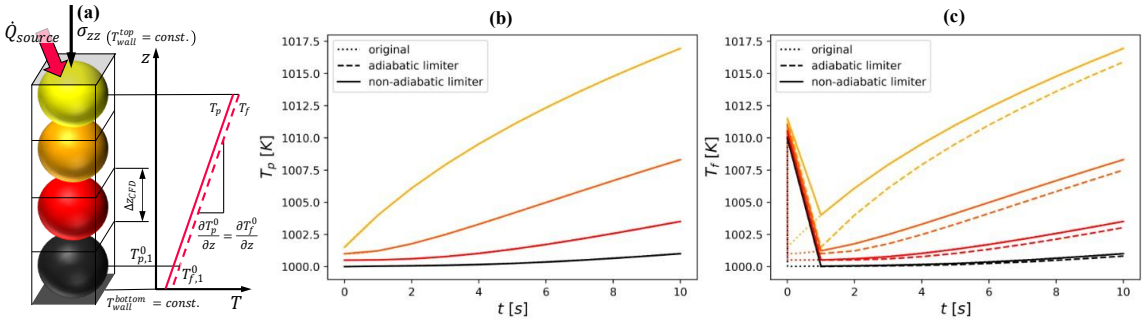

Figure 1. **(a)** Pearl chain test setup with a heat source at the top and a cold wall at the bottom. **(b)** Parcel temperatures. **(c)** Fluid temperatures original case with a CFD timestep = 10^{-4} s and the limited cases with 1 s.

To verify the correctness of our novel view factor correction, the setup from Figure 1a is employed with the exception that the top wall is fixed at a temperature and no heat source is applied. To match the effective bed conductivity with a non-coarsened simulation, the wall temperatures are fixed according to a predefined gradient (i.e., for higher CG, a higher top wall temperature is used) and the radiative heat flux is calculated. The resulting error is presented in Table 1, with its value expressed as a percentage

of the non-coarsened heat flux. Clearly, our implementation of this correction ensures a good match with a classical CFD-DEM simulation.

Table 1. Error for the heat flux for different coarse graining ratios with and without the correction.

CG	Error (uncorrected)	Error (corrected)
2	+300 %	0 %
5	+2420 %	1 %
10	+ 10110 %	2 %

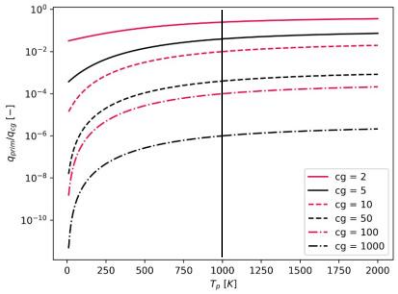

Figure 2. Parcel correction for various coarse graining ratios and the parcel temperatures. (nearby parcel temperature: 1000 [K])

Also, the P1 model performance was assessed by employing a pearl chain configuration as illustrated in **Figure 3a** in the CFDEM® software. This configuration consists of four parcels with a temperature of 300 [K] and two distinct wall temperatures (top = 1000 [K], bottom = 500 [K]). The $n_{CFD,p}$ metric is used to quantify the degree of refinement of the grid, ranging from a single cell per parcel to 100 cells per parcel. The heat flux is evaluated for the initial timestep, and results are plotted for different coarse-graining ratios in **Figure 3b**. The figure demonstrates that when the Eulerian grid is sufficiently fine, it is possible to obtain a fair match with analytical results: for a grid resolution ($\Delta z_{CFD}/l_m$) ranging up to 5, the most favorable outcomes are achieved. Thus, the P1 predictions are independent of the coarse-graining ratio, and the only significant factors are the grid resolution and the smoothing algorithm.

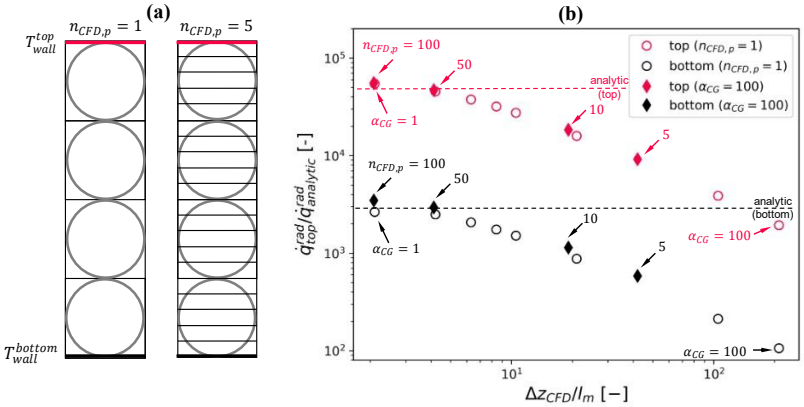

Figure 3. **(a)** Pearl chain test setup with finer grid resolution. **(b)** effect on radiative heat flux with different resolutions (open symbols: α_{CG} variation, filled symbols: $n_{CFD,p}$ variation).

Conclusion and outlook

Our present study significantly advances the applicability of CFD-DEM simulations by improving both (i) affordability and (ii) stability of these simulations. The introduction of a heat exchange limiter, corrections to radiative heat transfer models, and guidelines for efficient grid refinement increase the accuracy and reliability of coarse-grained simulations. These improvements pave the way for more accurate modeling of coarse-grained particulate systems. Future research may incorporate subscale models into the P1 radiation model to relax spatial grid resolution requirements, allowing even wider applications of the method.

References

[1] Kloss, C., Goniva, C., Hager, A., Amberger, S., & Pirker, S. (2012). *Models, algorithms and validation for opensource DEM and CFD–DEM*. Progress in Computational Fluid Dynamics, an International Journal, 12(2-3), 140-152.

[2] J. Mačak, C. Goniva, S. Radl, *Predictions of the P1 approximation for radiative heat transfer in heterogeneous granular media*, Particuology 82 (2023) 25–47. https://doi.org/10.1016/j.partic.2023.01.003.

Consistent Euler-Lagrange point-particle modeling using the volume-filtering framework

M. Hausmann[1*] and B. van Wachem[1]

[*]E-Mail: max.hausmann@ovgu.de

[1]Chair of Mechanical Process Engineering, University of Magdeburg, Universitätsplatz 2, 39106 Magdeburg, Germany

Background

When simulating particle-laden flows involving millions of particles, the Euler-Lagrange (EL) point-particle method is typically the best trade-off between computational cost and accuracy. In the EL point-particle approach, the particles are treated as points, and the unresolved fluid stresses acting on the particle surface are accounted for by (semi)empirical force correlations. In very dilute flows, i.e., in flows with a very small particle volume fraction, the influence that the particles have on the flow is weak, and the EL point-particle approach can often accurately predict the particle motion. As the particle volume fraction increases, however, the flow modification by the particles can become significant and source terms in the governing flow equations are required to account for the influence of the particles. The modeling of these source terms is typically ad hoc and not built upon a solid physical foundation, which can violate the conservation of kinetic energy of the particles and the fluid [1].

The so-called volume-filtering framework can provide a physical foundation if applied consistently. Volume-filtering a flow quantity, Φ, is defined as [3]

$$\epsilon_\mathrm{f}(\boldsymbol{x})\overline{\Phi}(\boldsymbol{x}) = \int_{\Omega_\mathrm{f}} \Phi(\boldsymbol{y}) g(|\boldsymbol{x}-\boldsymbol{y}|)\mathrm{d}V_y, \tag{1}$$

where Ω_f is the region occupied by the fluid, g is a uniform and symmetric filter kernel that we assume to be a Gaussian with a standard deviation σ, and ϵ_f is the fluid volume fraction, which is defined as

$$\epsilon_\mathrm{f}(\boldsymbol{x}) = \int_{\Omega_\mathrm{f}} g(|\boldsymbol{x}-\boldsymbol{y}|)\mathrm{d}V_y. \tag{2}$$

For a flow with constant fluid density, ρ_f, and constant dynamic viscosity, μ_f, the volume-filtered Navier-Stokes equations (NSE) can be derived to be [2]

$$\frac{\partial \epsilon_\mathrm{f}}{\partial t} + \frac{\partial u_{\epsilon,i}}{\partial x_i} = 0, \tag{3}$$

$$\rho_\mathrm{f}\frac{\partial u_{\epsilon,i}}{\partial t} + \rho_\mathrm{f}\frac{\partial}{\partial x_j}(u_{\epsilon,i}u_{\epsilon,j}) = -\frac{\partial p_\epsilon}{\partial x_i} + \mu_\mathrm{f}\frac{\partial^2 u_{\epsilon,i}}{\partial x_j \partial x_j} - s_i + \mu_\mathrm{f}\mathcal{E}_i - \rho_\mathrm{f}\frac{\partial}{\partial x_j}\tau_{\mathrm{sfs},ij}, \tag{4}$$

where $u_{\epsilon,i} = \epsilon_\mathrm{f}\bar{u}_i$ is the volume-filtered fluid velocity, and $p_\epsilon = \epsilon_\mathrm{f}\bar{p}$ is the volume-filtered pressure. Volume-filtering the NSE leads to three terms that depend on quantities that are not filtered, the particle momentum source, s_i, which arises from volume-filtering the pressure and viscous stresses across the particle surfaces, the viscous closure, $\mathcal{E}_i$, which arises from switching volume-filtering and spatial derivative in the viscous term, and the subfilter stress tensor, $\tau_{\mathrm{sfs},ij}$, which originates from volume-filtering the non-linear advective term. Little is known about these closure terms, and often these closures are neglected without much evidence. In the present contribution, our recent findings about the closures are presented and a consistent EL point-particle framework for dense particle-laden flows is derived.

Closures in the volume-filtering framework

The particle momentum source s_i contains the unfiltered pressure and viscous stresses at each of the particle surfaces. Since unfiltered quantities are not known in the volume-filtering framework, s_i is a

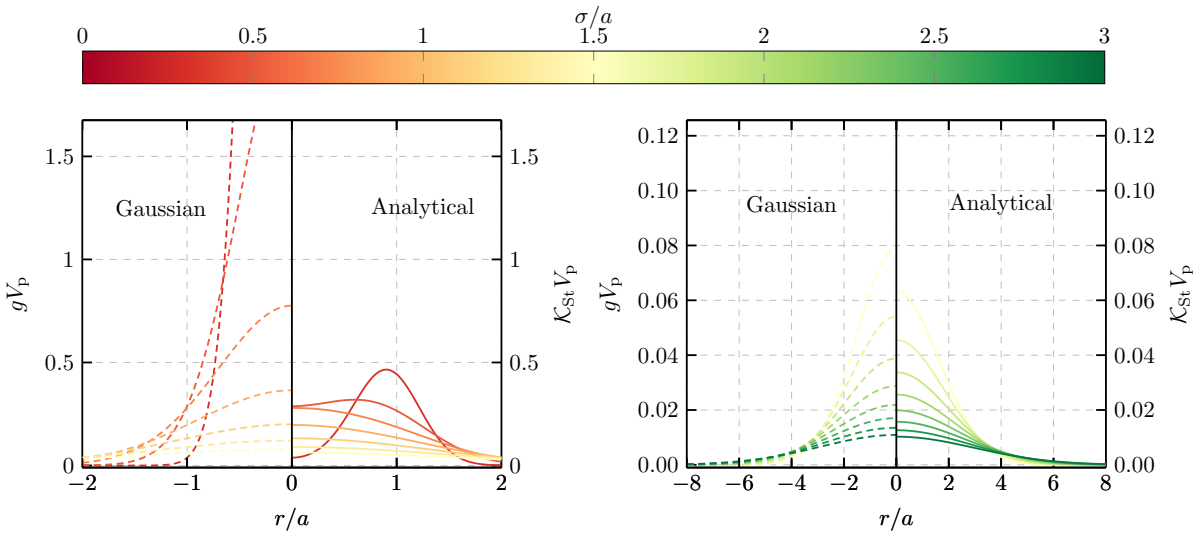

Figure 1: Normalized Gaussian and analytical regularization kernel of the particle momentum source, s_i, for different filter widths, σ. The left side shows filter widths up to $\sigma/a = 1.5$ and the right side shows filter widths in the range $1.5 \leq \sigma/a \leq 3$.

closure term and requires modeling. The particle momentum source associated to the particle with the index q is typically modeled as (see, e.g., Anderson & Jackson [3] and Capecelatro & Desjardins [4])

$$s_{q,i} = g(|\boldsymbol{x} - \boldsymbol{x}_{\mathrm{p},q}|)F_{\mathrm{h},q,i}, \tag{5}$$

where $\boldsymbol{x}_{\mathrm{p},q}$ is the position and $F_{\mathrm{h},q,i}$ the hydrodynamical force acting on the particle with the index q. It can be shown that equation (5) is correct for $\sigma/a \to \infty$, where a is the radius of the particle. However, it is not clear how large the ratio σ/a has to be such that equation (5) is an accurate approximation. In the case of a single particle in uniform Stokes flow, we derive the particle momentum source to be exactly

$$s_{q,i} = \mathcal{K}_{\mathrm{St}}(|\boldsymbol{x} - \boldsymbol{x}_{\mathrm{p},q}|)F_{\mathrm{h},q,i}, \tag{6}$$

where $\mathcal{K}_{\mathrm{St}}$ is the analytical regularization kernel valid in the Stokes regime. In figure 1, the commonly used Gaussian regularization kernel g is compared to $\mathcal{K}_{\mathrm{St}}$ normalized with the particle volume, V_{p}, for various σ/a. It is observed that for $\sigma/a \approx 2$ or larger, $g \approx \mathcal{K}_{\mathrm{St}}$, which means that in Stokes flow equation (5) is a good approximation for $\sigma > 2a$. Based on explicitly volume-filtered particle resolved direct numerical simulations around isolated particles, we observe that $\sigma > 2a$ is also required for larger Reynolds numbers for equation (5) to be valid.

The viscous closure $\mathcal{E}_i$ is often neglected due to the lack of appropriate models. We show that, in contrast to what is commonly believed, an analytical expression can be derived for the viscous closure, which is exact for all regimes and does not involve modeling. Therefore, the viscous closure is, strictly speaking, not a closure. We show that the expression

$$\mathcal{E}_i = \sum_q v_{q,i} \frac{\partial^2 \epsilon_{\mathrm{p},q}}{\partial x_j \partial x_j}, \tag{7}$$

holds exactly for spherical particles or not rotating non-spherical particles, where $\epsilon_{\mathrm{p},q}$ is the particle volume fraction of the particle with the index q and $v_{q,i}$ is the velocity of the particle with the index q. In order to satisfy Galilean invariance of the volume-filtered NSE, the viscous closure has to be included. The third closure, the subfilter stress tensor, is shown to have a significant contribution in the volume-filtered momentum equation, even in the absence of turbulence. Explicitly volume-filtered flow fields obtained from particle resolved simulations around an isolated sphere show that the subfilter stress closure has a magnitude of the same order as the particle momentum source for a particle Reynolds number equal to $\mathrm{Re_p} = 100$. This suggests that the subfilter stress tensor requires modeling, even in the absence of turbulence. We show that the non-linear gradient model, a subgrid-scale model known from single-phase

flow large eddy simulations, approximates the subfilter stress tensor well for relatively small filter widths. An additional contribution to the subfilter stress tensor is applied to exactly satisfy Galilean invariance.

Conclusions for Euler-Lagrange point-particle simulations

With the findings of the present study, conclusions can be drawn on how to consistently perform EL point-particle simulations of particle-laden flows. (i) For the uniform flow over spherical particles at low to moderate $\mathrm{Re_p}$, as they are often encountered in EL point particle simulations, the viscous closure and the subfilter stress closure can have a significant contribution to the momentum equation and should be included. Although the viscous closure is more important at small $\mathrm{Re_p}$ and the subfilter stress closure is more dominant at large $\mathrm{Re_p}$, there is not enough evidence that either of the closures can be neglected in one of the regimes. (ii) The filter width (standard deviation of the Gaussian filter) should be at least as big as the particle diameter because then, the particle momentum source can be approximated well with a Gaussian. At smaller filter widths, the shape of the particle momentum source is more complicated and generally not known. (iii) The filter width must be larger than the size of the fluid mesh cells to ensure that the discretization errors are small. A large filter width leads to a smoothly varying flow field that can be resolved with a relatively coarse fluid mesh.

It should be noted that the particle source in cell method (see Crowe *et al.* [5]) does not comply with the aforementioned recommendations because the momentum source is applied in the fluid mesh cell in which the particle lies, which means that the filter width is much smaller than the mesh cell size. This can cause a large discretization error because the flow structures are too small to be resolved by the fluid mesh.

References

[1] Xu Y. & Subramaniam S.: *Consistent modeling of interphase turbulent kinetic energy transfer in particle-laden turbulent flows*, Physics of Fluids, 19 (8), 085101, 2007.

[2] Hausmann M., Chéron V., Evrard F., van Wachem B.: *Study and derivation of closures in the volume-filtered framework for particle-laden flows*, Journal of Fluid Mechanics, 996, A41, 2024.

[3] Anderson T.B. & Jackson R.: *Fluid mechanical description of fluidized beds*, I and EC Fundamentals, 6 (4), 524-539, 1967.

[4] Capecelatro J. & Desjardins O.: *An Euler–Lagrange strategy for simulating particle-laden flows*, Journal of Computational Physics, 238, 1-31, 2013.

[5] Crowe C.T., Sharma M.P., Stock D.E.: *The particle-source-in cell (PSI-CELL) model for gas-droplet flows*, Journal of Fluids Engineering, 99 (2), 325-333, 1977.

Experimental study on sludge drying characteristics and optimized design of dryer base on CFD-DEM simulation

Gong Li[1,2], Hao Zhang[3], Zongyan Zhou[4], Ruiping Zou[1*], and Aibing Yu[1,2]

*E-Mail: ruiping.zou@monash.edu

[1] *ARC Research Hub for Smart Process Design and Control, Department of Chemical and Biological Engineering, Monash University, Clayton VIC 3800, Australia*
[2] *School of Energy and Environment, Southeast University, 210096 Nanjing, China*
[3] *School of Metallurgy, Northeastern University, 110819 Shenyang, China*
[4] *Jiangxi University of Science and Technology, 330013 Nanchang, China*

With the rapid growth of urbanization and industrialization worldwide, sludge production has increased significantly. Sludge drying plays a crucial role in reducing sludge volume while contributing to its stabilization, safe disposal, and resource recovery. Although extensive research has been conducted on the fundamental theory of particle material drying, there remains a lack of systematic understanding of the drying characteristics of physically complex sludge. In industrial applications, limited knowledge of material and flow field development within drying equipment presents significant challenges for dryer operation and structural design. To address this issue, a combination of physical experiments and numerical simulations has been employed to conduct a systematic and in-depth study on sludge drying characteristics and dryer optimization [1,2]. This presentation reports the major findings.

A small-scale material convection drying experimental system has been developed to monitor the moisture content and temperature of sludge particles, as well as the pressure, temperature, and humidity of the upstream and downstream flow fields, as shown in Figure 1. The influence of key drying parameters, including air velocity, temperature, humidity, particle size, and sludge pile thickness, on the sludge drying process has been systematically analyzed. Based on this, five typical drying kinetic models, as shown in Table 1, have been evaluated. The analysis indicates that the Page kinetic model is the most suitable for describing the sludge drying process.

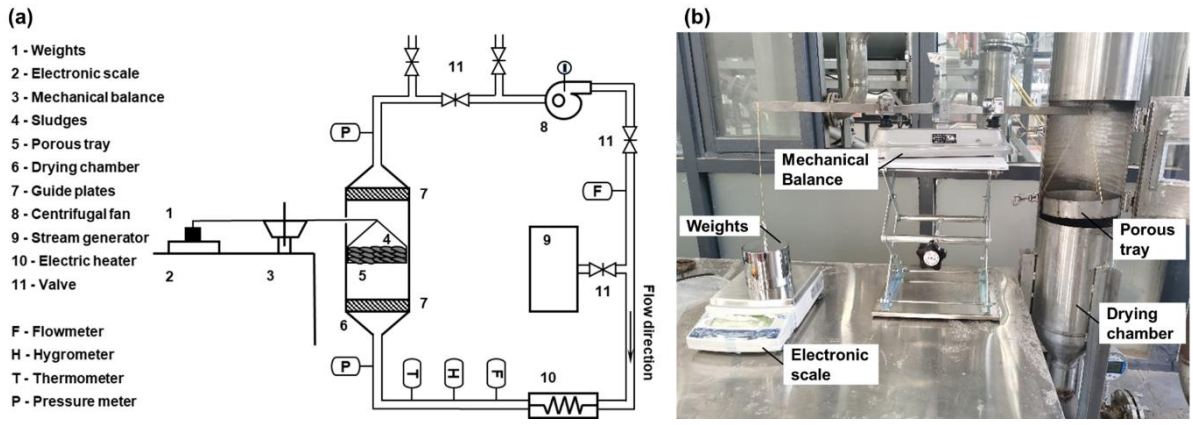

Figure 1. Small-scale material convection drying experimental system: (a) Schematic diagram, (b) Drying chamber and real-time weighing device.

Table 1. Typical drying kinetic models.

Model	Equations
Lewis [3]	MR=exp(-kt)
Page [4]	MR=exp(-kt^n)
Henderson and Pabis [5]	MR=a exp(-kt)
Parabolic [6]	MR=a+bt+ct^2
Logarithmic [7]	MR=a exp(-kt)+b

A CFD-DEM model has been established to accurately describe the sludge drying process. This model captures the flow, heat transfer, and mass transfer in a gas-solid system, where particle-scale evaporation is represented through a chemical reaction analogy. The model's ability to predict both the continuous-phase flow field and the sludge particle drying process has been validated through quantitative comparison with experimental data, as shown in Figure 2. Additionally, the approach used to enhance the applicability of the evaporation model can be extended to other porous materials similar to sludge.

The CFD-DEM model is further applied to numerically simulate the convective drying process in a sludge particle bed, with a particular focus on different sludge particle size distributions (PSD). The simulation considers five distinct cylindrical particle sizes with varying length-to-diameter (L/D) ratios, as well as four PSD types: Mono-type, Binary-type, Mean-type, and Gaussian-type. The study systematically reveals the effects of particle size parameters on reactor pressure drop, heat utilization, and moisture removal. Furthermore, a drying kinetics model is established to correlate particle size distribution with key factors such as L/D type number, average L/D, and dispersion.

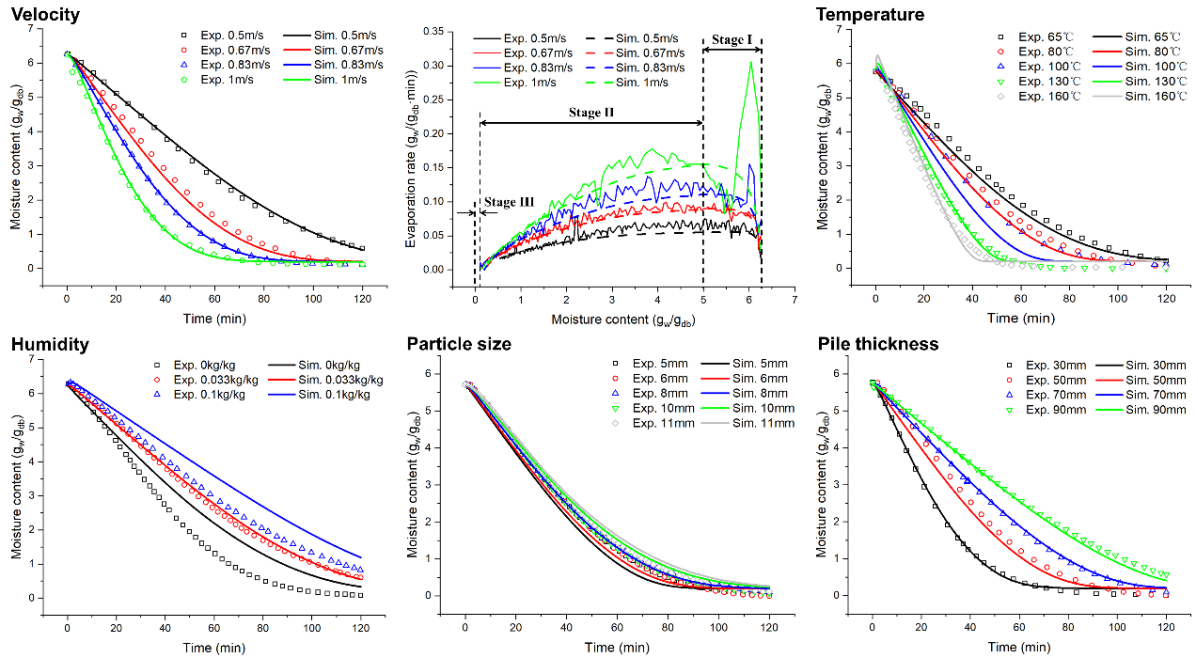

Figure 2. Simulation and experimental results of key parameters affecting sludge drying process.

A process simulation for an industrial-scale belt dryer has been developed, as shown in Figure 3, which can accurately predict the dynamic behavior of multi-layer sludge and flow field development within the dryer. Numerical simulations of belt dryer process parameters have been conducted to analyze the impact of sludge residence time on each layer, revealing its effects on the internal flow field and drying efficiency. Through this study, optimal process conditions and flexibility recommendations have been identified. In actual dryer operation, optimizing process parameters can achieve a maximum moisture reduction of 46%.

Additionally, numerical simulations have been performed to examine the belt dryer's equipment structure and air supply configuration. The drying environment and outcomes for each sludge layer under traditional air supply methods (Top-to-Bottom and Bottom-to-Top) have been analyzed. A novel side-assisted air supply method is proposed, and the relationships between optimal flow rate, total air volume, deflection angle, and side-air temperature have been thoroughly investigated. By optimizing both the equipment structure and air supply system in the dryer's design and operation, moisture content can be further reduced by up to 84%, while heat consumption can be lowered by 17%.

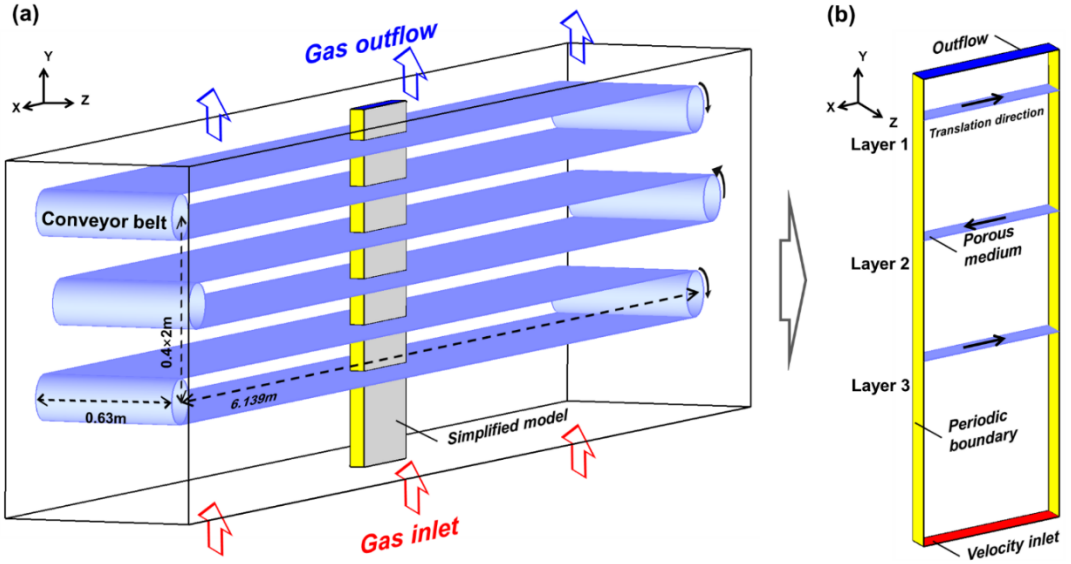

Figure 3. Belt dryer: (a) Schematic diagram, (b) Simplified model and boundary condition setting.

References

[1] Li, G., Zhang, H., Ye, X., Su, Y., Yu, A., Tan, Y.: *Numerical investigation on thermal drying process of sludges based on CFD-DEM*, Industrial & Engineering Chemistry Research, 62(42), 16990-17007, 2023.

[2] Li, G., Zhang, H., Ye, X., Su, Y., Yu, A., Wang, Y., Zhou, Z.: *Determination of optimal air supply form on sludge convective drying process: A CFD-DEM study*, Powder Technology, 444, 120052, 2024.

[3] Bruce, D.M.: *Exposed-layer barley drying: Three models fitted to new data up to 150°C*, Journal of Agricultural Engineering Research, 32(4), 337-348, 1985.

[4] Page, G.E.: *Factors influencing the maximum rates of air drying shelled corn in thin layers*, Ph.D. Thesis, Purdue University, 1949.

[5] Henderson, S.M., Pabis, S.: *Grain drying theory. 1. Temperature effect on drying coefficient*, 1961.

[6] Bi, J., Yang, A., Liu, X., Wu, X., Chen, Q., Wang, Q., Lv, J., Wang, X.: *Effects of pretreatments on explosion puffing drying kinetics of apple chips*, LWT-Food Science and Technology, 60(2), 1136-1142, 2015.

[7] Toğrul, İ.T., Pehlivan, D.: *Mathematical modelling of solar drying of apricots in thin layers*, Journal of food Engineering, 55(3), 209-216, 2002.

Locally resolved DEM/CFD simulations of a generic oxy-fuel kiln for lime production

M. Brömmer[1*], E. Illana[1] and V. Scherer[1]

*E-Mail: broemmer@leat.rub.de

[1] *Institute of Energy Plant Technology, Ruhr-University Bochum, Universitätsstraße 150, 44780 Bochum, Germany*

Introduction

Calcination of limestone is an energy-intensive thermo-chemical process. For an efficient production, shaft kilns used in industry are designed to optimize the temperature-time history of particles along their tracks through the kiln. The energy is typically provided by the combustion of a fuel-air mixture injected through lances into the moving particle bed with methane being the standard fuel. The design of those lances, their vertical position and arrangement within the shaft primarily determines the achievable calcination degree and product quality.

Due to the gas-phase combustion and even more so, due to the conversion of the limestone, CO_2 is generated during the process. To reduce the greenhouse gas CO_2 emissions, one possibility is the use of the oxy-fuel technology, where the oxidizer air is replaced by a mixture of oxygen and recycled CO_2. By the recirculation of the exhaust gas, a high concentration of CO_2 at the shaft kiln outlet is reached allowing for further processing through carbon capture and storage/usage technologies. But the change from a conventional air-fired reactor to an oxy-fuel mode comes with several challenges due to modified process conditions for the particles as temperature and CO_2 concentration differ strongly.

These complicating factors and the unfeasibility of experimental studies in industrial devices make high fidelity simulations a necessary tool to investigate the processes inside the reactor. The proposed contribution addresses the three-dimensional thermo-chemical simulation of the mutually reacting gas- and solid-flow in lime shaft kilns employing the combination of the Discrete Element Method with Computational Fluid Dynamics (DEM/CFD). The Eulerian description of the fluid flow (considering a porosity to mimic the solid phase) gives a reasonable approximation for the overall gas-phase conversion and subsequent particle reactions. This approach is often called unresolved DEM/CFD as details of the particle geometry are not known to the CFD solver. However, to increase the accuracy of intra-particle processes in thermally thick particles a more detailed representation of the local heat and mass transfer is desired, i.e. the representation of the particles as a porous medium on the CFD side is no longer adequate. This is especially important at the lance tips (gas inlets) and calls for a sufficient spatial resolution of the void spaces between the particles and the corresponding flow paths. Therefore, in such regions a resolved approach, the Blocked-Off (BO) method, a simple Immersed Boundary Method (IBM), is employed. Resolving the voids close to the lances enables more sophisticated combustion modelling compared to the unresolved case. Consequently, using more detailed modelling close to the important gas inlet regions aims for an improved description of the complete limestone conversion process.

Simulations are performed for a down-scaled generic single-shaft kiln, previously analysed with the non-resolved porous media approach by Bluhm-Drenhaus et al. for conventional firing [1] and by Illana et al. [2] in oxy-fuel mode. In contrast to previous simulations that simplified fuel injection using source terms, this study investigates a case incorporating real lance geometries. This approach results in more realistic particle tracks, influencing residence times and reaction progress of individual particles. In addition to simulations with the conventional porosity approach, locally resolved simulations are conducted comparing the degrees of calcination, as well as the gas phase fields. This study assesses the suitability of the locally resolved approach to be employed in large-scale shaft simulations.

Case description and Methods

A sketch of the cylindrical single-shaft lime kiln and an illustration of the principal features is given in **Figure 1**. Particles are fed into the reactor at the top and are moving downward during the process due

to gravity. At the bottom outlet, the end of the cone, particles exit the reactor. The discharge rate is controlled such that the mean particle residence time is 8h. A fuel-mixture is injected through four symmetrical lances, at approximately half of the reactor height. The exhaust gas leaves the reactor at the top, where particles are inserted. While particles are moving downward through the shaft, they are at first pre-heated by the exhaust gas until reaching the even hotter reaction zone where calcination takes place. At the bottom, cooling air is introduced to lower the particle temperature before they are discharged. The cooling air is extracted upstream by an annular ring at the kiln's side wall.

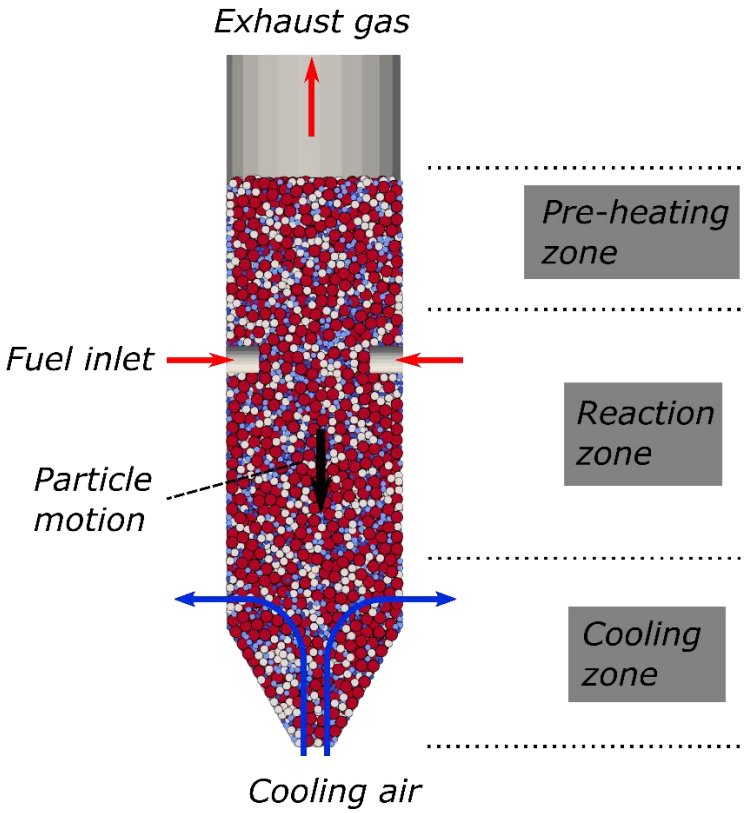

Figure 1. Down-scaled shaft kiln process sketch.

For the simulation of the particles coupled with gas flow including reactions in the solid and fluid phase, the DEM/CFD approach is used. Simulations are conducted using the Bulk-Reaction DEM/CFD framework which incorporates OpenFOAM v2012.
In the initial stage, utilizing the Discrete Element Method (DEM), particle tracks through the shaft are calculated. The positions and information about neighbouring contacts are stored and used in subsequent simulations.
The main stage consists of the coupled simulation of solid and gas. In the unresolved regions, particles are represented as porous media. In case of the locally resolved simulation, in the area close to the lances, a high mesh resolution in the CFD domain is established, enabling the use of the Blocked-Off method to resolve the fluid flow in the voids between individual particles. The Blocked-Off method is a simplified version of Immersed Boundary Methods where the particle geometry is resolved by applying source terms to the flow field such that no excessive re-meshing needs to take place. The transition between the resolved and unresolved particles needs special attention and is currently accomplished by an averaging technique. The combustion process is modelled with Flamelet Generated Manifolds (FGM) to consider detailed chemistry effects while laminar conditions are assumed. On the particle side, a radial calcination model for spherical particles is employed. Contact as well as radiative heat exchange among particles are considered.
The down-scaled shaft has dimensions of 2.5 m x 0.64 m x 0.64 m. Four symmetrical burner lances with an outer diameter $D_o = 10$ mm and an inner diameter of $D_i = 4\,mm$ are integrated into the DEM and CFD domain.

A polydisperse packing is generated, where particles are approximated as spheres. Four different particle diameters ranging from 17 mm to 45 mm are chosen. A cyclic condition at the particle outlet is set such that particles leaving the domain are reintroduced at the top of the shaft and the number of particles is constant over the whole process.

Results

Initial results of the locally resolved simulations are depicted in **Figure 2**. On the left, the locally resolved area is illustrated in red resolving the first few layers of particles in the direct vicinity of the fuel inlet. Cells occupied by resolved particles are omitted from the visualization. In blue, the unresolved area is shown, where the porosity approach is in use. Additionally, the reaction source term indicating the flame position in the bed is shown (**Figure 2**, right**)**. The premixed mixture reacts directly after being introduced into the reactor and is affected by the blockage of particles at the inlet. This influences the reaction progress and product quality of particles directly in the vicinity of lances, which will be investigated in this study.

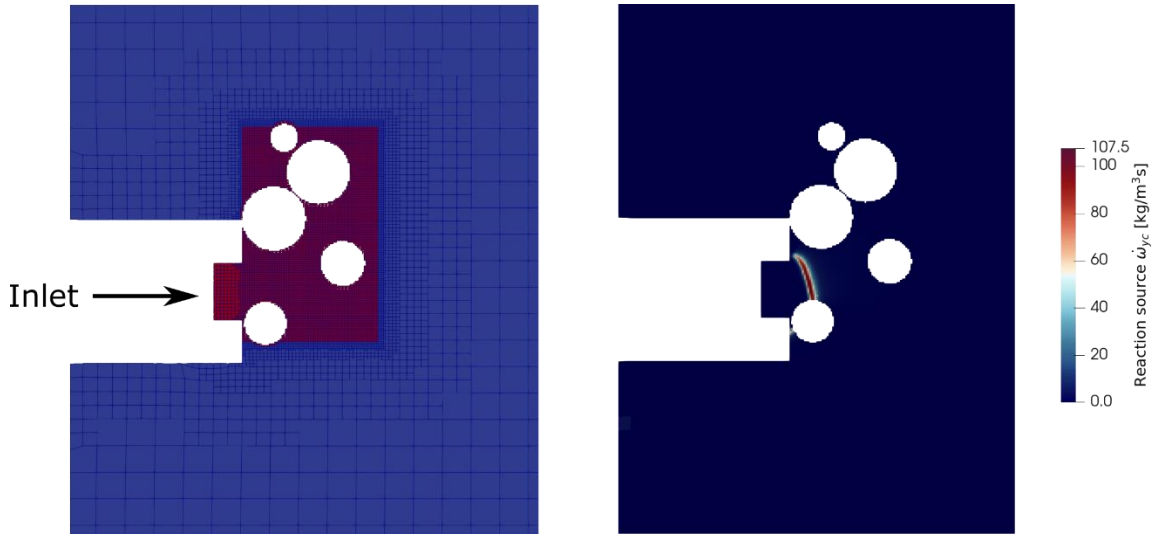

Figure 2. (left) CFD grid at one lance with mesh refinement in resolved particle zone in red and unresolved in blue. (right) Reaction source term indicating the position of flame.

References

[1] T. Bluhm-Drenhaus, E. Simsek, S. Wirtz, and V. Scherer, *A coupled fluid dynamic-discrete element simulation of heat and mass transfer in a lime shaft kiln*, Chemical Engineering Science, 65, 9, 2821–2834, 2010.

[2] E. Illana, H. Merten, S. Wirtz, V. Scherer, *DEM/CFD simulations of a generic oxy-fuel kiln for lime production*, Thermal Science and Engineering Progress, 45, 102076, 2023.

Acknowledgement

This work was funded by the Deutsche Forschungsgemeinschaft (DFG, German Research Foundation) – Project-ID 422037413 - TRR 287.

Mean flow properties in a packed bed with varying geometry

W. Sadowski[1*], H. Demir[1], and F. di Mare[1]

[*]E-Mail: wojciech.sadowski@ruhr-uni-bochum.de

[1]*Lehrstuhl für Thermische Turbomaschinen und Flugtriebwerke, Ruhr-Universität Bochum, Bochum, Germany*

Introduction

Packed-bed reactors typically contain an unordered assembly of particles which are passed by a gas. The random nature of the particle arrangement also results in irregular sizes and shapes of the interstices (voids created "between" particles) which force the flowing gas into tortuous recirculating paths, bolstering mixing of mass and momentum [1]. At the same time, these complex flow patterns influence the resistance encountered by the passing gas, typically expressed macroscopically as a pressure drop over the packing length, or as the *friction factor* in a non-dimensional way. For creeping flows, pressure drop varies linearly with Re_p, i.e., the Reynolds number defined using mean particle diameter, however, as soon as the flow enters inertial regime, the relationship between the pressure drop and Re_p becomes non-linear [2].

Although the pressure drop and other macroscopic properties of the packed bed are of high interest while designing such systems, their values and relationships with the mean flow properties or details of interstitial geometry are hard to predict. For example, the models available in the literature are often constructed under the assumption of sphericity of particles [3]. For non-spherical packing and other porous structures, there are models which try to incorporate analytically the influence of geometry [4], however, to our best knowledge the relationship between geometry of the interstitial space, flow tortuosity and the friction factor remains largely unexplored.

The most accurate way to investigate both micro- and macroscopic flow properties in packed-bed reactors is the use of particle-resolved direct numerical simulation (PRDNS) [1]. Although such simulations are costly and limited to laboratory scale configurations, they allow for the inspection of microscopic flow features without introducing any modelling error and minimizing numerical dissipation. PRDNS are especially effective when paired with the experimental measurements [5,6]. Even if measured data is limited only to a small region of the packing it allows for detailed validation of the simulation approach.

The goal of the current work is to study a model packed bed with prismatic solid elements, under different flow conditions and arrangements of interstitial space (described in detail in the following section), and formulate a model allowing for prediction of the pressure drop under different geometries.

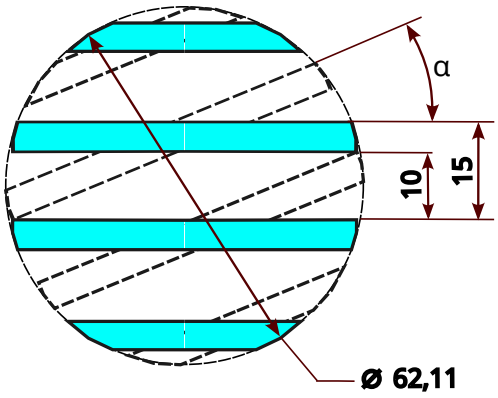

Figure 1: Schematic overview of the simulated domain: top view of the base module, showing the circle enclosing the 12-gon defining the outer geometry of the slits. The streamwise direction is oriented perpendicular to the surface of the paper.

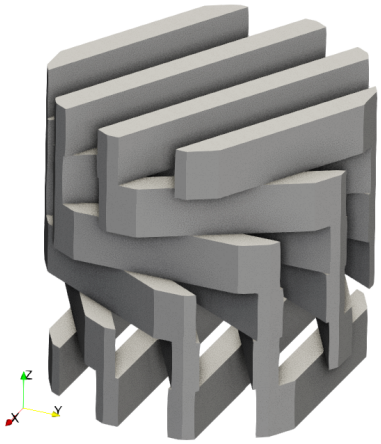

Figure 2: Periodic geometry used for the simulation with $\alpha = 30°$, consisting of six layers.

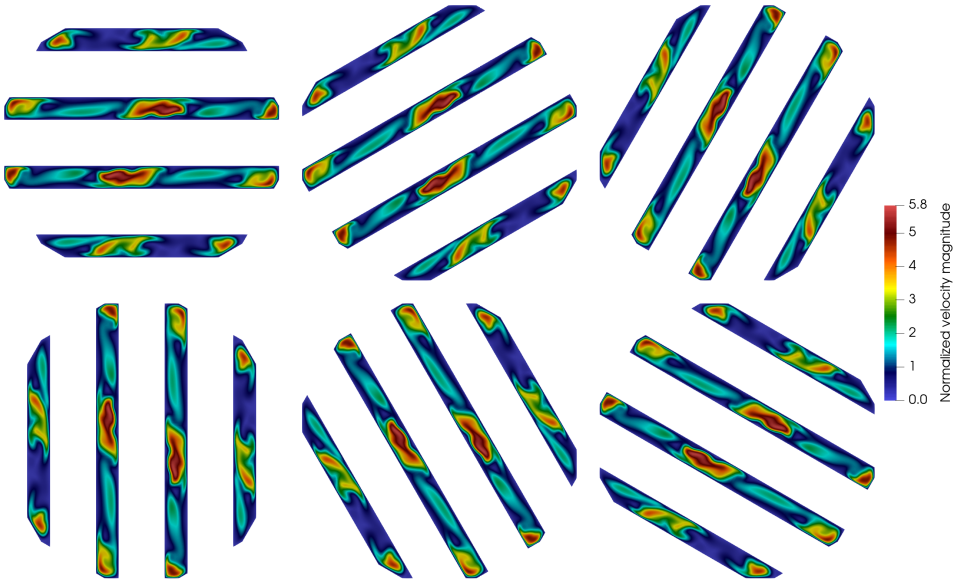

Figure 3: Velocity field at the middle plane of each layer for $\alpha = 30°$ at $\mathrm{Re}_p = 100$.

Furthermore, the analysis of microscopic flow features will help our project partners conducting experimental investigations of the same geometry to identify operating conditions which should be realized experimentally.

Reference configuration no. 2

All the studied geometries follow a similar design, closely resembling the modular packed bed studied experimentally in subproject A1 of the SFB287. The packed bed is assembled from disk-shaped elements, each 10 mm thick, with slits (arranged as in Fig. 1) forming the interstitial space. Each slit is 5 mm wide and the spacing between the slits (the bar width B) is equal to 10 mm. The outer sides of the slits are defined by a 12-gon inscribed into a circle with a diameter of 62.12 mm. The area of the circle is used to define the surface area of the packing A, and theoretical porosity of $\phi = 0.322$. Modules can be stacked on top of each other; successive layers can be rotated by α, allowing for different geometries of the interstitial space.

To characterize the flow conditions within the packing, Re_p, a Reynolds number based on the bar width, is introduced

$$\mathrm{Re}_p = \frac{\langle w \rangle B}{\nu} \tag{1}$$

where, $\langle w \rangle$ is the void-space (intrinsic) average of streamwise velocity and ν is the kinematic viscosity. The intrinsic velocity is related to superficial average $\langle w \rangle_s = Q/A$ (Q is the volumetric flow rate) using the Dupuit's formula $\phi \langle w \rangle = \langle w \rangle_s$.

Mathematical and numerical model

In current study, focus is placed on the characterization of interstitial flow w.r.t. different flow conditions and rotation angles. Hence, each of the simulations considers fully developed incompressible flow in a periodic geometry constructed from an appropriate amount of layers (see Fig. 2 for the example of the geometry with $\alpha = 30°$). The flow is driven by pressure gradient adjusted so that the value of bulk velocity results in a chosen Reynolds number. The computations are performed using Finite Volume Method based solver *OpenFOAM-v12*. The convective and diffusive terms are discretized using 2nd-order central differencing. Each slit is meshed with hexahedral-dominant mesh, constructed by extruding a surface mesh along the streamwise direction. The layer boundaries are connected using the Non-Conformal Coupling (NCC) interfaces, which allow for conservative solutions across non-matching boundary discriminations.

Results

As of now, the configuration with $\alpha = 30°$ at $\mathrm{Re}_p = 100$ and 150 was realized. For both Reynolds numbers the solution is stationary and dominated by many interacting recirculation regions. For the first case, the magnitude of the velocity field normalized by $\langle w \rangle$ for of each layer is visible in Fig. 3. The flow

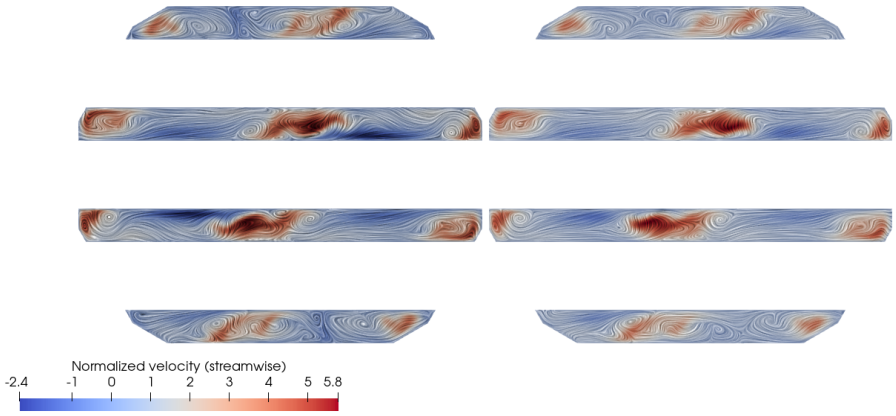

Figure 4: Velocity field and streamlines visualized with Line Integral Convolution method, at the middle of 1st layer at $\mathrm{Re}_p = 150$ (left) and $\mathrm{Re}_p = 100$ (right).

field is repeatable across the layers and exhibits an antisymmetry w.r.t. z coordinate axis (the rotation axis of the modules). The positions of small openings created between the consecutive layers determine the regions of high velocity fluid, which then travels along the slits.

Figure 4 compares the velocity fields and streamlines generated with Line Integral Convolution method between both Reynolds numbers. Although the velocity fields remain qualitatively similar, the higher Re_p results in a much higher vortical content in the flow field. Inspecting the fluid in the inner (larger) slits, which traverses the layers through the opening near the center of the domain, for lower Reynolds number, a pair of vortices are created near the region of high speed flow. In the same area, for higher Re_p one additional vortical structure is visible. The flow in smaller slits is highly complex for both flow conditions, presumably due to small inlets and outlets near the sharp corners, which result in high velocities in surrounding area.

Perspectives

In the future work, the presented configuration will be extended to other rotation angles and Reynolds numbers, up to turbulent flow for several chosen geometries. The studied configuration will also be extended into a fully periodic geometry without the polygonal end walls. This way, by comparing results from fully periodic and current setup, the influence of the wall effects on the whole flow field (visible for example in the smaller slits) could be isolated. Moreover, a detailed post-processing pipeline will be established allowing for averaging of the flow field across layers, resulting in a compact database of flow conditions in the experimental configuration, which could be used for model reduction.

Acknowledgment

We would like to express our gratitude towards Christin Velten and Katharina Zähringer for providing us with the geometry of their experimental apparatus. This work was funded by the Deutsche Forschungsgemeinschaft (DFG, German Research Foundation) – Project-ID 422037413 - TRR 287

References

[1] Dixon A. G., Partopour B.: *Computational Fluid Dynamics for Fixed Bed Reactor Design*, Annu. Rev. Chem. Biomol. Eng., vol. 11, no. 1, pp. 109–130, 2020

[2] Dullien F. A. L.: *Porous Media*, Academic Press, 1979, ISBN 9780122236501

[3] Woudberg S., Dumont É.: *Porous media models for packed bed characterization*, in *From Biofiltration to Promising Options in Gaseous Fluxes Biotreatment*, Elsevier, pp. 71–87., 2020

[4] Du Plessis J. P., Masliyah J. H.: *Mathematical modelling of flow through consolidated isotropic porous media*, Transp Porous Med, vol. 3, no. 2, pp. 145–161, 1988

[5] Sadowski W. *et al.*: *Particle-resolved simulations and measurements of the flow through a uniform packed bed*, Physics of Fluids, vol. 36, no. 2, p. 023330, 2024

[6] Neeraj T. *et al.*: *Modeling Gas Flows in Packed Beds with the Lattice Boltzmann Method: Validation Against Experiments*, Flow Turbulence Combust, vol. 111, no. 2, pp. 463–491, 2023

Using AI, positron imaging, and insider knowledge to digitally optimise industrial fluid- and particle-handling systems

C.R.K. Windows-Yule

*E-Mail: c.r.windows-yule@bham.ac.uk

[1] School of Chemial Engineering, the University of Birmingham, Edgbaston, Birmingham, B15 2TT

Introduction

Numerical methods such as the discrete element method (DEM), computational fluid dynamics (CFD), coupled CFD-DEM, and multiphase particle-in-cell (MP-PIC) simulations provide potentially powerful tools for the investigation and optimisation of diverse particulate, fluid, and multiphase systems, including gas-solid systems. However, without rigorous calibration and validation, their outputs may be inaccurate, or even entirely unphysical, and the processes of calibration and validation can prove highly time- and labour-intensive [1], [2].

For many industrial systems – which are typically housed in aluminium or steel, making them optically opaque – it can be highly challenging to extract meaningful dynamical information, and thus provide appropriate ground-truth data for the validation of numerical simulations [3]. For fast-moving systems such as fluidised beds, where the temporal resolution of techniques such as x-ray CT becomes too low for meaningful data reconstruction, the challenge is greater still [3].

In this talk, we provide an overview of the Positron Emission Particle Tracking technique, and its use as a tool for the calibration, validation, and ultimately optimisation of industrial systems. We provide real industrial case studies conducted with Unilever [4] and Jacobs Douwe Egberts [5], demonstrating how PEPT can be used to provide highly-validated, "true to life" simulations of industrial systems, and how these simulations in turn may be coupled to evolutionary AI algorithms to optimise the systems being modelled.

Positron Emission Particle Tracking

Positron Emission Particle Tracking (PEPT) is an imaging technique adapted from Positron Emission Tomography (PET) that enables the three-dimensional tracking of a single radioactive tracer within an opaque system. In the typical arrangement, a small particle is labelled with a positron-emitting radionuclide, most commonly such as Fluorine-18 or Gallium-68, though other radionuclides may also be used, for example Cobalt-55 to label iron-based particles. Once introduced into the system of interest, the labelled particle emits positrons as the radionuclide decays. These positrons interact almost immediately with nearby electrons, resulting in annihilation events that give rise to pairs of 511 keV gamma photons emitted in nearly opposite directions. By detecting multiple such pairs of Gamma-rays, it is possible to triangulate the position of the tracer and – for a suitably active tracer – follow its trajectory through three-dimensional space [6]. Under typical conditions, PEPT can achieve sub-millisecond temporal resolution and sub-millimetre spatial resolution [7].

Case Studies

Industrial case study 1: Jacobs Douwe Egberts

A laboratory-scale spouted bed was used for the PEPT experiments, wherein a positron-emitting tracer particle was tracked within the opaque system. The high temporal and spatial resolution of the PEPT technique enabled precise measurements of particle trajectories, providing detailed three-dimensional velocity and occupancy fields. These experimental data served as a benchmark for validating the CFD-DEM model, allowing for a direct, quantitative comparison of simulation outputs against the experimental results [5]. Specifically, a systematic workflow was developed to align the experimental and numerical data, allowing three-dimensional data to be compared piecewise across the entire three-

dimensional volume of the system. Care was also taken to ensure consistency in spatial and temporal resolutions during post-processing.

The study explored several drag force correlations to capture the fluid-particle interactions within the spouted bed. The Gidaspow model, incorporating equivalent intrinsic particle density, demonstrated superior performance in predicting particle trajectories, solid occupancy, and velocity distributions when compared to alternative drag models. The model was also validated across various operating conditions, such as differing particle bulk masses and airflow rates, to establish its robustness. Notably, the PEPT data facilitated the validation of transient and steady-state flow characteristics, including particle circulation times, residence times in the bulk bed and freeboard regions, and velocity distributions.

Interestingly, despite simplifying the particle geometries to spheres, the study demonstrated that accurate results could be achieved by incorporating appropriate rolling resistance and drag force adjustments to account for the aspherical nature of the particles – a valuable finding for industry, where such simplifications can greatly aid computational efficiency, and thus facilitate the efficient modelling of large, commercial-scale systems.

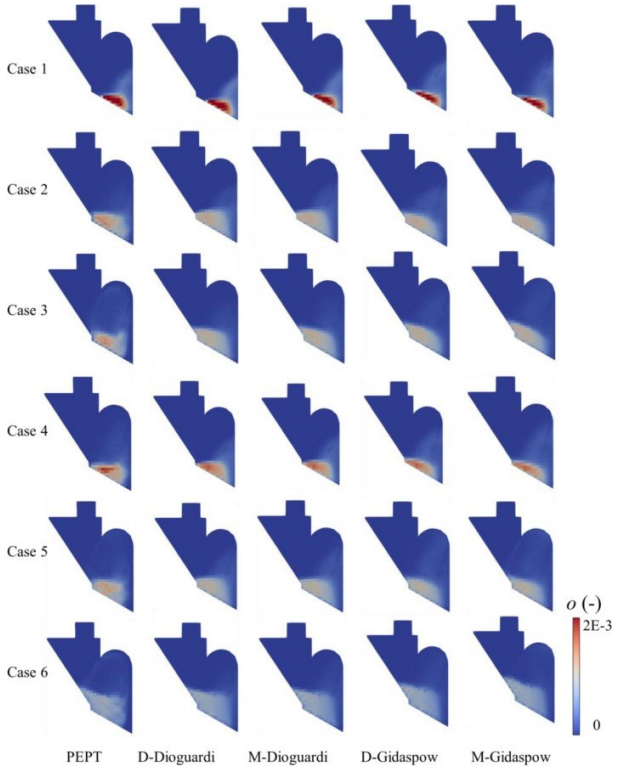

Figure 1: Comparison of PEPT-measured and numerically simulated occupancy fields for a spouted-bed coffee roaster.

Industrial case study 2: Unilever

In this study, a similar method of experimental-simulational comparison was used for a laminar mixing system. The research focused on a horizontal stirred tank operating with Newtonian glycerol under laminar flow conditions. Three CFD particle models—CFD-Massless, CFD-Lagrangian, and CFD-DEM—were compared against PEPT data to assess their accuracy in predicting particle motion and velocity fields.

PEPT was employed to capture high-resolution, three-dimensional Lagrangian particle trajectories within the opaque fluid system. These trajectories were processed to create time-averaged, three-dimensional velocity fields discretised onto a voxel grid. The experimental data were systematically compared to simulation outputs through the rigorous validation workflow described above, though this time using not only the R^2 coefficient, but also a novel metric labelled the *simulation quality coefficient*, Q_{sim}, incorporating a quantification of experimental noise to evaluate the degree of agreement between experiment and model.

The study found that the CFD-DEM and CFD-Massless models exhibited better agreement with the PEPT-derived velocity fields compared to the CFD-Lagrangian model. However, while the CFD-DEM approach demonstrated greater accuracy, it incurred significantly higher computational costs than the other methods. The Q_{sim} metric effectively highlighted the balance between model accuracy and computational efficiency, revealing that both the massless and DEM models performed well under the assumption of negligible particle inertia.

Conclusion

The case studies highlighted above showcase a novel workflow for the PEPT-based validation of two distinct sets of numerical simulations. In both cases, the results demonstrate that the respective simulation methods can provide faithful reproductions of the systems being modelled. Moreover, both illustrate those significant simplifications – in the former the modelling of aspherical coffee beans as spheres, in the latter the use of simple flow-following tracers as opposed to full DEM particles – can be implemented whilst still achieving highly realistic simulation models of multiphase industrial systems.

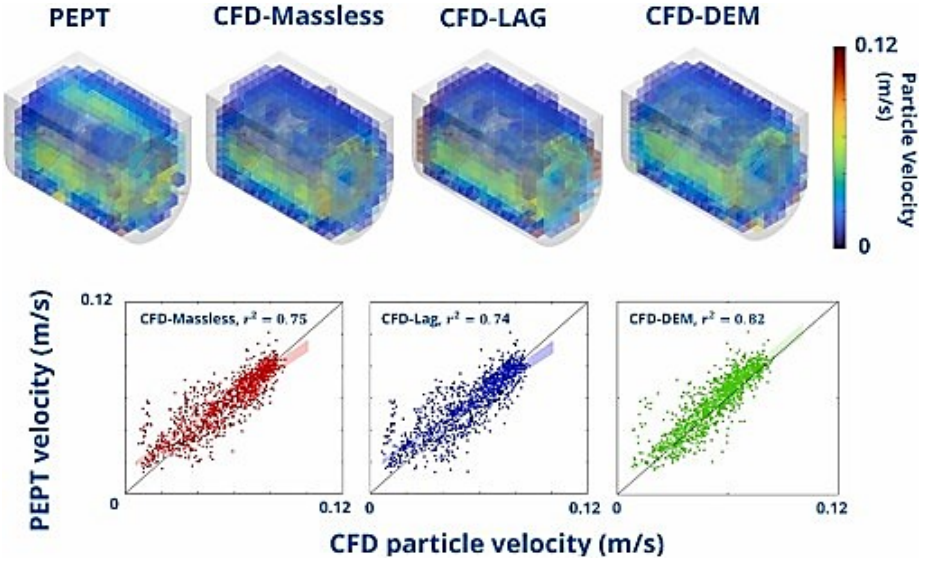

Figure 2: (Top) Three-dimensional 20 ×20 ×20 voxel grid of the particle velocity magnitude in each system, and (Bottom) a parity plot representing a 20×20×20 cell-by-cell comparison between simulation and experiment for the (red) massless, (blue) Lagrangian material, and (green) DEM particles.

References:

[1] Windows-Yule, C. R K., Tunuguntla, D. R.; Parker, D. J.,"Numerical modelling of granular flows: a reality check" *Computational particle mechanics,* 2016, 3, pp. 311-332.

[2] Windows-Yule, C. R. K., Neuveu, A., "Calibration of DEM simulations for dynamic particulate systems" *Papers in physics,* 2022, 14, 140010-140010.

[3] Windows-Yule, C. R. K., Buist, K. A., Taghizadeh, K., Finotello, G., Nicusan, A., "A multi-disciplinary perspective on the present and future of particle imaging", 2024, *Particuology*, https://doi.org/10.1016/j.partic.2024.04.009.

[4] Hart-Villamil, R., Ingram, A., Windows-Yule, C R K, Gupta, S., Nicusan, A., "On the autonomous validation and comparison of particle models for a Newtonian laminar flow mixing model using PEPT" *Chemical Engineering Research and Design*, 2024, 206, pp. 139-150.

[5] Che, H., Al-Shemmeri, M., Fryer, P. J., Lopez-Quiroga, E., Wheldon, T. K., Windows-Yule, C. R. K., "PEPT validated CFD-DEM model of aspherical particle motion in a spouted bed" *Chemical Engineering Journal*, 2024, 453, pp. 139689.

[6] Windows-Yule, K., Nicusan, L. Herald, M. T., Manger, S., Parker, D. "Positron Emission Particle Tracking: A Comprehensive Guide", 2022, IOP Publishing.

[7] Windows-Yule, C., Seville, J. P. K., Ingram, A., Parker, D. J., "Positron emission particle tracking of granular flows", *Annual review of chemical and biomolecular engineering*, 2020, 11(1), pp. 367-396.

State of the art of three selected techniques for advanced solids flow diagnostics: MPT, MST and high frequency radar

D.C. Guío- Pérez*, D. Pallarès

Division of Energy Technology, Chalmers University of Technology, Göteborg (Sweden)
*E-Mail: carolina.guioperez@chalmers.se

Background and Aim

The solid phases plays a key role in gas-solids systems in all of mass, momentum and heat transfer, as it often represents a reacting phase (or even the targeted main product/output), stands for the majority of the kinetic energy in the system, and governs the thermal mixing and the resulting temperature field. Thus, efficient design, control and scale-up of gas-solids operations are strongly dependant on the ability to diagnose the characteristics of the solids flow, i.e. its size distributions, conversion degrees, and concentration and velocity fields. From the latter two, key information such as residence time distributions and mixing rates can be derived.

The diagnostics of the solids flow were for many years based on the interpretation of wall pressure measurements in spatial, time and frequency domains (and combinations of these). This was followed by the introduction of direct measurement through tools for analysis of visual captures (though with limited penetration). Further development led to the development of probes (inserting e.g. pressure, impact or capacitance sensors into the flow) and eventually into non-invasive techniques, e.g. capacitance sensor systems, radioactive particle tracking, and laser and optical methods [1]. With time, the measurement techniques targeting the solids flow have diversified and become more specialized into enabling the measurement of specific parameters at the cost of certain limitations in terms of set-up and suitable flow scenario.

This work aims to provide updated insight into the state of the art for a selection of three advanced techniques in solids flow diagnostics: magnetic particle tracking (MPT), magnetic solids tracing (MST) and high frequency FMCW radar. For each technique, the measurement principles and uses are described, and limitations and possibilities are identified.

Magnetic particle tracking

Based on the anisotropic magnetoresistance effect, this measurement method assesses both position and orientation of one magnetic particle. Anisotropic magnetoresistance (AMR) sensors contain a ferromagnetic material, which resistance decreases when a magnetic field is applied. The change in resistance is proportional to the strength of the magnetic field. If the tracked particle is a permanent magnet of known magnetic strength, the distance between sensor and particle can be determined. Modern AMR sensors feature 3 AMR elements in different orientation, which allows for the determination of the orientation of the sensed magnetic field and therefore of the tracked magnet.

This technique has been used at laboratory scale to study solids movement in diverse systems [2,3,4]. Most common use of the technique regards the analysis of solids trajectories. Since early applications, the analysis of the 3D position with time has been in focus, and from there, the analysis of velocity and acceleration of a single particle. Volumes of few dm^3 can be well sensed with 4 to 5 sensors, with sufficient accuracy. The increase in the size of the sensed volume demands the use of more sensors and so, further considerations for the transfer and processing of signals.

Most limitations of this technique are related to the nature of the sensed particle: i) the unit and its surroundings must be free of magnetic fields and magnetic materials (polymers and aluminium are

preferred for the construction), ii) the density and size of the tracked particle can be adjusted by coating the magnet, but the density of neodymium and the required strength of the magnetic field set the limits for such adjustments (the magnetic field is proportional to the volume of the magnet). The maximum operating temperature is set by the Curie temperature (ranging from 80 °C to 230 °C, depending on the magnet). Regarding the method itself, it must be noted that there must be a balance between the sensitivity of the sensors and the strength of the sensed fields. Then, larger volumes are more challenging since the sensed fields vary strongly as the distances between sensor/s and tracer particle do.

Still the MPT technique delivers solids trajectories highly resolved in time and space. The quality of such measurements is sufficient for quantitative assessment of, for instance, lift and drag forces [5,6]. The technique is especially useful for the analysis of dense/opaque regions, where other techniques face strong interferences. It is a non- intrusive technique and can be used to analyse the movement of irregular particles (since the orientation can be acquired) [7]. Use of AI in the reconstruction of trajectories acquired through MPT is being explored as a way to further exploit the capacities of the technique [8,9].

Magnetic solids tracing

This method is based on the change in impedance of a coil when the susceptibility of its core changes. This phenomenon is used to quantify concentration of a solid phase in the system. The tracer material should be ferromagnetic. The measurements can be used to assess a number of different parameters depending on the configuration of the coil (or coils) and the experimental procedure.

This technique has been used to assess residence time of solids, mixing rates as well as solids circulation rates [10, 11]. In such configuration, coils are winded around the duct (pipe, or channel), they can be externally winded or embedded internally. The sensed volume would correspond to the core region of the coil. The experiments follow a regular peak injection methodology and are therefore suitable to investigate RTD, and from there, flow characteristics. The concentration measurements can also be used to investigate the solids dynamics in static beds, for instance, segregation or dispersion of a specific solid phase. This is done by immersing small coils in the bed to measure the concentration at specific locations. Instead of sensing in the core region of the coil, the area around the coil is sensed. Local concentrations acquired from different positions in the bed are the used to characterize the dynamics.

While showing satisfactory sensitivity, the sensors are susceptible to thermal drift, and electrostatics. Both can be filtered out during data processing. The most limiting aspect of the methodology is temperature, the Curie temperature for iron-based tracers is around 770 °C but the magnetic field of copper coils is not stable at temperatures beyond 200 °C. Since magnetic materials (e.g., in the walls) would introduce disturbances to the measurements, these should be avoided. The design of the coils is critical to the method, since it is important to achieve homogeneity of the magnetic field over the sensed region, so large coils can become problematic. It should also be noted that, the magnetic field must be strong enough to generate clear signals but should not affect the movement of the tracer particles.

As for today, the use of small coils is viewed positively, as specific local measurements have shown potential to reveal detailed descriptions of the solids flows. Coil geometries adjusted to the application (e.g., flat or elongated) are also interesting, but require careful characterization of the magnetic field.

High-frequency FMCW radar

The radar systems of the type Frequency-Modulated Continuous-Wave (FMCW) are capable of measuring both the distance and velocity of moving objects. This is achieved by continuously varying the frequency of the transmitted signal over a fixed period of time, the distance is calculated from the frequency difference between the transmitted and received signals, while the Doppler frequency is used to calculate the velocity. By using very high frequencies (GHz to THz), such a radar system can detect particles in the micron range of size.

Having been used for decades in remote sensing (of atmospheric precipitations and avalanches) and level measurements in industrial devices, this technique has been adapted to measure the solids velocity distribution and concentration (which, combined, yield the solids flux) in dispersed gas-solids industrial

systems [12,13,14]. The measurement is local, as it takes place along the radar beam with mm-scale spatial resolution, and it is inherently non-intrusive.

Some of the limitations of this technique relate to the measurement principle itself, as the central frequency and the frequency variation are simultaneously related to the resolution of the different measured parameters. For example, given a radar configuration, increasing the velocity resolution will reduce the range, and increasing the temporal resolution will reduce the range resolution. Similarly, using a higher central frequency improves the sensitivity to smaller particles but reduces penetration. A more practical limitation concerns the handling of large volume of data.

At the current stage of development, the technique still relies on calibration for the correct assessment of concentration. However, the non-intrusiveness, the absence of a temperature limit and the significantly high temporal and spatial resolutions, place this technique in a privileged position. Such information could for instance make it possible to close sub-grid momentum balances in CFD modelling [15].

References

[1] M. Errigo, C. Windows-Yule, M. Materazzi, D. Werner, P. Lettieri. *Non-invasive and non-intrusive diagnostic techniques for gas-solid fluidized beds – A review*. Pow. Tech. Vol. 431, 2024, 119098.

[2] E.E. Patterson, J. Halow, S. Daw. *Innovative Method Using Magnetic Particle Tracking to Measure Solids Circulation in a Spouted Fluidized Bed*. Ind. Eng. Chem. Res. 2010, 49, 11, 5037–5043.

[3] K.A. Buist, A.C. van der Gaag, N.G. Deen, J.A.M. Kuipers. *Improved magnetic particle tracking technique in dense gas fluidized beds*. AIChE Journal, 2014, 60(9), 3133-3142.

[4] A. Köhler, D. Pallarès, and F. Johnsson, *Magnetic tracking of a fuel particle in a fluid-dynamically down-scaled fluidised bed*. Fuel Process. Technol. 2017. 162, 147–156.

[5] I. Mema, V.V. Mahajan, B.W. Fitzgerald, J.T. Padding. *Effect of lift force and hydrodynamic torque on fluidisation of non-spherical particles.* Chem. Eng. Sci. 2019, 195, 642–656.

[6] D.C. Guío-Pérez, A. Köhler, A. Prati, D. Pallarès, F. Johnsson. *Effective drag on spheres immersed in a fluidized bed at minimum fluidization—Influence of bulk solids properties*. Can. J. Chem. Eng., 2023, 101(1): 210-226.

[7] I. Mema, K.A. Buist, J.A.M. Kuipers, J.T. Padding. *Fluidization of spherical versus elongated particles: Experimental investigation using magnetic particle tracking*. AIChE J. 2019, 66(4), e16895.

[8] M. Prashanth, P. Du, J.-X. Wang, H. Wu; *A neural network-based algorithm for the reconstruction and filtering of single particle trajectory in magnetic particle tracking*. Rev. Sci. Instrum. 2024; 95 (5): 055001.

[9] H. Wu, P. Du, R. Kokate, J-X. Wang. *A semi-analytical solution and AI-based reconstruction algorithms for magnetic particle tracking*. PLoS ONE, 2021, 16(7): e0254051.

[10] D.C. Guío-Pérez, T. Pröll, H. Hofbauer. *Solids residence time distribution in the secondary reactor of a dual circulating fluidized bed system.* Chem. Eng. Sci., 2013, Vol. 104: 269-284,

[11] G. Hofer, T. Märzinger, C. Eder, F. Pröll, T. Pröll. *Particle mixing in bubbling fluidized bed reactors with continuous particle exchange.* Chem. Eng. Sci., 2019, Vol. 195: 585-597,

[12] D.C. Guío-Pérez, M. Bonmann, T. Bryllert, M. Seemann, J. Stake, F. Johnsson, D. Pallarès. *Radar-based measurements of the solids flow in a circulating fluidized bed*. Fuel, Vol. 345, 2023, 128232.

[13] M. Bonmann, A. Moradikouchi, T. Bryllert, A. Sparén, S. Folestad, J. Johansson. *Terahertz Radar Observes Powder Dynamics for Pharmaceutical Manufacturing*. IEEE Sensors J., Vol. 24 (13): 20512-20522.

[14] J. Wei, X. Chen. *Blast furnace gas flow strength prediction using FMCW Radar.* ISIJ International. 2015, Vol. 55 (3): 600-604.

[15] H. Ström, H. Luo, Q. Xiong. *Perspectives on Particle–Fluid Coupling at Varying Resolution in CFD-DEM Simulations of Thermochemical Biomass Conversion*. Energy Fuels, 2024, 38 (18): 17179–17190,

Development of a PET-like system for particle tracking

Y. Hartych[1*], N. Böhle[1], M. Fink[1], M. Fritsch[1], F.H. Heinsius[1], T. Held[1], T. Holtmann[1], M. Huckestein[1], J. Oppotsch[1], M. Steinke[1], C. Wais[1], and U. Wiedner[1]

[*]E-Mail: yhartych@ep1.rub.de

[1]*Institute of Experimental Hadron Physics, Ruhr University Bochum, Universitätsstr. 150, 44780 Bochum, Germany*

Motivation

In the modern world of rapidly increasing importance of ecologically friendlier industrial processes going alongside the continuous refinement of economic efficiency, it is crucial to meticulously understand every stage of production. One of those stages is the processing of moving granular materials such as processing coffee beans in a roasting drum or sintering the raw mix for production of cement in a rotary kiln. These processes have shown to be difficult to examine due to dense packing of the macroscopic particles.

Method

Our approach to analysing the particles' behaviour is by using **p**ositron **e**mission **p**article **t**racking (PEPT) to be able to analyse the behaviour (e.g. trajectory, speed) of such macroscopic particles. PEPT is a modification of **p**ositron **e**mission **t**omography (PET) which is well established in the medical sector. As opposed to conventional PET detectors using ring scanners with circular arranged scintillators aligned with the expected photon origin and separate photomultipliers for every voxel (cf. [1]), this method is based on the idea of significantly reducing the count of photomultipliers. This is achieved by using elongated scintillators orthogonally (or with a large angle) to the propagation direction of the measured photons and read out those bars from both sides, as visualized in Figure 1a. Thus, we can not only reduce the need for SiPMs but also the number of **t**ime-to-**d**igital **c**onverters (TDCs) needed, both of which are very costly. Due to the dense packing of scintillators limiting the space, conventional **p**hoto**m**ultiplier **t**ubes (PMTs) need to be substituted by **si**licon **p**hoto**m**ultipliers (SiPMs) – just like in modern medical PET detectors as well – which possess significantly higher dark currents at a given temperature compared to the PMTs. Those scintillator bars, with the SiPM **p**rinted **c**ircuit **b**oards (PCBs) attached, are arranged as four walls, forming a cube in which one can track the movement of the given object. A visualisation of this setup, consisting of a generic grate system in the centre and a positron emitter within, is given in Figure 1b.

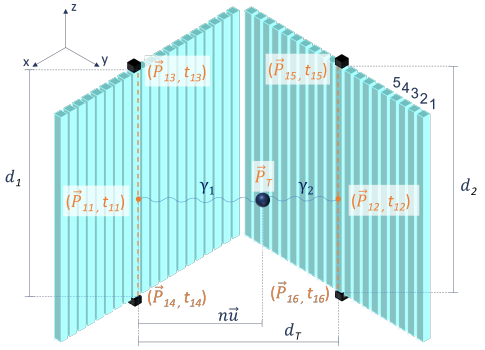

(a) Schematic illustration of time-of-flight analysis. [2, Fig. 4b]

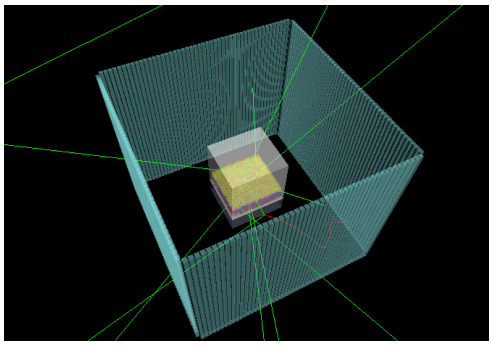

(b) Visualization of the experimental setup with trajectories of simulated photon emission (green) using Geant4 [3].

Figure 1. Illustration of underlying mathematics and expected mode of operation of the planned experimental setup. The generic grate system in the centre of the detector in Figure 1b is provided by working group C3 of the CRC/TRR 287 (cf. [4]).

The PEPT principle is based on a radioactive tracer emitting positrons. These positrons possess a very short mean free path before annihilating with an electron of the surrounding matter. With this, a pair

of 511 keV photons is emitted back-to-back, allowing the determination of their origin, for example by **t**ime-**o**f-**f**light (ToF) analysis. In our setup, this is supplemented by a second ToF calculation within the scintillator bars, as depicted in Figure 1a.

The positron emitter in use will be ^{68}Ge, producing positrons with a short mean free path of 3.1 mm [5]. The scintillator walls each consist of 22 scintillator bars whereby each bar has the dimensions $(20\times20\times1000)$ mm^3. The software used for **d**ata **acq**uisition (DAQ) and data processing – to reconstruct the observed trajectories – is tested through Monte Carlo simulations to validate the reliability of the analysis and estimate its accuracy.

Results

So far, the mounting structure for the scintillator bars and adjacent electronics was designed and constructed. Development of the PCB circuit for the SiPMs and their preamplifier was carried out. The placement of the preamplifier components (cf. Figure 2b) has been finished for all panelizations so that the SiPMs can be soldered on the opposing side, as illustrated in Figure 2a. To place the SiPMs, we use a universal assembly station, which consists of a digital microscope with a beam spitter to project the solder bumps onto the contacts on the PCB. In combination with micrometre screws for positioning the PCB underneath, this allows the high precision, needed for such delicate components. The assembly station is supplemented by a stencil printer to apply the soldering paste and an oven for the actual baking process. As SiPMs are particularly sensitive, we adapted the manufacturer's soldering profile to the conditions of our oven. The scintillator bars have been wrapped in one inner layer of highly reflective foil to minimize the loss of generated light, followed by two layers of black screening foil to shield the sensors from disruptive ambient light. In parallel, the first components of the DAQ and data analysis have been developed and validated with Monte Carlo simulations.

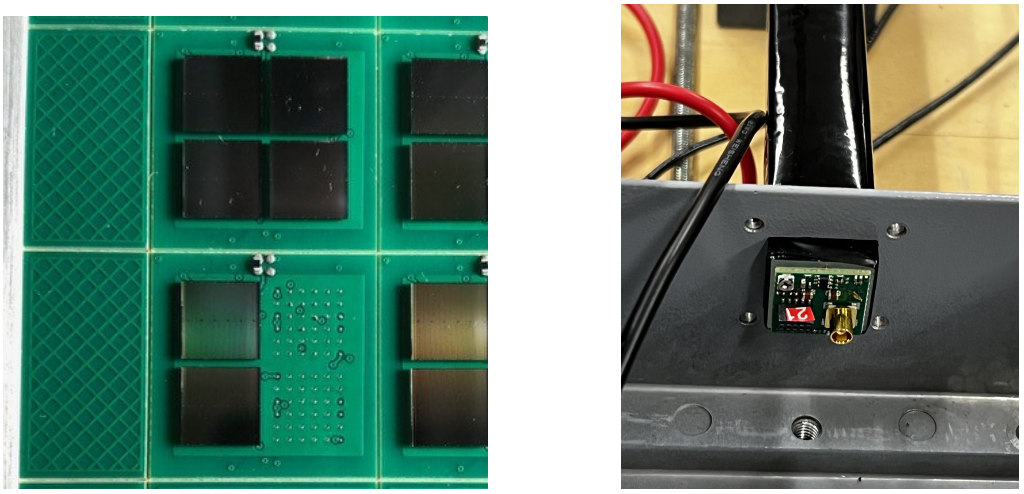

(a) Photo taken in the middle of a pick and place process of SiPMs on a panelization.

(b) Photo of assembled PCB glued onto a scintillator bar on a test stand.

Figure 2. Two photos demonstrating the process of manufacturing detector, focussing on the readout technology. In Figure 2b, the visible side consists of the preamplifier and the glued side is assembled with the SiPMs.

Currently, the assembling of almost all PCBs has been completed. To validate proper functioning and perform offset adjustment for every board, measurements of the dark current and test photopeak spectra, using ^{137}Cs positron emitter and $LaBr_3$ scintillators, are carried out. First tested boards have already been glued to the scintillator bars using the two component epoxy resin EPO-TEK 301-2 as shown in Figure 2b. Until summer, we are looking forward to having finished the soldering process, including all fixes of faulty boards. Further, we expect to have at least 22 scintillator bars with validated SiPM boards on each end to be able to set up two half-equipped detector walls to perform first measurements with a resting source. At this point, the conversion into a logic signal is done by commercial leading-edge

discriminators. In future, these will be substituted by self-designed constant fraction discriminators which satisfy our requirements more properly. The results of these measurements will be presented.

Outlook

After an initial proof of concept using measurements from the described partial setup, the next steps involve finalizing the entire detector with all four walls, consisting of 88 scintillator bars in total. In addition, the design of the discriminator circuit board needs to be completed, in order to start measuring with the desired total setup. In the next step, ^{68}Ge is incorporated into small wooden spheres which will be used in later measurements. With this, the proper functioning of the whole setup can be analysed, including the calibration of all components. If the analyses with all scintillators show an accuracy near the positron's mean free path, a better resolution might be obtained by replacing the Germanium isotope with ^{64}Cu, ^{22}Na or ^{52}Mn to reduce the mean free path of the positron by a factor of about 5 to 6 [6].

Once all these steps are taken, tracking of a moving tracer inside the generic grate system of dimensions $(320 \times 300 \times 300)\,\mathrm{mm}^3$, which is provided by project C3 within the CRC/TRR 287 (cf. [4]), will be conducted. Simultaneously, the simulation and analysis software will be refined and expanded. This will include the tracking of an expanding cloud of a nebulised radioactive isotope, for which the experimental setup has yet to be designed.

Acknowledgement

This work is funded by the Deutsche Forschungsgemeinschaft (DFG, German Research Foundation). Project-ID 422037413 – CRC/TRR 287 "Bulk-Reaction".

References

[1] Windows-Yule C.R.K., Herald M.T., Nicuşan A.L., et al.: *Recent advances in positron emission particle tracking: a comparative review*, Reports on Progress in Physics, 85, 016101, 2022.

[2] Oppotsch J., Athanassiadis A., Fritsch M., Heinsius F.H., Held T., Hilse N., Scherer V., Steinke M., Wiedner U.: *A simulation study for a cost-effective PET-like detector system intended to track particles in granular assemblies*, Particuology, 84, 117–125, 2024.

[3] Agostinelli S., Allison J., Amako K., et al.: *Geant4 — a simulation toolkit*, Nuclear Instruments and Methods in Physics Research Section A: Accelerators, Spectrometers, Detectors and Associated Equipment, 506, 250–303, 2003.

[4] Hilse N., Kriegeskorte M., Illana E., Wirtz S., Scherer V.: *Mixing and segregation of spheres of three different sizes on a batch stoker grate: Experiments and discrete element simulation*, Powder Technology, 400, 117258, 2022.

[5] de Jong H.W.A.M., Perk L., Visser G.W.M., Boellaard R., van Dongen G.A.M.S., Lammertsma A.A.: *High resolution PET imaging characteristics of ^{68}Ga, ^{124}I and ^{89}Zr compared to ^{18}F*, IEEE Nuclear Science Symposium Conference Record, Fajardo, PR, USA, 2005.

[6] Jødal L., Le Loirec C., Champion C.: *Positron range in PET imaging: non-conventional isotopes*, Physics in Medicine & Biology, 59, 7419–7434, 2014.

A Configurable Real-Time Data Acquisition System for PEPT in Particle-Gas Flow Measurement

D. Passaretti[1], E. Antonecchia[2], and N. D'Ascenzo[2,3*]

*E-Mail: nicoladascenzo@ustc.edu.cn

[1] *Forschungscampus STIMULATE, Otto-von-Guericke University of Magdeburg, Magdeburg, Germany*
[2] *Department of Life Science, BF Research, Jolanda di Savoja, Italy*
[3] *School of Information Science and Technology, University of Science and Technology of China, Hefei, China*

Introduction

Positron Emission Particle Tracking (PEPT) is an imaging technique able to observe quantitatively, in real-time and in 3-dimensions, the dynamics of liquid flows. Positron-emitting particles can be tracked in opaque vessels for mapping granular flows for engineering applications, for example, dynamic behaviour of catalysts in chemical reactors, mixing and segregation in mixers, dryers, rotating kilns, solid–liquid slip velocity in ball mills, particle rotation, solid flow structure, bubble flow pattern in fluidized beds and granulators, solid motion in food processors [1-5].

The PEPT technique is based on the detection of two collinear γ rays generated in the annihilation of a positron emitted by a radiolabelled particle. A 3-dimensional localization of the particle is possible in real time, making it possible to track quantitatively the movement of the particle in gas and fluid streams. High spatial resolution, temporal resolution and sensitivity are the key to image particles in stream [6].

We have recently developed a new detector for Positron Emission Tomography (PET) based on scintillator arrays read out by Silicon Photomultipliers (SiPMs), with a fast digitalization of the readout signal, reaching unprecedented count rate performance and sensitivity [7-10]. Due to the time consuming data post-processing involved in the digitalization process, real-time operation of the systems has been an issue, limiting the application of these detectors to PEPT.

In this work, we present a new Configurable Real-Time Data Acquisition System that collects the signal pulse generated by a single PET event, processes it on the fly, estimating its arrival time and period, and forwards it to the reconstruction system. Performing this first processing step at the early acquisition stage not only improves the consuming time of the acquisition data path, but it also allows the packet-size reduction of the single pulse and the bandwidth improvement of the communication with the reconstruction system.

Architecture design

The proposed Configurable Real-Time Data Acquisition System is designed to be implemented on the 7 series Field-Programmable Gate Arrays (FPGAs) of AMD [11], and can be configured at synthesis time for a different number of channels. The architecture, as shown in Fig. 1, consists of four pipelined stages: the *digitalization stage*, the *processing stage*, the *merging stage*, and the *transmitting stage*.

In the *digitalization stage*, the arrival time of the rising and falling signal is sampled through Time-to-Digital Converters (TDCs). Each TDC includes two Tapped Delay Lines (TDLs) for the fine time of the rising and the falling edges, an encoder to convert the detected fine time from thermometer code to number representation, and a shared counter for the coarse time. In the specific, as shown in Fig. 2 in the white block, the TDL has been implemented through a chain of CARRY4 modules. In order to process the period in real time, the arrival time of the rising signal is first stored in the "arrival time register" of 44 bits. Then, it is sent to the *processing stage* when the falling signal arrives. In this last stage, the period of the event is calculated in a single clock cycle, it is stored in the "pulse packet" which contains a register of 14 bits for the period, and the logic to encapsulate the arrival time, the period, and the pixel position in packets of 64 bits. While the packet is ready to be sent to the *merging stage*, the control unit in the digitalization stage sets the TDLs to sample the successive event. The *merging stage*, as shown in Fig. 1, consists of two sub-stages. In the first sub-stage (in the light yellow side), groups of 8 channels are formed to store the packets in buffers implemented with asynchronous First-In-First-Outs (FIFOs), and a round-robin scheduler, which is used to allocate ready packets to the single FIFO. Afterwards, in the second sub-stage (in the light orange side), another round-robin scheduler selects packets from

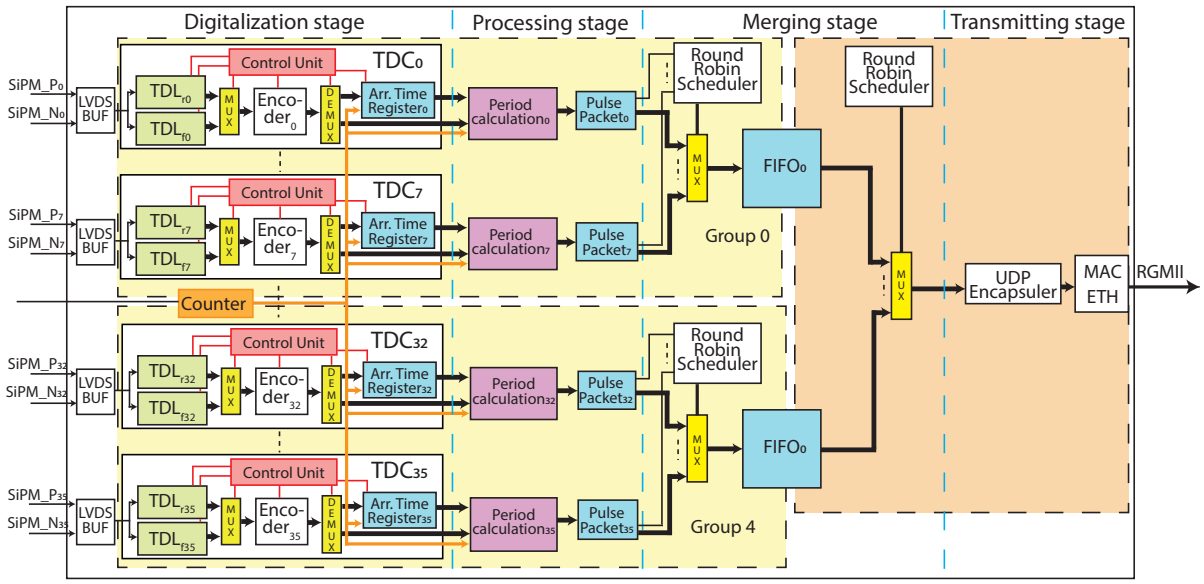

Figure 1: Configurable Real-Time Data Acquisition System

each non-empty FIFO and sends them to the transmission stage, where packets are encapsulated in UDP-IPv4 bigger packets and sent to the reconstruction system over Ethernet. The *scheduler stage* has the fundamental role of managing in real time the Clock Domain Crossing (CDC) between the sampling clock domain, which includes the modules in the light yellow boxes in Fig. 1, and the transmitting clock domain, which includes the modules in the light orange box in Fig. 1. The sampling clock domain is determined by the TDC sampling rate, and the transmitting clock domain, which is set to 125 Mhz, is determined by the transceiver data rate.

The proposed architecture has been designed, using SystemVerilog, and it has been implemented on the XC7S100FGGA676 FPGA [12]. For the implementation of the architecture and the experimental setup, we have configured the proposed architecture with 36 channels, matching a 6×6 detection elements array, with each element comprising a $2.0 \times 2.0 \times 20$ mm^3 Lutetium–yttrium oxyorthosilicate (LYSO) crystal (Epic Crystal) read out by a Complementary Metal-Oxide-Semiconductor (CMOS)-based SiPM that features up to nearly 4 mm^2. The analog signals from SiPMs, are individually shaped through readout analog electronics and connected to the XC7S100FGGA676 FPGA, through the Low-Voltage Differential Signaling (LVDS) interface. In order to estimate the performance of the proposed architecture in terms of resource utilization and time, as latency of the signal to be digitalized, processed, and prepared to be transmitted stage, we have simulated, synthesized, and implemented it with Vivado 2023.2. For the simulation, a SystemVerilog testbench module has been written, which randomly generates signals in parallel across the 36 channels, with each event having a random period in the range of 50-200 nanoseconds managing them in real-time.

Results

We validated the correct behavior of each module, the correct calculation of the period, and the scheduler stage to pack the data. Furthermore, by running the simulation of the entire system at clock cycle accuracy, we observed that the arrival time of the rising and falling edge has a delay of 8 clock cycles in the digitalization stage, and 1 clock cycle to calculate the period. This time is important because it defines the time in which the acquisition system can not acquire another signal from the same channel. Since the scheduler stage delay depends on the amounts of packets ready to be scheduled and the amounts of packets in the FIFOs, we considered the Best Case Execution Time (BCET) to define, which is 4 clock cycles, while the Worst Case Execution Time (WCET) is not considered because the FIFOs are stable. In fact, assuming that each channel acquires up to 25000 events/sec, the average amount of data to store in the FIFOs is 57,6 Mbit/sec for 36 channels, while the transmission link consumes data at the speed of 1 Gbit/sec. Finally, from the resource utilization results, excluding the Transmitter stage, we observed that the proposed architecture uses only 20 % of the Lookup Tables, and 31 % of the Flip-Flops.

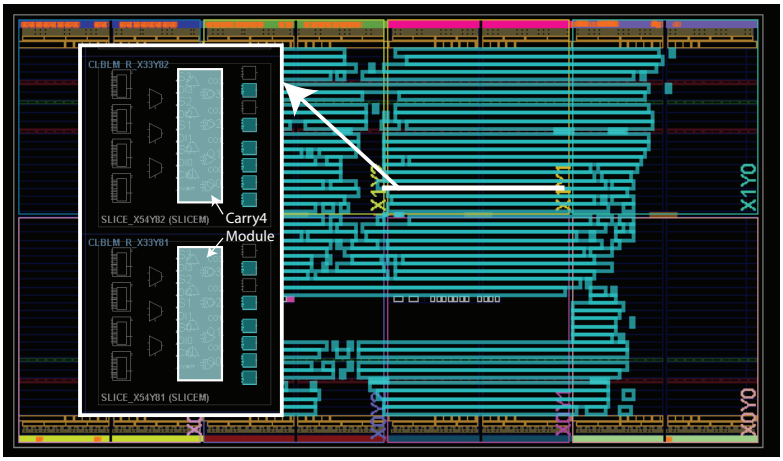

Figure 2: Floorplan implementation on the XC7S100FGGA676 FPGA

Outlook and conclusions

In this work, we have presented a new Configurable Data Acquisition System able to digitize, process on the fly, and forward single PET pulses in real time. Thanks to the implemented processing step, the proposed architecure not only improves bandwith, using only 64 bits per PET pulse, but also results in a low latency solution, enhancing the available time for data processing in the reconstruction system, which is crucial for PEPT imaging techniques.

Acknowledgment This work was partially funded by the European Regional Development Fund (ERDF) Project "Forschungscampus STIMULATE" and the European Union's Horizon 2020 research and innovation program H2020-MSCA-RISE-2020 "Project PETAL" (ID 101008114).

References

[1] Pellico, J., Vass, L., Carrascal-Miniño, A. et al., *In vivo real-time positron emission particle tracking (PEPT) and single particle PET* Nat. Nanotechnol. 19, 668–676, 2024.

[2] D.J. Parker, X. Fan, *Positron emission particle tracking—Application and labelling techniques*, Particuology, 6,16, 2008.

[3] Sommer, A.-E. et al. Application of positron emission particle tracking (PEPT) to measure the bubble–particle interaction in a turbulent and dense flow. Miner. Eng. 156, 106410, 2020.

[4] Mesa, D., van Heerden, M., Cole, K., Neethling, S. J. & Brito-Parada, P. R., *Hydrodynamics in a three-phase flotation system—fluid following with a new hydrogel tracer for positron emission particle tracking (PEPT)*. Chem. Eng. Sci. 260, 117842, 2022.

[5] Jones, C. R., Corona, A., Amador, C. & Fryer, P. J., *Dynamics of fabric and dryer sheet motion in domestic clothes dryers* Dry. Technol. 40, 2087–2104, 2022.

[6] Hampel, D. M., Manger, S., Parker, D. J. & Kokalova Wheldon, T. SuperPEPT: a new tool for positron emission particle tracking; first results. Nucl. Instrum. Methods Phys. (2022).

[7] E. Antonecchia et al., *Development and Evaluation of a Prototype of Shape-Adaptable and Portable All-Digital PET System for In-Lab and In-Field Plant Imaging*, in IEEE Transactions on Nuclear Science, vol. 71, no. 1, pp. 113-120, Jan. 2024

[8] F. Zhou et al., *Development and Evaluation of a Portable MVT-Based All-Digital Helmet PET Scanner*, in IEEE Transactions on Radiation and Plasma Medical Sciences, vol. 8, no. 3, pp. 287-294, March 2024

[9] J. Chen, N. D'Ascenzo, D. Passaretti, H. Lao, Y. Hua and Q. Xie, "Experimental Study of a Large Area High PDE SiPM in 0.11 μm CMOS process for PET Applications," in IEEE Transactions on Radiation and Plasma Medical Sciences, doi: 10.1109/TRPMS.2025.3534221

[10] N. D'Ascenzo et al., A Low-Noise High-Photon Detection Efficiency Silicon Photomultiplier in 0.11-μm CMOS, in IEEE Transactions on Electron Devices, vol. 72, no. 2, pp. 769-777, Feb. 2025

[11] AMD, "7 Series FPGAs Data Sheet: Overview." Xilinx, 2020, DS180 (v2.6.1). Product Specification.

[12] AMD, "SP701 Evaluation Kit." Xilinx, 2023, www.xilinx.com/products/boards-and-kits/sp701.html.

Unveiling the power and limitations in X-Ray imaging of organic materials.

Sebastian Gruber[1*], Nicole Vorhauer-Huget[2], Evangelos Tsotsas[2], Petra Först[1]

*E-Mail: sebi.gruber@tum.de

[1]Technical University of Munich, School of Life Sciences, Food Process Engineering, Weihenstephaner Berg 1, Freising, Germany

[2]Otto-von-Guericke University Magdeburg, Institute of Process Engineering, Thermal Process Engineering

Abstract:

X-Ray micro-computed tomography (XCT) is a non-invasive characterization method, which gain high importance in the field of drying in the last decade but is already present in life science for many more years. Two main methods are present for XCT imaging: 1. Absoprtion imaging and 2. Phase-contrast imaging. For absportion imaging X-Rays are absorbed based on the material of the sample and can be described by the Lambert Beer law (see equation 1)

$$I(x) = I_0 e^{-\mu dx} \quad (1)$$

Where *I(x)* is the intensity of the X-Ray beam measured at the detector, I_0 is the intensity of the attenuated X-Ray beam, μ is the linear attenuation coefficient and is depending on the sample composition and density and x is the sample thickness. For organic samples however, the density of the sample is quite low and also elements are used, which typically, have similar absorption coefficients (see figure 1).

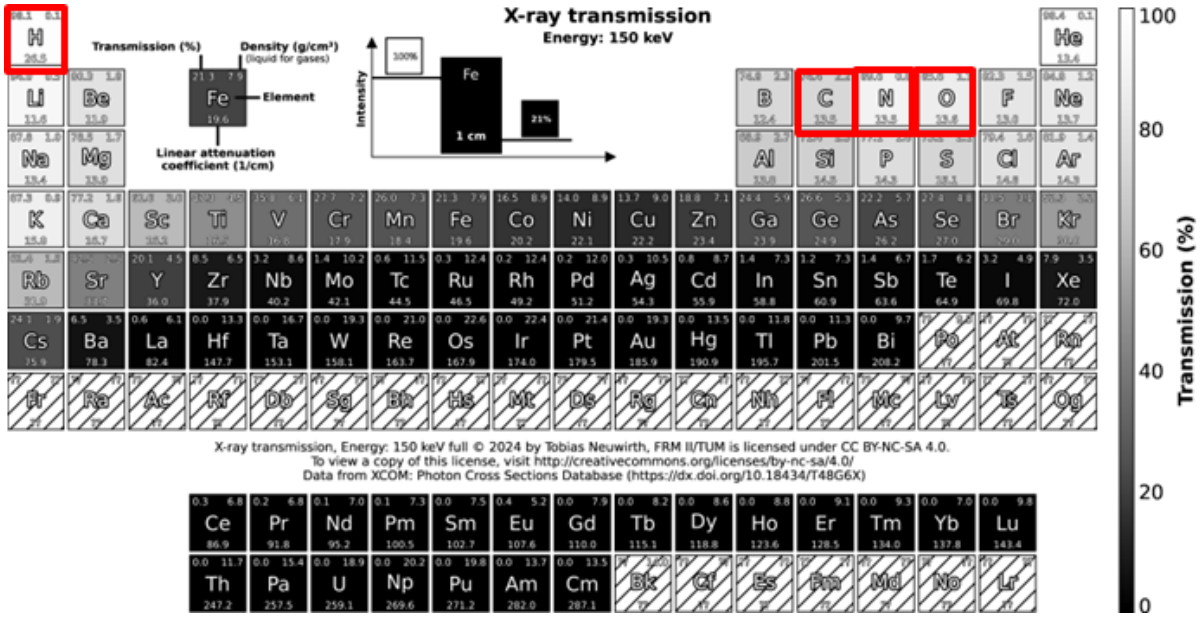

Figure 1: *Periodic table with X-ray transmission values for an energy of 150 keV. Black: high absorption, white: low absorption*

XCT is often used in the past to describe the microstructure of various materials and products. However, aiming for high resolution was always difficult. Newest generations of lab based XCTs overcome this deficit and allow high resolution measurements. While not only the spatial resolution of lab based XCTs increased also the power of such devices and thus the acquisition time is shortened. This results also in the possibility to investigate processes, such as freeze-drying. Freeze-drying is a gentle drying technique for high value products such as fruits, herbs and coffee. The process can mainly be separated in three steps. (1) The freezing step, here the actual

***Figure 2**: 3D-rendered illustration of the in-situ freeze-drying stage [3]*

microstructure of the final product can be formed. (2) The primary drying removes the ice out of the product by sublimation and is mainly controlled by heat and mass transport inside the porous structure. (3) The secondary drying is used to remove the bound water inside the matrix by desorption to get a stable product.

Freeze-drying typically happens by either drying the solid product or dispersing a solution into droplets or drying the solution by itself. While freeze-drying is still a very time and energy consuming process, it is still the aim to accelerate the process [1]. Here one important factor is the microstructure of the product [2]. In literature often the influence of the pore size is described and stated that bigger pores lead to a faster drying because of the lower mass transport resistance. However, other structural parameters such as pore shape and orientation are neglected.

In this presentation we want to demonstrate the power and limitations in X-Ray imaging for organic samples with freeze-drying of maltodextrin as an example. For that the UniTOM HR (Tescan XRE, Ghent, Belgium) was used as the XCT. This device allows spatial resolution up to 600 nm and temporal resolution down to 5s per 360° scans. As model substance maltodextrin was employed and samples with different solid concentrations (c=0.05 w/w up to 0.3 w/w) and freezing conditions (cooling rate and annealing treatment) were produced.

The samples where freeze-dried either as solutions or as particulate matter (see figure 3 and 4). For the in-situ measurements a custom-made freeze-drying stage was used (see figure 2). Here, different freezing protocols (different solid concentrations) are used to generate different microstructures. The freeze-drying occurred at various drying temperatures (-11, -15°C, and -33°C at 10 Pa). Continuous tomography is conducted during the experiment to observe the microstructural changes during freeze-drying. After the drying is completed, high-resolution scans are made for a more detailed microstructure visualization. All data (pore size, shape, and orientation) are analyzed by an in-house MATLAB and Python script.

The results show the power of XCT to analyze the microstructure during freeze-drying. Focus will be on microstructural changes over drying, even below critical temperatures. It will also be demonstrated that depending on the drying temperature, the changes in microstructure (pore size, shape, and orientation) are different [4,5]. Also limitations in terms of contrast will be demonstrated. In addition, samples with other conditions will be used for complementary information.

Overall, the presentation will show, why XCT is a powerful tool to study organic material and processes with some limitations.

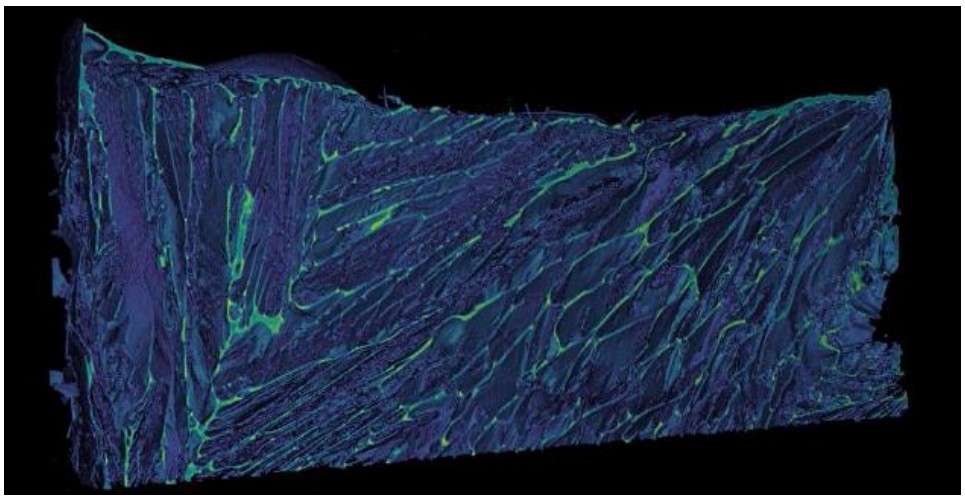

Figure 4: *3D-rendered visualization of a freeze-dried maltodextrin solution (annealing and c= 0.15 w/w)*

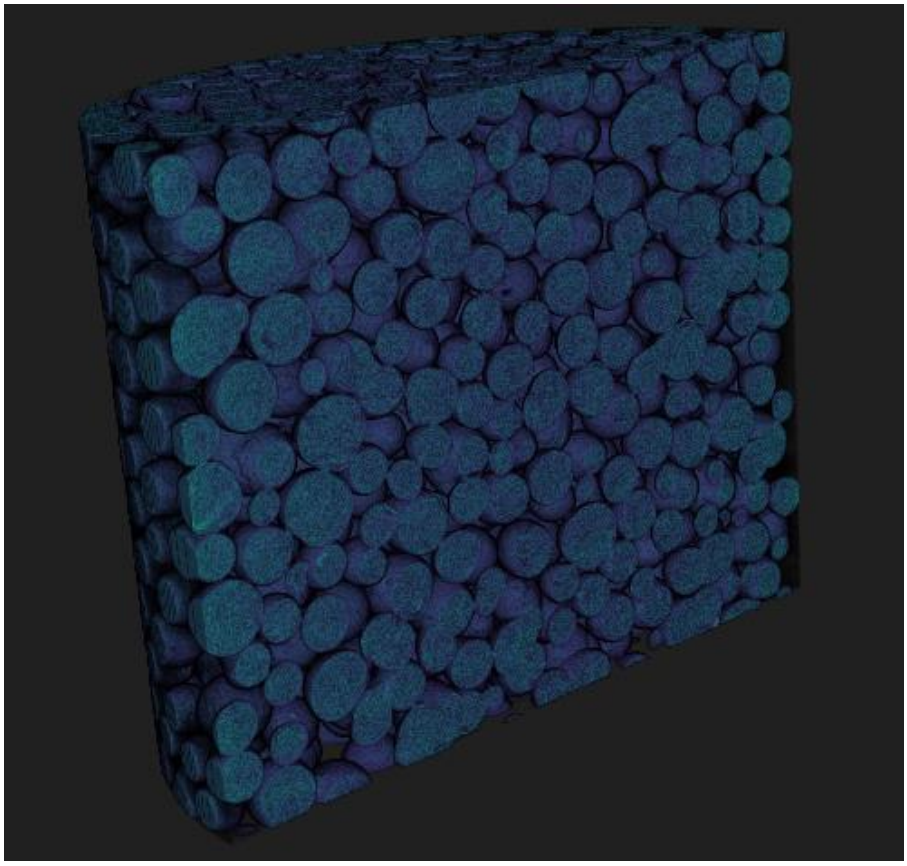

Figure 3: *3D-rendered visualization of freeze-dried maltodextrin particles (c= 0.2 w/w)*

Acknowledgments

This research was funded by the Deutsche Forschungsgemeinschaft (DFG, German Research Foundation)—413284489. This research made use of the XCT funded by the Deutsche Forschungsgemeinschaft (DFG-538007702). The authors would also like to thank Tescan XRE for offering free beam time at their DynaTOM system.

References

[1] Pikal, M.J. Freeze-Drying. In Encyclopedia of Pharmaceutical Technology, 3rd ed.; Swarbrick, J., Ed.; Informa Healthcare: New York, NY, USA, 2007; Volume 1, ISBN 0-8493-9396-5.

[2] Thomik,M.; Gruber, S.; Kaestner, A.; Foerst, P.; Tsotsas, E.; Vorhauer-Huget, N. Experimental Study of the Impact of Pore Structure on Drying Kinetics and Sublimation Front Patterns. Pharmaceutics 2022, 14, 1538.

[3] Hilmer, M., Gruber, S., & Foerst, P. (2020). Development of a Freeze-Drying Stage for In-Situ µ-CT Measurements. *Processes*, *8*(7), 869. https://doi.org/10.3390/pr8070869

[4] Gruber, S., Foerst, P., Thomik, M., Tsotsas, E., & Vorhauer-Huget, N. (2023). Pore Scale Investigation of Freeze-Drying. In E. F. Médici & A. D. Otero (Eds.), *Album of Porous Media* (p. 114). Springer International Publishing. https://doi.org/10.1007/978-3-031-23800-0_94

[5] Gruber, S., Greiner, J., Eppink, A., Thomik, M., Coppens, F., Vorhauer-Huget, N., Tsotsas, E., & Foerst, P. (2024). Pore shape matters - In-situ investigation of freeze-drying kinetics by 4D XCT methods. *Food Research International (Ottawa, Ont.)*, *193*, 114837. https://doi.org/10.1016/j.foodres.2024.114837

High-spatial-resolution Raman distributed temperature sensing system

J. López Bonilla[1*] and F. Beyrau[1]

[*]E-Mail: joel.lopez@ovgu.de

[1]*Institute of Fluid Dynamics and Thermodynamics, Otto von Guericke University Magdeburg, Universitätsplatz 2, 39106 Magdeburg, Germany*

Introduction

Understanding fluid temperature distribution in fluid-particle bulk systems is crucial for improving heat transfer models. A 2D or 3D spatial-temporal reconstruction of gas or liquid temperature within interstitial spaces reveals localized gradients that drive thermal and reaction heterogeneities. However, direct measurements in these complex environments require minimally intrusive methods. Conventional temperature sensors, such as thermocouples [1], provide high accuracy but suffer from different disadvantages, including sensitivity to radiation, potential catalytic effects and flow disruption due to extensive wiring.

Distribute temperature sensing (DTS) based on optical fibres offers a promising alternative, enabling continuous temperature measurements with minimal flow disruption. Rayleigh DTS [2] provides high spatial resolution but is highly sensitive to mechanical stress, often requiring rigid sheathing, which makes it impractical for measurements in complex geometries. In contrast, Raman DTS is less affected by mechanical stress, enabling flexible routing. However, to be viable for a fluid-particle bulk system, achieving high spatial resolution without compromising accuracy remains a challenge. Commercial systems offer 1 m resolution with 1°C accuracy [3], while recent advancements using special fibre materials [4] or advanced photodetectors [5] have improved this to sub-decimeter spatial resolution and sub-°C temperature resolution, though typically limited to fibres under 2 m. Achieving high spatial resolution with reliable accuracy over longer fibre lengths at an affordable cost remains a challenge.

This work presents a high-resolution Raman DTS system aimed to 3D temperature reconstruction in packed beds. Using a picosecond-pulsed green laser, avalanche photodiodes, and a gold-coated optical fibre, we achieved a spatial resolution and accuracy below 10 cm and <10 K, respectively, with reduced sensitivity to radiation effects and enabling measurements up to 600°C due to the gold-coating [6].

Experimental setup

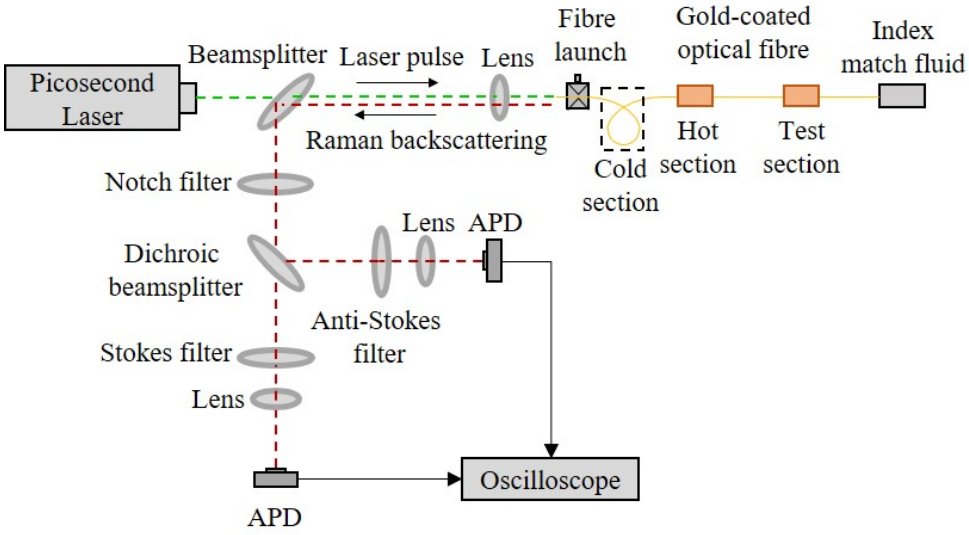

Figure 1. Optical setup for the Raman distributed temperature sensing system.

The optical setup for Raman distributed temperature sensing is shown in **Figure 1**. A picosecond-pulsed laser (532 nm, 20 ps pulse width, 100 kHz repetition rate) excites Raman scattering in a graded index multimode, gold-coated fibre (core: Ge-doped silica, 62.5 μm diameter; outer diameter: 155 μm). The 1.2 mm laser beam is focused by an aspherical lens and coupled into the fibre core using a 3-axis fibre launch. The backscattering is reflected by a beamsplitter (50:50) and filtered by a notch filter (532 nm, 17 nm bandwidth) to reject elastically scattered light. A dichroic beamsplitter (536 nm) separates Stokes (545 nm) and anti-Stokes (522 nm) shifts, which are further filtered using narrow bandpass filters. Two avalanche photodiodes (APDs, 1 GHz bandwidth) detect the Stokes and anti-Stokes scattering. The signals are recorded using a 2.5 GHz oscilloscope in fast frame acquisition mode.

The fibre is arranged in three sections. The cold section: 2 meters of the fibre isolated with foam rubber at room temperature (~24°C). Hot section: Fibre placed in a temperature-controlled heater set at 50°C. Test section: Fibre exposed to a temperature-controlled heat source at different temperatures. The cold and hot sections are used for calibration, while the test section is used to demonstrate the performance of the measurement system.

As the APD response time is comparable to the laser pulse width, impulse-induced oscillations appear in the measured signals. These are corrected using deconvolution in the frequency domain. The measured signals are deconvoluted by dividing their discrete Fourier transform (DFT) by the impulse response DFT, followed by an inverse Fourier transform. The deconvoluted Stokes ($I_{S(z)}$) and anti-Stokes ($I_{aS(z)}$) signals along the fibre (z) are used to determine the temperature profile via [6,7]:

$$T_{(z)} = \frac{\gamma}{\ln(C) - \ln(R_{(z)}) - \int_0^z \Delta\alpha \mathrm{zdz}} \tag{1}$$

where $R_{(z)} = I_{aS(z)}/I_{S(z)}$ is the Raman intensity ratio, $\Delta\alpha$ compensates the differential attenuation due to the wavelength differences, determined using the cold section, and the logarithm of C accounts for variations in filter transmission and APD response, calibrated using two fibre section at known temperatures (cold and hot section). The parameter γ can be determined experimentally or calculated as $\gamma = \frac{hc\Delta\nu}{k_B}$, where c is the speed of light, $\Delta\nu = 440\ cm^{-1}$ is the Raman shift for Ge-doped silica at 523 nm excitation, and h and k_B are the Planck's and Boltzmann's constant, respectively.

To demonstrate accuracy and spatial resolution, the test section was set to 6 temperatures between 24°C and 150°C. The heater length (6 cm) matches the expected spatial resolution of the system.

Results and discussion

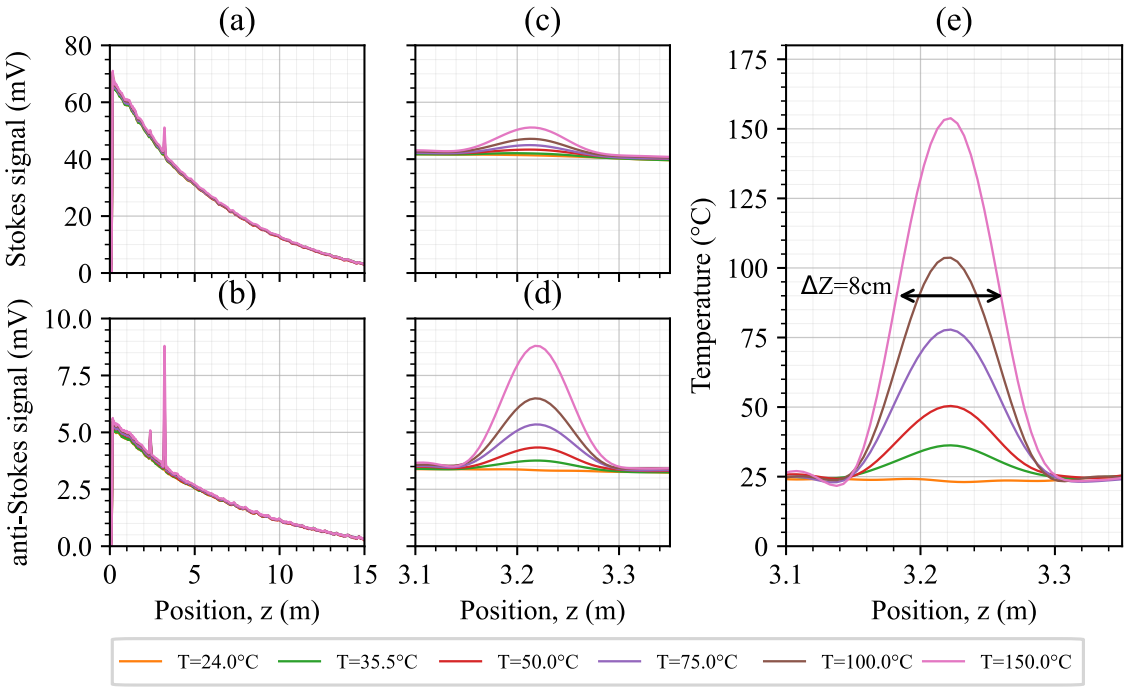

Figure 2. Deconvoluted Stokes (a) and anti-Stokes (b) signal along the first 15 m of the fibre. Stokes (c) and anti-Stokes (d) along the test section. Resultant temperature profile along the test section (e). Labels indicates the thermocouple readings inside the heater of the test section.

An initial experiment evaluates the spatial resolution and accuracy of the DTS system. **Figure 2 (a) and (b)** present the deconvoluted Stokes and anti-Stokes signals along the first 15 m of the fibre for different temperatures in the test section. A signal decay along the fibre with two temperature peaks is observed. The first peak correspond to the hot section (maintained at 50°C), while the second correspond to the test section, under six different temperatures ranging from room temperature to 150°C. As expected, the intensity of Stokes signal is stronger than the anti-Stokes signal. **Figure 2 (c) and (d)** show a detailed view of the temperature peak associated with the test section. The system successfully detects both signals, with anti-Stokes signal exhibiting higher temperature sensitivity.

Figure 2 (e) presents the resultant temperature profile based on the Raman intensity ratio and **Equation 1**. The labels indicates the thermocouple readings inside the heater of test section. The DTS temperature measurements align with the thermocouple readings, achieving an accuracy < 5°C for all cases. The spatial resolution is confirmed to be below 10 cm, with the temperature peak width measuring around 8 cm. This evaluation was performed at z=3.22 m, and further assessment is required along the first 15 m of the fibre, where signals remain detectable with the current system.

Conclusion

A Raman distributed temperature sensing system was developed to measure temperature gradients along the interstitial spaces in fluid-particle systems. High spatial resolution (<10 cm) and accuracy (<10 °C) were demonstrated in a controlled setup. Future work will focus on high temperature measurements and integrating the system into a pilot-scale reactor with uniform packing for investigation of heat transfer between gas and particles.

Acknowledgments

This work was funded by the Deutsche Forschungsgemeinschaft (DFG, German Research Foundation), Germany - Project ID 422037413 - TRR 287. The support and discussions with Ismail Laarossi and Fabian Reuter are also gratefully acknowledged.

References

[1] Wen, D., Ding, Y.: *Heat transfer of gas flow through a packed bed*, Chemical Engineering Science, 61(11), 3532–3542, 2006.

[2] Ahmed, Z., Jordan, C., Jain, P., Robb, K., Bindra, H., Eckels, S. J.: *Experimental investigation on the coolability of nuclear reactor debris beds using seawater*, International Journal of Heat and Mass Transfer, 184, 122347, 2022.

[3] Silva, L. C. B., Segatto, M. E. V., Castellani, C. E. S.: *Raman scattering-based distributed temperature sensors: A comprehensive literature review over the past 37 years and towards new avenues.*, Optical Fiber Technology, 74, 103091, 2022.

[4] Liu, X., Jie, R., Bera, S., Yan, T., Peng, W., Zhou, C., Rao, Y., Liu, B.: *High-speed and high-resolution YAG fiber based distributed high temperature sensing system empowered by a 2D image restoration algorithm.*, Optics Express, 31(4), 6170, 2023.

[5] Tanner, M. G., Dyer, S. D., Baek, B., Hadfield, R. H., Woo Nam, S.: *High-resolution single-mode fiber-optic distributed Raman sensor for absolute temperature measurement using superconducting nanowire single-photon detectors.*, Applied Physics Letters, 99(20), 2011.

[6] Laarossi, I., Ruiz-Lombera, R., Quintela, M. A., Mirapeix, J., Lima, D., Solana, D., Lopez-Higuera, J. M.: *Ultrahigh Temperature Raman-Based Distributed Optical Fiber Sensor with Gold-Coated Fiber*, IEEE Journal of Selected Topics in Quantum Electronics, 23(2), 296–301, 2017.

[7] Suárez, F., Aravena, J. E., Hausner, M. B., Childress, A. E., Tyler, S. W.: *Assessment of a vertical high-resolution distributed-temperature-sensing system in a shallow thermohaline environment*, Hydrology and Earth System Sciences, 15(3), 1081–1093, 2011.

The role of hydrogen flow rates in the direct reduction of iron ore pellets: Investigating external mass transfer limitations

M.L. Ali[1*], S. Fong[1], Q. Fradet[1] and U. Riedel[1]

*E-Mail: mohammed.ali@dlr.de

[1]*German Aerospace Center (DLR), Institute of Low-Carbon Industrial Processes, Äußere Oybiner Straße 14/16, 02763 Zittau, Germany*

Abstract

The successful transition to hydrogen-based direct reduction in ironmaking demands an in-depth comprehension of the complex reaction mechanisms and mass transfer dynamics at play. While high hydrogen flow rates in the reduction of single iron ore pellets are commonly used for mechanism development to neglect external mass transfer effects for simplification, this study critically examines the reduction behavior under low hydrogen flow conditions, where external mass transfer becomes significant, mirroring practical conditions more closely. Thermogravimetric analysis (TGA) experiments were conducted at 1073 K, 1173 K, and 1273 K, with H_2 flow-rates of 100 and 300 mL/min, revealing increased external mass transfer resistance at lower flow rates and higher temperatures. To numerically investigate this heterogeneous reacting system, a coupled 1D solid porous and 3D CFD modeling framework is employed, iteratively exchanging data of kinetic rates and gas concentrations at the pellet surface and validating the predictions against experimental data. This work advances reliable kinetic mechanisms for hydrogen-based reduction, addressing model scalability challenges.

Introduction

The steel industry is a substantial contributor to global CO_2 emissions, necessitating urgent decarbonization strategies aligned with climate goals. Hydrogen-based direct reduction (H_2-DR) offers a viable low-carbon alternative to conventional processes [1]. Single-pellet studies often neglect external mass transfer effects by using high flow rates [2]. While this simplifies modeling activities, relevance for industrial applications is limited, as real moving-bed systems exhibit localized flow effects, and steam, the inherent reaction product of the reduction, is abundantly present [3,4]. These conditions create mass transfer and chemical resistance, impacting the overall reduction rates and process efficiency. Models neglecting these effects will fail to predict furnace behavior at industrial-scales.

This study aims to develop a reliable kinetic mechanism for the reduction of single iron ore pellets under low H_2 flow-rates, explicitly addressing external mass transfer limitations. A 1D solid porous model [5] predicts reaction rates by solving mass conservation equations within the pellet, accounting for internal diffusion, porosity, and heterogeneous chemistry. A 3D CFD model [3] resolves gas flow and species concentrations throughout the pellet and reactor domain, resolving external mass transfer resistance. Through iterative data exchange, the coupled models ensure consistent and accurate kinetic predictions. The predictions of the coupled models will be validated against TGA-experiment results at various temperature and flow rates.

Experimental and Modeling Approach

Reduction experiments were conducted using a Linseis PT1600 TGA system on single DR-grade iron ore pellets (11.5 mm diameter, 27% porosity) in an H_2 atmosphere at 1073 K, 1173 K, and 1273 K, with flow rates of 100 and 300 mL/min. The setup featured a vertical furnace for uniform heating, an inert N_2 purge system to prevent oxidation, precise gas flow controllers, and a programmable temperature controller for accurate isothermal holds. The pellets were suspended on a quartz holder to ensure consistent gas exposure.

The H_2-DR modeling employed a 1D solid porous model and a 3D CFD model. The solid porous model was developed to circumvent the limitations of the traditional shrinking core model and its incompatibility with discretized CFD frameworks. The 1D model, assuming a spherical symmetry, solves the gas concentrations, the solid mass fractions, and the porosity across the pellet radius as a

function of time, capturing intrinsic reaction kinetics. However, since the 1D model considers only the pellet as the computational domain, it cannot resolve the external mass transfer. To address this, the 3D-CFD model was developed using a self-implemented solver in OpenFOAM, covering the entire reactor domain, including both the pellet and the surrounding gas flow. The models iteratively exchange information, with the 3D-CFD model providing external boundary conditions and the 1D model supplying reaction rates. Both models share governing equations for mass conservation, momentum conservation, species transport, and solid mass fraction evolution as shown in **Table 1**.

Table 1. Governing Equations in 1D and CFD models

1D	Gas concentration	$\frac{\partial C_i}{\partial t} = \frac{1}{\varepsilon}\nabla \cdot \left(D^{\text{eff}} \nabla C_i\right) + \frac{1}{\varepsilon}\dot{s}_i - \frac{C_i}{\varepsilon}\frac{\partial \varepsilon}{\partial t}$	(1)
1D/CFD	Solid mass fraction	$\frac{\partial X_j}{\partial t} = \frac{1}{1-\varepsilon}\frac{M_j}{\rho_j}\dot{s}_j + \frac{X_j}{1-\varepsilon}\frac{\partial \varepsilon}{\partial t}$	(2)
1D/CFD	Porosity	$\frac{\partial \varepsilon}{\partial t} = -\sum_j \frac{M_j}{\rho_j}\dot{s}_j$	(3)
CFD	Gas Continuity	$\frac{\partial \alpha_g \rho_g}{\partial t} + \nabla \cdot \left(\rho_g \mathbf{v}_g\right) = S_g$	(4)
CFD	Gas Momentum	$\frac{\partial \alpha_g \rho_g \mathbf{v}_g}{\partial t} + \nabla \cdot \left(\rho_g \mathbf{v}_g \mathbf{v}_g\right) = \nabla \cdot \bar{\bar{\tau}} - \nabla p + \rho_g \mathbf{g} + \mathbf{M}_{sg}$	(5)
CFD	Gas species transport	$\frac{\partial \alpha_g \rho_g Y_{g,i}}{\partial t} + \nabla \cdot \left(\rho_g Y_{g,i} \mathbf{v}_g\right) = -\nabla \cdot \mathbf{j}_{g,i}^{\text{eff}} + M_i \dot{\omega}_i + M_i s_i$	(6)

The gaseous reduction of iron ore occurs in the sequence: Fe_2O_3 (hematite) → Fe_3O_4 (magnetite) → FeO (wüstite) → Fe (metallic iron). The reactions in a pure hydrogen atmosphere above 840 K proceed as follows:

$$3\ Fe_2O_{3(s)} + H_{2(g)} \rightarrow 2\ Fe_3O_{4(s)} + H_2O_{(g)}, \quad (7)$$

$$Fe_3O_{4(s)} + H_{2(g)} \rightarrow 3\ FeO_{(s)} + H_2O_{(g)}, \quad (8)$$

$$FeO_{(s)} + H_{2(g)} \rightleftharpoons Fe_{(s)} + H_2O_{(g)}. \quad (9)$$

The backward reaction of equations (7) and (8) have been omitted, but not for equation (9), as the reverse rate is supposedly non-negligible.

Results and Discussions

The main evaluation criterion for model validation is the global conversion degree *F*, given by:

$$F = \frac{m_0 - m(t)}{m_0 - m_\infty}. \quad (10)$$

Here, m_0 represents the initial mass of the pellet, $m(t)$ is the mass at a given time *t*, and m_∞ corresponds to the theoretical mass after complete reduction. The value of *F* ranges from 0, indicating no conversion (Fe_2O_3 and gangue), to 1, indicting complete conversion (Fe and gangue).

Figure 1 demonstrates the effect of H_2 flow rates on the reduction kinetics of single iron ore pellets at various temperatures. **Figure 1** (a-c) show the conversion degree of the TGA experiments at 1073 K, 1173 K, and 1273 K, respectively. Higher flow rates (300 mL/min) consistently lead to a faster reduction. **Figure 1** (e) represents the TGA device arrangement and the gas flow dynamics around the pellet obtained by the CFD simulation. A close-up view at 300 seconds of the hydrogen mole fraction contour is given in **Figure 1** (d) for the two tested gas flow rate, 100 and 300 mL/min. The H_2 concentration in the gas phase is lower for the 100 mL/min flow rate due to greater external transport limitations. In addition, the concentration of hydrogen inside the pellet is also lower, which decrease the forward reduction rates and increase the rate of the reverse reaction between iron and wüstite. An inflection point is clearly visible in the experiments using 100 mL/min at around 30% conversion, which corresponds to the reduction from up to wüstite. After this point, the global conversion is controlled mostly by the equilibrium reaction (9) and by the flushing rate of water out of the pellet and subsequently out of the reactor. Only at the final reduction stage, where oxides near the pellet surface are depleted, does the system transition to a diffusion-controlled regime.

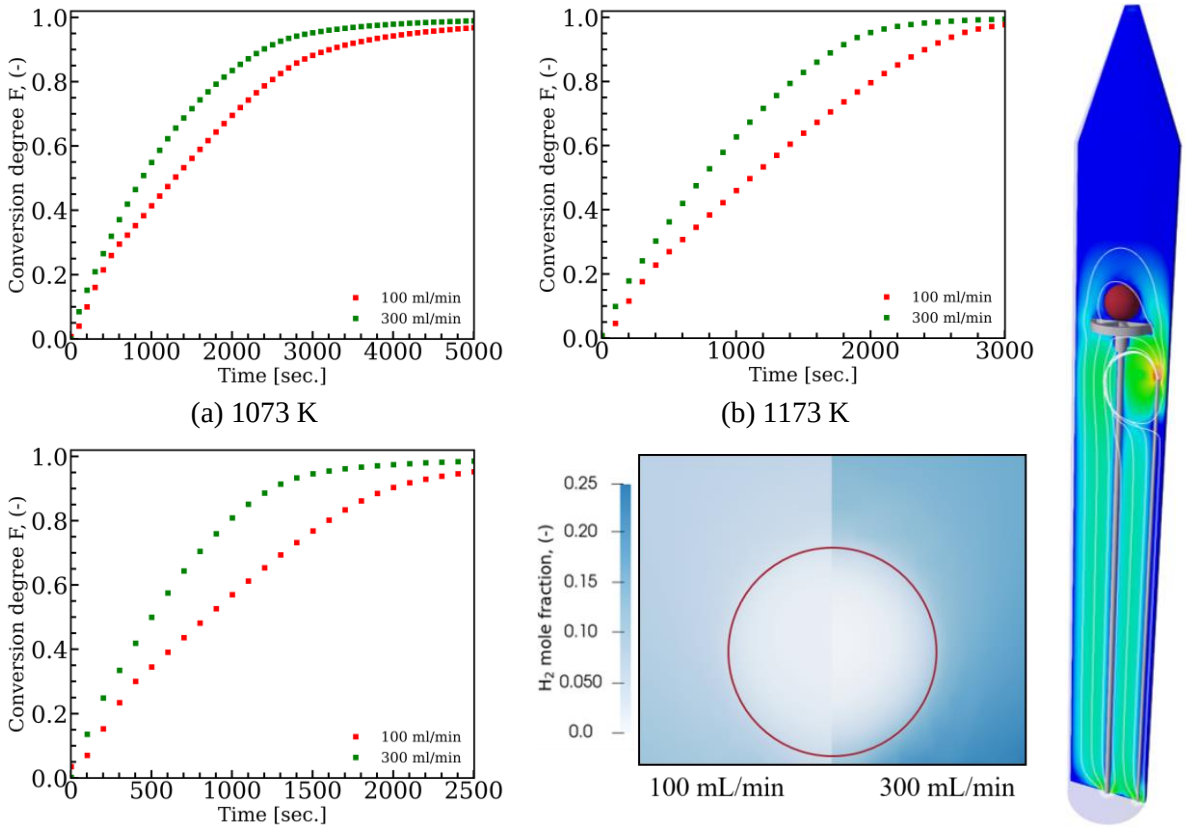

Figure 1. (a-c) Overall conversion degree over time for two flow rates and three different temperatures. (d) Contour plot of H_2 mole fraction inside and around the pellet at 1173 K at flow rates of 100 mL/min (left) and 300 mL/min (right). (e) CFD simulation showing velocity gradient and streamlines around a single iron ore pellet in the TGA furnace.

As previously described, the reduction process involves a complex interplay between flow field, internal diffusion, and reaction kinetics. The experimental and numerical methodology conducted here will allow to decouple all these effects. The next step is to forward the boundary condition information, as exemplary given in **Figure 1** (d), to the 1D model. The use of various temperatures and H_2/H_2O ratios at the boundary, while keeping other parameters (such as the pellet properties) constant, will allow to accurately determine kinetic parameters of both forward and backward reduction reactions. Such a robust kinetic mechanism is a pre-requisite to CFD simulations of multiple pellet cases.

Acknowledgements

We acknowledge funding by the European Union and by tax revenues on the basis of the budget adopted by the Saxon State Parliament. European Regional Development Fund (EFRE) project "BioFe - Biomassenutzung in der Eisenerzeugung unter wirtschaftlichen und CO_2-mindernden Randbedingungen".

References

[1] World Economic Forum. *Which technologies will enable a cleaner steel industry?* Available from: https://www.weforum.org/stories/2024/04/technologies-cleaner-steel-industry/, 2024.

[2] Kazemi M., Pour M., Sichen D.: *Experimental and Modeling Study on Reduction of Hematite Pellets by Hydrogen Gas*, Metall. Mater. Trans. B, 48, 2, 2017.

[3] Ali M. L., Fradet Q., Riedel U.: *Particle-resolved computational modeling of hydrogen-based direct reduction of iron ore pellets in a fixed bed. Part I: Methodology and validation*, International Journal of Hydrogen Energy, 87, 2024.

[4] Ali M. L., Mehlhose S., Fradet Q., Riedel U.: *Particle-resolved computational modeling of hydrogen-based direct reduction of iron ore pellets in a fixed bed. Part II: Influence of the pellet sizes and shapes*, International Journal of Hydrogen Energy, 86, 2024.

[5] Fradet Q., Ali M. L., Riedel U.: *Development of a Porous Solid Model for the Direct Reduction of Iron Ore Pellets*, Steel Research International, 93, 12, 2022.

CFD-DEM Investigation of Agglomeration Effects in Iron Powder Reduction

J.G. Ramírez[1], Y. Tang[2,3], M. van Sint Annaland[1,3], N.G. Deen[2,3], and I. Roghair[1,3*]

[*]E-Mail: i.roghair@tue.nl

[1]*Chemical Process Intensification, Department of Chemical Engineering & Chemistry, Eindhoven University of Technology, Eindhoven, the Netherlands*

[2]*Power and Flow Group, Department of Mechanical Engineering, Eindhoven University of Technology, Eindhoven, the Netherlands*

[3]*Eindhoven Institute for Renewable Energy Systems (EIRES), Eindhoven University of Technology, Eindhoven, the Netherlands*

Abstract

Iron powders represent a promising carbon-neutral energy carrier, offering benefits such as easy transport and storage, and high energy density. After releasing energy through oxidation, the iron must be regenerated (reduced), ideally using renewable energy sources like green hydrogen. However, this reduction process, commonly performed in high-temperature fluidized beds is hindered by particle agglomeration due to sintering. Using a Computational Fluid Dynamics–Discrete Element Method (CFD-DEM) approach, this research aims to understand how agglomeration impacts the efficiency of the reduction process. Given the small particle size of iron powders (~30-50 μm), the model employs a coarse-graining technique. Chemical reduction is represented using a well-known shrinking core model, while sintering is modeled with a solid bridge force based on surface diffusion mechanisms. The results indicate that under typical conditions, agglomeration can reduce the degree of reduction by around 40%. We propose strategies to mitigate this effect, such as integrating inert particles or alternative fluidized bed configurations.

Introduction

In recent years, global warming and the depletion of fossil fuels have accelerated the development of alternative carbon-neutral fuels, being green hydrogen one of the most attractive alternatives. Despite its potential, challenges related to transportation and high flammability pose significant drawbacks. A promising alternative is the use of metal powders. In particular, iron powders, which is the focus of this research, can be used and recycled in a oxidation-reduction cycle. Metal powders offer additional advantages, such as higher energy capacity per cubic meter compared to other energy carriers and the involvement of hydrogen as the reducing agent [1]. This reduction, that normally takes place in fluidized beds at high temperatures, is still sensitive to further optimization. One of the biggest challenges is particle agglomeration due to sintering. This numerical study focuses on understanding the effect of agglomeration on the reduction process yield and the effectiveness of potential countermeasures.

Given the particle-scale nature of the agglomeration process, a Computational Fluid Dynamics–Discrete Element Method (CFD-DEM) approach was chosen. This method tracks each particle's interaction with the gas phase and with the other particles in the system. Two key features of the model are particularly important. First, the way to compute the chemical reduction from iron oxides (Fe_xO_y) to iron (Fe). For fully oxidated iron powder, the reduction process follows a high-temperature pathway (T > 570°C) starting from hematite (Fe_2O_3) which is reduced first to magnetite (F_3O_4), subsequently to wünstite (FeO) and finally to iron. At lower temperatures, magnetite is reduced directly to iron without the formation of wünstite [2]. In our model, this reaction pathway is represented using the shrinking core model approach described by Kinaci et al. [2], where the particle is composed of concentric layers representing different reduction stages. The second important feature is the modeling of sintering between particles. The sintering mechanism governs the rate at which the solid bridge grows between particles. Kuczynski [3] found experimentally that, for iron powders, the early stage of sintering is governed by surface diffusion.

The implementation of this mechanism is explained below.

Numerical Methods

Our model incorporates features commonly found in CFD-DEM techniques for the simulation of fluidized beds, including particle collisions, and the inter-phase transfer and conservation of mass, momentum, heat and species concentration [4]. However, three key aspects are critical for accurately modeling iron powder reduction. First, the use of a coarse graining approach is crucial, due to the small size of the iron powders (~30-50 μm). Second, a shrinking core model that represents the multiple oxidation states of iron and the way hydrogen diffuses through these layers followed by chemical reactions is needed to track the reduction dynamically [2]. Figure 1a shows a circuit analogy of the mass transfer resistances encountered by hydrogen during reduction. Finally, a sintering model is implemented based on the surface diffusion of iron atoms, which move from the particles to form solid bridges. Figure 1b presents a sketch of the solid bridge force ($F_{sb,ij}$) and the time-dependence growth of the neck size considered here.

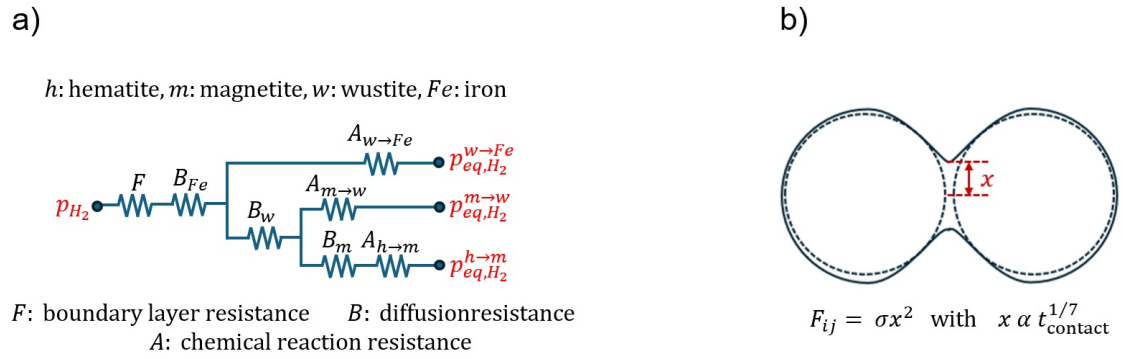

Figure 1. Sketches of the models used. a) Circuit representation of the resistances considered in the reduction shrinking core model. (Taken from Kinaci et al. [2]. b) Sintering force between two particles.

Preliminary results

Figure 2 presents snapshots of the fluidized bed with and without particle sintering. The particles are colored according to velocity magnitude, clearly showing that with sintering the particles quickly (t = 0.5 s) form a packed immobile structure. This behavior is expected to substantially reduce the interaction with the gas phase, as evidenced in the reduction yield comparison in Figure 3. From the very beginning the sintering slows the reduction rate, and the difference between sintered and non-sintered cases increase over time. Figures 2 and 3 also present the effect of using inert particles (glass beds of 37.5 μm diameter) as a countermeasure for sintering. Figure 2c shows that despite the formation of dark blue regions representing sintered particles, there is still a significant particle movement in the bed. The intermediate nature of the bed, lying between the behaviors of Figures 2a and 2b, is also evident in the reduced fraction predicted with inert particles in Figure 3, which consistently falls between the predictions for a fluidized bed with and without particle sintering. It is our current work a better characterization on how the use of inert particles helps to prevent the agglomerative nature of the reduction process as well as the effect of operational conditions.

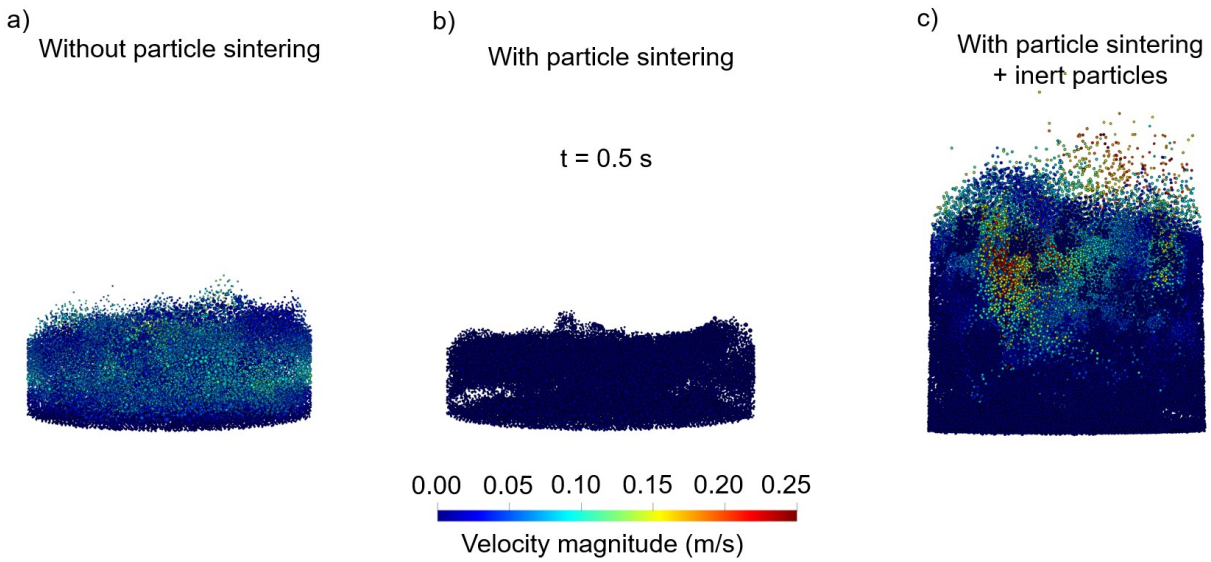

Figure 2. Snapshots of the fluidized bed when particle sintering is a) neglected, b) considered and c) with the addition of inert particles.

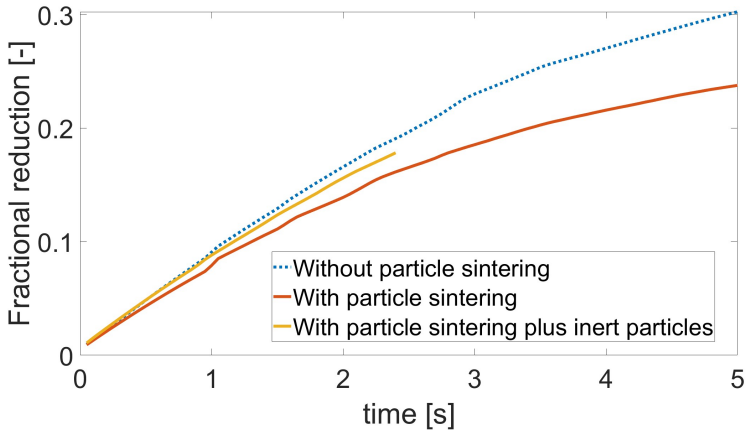

Figure 3. Average fractional reduction as a function of time.

References

[1] Liu, X., Hessels, C.J.M., Deen, N.G., Tang, Y.: *CFD-DEM investigation on the agglomeration behavior of micron-sized combusted iron fines.*, Fuel, 346,128319 2023.

[2] Kinaci M.E., Lichtenegger, T., Schneiderbauer, S.: *A CFD-DEM model for the simulation of direct reduction of iron-ore in fluidized beds*, Chemical Engineering Science, 227, 2020.

[3] Kuczynski, G. C.: *Self-diffusion in sintering of metallic particles.*, In S. Somiya & Y. Moriyoshi (Eds.), Sintering Key papers., pp. 509–527, 1990.

[4] de Munck M.J.A., Peters E.A.J.F., Kuipers J.A.M.: *CFD-DEM modeling and validation of solids drying in a gas-fluidized bed*, Chemical Engineering Science, 291, 2024.

Experimental and Numerical Investigation of Iron Ores in Conditions Relevant to Hydrogen-based Direct Reduction for Green Steelmaking

S. la Manna[1*], K. Qyteti[2], D. Barletta[1], E. Illana[2], S. Z. Ajabshir[1], V. Scherer[2] and M. Poletto[1]

*slamanna@unisa.it

[1] *Department of Industrial Engineering, University of Salerno, Via Giovanni Paolo II, 132, 84084 Fisciano, SA, Italy*

[2] *Department of Energy Plant Technology, Ruhr-University Bochum, Universitätsstraße 150, 44780 Bochum, Germany*

Introduction

The European Union is committed to reducing environmental impact through innovative technological advancements, including the transition to greener steel production using hydrogen for the direct reduction (DR) of iron oxides. This shift requires a thorough understanding of the behaviour of raw materials, particularly iron oxide pellets, which are fed counter currently with hydrogen in a shaft furnace [1]. The reaction involves elevated temperatures, up to a maximum of 950°C [2], significant compressive stresses, and the presence of a solid phase, necessitating a detailed study of the flow properties of the pellets. This understanding is crucial to predict and prevent undesirable effects such as aggregate formation, which can impede the normal gravitational motion of the pellets during reduction.

Experimental setup

To address this need, the University of Salerno has developed the Reacting High Temperature - Shear Tester (RHT-ST), an apparatus capable of replicating the high-temperature, higher than 1000°C, and high-compressive stress conditions found in shaft furnaces, up to 800kPa. The RHT-ST allows for analysing stress distribution and variation during the reduction phase, providing valuable data on compressive stress, shear stress, and sample density over time. The device includes a rotating trough and a vanned lid. With powders, the use of the vanes is needed to make a plane of shear in a given depth of the sample enabling the creation of a correlation between normal and shear stress, from which extrapolate characterisation parameters for particulate solids, such as the angle of internal friction and the angle of wall friction.

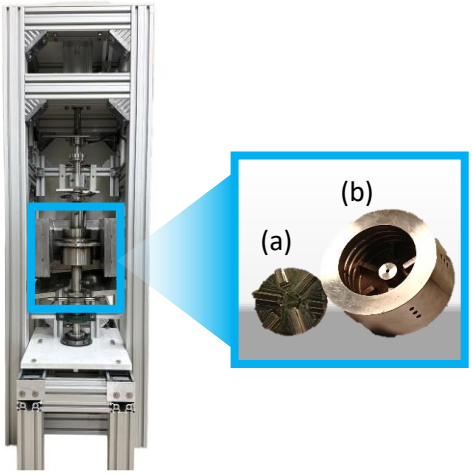

Figure 1. The design of the RHT-ST apparatus is reported on the left, the blue box shows the li (a) and trough (b).

The material examined in this study consists of iron ore pellets, primarily composed of hematite and coated with calcium carbonate, with sizes from 10 to 15 mm and an average aspect ratio of 1.13.

Using rotational shear testers, technologies and procedures [3] based on Jenike's frictional theory are effective for predicting flow properties of small particles [4]. However, for coarse particles such as the iron ore pellet to be tested, this approach is inadequate, leading to the failure of traditional methods and standard analyses.

To address this limitation, the flow properties of particles were observed using the RHT-ST by adapting the procedure to account for the average sample dimension. During the test, particles were subjected to constant vertical compression and step increases to change the compression level. The torque required to maintain the trough's rotation at an angular speed of 0.0015 rpm was recorded during the tests. The experimental results for three temperatures (25°C, 200°C, and 300°C) and fixed compressive steps (100, 200, 300, and 400 kPa) are presented in Figure 3.

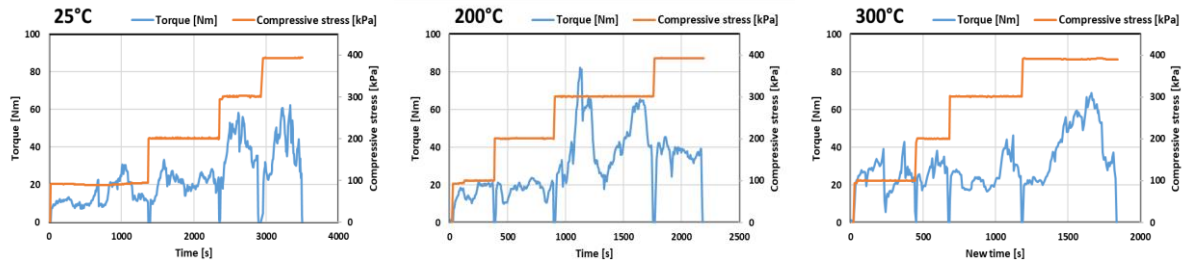

Figure 2. Experimental data recorded for the three temperatures investigated: the compressive stress applied in orange, and the torque measured in blue.

Despite the RHT-ST's capabilities, its limited trough volume and the particles size significantly impacts the measured torque due to the force chain, causing strong oscillations [5]. A preliminary analysis indicates that the torque required to ensure trough rotation increases with rising temperature, particularly at low compression stresses, while the amplitude of oscillations decreases with increasing temperature.

DEM/CFD Simulations

DEM/CFD simulations, which incorporate cohesion and reduction, effectively model the flow behaviour and cohesion of iron oxide pellets. These simulations are essential for understanding the flow properties of the pellets as they undergo reduction, particularly stress distribution and variation in the solid phase. The DEM-CFD coupling routines available combine the Discrete Element Method (DEM) with Computational Fluid Dynamics (CFD), creating a dual simulation framework.

DEM describes individual particle motion, including forces and contacts, solving simplified Newton's laws and Euler's equations in real-time [6]. In the case of a simultaneous gas flow, the drag forces formed by the relative velocity must be added to these sums.

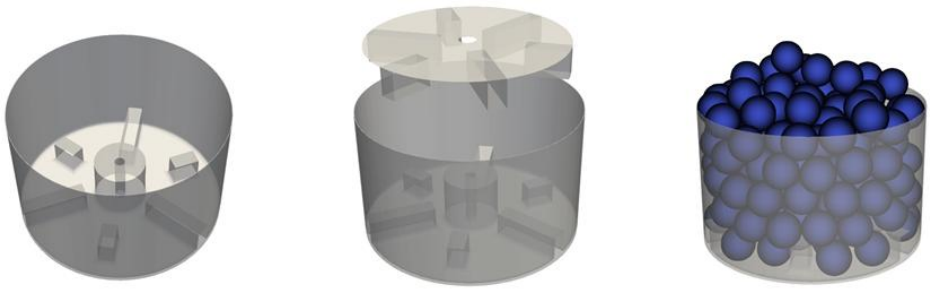

Figure 3. DEM Simulation of the experimental device (RHT-ST apparatus) with iron ores modelled as simple spheres

On the CFD side, the routine leverages the capabilities of OpenFOAM, a computational fluid dynamics platform. It excels in simulating fluid flow, as well as the transport of energy and species within the fluid domain. The integration of OpenFOAM enhances the applicability of fluid dynamics simulations for the intended use, providing an understanding of the complex interplay between simultaneously moving and reacting fluid and solid phases.

The code is fully parallelized on the DEM and CFD side in order to limit the computing times despite the unavoidable large computational effort. The coupling of the two software packages leads to DEM/CFD, where the two programs exchange data such as bulk material porosity and particle-resolved momentum transfer (from DEM to CFD) or gas phase velocity and flow resistance (from CFD to DEM).

Conclusions

The DEM/CFD model is essential for designing and validating equipment (such as RHT-ST) that support a greener steelmaking transition. By accurately simulating the motion of iron oxides during reduction, the model enables prediction and mitigation of potential process issues, contributing to the development of more sustainable steel production. The combined use of the RHT-ST apparatus and DEM/CFD simulations provides a powerful approach for investigating the behaviour of iron oxide pellets during reduction. This research is crucial for advancing green steelmaking technologies, aligning with European Union environmental targets, and fostering a more sustainable future.

Acknowledgements

The work in the paper was developed within project "Maximise H2 Enrichment in Direct Reduction Shaft Furnaces" (Ref. MaxH2DR), GA No.101058429, that received funding from Horizon Europe EU framework programme, which is gratefully acknowledged. Sole responsibility of issues treated in the paper lies with the authors; the Commission is not responsible for any use that may be made of the information contained therein.

References

[1] X. Jiang, L. Wang, and F. M. Shen, "Shaft Furnace Direct Reduction Technology - Midrex and Energiron," *Adv Mat Res*, vol. 805–806, pp. 654–659, 2013, doi: 10.4028/WWW.SCIENTIFIC.NET/AMR.805-806.654.

[2] J. Immonen and K. M. Powell, "Dynamic modeling of a direct reduced iron shaft furnace to enable pathways towards decarbonized steel production," *Chem Eng Sci*, vol. 300, p. 120637, Dec. 2024, doi: 10.1016/J.CES.2024.120637.

[3] A. W. Jenike, "Storage and flow of solids. Bulletin No. 123; Vol. 53, No. 26, November 1964," Nov. 1976, doi: 10.2172/5240257.

[4] "Test Method for Bulk Solids Using Schulze Ring Shear Tester," Oct. 2008, doi: 10.1520/D6773-08.

[5] W. Zhang, S. Zhang, J. Tan, J. Du, and N. Zhang, "Investigation on the friction mechanism and its relation to the force chains during powder compaction," *J Physical Soc Japan*, vol. 89, no. 12, Dec. 2020, doi: 10.7566/JPSJ.89.124602.

[6] H. Kruggel-Emden, "Analysis and Improvement of the Time-Driven Discrete Element Method," *Berichte aus der Energietechnik, Shaker Verlag,* Aachen, 2008, ISBN: 978-3-8322-6853-4

Development of a conversion model for the hydrogen reduction of iron ore based on single-pellet experiments

F. An[1*], F. Küster[1], M. Gallwitz[2], S. Guhl[1], M. Gräbner[1,2], G. , Herz[2] and A. Richter[1,2]

*E-Mail: fengbo.an@iec.tu-freiberg.de

[1] Institute of Energy Process Engineering and Chemical Engineering, TU Bergakademie Freiberg, Fuchsmühlenweg 9, 09599 Freiberg, Germany

[2] Fraunhofer Institute for Ceramic Technologies and Systems, Winterbergstr. 28, 01277 Dresden, Germany

Abstract

This study aims to develop a conversion model for the hydrogen direct reduction (H2DR) of the single iron ore pellet. The model's feasibility is evaluated based on experimental data. The goal is to apply this model to simulate hydrogen-based shaft furnaces, integrating kinetics and pellet properties into the conversion behavior. This study lays the foundation for developing a single-pellet conversion model to describe the hydrogen-based shaft furnace reaction process, based on experimental data, including thermogravimetric analysis (TGA), pellet temperature, and shape. These experimental observations can guide the development of a more accurate reduction model for pellets in a hydrogen atmosphere [1]. Computational Fluid Dynamics (CFD) is a powerful tool for incorporating these factors into a comprehensive model. By validating the conversion model against experimental results, CFD simulations can ensure a more precise understanding of the reduction process, allowing for better optimization and scaling of hydrogen-based direct reduction technologies.

Introduction

The HITECOM reactor at TU Bergakademie Freiberg is used to investigate the conversion process of isolated particle under defined gas velocities and temperatures. In previous work, the conversion processes of carbonaceous materials were observed using the HITECOM reactor, leading to the development of both the reactor and single-pellet conversion models [2]. In the field of direct reduction of iron ore pellet, the HITECOM reactor allows for the simultaneous measurement of pellet mass and temperature changes during the reduction process. A CFD model was also used to digitize this process, successfully validating the particle surface temperature under the influence of endothermic reactions and establishing a heat transfer model for the particle reaction process [3]. Building upon this, conducting experiments on the same raw materials at different temperatures and correlating the pellet reaction rate with particle temperature and reaction kinetics holds great potential for further advancements.

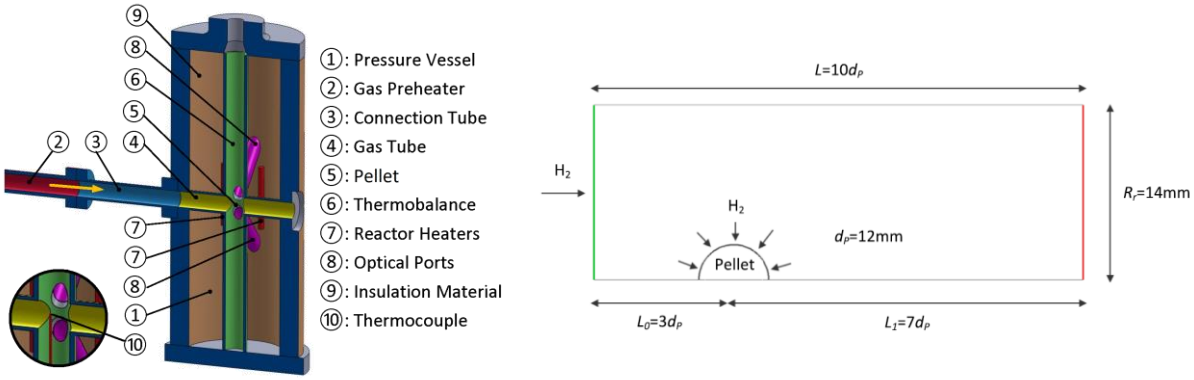

Figure 1. Geometry of the HITECOM reactor (left) and calculating domain (right).

The HITECOM reactor can operate at temperatures up to 1400 °C and pressures up to 40 bar. A schematic representation of the HITECOM reactor is shown in Figure 1 (left). The experimental setup consists of a water-cooled pressure vessel. The ceramic flow tube is horizontally positioned in the center of the reactor, while a vertical tube contains the particle fixation and thermobalance and is connected to the gas flow tube. The experiment was conducted under defined boundary conditions. The process gas used consisted of 100% H2. The operating pressure was maintained constant at 1 bar, while the gas flow velocity was set at 0.5 m/s. The iron carriers used had a particle size ranging from 8 to 12 mm, and the average particle mass was 2850 ± 50 mg to ensure homogeneous initial conditions.

Numerical Setup

In this model, a single spherical pellet of diameter d_p is placed in a large area, as shown in Figure 1 (right). For the axisymmetric 2D simulations the length upstream $L_0 = 3d_p$, the length downstream $L_1 = 7d_p$, and the radius of the reaction tube R_r = 14 mm is based on the HITECOM reactor. The properties of the gas phase are modelled using kinetic theory or polynomial expressions, assuming that the mixture behaves like an ideal incompressible gas. The chemical system consists of Fe_2O_3 as solid species and H_2, H_2O and N_2 as gaseous substances. ANSYS Fluent™ is used to solve the Navier-Stokes equations and the equations for mass and energy transport. Second-order schemes are used to discretize the differential equations in space. The number of grid cells used is about 23,000. The grid independence has already been confirmed in related investigations. The operating conditions, including temperature, composition and operating pressure of the gas phase, are taken from the experimental data.

Figure 2 (left) shows the temperature decrease within the pellet during the reduction reaction at different temperatures. The overall trend of the temperature distribution is similar at all temperatures, with the temperature gradually decreasing from the interior of the pellet towards its surface, influenced by the gas flow. Since the reduction of the pellet by hydrogen is an endothermic reaction, the pellet absorbs heat from the surrounding environment during the process, resulting in a temperature lower than the ambient temperature. Under these conditions, the area affected by the reduction reaction extends approximately half a pellet diameter upstream and one pellet diameter downstream. As the temperature increases, the reaction rate also rises, leading to a more significant temperature drop within the pellet. At 800 °C, the temperature drop is about 6 K, while at 1100 °C, the temperature drop increases to 15 K.

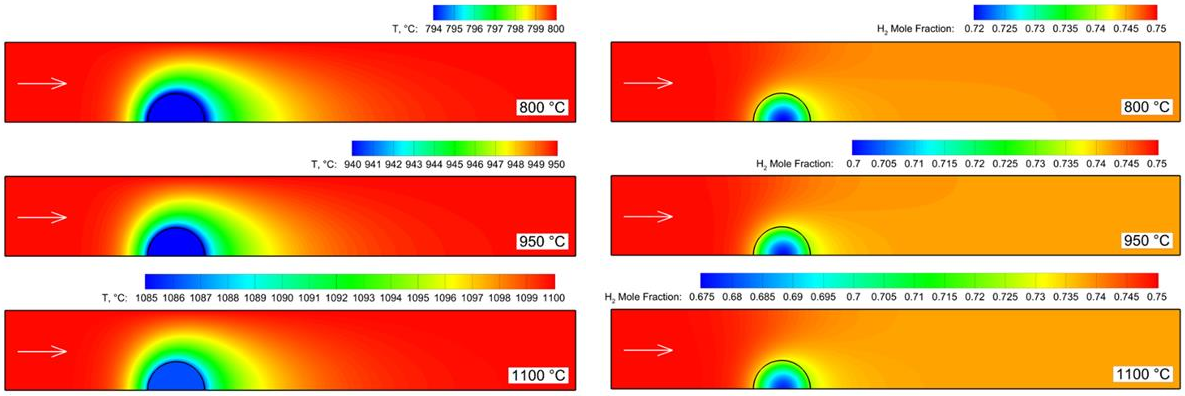

Figure 2. Distribution under different operating temperatures, Temperature (left) and H_2 mole fraction (right).

Figure 2 (right) shows the distribution of the H_2 mole fraction around and within the pellet during the reduction process. The distribution of the H_2 mole fraction remains similar across different temperatures, with the mole fraction set at 0.75 at the gas inlet. As the gas passes through the reacting pellet, the H_2 mole fraction gradually decreases, reaching its minimum at the outlet. At an operating temperature of 800 °C, the hydrogen mole fraction at the pellet surface is approximately 0.74. As the temperature increases, the surface mole fraction decreases, reaching 0.72 at 1100 °C. The central region of the pellet exhibits the lowest hydrogen mole fraction, dropping from 0.72 to 0.67.

The reaction rate inside the pellet is influenced by the partial pressure of the reacting gas and the reaction temperature. Due to the limitations in heat and mass transfer both inside and outside the pellet, the reaction rate is not uniform throughout the pellet. The surface reaction rate is higher than that in the core region due to the higher concentration of the reacting gas and the elevated temperature. Figure 3 illustrates the reaction rate distribution within the pellet at different temperatures. At 800 °C, the reaction rate ranges from 0.062 1/s m² to 0.064 1/s m². At this lower temperature, heat and mass transfer limitations are minimal. However, at 1100 °C, the reaction rate at the pellet surface increases to 0.18 1/s m², while the core region experiences a slightly lower rate of 0.165 1/s m², with a difference of about 10%.

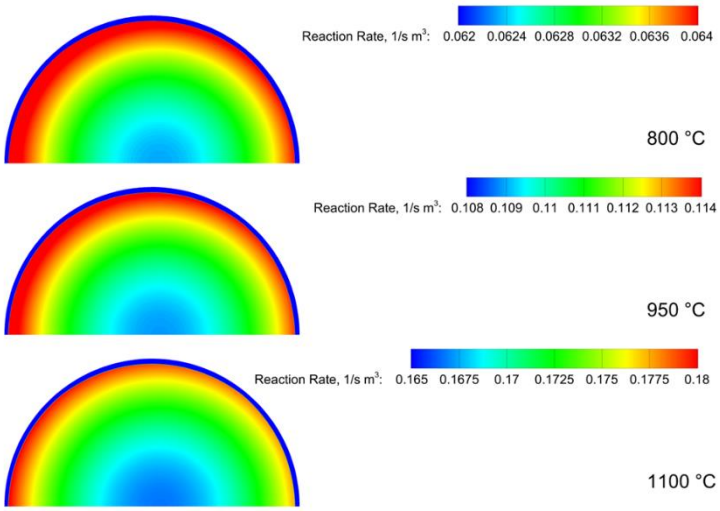

Figure 3. Reaction rate in the pellet under different operating temperatures.

Conclusion

This study presents an CFD-analysis of the reduction process of iron ore pellet in the HITECOM reactor, focusing on the heat and mass transfer within the pellet. The results indicate that the reduction reaction, being endothermic, leads to a temperature drop within the pellet due to the heat transfer limitation. The H_2 mole fraction decreases in the central region of the pellet, which results in a lower concentration of the reactant gas at the pellet surface compared to the set conditions in the reactor. Under these circumstances, where both the reaction temperature and partial pressure are significantly lower than the set values, the calculated reaction kinetics are underestimated. Therefore, a detailed heat and mass transfer analysis is necessary for each experimental point to determine the reaction temperature and concentration at different locations within the pellet. This will allow for the correction of the kinetic calculations under these conditions. These findings contribute to the understanding of pellet behavior during hydrogen direct reduction and provide valuable insights for developing more accurate models for the hydrogen-based reduction process, particularly in the context of shaft furnace simulations.

References

[1] R. Béchara, H. Hamadeh, O. Mirgaux and F. Patisson. *Optimization of the Iron Ore Direct Reduction Process through Multiscale Process Modeling*. Materials, 11: 7, 2018.

[2] F. An, F. Küster, R. Ackermann, S. Guhl and A. Richter. *Heat and mass transfer analysis of a high-pressure TGA with defined gas flow for single-particle studies*. Chemical Engineering Journal, 411: 128503, 2021.

[3] F. Küster, C. Scharm, F. An, M. Reinmöller, O. Volkova, A. Richter, S. Guhl and M. Gräbner. *Direct reduction of iron ore pellets by N2/H2 mixture: In-situ investigation and modelling of the surface temperature during reduction progression*. Minerals Engineering, 215: 108827, 2024.

Cross-Code Comparison of Carrier-Phase DNS of Turbulent Iron Particle Cloud Combustion

P. Ghofrani[1*], T.D. Luu[2], O.T. Stein[2], and A. Kempf[1]

*E-Mail: parsa.ghofrani@uni-due.de

[1] Chair of Fluid Dynamics, Institute for Energy and Materials Processes, University of Duisburg–Essen, Germany
[2] Engler-Bunte-Institut, Simulation of Reacting Thermo-Fluid Systems, Karlsruhe Institute for Technology, Germany

Introduction

Iron particle cloud combustion, presents a promising pathway for energy storage and utilization, yet its underlying physics remains poorly understood due to the complex interplay of turbulent flow dynamics and non-volatile heterogeneous combustion behavior. Direct numerical simulations (DNS) play an important role in understanding these multiphase interactions. However, a particle-resolving DNS of such systems is not feasible for cases with many particles due to the high computational cost of resolving the particle boundary layers. Therefore, the carrier-phase direct numerical simulation (CP-DNS) approach is used, which applies a point-particle assumption for the dispersed phase and models the interphase processes. CP-DNS has been conducted by many researchers for volatile-containing solid fuels such as coal and biomass [1-2]. Recently, Luu et al. [3-4] performed CP-DNS of monodisperse and polydisperse clouds of iron particles, investigating the ignition and combustion in a turbulent mixing layer. These CP-DNS simulations are typically considered nondeterministic. In this paper, we aim to build upon the previous CP-DNS simulation by Luu et al. [3] and compare the results of two independent CFD codes for both Quasi-2D and 3D instances of the turbulent reacting mixing layer setup in both a deterministic and a statistical way. The aim is to really compare the transient resolution of the velocity and scalar fields of the reacting two-phase flow predicted by the two different CFD codes, which is effectively the most stringent way of evaluating the validity of DNS results. To our knowledge, such a comparison has never been attempted unless for very simple cases like a Taylor Green Vortex [5].

Modeling

Within the context of CP-DNS, the gas phase is treated in an Eulerian framework by the conservation equations of mass, momentum, total enthalpy, and species mass fractions:

$$\frac{\partial \rho}{\partial t} + \frac{\partial}{\partial x_j}(\rho u_j) = \dot{S}_{\rho,p}, \tag{1}$$

$$\frac{\partial (\rho u_i)}{\partial t} + \frac{\partial (\rho u_i u_j)}{\partial x_j} = -\frac{\partial p}{\partial x_i} + \frac{\partial}{\partial x_j}\left(\mu\left(\frac{\partial u_i}{\partial x_j} + \frac{\partial u_j}{\partial x_i}\right) - \frac{2}{3}\mu\frac{\partial u_l}{\partial x_l}\delta_{ij}\right) + \dot{S}_{u,p}, \tag{2}$$

$$\frac{\partial (\rho h)}{\partial t} + \frac{\partial (\rho u_i h)}{\partial x_i} = \frac{\partial}{\partial x_i}\left(\frac{\mu}{Pr}\frac{\partial h}{\partial x_i}\right) + \dot{S}_{h,p}, \tag{3}$$

$$\frac{\partial (\rho Y_k)}{\partial t} + \frac{\partial (\rho u_i Y_k)}{\partial x_i} = \frac{\partial}{\partial x_i}\left(\frac{\mu}{Sc}\frac{\partial Y_k}{\partial x_i}\right) + \dot{S}_{k,p}, \tag{4}$$

These equations feature density ρ, velocity u_i, pressure p, total enthalpy h, and species mass fraction Y_k. The viscosity μ of the gas phase is calculated from kinetic gas theory, and the Schmidt and Prandtl numbers are assumed constant $Pr = Sc = 0.7$. The source terms in the equations $\dot{S}_{\phi,p}$ account for the interactions between particles and gas phase.

The iron particle phase, on the other hand, is described in a Lagrangian framework, interacting with the gas phase by means of mass, momentum, and energy exchange via $\dot{S_{\phi,p}}$. The particles are assumed to be spherical and driven only by drag force. The particle temperature is assumed to be uniform and be affected by convective heat exchange, radiation, and heat of combustion. Therefore, the governing

equations for the particle phase can be written using the gas-phase velocity $u_{g,i}$ and temperature T_g interpolated to the particle position:

$$\frac{du_{p,i}}{dt} = \frac{u_{g,i} - u_{p,i}}{\tau_p} \tag{5}$$

$$\frac{dT_p}{dt} = \frac{1}{\tau_{con}}(T_g - T_p) + \frac{\varepsilon_p A_p \sigma}{m_p c_{p,p}}(T_\infty{}^4 - T_p^4) + \frac{\dot{Q}_{FeO}}{m_p c_{p,p}} + \frac{\dot{Q}_{O_2}}{m_p c_{p,p}} \tag{6}$$

The term $u_{p,i}$ represents the particle velocity, and T_p denotes the particle temperature. The particle relaxation time τ_p is calculated based on particle Reynolds and Stokes number. Similarly, the particle convective heat transfer time scale is given by the Ranz-Marshal correlations [6]. To account for particle oxidation, the sub-model proposed by Mich et al. [7] is adopted. Thereby, iron particles are oxidized to FeO by the following heterogeneous reaction, considering both the effects of diffusion and reaction.

$$Fe_{(s)} + 0.5O_{2(g)} \longrightarrow FeO(s) \tag{7}$$

Consequently, the mass change of particles can be calculated from particle area A_d, oxygen mass fraction Y_{O_2} and reaction rate constant k_d according to:

$$\frac{dm_{p,Fe}}{dt} = -\frac{1}{s}\rho_f Y_{O_2} A_d k_d Da^* \tag{8}$$

Here, $Da^* = \frac{A_r k_r}{A_r k_r + A_d k_d}$ is the normalized Damköhler number that considers the diffusion-reaction balance.

Computational Setup

The turbulent reacting mixing layer is set up based on the previous work by Luu et al. [3]. The current configuration is defined by the initial development and temporal evolution of the momentum thickness δ_θ, forming self-similar turbulent structures driven by shear [8]. The setup involves two opposing streams: the upper stream (US) contains iron particles in air at an elevated temperature $T_{US} = 550K$, while the lower stream (LS) consists of hot air at $T = 1650K$. Both streams have equal velocities but are directed oppositely along the x-direction, creating a velocity difference of $\Delta u_x = 30m/s$, as shown in **Figure 1**.

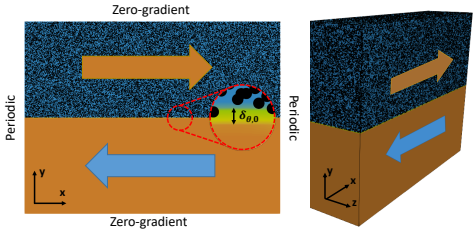

Figure 1. Initial and boundary conditions of the reacting mixing layer with iron particles.

A hyperbolic tangent profile based on momentum thickness $\delta_\theta$is used to initialise the streamwise velocity field $u_x = \frac{\Delta u_x}{2}\tanh\left(\frac{y - L_y/2}{2\delta_{\theta,0}}\right)$. The initial momentum thickness corresponds to a Reynolds number $Re_{\delta_\theta} = 44.018$.

The study involves two configurations: a quasi-2D and a full 3D case in which the computational domains have geometrical dimensions L_x, L_y and L_z discretized into a total of N_{cells} cubic Eulerian cells with a uniform grid spacing of Δ. A total of N_p spherical iron particles, each with an initial diameter of $d_{p,\text{init}} = 10\,\mu\text{m}$ are randomly distributed in the upper stream. The particle number is chosen to achieve an equivalence ratio of $\phi = 1$ in the upper stream, based on the oxidation of Fe to FeO. The initial particle velocities match the bulk gas velocity of the upper stream. Additionally, to accelerate the development of the mixing layer, isotropic velocity perturbations with magnitudes $u'u' = v'v' = w'w' = 0.01\,(\Delta u_x)^2$ and a characteristic length scale of $0.01 \cdot L_x$ are introduced in the center of the domain following the approach of Klein et al. [9]. The details of the computational domain for both cases are presented in **Table 1**. These cases were simulated using 2 independent CFD codes, PsiPhi and OpenFOAM, and cross-validated against each other to confirm the deterministic nature of the setup.

Table 1. Computational Domain for 3D and Quasi-2D Cases.

Case	L_x	L_y	L_z	N_{cells}	$N_{\text{particles}}$	Δ (µm)
3D	$320\times\delta_{\theta,0}$	$240\times\delta_{\theta,0}$	$80\times\delta_{\theta,0}$	84,934,656	4,900,000	100
Quasi-2D	$315\times\delta_{\theta,0}$	$236\times\delta_{\theta,0}$	$3.3\times\delta_{\theta,0}$	442,368	223,057	200

Results and Discussion

Figure 2 illustrates the temporal evolution of the gas and particle temperatures for the Quasi-2D test case, simulated using OpenFOAM (top) and PsiPhi (bottom). Initially, the particles and hot gas are separated, with the particles located in the upper stream and the hot gas in the lower stream. As the simulation progresses, a turbulent mixing layer develops at the interface between the upper and lower stream. During the early stages of the simulation, particle entrainment from the upper stream into the mixing zone is limited. However, as the mixing layer evolves, particles are drawn into the lower stream. Within the mixing zone, particles are accelerated upwards on the leading side of vortices before being convected downwards, following the gas stream. Once entrained into the lower stream, the particles are heated, ignited, and subsequently increase the gas temperature.

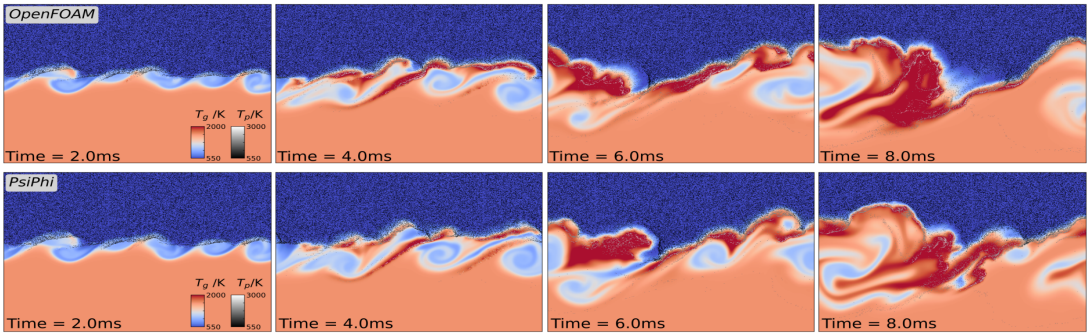

Figure 2. Snapshots of the gas phase and particle phase temperature at the mid-plane.

A comparison of the results from the two CFD codes reveals both similarities and differences. At 2 ms, both OpenFOAM and PsiPhi simulations show the formation of five distinct vortices within the mixing layer. These vortices play a key role in entraining particles into the lower stream. By 4 ms, the gas temperature fields from both codes exhibit similar features, including a streak of hot particles entrained into the lower stream, which locally increases the gas temperature. However, as the simulation progresses further, subtle differences emerge in the small-scale structures, even though the large-scale features remain largely consistent between the two codes.

This comparison provides strong evidence of the correct implementation of the models in both codes and represents an unusually strong validation of the DNS. Building on this validation, we aim to investigate the effect of higher turbulence levels on the ignition and combustion of iron particles, which require substantially greater computational resources.

Acknowledgement

We gratefully acknowledge the funding received from International Max Planck Research School for Sustainable Metallurgy (IMPRS SusMet).

References

[1] Rieth. et al.: *Carrier-phase DNS of pulverized coal particle ignition and volatile burning in a turbulent mixing layer*, Feul, 212, 364–374, 2018.

[2] Wang et al.: *Investigation of turbulent pulverized solid fuel combustion with detailed homogeneous and heterogeneous kinetics*, Energy & Fuels, 35, 7077–7091, 2021.

[3] Luu et al.: *Carrier-Phase DNS of Ignition and Combustion of Iron Particles in a Turbulent Mixing Layer*, Flow, Turbulence and Combustion, 112, 1083–1103, 2024.

[4] Luu et al.: *Carrier-phase DNS study of particle size distribution effects on iron particle ignition in a turbulent mixing layer*, Proceedings of the Combustion Institute, 40(1), 105297, 2024.

[5] Zirwes et al.: *Assessment of Numerical Accuracy and Parallel Performance of OpenFOAM and its Reacting Flow Extension EBIdnsFoam*, Flow, Turbulence and Combustion, 111(2), 567–602, 2023.

[6] Ranz et al.: *Evaporation from drops*, Chemical Engineering Progress, 48, 142–180, 1952.
[7] Mich. et al.: *A comparison of mechanistic models for the combustion of iron microparticles and their application to polydisperse iron-air suspensions*, Combustion and Flame, 256, 112949, 2023.
[8] O'Brien et al.: *Subgrid-scale backscatter in reacting and inert supersonic hydrogen–air turbulent mixing layers*, Journal of Fluid Mechanics, 743, 554–584, 2014.
[9] Klein et al.: *A digital filter based generation of inflow data for spatially developing direct numerical or large eddy simulations*, Journal of Computational Physics, 186(2), 652–665, 2003.

An equilibrium description of the envelope flame surrounding a burning magnesium particle

Z. Wang[1], S. Cheng[1] and F. Sewerin[2*]

*E-Mail: fabian.sewerin@ovgu.de

[1]*Department of Mechanical Engineering, The Hong Kong Polytechnic University, 11 Yuk Choi Road, Hung Hom, Kowloon, Hong Kong SAR, PR China*

[2]*Emmy Noether Group for Dispersed Multiphase Flows, Chair of Mechanical Process Engineering, Otto-von-Guericke-Universität Magdeburg, Universitätsplatz 2, 39106 Magdeburg, Germany*

Introduction

Magnesium particles can be burnt not only in air, but also in CO_2- and H_2O-containing atmospheres, rendering them versatile energetic materials. Besides their potential use as metal fuel [1, 2] or propellant [3], magnesium powders may also be involved in carbon sequestration and long-term carbon storage [4].

Focusing on the single-particle level, we present a systematic approach for modeling the reactive atmosphere in the vicinity of an individual burning magnesium particle based on first principles. By combining element and enthalpy conservation laws with the conditions for thermodynamic equilibrium and surface interaction constraints, the changes in the gas' thermochemical state from the particle surface through the far-field atmosphere are determined in a spatially resolved way [5]. The resulting profiles of the chemical composition and temperature allow us not only to elucidate the structure of the envelope flame, but also to predict the gas-particle mass and heat exchange rates and to estimate the emission of pollutants. Compared to previous modeling efforts [6, 7], the calibration of rate parameters for surface and gas phase reactions as well as smoke condensation is circumvented. Since the gas phase is assumed to rest in thermodynamic equilibrium, the relevant gaseous and condensed phase species are first identified from past investigations and supplementary ab initio molecular dynamics analyses. With the aid of quantum chemistry calculations, the thermodynamic properties of those species which are not included in the database of Burcat and Ruscic [8] are then determined. In a third step, the identified species sets and thermodynamic data are incorporated into the equilibrium-based boundary layer formulation and predictions of the radial species and temperature profiles near a burning magnesium particle are obtained for different oxidizing atmospheres.

Identification of species participating in Mg-oxidation chemistry

An account of the species that form during the oxidation of magnesium is crucial for an accurate determination of thermodynamic equilibria. In Mg-O_2 systems, O appears as a radical, while the primary product is magnesium oxide that occurs both as a gaseous species (MgO) and in condensed form (MgO(l, s)) [6, 9]. In the case of combustion in a CO_2 atmosphere, C, C(s), CO, MgO, MgO(l, s), O and O_2 [3, 6] as well as MgOC and MgOCO [10] have been identified as key species. In Mg-H_2O reactions, moreover, HMgOH, MgO, MgO(l, s) and species from the H_2-O_2 chemistry are formed and often accompanied by magnesium hydroxide (MgOH) and the magnesium water adduct ($Mg \cdot OH_2$) [11].

Although these previous investigations offer valuable insights into the relevant species, they are limited by particular experimental and computational conditions. In order to adequately identify the important intermediates and products formed during the oxidation of magnesium under different conditions, ab initio molecular dynamics simulations are performed using the CP2K software package [12]. The primary species are selected based on their participation in more than 10 % of the most frequent reactions and missing thermodynamic properties are then calculated using quantum chemistry methods.

Computation of thermodynamic properties

Since not all species involved in the Mg-oxidation reactions are covered by the database of Burcat and Ruscic [8], the missing thermodynamic properties are determined by following the approach of Yalamanchi et al. [13]. In particular, structural optimizations, vibrational analyses and zero-point energy calculations are performed at the B3LYP/6-311++G(d, p) level of theory. The single-point energies

(SPEs) of the optimized structures are further refined at the CCSD(T)/cc-pVXZ level of theory (with X = T and Q) and the resulting SPEs are extrapolated to the complete basis set (CBS) limit according to

$$E_{\mathrm{CBS}} = E_{\mathrm{CCSD(T)/cc\text{-}pVQZ}} + \left(E_{\mathrm{CCSD(T)/cc\text{-}pVQZ}} - E_{\mathrm{CCSD(T)/cc\text{-}pVTZ}}\right) \frac{4^4}{5^4 - 4^4}, \tag{1}$$

where E_* represents a computed SPE. Subsequently, the atomization method is employed to derive the enthalpies of formation at 0 K. The standard enthalpies of formation and the temperature-dependent enthalpies, entropies and heat capacities at constant pressure are determined using the MultiWell program suite [14]. In order to validate the computational approach, the thermodynamic data of CO_2 and $Mg(OH)_2$ are calculated first and compared with the data from Ref. [8] over the temperature range from 298 to 3000 K. The complete set of thermodynamic properties is further used to calculate the equilibrium composition throughout the reactive boundary layer surrounding a burning magnesium particle.

A reactive boundary layer in thermodynamic equilibrium

If the boundary layer that separates the surface of a reacting magnesium particle from the ambient atmosphere is spherically symmetric, then the state of the reactive gas at the radial distance $r \in [r_s, r_\infty]$ from the particle surface can be defined in terms of the radial mass flow rate $\dot{m}$, the mass fractions $Y_k(r)$ of species $k \in \mathcal{G}$ and the specific gas enthalpy $h(r)$. For simplicity, the species associated with condensed phase smoke are described in a similar way as gas species irrespective of their condensed nature or potential droplet/particle size-polydispersity. In view of the species' elemental composition, the species mass fractions $Y_k(r)$, $k \in \mathcal{G}$, are linked to the elements' mass fractions $Y_j(r)$, $j \in \mathcal{E}$, according to

$$Y_j(r) = W_j \sum_{k \in \mathcal{G}} a_{jk} \frac{Y_k(r)}{W_k}, \quad j \in \mathcal{E}, \tag{2}$$

where W_j is the atomic weight of element $j \in \mathcal{E}$, W_k denotes the molecular weight of species $k \in \mathcal{G}$ and a_{jk} is the number of atoms of element j in a single molecule of species k. The sets $\mathcal{E}$ and $\mathcal{G}$, moreover, encompass the labels of the relevant elements and species, respectively. As chemical reactions take place, the radial species mass flow rates $\dot{m}_k(r) = \dot{m}Y_k(r) - 4\pi r^2 \rho_g D dY_k(r)/dr$, $k \in \mathcal{G}$, change in the radial direction commensurate with the species-specific production rates $4\pi r^2 \dot{\omega}_k$ [15, Chapter 1]. The element mass fractions and the enthalpy, by contrast, are conserved scalars [16] and obey the conservation laws

$$\frac{d}{dr}\left(\dot{m}Y_j(r) - 4\pi r^2 \rho_g D \frac{dY_j(r)}{dr}\right) = 0, \quad j \in \mathcal{E}, \tag{3}$$

$$\frac{d}{dr}\left(\dot{m}h(r) - 4\pi r^2 \frac{\lambda_g}{C_{p,g}} \frac{dh(r)}{dr}\right) = 0 \tag{4}$$

in steady state [15, pp. 73–74]. Equation (4) is based on the assumption of a Lewis number of unity, $\lambda_g / C_{p,g} = \rho_g D$. Here, the boundary layer conductivity $\rho_g D$ involves the gas density ρ_g and the kinematic diffusivity D, but may alternatively be expressed in terms of the heat conductivity λ_g and the gas' heat capacity $C_{p,g}$. Note that the parenthesized terms in Eqs. (3) and (4) correspond to the element mass flow rates $\dot{m}_j$ and the enthalpy flow rate $\dot{h}$, respectively.

Since the gas phase reactions of metals and oxygen are very fast, the gas is assumed to rest in thermodynamic equilibrium at every radial location r. In order to additionally accommodate chemical reactions and phase transitions at the particle surface, we adopt a boundary layer formulation that has recently been presented in the context of aluminum combustion by Sewerin et al. [5]. For a given conductivity $\rho_g D$, a fixed particle temperature T_p and specified far-field conditions, the element and species mass fractions at the particle surface ($r = r_s$) are calculated from a single nonlinear system of equations, while the composition and temperature further away from the surface ($r > r_s$) are obtained in a post-processing step. In the following, the key rationale underlying this boundary layer model is briefly summarized and an extension is indicated.

If the element mass flow rates $\dot{m}_j$, $j \in \mathcal{E}$, and the enthalpy flow rate $\dot{h}$ through the spherical boundary layer were known, then Eqs. (3) and (4) could be integrated across the spherical shell $[r_s, r_\infty]$ to yield a relation between the element mass fractions $Y_{j,s} = Y_j(r_s)$ and the enthalpy $h_s = h(r_s)$ at the particle surface and their far-field counterparts $Y_{j,\infty} = Y_j(r_\infty)$, $h_\infty = h(r_\infty)$. By the conditions for thermodynamic

equilibrium, we may, in turn, link the elemental composition $(Y_j(r))_{j\in\mathcal{E}}$ and the gas enthalpy $h(r)$ to the species mass fractions $(Y_k(r))_{k\in\mathcal{G}}$ and the gas temperature $T(r)$ [17]. Denoting by $n_{j,s}$, $j \in \mathcal{E}$, and $n_{k,s}$, $k \in \mathcal{G}$, the element and species mole numbers at the particle surface, the equilibrium problem at $r = r_s$ reads in particular

$$G((n_{k,s})_{k\in\mathcal{G}}, T_s, p) = \underset{(n_{k,s})_{k\in\mathcal{G}}}{\text{Min!}} \tag{5}$$

subject to the constraints

$$n_{j,s} = \sum_{k\in\mathcal{G}} a_{jk} n_{k,s}, \quad j \in \mathcal{E}, \tag{6}$$

$$h_s = \left(\sum_{k\in\mathcal{G}} W_k n_{k,s}\right)^{-1} \sum_{k\in\mathcal{G}} h_k(T_s) W_k n_{k,s}. \tag{7}$$

Here, G represents the Gibbs free energy associated with a multicomponent ideal gas and h_k is the specific enthalpy of species $k \in \mathcal{G}$, while $T_s = T(r_s)$ and p denote the gas temperature at the surface and the ambient pressure, respectively. For given $(n_{j,s})_{j\in\mathcal{E}}$, T_s (or h_s) and p, the necessary conditions for optimality of $(n_{k,s})_{k\in\mathcal{G}}$ yield a nonlinear system of equations for the species mole numbers $n_{k,s}$, $k \in \mathcal{G}$, and the gas enthalpy h_s (or T_s). Retracing our steps, Eqs. (3) to (7) uniquely define the surface scalars $(Y_{k,s})_{k\in\mathcal{G}}$ and h_s in terms of the far-field values $(Y_{j,\infty})_{j\in\mathcal{E}}$, h_∞ and the flow rates $(\dot{m}_j)_{j\in\mathcal{E}}$, $\dot{h}$. In single-particle combustion experiments, the far-field composition $(Y_{k,\infty})_{k\in\mathcal{G}}$ and the far-field temperature T_∞ are commonly prescribed such that $(Y_{j,\infty})_{j\in\mathcal{E}}$ (by Eq. (2) with $r = r_\infty$) and h_∞ (by the counterpart of Eq. (7) at $r = r_\infty$) are available. In order to determine $\dot{m}_j$, $j \in \mathcal{E}$, and $\dot{h}$, by contrast, additional constraints are needed. Here, we specifically employ the conditions that there is no temperature jump at the particle surface, $T_s = T_p$, and that the particle's bulk Mg(l)-matter is in equilibrium with the gas at the particle surface. For the remaining element mass flow rates $\dot{m}_j$, $j \neq$ Mg, moreover, hypotheses on the gas-particle surface interaction are adopted. For example, in the case of combustion in air, $\dot{m}_\mathrm{N}$ is required to vanish, while $\dot{m}_\mathrm{O}$ is determined by the condition that the deposition of MgO(l) and MgO(s) is diffusion-limited.

After the flow rates $\dot{m}_j$, $j \in \mathcal{E}$, and $\dot{h}$ have been determined by jointly enforcing the conservation laws, the equilibrium conditions and the surface constraints, we may return to Eqs. (3) and (4) and recover the radial profiles $Y_j(r)$, $j \in \mathcal{E}$, and $h(r)$ for $r \in [r_s, r_\infty]$. In a post-processing step, the counterpart problem of Eqs. (5) to (7) for an arbitrary radius r is solved for given $n_j(r) = Y_j(r)/W_j$, $j \in \mathcal{E}$, and $h(r)$ across the boundary layer [18], yielding the equilibrium profiles $Y_k(r) = n_k(r)W_k$, $k \in \mathcal{G}$, and $T(r)$. Besides providing detailed insights into the structure of the enveloping diffusion flame, the equilibrium profiles also determine the gas-particle mass and heat exchange rates that control the progress and duration of the particle combustion.

A particular feature of burning magnesium particles is the presence of a porous oxide shell that impedes the access of the particle surface by the reacting gas and grows as the particle conversion proceeds [3, 6, 19]. Correspondingly, we intend to amend the conservation laws in Eqs. (3) and (4) by an r-dependent porosity field.

Summary

Magnesium is a versatile energetic material that may be used not only in propellants or as a fuel, but also to aid carbon capture and storage. The elementary reaction unit in these applications is a single magnesium particle that is suspended in an oxidizing atmosphere containing O_2, CO_2 or H_2O. Focusing on the steady combustion of an isolated magnesium particle with a spherical envelope flame, we present a three-stage, principle-based approach towards predicting the radial profiles of the gas phase composition, including magnesium oxide condensates, and the gas temperature. After the species that form during the gas phase combustion of magnesium were identified from past investigations and ab initio molecular dynamics simulations, missing thermodynamic properties are determined with the aid of dedicated quantum chemistry calculations. Complemented by data from Ref. [8], the species sets and thermodynamic data are used to inform an equilibrium-based boundary layer model which we plan to amend for the presence of a porous oxide shell. The radial composition and temperature profiles computed from the boundary layer formulation permit us to elucidate the envelope flame structure, identify relevant

surface chemistry and quantify gas-particle mass and heat exchange rates.

Acknowledgments
ZW and SC were supported by the Research Grants Council of the Hong Kong SAR, PR China (PolyU P0046985, ECS project, 2023/24 Exercise), while FS gratefully acknowledges the financial support by the Deutsche Forschungsgemeinschaft (Project number 443546539).

References

[1] Garra P., Leyssens G., Allgaier O., Schönnenbeck C., Tschamber V., Brilhac J.-F., Tahtouh T., Guézet O., Allano S.: *Magnesium/air combustion at pilot scale and subsequent PM and NO_x emissions*, Applied Energy, 189, 578–587, 2017.

[2] Bergthorson J. M.: *Recyclable metal fuels for clean and compact zero-carbon power*, Progress in Energy and Combustion Science, 68, 169–196, 2018.

[3] Shafirovich E. Y., Shiryaev A. A., Goldshleger U. I.: *Magnesium and carbon dioxide: A rocket propellant for Mars missions*, Journal of Propulsion and Power, 9 (2), 197–203, 1993.

[4] Chen Q., Bergthorson J., Schiemann M.: *A review of metal-carbon dioxide combustion*, Renewable and Sustainable Energy Reviews, 203, 114730, 2024.

[5] Sewerin F., Chu H., Finke J., Pitsch H.: *A point-particle model for burning aluminum particles based on a reactive boundary layer in chemical equilibrium*, 2nd Conference on the Metal-enabled Cycle of Renewable Energy (MeCRE), Darmstadt, Germany, 2024.

[6] Abbud-Madrid A., Modak A., Branch M. C., Daily J. W.: *Combustion of magnesium with carbon dioxide and carbon monoxide at low gravity*, Journal of Propulsion and Power, 17 (4), 852–859, 2001.

[7] King M. K.: *A simplified two-reaction zone model of magnesium combustion in carbon dioxide*, Proceedings of the Combustion Institute, 29 (2), 2931–2938, 2002.

[8] Burcat A., Ruscic B.: *Third Millennium Ideal Gas and Condensed Phase Thermochemical Database for Combustion with Updates from Active Thermochemical Tables*, ANL-05/20, Argonne, `http://garfield.chem.elte.hu/Burcat/burcat.html`, 2005.

[9] Cassel H. M., Liebman I.: *Combustion of magnesium particles I*, Combustion and Flame, 6, 153–156, 1962.

[10] Zhu X., Li Y., He P., Ren F., Sha Z., Hu X., Hu C.: *Reaction kinetics of an Mg/CO_2 power system for Mars exploration*, Acta Astronautica, 192, 233–244, 2022.

[11] Han Z.: *Study on the ignition and combustion model and high-temperature homogeneous reaction mechanism of magnesium with water*, Ph.D. Thesis (in Chinese), Zhejiang University, Hangzhou, 2012.

[12] Hutter J., Iannuzzi M., Schiffmann F., VandeVondele J.: *CP2K: Atomistic simulations of condensed matter systems*, WIREs Computational Molecular Science, 4 (1), 15–25, 2014.

[13] Yalamanchi K. K., Bai X., Fernando N. D., Lua A. S., Cheng S., Li Y., Zhou C.-W., Goldsborough S. S., Sarathy S. M.: *From electronic structure to model application of key reactions for gasoline/alcohol combustion: Hydrogen-atom abstractions by $CH_3\dot{O}$ radical*, Combustion and Flame, 252, 112742, 2023.

[14] Barker J. R., Nguyen T. L., Stanton J. F., Aieta C., Ceotto M., Gabas F., Kumar T. J. D., Li C. G. L., Lohr L. L., Maranzana A., Ortiz N. F., Preses J. M., Stimac P. J.: *MultiWell Program Suite User Manual*, University of Michigan, Ann Arbor, `https://multiwell.engin.umich.edu/`, 2016.

[15] Williams F. A.: *Combustion Theory*, Combustion Science and Engineering Series, 2nd ed., Addison-Wesley, Reading, Menlo Park, ISBN: 0-201-40777-9, 1985.

[16] Spalding D. B.: *The combustion of liquid fuels*, Symposium (International) on Combustion, 4 (1), 847–864, 1953.

[17] Zeleznik F. J., Gordon S.: *Calculation of complex chemical equilibria*, Industrial & Engineering Chemistry, 60 (6), 27–57, 1968.

[18] Gordon S., McBride B. J.: *Computer Program for Calculation of Complex Chemical Equilibrium Compositions and Applications. I. Analysis*, NASA RP-1311, Cleveland, 1994.

[19] Wang X., Liu Y., Xu X., Liu D., Yang Q.: *Combustion of single micron-sized magnesium particles in carbon dioxide*, Chemical Engineering Journal, 495, 153897, 2024.

Analysis of Iron Ore Reduction Using Hydrogen for Energy Storage and Transport

S. Schmitt[1*], O. Narin[1], B. Brosch[1], V. Scherer[2], C. Yannakis[2], F. Cerciello[3], A. Fabozzi[3] and O. Senneca[3]

*E-Mail: Sebastian.schmitt@doosan.com

[1] Doosan Lentjes, Daniel-Goldbach-Straße 19, 40880 Ratingen

[2] Department of Energy Plant Technology, Ruhr-University Bochum, Universitätsstraße 150, 44780 Bochum, Germany

[3] Istituto di Scienze e Tecnologia per l'Energia e la Mobilità Sostenibili (STEMS)-CNR, 80125, Napoli, Italy

Introduction

The reduction of iron ore using hydrogen derived from renewable energy sources offers a promising technology for energy storage and transport. Reduced iron can be oxidized to release energy as heat and/or to produce hydrogen. A fluidized bed reactor is ideal for this process due to its excellent gas-solid contact, uniform temperature distribution, and high heat and mass transfer rates. In these reactors, iron ore particles are suspended by an upward flow of hydrogen gas, ensuring efficient reduction.
This study focuses on the reduction of Khumani iron ore (90-200 µm) using hydrogen in a thermogravimetric apparatus (TGA). Explorative tests have also been carried out in a lab-scale Fluidized Bed Reactor (FBR) to identify suitable operating conditions and have a preliminary comparison with TGA results. The obtained kinetic data are then applied in a Multi-Phase Particle-In-Cell (MP-PIC) Computational Fluid Dynamics (CFD) model (Barracuda) to simulate fluidized bed reactors.

Reduction of Iron Ore Kumani with Hydrogen

The reduction of iron ore using hydrogen involves removing oxygen from iron oxides (Fe_2O_3) to produce metallic iron (Fe) and water vapor (H_2O). The reduction of iron ore by hydrogen is an endothermic process. The energy required to sustain this process can be supplied in two ways: by means of electric heating, or by supplying oxygen to the reduction reactor, where it combusts a portion of the hydrogen generated.

Experimental methods

TGA

Reduction tests were conducted in a TGA with hydrogen concentrations ranging from 6% to 32% at temperatures between 500°C and 850°C. Oxidation tests were performed in air. The reduction/oxidation cycles were also studied to evaluate the reactivity and stability of the iron ore over multiple cycles. Key results include mass loss/gain, reaction rates, and kinetic parameters derived from Arrhenius plots.

FBR

Reduction and oxidation experiments using hydrogen and water vapour were conducted in a lab-scale batch-operated fluidized bed reactor. The test facility consists of an electrically heated tube with a length of 1070 mm and an inner diameter of 42 mm. To monitor the process, sensors are installed to measure temperature and gas composition (H_2 & O_2). Additionally, bed material samples can be extracted. For the experiments, Khumani iron ore with a particle size of $150<x<250$ µm and a batch mass of 100–150 g was used. The raw ore was first reduced for 20 minutes at a bed temperature of 580°C in an atmosphere of 23 vol.-% H_2 (in N_2). Afterwards, the reduced sample was oxidized with steam at a bed temperature of 600°C for 16 minutes. Both the reduced and oxidized samples were analyzed by means of X-Ray powder Diffraction (XRD) analysis. The procedure described in [2] was used to evaluate the degree of reduction.

TGA Results

The reduction of iron ore exhibits two to three stages (aligning with the reaction pathways outlined in Table 1) depending on the temperature, with significant mass loss (28-30%) consistent with the

reduction of Fe_2O_3 to Fe. The oxidation tests showed mass gains of 25-40%, indicating effective re-oxidation.

Table 1. Reduction reaction scheme

$Fe_2O_3+H_2 \rightarrow 2Fe_3O_4+H_2O$ $\Delta m=3\%$	
T<570°C	T>570°C
$Fe_3O4+4H_2 \rightarrow 3Fe+4H_2O$	$(1-x)Fe_3O_4+(1-4x)H_2 \rightarrow 3Fe(1-x)O+(1-4x)H_2O$ $Fe_{(1-x)}O+H_2 \rightarrow {}_{(1-x)}Fe+H_2O$
$\Delta m=30\%$	

Performance in reduction/oxidation cycles: Khumani iron ore demonstrated robust performance during reduction/oxidation cycles conducted at 650°C with 16% hydrogen (H_2). The experiments revealed that residence times of approximately 20 minutes per cycle resulted in a conversion degree of around 70%. It was observed that increasing the hydrogen concentration enhances the conversion rate further.
Impact of reduction temperature on reactivity: High reduction temperatures have a negative impact on reactivity during re-oxidation. This suggests that maintaining moderate temperatures is crucial for preserving the iron ore's reactivity.
The outcome of the TGA experiments are the kinetic data for iron ore reduction. These data are listed in table 2. For further details on the kinetic studies, we refer to our previous work [1].

FBR results
The samples collected from the FBR tests, upon XRD analysis, revealed the presence of different phases (Figure 1). With 21% H_2 at 580°C after 20 min, the main phase obtained was Wüstite, accompanied by residual hematite and magnetite, and the overall degree of reduction increased from 0 (of the raw sample) to 40%. Upon reoxidation with steam at 600°C in 16 min magnetite was mainly obtained, together with a smaller fraction of hematite. The degree of reduction decreased from 40 to 10%.

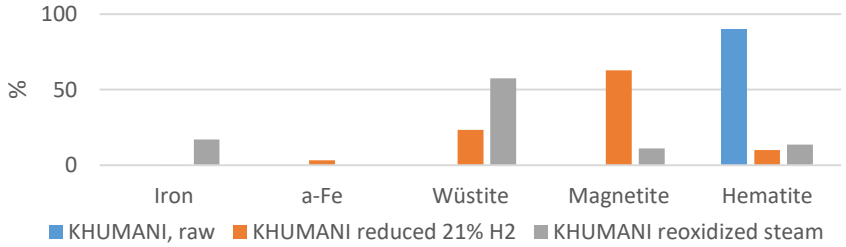

Figure 1. Results of XRD analysis on FBR samples

Implementation of kinetics into CPFD Barracuda
The simulation of the fluidised bed reduction of iron ore was conducted utilising the commercial CFD software, CFD Barracuda. This software employs a MP-PIC model to simulate the behaviour of particles. For the implementation of the TGA results, a simple kinetic law was chosen:

$$\frac{dx}{dt} = k_0 p_g \exp^{-\frac{E}{RT}}(1-x), \quad (4)$$

where p_g is the reactant gas concentration and x is the conversion degree.

Table 2. Reduction kinetics

T [°C]	E [KJ/mol]	k_0 [1/(min *atm)]
<550	133	3*10^8
550-700	33	17
>700	83	6700

An average temperature is calculated for each particle parcel at each time step from the particle temperature and the gas temperature of the surrounding CFD cell.
To test the reduction model, a fixed single particle was first simulated, and the reduction time was then compared with the reaction time of the TGA tests. Deviations were below 5%. In a next step, a bubbling bed fluidized bed reactor with a diameter of 150 mm was simulated. Figure 1 shows the local mass fraction of Fe_2O_3 within the bed.

Figure 2. Simulation of a bubbling bed iron reduction reactor

Conclusion and outlook

Preliminary kinetic models have been proposed based on TGA data. The kinetic data were implemented in a CFD model to simulate a stationary fluidised bed. A lab-scale fluidized bed reactor for reduction and oxidation has been setup allowing for comparison with the simulation results. In future work, more detailed modeling of single particle reduction and oxidation including intraparticle transport processes is required to enhance the understanding of these processes. Additionally, future research should include comprehensive physicochemical analyses, such as porosimetric analysis and X-ray diffraction (XRD), on samples prepared in fluidized bed reactors (FBR) at different temperatures and after multiple reduction/oxidation cycles. In addition, effects such as thermal annealing need to be added to improve the predictive accuracy of the model. Based on the refined models, simulations can be carried out to find an optimal reactor design for a reduction/oxidation plant.

Ackowledgement

SPONSORED BY THE
Federal Ministry of Education and Research

Sponsored by the German Federal Ministry of Education and Research

Ministero degli Affari Esteri e della Cooperazione Internazionale
MUR

Sponsored by Italian Ministry of University and Research (MUR) and Ministry of Foreign Affairs (MAECI)

References

[1] F. Cerciello, A. Fabozzi, C. Yannakis, S. Schmitt, O. Narin, V. Scherer, O. Senneca, Kinetics of iron reduction upon reduction/oxidation cycles, International Journal of Hydrogen Energy, 65, 2024, Pages 337-347

[2] A. Fabozzi, F. Cerciello, F., O. Direct reduction of iron ore using biomass biochar: Reduction rate, microstructural and morphological analysis. Fuel, 2025, 383, 133976. 10.1016

Molecular Dynamic Investigation of Nanoparticle Formation during Iron Microparticle Combustion

L. Elsäßer[1], Y. Gao[2], A. Dreizler[1], and T. Li[1*]

*E-Mail: tao.li@rsm.tu-darmstadt.de

[1]Reactive Strömungen und Messtechnik, Technische Universität Darmstadt, Otto-Berndt-Staße 3, 64287 Darmstadt, Germany
[2]Department of Mechanical Engineering, Pennsylvania State University, University Park, 16802, PA, United States

Introduction

The formation of iron oxide nanoparticles (NPs) during iron powder combustion poses efficiency and emission challenges, necessitating deeper insights into precursor formation and agglomeration mechanisms. Although previous experiments suggest the critical role of temperature for the nanoparticle formation [1], the underlying pathways remain poorly understood. This study employs molecular dynamics (MD) simulations using ReaxFF to investigate (I) precursor formation at the solid-gas interface and (II) agglomeration mechanisms leading to NP formation. Dry air and humid air environments were used to understand influences of water vapor on precursor suppression and NP growth.

Numerical Setup

To gain a fundamental understanding of nanoparticle formation, we conducted MD simulations using the reactive force field (ReaxFF) method. Shin's force (Fe/O/H) field [2] was used as it provides good predictions of liquid iron and iron oxide mixing enthalpies, as well as coordination numbers in the mixing phase, according to Thijs [3]. The present simulations are divided into two phases, making the NP formation process accessible within the length and time scales of MD simulations, which are usually on the nanometer and nanosecond scale, respectively. The configurations of the two phases are as follows.

- Phase I focuses on the precursor formation, see **Figure 1(a)**: A 500-atom BCC-Fe nanoparticle was placed in a periodic simulation box (80 Å × 80 Å × 80 Å) containing a gas of 500 O_2 molecules (dry air case) or 250 H_2O + 375 O_2 molecules (humid air case). The system evolved in the microcanonical ensemble (NVE) for 500 ps at a 0.1 fs time step from a 1500 K initial temperature.
- Phase II focuses on nanoparticle agglomeration, see **Figure 1(b)**: Precursor mixtures extracted from Phase I were dispersed in a cubic simulation box with added O_2 (dry air case) or O_2 + H_2O molecules (humid air case). Simulations were conducted at constant temperatures 1000 K, 2000 K, and 3000 K over 2 ns at a 0.25 fs timestep in the canonical ensemble NVT ensemble using the Nose Hoover thermostat.

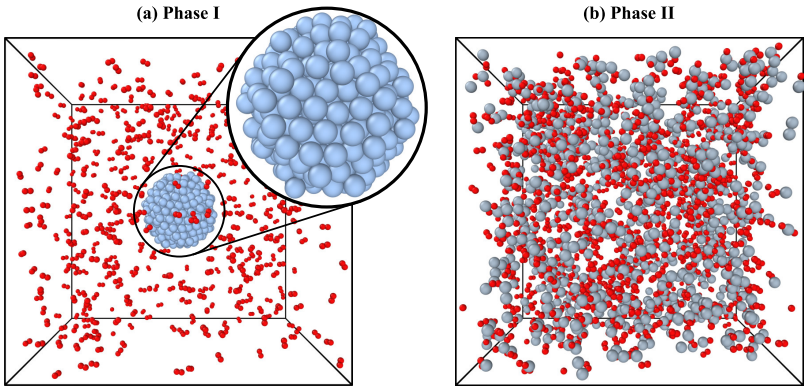

Figure 1: Initial configurations for MD simulation for (a) Phase I and (b) Phase II. Atom colors: Fe (ice blue) and O (red).

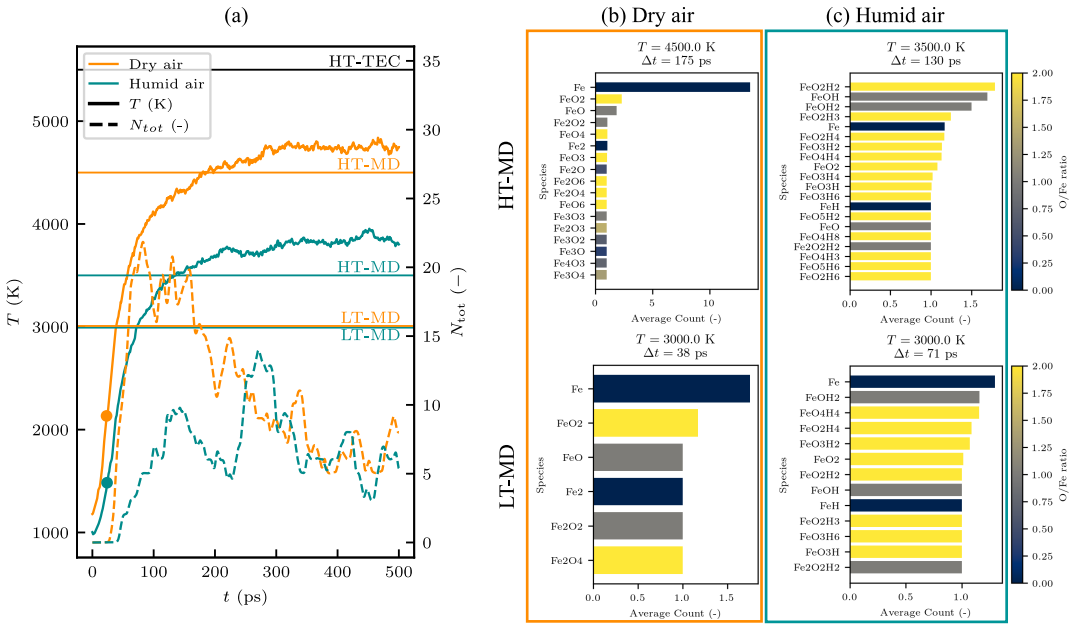

Figure 2: Phase I: (a) Temperature and total precursor count N_{tot} over time and the HT-MD and LT-MD precursor mixtures for the (b) dry air and (c) humid air cases.

To ensure the comparability across all cases, the O/Fe atomic ratio was set to 2 and the initial number density in Phase II was $1/256$ Å^{-3}. All cases underwent an initial energy minimization and atomic charges were updated at every step.

Precursor formation

As indicated in **Figure 2(a)**, the precursor count initially rises as Fe atoms detach from the nanoparticle (first detachment marked by a circle) and react with oxygen or hydroxyl species. Over time, these precursors recombine to intermediates, reducing the overall precursor concentration and leading to nanoparticle nucleation. The precursor composition is probed at high temperatures (HT) and low temperatures (LT) marked by the horizontal solid lines, and the main characteristics are highlighted below.

- In the dry air case, shown in **Figure 2(b)**, Fe reacts with O_2 to predominantly form FeO and FeO_2, which contribute to a recombination cycle that was found to be essential for NP synthesis [4].
- In the humid air case, shown in **Figure 2(c)**, Fe reacts with both O_2 and H_2O, forming iron hydroxides ($Fe(OH)_n$), primarily FeOH and $Fe(OH)_2$ at high temperatures. These species stabilize the precursor pool and reduce overall precursor formation.

The temperature conditions further influence precursor dynamics. High-temperature cases favor atomic Fe evaporation (HT-MD), while low-temperature (LT) conditions lead to a more evenly distributed precursor mixture (LT-MD). Water vapor lowers reaction temperature and reduces precursor concentration compared to the dry air case.

Nanoparticle Agglomeration

Clustering and oxidation co-occur, following a Yasuoka-Matsumoto nucleation curve, see **Figure 3(a)**. The precursor mixtures from Phase I (LT-MD and HT-MD) and a theoretical high-temperature case of pure iron evaporation (HT-TEC) [5], are used to determine early-stage NP nucleation dynamics. In the dry air cases, the final oxidation state depends on the agglomeration temperature, not the precursor mixture, see **Figure 3**(b) orange lines: $\sim Fe_2O_3$ at 1000 K, $\sim Fe_3O_4$ at 2000 K (excluded from figure) and $\sim$ FeO at 3000 K. Here, agglomeration is on the nanosecond scale, while the transport of NPs in the parent particle boundary layer is on the millisecond scale in experiments [5]. Thus, NPs have ample time to adapt their oxidation state to their ambient temperature.

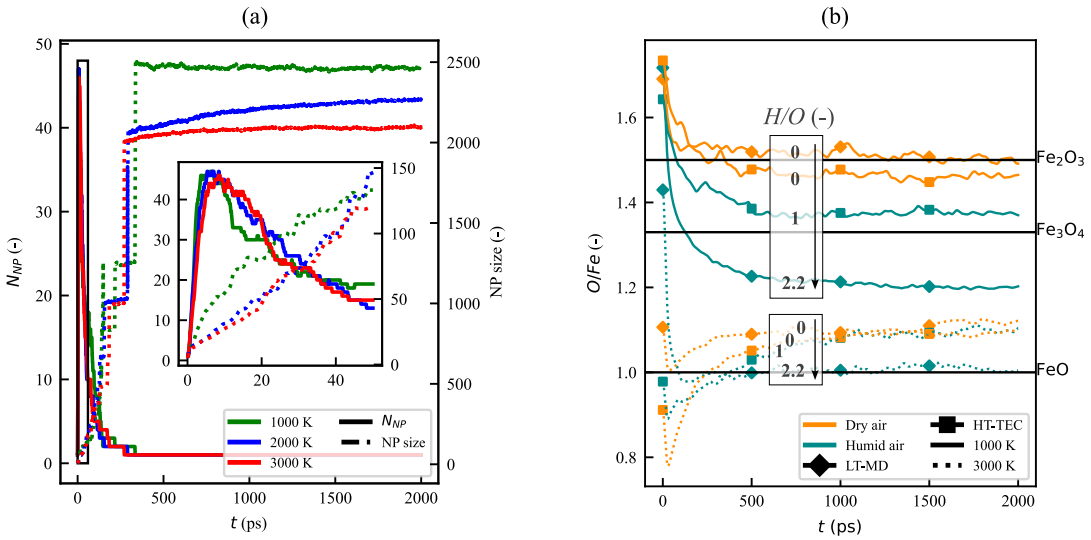

Figure 3: Phase II: (a) NP formation of HT-TEC dry air case. Particle size N_{NP} in solid lines and NP size in dashed lines (b) O/Fe ratios with H/O ratio influence with HT-TEC and LT-MD mixtures.

Figure 3(b) compares dry air and humid air cases at 1000 K and 3000 K, considering HT-TEC and LT-MD. While Fe and O atom counts remain constant, the H atom count varies due to the different H content in humid air precursor mixtures. This allows analysis of the H/O ratio effect: At a constant temperature, dry air cases show a consistent final O/Fe ratio, whereas increased H/O ratios lead to lower O/Fe ratios due to hydrogen's reducing influence.

Summary and Perspectives

This MD study reveals that humid air curbs nanoparticle precursor evaporation, while ambient temperature dictates the final oxidation state—favoring FeO at 3000 K and Fe_2O_3 at 1000 K. The presence of water vapor introduces hydrogen, which acts as an oxygen sink, further limiting oxidation.

The current findings from MD simulations provide insightful guidance for single microparticle combustion experiments in a drop tube reactor, investigating NP formation in water-enriched air. Optical diagnostics, including high-speed shadowgraphy and emission spectroscopy, will be employed to validate the computational predictions. The MD results provide insight into nanoscale processes inaccessible by experiments, enabling better control over nanoparticle formation in practical combustion systems.

References

[1] Tao Li, Franziska Heck, Felix Reinauer, Benjamin Böhm, and Andreas Dreizler. Visualizing particle melting and nanoparticle formation during single iron particle oxidation with multi-parameter optical diagnostics. *Combustion and Flame*, 245:112357, November 2022.

[2] Yun Kyung Shin, Hyunwook Kwak, Alex V. Vasenkov, Debasis Sengupta, and Adri C.T. van Duin. Development of a ReaxFF Reactive Force Field for Fe/Cr/O/S and Application to Oxidation of Butane over a Pyrite-Covered Cr2O3 Catalyst. *ACS Catalysis*, 5(12):7226–7236, December 2015. Publisher: American Chemical Society.

[3] Leon C. Thijs, Efstratios M. Kritikos, Andrea Giusti, Marie-Aline van Ende, Adri C. T. van Duin, and XiaoCheng Mi. Effect of Fe–O ReaxFF on Liquid Iron Oxide Properties Derived from Reactive Molecular Dynamics. *The Journal of Physical Chemistry A*, 127(48):10339–10355, December 2023. Publisher: American Chemical Society.

[4] Igor Rahinov, Johannes Sellmann, Matthieu R. Lalanne, Monika Nanjaiah, Thomas Dreier, Sergey Cheskis, and Irenäus Wlokas. Insights into the Mechanism of Combustion Synthesis of Iron Oxide Nanoparticles Gained by Laser Diagnostics, Mass Spectrometry, and Numerical Simulations: A Mini-Review. *Energy & Fuels*, 35(1):137–160, January 2021.

[5] Daoguan Ning, Yuriy Shoshin, Martijn van Stiphout, Jeroen van Oijen, Giulia Finotello, and Philip de Goey. Temperature and phase transitions of laser-ignited single iron particle. *Combustion and Flame*, 236:111801, February 2022.

Modeling of Plastic Pyrolysis

F. Zhang[1*], M. Li[1], S. Tavakkol[1], T. Zirwes[2], and D. Stapf[1]

[*]E-Mail: feichi.zhang@kit.edu

[1]Institute for Technical Chemistry, Karlsruhe Institute of Technology, Kaiserstr. 12, 76131, Karlsruhe, Germany
[2]Institute for Reactive Flows, University of Stuttgart, Pfaffenwaldring 31, 70569 Stuttgart, Germany

Introduction Currently, chemical recycling through pyrolysis is recognized as a key technology to address the environmental and climate challenges posed by plastic waste. Unlike conventional mechanical recycling, which is limited to high-purity thermoplastics, pyrolysis can effectively recycle contaminated and mixed plastic waste. The potential of pyrolysis for plastic recycling has been extensively demonstrated in laboratory-scale experiments [1]. However, the reaction conditions in large-scale industrial pyrolysis plants differ significantly from the idealized conditions used in small-scale experiments, which often overlook real-world factors such as heat transfer, heat losses, and particle morphology. Experimental studies of pyrolysis processes are challenging due to the multi-scale coupling between hydrodynamics, transport phenomena, and reaction kinetics. As a result, numerical modeling has become an essential tool for studying pyrolysis in greater detail, providing deeper insights into the underlying thermo-chemical processes and facilitating the scale-up of plastic pyrolysis technologies.

Simulation Setups
This work highlights recent numerical studies on plastic pyrolysis conducted at the Institute for Technical Chemistry (ITC) at KIT. The primary objective of these studies is to develop and optimize plastic pyrolysis processes for industrial applications. The research systematically examines various setups, ranging from a single plastic particle to a fully resolved laboratory-scale fluidized bed reactor:

1. **Single-particle model (0D):** The plastic particle was modeled as a homogeneous, thermally thin sphere, which was heated and pyrolized in a nitrogen environment at an elevated temperature as illustrated in Fig. 1 (a). Two balance equations were solved for the particle mass and temperature, with the external heat transfer coefficient being adjustable. The pyrolysis reaction rate was determined using a global, single-step reaction model derived from thermogravimetric measurements. This setup was employed to investigate the effects of various operating parameters, such as plastic particle size and reactor temperature, as well as the interplay between heat transfer and pyrolysis chemistry on the overall conversion process [2].
2. **Particle-resolved simulation (3D):** An Eulerian-Eulerian approach was employed to simulate the pyrolysis process of a single plastic particle, enabling the resolution of velocity and thermal boundary layers around a non-ideal plastic particle, as well as internal gradients of chemical scalars within the particle. Two sets of balance equations in the Eulerian framework were solved for both the gas and solid phases, coupled through source terms for mass, heat, and momentum exchange. The void fraction, ε, was used to distinguish between phases, where $\varepsilon = 1$ represents the pure gas phase and $\varepsilon = 0$ corresponds to the pure solid phase. The particle shape was accounted for by initializing the ε field to 0 in the regions occupied by the particle. As pyrolysis progresses, the plastic particle shrinks until it is fully converted. This setup was used to investigate the influence of particle morphology (size and shape) on pyrolysis conversion [3].
3. **Fluidized bed (3D):** Eulerian-Lagrangian simulations were conducted to study the pyrolysis process of plastics in a fluidized bed reactor with dense gas-solid flow. The Multiphase Particle-in-Cell (MP-PIC) method was employed to model inter-particle collisions [4]. The simulations accounted for contact heat transfer between plastic particles and bed materials, as well as a lumped kinetic model to calculate product yields. The effects of various operating parameters, such as particle size, reactor temperature, and plastic loading, on both the hydrodynamic behavior of the fluidized bed and reaction selectivity were systematically evaluated [5].

The 3D simulations were performed using the open-source Computational Fluid Dynamics (CFD) code OpenFOAM, with newly implemented thermo-chemical models. The numerical methods for all setups were validated by comparing the results with experimental data, showing reasonably good agreement between the calculated and measured values.

Results

Figure 1 (b) illustrates the normalized pyrolysis time, τ_{py}/τ_c, derived from the single-particle setup (0D) as a function of the pyrolysis number, Py, for low-density polyethylene (LDPE: points) and high-density polyethylene (HDPE: triangles). τ_{py} is defined as the time duration from 1% to 99% of full conversion of the plastic particle and the characteristic time scale of chemical reactions τ_c is proportional to the rate coefficient of the pyrolysis reaction. The pyrolysis number Py is defined as the ratio of τ_c to the time scale of convective heat transfer τ_h. Variations in reactor temperature (T_R), particle size (d_P), and heat transfer coefficient (α) result in different values of τ_c and τ_h, representing distinct scenarios of the competing interactions between heat transfer and chemical reactions. When the pyrolysis reaction is slower than the heat transfer process ($\tau_c > \tau_h$, $Py > 1$), the overall conversion is limited by chemical kinetics. Conversely, when the heating process is slower than the pyrolysis reaction ($\tau_c < \tau_h$ or $Py < 1$), the conversion is limited by heat transfer. A strong correlation between τ_{py}/τ_c and Py was observed, which holds for all examined cases, including different plastic types, reactor temperatures, particle sizes, and heat transfer coefficients. The results demonstrate that pyrolysis conversion can be effectively accelerated at small Py values, where heat transfer is the limiting factor. In contrast, enhancing heat transfer at $Py >> 1$ does not significantly improve conversion, as the process is constrained by the slower chemical reaction. The relationship between τ_{py}/τ_c and Py was modeled using an inversely proportional function, as shown by the solid lines in Fig. 1 (b). This correlation provides a first-order estimate for predicting the required pyrolysis time under given operating conditions, highlighting the critical role of the interplay between pyrolysis reactions and heat transfer in determining overall conversion efficiency [2].

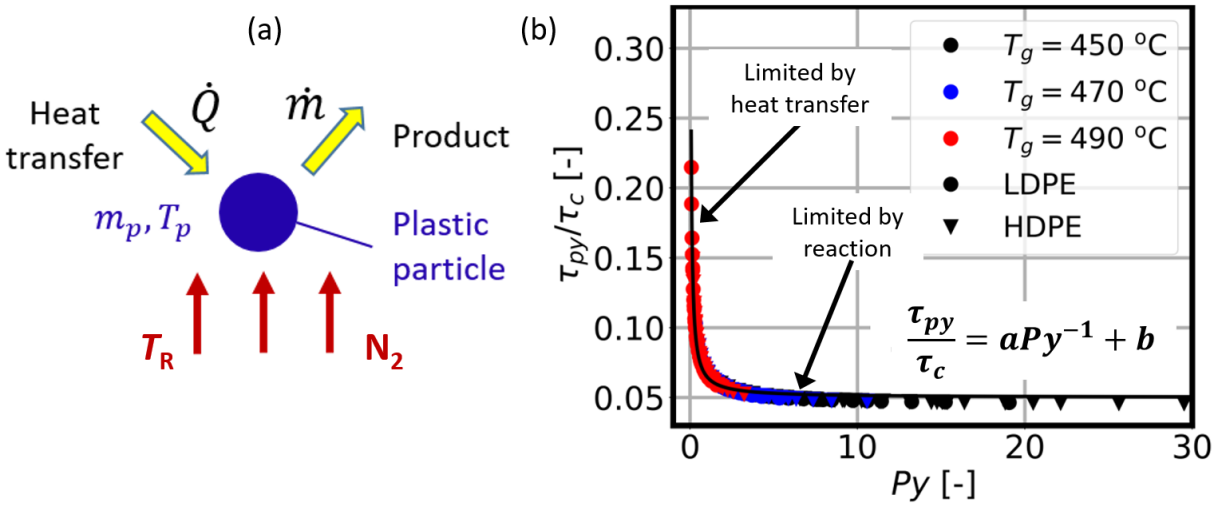

Figure 1: Schematic setup used for the simulation of pyrolysis of an ideal, homogeneous plastic particle (a) and correlation of normalized pyrolysis duration τ_{py}/τ_c with pyrolysis number Py (b).

In the second case, particle-resolved simulations were conducted to study the pyrolysis process of non-ideal HDPE particles with varying shapes and sizes in an inert hot nitrogen flow. Figure 2 (a) displays instantaneous contours of the particle temperature (T_P) and streamwise gas velocity (v) on a meridian cutting plane passing through the symmetry axis for a particle with a diameter of 6 mm. The flow direction is indicated by arrows. The gas velocity decreases to zero at the particle surface due to the no-slip boundary condition, while the gas temperature decreases to match the particle temperature near the gas-solid interface, forming both velocity and thermal boundary layers around the particle. Large temperature gradients were observed within the particle, with differences of up to 10 K between the core and the external surface. Since the reaction kinetics are highly sensitive to particle temperature, this led to notable deviations between the particle-resolved simulations and the conventional Lagrangian

method, which assumes a uniform temperature distribution across the particle. These results indicate that the Lagrangian approach is not suitable for modeling plastic pyrolysis when the particle diameter exceeds 2 mm. Additionally, the particle shape (sphere, cylinder, or shell) and flow direction (parallel or perpendicular to the cylinder axis) were found to significantly influence pyrolysis conversion, underscoring the critical role of heat transfer in the pyrolysis process [3].

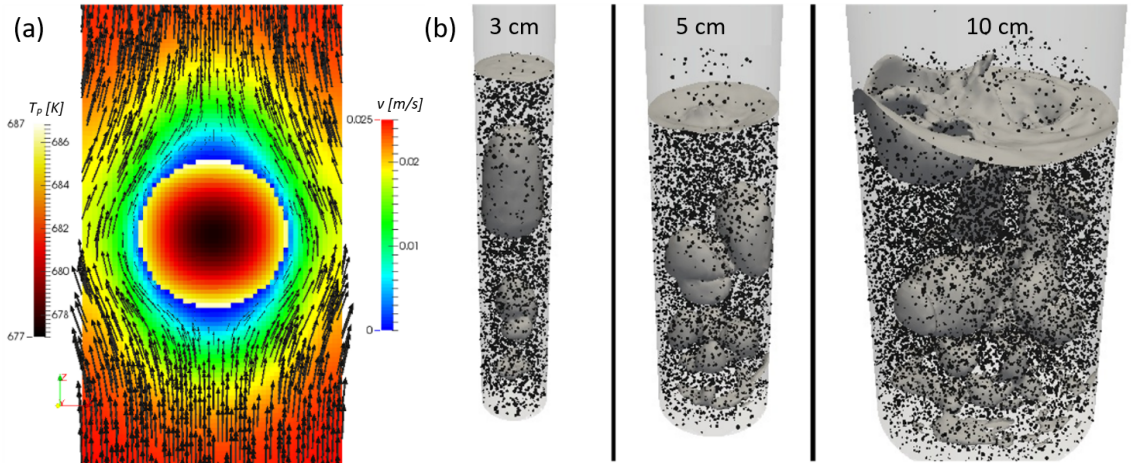

Figure 2: Contours of calculated particle temperature and gas flow velocity from a particle-resolved simulation of pyrolysis process of a HDPE particle (a) and comparison of bubble surfaces calculated from simulations of fluidized beds using different reactor diameters (b).

Fluidized bed reactors are considered a promising reactor concept for industrial-scale plastic pyrolysis due to their ability to provide homogeneous and enhanced heating as well as support continuous operation. To explore this potential, a laboratory-scale fluidized bed reactor was simulated, using inert sand particles as the bed material and air as the fluidizing agent. The simulations incorporated a particle size distribution based on experimental data and employed up to 1.6 kg sand along with 32 million Lagrangian parcels. The calculated fluidization morphology, pressure drop (Δp), and bed height (h_B) at varying bed inventory (m_S) and superficial gas velocity (u_G) showed excellent agreement with corresponding experimental results. In addition to Δp and h_B, the specific kinetic energy of the bed material (k_S) and the bubble frequency (f_B) were introduced to enable a more detailed analysis of the hydrodynamic behavior of the fluidized bed. These parameters were found to exhibit strong correlations with operating conditions such as u_G and m_S. Figure 2 (b) illustrates iso-surfaces of void fraction calculated for cold-mode fluidized beds with different reactor diameters (d_R), highlighting the structures of the bubbles and their interactions with the particles. The formation of bubbles was significantly enhanced during the up-scaling of the fluidized bed, which is attributed to the reduced influence of the reactor wall on the gas-solid flow. Furthermore, f_B was observed to increase with d_R, while Δp, h_B and k_S remained nearly constant. The reactor temperature had a minor influence on Δp, h_B and f_B, but k_S was found to increase significantly at elevated reactor temperatures [5].

Further simulations of plastic pyrolysis in fluidized bed reactors incorporated the effects of particle-particle heat transfer and pyrolysis chemistry. Figure 3 (a) presents a snapshot of the void fraction α_c and the spatial distribution of particles. The bubbles are identified by red zones with $\alpha_c = 1$, representing pure gas. The sand particles are depicted by teal dots, while the plastic particles are represented by blue points. The movement of these bubbles enhances the mixing of both particle types, resulting in a homogeneous temperature distribution throughout the reactor. Figure 3 (b) illustrates the temporal evolution of product yields, including the heavy fraction (HF), light fraction (LF), and gas (Gas), at a reactor temperature of 500°C. These yields are calculated by integrating the corresponding mass flow rates over the outlet area of the fluidized bed. As shown in Fig.3 (c), the final yield or selectivity in the stationary state indicates an increasing share of Gas and a decreasing share of LL with rising reactor temperature. This trend is attributed to differences in the activation energies of the corresponding reactions. Additionally, the size of the plastic particles, as well as the choice between batch-wise or continuous feeding modes, has been found to have a subordinate impact on the selectivity of the process.

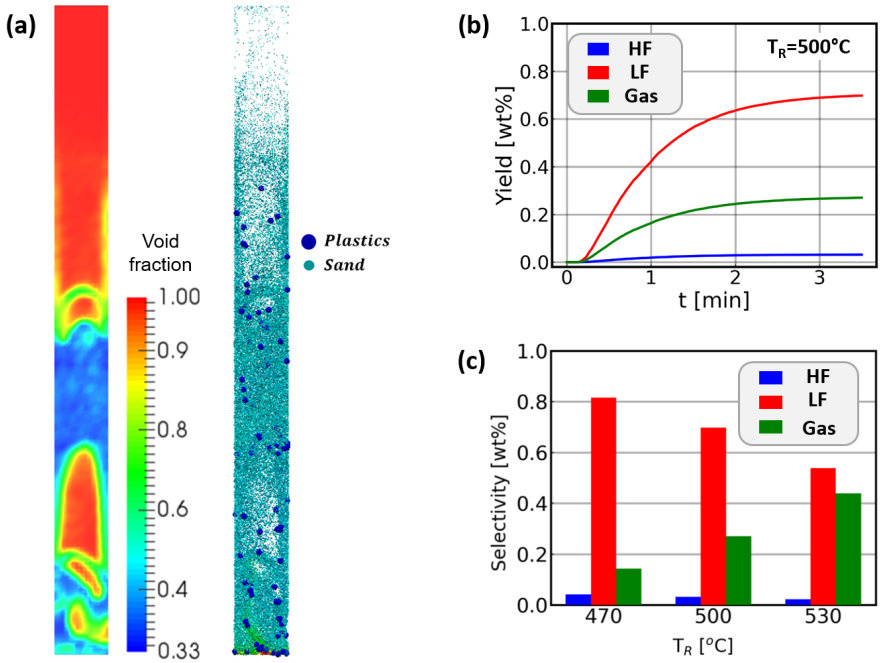

Figure 3: Contours of calculated void fraction and particle distribution from simulations of plastic pyrolysis in a fluidized bed (a), time evolution of product species at the outlet of the fluidized bed (b) and selectivity of plastic pyrolysis at different reactor temperatures (c).

The results demonstrate that the operating performance, in terms of product selectivity, can be adequately reproduced by numerical simulations across various operating conditions, such as reactor temperature, particle size, and operating modes (e.g., continuous or batch-wise feeding). However, the simulations rely on several closure models to compute the multiphase reactive flows, and certain factors—such as the influence of nonspherical particles, melting behavior, and detailed chemical kinetics—have not been accounted for. Addressing these limitations requires ongoing advancements in both theoretical and experimental research to deepen the understanding of the plastic pyrolysis process. Such insights are essential for developing more accurate and comprehensive chemo-physical models.

Acknowledgments

The authors gratefully acknowledge the financial support by the Helmholtz Association of German Research Centers (HGF), within the research program Materials and Technologies for the Energy Transition (MTET), topic Resource and Energy Efficiency. This work utilizes computing resources from the supercomputer HoreKa at the Scientific Centre for Computing (SCC) at KIT, Germany.

References

[1] Dogu O., Pelucchi M., Van de Vijver R.: *The chemistry of chemical recycling of solid plastic waste via pyrolysis and gasification: State-of-the-art, challenges, and future directions*, Prog. Energy Combust. Sci., 84, 100901, 2021.

[2] Zhang F., Cao J., Zirwes T., Netsch N., Tavakkol S., Zhang R., Bockhorn H., Stapf D.: *Numerical simulation of thermal decomposition of polyethylene with a single-particle model*, In Advances in Computational Heat and Mass Transfer, vol. 1. A.C. Benim, R. Bennacer, A.A. Mohamad, P. Oclon, S.H. Suh, J. Taler (eds), Springer Cham, 2024.

[3] Zhang F., Tavakkol S., Galeazzo F.C.C., Stapf D.: *Particle-resolved simulation of pyrolysis process of a single plastic particle*, Heat Mass Transf. 61(12), 2025.

[4] Alobaid F., Almohammed N., Farid M. M.: *Progress in CFD Simulations of Fluidized Beds for Chemical and Energy Process Engineering*, Prog. Energy Combust. Sci., 91, 100930, 2022.

[5] Zhang F., Tavakkol S., Dercho S., Zhou J., Zirwes T., Zeller M., Vogt J., Zhang R., Bockhorn H., Stapf D.: *Assessment of dynamic characteristics of fluidized beds via numerical simulations*, Phys. Fluids 36(2), 023348, 2024.

Interplay of primary and secondary reactions during PMMA pyrolysis – Experiments and modeling

S. Pielsticker[1*], K. Gfall[1,2], and R. Kneer[1]

[*]E-Mail: pielsticker@wsa.rwth-aachen.de

[1]*Institute of Heat and Mass Transfer, RWTH Aachen University, Augustinerbach 6, 52056 Aachen, Germany*
[2]*Leibniz Institute of Polymer Research Dresden, Hohe Straße 6, 01069 Dresden, Germany*

Introduction

The growing plastic waste problem has intensified the global pursuit of effective recycling strategies. Polymethyl methacrylate (PMMA), a widely used thermoplastic known for its transparency and weather resistance, poses challenges in waste management due to its durability and widespread use. Chemical recycling through pyrolysis is a promising way to convert PMMA waste into valuable resources and foster a circular economy [1]. Pyrolysis of PMMA involves thermal decomposition in an inert atmosphere, generating the monomer methyl methacrylate (MMA) and other valuable compounds. Process efficiency depends on understanding the reaction kinetics of thermal degradation. Factors such as temperature, heating rate, molecular weight, and catalysts or impurities influence the depolymerization and degradation pathways. Primary reactions break down PMMA chains to yield MMA monomers, but secondary reactions can alter these products, affecting yield and selectivity. Understanding the interplay between primary and secondary reactions is crucial for optimizing pyrolysis, especially when particle and gas residence times can be controlled separately [2]. To clarify the role of secondary pyrolysis and relevant mechanisms, experiments are conducted with reacting solid PMMA particles and pure gaseous MMA. For both the primary degradation of the solid and subsequent gas-phase decomposition reactions, models of varying complexity are evaluated.

Experimental investigation

For the experimental investigation, a fluidized bed reactor setup in two slightly different modifications is used. In both configurations, the reaction temperature (T_{FB} = 623–1073 K) is set via an electrically heated furnace, where the reactor is placed. The bed consisting of Al_2O_3 particles (d_{p} = 100–180 µm) is fluidized with an N_2 stream.

To investigate the pyrolytic decomposition of the solid PMMA particles, fuel samples are injected batch-wise (m_{PMMA} = 15 mg, d_{p} = 600–800 µm) via a lock system and a purge gas flow to the bed, as illustrated in **Figure 1**. While the particles stay until final decomposition in the reactor, the gaseous reaction products, fluidization gas and purge gas mix with each other and leave the reaction zone via a heated exhaust gas pipe. For the used fluidization volume flow of 80 L_n/h, the gas residence time in the hot reaction zone is around 6 to 8 s. In the case of MMA pyrolysis, a slightly modified reactor is used. The purge gas flow first bubbles through a tempered bath of liquid MMA before it is cooled down to a specific temperature to generate a saturated flow similar to the calibration process described in the study by Pielsticker et al. [4]. Afterward, the stream is guided through a small ceramic pipe to the bottom of the FBR and mixes with the bed. By changing the fluidizing volume flow between 50 and 150 L_n/h, the gas residence time is varied between 6 and 18 s.

In both cases, the composition of the exhaust gas stream is measured with a Fourier-transform infrared spectrometer (Ansyco GASMET DX-2000, 2.0 m optical path length) with a frequency of 0.38 Hz in the mid-infrared wavenumber region ν = 600–4200 cm^{-1}. In total, 13 relevant gas species including MMA and smaller side products are quantitatively determined. By closing the mass balance around the reactor, yields and decomposition rates are determined with methods previously developed for biomass [5].

Modelling

Modeling the thermal decomposition of the solid PMMA involves three main approaches. The single first-order (SFOR) model assumes a single reaction with constant kinetic parameters, providing a basic

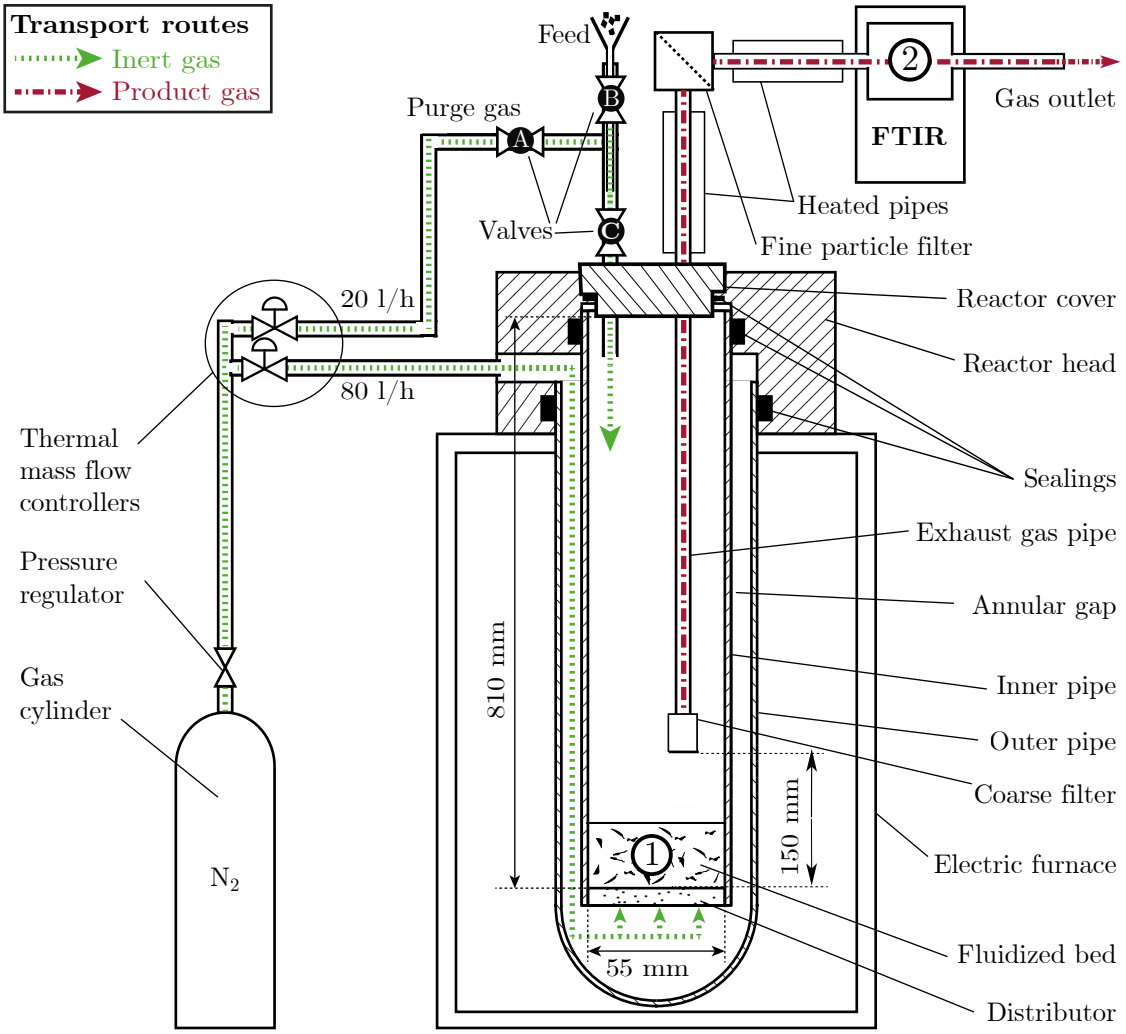

Figure 1. Experimental setup for PMMA pyrolysis in a fluidized bed reactor [3].

understanding but may simplify the complex degradation. However, a previous study by Gfall et al. [3] has shown that the SFOR approach is suitable to describe the conversion rate in the FBR. The multi-step model (MSM) considers multiple sequential or parallel reactions, each with its kinetics, offering a more detailed representation. For the most comprehensive analysis, the chemical percolation devolatilization (CPD) network model treats decomposition with a physics-based approach including, e.g., bond-breaking reactions and a vapor-liquid equilibrium. Similar to the solid-phase reactions, the gas-phase decomposition is also mapped with models of varying complexity, including a global simple first-order decomposition of MMA and a more detailed reaction mechanism with multiple reactions involved.

Results

Experiments with pure MMA as an educt serve to determine the gas-phase reaction kinetics. **Figure 2** shows the yields of MMA and light gas decomposition products at different temperatures T_{FB} and volume flows $\dot{V}$. Changing the volume flows allows for the investigation of different gas residence times under hot conditions. Higher temperatures and longer residence times promote the decomposition.

Assuming a plug flow reactor and a one-step global reaction, the reaction rate r_{sec} is determined by

$$r_{sec} = \ln\left(1 - y_{LG}\right) \cdot \frac{\dot{V}}{V} \tag{1}$$

with y_{LG} being the light gas yield and V the reactor volume between the bed and reactor exit. With an Arrhenius approach, kinetic parameters such as activation energy $E_a = 99.1\,\mathrm{kJ\,mol^{-1}}$ and pre-exponential factor $A = 1.02 \cdot 10^5\,\mathrm{s^{-1}}$ are determined via a least-square fit procedure. The corresponding kinetic is

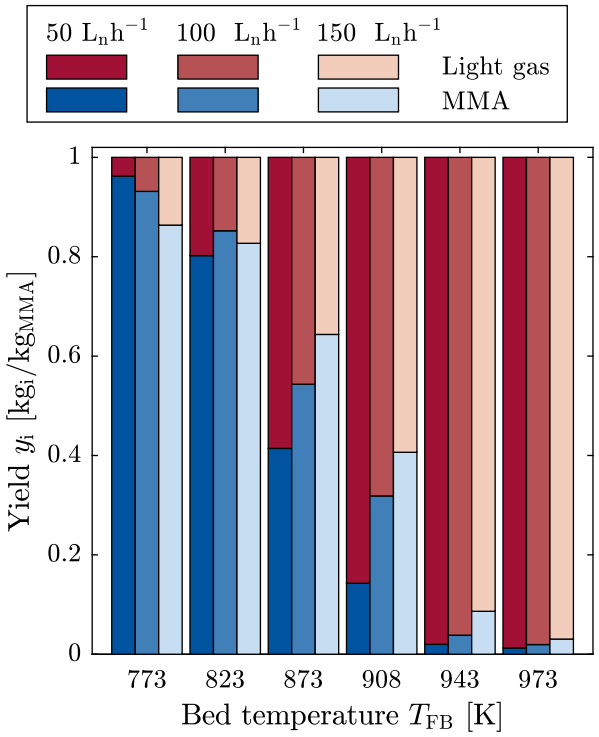

Figure 2. Measured yields of MMA and light gas decomposition products from MMA pyrolysis.

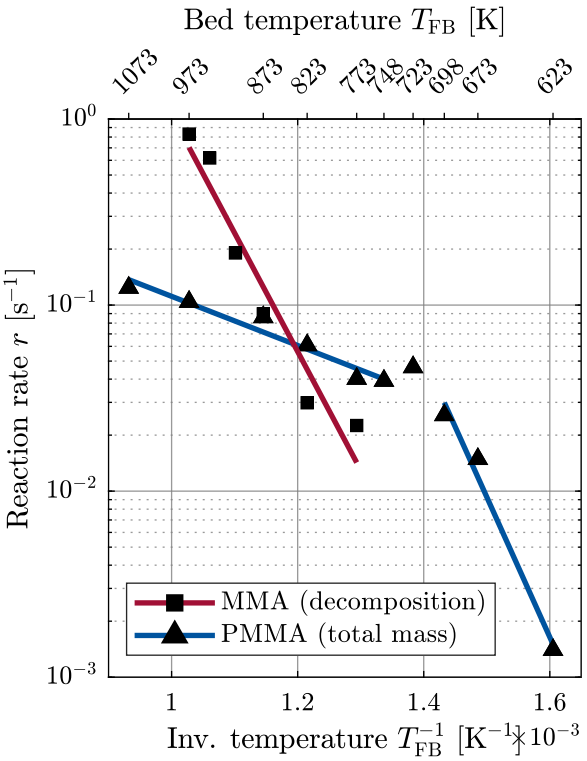

Figure 3. Arrhenius diagram for MMA gas-phase decomposition and PMMA pyrolysis.

depicted in the Arrhenius diagram in **Figure 3** (red curve).

Additionally, **Figure 3** shows apparent reaction kinetics obtained with experiments using solid PMMA particles as fuel feed [3]. The blue line indicates the total mass loss kinetic including MMA and light gas volatiles under the assumption of a single first-order release characteristic. The two visible reaction regimes can be attributed to pure reaction kinetics controlled behavior at low temperatures and a heat transfer limited regime at high temperatures. For the kinetics controlled regime, the kinetic parameters $E_a = 144.2\,\mathrm{kJ\,mol^{-1}}$, $A = 1.85 \cdot 10^9\,\mathrm{s^{-1}}$ have been derived [3].

To evaluate the interplay of primary and secondary pyrolysis reactions, yields of the three species PMMA, MMA, and the group of lumped light gases are calculated from the PMMA pyrolysis experiments. Since no direct sampling of the solid material is possible, PMMA yields are calculated from difference. **Figure 4** shows the experimentally gained yields in comparison to the model prediction using a two-step decomposition mechanism. For simplification, the gas-phase temperature is set equal to the bed temperature, and a constant gas residence time $t_g = 10\,\mathrm{s}$ is assumed.

Figure 4 shows a steady decrease of the MMA yield at the expense of formed light gases with increasing temperature for both, the experimentally obtained results and the model predictions. The model tends to slightly overpredict the decomposition at higher temperatures, while the modeled MMA yields exceed the experimental ones for T_{FB} between 673 and 773 K. Due to the different bed temperatures and the temperature profile along the exhaust gas line, the gas residence time may slightly deviate from the assumed constant value. In addition, the model makes the assumption that the light gas products only result from the decomposition of MMA. However, light gases can also be produced along with the depolymerization reactions [6]. This effect is particularly significant when PMMA decomposition is slow and the residence time of the solid phase is significantly longer than the one of the gas phase.

Except for $T_{FB} = 623\,\mathrm{K}$, a full conversion of PMMA into gaseous products is observed in the experiment time t_{exp}. Note, that the experimental time is in most cases significantly longer than the conversion time, to ensure that the entire conversion process is captured in the experiment. Model predictions using the primary SFOR decomposition model with the kinetic parameters presented by Gfall et al. [3] support the above-mentioned observation as they only show a remaining PMMA fraction for 673 K.

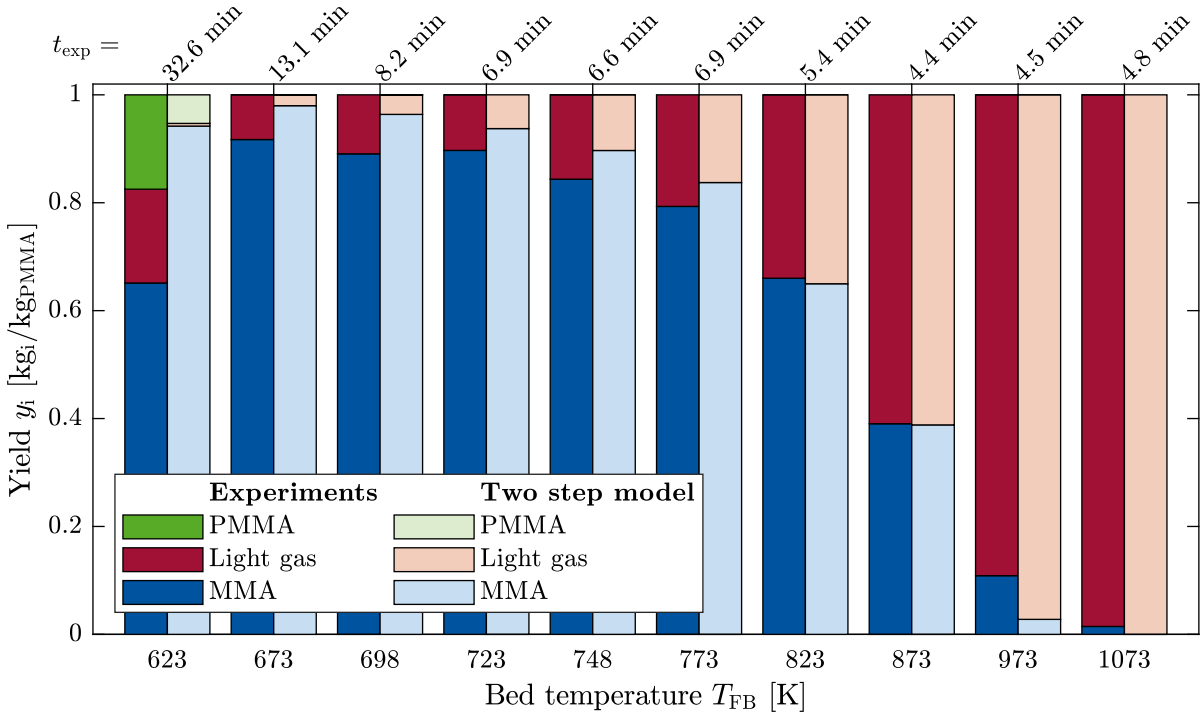

Figure 4. Yields of PMMA (by difference), MMA, and light gas decomposition products obtained from experiments in the FBR in comparison with model predictions using a gas residence time t_g = 10 s.

Conclusion

This study demonstrates that pyrolysis is an effective method for recycling PMMA waste, converting it into valuable monomers like MMA. The experimental results in a fluidized bed reactor, supported by modeling using a single first-order reaction approach, show that primary degradation of PMMA is well-predicted, though secondary gas-phase reactions at higher temperatures affect yields by increasing light gas formation. Understanding and modeling the interplay between primary and secondary reactions are thus crucial for optimizing the pyrolysis process to enhance MMA yields and overall efficiency.

Acknowledgement

The authors thank for funding from the Exploratory Research Space – ERS, RWTH Aachen under grant agreement PFKA008 ”Cluster 4 Plastics Recycling” and the German Research Foundation (DFG) – project number 215035359 – within the CRC/TRR 129 ”Oxyflame”.

References

[1] Kikuchi, Y., Hirao, M., Ookubo, T., Sasaki, A.: *Design of recycling system for poly(methyl methacrylate) (PMMA). Part 1: Recycling scenario analysis*, The International Journal of Life Cycle Assessment, 19(1), 120–129, 2014.

[2] Zeng, W.R., Li, S.F., Chow, W.K.: *Review on chemical reactions of burning poly(methyl methacrylate) PMMA*, Journal of Fire Sciences, 20(5), 401–433, 2002.

[3] Gfall, K., Kneer, R., Pielsticker, S.: *Determination of PMMA pyrolysis kinetics and the role of heat transfer limitations*, 13th Mediterranean Combustion Symposium, 2025.

[4] Pielsticker, S., Hendricks, K., Knevels, C., Lehnertz, M.S., Palkovits, R., Kneer, R.: *Experimental determination of quantitative yields from polymethyl methacrylate (PMMA) flash pyrolysis in a fluidized bed reactor via online FTIR gas analysis*, Fuel, p. 134827, 2025.

[5] Pielsticker, S., Schlögel, K.U., Kreitzberg, T., Hatzfeld, O., Kneer, R.: *Biomass pyrolysis kinetics in a fluidized bed reactor: Measurements and plausibility verification for reaction conditions*, Fuel, 254, 115589, 2019.

[6] Brandrup, J., Bittner, M., Michaeli, W., *Die Wiederverwertung von Kunststoffen*, Hanser Verlag, 1995.

Temperature Measurement during the Ignition and Combustion of Particle Clouds using Two-Color-Pyrometry

M. Giesen[1*], D. Bernhardt[1] and M. Beckmann[1]

*E-Mail: matteo.giesen@tu-dresden.de

[1] Chair for Energy Process Engineerung, Technical University Dresden, George-Bähr-Str. 3b, 01069 Dresden, Germany

Introduction

In order to reduce fossil CO_2-emissions biogenic fuels are used as a substitute for fossil fuels in combustion processes. However, many biogenic residues are not considered for substitution due to their different ignition and combustion properties. In this case, laboratory analyses of the substitute fuels or fuel mixtures can provide initial indications of the possibly changed combustion behavior. So far, however, there is no standardized method for determining the ignition and combustion behavior of powdered fuels. Therefore, special attention will be paid here to the investigation of the ignition and combustion behavior of pulverized fuels, which can be carried out on individual particles or particle clouds.

Using single particle methods like the FIELD tube kinetic parameters of the ignition and combustion of particles can be determined as a function of external conditions as well as fuel properties [1]. This high number of dependent variables leads to considerable measurement uncertainties, high costs and difficulties in the representative application to inhomogeneous or time-varying fuels such as biomasses. In addition, the essential influencing factor of particle-wall and particle-particle interactions cannot be considered.

To include these essential processes in the combustion of particle clouds, the Zelkowski ignition oven method can be used [2]. Using this method the ignition delay time, which measures the change in light intensity, and its dependence on the above parameters is determined. If the ignition delay time is plotted against the combustion gas temperature, the ignition hyperbola is obtained, which can be used to derive the burner design and adjustment. To get further information about the ignition and combustion behavior the existing ignition oven method is combined with spectroscopy in the UVVIS- and NIR-range to gain temporal and spectral data of the ignition and combustion behavior of powdered fuels. From spectral emissions information about occurring species and, using two-color-pyrometry, the temperature in the particle cloud can be determined. In this contribution the combined ignition oven and spectroscopy method will be described, experimental results will be shown and discussed.

Experimental Setup

The experimental setup consists of an ignition oven [2] where the measurement setup is extended using UVVIS- and NIR-spectroscopy (s. Figure 1). For the experiments fuel samples get injected into the electrically heated combustion chamber (up to 1000°C) using an injection lance and pressured air. The fuel samples are manually placed in the water-cooled injection lance. The injection of the fuel sample is synchronized with the measurement setup to establish a temporal correlation between the ignition and combustion process and the injection into the combustion chamber.

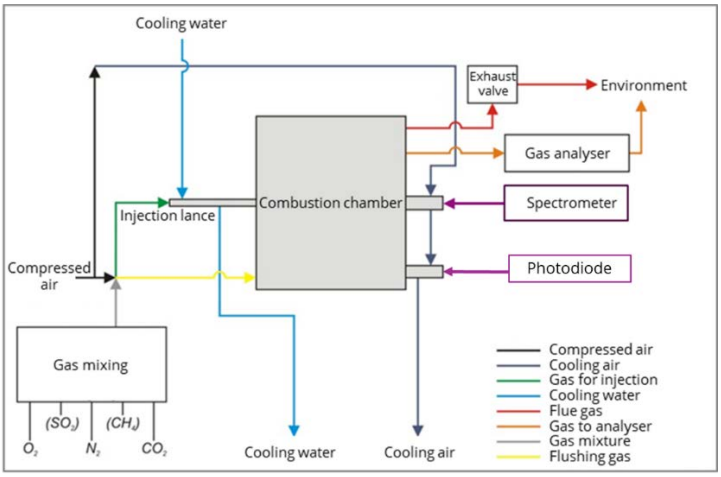

Figure 1. Scheme of the experimental setup

The emitted radiation during the ignition and combustion process, which consists of thermal and atomic/molecular radiation, is focused on an optical fiber using a coupling optic. The optical fiber transmits the radiation to a UVVIS-spectrometer (AVASPEC-ULS2048CL-EVO, 200-1100 nm) and a NIR-spectrometer (HORIBA MicroHR, 800-1700 nm, 150 lines/mm grating). The temporally resolved radiation in the NIR is obtained using a linescan camera (Sensors Unlimited 1024 LDM) and the corresponding SUI Image Analysis Software. In the UVVIS the data is acquired using AvaSoft software.
The experiments are conducted in a temperature range from 450°C to 900°C in 50K steps. At every temperature three repetitions are carried out. The biomass samples were ground, sieved to a particle size of less than 63 µm and dried. The fuel samples were weighed to 0.2 g.
Five fuels were investigated: Wood dust, olive cake (residues from olive oil production), draff, barley husk and bio coal. These fuels were chosen to represent a wide spectrum of different biogenic fuels. The fuels not only have a different composition regarding the elemental analysis and the volatile content but also differ in their structure. While wood dust has a structure mainly made of cellulose, hemicellulose and lignin, olive cake has a higher content of oils and fats, and Bio Coal consists of a Carbon structure. These properties are the main influencing factors for the ignition and combustion behavior [3].

Table 1: Fuel compositions

		Wood Dust	Olive Cake	Draff	Barley Husk	Bio Coal
Ash	Ma.-%	2.13	6.58	3.71	7.34	1.90
Volatiles	Ma.-%	79.28	73.27	80.47	74.36	44.18
Fixed Carbon	Ma.-%	18.28	18.44	15.69	17.96	53.92
Carbon	Ma.-%	51.11	48.53	48.67	44.44	69.87
Hydrogen	Ma.-%	5.49	6.49	6.65	5.89	4.44
Oxygen	Ma.-%	40.61	34.74	38.23	40.77	23.21
Nitrogen	Ma.-%	0.32	1.59	2.35	1.11	0.44
Sulfur	Ma.-%	0.03	0.36	0.26	0.12	0.10
Heating Value	MJ/kg	19.05	18.34	18.69	16.74	26.38

Two-Color-Pyrometry
The temperature of the particle cloud is determined using two-color pyrometry comparing the intensity at 750 nm and 940 nm. Following the approach described by [4,5] the temperature can be calculated by Wien`s law:

$$T = c_2 \frac{\lambda_1 - \lambda_2}{\lambda_1 \lambda_2} \left(\ln\left(\kappa \left(\frac{\lambda_1}{\lambda_2} \right)^5 \right) + \ln\left(\frac{I_1}{I_2} \right) \right)^{-1} \quad (1)$$

where c_2 is the second radiation constant, λ_1= 750 nm, λ_2= 940 nm, I_1 and I_2 are the intensities at λ_1 and λ_2 respectively. The calibration constant κ is determined for this measurement setup using calibration measurement with a blackbody reference radiation source. The radiation of the blackbody radiation source was measured at a temperature range from 300°C to 1500°C in 10K steps. Thus, the calibration constant was determined to be $\kappa = 0.689277 \pm 0.007961$.

Results
The course of the temperature of the particle cloud during the ignition and combustion process shows the rise of the temperature when the ignition starts. Thus, also the point of ignition can be determined using this method. However, the focus of this work is on the temperature changes in the particle cloud during the ignition and combustion process and the comparison of different biogenic fuels. Figure 2 shows the calculated temperature of the particle cloud for wood dust and olive cake of the experiments with an ignition oven temperature of 900°C. The fuels samples are injected at 2000 ms. Therefor the first part, until the temperature increases due to the ignition, shows the temperature of the ignition oven. The determination of the oven temperature is connected with uncertainties, because the accuracy of the calibration method increases with increasing temperatures. During the whole ignition and combustion process the temperature of wood dust is higher. Wood dust has a higher heating value and amount of volatiles, while olive cake has a higher content of ash, which are connected to the temperature of the particle cloud. The differences in the structure of both fuels can also influence the temperature of the cloud, while the structure is also a main influencing factor for the devolatilization and the start of the ignition. For both fuels the temperature reaches the level of the oven temperature at 2270 ms, indicating a similar timespan for the ignition and combustion process.

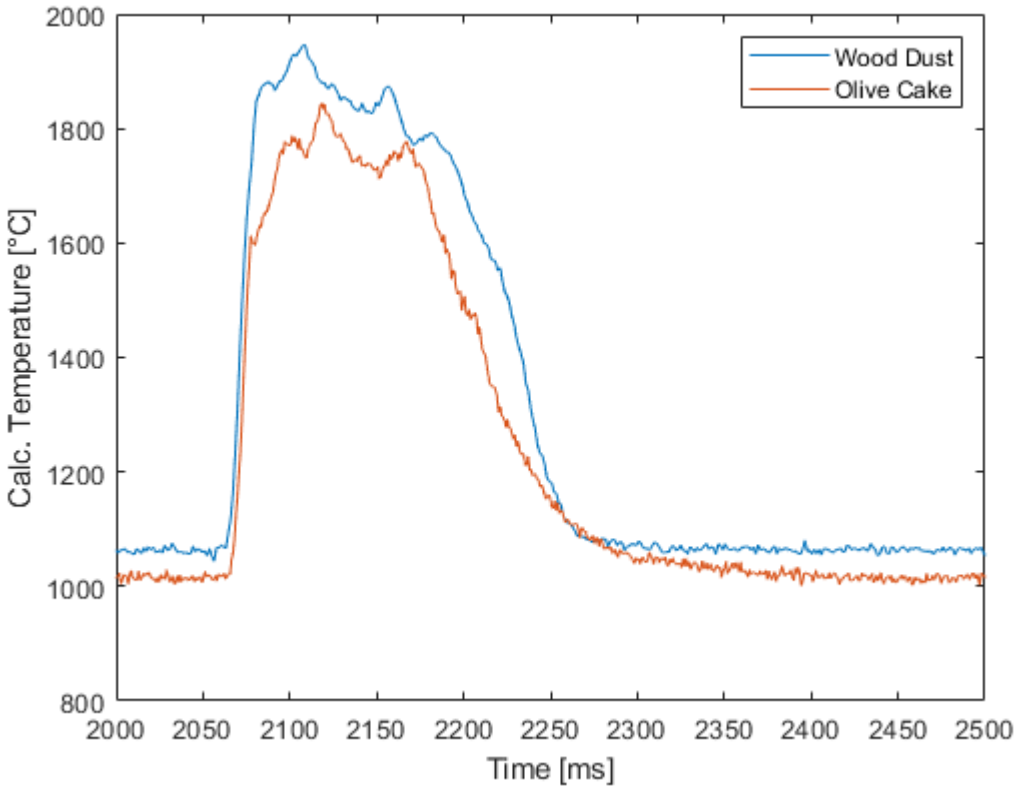

Figure 2: Temperature of the particle cloud for Wood Dust and Olive Cake ($\vartheta_{Oven} = 900°C$)

Conclusion

The presented method, combining the ignition oven with spectroscopy and using two-color pyrometry, is a novel approach to determine the temperature inside a particle cloud during the ignition and combustion process while accounting for particle-particle interactions in particle clouds. As a first result the temperature course of wood dust and olive cake at an ignition oven temperature of 900°C is presented. Further investigations regarding other biogenic fuels and experimental conditions will be conducted to get further insight into the process of ignition and combustion as well as determining influencing factors of the temperature in the particle cloud.

Acknowledgement

The investigations presented were part of the AiF-IGF research project "Methodenentwicklung zur Charakterisierung der Zündung staubförmiger Brennstoffe mittels Spektroskopie an einem Zündofen" with the funding reference 22159 BR / 1, which was funded by the Federal Ministry for Economic Affairs and Climate Action based on a resolution of the German Bundestag.

References

[1] Field, M. A. (1969): Rate of Combustion of Size-Graded Fractions of Char from a Low-Rank Coal between 1200K and 2000K. In: Combustion and Flame 13 (3), S. 237–252, zuletzt geprüft am 25.07.2024.
[2] Zelkowski J. Kohlecharakterisierung und Kohleverbrennung. 2nd ed. Essen: VBG PowerTech Service GmbH; 2004.
[3] Mularski, Jakub; Li, Jun (2023): A review on biomass ignition: Fundamental characteristics, measurements, and predictions. In: FUEL 340, S. 127526. DOI: 10.1016/j.fuel.2023.127526.
[4] Pörtner L, Gu Y, Schiemann M. Investigation of Pulverized Biomass and Coal Char Emissivity. Energies 2020;13(18):4620. https://doi.org/10.3390/en13184620.
[5] Graeser P, Schiemann M. An attempt to measure the emissivity of burning coal particles in oxy-fuel atmospheres: test rig calibration and first results. The 40th International Technical Conference on Clean Coal & Fuel Systems 2015. https://doi.org/10.13140/RG.2.1.2840.8483.

Methodology for derivation of effective heat transfer properties by pore network modeling

F. Faber[1*], S. Bhaskaran[1], A. Dieguez-Alonso[2], and N. Vorhauer-Huget[1]

[*]E-Mail: felix.faber@ovgu.de

[1]*Thermal Process Engineering, Otto-von-Guericke-University Magdeburg, Universitätsplatz 2, 39106 Magdeburg, Germany*
[2]*Transport Processes, Technical University Dortmund, Emil-Figge-Str. 68, 44227 Dortmund, Germany*

Introduction

Heat transfer in porous media plays a tremendous role for thermochemical conversion processes, e.g. pyrolysis, gasification, or chemical syntheses under heterogeneous catalysis conditions, but also in other processes like drying or combustion. In cases where the product quality is of importance, or when the product composition, yield and conversion rates are dependent on the local temperature, a detailed understanding of the pore-level temperature field, but also heat transfer rates inside the porous material, are of interest. Especially when naturally grown materials like wood are used as feedstock, models are needed that describe the heat and mass transfer accurately with respect to the anisotropic character of the material. In this regard, heat dissipation by electromagnetic waves imposes challenging new research tasks that highly demand for a fundamental understanding of the complex and strongly coupled heat and mass transfer processes.

While for the mass transfer only the void space of a porous sample is of relevance, heat transfer as well as dielectric heating with microwaves occurs in and through the solid. In case of wood, its anisotropic character results especially in different effective properties for the mass transfer [1], but also for the thermal conductivity [2] as well as dielectric constant and loss [3], depending on the direction.

Methodology

A Pore network model (PNM) is a versatile tool for deterministic simulations of pore-scale phenomena, especially when it comes to kinetically limited processes. Our PNM approach builds on tomographic data that is obtained by 3D X-ray tomography, in Figure 1a shown for the selected region of interest (ROI) of a beech wood sample.

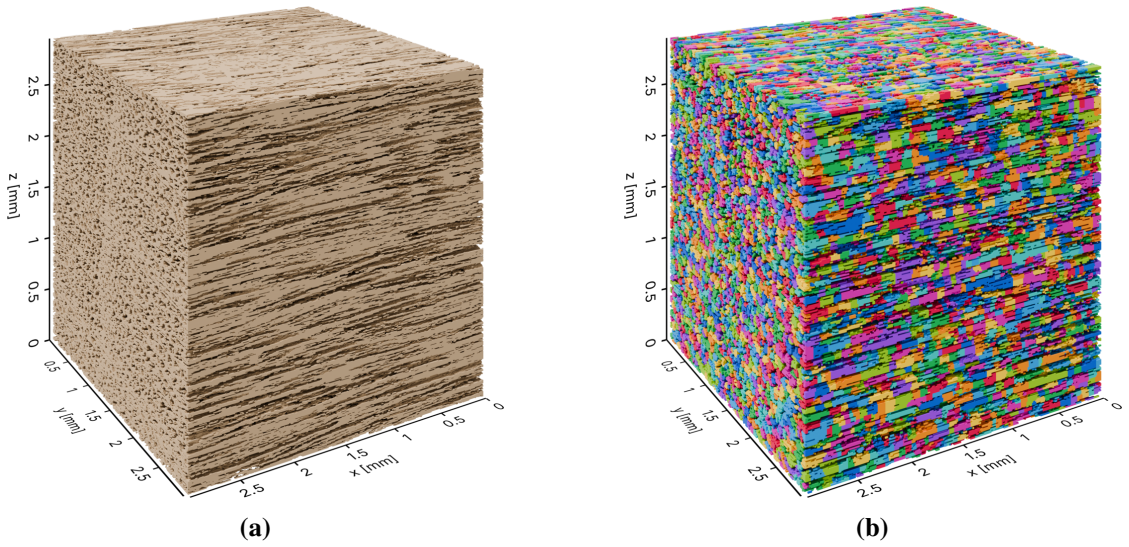

Figure 1. The solid structure of a beech wood sample (a) obtained by X-ray tomography (voxel edge length: 5.9 µm) and subsequent binarization, and (b) segmentation of the void space into pores for determination of local transport properties. Visualizations are created with our in-house Python package "PoreScene" for Blender.

In a first step, the void space of the porous material is segmented into individual pores using a marker-based watershed algorithm that was already presented in Faber et al. [4]. The resulting pore bodies are shown in Figure 1b. This segmentation of only the void space provides first hand a foundation for the computation of effective mass transfer permeabilities by calculating fluid flow from pore to pore, employing the Hagen-Poiseuille-Equation between them [5, 6].

We propose an analogous scheme for the computation of the effective thermal conductivity of porous materials, i.e., computing the heat transport pore-resolved to obtain the macroscopic, therefore effective, thermal conductivity. For this, a control volume (CV) is wrapped around each pore from Figure 1b by using a Voronoi tessellation [4]. Each CV is assigned with a local porosity ε_i extracted from the binary image (cf. Figure 1a) , which yields a spatial distribution of the porosity that is (corresponding to the solid structure from Figure 1a) shown in Figure 2a, mapping both, the denser regions of the annual rings of the wooden structure (visible between $y = 1$ mm to 1.5 mm), as well as the longitudinal pores in x-direction, clearly.

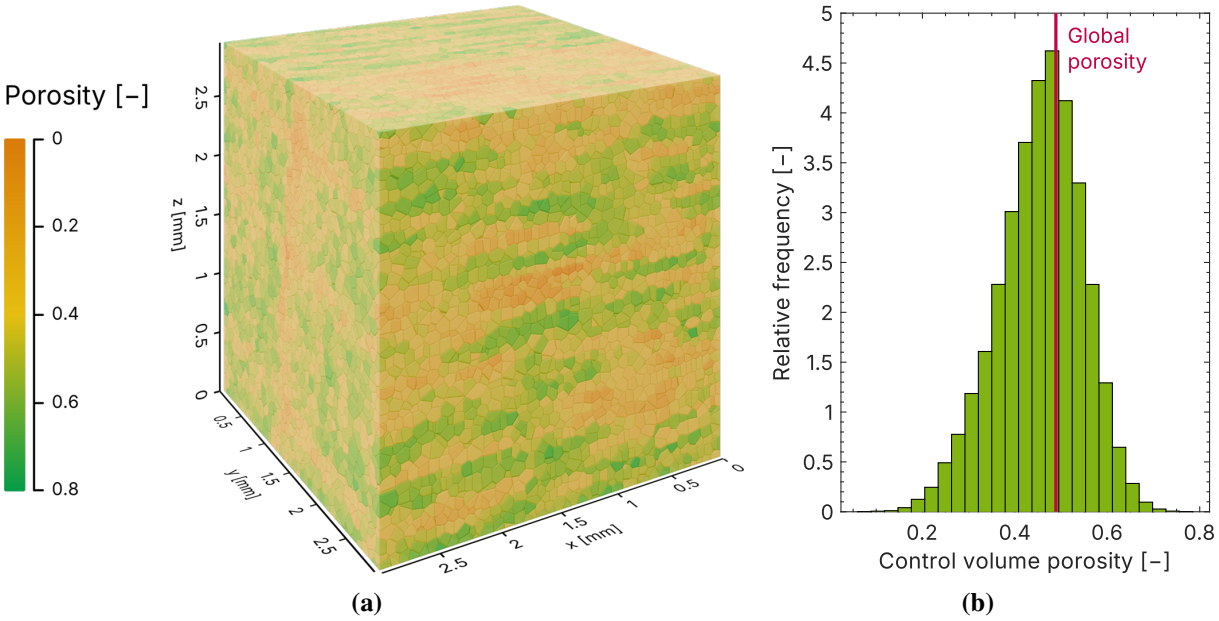

Figure 2. (a) Spatial distribution of the local porosity ε_i for the sample from Figure 1a that builds the foundation for the pore-scale distribution of thermo-physical properties, e.g., thermal conductivity, density, dielectric loss, and (b) the corresponding relative frequency distribution of the control volume porosities.

For the computation of heat transfer between adjacent pores we use an approach following Tsotsas [7] that calculates the effective thermal conductivity based on serial and parallel arrangement of heat transfer resistances, described with a fraction of serial heat conductivity a_{serial} and the material properties of the pure phases λ_{solid} and λ_{void}:

$$\lambda_{\text{parallel},i} = \varepsilon_i \lambda_{\text{void}} + (1 - \varepsilon_i)\lambda_{\text{solid}} \tag{1}$$

$$\lambda_{\text{serial},i} = \left(\frac{\varepsilon_i}{\lambda_{\text{void}}} + \frac{1 - \varepsilon_i}{\lambda_{\text{solid}}} \right)^{-1} \tag{2}$$

$$\lambda_{\text{eff},i} = \left(\frac{a_{\text{serial}}}{\lambda_{\text{serial},i}} + \frac{(1 - a_{\text{serial}})}{\lambda_{\text{parallel},i}} \right)^{-1} \tag{3}$$

Employing Eqs. (1) to (3) to each CV, establishes a spatial distribution of the local thermal conductivity $\lambda_{\text{eff},i}$, mapping in total the spatial differences of the material morphology. In case of heterogeneous, or even anisotropic structures like wood, a careful consideration of the fraction of serial heat conductivity a_{serial} is necessary, which might be achieved with a local, directional dependent determination of the parameter.

The overall heat flux through the ROI $\dot{Q}_{\text{tot}}$ is computed by imposing a thermal gradient across the ROI, i.e., applying a constant temperature to the boundary pores opposite to each other, and by computing

the heat transport between a neighboring pair of pores i and j using Fourier's heat conduction approach:

$$\dot{Q}_{ij} = \left(\frac{0.5 L_{ij}}{\lambda_{\mathrm{eff},i}} + \frac{0.5 L_{ij}}{\lambda_{\mathrm{eff},j}} \right)^{-1} A_{\mathrm{CV},ij} \left(T_j - T_i \right), \tag{4}$$

with L_{ij} as distance between both pore centers and $A_{\mathrm{CV},ij}$ as shared interface of the polyhedral Voronoi cells. The effective thermal conductivity of the sample is subsequently available from

$$\lambda_{\mathrm{eff,ROI}} = \frac{\dot{Q}_{\mathrm{tot}} L_x}{A_{\mathrm{ROI,yz}} \left(T_{\mathrm{out}} - T_{\mathrm{in}} \right)}, \tag{5}$$

by regarding the selected temperatures T_{in} and T_{out} at the lateral ROI interfaces of size $A_{\mathrm{ROI,yz}}$ opposite to each other and the distance L_x between them. By switching the direction of the thermal gradient, the heat transfer parallel as well as perpendicular to the longitudinal pores of the wood sample can be assessed.

Outlook

The proposed methodology allows not only the computation of effective thermal properties, even more importantly, it allows as well the simulation of the transient heat transfer under consideration of local, volumetric heating, e.g. occurring during microwave pyrolysis of wood. The thermal conductivity as well as dielectric loss (but also density and heat capacity) are functions of the local pore-solid structure, which are expected to be precisely mapped with the PNM approach. However, the comparison to direct numerical simulation of flow and heat transfer on the pore scale remains an open task.

Acknowledgments

This work was funded by the Deutsche Forschungsgemeinschaft (DFG, German Research Foundation) – Project-ID 422037413 – TRR 287.

References

[1] Dernbecher A., Bhaskaran S., Vorhauer-Huget N., Seidenbecher J., Gopalkrishna S., Briest L., Dieguez-Alonso A.: *Investigation on the intra-particle anisotropic transport properties of a beech wood particle during pyrolysis*. Submitted to Particuology.

[2] Sonderegger W., Hering S., Niemz P.: *Thermal behaviour of Norway spruce and European beech in and between the principal anatomical directions*, Holzforschung, 65, 369–375, 2011. DOI: 10.1515/hf.2011.036.

[3] Sahin H., Ay N.: *Dielectric properties of hardwood species at microwave frequencies*, Journal of Wood Science, 50, 375–380, 2004. DOI: 10.1007/s10086-003-0575-1.

[4] Faber F., Vorhauer-Huget N., Thomik M., Gruber S., Först P., Tsotsas E.: *Pore-scale study of coupled heat and mass transfer during primary freeze-drying using an irregular pore network model*, Drying Technology, 2025. DOI: 10.1080/07373937.2024.2407062.

[5] Neumann R. F., Barsi-Andreeta M., Lucas-Oliveira E., Barbalho H., Trevizan W. A., Bonagamba T. J., Steiner M. B.: *High accuracy capillary network representation in digital rock reveals permeability scaling functions*, Scientific Reports, 11, 11370, 2021. DOI: 10.1038/s41598-021-90090-0.

[6] Vorhauer N., Altaf H., Tsotsas E., Vidakovic-Koch T.: *Pore Network Simulation of Gas-Liquid Distribution in Porous Transport Layers*, Processes, 7, 558, 2019. DOI: 10.3390/pr7090558.

[7] Tsotsas E.: *D6.3 Thermal Conductivity of Packed Beds*. *VDI Heat Atlas*. 2nd ed. Berlin, Heidelberg: Springer, 2010, 570–580. ISBN: 978-3-540-77877-6.

Reaction Kinetics of Biogenic Fuel Gasification for Chemical Looping

M. Schmitt[1*], L. Lindmüller[1], and S. Heinrich[1]

[*]E-Mail: marian.schmitt@tuhh.de

[1]*Institute of Solids Process Engineering and Particle Technology, Hamburg University of Technology, Germany*

Motivation

In response to increasingly stringent global climate targets and the urgent need to reduce CO_2 emissions, novel combustion processes that enable inherent carbon capture are garnering significant attention. Chemical looping combustion (CLC) is one such process, originally developed to produce pure CO_2 streams. By circulating an oxygen carrier between a fuel reactor (where reduction occurs) and an air reactor (where reoxidation takes place), CLC inherently sequesters CO_2 without requiring additional downstream treatment. This capability positions CLC as a promising candidate for biomass-based energy production, particularly when combined with carbon capture and sequestration (BECCS) strategies aimed at achieving negative emissions [1]. The shift towards biogenic fuels, accelerated by policies such as the German coal phase-out act, necessitates efficient use of solid biofuels in industrial applications. However, conventional fluidized bed reactors face challenges when handling biomass due to its wide particle size distribution, high volatile content, and complex ash behavior. These factors impair the interaction between the fuel and the oxygen carrier, reducing heat and mass transfer efficiencies and complicating fluidization [3]. Thus, a detailed kinetic understanding of biomass devolatilization and char gasification is crucial for optimizing the design and operation of CLC reactors [2]. This study focuses on quantifying the gasification kinetics of woody biomass coke produced by controlled devolatilization and investigates the impact of reactor design and particle size distribution on conversion efficiency.

Experimental Setup

Experiments were conducted in a lab-scale hot plant specifically designed to replicate the conditions of chemical looping combustion (CLC) processes. The reactor consists of a chrome-nickel steel tube 500 mm in length and 53 mm in diameter, heated by a 4 kW electrical unit with PID control, which allows the system to reach and maintain temperatures up to 1100 °C. Pre-heated fluidizing gases are uniformly introduced through a sintered metal distributor, ensuring consistent gas flow and proper fluidization. Temperature sensors and pressure gauges are positioned below and above the distributor, within the freeboard phase, and at the outlet to provide real-time monitoring to guarantee stable operating conditions. The biomass feedstock comprised softwood pellets that were first milled and subsequently degassed. During degassing, approximately 300 grams of shredded biomass was processed at 900 °C under a continuous flow of nitrogen. This treatment removed volatile compounds, leaving behind coke residue. The resulting coke was crushed and sieved into several size fractions, with particles smaller than 50 μm classified as dust and excluded from further analysis. The coke's particle size distribution was determined using dynamic image analysis (Camsizer XT by Retsch), and its composition was assessed through both ultimate analysis, which provides elemental composition, and proximate analysis, measuring moisture, ash, and volatile contents. The results for both are shown in table 1.

Gasification experiments were conducted under two distinct conditions to simulate both inert and reactive environments. In the inert experiments, quartz sand was used as the bed material to provide a non-reactive medium, ensuring that the gasification kinetics were measured without additional chemical reactions from the bed material. For reactive experiments a synthetic oxygen carrier composed of 9 wt.% CuO supported on Al_2O_3 was used. With the reactive bed material, the oxygen transfer characteristics of an operational CLC system were reproduced, enabling the study of both thermal and chemical reaction influences on gasification kinetics. In both cases a 50/50 volumetric mixture of CO_2 and N_2 was used as the fluidizing and gasification gas. An inline process gas analyzer measured concentrations of key species, including CO_2, CO, CH_4, and H_2, using a thermal conductivity detector for the latter

Table 1: Results of the Proximate Analysis (left) and Ultimate Analysis (right) for the raw biomass feedstock and produced coke.

Proximate Analysis		**raw**	**coke**
Moisture	wt.% (raw)	8.1	3.2
Volatiles	wt.% (raw)	76.6	1.7
Ash	wt.% (raw)	0.1	1.5
Fixed Carbon	wt.% (raw)	15.1	93.6

Ultimate Analysis		**raw**	**coke**
N	wt.% (raw)	<0.1	0.39
C	wt.% (raw)	47	89
H	wt.% (raw)	6.5	0.4
S	wt.% (raw)	<0.2	0.2
O	wt.% (raw)	38.4	7.4

and nondispersive infrared sensors for the other species. Additionally, a conical spouted bed reactor was constructed to evaluate the impact of the reactor configuration on gasification kinetics. In this configuration, gas is injected through a localized nozzle to create a central spout that promotes back-mixing and thereby improves heat and mass transfer [4]. High-frequency pressure sensors, coupled with Fast Fourier Transformation (FFT) analysis, were used to monitor and confirm the stability of the spouted bed operation across various temperature and flow conditions according to equation (1) [5]:

$$F(k) = \sum_{j=1}^{N} x(j) e^{-i\frac{2\pi}{N}(j-1)(k-1)} \tag{1}$$

Results

Detailed stability analyses were conducted to ensure reliable reactor operation. By recording high frequency pressure data and applying FFT, operating conditions that yielded a clear dominant frequency (free of low-frequency disturbances due to fixed bed particle movements) were identified. This analysis was critical to provided a stable and reproducible working range for the spouted bed reactor setup to investigating biomass gasification kinetics. Using this method, stable working ranges could be determined for different gases and flow rates as a function of temperature. The data shown in figure 1 is an example of the stability analysis with nitrogen at 800 °C and a flow rate of the fluidization gas of 4.4 L/min. The FFT analysis of the spouted bed's pressure signals confirmed the presence of a stable operating regime, as evidenced by a dominant frequency peak in the 5–15 Hz range.

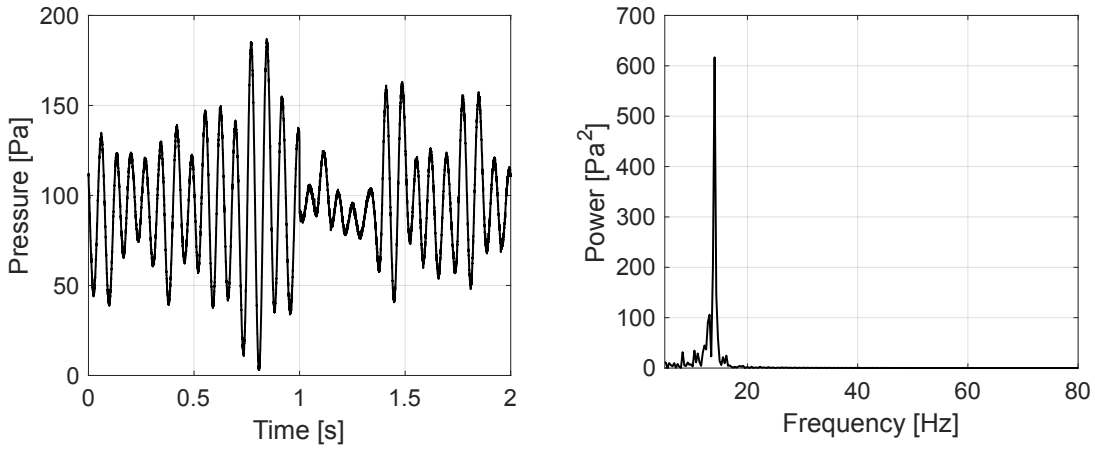

Figure 1: Total relative pressure signal against atmosphere over time (left) and transformed signal in using FFT (right) for nitrogen fluidization with quartz sand at 800 °C and 4.4 L/min.

The experimental investigations revealed that the particle size distribution (PSD) of the biomass coke is a key factor influencing gasification kinetics. In the fluidized bed setup with inert bed material, experiments conducted at 1000 °C using a 50/50 volume mixture of CO_2 and N_2 showed that smaller coke particles, with their higher specific surface areas, exhibited accelerated reaction rates due to enhanced heat and mass transfer. The conversion data shown in figure 2 clearly indicated that finer particles achieved higher carbon conversion in a shorter period than coarser fractions, confirming that particle size plays a critical role in the overall efficiency of gasification process.

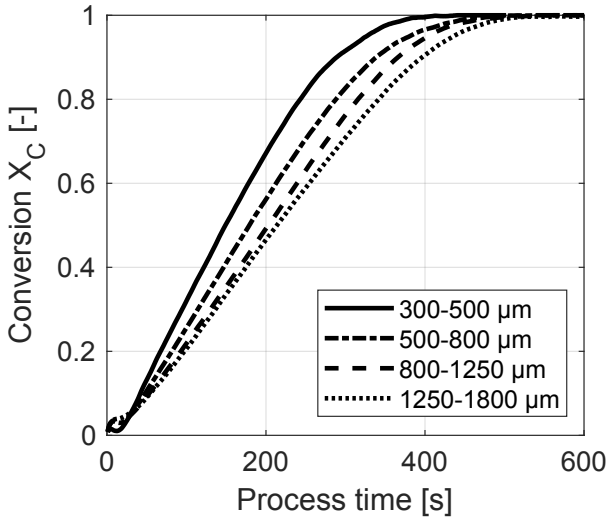

Figure 2: Relative carbon conversion for different PSDs at 1000°C in inert sand and 50 vol.% CO_2 atmosphere.

For devolatilization processes, the spouted bed reactor already demonstrated enhanced performance in previous studies. Compared with conventional fluidized bed design, the spouted bed design yielded improvements in both conversion efficiency and reaction rate. Specifically, the spouted bed experiments demonstrated an increase in total carbon conversion by up to 24%, along with a 17% improvement in carbon conversion rates. In general, the experimental results validate the importance of particle size in optimizing the gasification of biomass coke. Furthermore, the improved performance observed in the spouted bed reactor highlights the significant role that reactor design can play in enhancing process efficiency, a factor that will be crucial for scaling up CLC systems for industrial applications. An efficient description of kinetic factors will be crucial for the accurate modeling and simulation of chemical looping processes.

Acknowledgments
The financial support of the German Research Foundation DFG (Deutsche Forschungsgemeinschaft) under project number 495012431 is gratefully acknowledged.

References

[1] J. Adánez, A. Abad, T. Mendiara, P. Gayán, L.F. de Diego, and F. García-Labiano. Chemical looping combustion of solid fuels. *Progress in Energy and Combustion Science*, 65:6–66, March 2018.

[2] Johannes Haus, Matthis Goltzsche, Ernst-Ulrich Hartge, Stefan Heinrich, and Joachim Werther. Gasification kinetics of lignite char in a fluidized bed of reactive oxygen carrier particles. *Fuel*, 236:166–178, January 2019.

[3] Lennard Lindmüller, Johannes Haus, and Stefan Heinrich. High Volatile Conversion in a Chemical Looping Combustion System with Three Different Biomasses. *Energy & Fuels*, 36(17):9529–9537, September 2022.

[4] K. B. Mathur and P. E. Gishler. A technique for contacting gases with coarse solid particles. *AIChE Journal*, 1(2):157–164, June 1955.

[5] Navid Mostoufi, Gorkem Kulah, and Murat Koksal. Flow structure characterization in conical spouted beds using pressure fluctuation signals. *Powder Technology*, 269:392–400, January 2015.

Effect of pyrolysis atmosphere on biochar production from spruce bark, needle, twig and forest residue

Wang Liang [1*], Elisa Magnanelli [1] and Alba Dieguez-Alonso [2]

*E-Mail: liang.wang@sintef.no

[1] *SINTEF Energy Research, Sem Sælands vei 11, 7034 Trondheim, Norway*

[2] *Laboratory of Transport Processes, Faculty of Biochemical and Chemical Engineering, TU Dortmund University, Emil-Figge-Straße 68, 44227 Dortmund, Germany*

Background

Growth of biomass is considered the most naturally efficient method currently available to extract carbon dioxide from the atmosphere. As biomass is pyrolyzed, the organic carbon can be converted into solid biochar, liquid and gases products for various uses. Depending on production technology and process settings, for every tonne of infeed biomass around a third (and up to a half) of the carbon can be sequestered into solid biochar. Burying biochar in soils could play a key role in soil fertility and represents the largest terrestrial sink of carbon. Biochar can also improve agricultural productivity with benefits of reversing climate change while supporting sustainable farming. Biochar bioenergy systems are currently the main available technologies that can concurrently provide both energy and significant carbon sequestration. In addition to the sequestered carbon within carbon with biochar itself, production and use of biocarbon can also " turbocharge" other key technologies through integrating with other net emission technologies (NETs) such as CCS and CCU. The aim of this work is study biochar production under different atmospheres and further characterizing properties of produced biochar, which are relevant to environmental and industrial applications for reducing CO_2 emissions. This work investigated the impact of highest treatment temperature (HTT), atmosphere (CO_2 and N_2) and feedstock on yield of solid, liquid and gas products from pyrolysis of spruce bark, needles, twigs and forest residues as well as characteristics of the produced biochar.

Methodology

Spruce bark, needles, twigs and forest residues were pyrolyzed in a fixed bed reactor under slow heating conditions with presence of nitrogen and carbon dioxide, with continuous monitoring gases products. The produced biochars were characterized by a combination of proximate analysis, elemental analysis, N_2 and CO_2 adsorption for BET surface area and porosity analysis, Raman spectrometry, Fourier transform infrared spectroscopy (FTIR), X-ray diffraction and Scanning electron microscopy with energy dispersive X-ray spectroscopy (SEM/EDX) analysis.

Results

It was found that products distribution from pyrolysis of the studied feedstocks are considerably different, mainly owing to the differences in physical and chemical properties of them. More evident shrinkage was observed from the spruce bark after the pyrolysis in N_2 atmosphere as shown in Figure 1 (a). The experimental and analysis results indicate that pyrolysis behaviours of the biomass in N_2 and CO_2 is different. Gas release behaviours were monitored for each experiment. The CO_2 seems to enhance cracking of volatile organic carbons, leading to extension of release of CO and H_2, which was not observed from pyrolysis of studied biomass in presence of N_2 (Figure 2). In addition, compositions of the produced gases were also different as shown in Figure 3. Pyrolysis in CO_2 led to different extents of pyrolysis reactions and produced biochar with different physiochemical properties compared to those produced in N_2 atmosphere. The biochars produced in presence of CO_2 have generally slightly higher fixed carbon and volatile content, which also have higher carbon content as well (Figure 4). ICP analysis results indicated that there are almost no differences regarding inorganic elements in the spruce tree needles char (SNC) and spruce tree twigs char (STC) with purging of N_2 and CO_2. However, XRD analysis on the produced biochar revealed that higher intensity of calcium containing mineral phases CaO and $CaCO_3$ were detected from the biochars produced with presence of CO_2 (Figure 6).

Figure 1. Norwegian (a) birch bark, (b) spruce tree needles, (c) twigs and (d) forest residues and biochar samples produced from them (e-h)

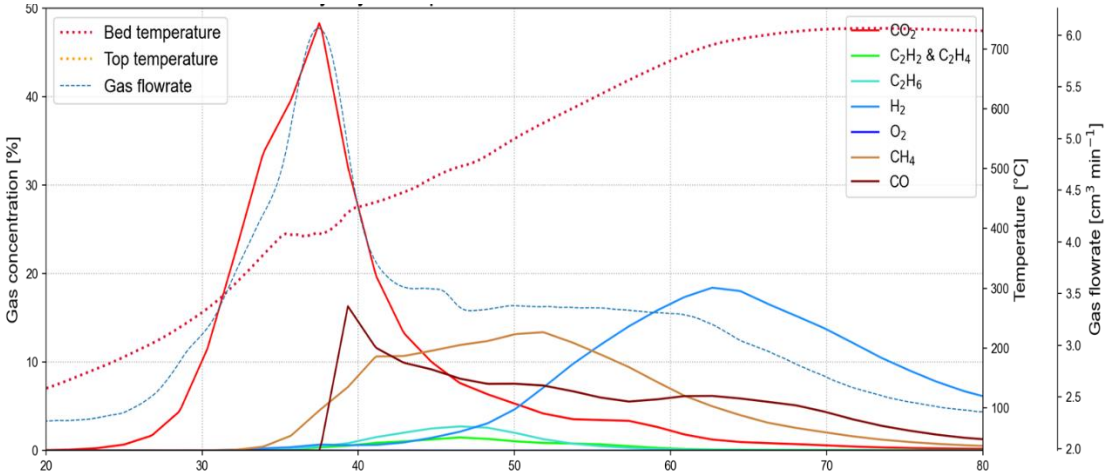

Figure 2. Temperature and gas release profile of pyrolysis of birch bark in N2

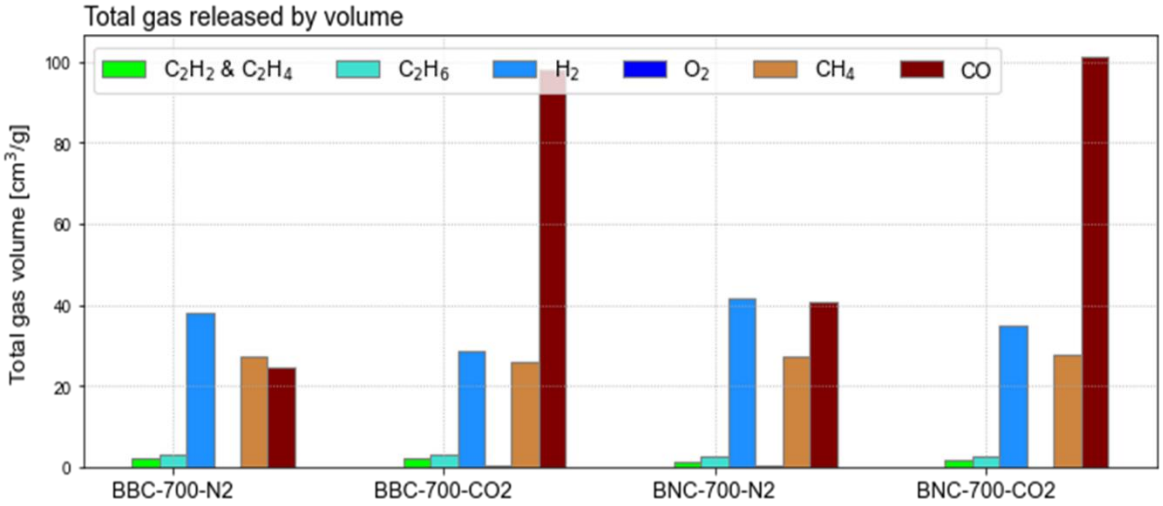

Figure 3. Comparison of main gases released from pyrolysis of bark and forest residues in N2 and CO2.

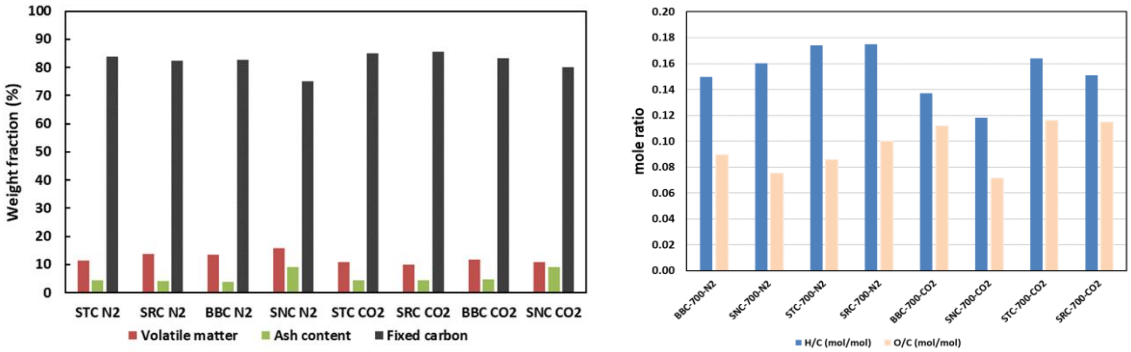

Figure 4. Proximate analysis, H/C and O/C mole ratios of the birch bark char (BBC), spruce tree needles char (SNC), (c) spruce tree twigs char (STC) and (d) spruce forest residues char (SRC)

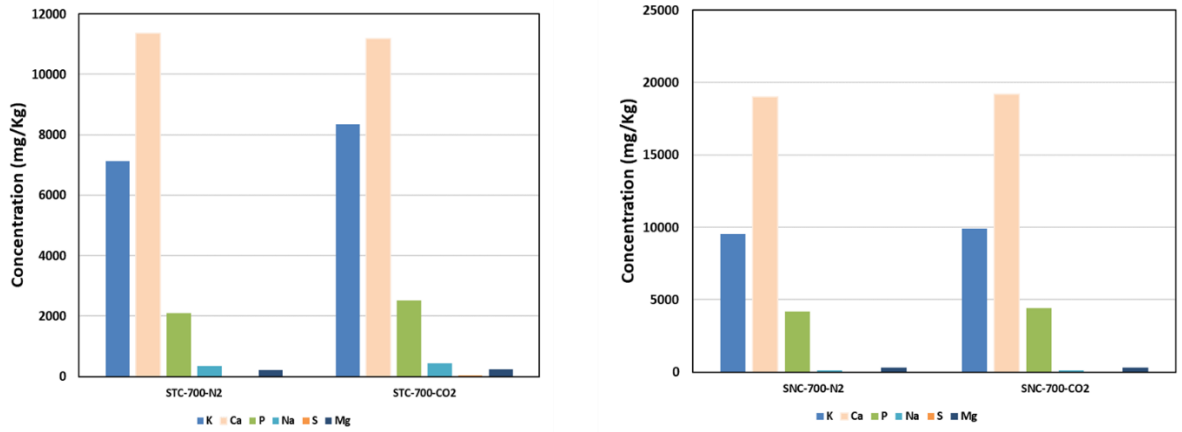

Figure 5. Concentration of K, Ca, P, Na and Mg in spruce twig and needle biochar.

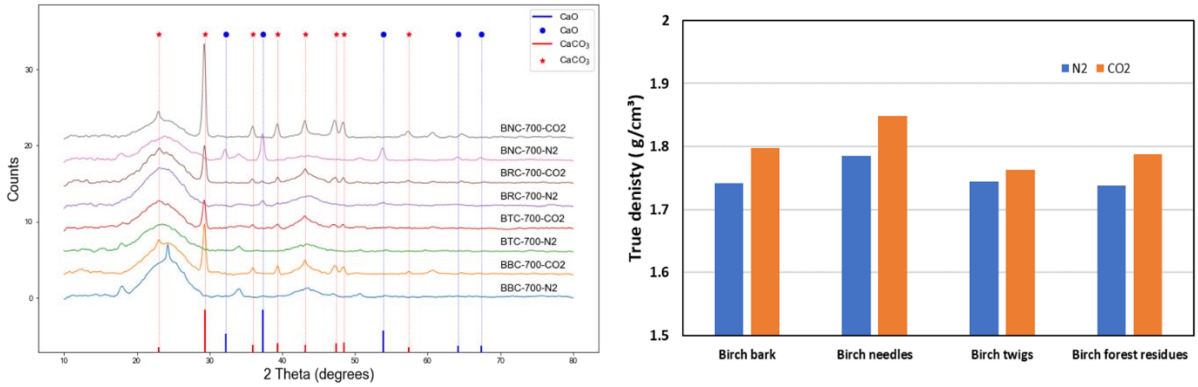

Figure 6. (a) XRD spectra and (b) true density of the produced biochar.

Conclusion

The experimental findings in this study indicate that the carbon neutral biomass and CO_2 could be co-utilized as feedstock and influencing carrier gas with multi benefits for biochar production, energy generation and waste management. Utilization of CO_2 as pyrolysis purging gas can alter reaction chemistry, affecting yield and properties of products.

Acknowledgement

This work was supported by the project BioOxyChar which is entirely funded by the SINTEF Climate Fund, a program that supports solutions and technologies that remove climate gases from the atmosphere and the project Cascading recycling of organic N-sources with next-generation biochar fertilizer for Norwegian agriculture (AgriCascade) funded by the Research Council of Norway.

Cascade utilization of chemical component in biomass with supercritical carbon dioxide

H. Jin[1*], X. Li, L. Guo

*E-Mail: jinhui@mail.xjtu.edu.cn

[1] *State Key State Key Laboratory of Multiphase Flow in Power Engineering, Xi'an Jiaotong University, 28Xianning West Road, Xi'an 710049, Shaanxi, China*

Bottleneck in biomass conversion

Biomass is a diverse and highly usable material. It contains very valuable chemical components with fine and complicated structure. However, the utilization of biomass has always been a challenging issue. Traditional methods of handling biomass can severely pollute the soil, release harmful gases, waste resources and are low efficiency. More importantly, these treatment methods break most of the chemical bonds, including very valuable ones. Therefore, cascade utilization is an effective method for processing biomass. It is important to directly obtain the valuable substance directly to realize the cascade utilization of biomass from the point of view of substance. Supercritical carbon dioxide (SC-CO_2) has the potential to separate waste biomass into bioactive substance, fuel-gas, bio-oil and biochar due to its adjustable physical and chemical properties in one temperature heat-up process. Moreover, at different reaction temperature stages, the SC-CO_2-biomass mixture can be used for various industrial processes. Therefore, this concept of cascade utilization is significant for addressing the challenges of biomass utilization.

Heat, mass, and momentum transfer of biomass particle

Through the simulation works of heat transfer and drag force of biomass particles in SC-CO_2, it is found that temperature significantly affects the heat transfer Nusselt number (Nu) and drag coefficient (C_d) under trans-critical conditions. The most important influencing factors are dynamic viscosity μ and specific heat capacity Cp. To address the effects of properties variations, the correlations for the property-corrected Nu and C_d are established, which shows good predictive performance, as shown in Figure 1.

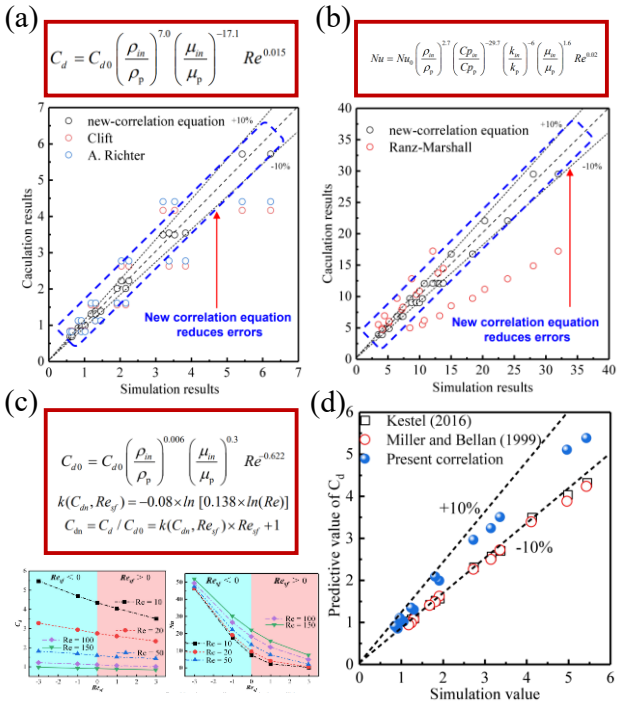

Figure 1. Heat transfer and drag force models of biomass particle in trans-critical conditions of CO_2.

During the reaction process, the Stefan flow phenomenon also occurs with the particles. The simulation works are conducted for the effects of Stefan flow on heat transfer and drag force characteristics. The simulation results indicate that Stefan flow can reduce the *Nu* and C_d of the biomass particles. By correcting for the influence of Stefan flow, a model for the influencing factor *k* was obtained, which was coupled with the aforementioned model of C_d, leading to a correlation for the particle C_d under the influence of Stefan flow in SC-CO_2. Furthermore, it is found that direct liquefaction and supersonic nozzles can effectively achieve the separation of SC-CO_2 and other gaseous products.

Through simulations of the molecular diffusion process in SC-CO_2, it is found that the physical property of CO_2 in trans-critical region appears to decrease heavily. The Arrhenius relation curve of self-diffusion coefficient of CO_2 in trans-critical region suddenly changes its slope, as illustrated in Figure 2. Traditional empirical formulas are limited by gas/liquid phase constraints and cannot be applied to the supercritical region. Therefore, new formulas for the diffusion coefficients of various molecules have been established. The new model has a simpler form with fewer parameters and demonstrates good accuracy in the critical region. It is found that the interaction energy between PAHs and SC-CO_2 is primarily determined by van der Waals interaction energy. The variation trend of the interaction energy between PAHs and SC-CO_2 molecules with temperature and pressure is consistent with the variation trend of PAHs diffusion coefficient with temperature and pressure. The variation trend of the interaction energy and diffusion coefficient is not consistent when the molecule size varied. The molecule size effect is stronger than interaction force between molecules for PAHs diffusion in SC-CO_2. Furthermore, it is found that only ethanol, acetic acid, methanol, and 1-propanol can produce strong hydrogen bonds with SC-CO_2, thus enhancing the interaction between SC-CO_2 and cosolvent molecules. The hydrogen bonding interaction energy has a significant impact on the enhancement of the solubility parameter. The polarization ability of the cosolvent is not the only factor that helps increase the solubility parameter of SC-CO_2.

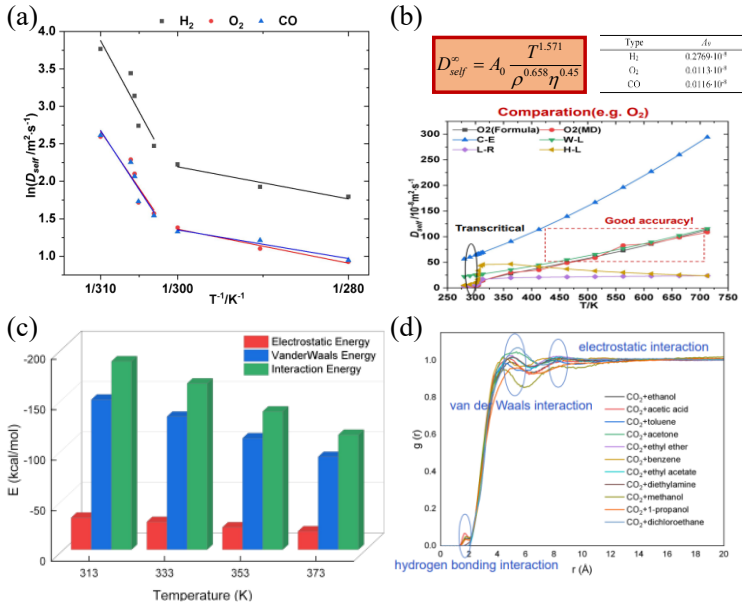

Figure 2. Diffusion process results of simulation and solubility parameter of cosolvent.

Reaction characteristics of biomass particle

Under the catalysis of KOH, activated carbon is prepared from walnut shells in a SC-CO_2 environment at 700 °C. After a reaction time of 90 minutes, not only is activated carbon successfully obtained, but various gases and liquids are also produced, as shown in Figure 3. The main component of the gaseous byproducts was still CO_2, along with some high-value gases such as H_2, CH_4 etc. The liquid byproducts are phenol-rich bio-oil containing more than 67% phenols, with 2,6-dimethylphenol content up to 40.1 %. Biochar with specific surface area more than 2900 m^2/g is obtained from walnut shell with treatment of SC-CO_2. In sewage treatment using the obtained biochar, the kinetics of the adsorption are better represented by the pseudo-second-order model, which indicates that the adsorption of MB by the activated carbon is chemisorptive. By doping N into the activated carbon, the carbon can achieve a richer

pore structure, with more pores and wider pore sizes. This method can also enable direct CO_2 capture from the air.

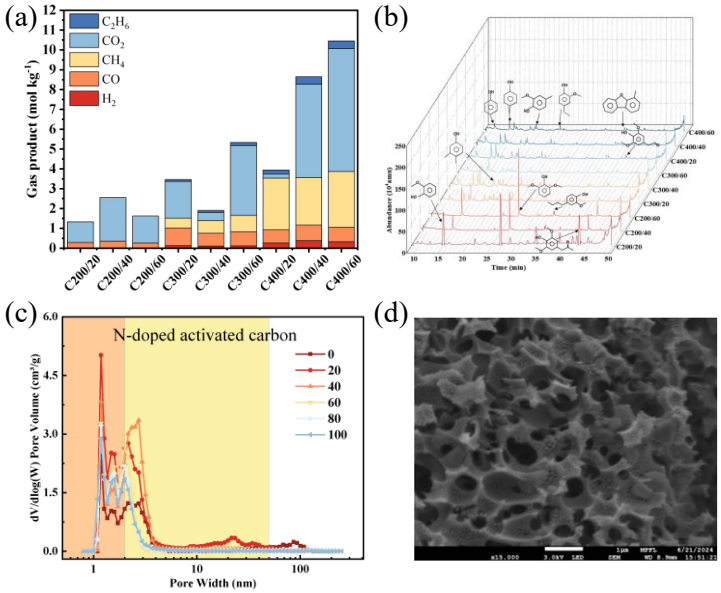

Figure 3. Reaction results of walnut shell in a SC-CO_2 environment

Through conversion experiments of rapeseed flower pollen and eucalyptus sawdust in SC-CO_2, various products are also discovered, with gas products remaining the most significant. In the conversion experiment of rapeseed flower pollen, pyrolysis is almost complete before the temperature reaches 400 °C. Pyrolysis is fastest at 240-390 °C, the total weight loss ratio is 81.49%, as shown in Figure 4. Pleiocarpamine and 3-Ethyl-5-(2-ethylbutyl) octadecane is extracted by SC-CO_2 from pollen particle. In the conversion experiment of eucalyptus sawdust, CO_2 is consumed by eucalyptus thermal chemical process with the amount of 8.83 mol/kg and meanwhile, hydrogen, carbon dioxide and methane were produced, which provides a way for carbon collection for fuel gas. Guaiacol was involved in four main processes during pyrolysis; cleavage of free radicals; isomerization of free radicals; secondary cleavage of free radicals and recombination of free radicals. Phenols are released from biomass as volatile in SC-CO_2 environment. By depressurization, the mixture can naturally separate into CO_2 and other substances. This method can transform contaminated soil into clean soil and achieve the recycling of SC-CO_2. The aforementioned research can be linked together to realize the comprehensive utilization of biomass.

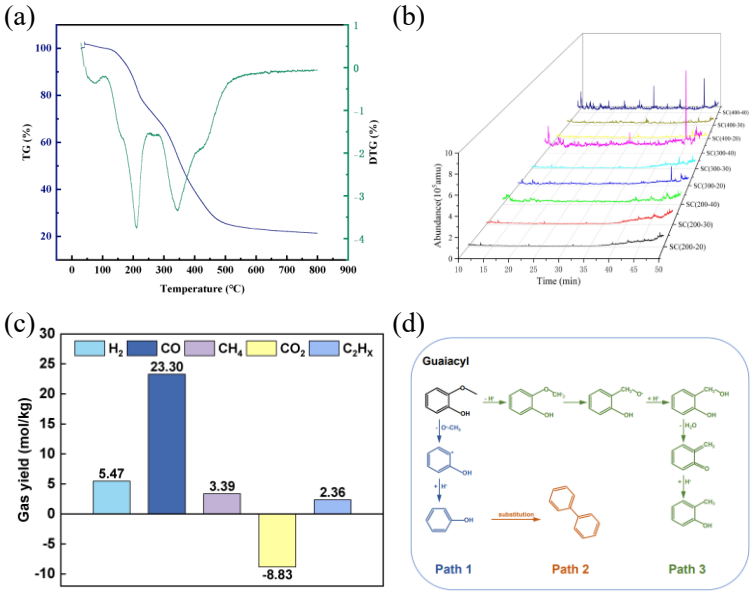

Figure 4. Treatment process of rapeseed flower pollen and eucalyptus sawdust in SC-CO_2.

Rheology model for simulation of particle flow in moving-bed reactors

Y. Kaymak[1*], T. Piontek[1], T. Hauck[1], K. Qyteti[2], and V. Scherer[2]

*E-Mail: Yalcin.kaymak@bfi.de

[1] Department Process optimisation Iron and Steel Making, VDEh-Betriebsforschungsinstitut, Sohnstraße 69, 40237 Düsseldorf, Germany

[2] Department of Energy Plant Technology, Ruhr-University Bochum, Universitätsstraße 150, 44780 Bochum, Germany

Abstract

The movement of the solid material (i.e., pellets) has a significant influence on the reactions and overall process in a moving-bed reactor. However, most of the continuum models for such reactors (e.g., iron blast furnace, direct iron reduction reactor, etc.) reported in the literature use a predefined solid descent velocity approach [1]. The main objective of this study is to improve this assumption by means of the laboratory experiments, discrete element method (DEM) modelling, and FEM modelling. A rheology model (i.e., a non-Newtonian flow model) has be adapted to approximate the movement of pellets in such counter-flow shaft reactors. That means the collection of solid particles flows macroscopically like a liquid which can be described by Bingham-Papanastasiou model [2], [3]. The validity of the model is tested by the laboratory experiments as well as available discrete element method (DEM) modelling results.

Rheology Model Description

A collection of solid grains can behave macroscopically like a liquid and flow. In the present work, the movement of pellets in the DR reactor vessel is described by Bingham-Papanastasiou model. The yield stress and the apparent viscosity are given by equation 1 below.

$$\mu = \mu_p + \tau_y \frac{1-\exp(-m_p\dot{\gamma})}{\dot{\gamma}} \quad (1)$$

$$\tau_y = p \sin\phi \quad (2)$$

where τ_y is the yield stress, p pressure, ϕ internal friction angle, $\dot{\gamma}$ shear rate, μ_p and m_p are model parameters. The yield stress calculation in equation 2 corresponds to the Terzaghi's theory of shear strength which is an extension of Mohr-Coulomb flow criteria which is commonly used for the slope stability calculations in the field of soil mechanics.

Rheology Model Results vs Experimental Results

The performance of the model has been initially evaluated by comparison to reported experimental results. So-called dam break experiments were performed by Balmforth and Kerswell [4] for various initial heights of granular material as shown in **Figure 1**. Figure 1.a-b show the photos of experimental set-up, while the measured profiles of the granular material are given in Figure 53.c.

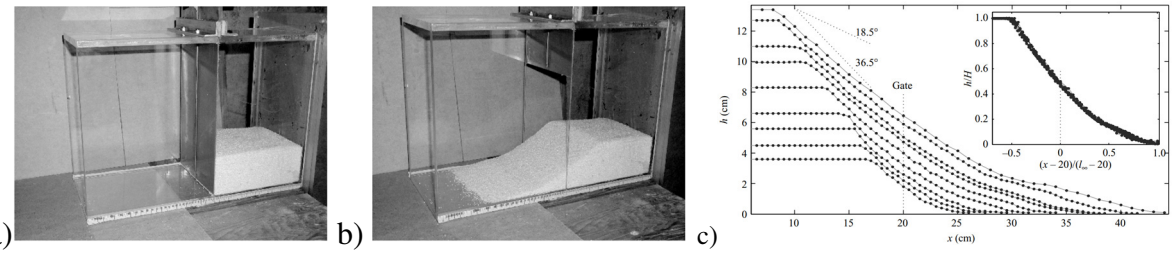

Figure 1. Dam break experiments, a) initial state, b) slope shape after collapse; c) slope shapes for various initial filling levels [4].

The results of the Bingham-Papanastasiou model computed with rheology model parameters $\mu_p = 0.1\ Pa \cdot s\ m_p = 100\ s$ are compared to those experiments reported in [4] as given in **Figure 2**. Although there are some small discrepancies, the model can fairly well estimate the slope shape after the collapse.

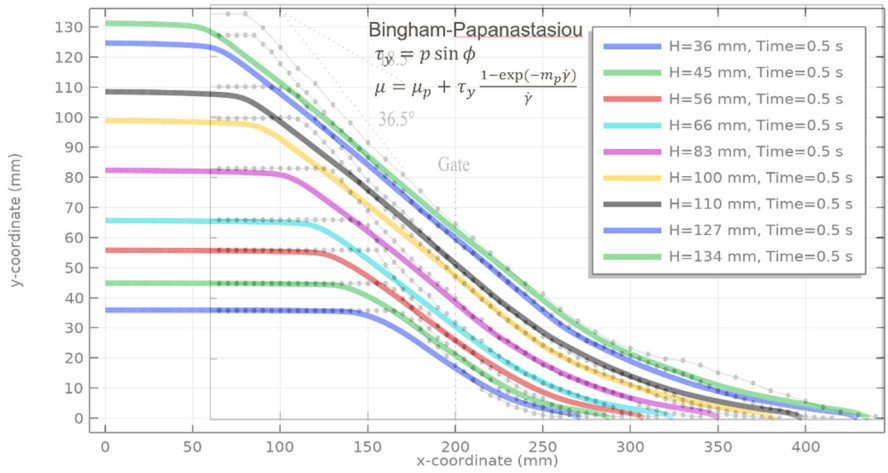

Figure 2. Comparison of the Bingham-Papanastasiou model with dam break experiments.

Steady state dynamics of particle movement in a rotating drum can be also modelled. The results of the rotating drum experiment reported in [5] are used model validation. The typical steady state surface shape observed in the experiment is shown in upper left photo in **Figure 3**. The simulated surface shape is given in the left plot in Figure 3. The wooden spheres have bulk density of ρ=400kg/m³, and internal friction angle of θ=27°. The rheology model parameters are $\mu_p = 2\ Pa \cdot s$ and $m_p = 10\ s$. The variation of the average slope angle over time for a 10s duration is shown in lower left plot in Figure 3. Note that the quasi-stationary state is achieved in a quite short time. The particle flow occurs near free surface and other regions rotate with the drum as expected.

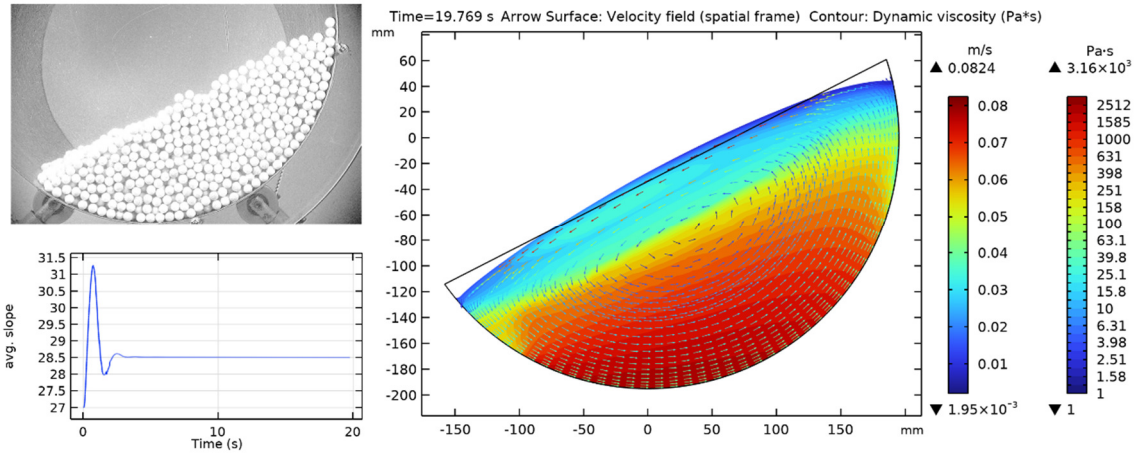

Figure 3. Steady state dynamics of particle movement in rotating drum experiments [5] vs model.

The movement of the pellets in a direct reduction reactor has a significant influence on the reactions and over-all process. A predefined solid descent velocity approach is not accurate due to the mechanisms used for sticking prevention (e.g., three small cylinders and Christmas tree as shown in **Figure 4a**). A physical model has constructed to measure the movement of the real pellets as well as the interaction with gas flow. The particle movements are recorded with a digital camera. The total gas flow rate and the gas pressures at several positions are measured. The weight of the discharged particles is also continuously measured. The experimental results are used for the calibration of the numerical models. For example, the total flow rate and pressure measurements are used to determine bed-permeability whereas the descent velocity and discharged particle weight are used to determine the rheology model parameters (e.g., μ_p and m_p). The average bed-height variations for two different discharge slot sizes as

well as experiment repeatability are shown in Figure 4b. This particular example is without gas flow. The rheology model with $\mu_p = 267\ Pa \cdot s$ and $m_p = 1\ s$ computes a descent rate of 8.9 mm/s for case 1 and 14.4 mm/s for the case 2. Typical fields of apparent viscosity, pressure, shear rate, and velocity for the case 1 are shown in Figure 4c.

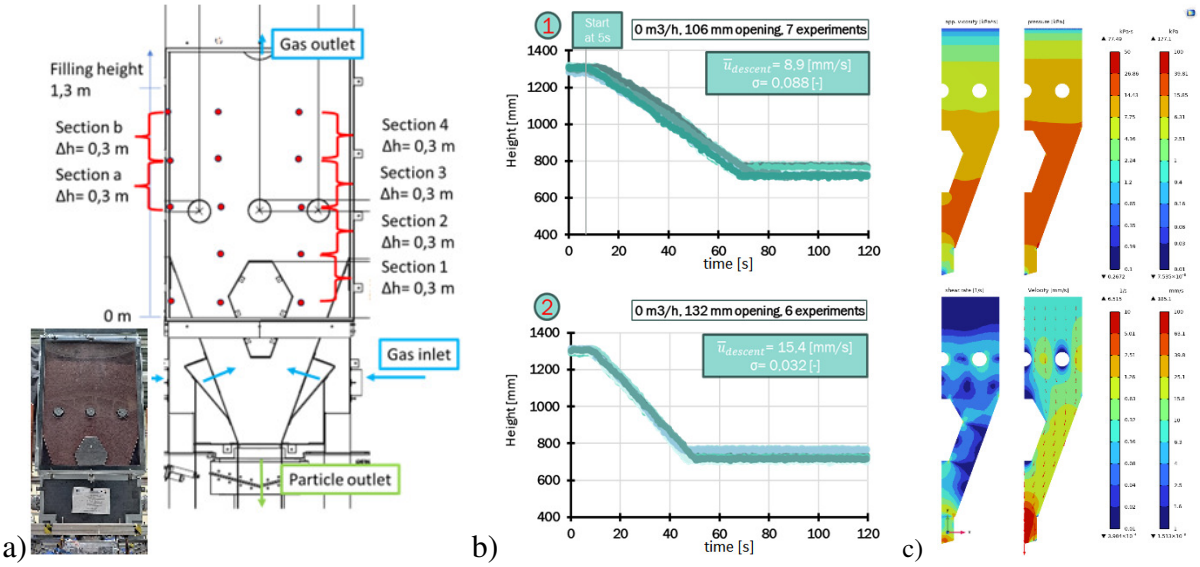

Figure 4. a) experimental setup, b) measured surface descent, c) rheology model results.

Conclusions

A rheology model for computing the movement of pellets in moving-bed shaft reactors has been presented. The apparent viscosity of the equivalent non-Newtonian flow is modelled by Bingham-Papanastasiou model [2], [3]. The main model parameter plastic viscosity μ_p can be estimated from the observed descent velocity. The model results are in good agreement with the dam-break experiments reported in [4] and rotating drum experiments in [5]. The main motivation of this study is to accurately describe the pellet descent in blast furnace and direct reduction reactor models. Therefore, a large-scale experimental setup is constructed to study the real particle descent and its interaction with the gas flow. Initial comparison of rheology model and experimental observations are very promising.

Acknowledgement

The work in the paper was developed within project "Maximise H2 Enrichment in Direct Reduction Shaft Furnaces" (Ref. MaxH2DR), GA No.101058429, that received funding from Horizon Europe EU framework programme, which is gratefully acknowledged. Sole responsibility of issues treated in the paper lies with the authors; the Commission is not responsible for any use that may be made of the information contained therein.

References

[1] Hamadeh H., Mirgaux O., Patisson F.: *Detailed Modeling of the Direct Reduction of Iron Ore in a Shaft Furnace,* Materials, v11, pp1865; doi: 10.3390/ma11101865, 2018.

[2] Bingham E. C.: *Fluidity and plasticity*, McGraw-Hill. ISBN 9781377929613, 1922.

[3] Papanastasiou T. C.: *Flows of Materials with Yield*, Journal of Rheology. 31 (5): pp. 385; doi:10.1122/1.549926, 1987.

[4] Balmforth N.J., Kerswell R.R., *Granular collapse in two dimensions,* J. Fluid Mech., vol. 538, pp. 399, 2005.

[5] *Wechselwirkung von Fließverhalten und Durchströmung in Schachtöfen,* Schlussberichts zu IGF-Vorhaben Nr. 20409 N, pp. 33, 2022.

Hydrodynamic interactions between particles suspended in a fluid medium

Sina Hassanzadeh Saraei[1*] and Bernhard Peters[1]

[*]E-Mail: sina.hassanzadeh@uni.lu

[1]*Department of Engineering, University of Luxembourg, Maison du Nombre, 6 Avenue de la Fonte, 4364 Esch-sur-Alzette, Luxembourg*

Abstract

A correct evaluation of suspensions behavior requires a detailed understanding of their rheology. The volume fraction of particles within the suspension is a crucial parameter that can influence the suspension's rheological behavior. The objective of this study was to elucidate the interaction between solid and fluid phases by coupling our in-house DEM code (XDEM) with a CFD solver. To obtain a more accurate assessment of the hydrodynamic forces, without relying on any drag law approximation, we developed a variant of the immersed boundary method as a fully resolved CFD solver. This approach also enables us to achieve a high resolution field data around particles, facilitating the interpretation of the underlying physics in suspensions. To validate the model, we conducted a series of tests to investigate the suspension by comparing our CFD-DEM results with theoretical predictions.

Keywords: CFD-DEM; IBM; Rheology

Introduction

Suspensions can be regarded as solid particles suspended in a fluid domain. The rheological behavior of a suspension differs from that of the base fluid due to the disturbance caused by the particles. Therefore, it is imperative to assess their rheological behavior, given their extensive range of industrial applications. Computational Fluid Dynamics coupled with Discrete Element Method (CFD-DEM) simulations could be used to address this problem by simulating the suspension between two parallel plates, as illustrated in **Figure 1**[1-2].

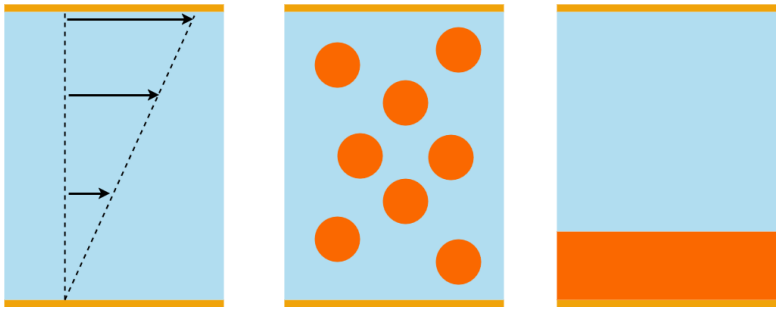

Figure 1. Schematic representation of the suspended particles in the fluid domain [2].

In this figure, the fluid domain (depicted in blue) is confined between two parallel plates, with the upper plate acting as a moving wall and the lower plate maintaining a stationary. The velocity distribution of the fluid is also depicted in this figure. The applied shear rate can be calculated as follows:

$$\dot{\gamma} = \frac{U_{wall}}{l} \tag{1}$$

where l and U_{wall} present the gap distance between the plates and moving wall velocity, respectively. As demonstrated in **Figure 1** and previously reported by Gleissle et al. [2], the presence of the particles could result in a decrease in the effective gap distance between plates for the fluid, resulting in a higher shear rate than the applied shear rate. This manner results in a higher shear stress compared to the base

fluid without particles. The aim of the present work was to develop a fully resolved CFD-DEM model to predict the behavior of the fluid under the applied shear rate.

Method

In this work, the immersed boundary method was used as a CFD solver to account for the hydrodynamic interaction between the particles, as follows [3]:

$$\nabla \cdot \vec{u} = 0 \tag{2}$$

$$\frac{\partial \vec{u}}{\partial t} = -\nabla \cdot (\vec{u} \otimes \vec{u}) + \frac{1}{\rho_f} \nabla \cdot \vec{\tau} + \vec{f} \tag{3}$$

The IBM force was integrated over the particle surface to account for the drag force it faced. Then, this force was transferred to our in-house discrete element method (DEM) code, named XDEM, as follows [4-6]:

$$\vec{f_{h,i}} = \frac{d}{dt} \int_{\Omega_p} \rho_f \vec{u} \, dV - \int_L \rho_f \vec{f} \, dV \tag{4}$$

A detailed discussion of the governing equation and the IBM can be found in our previous publication, to which readers interested in further details are encouraged to refer [5].

Results

Following the execution of the CFD-DEM simulations, post-processing of the results was performed to assess the rheological behavior of the suspension. Our investigative approach involves a comparative analysis of the relative viscosity measurements derived from CFD-DEM simulations and those obtained from the Krieger–Dougherty model with the following equation [7-8]:

$$\mu_r = \frac{\mu}{\mu_s} = (1 - \frac{\phi}{\phi_m})^{-1.82} \tag{5}$$

After successfully validating our CFD-DEM model with the Krieger–Dougherty model, further postprocessing of the results was conducted for the purpose of assessing the relationship between the shear rate and the volume fraction of the particles. The concept of effective inner shear rate, as introduced by Gleissle et al. [2], was employed in this analysis. The reference work reported the amplification factor for three different volume functions (10%, 20%, and 25%), with which our results for normalized wall shear rate align with them [2]. To normalize the results, the simulated wall shear rate was divided by the applied shear rate, which was calculated by using **Equation 1**.

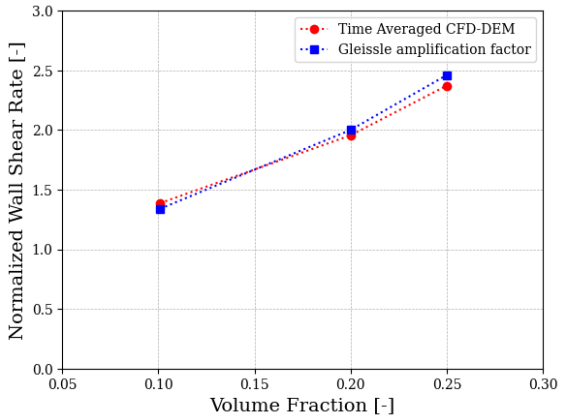

Figure 2. Shear rate comparison between the present work and amplification factor from the reference work [2].

Because we performed a fully resolved simulation, we could visualize the shear rate distribution in the fluid domain, as shown in **Figure 3**.

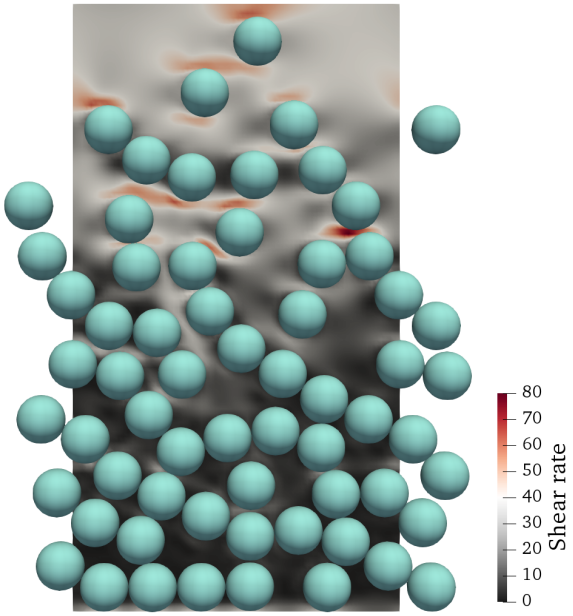

Figure 3. Shear rate distribution in the fluid domain.

Conclusion

A comparison of the CFD-DEM results with analytical and theoretical approaches confirms the validity of our model. This is of particular importance because the CFD-DEM model can be regarded as a digital twin for predicting the rheological behavior of the suspension. Additionally, the fully resolved field data surrounding the particles can be utilized to elucidate the underlying physics governing particle migration from regions of higher shear rates to those of lower shear rates.

Acknowledgment

This project was Founded by Luxembourg National Research Found (INTER/DFG/20/14843353 - ConMicMac). As a member of the XDEM group, we used the XDEM code as a DEM solver under the supervision of Professor Peters. We would like to acknowledge all previous colleagues who contributed to the XDEM code, its coupling interface, and immersed boundary method.

References

[1] Saraei, S.H. and Peters,B.: *Analysis of the rheological behavior of suspensions by using the Immersed Boundary Method (IBM) coupled with the Discrete Element Method (DEM)*, Powder Technology, 446, p.120165, 2024.

[2] Gleissle W, Hochstein B.: *Validity of the Cox–Merz rule for concentrated suspensions*, Journal of rheology, 47(4), 897-910., 2003.

[3] Municchi, F. and Radl, S: *Consistent closures for Euler-Lagrange models of bi-disperse gas-particle suspensions derived from particle-resolved direct numerical simulations*, International journal of heat and mass transfer , 111 (2017): 171-190, 2017.

[4] Aminnia, N., Adhav, P., Darlik, F., Mashhood, M., Saraei, S.H., Besseron, X. and Peters, B.: *Aminnia N, Adhav P, Darlik F, Mashhood M, Saraei SH, Besseron X, Peters B. Three-dimensional CFD-DEM simulation of raceway transport phenomena in a blast furnace*, PFuel. 2023 Feb 15;334:126574, 2023.

[5] Adhav P, Besseron X, Peters B.: *Development of 6-way CFD-DEM-FEM momentum coupling interface using partitioned coupling approach.*, Results in Engineering. 2024 Jun 1;22:102214,2024.

[6] Saraei, S.H. and Peters,B.: *Immersed boundary method for considering lubrication effects in the CFD-DEM simulations*, Powder Technology, 426, p.118603, 2023.

[7] Krieger, I.M. and Dougherty, T.J.: *A mechanism for non-Newtonian flow in suspensions of rigid spheres*, Trans. Soc. Rheol, 3(1), pp.137-152. 1965.

[8] Phillips RJ, Armstrong RC, Brown RA, Graham AL, Abbott JR.: *A constitutive equation for concentrated suspensions that accounts for shear-induced particle migration*, Fluid Dynamics, 4(1), pp.30-40, 1992.

Coarse graining / multi-level coarse graining and its application to fluidized systems

H. Kruggel-Emden[1*], V. Brandt[1]

*E-Mail: kruggel-emden@tu-berlin.de

[1] Chair of Mechanical Process Engineering and Solids Processing, Technische Universität Berlin, Ernst-Reuter-Platz 1, 10587 Berlin, Germany

Introduction

Fluidized systems play an important role in various applications for the chemical and process industry as they can be used for coating or drying of particles as well as chemical reactions to name only a few [1].

The complex physical behaviour of fluidized systems on multiple time and length scales leads to challenges when building mathematical models to simulate the underlying solid-gas or solid-liquid multiphase flow. To do so, several modelling approaches have been developed to date, encompassing various strategies and complexities.

Particle resolved direct numerical simulations (PR-DNS) can be performed to gain highly resolved information of the flow field of multiphase systems while the solid phase is represented with the discrete element method (DEM). DEM is a Lagrangian approach capable of tracking the trajectory of each particle [2]. Flow around individual particles is resolved in PR-DNS so that interaction forces between the solid and the fluid phase are directly obtained. However, the use of PR-DNS for fluidized systems is highly computationally intensive and thus reserved for reference simulations [3].

In contrast, continuum based two-fluid models (TFM) [4] and coupled DEM-CFD are well-known and less computationally demanding modelling approaches to describe fluidized systems. In TFM, both the solid and fluid phase are treated continuously as Eulerian phases whereby information on the discrete nature of the solid phase is lost. In contrast to TFM, DEM-CFD is a numerical method where the solid phase is solved using the DEM. In contrast to PR-DNS, forces between the solid and the fluid phase are realized by closures as part of the DEM-CFD, which is reducing computational cost.

Nonetheless, the computation of fluidized systems with the DEM-CFD with more than 10^6 particles quickly saturates the computation capacity of modern computers, even using highly parallelized and optimized DEM-CFD codes. A common approach to overcome the named limitation is to compute large-scale systems with the DEM-CFD by bundling multiple original particles into large-sized particles, so-called grains. The resulting coarse-grained DEM-CFD is less computationally demanding because of a reduced number of particles (see Figure 1). However, scaling models need to be applied to the hydrodynamic and contact forces to achieve accurate results.

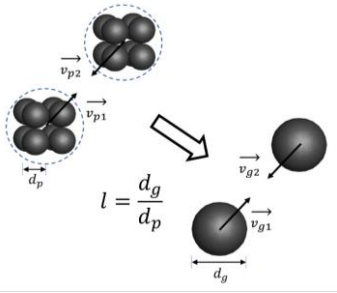

Figure 1. Principle of coarse graining.

Coarse graining and accuracy

Lumping a pre-set number of particles into a spherical grain is the main principle of coarse graining. From the solid's phase perspective, a reduced number of entities needs to be tracked by the Lagrangian DEM approach consequently, which leads to a large reduction of computational cost. In the context of coarse graining a fundamental parameter is the ratio of grain to particle diameter, the so-called coarse

graining factor $l = d_g/d_p$ (see Figure 1). A short overview of the most common available coarse graining approaches is given in Figure 2 for hydrodynamic and contact forces.

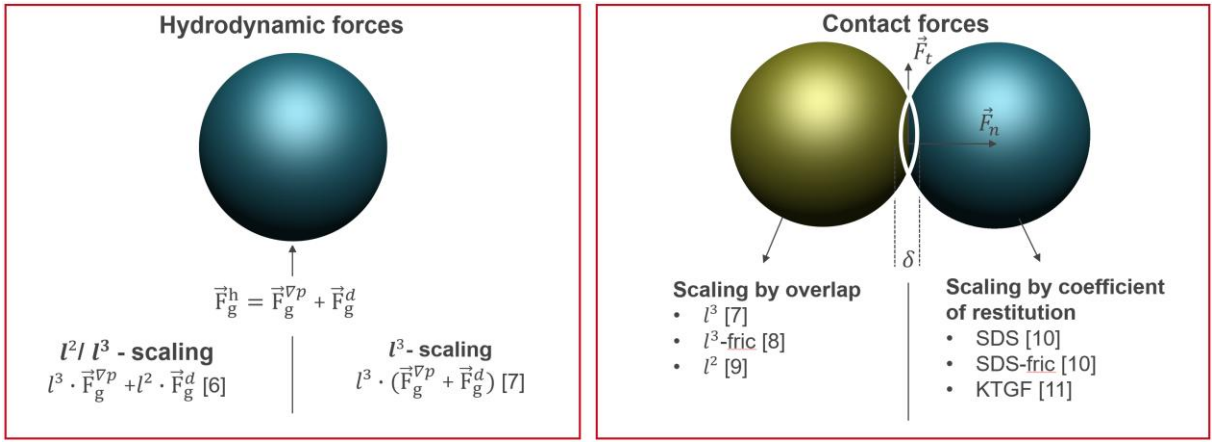

Figure 2. Possible hydrodynamic and contact force scaling as part of coarse graining (see also [5]).

Ideally, simulations with representative coarse grained particles lead to identical results as unscaled particle simulations. That this is only achievable to a limited extend can be exemplarily seen in Figure 3 for a mechanically agitated system. Accuracy of average particle height, granular temperature, mixing time and particle velocity distribution has been evaluated for a system where particles are set in motion by a moving bottom plate (see Figure 3 (right)). It can be clearly seen that the SDS [10] and SDS-fric [11] approaches are associated with the lowest deviations with regard to a reference simulation with a coarse graining factor of $l = 1$.

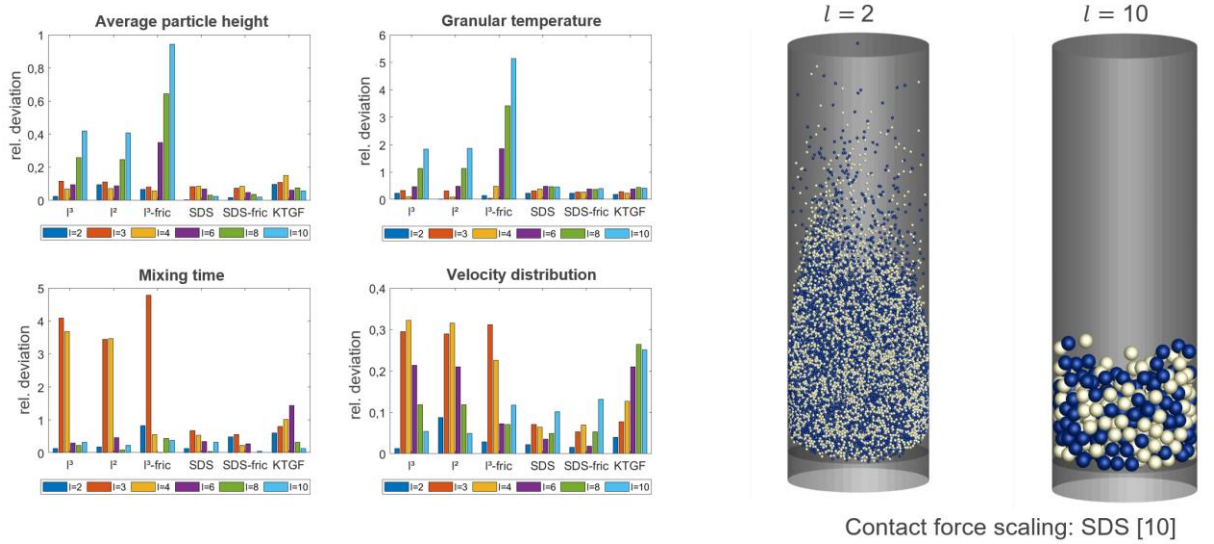

Figure 3. Accuracy of different contact force scaling approaches for different coarse graining factors for a mechanically agitated system (see also [5] for further details).

Multi-level coarse graining

In many industrial fluidized systems, the macroscopic behavior depends on the size of particles / grains. Exceeding a critical grain size at local geometry constrictions in a coarse grained DEM simulation can lead to erroneous results. As an example, according to [12], the application of coarse graining to a conical hopper causes the ratio between the particle / grain diameter and the size of the orifice to change. This leads to a temporal choking and an overall incorrect prediction of the discharge rate for a sufficient coarse graining factor of l= 8 as depicted in Figure 4 (left). Multi-level coarse graining originally proposed by [12] and others addresses this issue, by using multiple grain sizes in the simulation. The used coarse graining factor represents the local resolution. While [12] and others only applied refinement

within their multi-level coarse graining (see e.g. Figure 4 (left)), in the proposed multi-level coarse graining close to critical geometry constrictions the grains are refined, to achieve a higher resolution. Away from critical regions, particles or grains are bundled to reduce the number of modeled entities and achieve a computational speed-up (see Figure 4 (right), where differently placed refinement zones are applied).

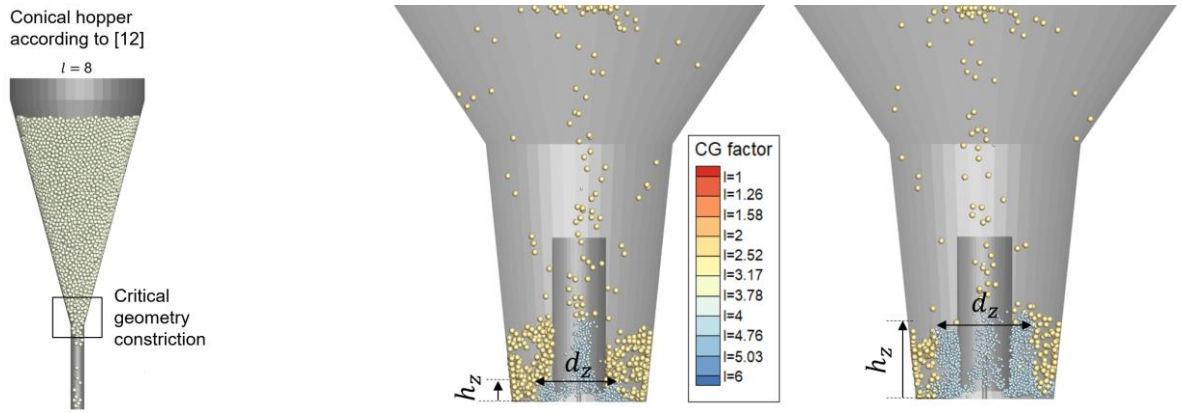

Figure 4. Coarse graining applied to a hopper [12] (left) and multi-level coarse graining applied to a Wurster coater as part of a DEM-CFD with different refinement zones (right) (see [13] for details).

Acknowledgments

Financial support was funded by the Deutsche Forschungsgemeinschaft (DFG, German Research Foundation) – Project-ID 456827728. Computing resources were funded by the DFG – Project-ID 463921749.

References

[1] Grace J., Bi X., Ellis N.: *Essentials of Fluidization Technology*, Wiley, 2020.

[2] Cundall P.A., Strack O.D.L.: *A discrete numerical model for granular assemblies*, Géotechnique, 29(1), 47–65, 1979.

[3] Esteghamatian A., Bernard M., Lance M., Hammouti A., Wachs A.: *Micro/meso simulation of a fluidized bed in a homogeneous bubbling regime*, Int. J. Multiph. Flow, 92, 93–111, 2017.

[4] Gidaspow D.: *Multiphase flow and fluidization: Continuum and kinetic theory descriptions*, Acad. Press, 1994.

[5] Brandt V., Grabowski J., Jurtz N., Kraume M., Kruggel-Emden H.: *A benchmarking study of different DEM coarse graining strategies*, Powder Technology 426, 118629, 2023.

[6] Bierwisch C., Kraft T., Riedel H., Moseler M.: *Three-dimensional discrete element models for the granular statics and dynamics of powders in cavity filling*, J. Mech. Phys. Solids, 57(1), 10–31, 2009.

[7] Sakai M. , Koshizuka S.: *Large-scale discrete element modeling in pneumatic conveying*, Chem. Eng. Sci., 64(3), 533–539, 2009.

[8] Cai R., Zhao Y.: *An experimentally validated coarse-grain DEM study of monodisperse granular mixing*, Powder Technol., 361, 99–111, 2020.

[9] Radl S., Radeke C., Khinast J. G., Sundaresan S.: *Parcel-Based Approach For The Simulation Of Gas-Particle Flows*, 8th Interantional Conf. CFD Oil Gas, Metall. Process Ind., 1–10, 2011.

[10] Benyahia S., Galvin J. E.: *Estimation of Numerical Errors Related to Some Basic Assumptions in Discrete Particle Methods*, Ind. Eng. Chem. Res., 49(21), 10588–10605, 2010.

[11] Lu L., Xu J., Ge W., Yue Y., Liu X., Li J.: *EMMS-based discrete particle method (EMMS-DPM) for simulation of gas-solid flows*, Chem. Eng. Sci., 120, 67–87, 2014.

[12] De T., Chakraborty J., Kumar J., Tripathi A., Sen M., Ketterhagen W.: *A particle location based multi-level coarse-graining technique for Discrete Element Method (DEM) simulation*, Powder Technology, 398, 117058, 2022.

[13] Brandt V., Grabowski J., Jurtz N., Kraume M., Kruggel-Emden H.: *DEM and DEM-CFD modeling of systems with geometric constrictions using a new particle location based multi-level coarse graining approach*, Powder Technology 436, 119447, 2024.

Simulation of Plastics Pyrolysis in Fluidized Bed with a Lumped Reaction Kinetic Model

M. Li[1], F. Zhang[1*], S. Tavakkol[1], T. Zirwes[2], O.T. Stein[3], and D. Stapf[1]

[*]E-Mail: feichi.zhang@kit.edu

[1]Institute for Technical Chemistry, Karlsruhe Institute of Technology, Kaiserstr. 12, 76131, Karlsruhe, Germany
[2]Institute for Reactive Flows, University of Stuttgart, Pfaffenwaldring 31, 70569 Stuttgart, Germany
[3]Engler-Bunte-Institute/Division for Combustion Technology, Chair for Simulation of Reacting Thermo-Fluid Systems, Karlsruhe Institute of Technology, Kaiserstr. 12, 76131, Karlsruhe, Germany

Introduction

The production of plastics is continuously increasing, and has reached 400 Mt in 2022 alone [1]. As a result, the generation of plastic waste has also increased dramatically. According to the OECD, approximately 353 Mt of plastic waste were generated in 2019, around 70% of it has been landfilled and incinerated, while another 20% has leaked into the environment due to mismanagement, leading to serious environmental issues such as microplastics [2]. While the conventional mechanical recycling is limited to thermoplastics with high purity, chemical recycling can be used to recycle mixed and contaminated plastics. Among the current chemical recycling technologies, pyrolysis shows the best balance between investment cost, operating cost and product quality compared to other technologies such as gasification or hydrothermal liquefaction [3,4]. During the pyrolysis process, plastic waste is decomposed in a high-temperature, oxygen-free environment into chemical building blocks, which can be reused to produce new plastic products. The feasibility of pyrolysis for recycling plastic waste has been proven extensively through laboratory-scale experiments over the past decades [3]. The development of industrial-scale, high-throughput (continuous) plastics pyrolysis processes is imperative to address the increasing production of waste plastics. However, the widespread industrial application of waste plastics pyrolysis is mainly limited by the technical feasibility of reactor scale-up and the high cost of large-scale experiments.

Among the various reactor types, fluidized bed reactors are considered highly promising for large-scale applications due to their superior heat and mass transfer capabilities, as well as excellent mixing characteristics. To develop a thorough understanding of the underlying processes while minimizing experimental costs, computational fluid dynamics (CFD) simulations can serve as a cost-effective tool for process optimization and risk reduction. The primary objective of this study is to develop a CFD model for simulating waste plastic pyrolysis in fluidized beds, capturing key phenomena such as dense gas-particle flow, heat transfer, and pyrolysis reactions. A lumped kinetic model is employed to balance computational efficiency with accuracy. The simulations are first applied to batch-operated fluidized beds and subsequently extended to continuously fed systems, providing valuable insights for future process development.

Simulation Setup

A cylindrical fluidized bed with a diameter of 5 cm and a length of 60 cm was used, along with 695 g of quartz sand as bed material and methane as fluidizing agent. The sand particles were assumed to be spherical and have a particle size distribution (PSD) with a mean diameter of 0.21 mm. Spherical, monodisperse polypropylene (PP) particles with diameters d_P ranging from 1.5 to 2.5 mm were fed into the reactor at an initial temperature of 25°C. The mass load of plastics compared with the bed inventory was set to 2%. The superficial gas velocity u_G and the reactor temperature T_R were set to $u_G = 15 - 30$ cm/s and $T_R = 470 - 530$ °C.

A Eulerian-Lagrangian approach was used to model the multiphase flow, where the collisions and heat exchange between the particles was considered (4-way coupling). A lumped 5-step kinetic model (adopted

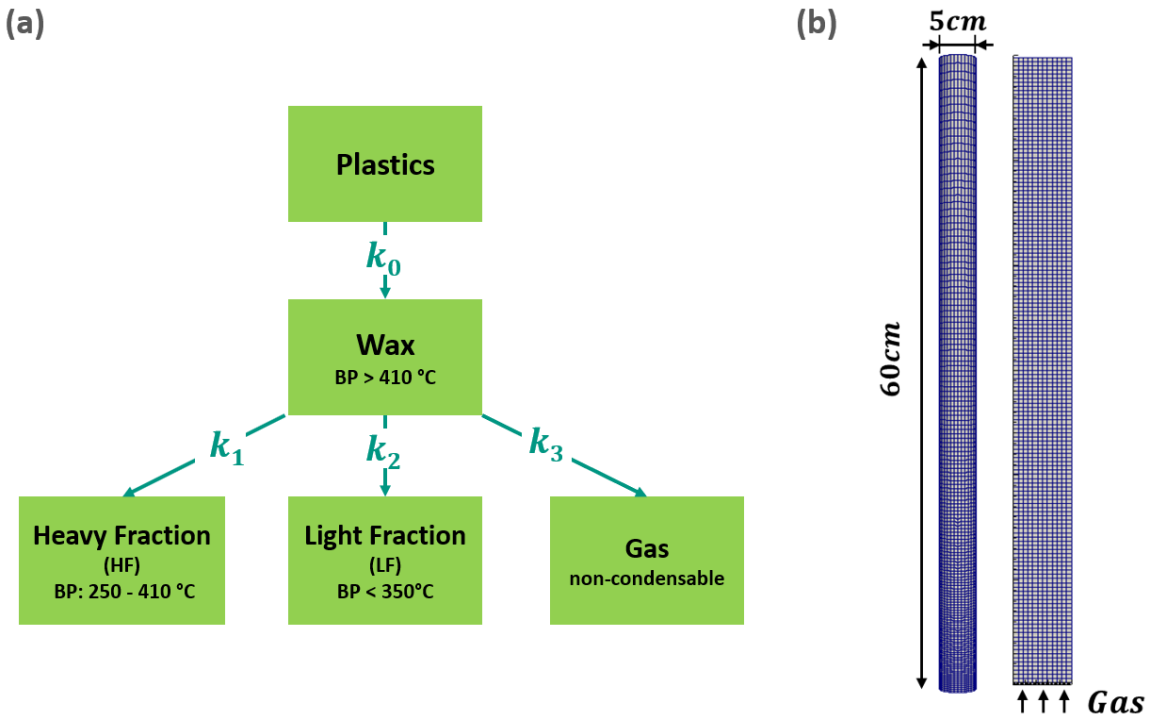

Figure 1: Illustration of the simulation setup: (a) 5-lump kinetic model (adopted from [5]) and (b) computational grid.

from [5]) was applied to characterize the pyrolysis reactions. As shown in Fig.1 (a), the degradation of polyolefins undergoes a formation of long-chained intermediates (Wax), which is followed by secondary decomposition into gaseous heavy fraction (HF), light fraction (LF) and gas (Gas). Since the boiling points of these final products are relatively lower than the reactor temperature, they are assumed to be immediately released to the gas phase after their formation. Additionally, due to the short residence time (2 - 4 s) of the gas phase, chemical reactions among the gaseous products were neglected.

Due to the long pyrolysis time (time to reach 99% conversion of plastic mass) of up to tens of minutes, the original cylindrical computational domain was simplified to a thin slice with a width of 5 cm, corresponding to the diameter of the cylindrical fluidized bed, as illustrated in Fig.1 (b). The thickness of the slice was set to 4 mm, which allows the use of particle sizes up to 2.5 mm for plastic particles. In this way, the volume of the domain was reduced to 1/10 of the original cylindrical domain of the full fluidized bed, leading to a speed-up of the computing time by a factor of 10. A modified OpenFOAM solver was used for the numerical simulations, where the heat transfer model [6] and lumped pyrolysis reaction model was implemented. The numerical setup was first validated against cold model experiments with regard to the hydrodynamics of the fluidized bed [7], which was then used for modeling plastics pyrolysis considering heat transfer and chemical reaction.

Results

Batch-wise feeding

The simulations were conducted first with batch-wise feeding of plastics. In this case, the simulation was started with an overheated fluidized bed reactor. After the formation of stable bubbling in the fluidized bed, plastic particles with 2% mass share of bed inventory were added to the reactor at once. The simulation was first conducted for T_R = 500 °C and d_p = 2.0 mm, which was treat as the reference case for further simulations. Figure 2 (a) illustrates contours of the instantaneous void fraction α_c, particle spatial distribution and temperature distribution in both gas phase and particle phase of the reference case. The bubbles can be detected by the red zones with $\alpha_c = 1$, corresponding to pure gas. The sand particles are indicated by the teal dots and plastic particles by the blue points. Due to the movement of the bubbles, the mixing of both particles was enhanced, leading to a relative uniform temperature distribution throughout the whole reactor.

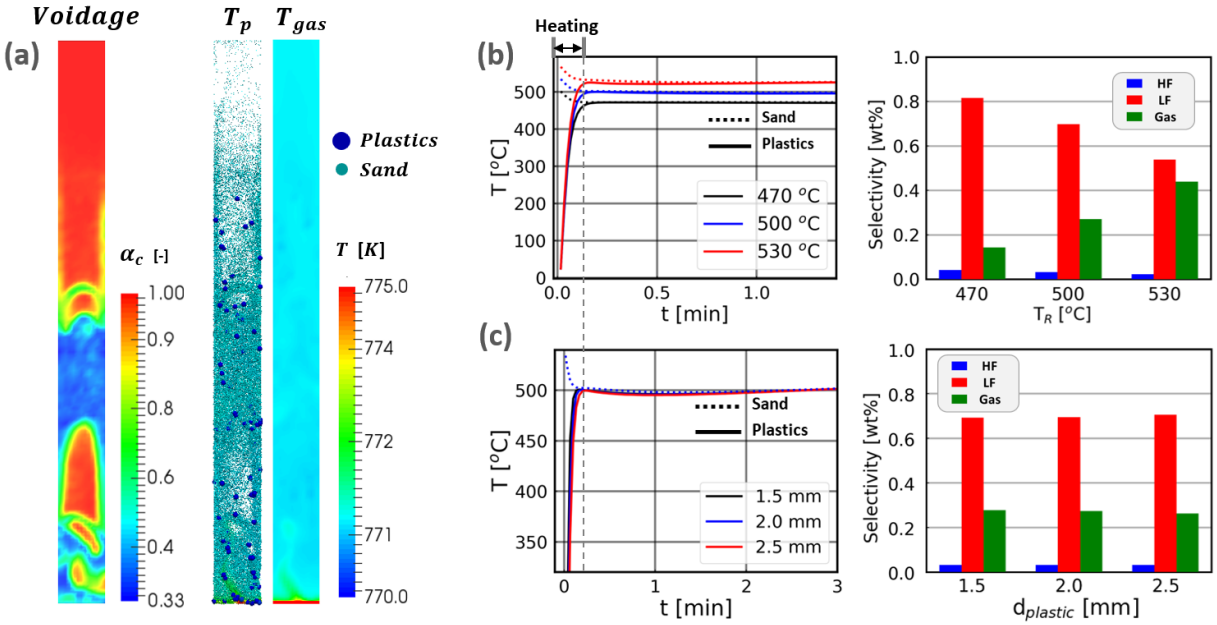

Figure 2: (a) Contours of instantaneous void fraction, particle distribution and gas phase temperature in the reference case (T_R = 500 °C, d_p = 2.0 mm); temporal evolution of temperature and product selectivity under batch-wise feeding for varying reactor temperature (b) and particle size (c).

As presented in Fig.2 (b), an increase in reactor temperature resulted in a decrease in LF's selectivity and an increase in Gas, which can be attributed to the difference in activation energy of the corresponding reactions ($E_{a,2}$ = 100 kJ/mol, $E_{a,3}$ = 249 kJ/mol). In contrast to the reactor temperature, the size of the plastic particles only have a minor influence on reaction selectivity, although smaller particles are heated up faster, as shown in Fig.2 (c). It has been found in the reference case that only approximately 1% of the particles were converted during the heating process (time to reach $T_{R,steady}$, approximately 10 s) from room temperature to reactor temperature. Therefore, despite different heating rates in the heating stage, all three sizes of particles demonstrate 1-2% discrepancy in selectivity. Moreover, the Euler-Lagrangian method treats all particles as having a homogeneous temperature, thereby further minimizing the impact of particle size. Although not shown here, the effect of plastic mass load and superficial velocity on the product selectivity were also negligible.

Continuous feeding

Under continuous feeding of plastics, the inlet gas temperature was kept constant during the simulation, which was higher than the desired reactor temperature T_R to provide the required heat for the endothermic pyrolysis process. The primary challenge in achieving continuous feeding is the establishment and maintenance of a stationary process condition at desired reactor temperature and plastic loading. In the initial stage of the simulation, the plastic particles will gradually accumulate in the reactor until the reaction rate reaches a dynamic equilibrium with the feeding rate. During this process, the boundary conditions (i.e., operating parameters) must be dynamically adjusted in order to stabilize the reactor temperature. In this study, the consumption rate of plastic under different operating conditions and the corresponding energy demand were estimated based on the given target operating conditions. These estimates were further employed in the calculations of mass and energy balance of the reactor system to determine the boundary conditions to achieve a steady state.

Figure 3 (a) demonstrates the time evolution the reactor temperature T_R starting from different initial states. With the aforementioned parameter setting strategy, the reactor can reach the steady state under all three conditions. During the startup stage, due to low mass share of plastics in the fluidized bed, the thermal energy supplied by the gas phase exceeded the energy demand, leading to energy accumulation and an increase of T_R. As the energy supplied by the hot gas and the consumption of heat for pyrolyzing

the plastics gradually reached equilibrium, the reactor temperature stabilized at a constant value. As shown in Fig.3 (b), a similar tendency in terms of product yield can be observed, where an increase of the reactor temperature led to the shift of selectivity from LF to Gas. Moreover, the size of the plastic particles d_P was found to have only a limited effect on the product selectivity during continuous feeding, although a slight decrease of T_R at smaller d_P was confirmed in the simulations.

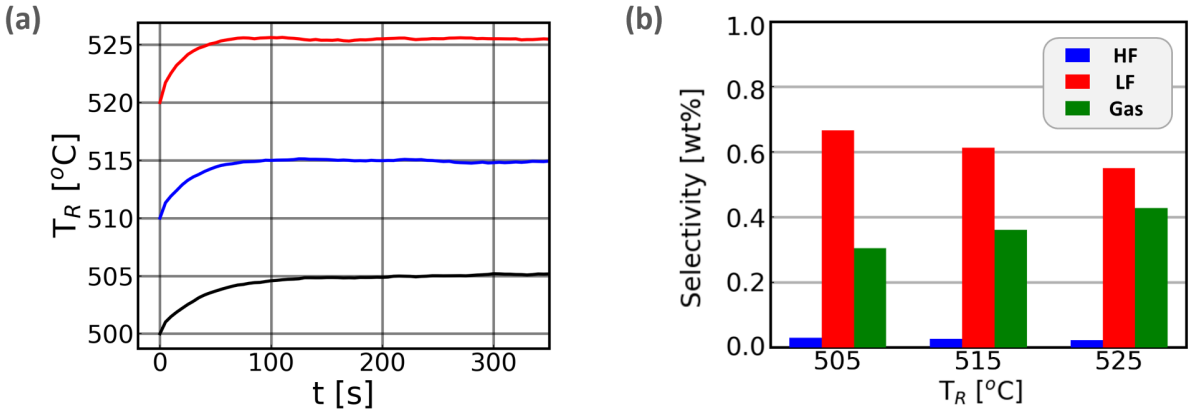

Figure 3: (a) Temporal evolution of reactor temperature under continuous feeding; (b) Selectivity of products at different reactor temperatures.

Conclusion

This study presents time-resolved Eulerian-Lagrangian simulations of plastic pyrolysis in a laboratory-scale fluidized bed, accounting for particle-gas dynamics, heat transfer, chemical reactions, and their mutual interactions. Simulations were conducted for both batch and continuous feeding operations. The promising simulation results across varying operating conditions demonstrate the potential of CFD-driven design to advance plastic pyrolysis technology on industrial scales. In future work, this modeling approach will be applied to guide the design and scale-up of plastic pyrolysis processes.

Acknowledgments

The authors gratefully acknowledge the financial support by the Helmholtz Association of German Research Centers (HGF), within the research program Materials and Technologies for the Energy Transition (MTET), topic Resource and Energy Efficiency. This work utilizes computing resources from the supercomputer HoreKa at the Scientific Centre for Computing (SCC) at KIT, Germany.

References

[1] PlasticsEurope: *The Circular Economy for Plastics – A European Analysis*, PlasticsEurope, Brussels, 2024.

[2] OECD: *Global Plastics Outlook: Economic Drivers, Environmental Impacts and Policy Options*, OECD Publishing, Paris, 2022.

[3] Dogu O., Pelucchi M., Faravelli T., Van Geem K. M.: *The chemistry of chemical recycling of solid plastic waste via pyrolysis and gasification: State-of-the-art, challenges, and future directions*, Prog. Energy Combust. Sci., 84, 100901, 2021.

[4] Dai L., Zhou N., Lv Y.: *Pyrolysis technology for plastic waste recycling: A state-of-the-art review*, Prog. Energy Combust. Sci., 93, 101021, 2022.

[5] Lechleitner A. E., Schubert T., Hofer W., Lehner M.: *Lumped kinetic modeling of polypropylene and polyethylene co-pyrolysis in tubular reactors*, Processes, 9(1), 34, 2020.

[6] Gunn D.J.: *Transfer of heat or mass to particles in fixed and fluidised beds*, Int. J. Heat Mass Transf., 21(4), 467-476, 1978.

[7] Zhang, F., Tavakkol, S., Dercho, S., Zhou, J., Zirwes, T., Zeller, M., Vogt, J., Zhang, R., Bockhorn, H. and Stapf, D.: *Assessment of dynamic characteristics of fluidized beds via numerical simulations*, Phys. Fluids, 36(2), 2024.

Scale-up of CFD-DEM simulation of fluidized bed gasification by GPU acceleration

C. Graf[1*], Y. Lichtmannegger[1], J. Ströhle[1] and B. Epple[1]

*E-Mail: christoph.graf@est.tu-darmstadt.de

[1] Technical University Darmstadt,Department of Mechanical Engineering, Institute for Energy Systems & Technology, Otto-Berndt-Str. 2, 64287 Darmstadt, Germany

Introduction

In light of anthropogenic carbon dioxide emissions contributing to climate change, increasing efforts have been made to reduce greenhouse gas emissions and transition the global economy from a fossil-based to a circular system. While carbon emissions have been reduced in the energy and industrial sectors in Europe, emissions are steadily increasing in the transport sector [1]. For land-based transportation, efforts to transition to electric propulsion systems were made; however, this is not feasible for air and sea travel due to the lower energy densities of battery storage compared to liquid fuels. This shows the need for renewable, carbon-neutral liquid fuels. One possible pathway for the production of such fuels is fluidized bed gasification of solid biomass residues with subsequent synthesis to products, such as green methanol or Fischer−Tropsch products. Gasification is achieved by partial oxidation of the feedstock to a raw syngas consisting of H_2, CO, CO_2, CH_4, and H_2O along with other trace components, which is subsequently purified for synthesis.

To improve reactor designs and to scale up fluidized bed gasification processes to industrial scales, computational fluid dynamics (CFD) simulation can be a powerful and cost-efficient tool. However, while pilot scale simulations have shown that reasonable accuracies can be achieved, simulation of large-scale fluidized bed reactors with the CFD-DEM method comes at very high computational costs due to high number of particles combined with complex chemical processes [2].

Large scale systems are typically simulated on high performance clusters (HPC) using large numbers of processing units (CPU). However, this results in a relatively low speed-up due to a low degree of parallelization. This could be improved by outsourcing the particle calculations to the graphical processing unit (GPU) which offers a much higher number of parallel cores, even on workstation PCs.

In this work, the acceleration potentials by using GPU for particle calculations in fluidized bed gasification will be evaluated. The major parameters and bottlenecks of GPU simulation and GPU-CPU coupling will be identified as well as assessing the influence of adding heterogeneous and homogeneous reactions. The feasibility of simulations of industrial scale systems on widely available and cheap consumer hardware will be determined and best practice guidelines derived.

Theory

Conventional CFD programs such as ANSYS Fluent are typically optimized for fluid simulations and thus come with drawbacks when particles are included. This affects both stability and speed of the calculations. In particular, the parallelization is performed based on the computational mesh of the domain. Fluidized beds typically have an uneven distribution of particles in the reactor. This leads to an uneven particle distribution to the computational threads and thus an imbalance in processor loads. Furthermore, particles frequently move across subdomain borders resulting in frequent data transfers between processors which causes higher computational time and lower CPU efficiency. This also prevents an effective transfer of the computations to the GPU as the computation time is determined by the slowest thread and the passing of memory between cores. Thus, the potential of large amounts of parallel cores offered by the GPU is not utilized.

In this work, this issue is prevented by decoupling fluid and particle calculations. To achieve this, two commercial codes were coupled. ANSYS Fluent was used for calculations of fluid flow and gas phase reactions, while ANSYS Rocky was chosen for particle tracking and heterogeneous reactions. The gas phase calculations are run on CPU while the particle calculations are performed on the GPU.

This allows for an even load balancing due to parallelization based on particle count. Furthermore, for fluidized beds a high number of particles has to be considered which profits from the high degree of parallelization offered by the GPU allowing for significant speed-up.

Methodology

In this work, several steps are considered to evaluate the performance boost achieved by utilizing GPU for DEM calculations for large scale fluidized bed gasification. All GPU simulations were conducted on a workstation PC with cheap and widely available consumer hardware, namely 1 NVIDIA GeForce RTX3060 GPU and 4 cores of an Intel 11th Gen I9-1190K CPU. CPU only simulations were conducted on a high-performance cluster (HPC) using 32 cores of Intel Cascade Lake AP processors using AVX-512 architecture.

First, a cold-flow benchmark case is created to set a baseline for the potential speed-up with the available hardware compared to HPC CPU-only computing. Second, a pilot scale 1 MW_{th} reactive fluidized bed gasifier is considered to evaluate the influence of reactions on simulation performance and provide a basis for scale-up of the process to industrial scale.

Preliminary results

The acceleration of particle calculation on GPU vs CPU is shown in **Figure 1** for the benchmark case. It is evident, that GPU offers a significant performance boost of 40 to 80 times faster calculations even with consumer hardware compared to an HPC. The speed-up is especially apparent when increasing particle number as the overall computation effort is shifted towards calculating particles. For CPU-only calculation even with 30,000 particles more than 99% of the calculation time is used for the particles. In contrast, with the coupled approach the fluid calculations are the bottleneck with the particles only accounting for 40% of the computational time for 30,000 particles. This shifts to approximately 75% at 300,000 particles in the domain. This shows the possibility to achieve further acceleration when using more CPU cores for parallelization of the gas phase.

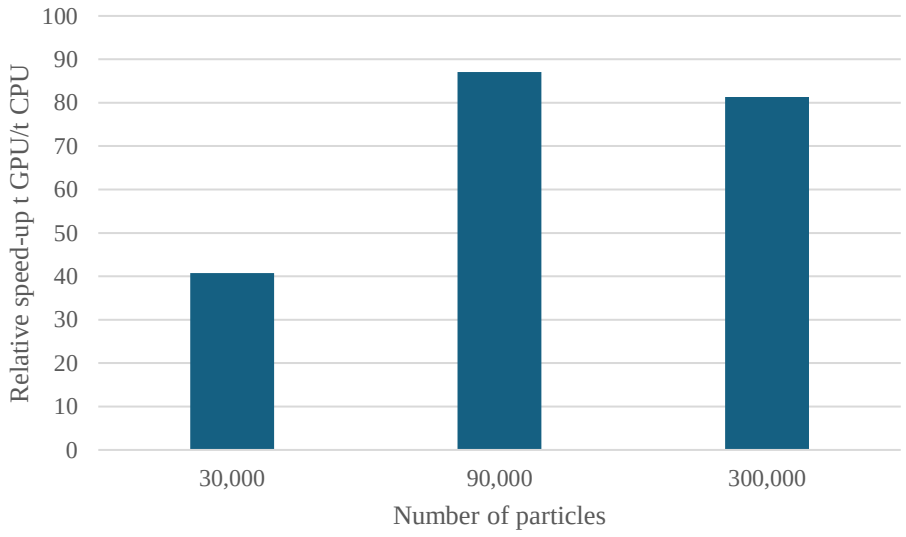

Figure 1. Relative speed-up for cold-flow simulations using GPU over CPU for particle processing.

Figure 2 shows the individual contributions of particle and fluid calculations as well as data transfer between CPU and GPU towards the total calculation time. The cold-flow cases with 30,000 to 300,000 were simulated as benchmark cases whereas the 500,000 particle cases correspond to the 1 MW_{th} bubbling fluidized bed gasification reactor using a coarse-grain approach. It can be seen that along with increasing number of particles not only the time for particle calculation but also for data transfer rises as values such as position, velocity and source terms have to be transferred for each individual particle. Overall, the data transfer accounts for 10-20% of the total calculation time, making it a significant limiting factor in GPU acceleration. The fluid solve time on the contrary decreases with increasing particle numbers, likely due to less variations in volume fractions and thus faster convergence.

For the bubbling bed gasification reactor lower particle calculation times are achieved although the number of particles increases. This highlights another major influence, namely the particle time step. As the particles in the gasification reactor are larger, larger time steps can be used while ensuring small overlaps and stable simulation conditions. This leads to less particle iterations and thus fast calculation times albeit higher processing times for individual iterations. The contribution of the fluid iterations increases significantly due to higher cell count and complex geometry and flow heterogeneities leading to slower convergence.

When accounting for reactions, both particle and fluid computation times increase significantly, while the data transfer is unaffected. In this case the addition of five heterogeneous reactions lead to a twofold increase of simulation time. On the fluid side, the addition of homogeneous reactions as well as slower convergence due to higher species and temperature gradients lead to higher calculation times. Overall, the reactive model requires an overhead of 67% on the calculation time.

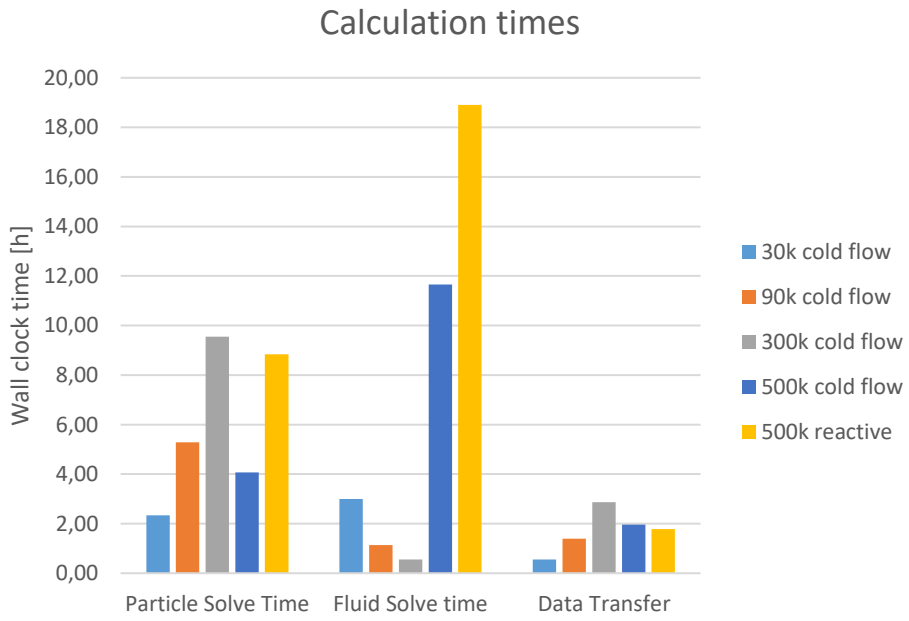

Figure 2. Calculation times of particle and fluid calculations and data transfer between CPU and GPU for 10 seconds of simulated time.

Outlook

As shown, by outsourcing the particle calculations to the GPU, significant acceleration of CFD-DEM simulation can be achieved. This allows for steady state simulation of a 1 MW_{th} pilot scale bubbling bed gasifier within 2-3 days on consumer hardware. Due to speed-up of particle calculations, the impact of fluid calculations is significant up to particle numbers needed for large scale systems, thus effective CPU parallelization of the gas phase should be ensured.

Further investigations are planned regarding scale up to industrial scale to evaluate model performance and computational requirements to enable the use of CFD-DEM as a scale-up tool for fluidized bed gasification.

References

[1] W. F. Lamb *et. al.*, *A review of trends and drivers of greenhouse gas emissions by sector from 1990 to 2018*, *Environ. Res. Lett.*, 16, 073005, 2021.

[2] C. Graf *et. al.*, *Development of a CFD-DEM Model for a 1 MW $_{th}$ Chemical Looping Gasification Pilot Plant Using Biogenic Residues as Feedstock*, *Energy Fuels*, 38, 19, 18660-18673, 2024.

Transient Drag Behaviour on non-Spherical Geldart B Coal particle in Air Fluidised bed Reactor

Ravisha Goswami[1*] and Vimal Kumar[1]

*E-Mail: rgoswami@ch.iitr.ac.in, vimal.kumar@ch.iitr.ac.in

[1] Department of Chemical Engineering, Indian Institute of Technology Roorkee, Roorkee, Uttarakhand – 247667, India

Abstract

In the present work the hydrodynamics of gas-solid 2-D approximated fluidised bed reactor for Geldart B particles (300μm) is studied. Eulerian-Eulerian approach combined with quantity granular property for modelling solid particles is applied for the prediction of void fraction and granular temperature in the bubbling fluidised bed reactor. Seven drag models are chosen for a comprehensive comparison for different values of bed voidage (ε) for coal particle, considering spherical (sphericity, Ψ=1) shape. Compared to already established experimental data in the literature with glass particles, it is found that Huilin Gidaspow and parameterised Syamlal O'Brien drag models provided the closest approximation at different bed voidages. Furthermore, granular temperature prediction in different regions of fluidised bed is reported. The Gidaspow drag model predicted the bed voidage more accurately, however bubble prediction is more accurate in the case of the Syamlal O'Brien drag model.

Introduction

Coal remains to be the predominant energy source worldwide, according to the IEA report 2024 (July 2024) [1]. However, shifting towards clean energy remains a target worldwide and hence in this context fluidisation is the technology which can provide clean coal energy. Application of fluidisation-based technologies for coal processing has been studied widely through several decades. Bubbling fluidisation regime is the most widely used configuration for the coal gasification. Momentum exchange between gas and solid particles plays a vital role in dictating the overall flow pattern in fluidised bed reactors and hence influences the physics of fluidised bed reactors. Drag force is influenced by solid volume fraction, causing a difference in drag force experienced by particles. Wen Yu, Gidaspow, and Syamlal O'Brian models are the standardised models, widely used to compare findings of drag laws for monodisperse systems. More recent models [2] are based on the polydisperse system and are derived on the basis of Lattice Boltzmann method. Tenneti et al. [3] proposed drag law for monodisperse systems, which is limited to static assembly of spheres. As observed from the literature [4], granular temperature is a very important parameter in fluidised bed reactors, since it influences the drag force value predominantly, and hence gas-solid chemistry interaction. In the present work both void fractions (bed voidage) and granular temperature variation is studied using different drag models. It is expected that experimental data for coal particles will provide closer estimation with present simulation data.

Mathematical Framework for Drag Dynamics in Fluidisation:

The Eulerian-Eulerian two-fluid modelling (TFM) approach was used in this work considering both solid and gas phase as interpenetrating continua. The model is derived based on conservation laws of mass and momentum and principle of fluid mechanics. ANSYS Fluent 2024R1 was used to solve the governing equations for mass and momentum in the considered domain. Time average bed voidage and granular temperature for solid fraction packing of 0.6 is reported. Air is passed through the bed at a Reynolds number of 24.5. Phases are solved based on continuity and RANS equations. Drag-solid interactions are modelled using drag equations shown in Table 1.

The computational domain, fluid and solid particles considered are two-dimensional (2D), air and coal particles, respectively. The present numerical predictions of bed voidage and granular temperature were compared with the experimental data of Taghipour et al. [5] and Jung et al. [6], respectively.

Table 1. Classical drag models considered for bed voidage and granular temperature predictions

Wen-Yu Model $$F_{gs} = \frac{3}{4} C_d \frac{\alpha_s \alpha_g \rho_g \lvert u_s - u_g \rvert}{d_s} \alpha_g^{-2.65}$$ $$C_d = \frac{24}{\alpha_g Re_s}\left[1 + 0.15\left(\alpha_g Re_s\right)^{0.687}\right] \quad Re < 100$$ $$C_d = 0.44 \qquad Re \geq 1000$$	Homogeneous model Based on drag force calculation which is being a function of bed voidage experienced by a single particle falling in an expanse of infinite fluid
Gidaspow Model $$F_d = \{\left(\frac{3}{4} C_D \frac{\alpha_p \alpha_g \rho_g \lvert \overrightarrow{u_s} - \overrightarrow{u_g} \rvert}{d_s}\right) \cdot \alpha_g^{-2.65}, \alpha_g > 0.8$$ $$F_d = \frac{\alpha_s 150(1-\alpha_g)\mu_g}{\alpha_g d_s^2} + \frac{\alpha_s 1.75 \rho_g \lvert u_s - u_g \rvert}{d_s}, \alpha_g \leq 0.8$$ $$C_D = \begin{cases} \frac{24}{Re_s}(1 + 0.15 Re_s^{0.687}) & Re_p \leq 1000 \\ 0.44 & Re_s > 1000 \end{cases}$$	Homogeneous model This model uses Wen Yu model for dilute conditions($\alpha_s \leq 0.2$) and Ergun model for dense regions($\alpha_s > 0.2$)
Syamlal O'Brian Model $$F_d = \frac{3\alpha_s \alpha_g \rho_g}{4 u_{t,s}^2 d_s} C_d \left(\frac{Re_s}{u_{t,s}}\right) \lvert u_s - u_g \rvert$$ $$C_d = \left(0.63 + \frac{4.8}{\sqrt{\frac{Re_s}{u_{r,s}}}}\right)^2$$ $$u_{r,s} = 0.5(A - 0.06)Re_s + \sqrt{(0.06 Re_s)^2 + 0.12 Re_s (2B - A) + A^2}$$ where A=$\alpha_g^{4.14}$, $B = 0.8\alpha_g^{1.28}$ for $\alpha_g \leq 0.85$ A=$\alpha_g^{4.14}$, $B = \alpha_g^{2.65}$ for $\alpha_g > 0.85$	Homogeneous model The derivation of this model starts from the basics of velocity and voidage relationship. The formula has given good predictions with both gas and liquid fluidised bed.
Gibilaro Model $$F_d = C_D \frac{\rho u^2}{2} \frac{\pi d^2}{4}$$ $$C_D = \frac{4}{3} f_p \alpha^{-3.8}$$ where, $f_p = \frac{17.3}{Re} + 0.336$	Homogeneous model Formula is based on pressure drop correlation. Predictions through this equation are not good in transition flow conditions (in between laminar and turbulent)

Results and Discussion:

Simulations were performed for a flow time of 15-20s, and time averaging of physical quantities were started after 3s, since bed expands up to a stable height and flow pattern is developed at 3s and does not expand further. Figure 1(a) shows the time mean phases, calculated at a height of 0.2m from the bottom of the column. It can be observed that there is an overestimation of bed voidage through the Syamlal O'Brien and Wen-Yu drag models, while the Gidaspow drag model gives good agreement with experimental data. The difference between experimental results and numerical prediction can be accounted for by the reason that the experimental data recorded at a frequency of 100 Hz and numerical data sampling is done at 500 Hz frequency and hence there is an overprediction of the drag force. Formation of bubbles at different instants of time and their coalescence at the upper surface of bed through different models, marks the difference between the models.

Figure 1(b) shows fairly good agreement between present granular temperature numerical predictions and the experimental results of Jung et al. [6]. Figure 2(a-c) shows the granular temperature predicted in different zones (dilute, intermediate and dense). Magnitude of time average granular temperature is of the order of 0.0015 m^2/s^2 in the dense region and is found to increase by an order of 10 in the intermediate region, and again by factor of 10 in the dilute region. The granular temperature of a particle arises due to oscillations of particles in a small region for a very short period. The random kinetic energy of a particle is given through granular temperature and varies with space and time.

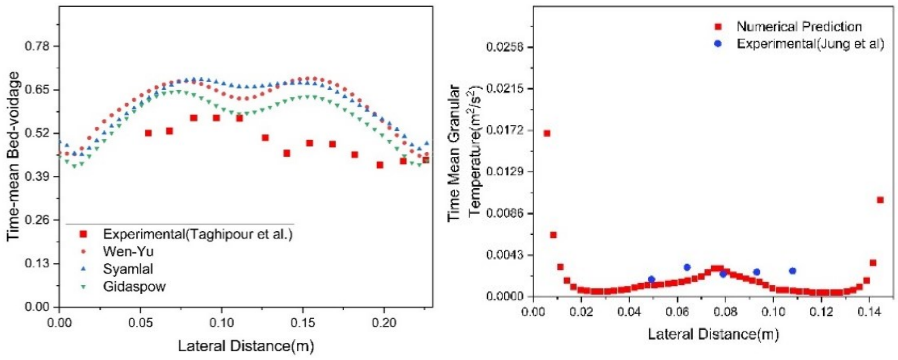

(a) (b)

Figure 1. Comparison of present predictions with the experimental data of (a) Taghipour et al. [5] for spherical glass beads, and (b) Jung et al. [6] for 500 μm particles using Huilin-Gidaspow model.

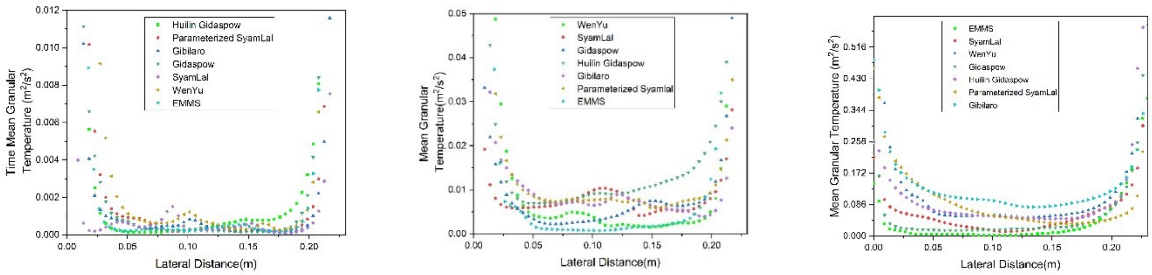

(a) (b) (c)

Figure 2. Estimation of time mean granular temperature for 300 μm particle in (a) dense (b) intermediate, and (c) dilute regions

Conclusion

The hydrodynamics of fluidised bed reactor is investigated, by considering 2-D flow field for the coal fluidised bed system considering different drag models. Expanded bed height was found to be in the range of 0.6 to 0.7m through all the models, except the EMMS model which predicted bed height up to 0.5m. The present predictions for bed voidage and granular temperature are found in good agreement with the experimental data reported in the literature. Hydrodynamics for transient study of fluidisation is unique for every system under consideration and hence need to be done, before planning reacting gas-solid systems.

References

[1] World Energy Outlook 2024, https://www.iea.org/reports/world-energy-outlook-2024 (accessed on April 10th, 2025)

[2] Beetstra R., van der Hoef M.A., Kuipers J.A.M.*: Drag force of intermediate Reynolds number flow past mono- and bidisperse arrays of spheres*, AIChE J. 53, 489–501, 2007.

[3] Tenneti S., Garg R., Subramaniam S.: *Drag law for monodisperse gas–solid systems using particle-resolved direct numerical simulation of flow past fixed assemblies of spheres*, International Journal of Multiphase Flow 37(9), 1072-1092, 2011.

[4] Mineto A. T., Braun M. P. S., Navarro H. A., Cabezas-Gómez L.: *Influence of the granular temperature in the numerical simulation of gas-solid flow in a bubbling fluidized bed*, Chemical Engineering Communications 201(8), 1003-1020, 2014.

[5] Taghipour F., Ellis N., Wong C.: *Experimental and computational study of gas–solid fluidised bed hydrodynamics*, Chemical Engineering Science 60, 6857–6867, 2005.

[6] Jung J., Gidaspow D., Gamwo I. K.: *Measurement of two kinds of granular temperatures, stresses and dispersion in bubbling beds*, Industrial Engineering Chemistry Research 44, 1329–1341, 2005.

Continuum Model and Benchmarking Experiment of Powder Mixing in a Cylindrical Bladed Mixer

A. M. Baecke[1*], A. P. Ganesh Ruthraruba[1], U. Hampel[1,2] and G. Lecrivain[1]

*E-Mail: a.baecke@hzdr.de

[1] Institute of Fluid Dynamics, Helmholtz-Zentrum Dresden-Rossendorf, Bautzner Landstraße 400, 01328 Dresden, Germany

[2] Chair of Imaging Techniques in Energy and Process Engineering, TU Dresden, 01062 Dresden, Germany

Introduction & Motivation

Industrial processes are inevitably associated with generating fine-grained particulate matter. Such fine-grained residues rarely find re-entry into industrial value chains; typically, they are disposed and become an environmental burden. The Helmholtz project FINEST addresses this challenge to process different residues in an optimized manner to generate value and to minimize hazards. One approach is targeted merging of material streams that are extremely different in terms of chemical and phase composition. This involves a mixing and agglomeration step, followed by pyrometallurgical treatment.

In powder mixing, differences in particle properties cause segregation. In the context of our project, focus is on different densities, because the occurring particles range from plastics to metals. We first choose a non-invasive technique to investigate the process, Microfocus X-Ray Computed Tomography. Complementary to the experimental study, continuum modelling is chosen to simulate the mixing as a Finite Volume Model in OpenFOAM. We are implementing μ(I)-rheology and a density segregation term and validating it against the experimental results. This combines previous continuum models for bladed mixer considering only size-segregation [1], other geometries being investigated for density segregation [2] and implementations of the rheology in free surface flows [3].

Method for Experiment

Our experiment is intended as a benchmarking and validation case for mixing of powders with different densities in cylindrical bladed mixers on a lab scale. Combinations of particles from 150 – 250 μm with densities between 0.5 – 5 g/cm³ are mixed in a vessel of 9 cm inner diameter with a 3-bladed impeller. The μCT scans of powder mixtures are acquired with voxel size of 100 μm. They provide insight into the composition of the powder mixture at any point in space and allow to analyse the powder flow. Using a 3D analysis method, the quality of mixture is described by a variance measure. The method features a direct analysis of intensity/grey scale values from the μCT data. It needs no segmentation or binarization step. Instead, a normalization is applied based on histogram analysis. The known principle of sampling bulk powders and sample statistics are adapted [4]. In analogy to physical samples, grid cells are constructed over the image data. Within those, a mean intensity value is determined and variance of those mean values calculated. The evolution of variance describes the evolution of mixing quality over time. A mixing index, following classical variance based mixing index approaches, can be formulated on this basis.

Method for Simulations

In the modelling of particle processes, DEM is highly popular despite high computational cost [1]. Since we are specifically dealing with a fine powder system, where the cylindrical bladed mixer exceeds the size of particles by far, we choose a continuum modelling approach.

This approach necessitates a rheological model to characterize the bulk powder's flow behaviour. We employ the commonly used μ(I)-model which offers a flexible framework for analysing dense granular flows, adeptly explaining the transition between behaviours resembling solids and fluids [5]. It requires a regularization method to address some mathematical and physical limitations.

For the description of the mixing among particles and the development of concentration profiles we investigated Advection-Dispersion-Segregation Models first [1]. Our model now has all terms for transport mechanisms, including segregation between particle species, implemented into the respective

volume fraction equations. Momentum conservation is formulated based on the bulk mixture model, ensuring that the collective motion of particles and carrier phase is accurately captured while accounting for the interactions between different phases within the continuum framework.

Results of Experiment

From the µCT scans, we get 3D datasets of the composition of different powder mixtures after defined durations of mixing. **Figure 1** shows a scan of two powders (density 1 g/cm³ and 2,5 g/cm³) mixed at Froude-Number = 1 (here equal to 142 rpm) for 5 impeller rotations. Horizontal and vertical slices of the image are provided for detailed insight. Lightweight particles are represented by areas of lower attenuation, here medium blue. Higher attenuation, caused by high density particles, is shown in orange. Different degrees of mixing result in a range of colour in between. In these images, the impeller is visible in a light blue colour. These are the areas that will be masked for further calculations on the data.

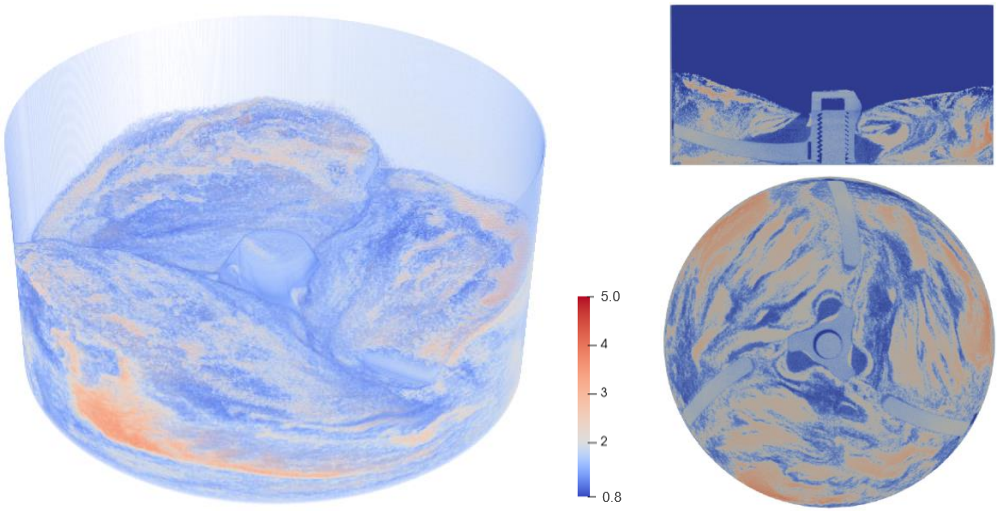

Figure 1. Experimental Results - µCT scan of powder mixture, 3D view, vertical and horizontal slice

Quantitative results are achieved through the normalization and variance calculation method. With the method applied to a variety of mixtures, we can give a full image of parameters, such as mixing speed, density ratio and mixing duration, that lead to segregation and the dependency of the variance measure (representing mixing quality) on those.

Results of Simulations

Our results so far demonstrate the successful implementation of µ(I)-rheology in OpenFOAM. Both regularized and unregularized µ(I)-rheology [3] are implemented for OpenFOAM 12 for two phase non-newtonian flow. This was also based on an implementation in OpenFOAM 2406, which did however lack multiphase capabilities and validation [6].

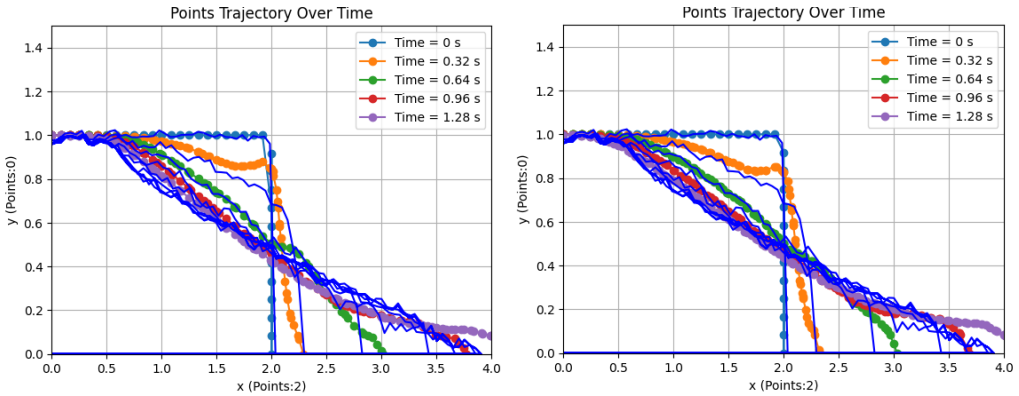

Figure 2. Graphs for validation of µ(I)-implementation, left: unregularized, right: regularized model

The implementation of the μ(I)-rheology model as a user-defined executable library, libmuI, has so far been verified based on the results of the 2D column collapse simulations. A qualitative comparison, with DEM results [7] demonstrates the reliability of the μ(I)-rheology model. **Figure 2** shows the comparison of flow trajectory over time with an aspect ratio (column's height to base length) a = 0,5. The findings indicate that the regularized version achieves better agreement with the reference data, confirming that the regularization effectively addresses known limitations of the unregularized μ(I)-rheology.

Further improvements to the numerical model were achieved by developing a more robust approximation for the maximum and minimum viscosity limits to enhance the fidelity of the rheological behaviour and tightening the convergence tolerances of the numerical solvers to minimize residual errors and improve overall solution accuracy. These refinements will improve the accuracy of the μ(I)-rheology model and enhance its applicability to a broader range of granular flow problems.

After implementing the rheology model, the multiphase VoF solver was modified to incorporate our adjustments in the volume fraction equation. To ensure stability and accuracy, we conducted initial tests on a rotating drum case [3]. The next phase involves validating the model for size segregation, comparing results with [1], before proceeding to density segregation simulations in the cylindrical mixer. These final simulations will be cross-validated against experimental results from our parallel study, ensuring the model's accuracy and applicability to granular mixing process.

Conclusions

The insights gained from our experimental methodology will be used to further investigate the relevant parameters in powder mixing, such as density combinations and mixing intensity to result in a parameter/regime map for this process.

We could successfully implement μ(I)-rheology in regularized and unregularized form in OpenFOAM for powder flow. In particular, the regularized μ(I)-rheology model shows great promise for advancing the predictive capabilities of numerical simulations in granular flow problems.

Our multiphase VoF solver, with modified volume fraction equations, effectively captures mixing and size-based segregation in the cylindrical bladed mixer. However, density-driven segregation cases require further validation against experimental data. Additionally, the role of compressibility in the system remains for further discussion and analysis.

Acknowledgement

The project FINEST is funded by the Investment and Networking Fund of the Helmholtz Association under grant agreement no. KA2-HSC-10.

References

[1] Yang L., Zheng Q., Yu A.: *A continuum model for the segregation of bidisperse particles in a blade mixer*, AIChe Journal, 68, e17734, 2022.

[2] Tirapelle M., Santomaso A.C., Richard P., Artoni R.: *Experimental investigation and numerical modelling of density-driven segregation in an annular shear cell*, Advanced Powder Technology, 32, 1305, 2021.

[3] Barker T., Rauter M., Maguire E.S.F., Johnson C.G., Gray J.M.N.T.: *Coupling rheology and segregation in granular flows*, Journal of Fluid Mechanics, 909, A22, 2021.

[4] Stieß M.: *Mechanische Verfahrenstechnik – Partikeltechnologie 1*, Springer Berlin, Heidelberg, ISBN 978-3-540-32552-9, 2008.

[5] Jop P., Forterre Y., Pouliqen O., *A constitutive law for dense granular flows*, Nature, 441, 727, 2006.

[6] Jarosch A.H., Jóhannesson T., *alexjarosch/OpenFOAM-muI: v1.1.0 OpenFOAM mu(I) rheology*, v1.1.0, Zenodo, 2024, DOI: 10.5281/zenodo.13354106

[7] Lagrée P-Y, Staron L, Popinet S.: *The granular column collapse as a continuum: validity of a two-dimensional Navier–Stokes model with a μ(I)-rheology*, Journal of Fluid Mechanics, 686, 378, 2011.

Ignition and flame propagation in mixtures of combustible dusts with hydrogen

P. Zhao*, D. Gabel and U. Krause
*E-Mail: zhao.peng@ovgu.de
Chair of Plant Design and Process Safety, University of Magdeburg, Universitätsplatz 2, 39106 Magdeburg, Germany

Abstract:
The ignition process and the flame propagation behavior of hybrid mixtures of iron dust and carbon black powder with hydrogen were experimentally investigated in a transparent vertical tube of 60 mm in diameter and 1 m in length. An electrical spark ignitor with 10J energy was used as the ignition source and ignition and flame propagation were observed with a high speed-infrared camera. Carbon black and iron were chosen as dusts because they do not contain any volatiles and in combination with hydrogen the simplest possible reaction mechanisms for hybrid mixtures occur. The experiments showed that the minimum explosible concentration (MEC) of iron dust was determined as 560 g/m^3 and there was no significant change in MEC with the addition of 1 vol% and 2 vol% hydrogen. But the MEC was decreased to 250 g/m^3 when 3 vol.% hydrogen was added (with the lower explosion limit of H_2 being at 4.2 vol%). A similar trend emerged for carbon black and hydrogen in which the addition of 50 g/m³ of the former led to stable flame propagation at only 3 vol.% of hydrogen.

Keywords: Hybrid mixtures, hydrogen, ignition, dust explosion, minimum explosible concentration, flame propagation velocity

Introduction

The explosion and flame propagation characteristics of hybrid mixtures related to flammable gases and metal dust have attracted a lot attention from researchers worldwide for many years [1]. Denkevits [2] studied the explosion indices and explosion behavior of Al dust/H_2/air mixtures and found that the explosion regime depends on the hybrid fuel concentration. The combustion behaviors of hybrid Al/H_2 were investigated by [3], the results show that the addition of H_2 can increase the flame brightness and improve the continuity of the flame front.
Iron (Fe), as a traditional multi-purpose material, has attracted renewed attention in recent years for its high energy density and abundant reserves, making it a potential candidate material in the field of renewable energy [4]. Additionally, iron dust can also serve as a source of hydrogen generation by reacting with water to produce hydrogen gas, enabling the production of clean energy. Carbon black can be produced from biomass by hydrothermal carbonization, has a water content of less than 5 % in mass and is free of volatiles. In contrast to dusts with a more complex chemical structure for both iron and carbon black the reactions with oxygen follow comparatively simple reaction mechanisms. Basically, there is no devolatilization and consequently no oxidation of a gas phase, just a burning of the particles. Thus, in case of hybrid mixtures the contribution of the particles and the added flammable gas to the flame propagation can be distinguished quite clearly.

Experimental setup and procedure

The main setup used in this work is a vertical tube of 60 mm in diameter and 1000 mm in height, as used by Krause et al. [5] for flame propagation experiments in dust/air mixtures, see Figure 1. The bottom of the tube was mounted to a cup of the same inner diameter inside which the dust particles were initially layered on a porous filter plate. The gas inlet was mounted to the wall of the cup underneath the level of the filter plate. The upper end of the tube remained open. The dust concentration inside the tube was measured by

infrared light attenuation at two height levels. The ignition source consisted of a high voltage discharge arc with approximately 10 J energy, and was placed at a level of 330 mm from the bottom of the tube. Spark duration was 50 ms. The flow rate, flow time and ignition delay time of gases were set to 2000 L/h, 20 s and 20 ms respectively. The flame propagation was observed with a high-speed video camera at 2000 fps. A high-speed infrared camera was also used operated at a frame rate of 600 fps.

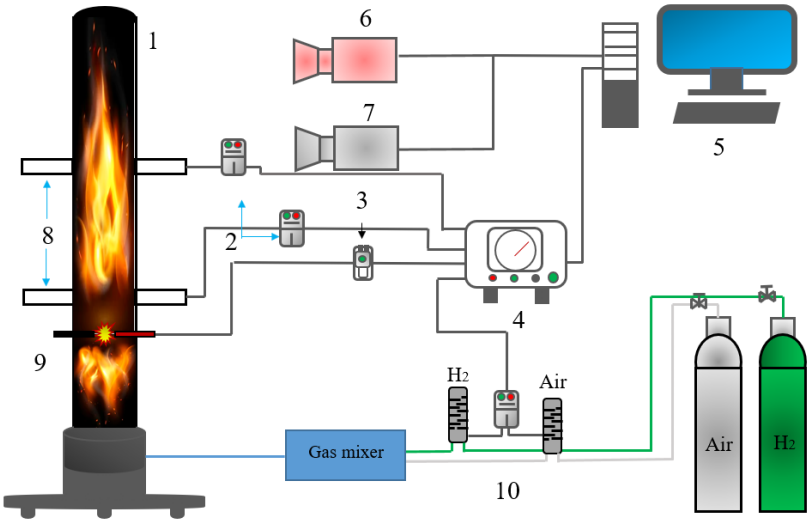

1-Acrylic vertical tube 2-Data acquisition unit 3-High voltage transformer
4-Time controller 5-PC 6-Infrared camera
7-High speed camera 8-Conc. measurement probes 9-Spark electrodes
10-Digital flowmeter

Figure 1. Schematic diagram of the experimental setup for flame propagation experiments.

For each experiment the intended amount of dust was layered on the filter plate and elutriated by the pre-mixed hydrogen/air mixture. The dust/gas mixture passed the two dust concentration probes. When the deviation in the signals of both was less than 10 % the dust/gas mixture was considered as "homogeneous" and the ignition spark was triggered. Flame propagation was observed with both the high-speed and the infrared camera. A trial was counted as "ignition" when the flame kernel started to grow beyond and detached from the ignition source. Each trial was repeated at least five times to assess uncertainties in the measured parameters.

Results

The lower explosion limit (LEL) of pure hydrogen mixed to air is at 4.2 vol.% [6]. This means a mixture with a volume fraction less than that value cannot ignite. For carbon black the minimum explosible concentration (MEC) was found at 125 g/m³ which also means a mixture with less dust cannot ignite. Correspondingly, the MEC of iron dust was found at 560 g/m³. Hybrid mixtures, however, are able to ignite at concentrations below the individual LEL and MEC of their constituents. Figure 2 shows thermal imaging snapshots of a mixture of 3 vol.% H_2 and 50 g/m³ of carbon black at 25 ms to 100 ms after activation of the ignition source. Clearly, the ignition energy was applied to the particles firstly before the hydrogen molecules (which are insufficient in concentration to sustain a flame without the dust) were starting to react. At 100 ms a reaction front, visible a light-yellow pattern, has detached from the ignitor electrodes.

The effect of the addition of hydrogen on the reaction front velocity of iron dust shows figure 3 based on frames taken from the high-speed camera in visible range. The time span between two frames was 100 ms. The frames show a clear acceleration of the reaction front with increasing concentration of hydrogen despite the highest hydrogen concentration of 5 vol.% was still close to its LEL.

Conclusions

The experimental results show that in flames through hybrid mixtures first of all a sufficient number of particles has to be ignited before the gas phase component can start to react. Further, already a small amount of added flammable gas considerably accelerates the velocity of the reaction front.

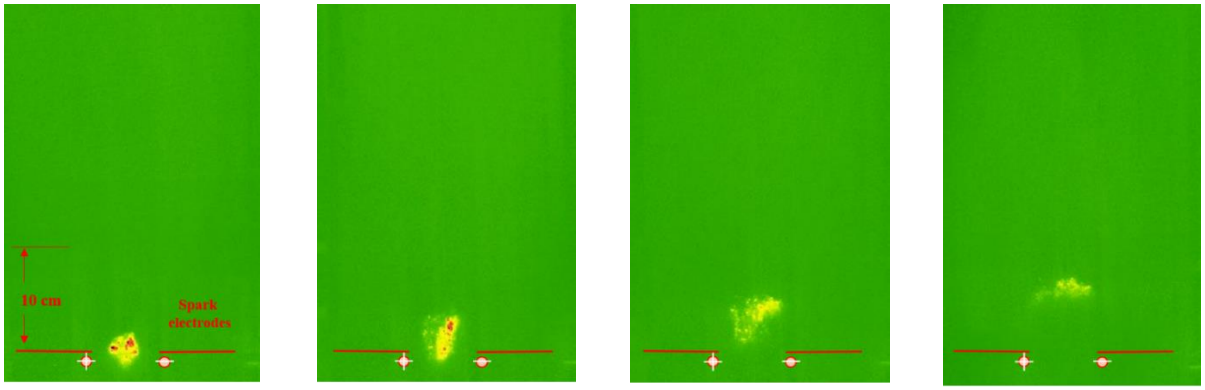

Figure 2. High-speed thermal imaging camera frames. Formation and extinction of a flame kernel in a hybrid mixture of H_2 and carbon black dust (3 vol.% H_2 and 50 g/m^{3}carbon black).

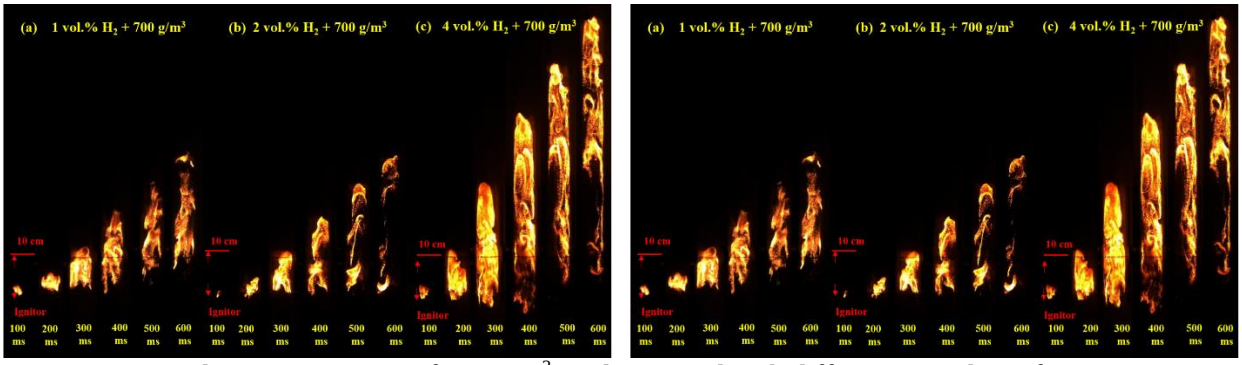

Fig. 3. Flame propagation of 700 g/m^3 Fe dust mixed with different H_2 volume fraction.

References

[1] Wu, D., Zhao, P., Spitzer, S. H., Krietsch, A., Amyotte, P., Krause, U., A review on hybrid mixture explosions: Safety parameters, explosion regimes and criteria, flame characteristics. Journal of loss prevention in the process industries, 82, 104969. 2023

[2] Denkevits, A., Hoess, B., Hybrid H_2/Al dust explosions in Siwek sphere. J. Loss Prev. Process. Ind. Elsevier Ltd 36, 509-521. 2015.

[3] Ji, W., Wang, Y., Yang, J., He, J., Lu, C., Wen, X., Wang, Y., Explosion overpressure behavior and flame propagation characteristics in hybrid explosions of hydrogen and magnesium dust. Fuel, 332, 125801. 2022

[4] Debiagi, P., Rocha, R.C., Scholtissek, A., Janicka, J., Hasse, C., Iron as a sustainable chemical carrier of renewable energy: Analysis of opportunities and challenges for retrofitting coal-fired power plants. Renew Sust Energ Rev. vol.165, 112579. 2022

[5] Krause, U., Kasch, T., Gebauer, B., Velocity and concentration effects on the laminar burning velocity of dust-air mixtures. Arch. Combust. 16, 159-176. 1996.

[6] Database ChemSafe. www.chemsafe.ptb.de, Physikalisch-Technische Bundesanstalt Braunschweig.

Comparison of 1D and 3D models for the thermochemical conversion of carbonaceous pulverized particles

Matthias Kiss[1], Thomas Nanz[2], and Markus Bösenhofer[3*]

*E-Mail: markus.boesenhofer@tuwien.ac.at

[1]Area 3 - Simulation and Analyses, K1-MET GmbH, Stahlstraße 14, 4020, Linz, Austria
[2]Area 1 - Metallurgical Process Efficiency & Circularity, K1-MET GmbH, Stahlstraße 14, 4020, Linz, Austria
[3]Institute of Chemical, Environmental and Bioscience Engineering, TU Wien, Getreidemarkt 9/166-2, 1060, Vienna, Austria

Introduction

Detailed modeling of the thermochemical conversion of pulverized particles is essential for high heating rate applications, e.g., in the blast furnace, dust boilers, or other high-temperature industrial processes. Pulverized particles can experience significant intra-particle temperature gradients under high heating rate conditions [1]. These non-uniform particle temperatures influence the thermochemical conversion process; typically, the overall conversion rate decreases. While 1D resolved particles can model non-uniform temperature distributions it is necessary to utilize fully resolved 3D models to model changes in reaction kinetics inside the particle due to the inhomogeneous temperature distribution.

Since measurements are impossible in the blast furnace raceway zone, we use a simplified experimental setup, the ARA Reactor, to better control the experimental conditions [2, 3], which aims to reproduce raceway conditions. Furthermore, a Computational Fluid Dynamics (CFD) model of the ARA Reactor is implemented and employed to extract additional information from the experiments. Representative particle trajectories were extracted from the CFD model to investigate the thermochemical conversion process at particle scale in detail. A 1D Euler-Lagrangian and a 3D particle resolved approach are used to investigate these intra-particle scales. The open-source CFD toolbox OpenFOAM is used for the simulations.

The subsequent sections first give an overview of the experimental setup and procedures before the 1D approach is explained and the results are presented. Finally, the 3D approach is introduced and validated. At the current state, the particle-resolved 3D simulations are ongoing. Therefore, only model validation results can be presented here.

Experiments

The experiments are conducted using the ARA Reactor of K1-MET located at and operated with TU Wien, which is an entrained flow reactor for high heating rates (up to 10^6 K/s), high temperatures (up to 1500 K), and pressures up to 7 $bar_{(a)}$ [2, 3]. Figure 1 sketches the ARA Reactor and its main components, and Table 1 summarizes the experimental and simulation boundary conditions.

Table 1. Investigated experimental conditions.

	Flow rate (Nm^3/h)	Temperature (K)
Co-flow (air)	24.9	1245
Coal lance (N_2)	1.3	303
Burner (air)	2.5	303
Burner (H_2)	0	-
Quench (N_2)	10	303
Heating zones	-	1585

The same conditions are used to simulate the reactive zone, extract representative particle trajectories by Lagrangian particle tracking and, and derive representative particle conversion conditions. The extracted conversion conditions are depicted in Figure 1.

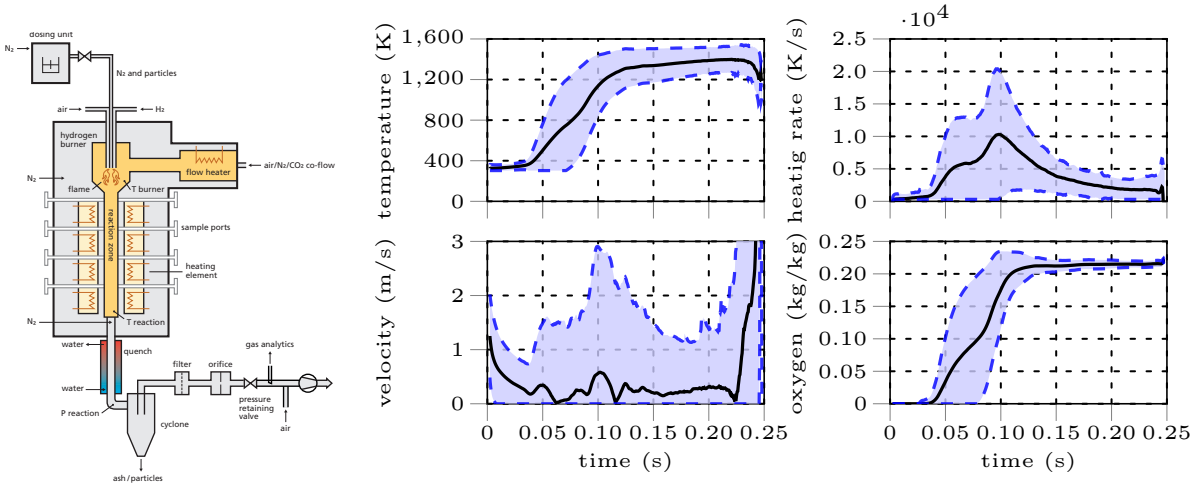

Figure 1. Schematics of the ARA Reactor (left) and representative particle conversion conditions extracted from the ARA Reactor CFD model (right).

1D Simulations

The 1D simulations are based on an Euler-Lagrange simulation framework. The employed resolved Lagrangian particle model (RLPM) resolves the Lagrangian particles in 1D, assuming radial symmetry. The particles consist of three phases: i) gas, ii) liquid, and iii) solid. The individual phases consist of multiple species. The solid and liquid phase are assumed to be stationary, while the gas phase can move. As a result, the species transport equations are only solved for the gas phase, while the energy equation considers all three phases. The transport equations are coupled to the surrounding gas phase (carrier phase) via suitable boundary conditions. Details about the model can be found elsewhere [4, 5].

The detailed investigations were carried out for the average, low, and high temperature cases temperature cases indicated by the black line and the two dashed blue lines in Figure 1, respectively. The simulation setup for the 1D cases consists of a single particle in a box and is described in detail in [6].

Figure 2 shows the 1D modeling results for the three cases. As expected, the carrier phase temperature has a significant effect on the devolatilization (DO) and burnout (BO) ratios. The particle is fully converted after 0.16 s in the high-temperature case, while the BO is roughly 0.4 after 0.25 s for the low-temperature case. Peak particle temperatures are delayed and reduced for lower carrier temperatures.

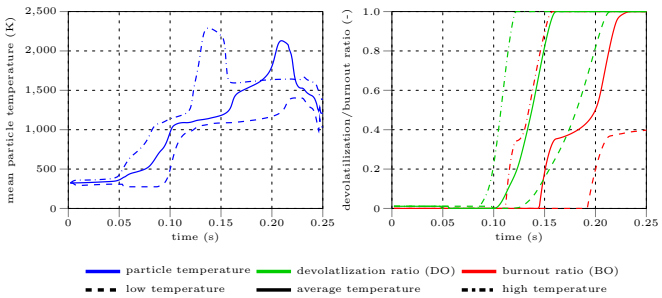

Figure 2. Schematics of the ARA Reactor (left) and representative particle conversion conditions extracted from the ARA Reactor CFD model (right).

3D Simulations

An OpenFOAM based multi-region solver has been implemented to enable particle-resolved 3D simulations. The particle model consists of a surrounding fluid region, and the particle region is modeled as an Euler-Euler multiphase region. The two regions are coupled using a suitable set of coupling boundary conditions. The particle pore structure is not resolved, but porosity, tortuosity, and pore size are modeled by conversion-dependent functions. The Surface CHEMKIN formalism is used to model char conversion.

The detailed 3D particle model is currently validated using simultaneous mass and diameter measurements from literature [7]. The validation results show that the model can reproduce the d_0^2-law for char burnout and predicts similar conversion times as the experiments. Figure 3 shows a snapshot of the CO_2 and O_2 mass fractions in and around the particle and the comparison between the simulated particle size and

mass change to the experimental one. The particle model fails to predict the deviation of the d_0^2-law at 873 K. However, this deviation is unique in literature data and is assumed to be irrelevant for most applications.

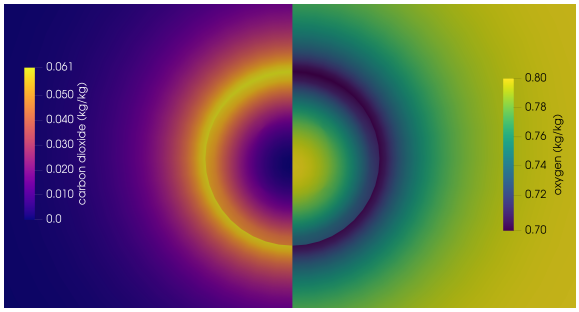

Figure 3. Snapshot of the CO_2 and O_2 concentration inside and surrounding the particle (left) and the comparison of the simulation results at 873 K (black line) and experimental results for temperatures of 673 K (red) and 873 K (blue).

Summary and Outlook

The experiments and reactor simulations allow the identification of representative particle tracks and, subsequently, detailed analysis of thermochemical conversion processes. The 1D particle simulations are useful to identify bottlenecks occurring during the conversion process. A novel 3D detailed particle model will be used to simulate the same conversion processes to get more insights into the ongoing processes. The 3D particle model has been thoroughly validated, and the detailed simulations are continuing.

The combined approach of experiments and macro- and microscopic simulations has enormous potential to provide novel insights into the ongoing processes during the thermochemical conversion of solids. The presented method will be applied to investigate high heating rate and high-temperature processes.

Acknowledgments

The authors acknowledge the funding support of K1-MET GmbH, whose research program is supported by COMET (Competence Center for Excellent Technologies), the Austrian program for competence centers. COMET is funded by the Austrian ministries BMK and BMDW, the provinces of Upper Austria, Tyrol, and Styria, and the Styrian Business Promotion Agency (SFG).

Apart from funding, the project activities are financed by the industrial partners Primetals Technologies Austria, voestalpine Stahl, voestalpine Stahl Donawitz, RHI Magnesita

References

[1] Markus Bösenhofer, Mario Pichler, and Michael Harasek. Heat transfer models for dense pulverized particle jets. *Processes*, 10(2), 2022.

[2] Thomas Nanz, Markus Bösenhofer, Johannes Rieger, Christoph Feilmayr, Franz Hauzenberger, Hugo Stocker, and Michael Harasek. A novel test rig for the evaluation of auxiliary reducing agents (ARAs). In *AISTech 2023 Proceedings*. AIST, 2023.

[3] Thomas Nanz, Markus Bösenhofer, Johannes Rieger, Hugo Stocker, Christoph Feilmayer, and Michael Harasek. Evaluating auxiliary reducing agents in a test rig under raceway conditions. In *AISTech 2024 Proceedings*, page 192–200. AIST, 2024.

[4] Matthias Kiss, Markus Bösenhofer, Franz Hauzenberger, Hugo Stockerand Christoph Feilmayr, and Michael Harasek. Investigation of the thermally thick alternative reducing agent behavior in the raceway zone. In *AISTech 2023 Proceedings*. AIST, 2023.

[5] Matthias Kiss, Markus Bösenhofer, Eva-Maria Wartha, Franz Hauzenberger, Markus Gruber, Christoph Feilmayr, Hugo Stocker, Christine Gruber, and Michael Harasek. Numerical evaluation of

the suitability of thermally thick alternative reducing agents in the raceway zone. In *AISTech 2024 Proceedings*, page 201–209. AIST, 2024.

[6] Markus Bösenhofer, Thomas Nanz, Matthias Kiss, Christine Gruber, Johannes Rieger, Hugo Stocker, Christoph Feilmayr, and Michael Harasek. Simulation-aided evaluation of alternative reducing agent conversion experiments. In *AISTech 2024 Proceedings*, page 1838–1848. AIST, 2024.

[7] N. Mohammed Asheruddin, Anand M. Shivapuji, and Srinivasaiah Dasappa. Analysis of deviation from classical d_0^2 -law for biochar conversion in an oxygen-enriched and temperature-controlled environment. *Scientific Reports*, 12(1):18391, 2022.

Scalable Production of Nanostructured Materials for Energy and Health Applications using Gas Phase Deposition

J. R. van Ommen[1*]

*E-Mail: j.r.vanommen@tudelft.nl

[1]Chemical Engineering, Delft University of Technology, Van der Maasweg 9, 2629 HZ Delft, the Netherlands

Introduction

Nanostructured solids (for example, core-shell nanoparticles or porous micro-particles containing nanoparticles) hold great potential for energy and health applications. However, to come from product design incorporating nanostructuring to actually making such materials at industrial scale is not trivial at all. Gas phase coating using reactive techniques such as chemical vapour deposition (CVD), atomic layer deposition (ALD), and molecular layer deposition (MLD) can be used to provide the surface of a particle with either an ultrathin continuous coating or a decoration of nanoclusters. This allows us to take benefit from the vast range of chemistries that has been developed over the years for CVD, ALD, and MLD.

Gas phase deposition is also attractive for manufacturing nanostructured particles on a large scale when implemented in a system where particles are suspended in the gas phase, such as a fluidized bed or a pneumatic transport reactor. Even nanopowders can be processed using this method, although they form very dilute agglomerates – typically in the order of 100 µm in diameter – and are not fluidized as individual particles. Since we often process cohesive materials, an effort has been made to obtain proper dispersion of the particles.

Applications

In this presentation, experimental evidence will be given for the benefits of applying gas phase deposition to powders. The first application we will discuss is making an enhanced photocatalyst using gas phase deposition. When we use TiO_2 nanoparticles (P25) as the substrate, we can modify it using SiO_2 to enhance the binding of the reactant. Decoration with Pt nanoclusters is a way to prevent electron-hole-pair recombination and enhance the photocatalytic activity [1]; see Fig. 1.

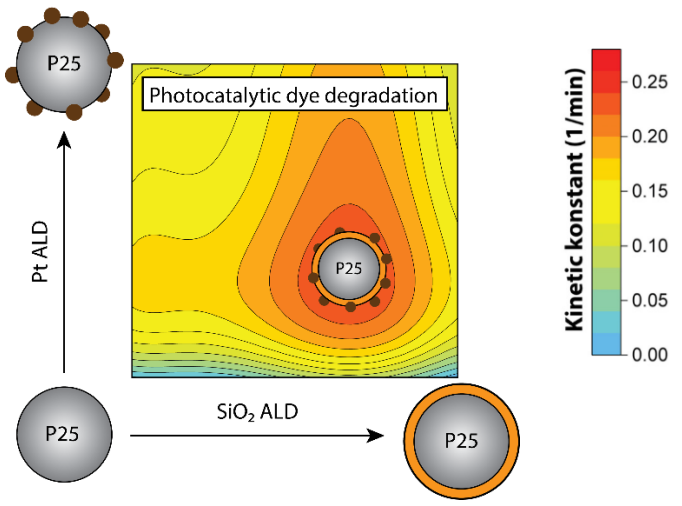

Figure 1. Combined Pt:SiO_2:TiO_2(P25) photocatalyst with different loadings of Pt and Si. The colour indicates the photocatalytic activity.

The second application that will be discussed is in electrocatalysis. Pt is also an important electrocatalyst for the production of hydrogen using proton exchange membrane (PEM) electrolysis. When PEM electrolysers are becoming applied at large scale, it if of uttermost importance to maximize the lifetime of the catalyst. We show that using ALD to make an ultrathin SiO_2 coating on the Pt electrocatalyst enables stable hydrogen production [2]; see Fig. 2.

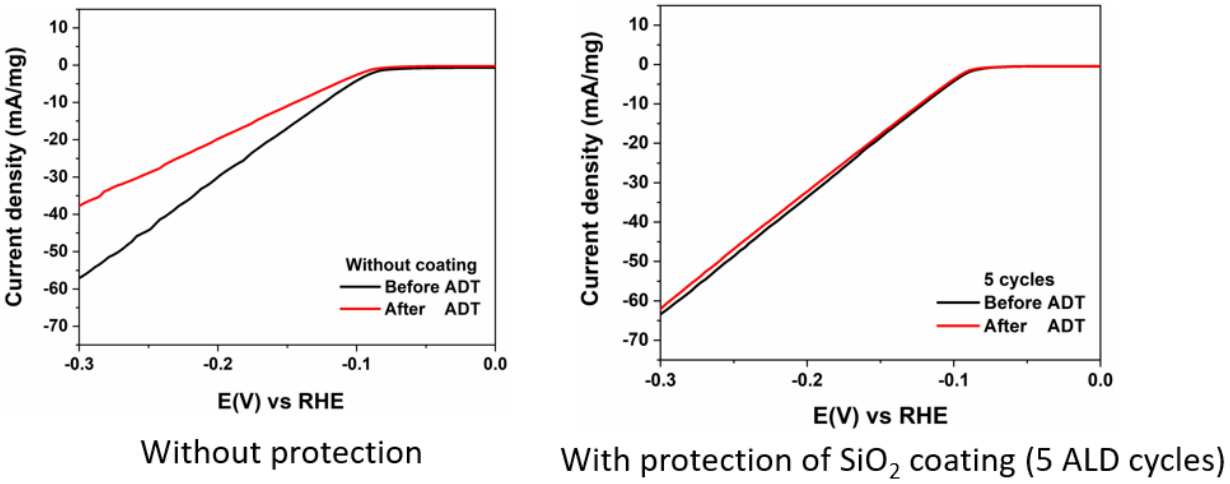

Figure 2. Stabilization of a Pt electrocatalyst (supported on carbon) using SiO_2 ALD. The stability is tested using an accelerated durability test (ADT) [2].

The third and final application is in the enhancement of pharmaceutical powders. Coating the surface of grains of a pharmaceutical powder (see Fig. 3) – as used for example in dry powder inhalers for treating respiratory diseases – can increase the powder flowability while also adding a controlled release functionality. In this way, the powder is used more effectively and side-effects in the patient can be reduced strongly [3].

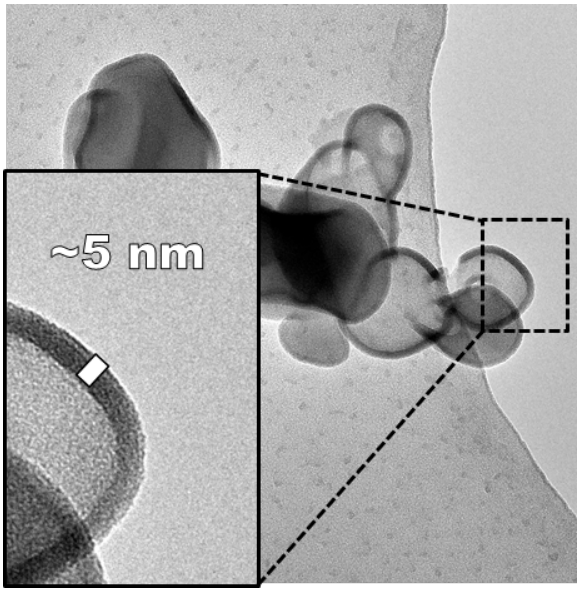

Figure 3. SiO_2 coating on budesonide particles made using ALD.

Scale-up

In our lab, we typically produce a few up to 100 g of the coated particles using our lab-scale fluidized beds. This could also easily be done in larger fluidized beds to produce kilograms or even tons of material, when this process is taken to industry. The exact amount needed will strongly depend on the

specific application. However, the production in fluidized beds is batch-wise with respect to the particles (one amount after the other), while in many industrial processes, continuous production is preferred. We have also been developing an approach for that: the so-called pneumatic transport reactor. In this reactor, the particles are blown through a long tube, and the precursor is added along the way [4]. This indeed leads to a continuous flow of nanostructured particles. Powall, a spin-off company from our research group, is working on further scaling up this approach for various gas-phase coating processes. They developed and constructed a reactor that can produce 100 kg of coated particles per hour.

Conclusions

Gas phase coating methods such as atomic layer deposition, molecular layer deposition, and chemical vapor deposition can be used to provide powdered substrates with a thin film or with nanoclusters of the required materials. The high degree of control makes it ideally suited to produce nanostructured materials for a range of applications; the scalability of the method makes a smooth translation to industrial practice feasible.

References

[1] Benz D., Van Bui H., Hintzen H.T., Kreutzer M.T., van Ommen J.R.: *Synthesis of a Rationally Designed Multi-Component Photocatalyst Pt:SiO_2:TiO_2(P25) with Improved Activity for Dye Degradation by Atomic Layer Deposition*, Nanomaterials, 10, 1496, 2020.

[2] Li M., Saedy S., Fu S., Stellema T., Kortlever R., van Ommen J.R.: *Enhancing the durability of Pt nanoparticles for water electrolysis using ultrathin SiO_2 layers*, Catalysis Science & Technology, 14, 1328, 2022.

[3] La Zara D., Sun F., Zhang F., Franek F., Balogh Sivars K., Horndahl J., Bates S., Brännström M., Ewing P., Quayle M.J., Petersson G., Folestad S., van Ommen J.R.: *Controlled pulmonary delivery of carrier-free budesonide dry powder by atomic layer deposition***,** ACS Nano, 15, 6684, 2021.

[4] van Ommen J.R., Kooijman D., Niet M.D., Talebi M., Goulas A.: *Continuous production of nanostructured particles using spatial atomic layer deposition*, Journal of Vacuum Science & Technology A, 33, 021513, 2015.

Investigation of the hetero-aggregation mechanisms of nano particles by desublimation in the supersonic flow

M. Nestriepke*, M. Weirich, D. Misiulia and S. Antonyuk

*E-Mail: malte.nestriepke@mv.rptu.de

Institute of Particle Process Engineering, University of Kaiserslautern-Landau (RPTU), Gottlieb-Daimler-Str. 47, 67663 Kaiserslautern, Germany

The utilization of particles in the submicrometer and nanoscale particle size range has significantly increased in industrial applications as a result of their unique chemical, physical, and morphological properties. At the same time, particulate functional materials such as catalysts, high-quality pigments, battery cathodes and electronic components are becoming increasingly complex. These functional particles consist of several different particulate materials whose primary particles can be bonded in a hetero-aggregate structure by different binding mechanisms. The controlled production of hetero-aggregates composed of titanium dioxide (TiO_2) and copper phthalocyanine (CuPc) is significant for numerous applications such as photocatalysis [1]. In this work, a novel aerosol process was developed that combines desublimation and mixing in a supersonic flow to synthesize TiO_2/CuPc hetero-aggregates in a targeted manner.

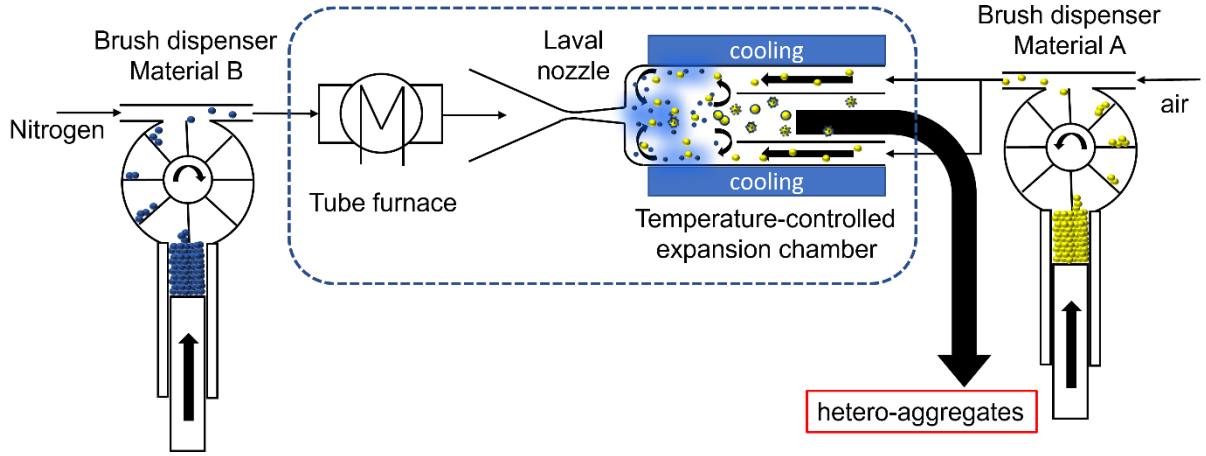

Figure 1. Process scheme of the hetero-aggregation experimental setup.

In this process, a CuPc-loaded aerosol (Material B in Figure 1) is generated by heating CuPc in a nitrogen carrier flow within a high-temperature furnace until sublimation occurs. The resulting gas mixture is accelerated to supersonic speed in a Laval nozzle and directed into a temperature-controlled expansion chamber. The rapid cooling during expansion initiates the desublimation of CuPc. Simultaneously, a TiO_2-loaded gas flow (Material A) is introduced into the recirculation zone of the nozzle flow, bringing TiO_2 nuclei into the supersaturation region of the expansion chamber. Different formation mechanisms can be involved in the formation of hetero-aggregates (see Figure 2).

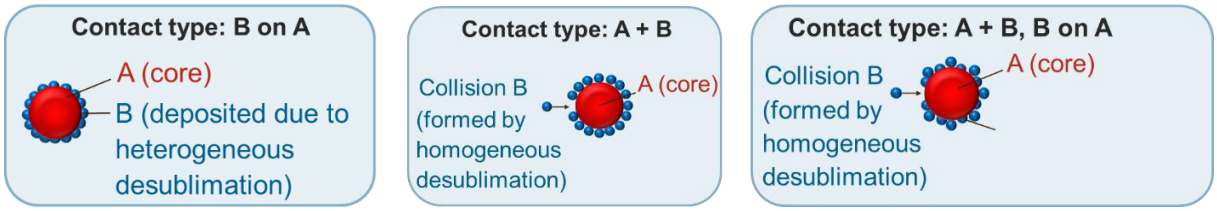

Figure 2. Hetero-aggregation mechanisms of particles in the developed process.

In the case of homogeneous desublimation, CuPc particles are initially desublimated in the supersaturation zone and subsequently collide with TiO_2 particles downstream, forming hetero-aggregates (Figure 2 middle). Conversely, in the heterogeneous desublimation, the presence of TiO_2 nuclei directly within the supersaturation zone results in the desublimation of CuPc on the TiO_2 (Figure 2 left). The interplay of these phenomena gives rise to a hybrid mechanism (Figure 2 right). By varying the process parameters, certain formation mechanisms can be enhanced while others can be suppressed.

The flow field (Figure 3) and particle movement in the expansion chamber were numerically investigated using Computational Fluid Dynamics (CFD). The supersonic gas flow was treated in an Eulerian manner using the Large Eddy Simulation by solving the compressible Navier-Stokes equations. The gas flow was modelled as a mixture, applying mixture properties depending on the volume fraction of the separate components. The local saturation of CuPc was determined at each position of the flow field from the local pressure and the concentration of the CuPc. The movement of particles was investigated using a Lagrangian approach, whereby the particles are tracked as Lagrangian points within the Eulerian flow field. The simulations helped to understand the flow dynamics, particle distribution, and formation of supersaturation regions. This enabled the precise visualization of desublimation regions, pointing out zones of mass transfer from gas to solid phase.

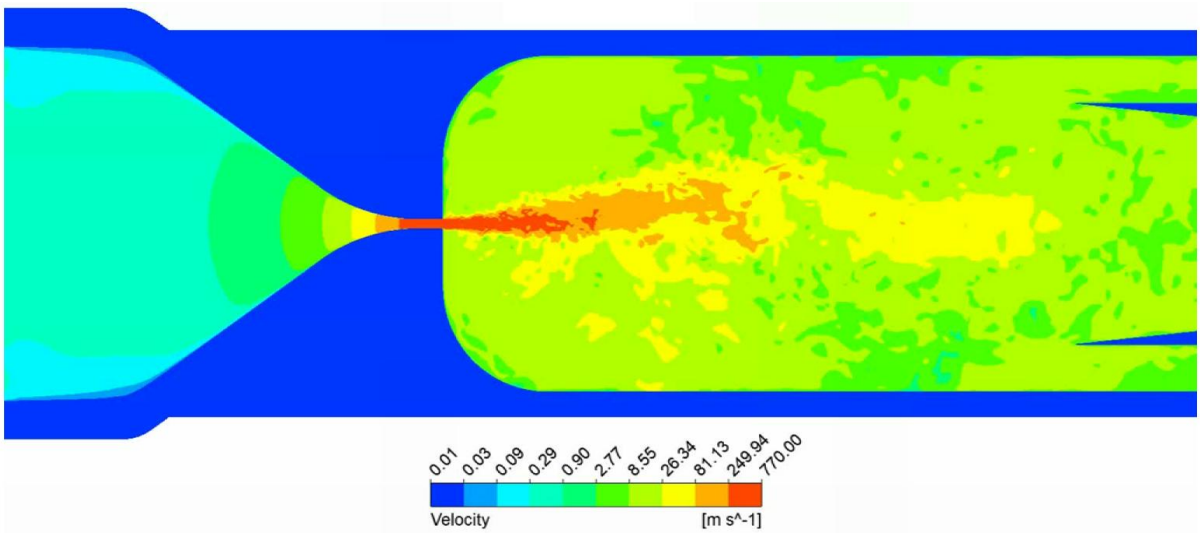

Figure 3. Instantaneous gas flow velocity field in the expansion chamber.

These insights revealed the key factors influencing particle growth, whether homogeneous or heterogeneous occurs, and the conditions under which nucleation is initiated in the absence of desublimation nuclei. The CFD results can help comprehensively understand the peculiarities of the flow field and particle dynamics paving the way for optimized control strategies to achieve the desired material properties and process efficiencies.

In addition to the CFD simulations, a parameter study was performed using the experimental setup to examine their influence on particle properties, such as size and shape, in more detail. The particle size distributions of the generated aerosols were determined by an Aerodynamic Particle Sizer (TSI Incorporated, USA) and a Scanning Mobility Particle Sizer (TSI Incorporated, USA). Furthermore, imaging techniques, including scanning and transmission electron microscopy, were utilized to analyse the morphology of hetero-aggregates. The elemental composition of the primary particles within hetero-aggregates was analysed using a combination of the Transmission Election Microscope (TEM) with energy dispersive X-ray spectrometry (EDX) (Figure 4).

A 3D Light Scattering Sensor (see Figure 5) was used to analyze the morphology of the aerosol particles. This measuring device was developed in-house to assess the shape of submicron aerosol particles in the size range of 0.5 to 5 µm [2]. In contrast to the aforementioned imaging techniques, the 3D Light Scattering Sensor (3D-LSS) allows the online assessment of the particle shape. The sensor system is

based on the determination of the intensity of the scattered light caused by the aerosol particles as they pass through a circular polarized laser beam. The scattered light intensity is recorded by seven detectors located in the scattering chamber at various points (azimuth angles). Based on the measured scattered light intensity distribution of the produced hetero-aggregates, a shape index (SPX) was calculated (see Figure 5), which characterize the shape of the hetero-aggregates.

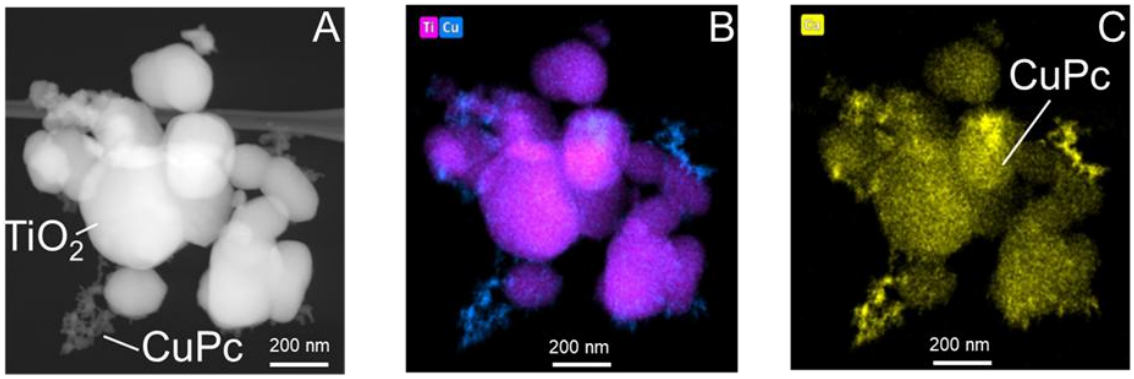

Figure 4. TEM sample of a TiO2/CuPc hetero-aggregate without EDX (A) and with EDX (B and C).

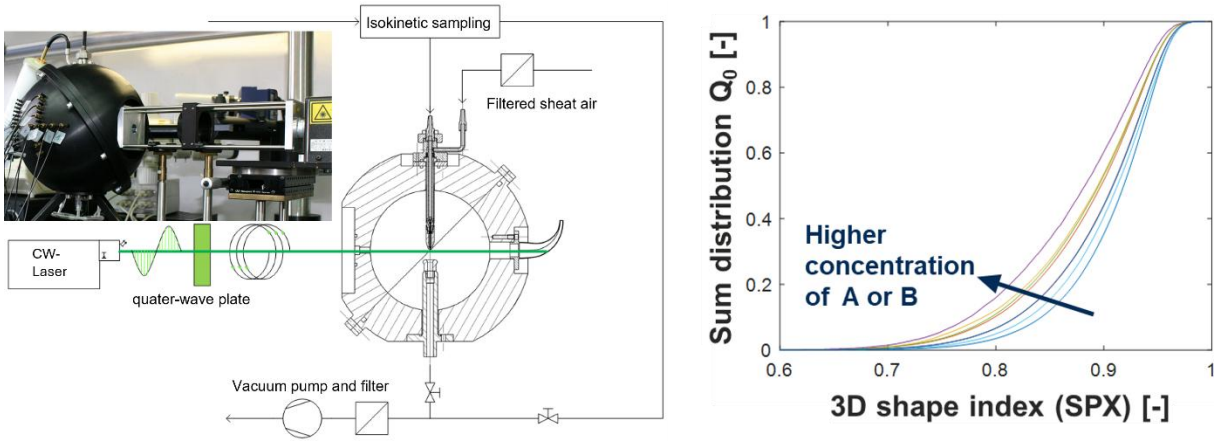

Figure 5. Schematic drawing of the 3D-LSS setup (left) and distributions of the shape index for different generated aerosols measured by the 3D-LSS (right) [2].

The obtained properties of the hetero-aggregates, including size, elemental composition, and morphology, can be leveraged to enhance comprehension of the impact of process parameters on these particle properties. This enhanced understanding facilitates the precise control of particle properties through adjustments of process parameters.

Acknowledgement:
This work was funded by the German Research Foundation (DFG) within the Priority Program (SPP 2289) – Project-ID: 462536406.

References:

[1] Moon, H.S.; Yong, K.: *Noble-metal free photocatalytic hydrogen generation of CuPc/TiO_2 nanoparticles under visible-light irradiation*. Applied Surface Science, 530, 147215, 2020.

[2] Weirich, M., Misiulia, D., Antonyuk, S.: *Characterization of particle shape with an improved 3D Light Scattering Sensor (3D-LSS) for aerosols*. Sensors 24, 955, 2024.

Simulation of methanol steam reforming in packed bed reactors – comparison of wall-heated and induction-heated configurations

M. Dal Belo Takehara[1], K. Umeki[1*]

*E-Mail: kentaro.umeki@ltu.se

[1] Div. Energy Science, Luleå University of Technology, Laboratorievägen 10, 971 87 Luleå, Sweden

Introduction

Rapid, significant increase in extremely cheap, but intermittent renewable electricity calls for the development of long-term storage and long-distance transport careers for surplus electricity. Power-to-X technologies, such as production of methanol, ammonia, and liquid hydrocarbon, would open a new opportunity to maximize the utilization of green electricity by decoupling the regional and temporal mismatching of renewable electricity availability and energy and/or hydrogen demand. This work focuses on the use of methanol as a storage option and investigate how electrification of steam reforming technologies can reduce the required reactor volumes for the same throughput in comparison with the wall-heated reactors. The application areas of the technologies can be, for example, metallurgical and petrochemical industries, which may benefit from carbon atoms in syngas as raw materials in their production processes.

The reactor size of catalytic reactors tends to be large because heat transfer from combustion gas via reactor wall ends up with unevenly heated catalyst. Recently, many researchers have been trying to minimize reactor sizes by electrification via directly heating catalyst with Joule heating, microwave heating, or induction heating [1,2].

The objective of this study is to investigate the effects of reactor scaling and reaction conditions on the methanol conversion in induction-heated packed-bed reactors. The reactor simulation model was developed to carry out the comparison with conventional wall-heated reactors.

Experimental

The experimental investigation was conducted using two different configurations: an induction-heated reactor and a wall-heated reactor with resistance heating. Both setups were equipped with feed supplies of methanol, water, and carrier gas, and the same catalyst bed was evaluated in each configuration. The methanol/water mixture was evaporated before injection, with the flow rate controlled by a syringe pump. To prevent condensation, both upstream and downstream piping connections to the reactor were heated. The reactor itself was a vertical quartz tube with an internal diameter of 25 mm. Temperature measurements were taken before and after the catalyst bed, both inside and outside the reactor.

For the induction-heated reactor, a water-cooled induction coil was placed around the reactor's centre. An infrared pyrometer was used to monitor the catalyst bed temperature due to the magnetic field. The induction heater was an Ultraflex unit (HS-4W, 4kW/250kHz). After the reactor, a condensate trap was used to separate water, and the dried gas was analysed using a micro gas chromatograph and NDIR instrument.

Modelling

The gas continuity equation represents the mass balance of total gas volume. The equation is written as:

$$\rho_g \nabla \cdot (\boldsymbol{u}) = Q_m, \quad (1)$$

where ρ_g is gas density (kg m^{-3}), $\boldsymbol{u}$ is the gas velocity vector (m s^{-1}), Q_m is the rate of gas generation (kg m^{-3} s^{-1}). The conservation of momentum was calculated by Brinkman equation, which can be written as:

$$0 = \nabla \cdot \left[-p\boldsymbol{I} + \frac{\mu}{\epsilon}(\nabla \boldsymbol{u} + (\nabla \boldsymbol{u})^T) - \frac{2}{3}\frac{\mu}{\epsilon}(\nabla \cdot \boldsymbol{u})\boldsymbol{I}\right] - \left(\mu\kappa^{-1} + \frac{Q_m}{\epsilon^2}\right)\boldsymbol{u} + \boldsymbol{F} \quad (2)$$

Where ϵ is a void fraction (-), κ is permeability (m^2), μ is dynamic viscosity (Pa s), p is the gas pressure (Pa). For the calculation of temperature, the heat transfer equation was used, which can be written as:

$$\rho_g C_{p,g} \boldsymbol{u} \cdot \nabla T = \nabla \cdot \left(k_{eff} \nabla T\right) + Q, \quad (3)$$

where $C_{p,i}$ is the specific heat capacity of phase i (J kg^{-1} K^{-1}), T is the temperature (K), k_{eff} is effective thermal conductivity (W m^{-1} K^{-1}) and Q is the sum of the heat of reactions and induction heating from the magnet field (J m^{-3} s^{-1}). Mass fractions of individual gas species are calculated from species transport equation written as:

$$\rho_g(\boldsymbol{u} \cdot \nabla)Y_i = \nabla \cdot \left(\rho_g D_i \nabla Y_i + \rho_g D_i Y_i \frac{\nabla M_n}{M_n} - \rho_g Y_i \sum_k \left(\frac{M_i}{M_n} D_k \nabla x_k\right)\right) = R_i, \quad (4)$$

where Y_i is the mass fraction of gas species i (-), D_i is effective mass diffusivity of gas species i (m^2 s^{-1}), M_n is the mean molecular mass (kg mol^{-1}), and R_i is the rate of generation/consumption for gas species i due to chemical reactions (kg m^{-3} s^{-1}). Methanol reforming reactions were expressed as the combination of irreversible methanol decomposition reactions,

$$CH_3OH \rightarrow CO + 2H_2, \quad (5)$$

and reversible water-gas shift reaction,

$$CO + H_2O \leftrightarrow CO_2 + H_2. \quad (6)$$

The kinetic parameters were taken from the literature [3]. The simulation model was implemented in COMSOL Multiphysics 6.2. **Figure 1** shows the schematic figures of simulation domains. The reactor was cylindrical shape with variable diameter and temperature. Inlet gas was the mixture of methanol and steam at constant velocity and temperature. For the wall-heated reactors, wall temperature was kept constant at target reaction temperature. For the induction-heated reactors, magnetic field was calculated by using Maxwell equations using the current and alternate frequency through the coil surrounding the reactor, and the heat sources inside the catalyst bed were estimated by the sum of resistive and magnetic losses.

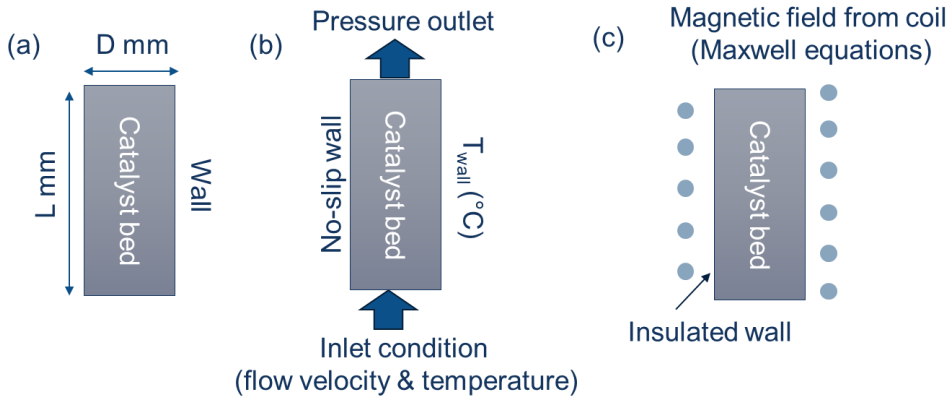

Figure 1. The schematic representation of the simulation domain. (a) reactor dimension; (b) boundary conditions for wall-heated reactor configuration; and (c) additional conditions for induction-heated reactor.

First results

Figure 2 shows the initial results of the simulation. The results are shown for the reactor diameter of 50 mm and the length of 120 mm. The results from wall-heated reactors show clear indications of non-uniform heating profiles where temperatures near the wall reach relatively close to the wall temperature while the temperature at the middle of the reactor remains close to the inlet temperature. This, in turn, results in the unconverted methanol. Such a disadvantage of wall heated reactors became more apparent as the reactor capacity, inlet velocity, or the reactor diameter increase. In contrast, the induction heating showed extremely uniform temperatures (below 1 °C difference inside the domain). Since heat source is distributed throughout the reactor volume, such an advantage to keep the uniform temperature inside the reactor is expected to be more significant when the performance of wall-heated reactors decreases due to non-uniform temperature. The results from the simulation will be validated by the experiments in future, and extended parametric studies will be carried out.

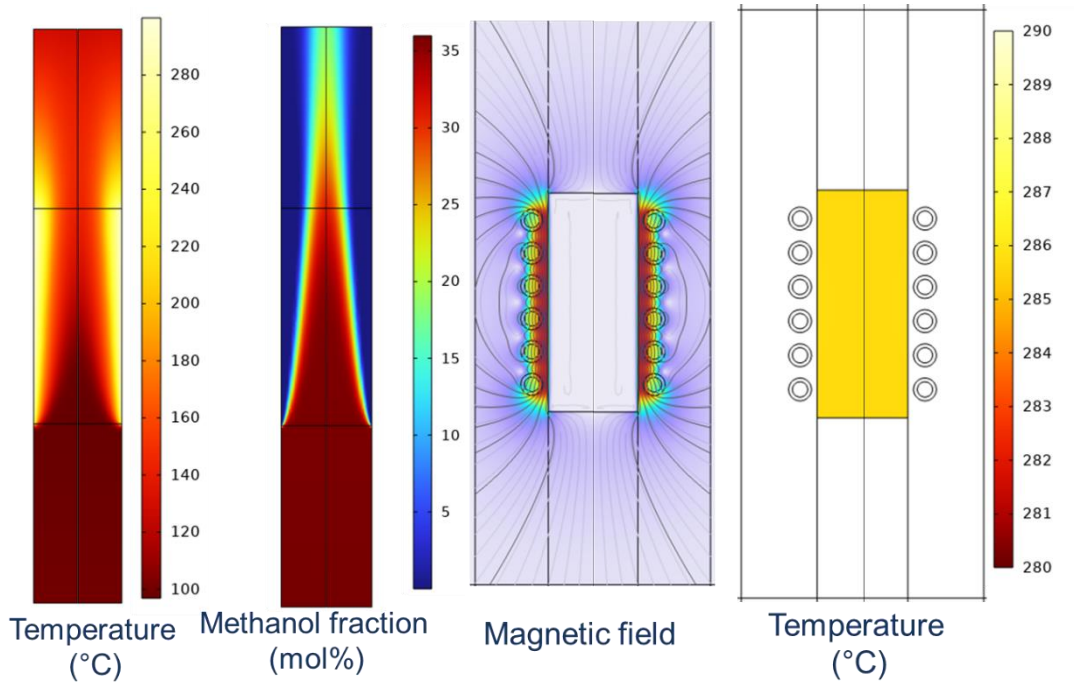

Figure 2. The initial results of the distribution of temperature and methanol molar fraction in conventional wall-heated reactor (left). Magnetic field and the resulting temperature distribution for the non-reactive case of induction heating (right).

References

[1] Wismann, S.T., Engbæk, J.S., Vendelbo, S.B., Bendixen, F.B., Eriksen, W.L., Aasberg-Petersen, K., Frandsen, C., Chorkendorff, I. and Mortensen, P.M.: *Electrified methane reforming: A compact approach to greener industrial hydrogen production*. Science, *364*, 756-759, 2019.

[2] Kim, Y.T., Lee, J.J. and Lee, J.: *Electricity-driven reactors that promote thermochemical catalytic reactions via joule and induction heating: a review*. Chemical Engineering Journal, 470, 144333, 2023.

[2] Özcan, O., Akin, A.N.: *Methanol steam reforming kinetics using a commercial CuO/ZnO/Al2O3 catalyst: Simulation of a reformer integrated with HT-PEMFC system*, International Journal of Hydrogen Energy, 48, 22777-22790, 2023.

Dynamic Microwave Freeze-Drying with In-Situ Neutron Imaging: Insights in the Drying of Particle Bulks

Hilmer, M.[1*], Kis Z.[2], Schulz M.[3], Foerst, P.[1]

*E-Mail: mathias.hilmer@tum.de

[1] *Technical University of Munich, School of Life Sciences, Professorship of Food Process Engineering, Freising*

[2] *HUN-REN Centre for Energy Research*

[3] *Technical University of Munich, Heinz Maier-Leibnitz-Zentrum, Garching*

The gentle yet cost-efficient drying of sensitive products in the food and pharmaceutical industries is becoming increasingly important. However, the freeze-drying process is very time-consuming and costly, which is due to poor mass and heat transport. Therefore, a dynamic microwave freeze-drying process was developed, in which the bulk material is continuously mixed in a rotating drum during drying.

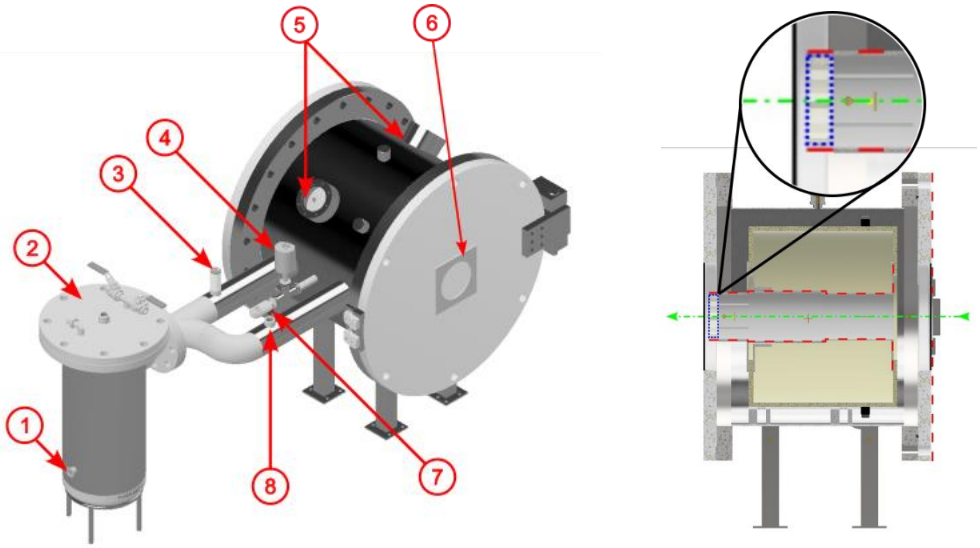

Figure 1. Left: 3D model of the in-situ microwave freeze dryer. (1) Vacuum connector (2) condenser (3) Dewpoint sensor (4) Capacitive pressure sensor (5) microwave couplings (6) neutron shielding (7) Pirani pressure sensor (8) temperature sensor. Right: Half section of the in-situ setup of the microwave freeze dryer. Green: Neutron beam; Red: Shielding; Blue: Sample drum. [1]

To determine the influence of the microwave power input and the bulk characteristics on the drying process non-invasively, the drying process was observed using in-situ neutron imaging at the Centre for Energy Research in Budapest. This imaging technique allows for monitoring the decreasing water content of the sample as well as the changes in particle bulk. For this purpose, a dryer suitable for the requirements of dynamic microwave freeze-drying and neutron imaging was first developed (Figure 1).

Then, the drying process was imaged for different particle sizes and rotational speeds. Nine sample images are shown in Figure 2. The letters A to C indicate different experiments, while the processing time is from 0 to 2. Experiments A and B were conducted with a particle bulk of ~ 3 mm particles, and experiment C with a bulk of ~ 1 mm particles. As can be seen in the figure, pictures A and C were conducted with a higher resolution to ensure a better visibility of the single particles in the bulk.

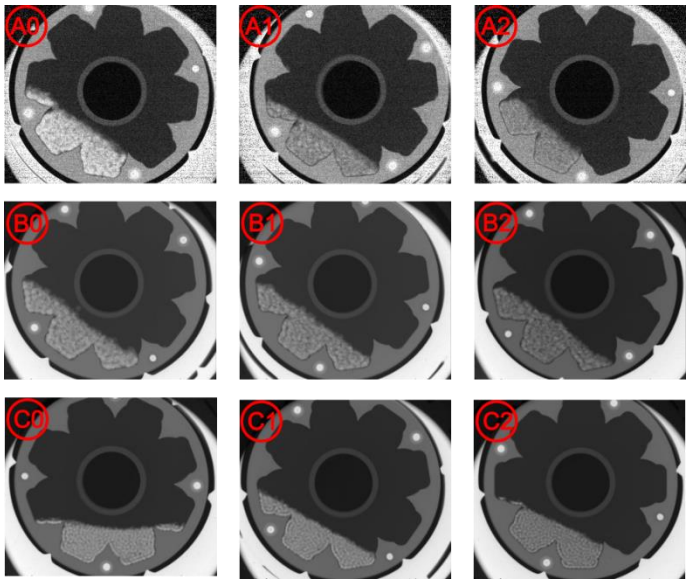

Figure 2. Resulting images (after image correction) of three experiments 1 (A0 - A2), 2 (B0 – B2) and 3 (C0 - C2). Bright grey equals high absorption and, therefore, high D2O content. [1]

The transmission images – bright grey equals high absorption and, therefore, high water content – show an apparent decrease in grey value over time. Indicating the sublimation of the solvent and, hence, the drying process. The images of the bulk were then used to determine changes in bulk characteristics and drying kinetics during the drying process. The advantages and drawbacks of this method will be discussed.

[1] Mathias Hilmer, Sebastian Gruber, Zoltán Kis, Michael Schulz, Petra Foerst; Design of a pilot-scale microwave freeze dryer for in situ neutron imaging. Rev. Sci. Instrum. 1 August 2024; 95 (8): 083704. https://doi.org/10.1063/5.0213685

Modelling of a lab-scale microwave dryer for thermally thick materials

A. Ujjani Narasimhaiah[1*], A. Schmidt[2], L. Briest[1], A. Tretau[2], R. Wagner[2], E. Tsotsas[1], N. Vorhauer-Huget[1]

*E-Mail: akshay.narasimhaiah@ovgu.de

[1] *Chair of Thermal Process Engineering, Otto-von-Guericke-University Magdeburg Germany*

[2] *Materials Research and Testing Institute (MFPA) Weimar Germany*

Introduction

Absorption efficiency and thus heating of thermally thick materials is strongly dependent on the cavity geometry, the connection of waveguides as well as the positioning of the sample inside of the cavity and its rotation. Mode stirrers (MS) are often used to homogenize the electromagnetic field. However, only a small number of studies modelled absorption with the product rotating on a turntable [1] and in presence of a MS [2]. Discrete rotation angles are employed to reduce computational efforts in these studies [3].

Since both, the sample rotation and the implementation of a MS (rotating or at least at variable positions), are expected to strongly alter the absorption efficiency and finally also the heating conditions, we implemented the batch microwave dryer from [4] to study this aspect numerically. We start our study with the simulation of a few discrete positions of sample and MS, adopting the material properties of wet clay bricks [5]. The first simulations results indicate that the MS has no positive effect on the absorption efficiency but that positioning of the sample significantly affects the fraction of absorbed power.

Methodology

For this study we used COMSOL 6.0 and a finite element approach for solving Maxwell's equation in the frequency domain. The simulations were conducted on a workstation equipped with a 2.30 GHz AMD EPYC 7352 24-Core Processor, 256 GB of RAM, and a 64-bit Windows 10 Pro operating system.

A COMSOL graphic interface was used to construct the geometric model of the cavity with the sample in it. The implemented cavity dimensions agree with the actual experimental setup used in [4] and are 880x750x595 mm³ (Fig. 1). The electromagnetic waves are excited by transverse electromagnetic standing wave fields in x-direction and enter the cavity via two (lateral) rectangular waveguides. This way, two magnetrons with a single power of 350 W and 2.45 GHz are represented. The cavity, the rectangular waveguides and the sample were all implemented with the experimental dimensions adopted from [4]. In addition to that, the turntable and the MS were realized in the simulation domain.

The waveguides operated in TE10 mode, the dominant transverse electric mode with the lowest cut-off frequency, serving as microwave inlets. Except for the turntable and brick, the steel cavity was treated as perfect electric conductor. The complex permittivities, $\varepsilon = \varepsilon' - j\varepsilon''$, of all materials are given in Table 1, where ε' is the dielectric constant and ε'' represents the dielectric loss.

Table 1: Dielectric properties of the materials used in the simulation.

Brick	14.83 – 2.32j
Steel	4.134
Glass	5.8
Air	1

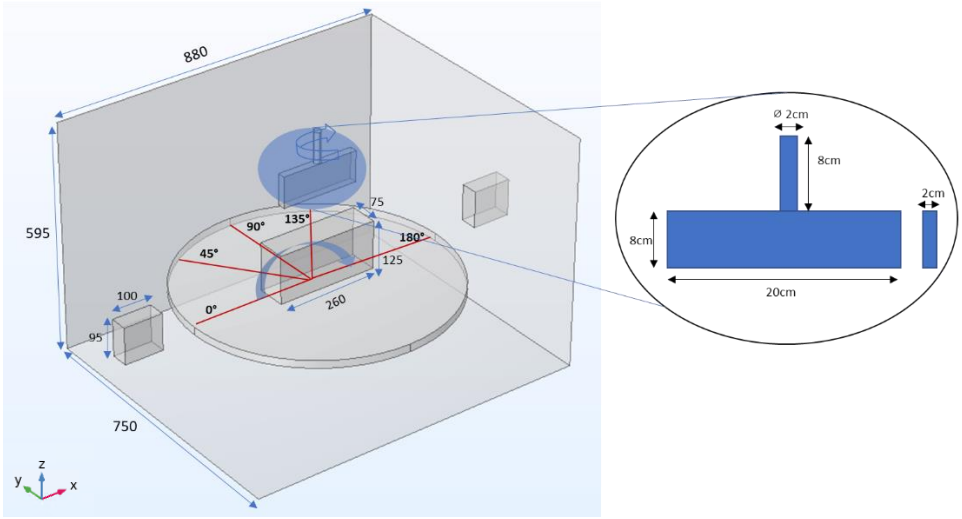

Figure 1. Geometry of the cavity, including turntable, MS (detailed view on the right) and sample.

Results

A reference case simulation (test case "Microwave Oven" [6]) was initially conducted to validate the multiphysics model available in COMSOL, using the setup illustrated in Fig. 1. Fine quadrilateral elements were realized for meshing of the brick sample and much coarser tetrahedral elements were used for the surrounding air and the table. The average dissipated power (W/m^3) for the simulated clay brick remained nearly in the same magnitude for a mesh size exceeding 256,000 elements.

At first the optimal sample position was studied. For this purpose, five vertical positions were considered (Fig. 2a). The MS was not implemented in this study to avoid additional complexities in the interaction between electromagnetic waves and the clay bricks. In each case, the turntable along with the sample was rotated at a step angle of 45° between 0° and 180°, i.e., 0°, 45°, 90°, 135°, and 180°. Extending the simulation beyond 180° was unnecessary, as the geometric symmetry of the model and clay brick ensures identical results for further rotations.

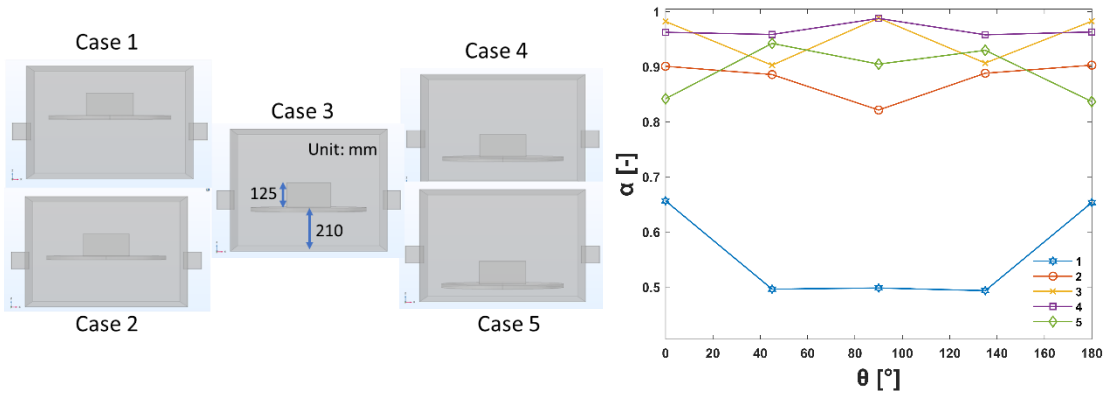

Figure 2. a) Variable vertical brick position; b) Power absorption ratio (α) over rotation angle (θ).

The power absorption ratio, denoted as α, is given by $\alpha = 1 - |\Gamma|^2$, where Γ represents the reflection coefficient. Figure 2b shows the power absorption ratio for the five cases given in Fig. 2a. It reveals that case 4 (purple line) yields the highest absorption efficiency. In contrast, the standard set height (yellow line) yields a slightly lower absorption efficiency. Based on this finding, the apparatus used in experiments will be re-designed to realize optimal absorption conditions.

To analyse further the influence of the MS on the dispersion of the electromagnetic field, 4 different cases were examined (Table 2 and Fig. 3a). The simulations were realized with sample position as in the standard case 3 in Fig. 2a.

Table 2: Variation of MS operation (w or w/o MS) and position.

Case	MS position
1	No MS, sample rotation 0° - 180° and back in 45° steps
2	MS fixed at 0°, sample rotation 0° - 180° and back in 45° steps
3	MS fixed at 45°, sample rotation 0° - 180° and back in 45° steps
4	MS fixed at 90°, sample rotation 0° - 180° and back in 45° steps

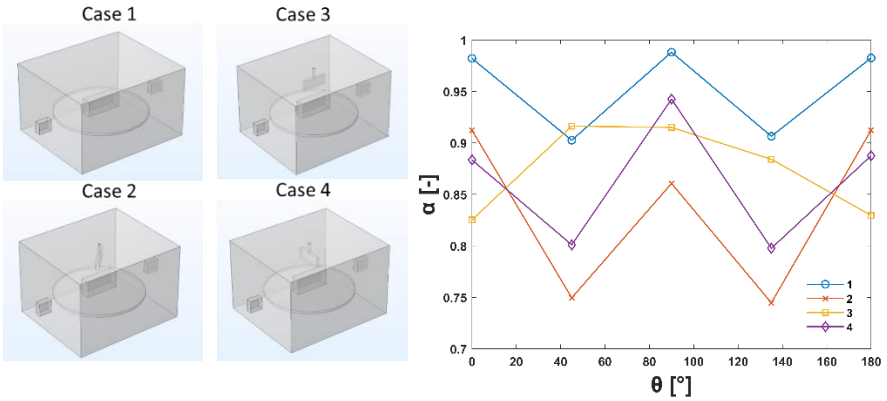

Figure 3. a) Variable MS configuration; b) Power absorption ratio (α) plotted against step angle (θ).

Surprisingly, the highest absorption efficiency is achieved when no MS is present in the cavity. As depicted by Fig. 3b, the highest absorption efficiency is always observed when the brick is at θ = 90°, independent of the MS configuration. At this position, the largest interface faces the magnetrons (cf. Fig. 1).

Besides absorption efficiency the penetration of the electromagnetic field inside the material is of utmost interest to control heating conditions. We will therefore also study the distribution of the field strength in dependence of (vertical) sample position, rotation and the presence of the MS in a next step.

Acknowledgement

The project "Influence of process control on the energy demand of microwave dryers (German: Einfluss der Prozessführung auf den Energiebedarf von Mikrowellentrockner)" is funded by the Federal Ministry of Economics and Climate Protection as part of the "Industrielle Gemeinschaftsforschung (IGF)" program on the basis of a resolution of the German Bundestag. The authors N. Vorhauer-Huget and E. Tsotsas additionally acknowledge the funding by the Deutsche Forschungsgemeinschaft (DFG, German Research Foundation) – Project-ID 422037413 – TRR 287 for their contributions to the study.

References

[1] S. Geedipalli, V. Rakesh, A.K. Datta, Modeling the heating uniformity contributed by a rotating turntable in microwave ovens, Journal of Food Engineering 82 (2007) 359–368. https://doi.org/10.1016/j.jfoodeng.2007.02.050.

[2] P. Plaza-Gonzalez, J. Monzo-Cabrera, J.M. Catala-Civera, D. Sanchez-Hernandez, Effect of mode-stirrer configurations on dielectric heating performance in multimode microwave applicators, IEEE Trans. Microwave Theory Techn. 53 (2005) 1699–1706. https://doi.org/10.1109/TMTT.2005.847066.

[3] K. Pitchai, J. Chen, S. Birla, D. Jones, R. Gonzalez, J. Subbiah, Multiphysics Modeling of Microwave Heating of a Frozen Heterogeneous Meal Rotating on a Turntable, J. Food Sci. 80 (2015) E2803-14. https://doi.org/10.1111/1750-3841.13136.

[4] L. Briest, R. Wagner, A. Tretau, E. Tsotsas, N. Vorhauer-Huget, Microwave-assisted drying of clay roof tiles, Drying Technology 40 (2022) 1804–1818. https://doi.org/10.1080/07373937.2021.1878369.

[5] N. Vorhauer-Huget, L. Briesta, R. Wagnerb, A. Tretaub, A. Rahimic, E. Tsotsasa, Using microwave heating for electrification of the dryingof green heavy clay products (2022).

[6] COMSOL, Microwave Oven. https://www.comsol.com/model/microwave-oven-1424.

Regenerative Absorption and Desorption between CO_2 and Dolomite Particles for CCS Processes

A. Kropman*, W. Aliyu, E. Specht and F. Beyrau

*E-Mail: alexey.kropman@ovgu.de

Institute of Fluid Dynamics and Thermodynamics, University of Magdeburg, Universitätsplatz 2, 39106 Magdeburg, Germany

In many processes in the industry of primary commodities, most carbon dioxide emissions originate from the chemical conversion of raw materials. Examples include cement and lime production ($CaCO_3 \rightarrow CaO + CO_2$) and crude steel production ($Fe_2O_3 + 2\ C \rightarrow 2\ Fe + CO_2 + CO$). To achieve climate neutrality in these processes, the CO_2 must be separated from the flue gases and sequestered, which is known as carbon capture and storage (CCS). However, all existing CO_2 capture processes are very energy-intensive and therefore uneconomical. Oxyfuel processes involve cryogenic air separation, which requires a large amount of electricity. In post-combustion CO_2 capture processes, such as amine scrubbing and calcium looping, the heat of the exothermic absorption cannot be utilised for the energy demand of the endothermic desorption, as absorption always takes place at a lower temperature level than desorption.

In the innovative packed bed pressure swing calcium looping process, the temperature level of the absorption is raised by compressing the flue gas. Desorption is carried out at vacuum, which lowers the temperature level below that of absorption. As a result, the reaction enthalpy of the absorption can be regeneratively utilised for desorption. The flue gases from kilns used in cement, lime and crude steel production contain around 20 %vol. CO_2. If, for example, the flue gas is compressed to 5 bar, which corresponds to a CO_2 partial pressure of 1 bar, and then passed over burnt dolomite particles, these absorb the CO_2 ($CaO \cdot MgO + CO_2 \rightarrow CaCO_3 \cdot MgO$) and heat up to the equilibrium temperature of 900 °C. Absorption is then complete. If the particles are then placed under vacuum, e.g. 0.2 bar(a), the CO_2 desorbs and the particles cool down to the equilibrium temperature of 800 °C. Subsequently, the particles can absorb CO_2 again. The description of the entire process with energy requirements and separation efficiency is not described in detail here, but reference is made to [1]. In contrast, this study focuses on the absorption and desorption behaviour of the dolomite particles. Particularly, the dynamics of the absorption reaction has hardly been studied so far for particles with sizes exceeding a few millimetres.

In the experiments, cylindrical dolomite particles were hung on a thermobalance in an electrically heated steel tube in order to regulate their temperature. The increase in weight during absorption and the decrease during desorption were measured continuously. Thermocouples were placed in the centre of the cylinders to measure the sample temperature. The two end faces were covered with wool in order to obtain conditions that were as one-dimensional as possible. The cylinders were subjected to a flow of pure CO_2, which corresponds to a partial pressure of 1 bar. Afterwards, the flow was switched to ambient air for desorption, which corresponds to a CO_2 partial pressure of about 400 ppm (CO_2 content in the atmosphere). The particle diameter was varied from 24 to 40 mm, the furnace temperature from 550 to 850 °C as well as the flow velocity. As an example, Figure 1 shows the profiles of the core temperature and absorption degree (for the absorption phase) at different furnace temperatures for a dolomite cylinder with a diameter of 24 mm. It can be seen that the core temperature always rises up to the equilibrium temperature of 900 °C. A degree of absorption of approximately 0.95 is achieved. The CO_2 is therefore almost completely reabsorbed by the dolomite. This was also observed for spherical dolomite particles under slightly different boundary conditions [2]. Once the exothermic absorption is complete, the temperature of the cylinders decreases due to radiative heat transfer to the colder furnace wall. The higher the kiln temperature, the lower the rate of absorption.

It is shown that the rate of absorption is a monotonically increasing function of the difference between the CO_2 partial pressure (1 bar in this study) and the equilibrium pressure at the temperature of the cylinder, which in turn depends on the furnace temperature. An increased furnace temperature therefore leads to a smaller difference and thus a reduced absorption rate. This is in agreement with kinetic measurements known from the literature (e.g. [3]). Furthermore, it was found that the dimensionless absorption rate (*dX/dt*) of the reacting dolomite follows an empirical relation

$$dX/dt = c \cdot (1-X) \tag{1}$$

for most of the reaction time, including only the absorption degree (*X*), and a constant (c). The rate of desorption, on the other hand, is proportional to the difference between the equilibrium pressure at the temperature of the dolomite cylinder and the partial pressure of CO_2 in the environment, in this case approx. 400 ppm. The associated reaction coefficients are discussed for dolomite from various origins in [4]. A numerical model, which covers both, the absorption and desorption reaction has been implemented and validated based on these results. It can cover radiative as well as adiabatic boundary conditions, with the latter being of particular significance for the mathematical description of the pressure swing calcium looping process.

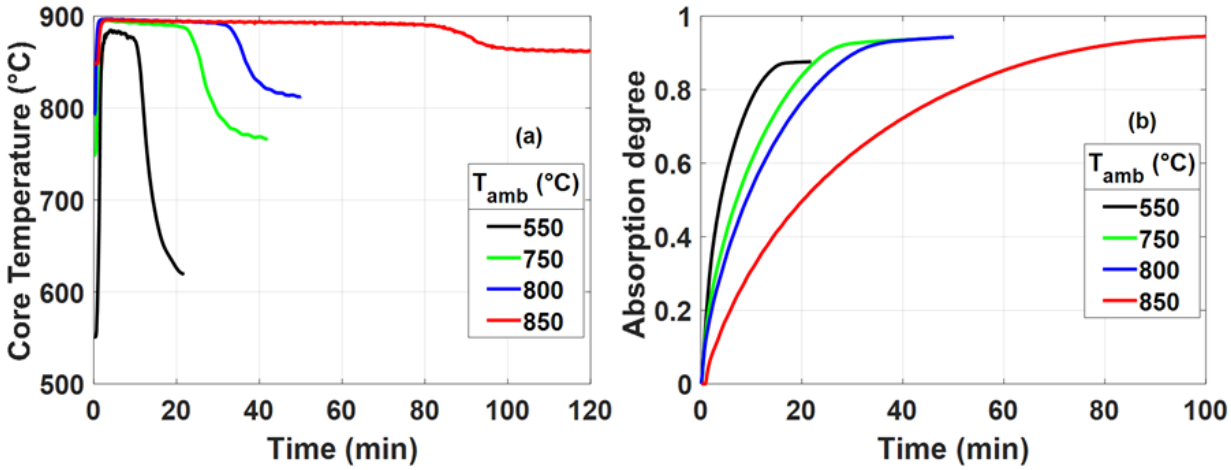

Figure 1. Profiles of temperature and absorption rate for different kiln temperatures for a dolomite cylinder of 24 mm diameter.

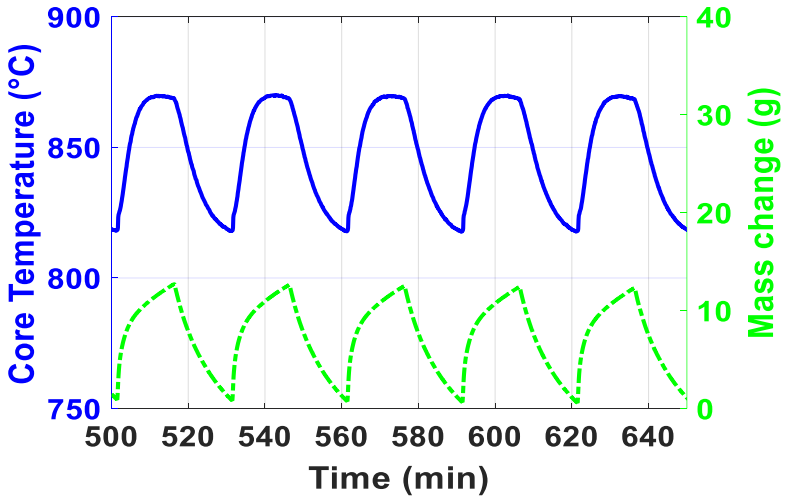

Figure 2. Profiles of temperature and mass of a dolomite sample during regenerative alternations between carbon dioxide and air flow.

Figure 2 shows the regenerative behaviour of a lumpy dolomite particle. This was exposed to pure carbon dioxide for 15 minutes and then to air for 15 minutes. Obviously**,** the weight and temperature increase and decrease cyclically. The cycles are shown after 10 hours of testing. A change in the absorption and desorption rate is not recognisable. This was also not the case after 1000 cycles. Dolomite thus proves to be a stable absorption material for CO_2 from flue gases. In contrast, particles of pure limestone ($CaCO_3$) proved to be an unstable absorption material. After only a few cycles, CO_2 can no longer be absorbed as lime sintering occurs and the inner surface decreases. This has often been pointed out in the literature (e.g. [5]). The magnesite content in dolomite (MgO), on the other hand, appears to prevent sintering.

The subsequent phase in the development of the pressure swing calcium looping process involves its implementation in a semi-industrial reactor, operating under the same boundary conditions as previously outlined. However, this time the reactor is configured as a thermally insulated cylindrical packed bed with a diameter of 390 mm and a height of 1500 mm. To assess the performance of the process, three distinct experimental campaigns have been conducted, each comprising 3, 6 and 21 cycles of absorption and desorption, respectively. During the most extensive of these campaigns, 120 kg of CO_2 were supplied to the reactor during the absorption phases. The desorption phases released approximately 115 kg of CO_2, without the provision of any additional energy to the reactor.

References

[1] Aliyu, W., Specht, E., Bergold, T., Scherer, V., Kropman, A., Beyrau, F.: *Lime Based CO_2 Capture from Flue Gases with Regenerative Recovery of the Reaction Enthalpy in the Solid-State-Reactor*. 31. Deutscher Flammentag, Berlin, 27.-28. September 2023.

[2] Kropman, A., Schulz, F., Specht, E., Aliyu. W., Beyrau, F. *Recarbonation of large dolomite particles for Calcium Looping.* Experimental Thermal and Fluid Science, *163*, 111392, 2025.

[3] Sun, P., Grace, J. R., Lim, C. J., & Anthony, E. J. *Determination of intrinsic rate constants of the CaO–CO2 reaction.* Chemical Engineering Science, 63(1), 47-56, 2008.

[4] Aliyu, W., Specht, E.: *Decomposition Mechanism of Lumpy Dolomite Particles.* Chemical Engineering Science, 288, 119801, 2024.

[5] Abanades, J. C. *The maximum capture efficiency of CO2 using a carbonation/calcination cycle of CaO/CaCO3*. Chemical Engineering Journal, 90(3), 303-306, 2002.

Investigation of flame–particle interactions in model packed beds using dual-phosphor thermometry and CH* chemiluminescence imaging

Hassan Khodsiani[1†], Mohammad Rashik Niaz[1*], Frank Beyrau[1], and Benoit Fond[2]

[*]E-Mail: mohammad.niaz@ovgu.de

[1]*Institute of Fluid Dynamics and Thermodynamics, Otto-von-Guericke-Universität Magdeburg, Universitätsplatz 2, 39106 Magdeburg, Germany*

[2]*ONERA, the French Aerospace Lab, Department of Aerodynamics and Aeroacoustics (DAAA), Paris-Saclay University, Meudon, France*

[1†]*Currently affiliated with MAN Energy Solutions SE, Stadtbachstrasse 1, 86153 Augsburg, Germany*

Introduction

Investigating the interaction between flames and particles in packed beds is crucial for understanding particle thermal processing. The particle temperature influences the flame's position and extent, which in turn affects particle transformation [1]. Phosphor thermometry has proven to be a reliable method for remote surface temperature measurements particularly in reactive environments [2] over wide temperature ranges [3]. In a previous study [4], the interaction of a CH_4/air premixed flame with cooled particles was investigated. In the case of cooled particles, as the particles bounding the flame were maintained at similar temperatures, phosphor thermometry for surface temperature measurement used a single type of phosphor. However, this study investigates flame-particle interaction in a more realistic uncooled case and employs a dual-phosphor approach to address the issue of the top particle existing at a significantly higher temperature compared to the bottom particles. A similar model packed bed of parallel cylindrical particles [4], providing good optical access for observing flame-particle interactions, is used. The setup stabilizes a uniform 2D flame along the particle length. The dual-phosphor thermometry approach measures the 2D temperature distribution around the flame, while CH*- chemiluminescence imaging captures the flame's position and structure [4].

Methods

Figure. 1a shows a 3D isometric view of the test rig, comprising a cylindrical packed bed atop a slit burner. The burner ensures uniform CH_4/air flow, generating a 2D flame between the first and second particle rows. The hexagonal particle arrangement creates 40% porosity in the packed bed. The white region marks the holder plate opening, enabling chemiluminescence imaging and dual-phosphor thermometry of the flame and three particle surfaces. As shown in Fig. 1c, a particle is coated with a narrow strip of phosphor (YAG:Cr^{3+} or GAP:Cr^{3+}). In Figure. 1d, an sCMOS camera equipped with a

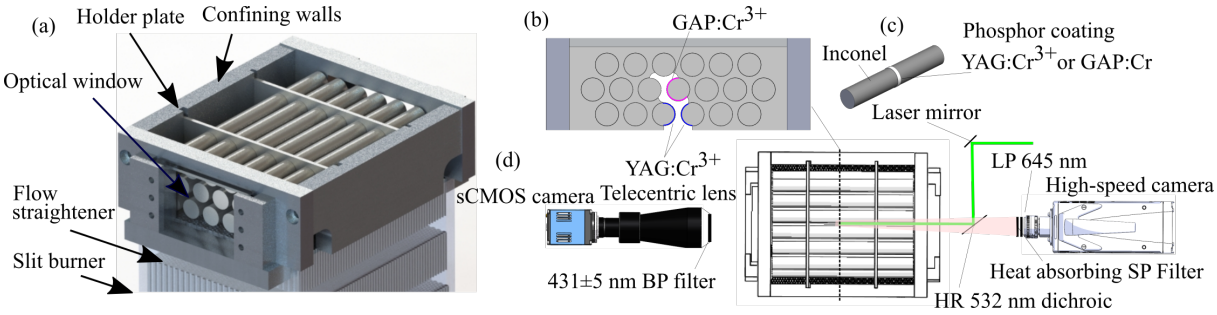

Figure 1. A 3D view of the cylindrical packed bed (a), section view of the packed bed (b), narrow strip of phosphor on the perimeter of the cylinder (c), schematics of the setup to perform phosphor thermometry and chemiluminescence imaging.

telecentric lens is placed on one side of the packed bed. The telecentric lens ensures minimal perspective distortion, preventing the loss of spatial resolution. The lens is fitted with a band-pass filter with a central wavelength of 431 nm and a bandwidth of 10 nm to isolate the CH* chemiluminescence at 431 nm. From the opposite side, a 532 nm Nd:YAG pulsed laser is guided into the packed bed through the opening using a dichroic filter to simultaneously excite the phosphor strips on the three particles. The excitation results in decaying luminescence of the phosphor coating, which is recorded using a high-speed CMOS camera. The high-speed camera is fitted with filters to isolate the phosphorescence signal from background noise and blackbody radiation. When exposed to the flame, the particle on top has a higher temperature than the particles on either side at the bottom of the flame. The dual-phosphor approach enables simultaneous measurement at two different temperature ranges. YAG:Cr^{3+} (YAG phosphor doped with Cr^{3+}) is coated on the two particles situated on the bottom, and GAP:Cr^{3+} is coated on the particle at the top of the flame.

Table 1. Operating conditions

label	Mixture velocity (u), Equivalence Ratio (ϕ)
a	u = 0.25 m/s, ϕ = 1.00
b	u = 0.25 m/s, ϕ = 0.95
c	u = 0.25 m/s, ϕ = 0.91
d	u = 0.30 m/s, ϕ = 1.00
e	u = 0.30 m/s, ϕ = 0.95
f	u = 0.30 m/s, ϕ = 0.91

Results

Table 1 shows the six different operating conditions under which measurements were taken. The results are presented in Figures 2 and 3, which consist of six subplots corresponding to the six operating conditions. In Figure 2, the red arcs indicate the CH_4/air flame front position obtained from the CH*-chemiluminescence images, while the larger circular segments delineate the position of the particle surfaces as well as the temperature distribution with respect to the flame position. Two different temperature scales, 390 °C to 520 °C and 800 °C to 920 °C, are used for the bottom particles and the particle at the top, respectively. The black crosses on each of the right and left bottom particles indicate the locations of flame quenching. Based on preliminary observations, the top particle experiences much higher temperatures compared to the bottom particles. An increase in flow velocity pushes the flame front towards the downstream region, and a reduction in the equivalence ratio ϕ shows a similar effect due to the resulting decrease in laminar flame speed. A detailed illustration of the temperature distribution along the surface of the bottom-left cylinder near the flame is shown in Figure 3, where the temperature is plotted against the angle θ within the range of $-20°$ to $70°$ for the six different operating conditions. The blue and orange dashed horizontal lines mark the maximum and minimum surface temperatures within the θ range, and the magenta dash-dotted line represents the core temperature of the particle, measured using a K-type

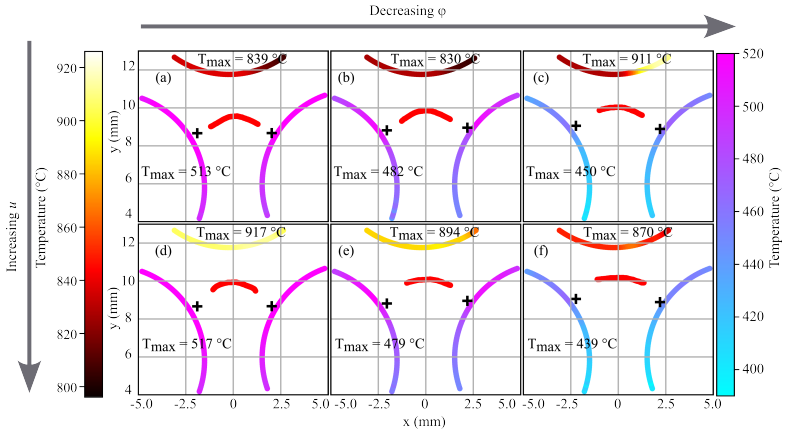

Figure 2. Detected flame skeletons are shown with red arcs, superimposed on the measured cylinder surface temperature distribution for the top and bottom cylinders for the different operating conditions a-f (Table 1).

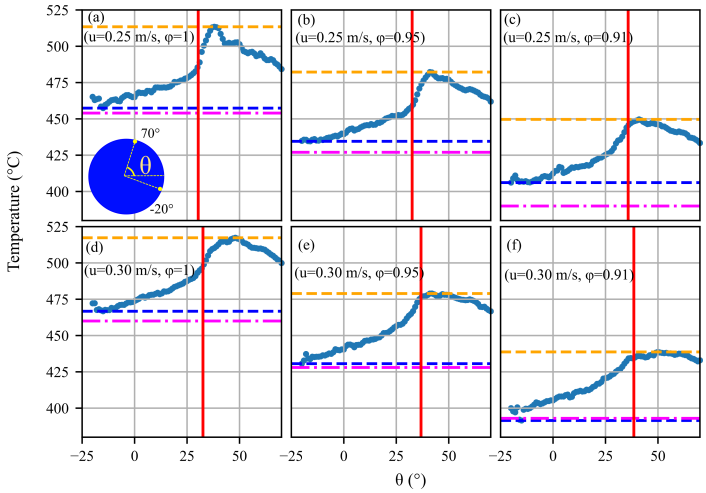

Figure 3. The measured surface temperature of the left cylinder for conditions a–f (Table 1) is shown. Orange and blue dashed lines indicate max/min temperatures, while the magenta dash-dotted line represents the core temperature.

thermocouple. The red vertical line marks the angular position at which flame quenching is identified. The maximum temperature on the particle surface, as well as the core temperature, decreases with a reduction in the equivalence ratio ϕ due to the decrease in flame thermal power. On the other hand, an increase in the mixture flow velocity from 0.2 to 0.3 m/s increases the flame thermal power, resulting in higher core and maximum surface temperatures. The increase in mixture velocity and decrease in equivalence ratio also shift the quenching point to a higher angular position.

Conclusion

Dual-phosphor thermometry for measuring the temperature distribution along the particle surface and telecentric chemiluminescence imaging of CH* radicals for flame position were successfully implemented. This enabled the measurement of particle surface temperatures, flame position, and quenching points for different CH_4/air compositions and mixture velocities. A decrease in the equivalence ratio ϕ reduces the flame speed, causing the flame to move downstream and settle in regions of lower gas velocity. Additionally, it reduces the flame's thermal power, resulting in a reduction in particle temperature. In a similar way, an increase in mixture velocity pushes the flame and the flame quenching points downstream, but an increase in particle temperature is also observed due to the increased flame thermal power. These results provide valuable data for validating CFD simulations of interactions between solids and flames.

Acknowledgment

This work was funded by the Deutsche Forschungsgemeinschaft (DFG, German Research Foundation), Germany - ProjectID 422037413 - TRR 287.

References

[1] Krause B., Liedmann B., Wiese J., Wirtz S., Scherer V.: *Coupled three dimensional DEM-CFD simulation of a lime shaft kiln-Calcination, particle movement and gas phase flow field*, Chemical Engineering Science, 134, 834-849, 2015.

[2] Cai T., Khodsiani M., Hallak B., Abram C., Beyrau F., Specht E.: *Phosphor thermometry at the surface of single reacting large-diameter spherical coke particles to characterise combustion for packed bed furnaces*, Proceedings of the Combustion Institute, 38, 4225–4232, 2021.

[3] Brübach J., Pflitsch C.,Dreizler A., Akatan B.: *On surface temperature measurements with thermographic phosphors: A review*, Progress in Energy and Combustion Science, 39, 37-60, 2013.

[4] Khodsiani M., Namdar R., Varnik F., Beyrau F., Fond B.: *Spatially resolved investigation of flame particle interaction in a two dimensional model packed bed*, Particuology, 85, 167-185, 2024.

Eulerian-Eulerian Modelling of Biomass Thermal Conversion in a Rotary Kiln

C. Álvarez-Bermúdez[1*], H. Khodaei[2,3], S. Chapela[1], M. A. Gómez[1], S. Adhikari[2,3] and J. Porteiro[1]

*E-Mail: cesalvarez@uvigo.gal

[1] *CINTECX, Universidade de Vigo, Grupo de Tecnoloxía Enerxética (GTE), Vigo, 36310, Spain*

[2] *Biosystems Engineering Department, 200 Corley Building, Auburn University, Auburn, AL 36849, USA*

[3] *Center for Bioenergy and Bioproducts, 519 Devall Drive, Auburn University, Auburn, AL 36849, USA*

Abstract

This study presents the CFD modelling of a lab-scale rotary kiln for biochar production. An Eulerian porous media based model is used to characterise the solid fuel bed. The model can accurately represent the thermal conversion of biomass and the movement of the fuel bed induced by the kiln's rotation. Two simulations were conducted using different heating configurations—single-zone and multi-zone—to evaluate thermal efficiency and char production yield. The lower temperature in the first heated section of the kiln in the multi-zone case leads to a more gradual and lower-temperature pyrolysis process. As a result, char production yield increases to 15%, compared to 11% in the single-zone configuration. Additionally, the multi-zone case exhibits lower energy consumption (1004 W) compared to the single-zone case (1184 W), resulting in higher thermal efficiency. These findings highlight the advantages of multi-zone heating for optimizing biochar production in rotary kilns.

Introduction

Numerical modelling is a powerful tool for analysing and optimizing reacting particle-gas systems, enabling the prediction of flow behaviour, heat and mass transfer, chemical reactions, and phase interactions under various operating conditions. Among the available modelling methodologies, Computational Fluid Dynamics (CFD) stands out for its ability to provide detailed insights into the complex phenomena governing particle-gas interactions. Given the multiphase nature of these systems, advanced CFD modelling frameworks, such as Eulerian-Eulerian and Eulerian-Lagrangian approaches, are needed to characterize fluid-particle interactions.

Lagrangian methods, such as the Discrete Phase Model (DPM) and Discrete Element Method (DEM), are commonly coupled with CFD to model the solid phase. These approaches track individual particles within a continuous gas phase, enabling detailed modelling of particle trajectories, collisions, and dispersion. While they offer high accuracy in predicting particle movement and interactions, their computational cost rises significantly when simulating large particle populations, making them less practical for dense flows and large-scale systems. On the other hand, the Eulerian-Eulerian approach treats both the gas and particle phases as interpenetrating continua, without tracking individual particles. This provides a more computationally efficient alternative but usually comes at the expense of accuracy.

CFD techniques have been widely used to model solid biomass thermal conversion systems, with both Eulerian-Lagrangian and Eulerian-Eulerian methods applied to model the solid fuel bed [1]. In this work, the CFD modelling of a lab-scale rotary kiln for biochar production is presented [2]. To accurately characterize the thermal conversion of biomass in the rotary kiln, it is crucial to model the movement and mixing of the fuel throughout the system [3]. Although the most common approach in such cases would be to use a Lagrangian model to individually track solid particles [3, 4], this work proposes the use of a porous media Eulerian bed model, aiming to develop a methodology with lower computational cost. The model can characterize bed morphology and temperature distribution throughout the unit, enabling the prediction of biochar production yield. Two thermal configurations are analysed to determine the optimal setup for maximizing biochar production and enhancing the system's thermal efficiency. This modelling approach can also be applied to analyse the impact of various parameters, such as feedstock composition, kiln rotation speed and heating temperature.

Model and methodology

The simulations were done using the commercial CFD software ANSYS Fluent. To model the solid fuel bed, the Eulerian Biomass Thermal Conversion Model (EBiTCoM), developed by the GTE research group at the University of Vigo, was implemented. The fuel bed is represented as a dispersed porous medium, with the solid and gas phases coexisting. A scalar (solid fraction) controls the ratio of solid volume to the total cell volume in each computational cell. More Eulerian scalars are employed to define the average properties of the fuel, including temperature, moisture content, wood density, char density, ash density, and the average particle diameter. The model considers three thermal conversion processes: drying, pyrolysis and char heterogeneous reactions. More details of the model can be found in the authors' previous works [5].

To model bed movement, a custom-developed algorithm is used [6]. This code, through geometric calculations on the CFD mesh, moves the solid fraction between cells in a way that mimics the natural settling of granular materials under gravity. As a result, the solid forms piles with slopes defined by the characteristic angle of repose of the material. The rotation of the kiln is modelled using the Mesh Motion technique, which enables the CFD mesh to rotate at a specified speed around a central axis. This mesh movement, combined with the settling algorithm, causes the solid fuel to progress along the kiln, as it is slightly inclined relative to the horizontal.

A lab scale kiln working under two different operating conditions to evaluate which configuration achieves the highest thermal efficiency has been studied. The kiln measures 1820 mm in length and 120 mm in internal diameter and is made of quartz. This kiln features a 1016 mm long electric heater that heats it from the outside, providing heat to the central portion of the kiln while leaving the ends unheated. The heater can operate either uniformly (600°C) or independently in three separate sections (350°C, 600°C and 450 °C respectively). The kiln is equipped with multiple radiation shields at its ends to confine the high-temperature zone to the section surrounded by the heater. The material used for biochar production is pine wood chips with a moisture content of 7.7%, fed at a rate of 12 g/min. The kiln is inclined at 3.5° relative to the horizontal and rotates at 6 rpm. It operates in an inert atmosphere by purging nitrogen into the chamber.

Results

Figure 1 shows the bed temperature contours for the two simulated cases. The bed temperature distribution is directly influenced by the heater temperature. The solid fuel reaches a temperature close to that of the wall it is in contact with in the section of the kiln surrounded by the heater. In the single-zone case, this results in a steep temperature gradient in the bed, causing both drying and pyrolysis to occur within a short section at the beginning of the heated zone. In the multi-zone case, the fuel temperature increases more gradually along the first heated section.

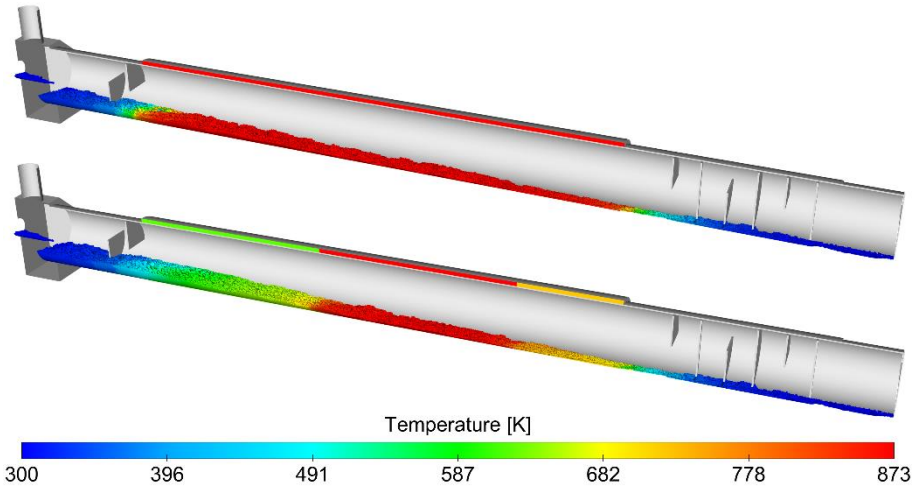

Figure 1. Contours of temperature of the heater and solid fuel bed for the single-zone (top) and multi-zone (bot) scenarios

As seen in the char contours (Figure 2), the difference in the heating rate leads to a faster conversion of wood into char in the single-zone case, while in the multi-zone case, the conversion occurs more gradually. This leads to a higher char production yield (15%) than the single-zone case (11%).

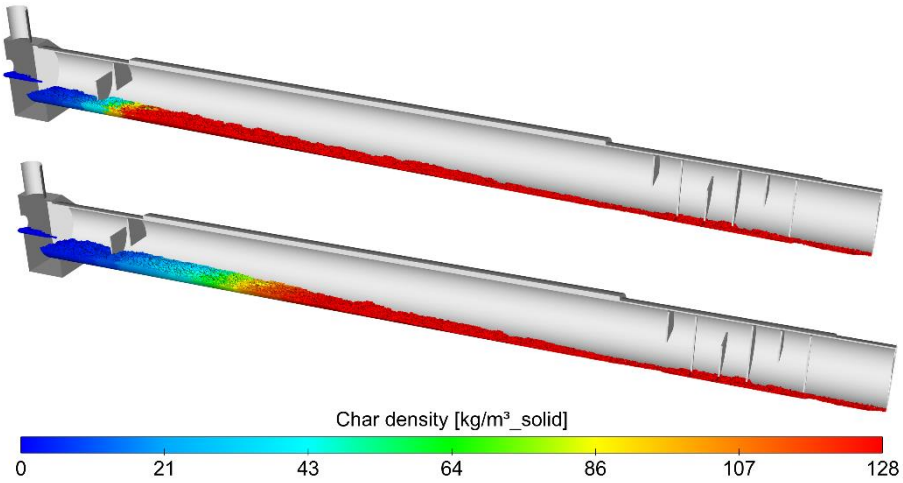

Figure 2. Contours of char density for the single-zone (top) and multi-zone (bot) scenarios

Conclusions

A rotary kiln for biochar production has been simulated in an Eulerian-Eulerian framework. The results show that the heating strategy significantly influences the thermal conversion process and char yield. The single-zone case, with a steeper temperature gradient, leads to a faster pyrolysis process but results in a lower char yield (11%) and higher energy consumption (1184 W). In contrast, the multi-zone case provides a more gradual temperature increase, leading to a higher char yield (15%) and improved energy efficiency (1004 W). These findings highlight the potential benefits of controlled multi-zone heating for optimizing biochar production and thermal efficiency in rotary kilns.

Acknowledgments

This research was funded by the project PID2021-126569OB-I00 of the Ministry of Science and Innovation (Spain). The work of César Álvarez-Bermúdez has been supported by the grant PRE2019-090110 of the Ministry of Science and Innovation (Spain).

References

[1] Rahdar M. H., Nasiri F., Lee B.: *A Review of Numerical Modeling and Experimental Analysis of Combustion in Moving Grate Biomass Combustors*, Energy & Fuels, 33, 9367–9402, 2019.

[2] Kavan Kumar V., Panwar N. L.: *Pyrolysis technologies for biochar production in waste management: a review*, Clean Energy, 8, 61–78, 2024.

[3] Pichler M., Haddadi B., Jordan C., Norouzi H., Harasek M.: *Influence of particle residence time distribution on the biomass pyrolysis in a rotary kiln*, Journal of Analytical and Applied Pyrolysis, 158, 105171, 2021.

[4] Tavakkol S., Zirwes T., Denev J. A., Jamshidi F., Weber N., Bockhorn H., et al.: *An Eulerian-Lagrangian method for wet biomass carbonization in rotary kiln reactors*, Renewable and Sustainable Energy Reviews, 139, 110582, 2021.

[5] Álvarez-Bermúdez C., Chapela S., Gómez M. A., Porteiro J.: *CFD simulation of a 4 MW biomass grate furnace using an Eulerian fixed-bed model: Validation of in-bed and freeboard results*, Fuel, 387, 134378, 2025.

[6] Varela L. G., Bermúdez C. Á., Chapela S., Porteiro J., Tabarés J. L. M.: *Improving Bed Movement Physics in Biomass Computational Fluid Dynamics Combustion Simulations*, Chemical Engineering & Technology, 42, 2556–2564, 2019.

Investigation of granule mixing in a rotating drum with Camera, ultrafast-Xray and numerical simulations

Theodoros Nestor Papapetrou,[1,2],* Martina Bieberle[1], Frank Barthel[1], Uwe Hampel[1,2], Gregory Lecrivain[1*]

*E-Mail: g.lecrivain@hzdr.de

[1] *Helmholtz-Zentrum Dresden – Rossendorf, Institute of Fluid Dynamics, Bautzner Landstraße 400, 01328 Dresden, Germany*

[2] *Technische Universität Dresden, Institute of Power Engineering, Chair of Imaging Techniques in Energy and Process Engineering, Dresden, Germany*

Context

The mixing of granular solids, hereafter called particles, is found in many industrial applications, among which stand out pharmaceuticals, food and concrete processing. In this work, we are interested in the mixing of two particle phases, namely 4-mm spherical polypropylene and glass beads in a rotating drum. Because of the density difference between the two phases, radial segregation rapidly occurs. Here, Ultrafast X-ray computed tomography (UFXCT), camera and simulation with the Discrete Element Method (DEM) are used to investigate the segregation dynamics. In this academic scenario, we vary the drum filling from 20 to 50 % and report two different segregation regimes. The filling degree in Figure 1 is calculated with the help of elementary trigonometry as $f = \theta - \sin\theta/2\pi$, where $\theta = 2\cos^{-1}(1 - h/R)$ is the central angle.

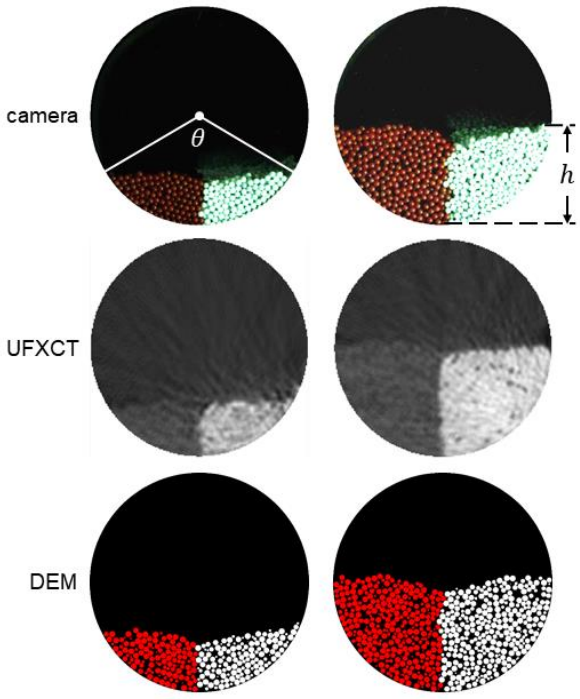

Figure 1.: Images of the bed at t = 0 s for the two experimental scenarios. Top row: camera images at the front-end of the drum. Middle row: UFXCT images in the bulk. Bottom row DEM cuts through the bulk. Polypropylene particles are red and glass particles white. Images are shown for f = 0.2 and 0.5, where is f the filling degree.

State of the art – Experimental techniques

Camera is one of the most conventional visualization techniques to capture the segregation dynamics in drum. With it, only the visible parts of the bed can be analysed. In a rotating drum, these visible parts are the free surface of the granular bed and those in contact with the circular caps and the drum cylinder. For these reasons, radial mixing has mostly been extensively studied in quasi-2D drums using video camera. Alternative experimental techniques can also be used to investigate the segregation dynamics across an opaque granular bed [1-2]. Among them, there exists magnetic resonance imaging, radioactive particle tracking and positron emission particle tracking. They have successfully been used to investigate particle segregation in rotating drums. Lately, granular segregation has been studied with X-ray computed tomography too. A relatively new technique, namely the ultrafast X-ray computed tomography (UFXCT), is of increasing interest for the visualization of rapid granular flows. It has only been used a few times for granular systems. In our recent work [3], we showed that UFXCT is also well applicable to visualize the transient segregation patterns in the bulk of a rotating drum. Yet, there exist no studies where UFXCT data are compared to other bulk data from experiments, simulations or theories. In this context, we use UFXCT, camera and DEM to investigate the effect of the filling degree on both the granular flow and the segregation dynamics in a rotating drum.

Objectives

The objectives of this work are twofold. First, we seek to compare UFXCT data to DEM data and so, showcase the advantages and limits of UFXCT compared to other techniques. Second, we investigate the effect of the filling degree on the active layer, where particle dispersion is highest. In the following, we present results on the transient and steady-state radial segregation patterns in two planes normal to the rotation axis. The first plane is the visible front-end of the drum and the second plane is in the bulk. Concentration and velocity fields are also used to further compare the three methods and to draw conclusions about how the filling degree correlates with the segregation patterns. Notable difference between the bulk and the front plane are observed.

Experimental set up

The present experimental set-up consists of a horizontal rotating drum partly filled with a binary bed of spherical particles. For the sake of conciseness, only the most salient features of the set-up are here presented. The particles in each granular species have the same diameter (4 mm) and only differ in density and colour. The polypropylene particles are red and the glass particles are white. Initially, that is at time t=0 s, the bed is in a side-by-side segregated state as shown in Figure 1-2.

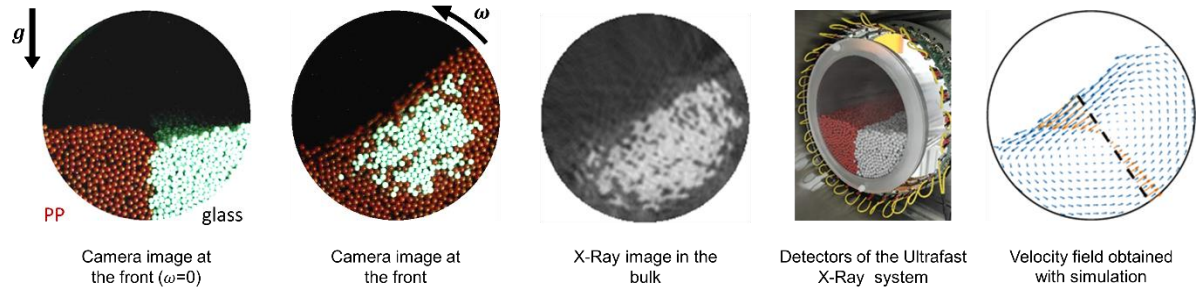

Figure 2. At high filler degree, that is f = 0.5, a white core of glass white particles eventually forms.

The drum rotates about its long axis with a constant rotational speed. In each experiment, the drum accelerates and decelerates for about 0.1 s. This time is minimal and corresponds to less than 5% of a full drum rotation. Typically, three to five rotations are needed to reach the steady-state. The drum speed is conveniently converted to a non-dimensional Froude number given by Fr = 0.06. The latter provides indication about the mixing regime, which is here rolling to cascading. These two regimes are typical for industrial mixing applications. In the rolling regime, the free surface of the bed is a flat, inclined plane. In the cascading regime, the free surface turns into a sigmoid (Figure 2)

Selected results

In this abstract, we select the scenario with the greatest filling degree, because it is one of the most investigated scenarios in the literature. We see, that the blue velocity fields obtained with UFXCT and DEM match well. The orange velocity profile along the segment AB in Figure 3 is also compared to literature data [4-5]. The agreement is excellent along the entire segment AB. The position at which the velocity equals zero, separates the active from the passive layer. The active and passive layers, well-established in the literature are well seen in the two bulk slices obtained with UFXCT and DEM.

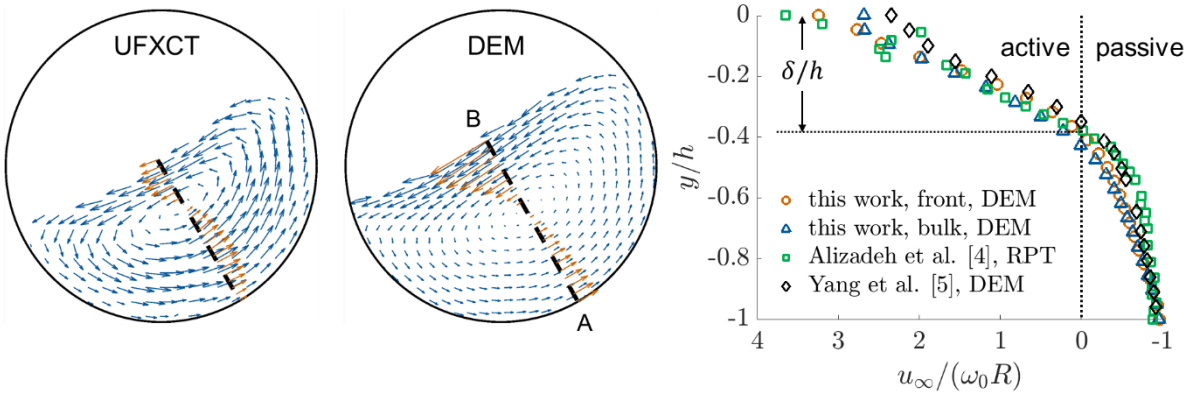

Figure 3: Comparison of UFXCT and DEM steady-state streamwise velocity along the line segment AB for the scenario ($f = 0.5$). The plot compares the orange velocity profile along the line AB with literature data for the same filling degree. The vertical line indicates the transition from the active ($u_\infty > 0$) to the passive ($u_\infty < 0$) layer. u_∞ is the maximum granular velocity, R the drum radius and ω_0 the rotation speed of the drum.

Further results

Despite a few limitations, the results from all three techniques are in good agreement with one another and compare well to literature data. Unlike UFXCT, camera and DEM methods are now well established. We have shown that UFXCT is a robust experimental technique and is particularly suited to the study of bulk granular flows, which are opaque. We believe that the data presented here can be used for the further validation of DEM and continuum models.

During the presentation, mixing indices as well as concentration and velocity fields for varying filling degree, both at the front place and in the bulk, will be shown. We find that, at low filling degree, typically for $f < 0.35$, the particles in the passive layer do not stick to the drum, as it rotates. Instead, they slip. This has considerable effect on the concentration fields.

Acknowledgement

This work was funded with a Scholarship provided by the Free State of Saxony.

References

[1] Hill, K.M., Caprihan, A., Kakalios, J.: *Bulk segregation in rotated granular material measured by magnetic resonance imaging*. Physical Review Letters 78, 50–53, 1997

[2] Parker, D.J., Dijkstra, A.E., Martin, T.W., Seville, J.P.K.: *Positron emission particle tracking studies of spherical particle motion in rotating drums*. Chemical Engineering Science 52, 2011–2022, 1997

[3] Papapetrou, T.N., Bieberle, M., Barthel, F., Hampel, U., Lecrivain, G.: *Investigating binary granular mixing in a rotating drum using ultrafast X-ray computed tomography*. Powder Technology 443, 119964, 2024)

[4] Alizadeh, E., Dubé, O., Bertrand, F., Chaouki, J.*: Characterization of mixing and size segregation in a rotating drum by a particle tracking method.* AIChE J. 59, 1894–1905, 2013

[5] Yang, S., Sun, Y., Zhang, L., Chew, J.W.: *Segregation dynamics of a binary-size mixture in a three-dimensional rotating drum*. Chemical Engineering Science 172, 652–666, 2017)

Influence of moisture reduction of conidiated rice on particle collision in rotating drum

D. B. Ferreira[1*], N. Vorhauer-Huget[2], E. Tsotsas[2] and J. C. Thoméo[1]

*E-Mail: daiane.b.ferreira@unesp.br

[1] Laboratory of Bioprocess, São Paulo State University "Júlio de Mesquita Filho", Cristovão Colombro 2265, 15054000 São José do Rio Preto, Brazil

[2] Institute of Process Engineering, University of Magdeburg, Universitätsplatz 2, 39106 Magdeburg, Germany

Introduction

The growing awareness of the adverse effects of excessive agrochemical use [1] has driven the adoption of more sustainable agricultural practices, such as the use of biopesticides [2]. Effective against more than 200 insect species, *Metarhizium anisopliae* is widely used for pest control in sugarcane fields, agricultural crops, and pastures [3, 4]. Its production mainly occurs through solid-state fermentation (SSF), using rice as a substrate packaged in plastic bags. Spore extraction is a critical step in this process, traditionally performed using vibrating sieves, which have low efficiency and cause significant environmental losses [5]. To optimize this step, a system based on a rotary drum, coupled with cyclones for spore collection, was developed. During extraction, it was observed that reducing the moisture content of rice particles decreases the adhesive forces between the spores and the substrate, requiring lower collision forces for detachment. However, parameters such as the number and intensity of collisions, as well as the influence of moisture, cannot be directly determined through experimental methods, posing challenges to process optimization. To address this limitation, numerical simulations based on the Discrete Element Method (DEM) prove to be a valuable tool. DEM enables a quantitative understanding of phenomena that are difficult to observe experimentally and has already demonstrated its effectiveness in predicting the dynamics of large particle assemblies. This study aimed to apply DEM to predict the motion regime and collisions of rice particles during spore extraction from *M. anisopliae* in a rotary drum. The method evaluated the impact of rotation speed and moisture content on the velocities and forces exerted on the rice grains, providing insights for designing and scaling more efficient rotary drums, including the internal arrangement and geometry required to achieve collision forces suitable for spore detachment.

Materials and Methods

- **Particle**

The conidiated rice (CDR) particles used in this study were obtained through solid-state fermentation in polypropylene plastic containers, each containing 400 g-ds of long-grain rice (*Oryza sativa*). The substrate was moistened and sterilized in an autoclave at 121°C for 30 minutes. After cooling in a laminar flow chamber, the spore suspension was incorporated, resulting in a substrate with a final moisture content of 0.923 kg of water per kg of dry substrate (kg-w/kg-ds). The fungus was incubated for 10 days in a climatic chamber at 28°C. After the incubation period, the containers were opened, and the CDR was placed in trays, which were kept in a climatic chamber at 30°C until reaching three distinct moisture levels: 0.250, 0.111, and 0.053 kg-w/kg-ds. These moisture levels correspond to the initial moisture and the levels after 4 and 8 hours of extraction, respectively. To adequately represent the CDR particles in the DEM simulation environment, their dimensions and bulk density (ρ_{bulk}) were determined.

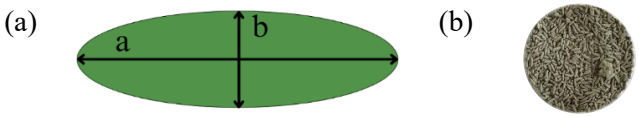

Figure 1. (a) Measurements for characterizing particle size, where a represents the length and b the width of the CDR particles and (b) CDR particles.

Figure 1 illustrates the measurements used for particle sizing, considering that the width (*b*) is equivalent to the thickness, while *a* represents the particle's length. The dimensions were obtained from photographic images of samples containing over 100 CDR grains with different moisture contents, analyzed using ImageJ software. The bulk density, ρ_{bulk}, was determined using the volumetric method in a 50 mL measuring cylinder.

- **Particle collisions**

The simulations were conducted using the LIGGGHTS software, adopting the non-linear Hertz-Mindlin contact model. The drum, with a diameter of 20 cm and a length of 33 cm, was designed using SolidWorks (Dassault Systèmes, France) to accurately represent the experimental setup. Inside the drum, two straight longitudinal blades, each 2 cm wide, were positioned perpendicularly to the drum wall. The reduction in the moisture content of the CDR particles during the extraction process was considered. To this end, the number of particles was kept constant (315,000 particles) across all experiments, while the particle diameter was adjusted. The simulations were conducted with a bed filling degree of 0.50 and drum rotation speeds of 30 and 60 rpm. The collision forces and velocities achieved by the particles, were quantified using Python. In addition to collisions, the bed movement regime during the extraction process was evaluated, an analysis that could not be performed experimentally due to spore release, which obstructed visualization. To ensure numerical stability during the simulations, a time step of $1x10^{-4}$ seconds was employed. The rice particles were modeled as spheres, with their volume adjusted to match that of real particles. The restitution coefficients, rolling friction, and static friction were experimentally obtained for conidial rice particles at different moisture levels and calibrated to reflect the real behavior of the particles. The restitution coefficient values used in the simulations were directly based on the experimental data, being 0.164, 0.187, and 0.215 for particle-particle (PP) interactions and 0.297, 0.314, and 0.343 for particle-wall (PW) interactions, corresponding to CDR particles with moisture contents of 0.250, 0.111, and 0.053 kg-w/kg-ds, respectively. Additionally, the static and rolling friction coefficients for both PP and PW interactions were defined as 0.267 and 0.818; 2.711 and 0.470, respectively, and were considered constant regardless of the particle moisture.

Results and Discussion

The movement regimes obtained from the DEM simulations with drum rotations of 30 and 60 rpm are shown in **Figure 2**.

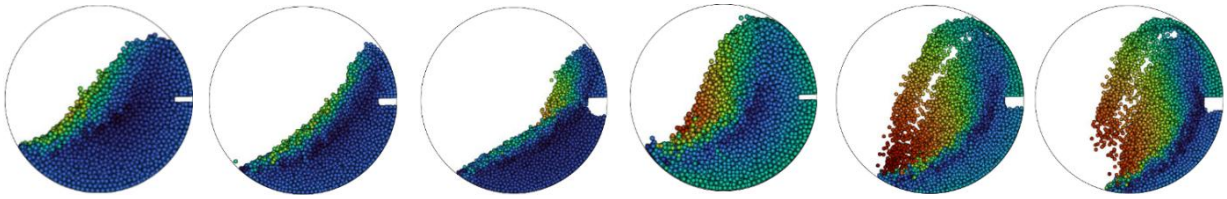

Figure 2. Movement of conidial rice in the extraction drum rotating at 30 rpm for particles with moisture of (a) 0.250, (b) 0.111, and (c) 0.053 kg-w/kg-ds, and at 60 rpm for particles with moisture of (d) 0.250, (e) 0.111, and (f) 0.053 kg-w/kg-ds.

During the simulations, the number of particles was kept constant, while their dimensions were adjusted to represent the size reduction caused by drying throughout the process. Thus, the CDR spheres with moisture contents of 0.250, 0.111, and 0.053 kg-w/kg-ds were modeled with radii of 1.26 mm, 1.07 mm, and 0.97 mm, respectively. As a result, a significant reduction in the drum's filling degree was observed. The drum's rotation speed directly influences the particle movement regimes within the bed. Particle movement inside drums can generally be divided into three distinct regions: the active layer, where most particle motion and interactions occur; the passive layer, characterized by a more stable and cohesive flow; and the interface region, which separates these two layers and affects material transitions within the system [6]. When the particles predominantly remain in the active layer, interactions between them increase, intensifying friction. For both drum rotation speeds, it was observed that the reduction in the filling degree decreased the extent of the interface region. The lower filling degree also increased the frequency with which particles entered the active layer of the bed, where more intense collisions occur,

particularly at a drum speed of 60 rpm. These stronger impacts enhance spore detachment, further highlighting the influence of reduced particle moisture on extraction efficiency, as verified experimentally. The particle velocities and average collision forces are summarized in **Figure 3**. Overall, both velocities and collision forces increase as the moisture content decreases. This behavior can be partially explained by the higher restitution coefficients observed in particles with lower moisture content. These higher coefficients result in less energy dissipation during collisions [7]. Consequently, the particles rebound with relatively higher velocities, leading to more intense collisions. Additionally, the average collision forces are higher when the drum is rotated at 60 rpm, justified by the greater average velocities reached by the particles. Since spore release often occurs through collisions, higher forces are desirable to enhance the efficiency of the extraction process.

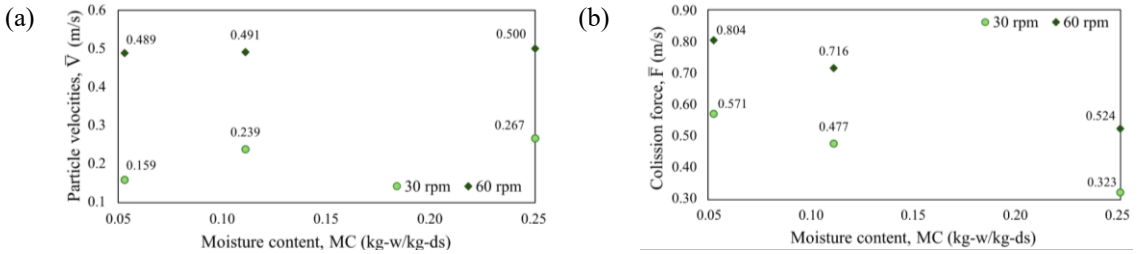

Figure 3. (a) Velocities and (b) collision forces reached inside the drum by CDR particles with different moisture contents).

Conclusion

It is concluded that the reduction in the moisture content of particles during the spore extraction process of *Metarhizium anisopliae* in a rotary drum positively influences the particle motion regime, as well as their velocities and collision forces. Among the tested conditions, a drum rotation speed of 60 rpm was deemed ideal, as it promotes a more efficient motion regime for the extraction process. These findings open new possibilities for the implementation of more efficient extraction systems, with the potential to enhance the economic and productive feasibility of large-scale bioinsecticide production, contributing to sustainability in agricultural pest control.

Acknowledgement

The authors D. Bortolote Ferreira and J. Cláudio Thoméo acknowledge the funding by the Coordination for the Improvement of Higher Education Personnel (CAPES - Finance Code 001) and the Brazilian National Council for Scientific and Technological Development (CNPq - PROC 406950/2023-7) for their contributions to the study. The authors N. Vorhauer-Huget and E. Tsotsas acknowledge the funding by the Deutsche Forschungsgemeinschaft (DFG, German Research Foundation) – Project-ID 422037413 – TRR 287 for their contributions to the study.

References

[1] Bagheri, A.; Shirzadi, Z.; Shokohian, A. A.; Bondori, A.; Damalas, C. A. *Occupational Exposure to Pesticides, Personal Protection, and Willingness to Reduce Chemical Sprayings Among Iranian Greenhouse Farmers*. Journal of Agromedicine, *30*, 14–26, 2025.

[2] Ferreyra-Suarez, D.; García-Depraect, O.; Castro-Muñoz, R. *A Review on Fungal-Based Biopesticides and Biofertilizers Production*. Ecotoxicology and Environmental Safety, *283*, 116945, 2024.

[3] Nishi, O.; Sato, H. *Species Diversity of the Entomopathogenic Fungi Metarhizium Anisopliae and M. Flavoviride Species Complexes Isolated from Insects in Japan*. Mycoscience, *58*, 472–479, 2017.

[4] Fontes, E. M. G. *Controle biológico de pragas da agricultura*; Embrapa, 2020.

[5] Liu, H.; Wang, P.; Hu, Y.; Zhao, G.; Liu, H.; Li, Z.; Wu, H.; Wang, L.; Zheng, Z. *Optimised Fermentation Conditions and Improved Collection Efficiency Using Dual Cyclone Equipment to Enhance Fungal Conidia Production*. Biocontrol Science and Technology, *25*, 1011–1023, 2015.

[6] Mellmann, J. The *Transverse Motion of Solids in Rotating Cylinders—Forms of Motion and Transition Behavior*. Powder Technology, *118*, 251–270, 2001.

[7] Xie, C.; Zhao, Y.; Song, T.; Zhao, Y. *Investigation of the Effect of Filling Level on the Wear and Vibration of a SAG Mill by DEM*. Particuology, *63*, 24–34, 2022.

Experimental and DEM analysis of transverse particle motion in a rotary drum with cross section internals

J. Hahne[1*] and F. Herz[1]

*E-Mail: jannes.hahne@hs-anhalt.de

[1] University for Applied Sciences - Anhalt., Bernburger Str. 55 06366 Köthen (Anhalt), Germany

Introduction

Rotary kilns are essential for the thermal treatment of bulk materials, characterized by high throughput rates and homogenization. Energy input is typically from heating gas, with heat transfer through radiation at temperatures above 600 °C. Below these temperatures, the impact of thermal radiation is minimal. For this reason, internal structures are added to elevate bulk materials and ensure continuous discharge over the cross section, improving heat transfer. However, this can lead to abrasion and fracture of particles, risking product quality and increasing dust generation. To reduce this, a drum reactor with cross internals has been developed. This paper aims to investigate the transverse particle motion in this rotary drum with cross section internals using experimental and numerical data.

DEM analysis

This publication employs the open-source software LIGGGHTS to simulate the dynamics of bulk materials. The mathematical model code systematically monitors each particle over discrete time steps within the simulation environment. This temporal resolution enables a detailed analysis of bulk material dynamics at the microscopic level within a rotary drum featuring cross section internals. Specifically, the discrete element method (DEM) analysis aims to complement macroscopic findings – such as those derived from experimental analyses – with particle velocity distributions (see [1–3]). Newton's second law of motion allows calculating individual particle movements resulting from interactions between particles and boundaries. To accurately represent the contact behavior between particles in DEM simulations, contact models are utilized. Hard and soft sphere models are distinguished. This paper employs a nonlinear Hertzian contact model, which enables the computation of both normal and tangential forces, along with tracking tangential interactions stemming from elastic particle collisions.
The numerical analysis presents the motion behavior of glass spheres with a diameter of 3 mm in a rotating drum, with and without cross internals. The dimensions of the rotary drums are consistent with those used in the experimental setup. To achieve a filling degree of 30%, 135,000 glass particles were introduced into the rotary drum without internals. In contrast, for the drum with cross internals, the particle collective was evenly distributed across the eight segments, resulting in 16,875 particles per segment. Both simulations used identical contact parameters for the glass balls, thereby allowing a direct comparison.

Experimental analysis

A discontinuous test facility was established to experimentally investigate the motion dynamics of bulk materials in a rotary drum with cross section internals. The horizontally mounted experimental rotary drum has a diameter of 300 mm and a length of 150 mm, and is divided into eight sections by a cross section internals structure. A three-phase motor mounted at the rear drives the drum and the particles (with a diameter of 2 mm). A glass window at the front allows observing the particles during the experiment. Particle movement was recorded using a high-resolution camera; alternatively, a high-speed camera can be used. The rotational speed range investigated was between 0.5 rpm and 8.0 rpm. The experimental setup of the test facility is shown in **Figure 1**. Geometric relationships and balance equations within the drum's cross section were used to describe the transverse motion behavior within rotary drums equipped with cross internals. The cross section of the rotary drum is schematically represented in **Figure 2**, where the bulk bed is indicated as the red area. The eight sections are arranged at an angle of $\alpha = 45°$ and are defined by the segment $B_1B_2C_2C_1$. The bulk material is evenly distributed

among the eight sections, with a filling degree of 30%. The center of the rotary drum serves as the origin of the cartesian coordinate system, with rotation starting clockwise from the negative horizontal semi-axis at a rotation angle of δ = 0°. The rotation angle is defined by the line OC1, covering a full rotation of 360°. Only the cross section of the rotary drum is analyzed, with the contact area treated as a linear. In this context:

- I_{SG} refers to the free bed surface between the bulk bed and the gas phase.
- P_1 denotes the contact length between particle bed and B_1C_1.
- W_i represents the contact length between particle bed and the inner arc B_1B_2.
- P_2 indicates the contact length between particle bed and B_2C_2.
- W_o refers to the contact length between particle bed and outer wall of the rotary drum C_1C_2.

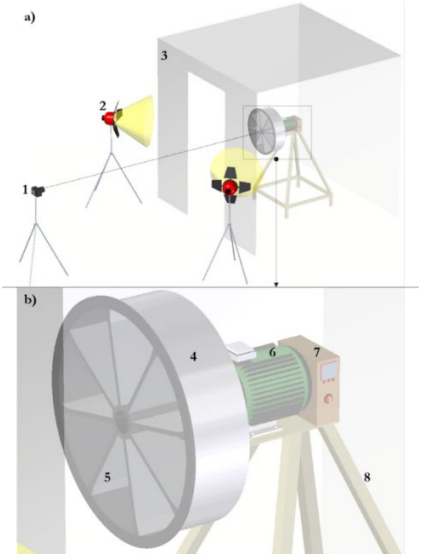

Figure 1. Setup of the experiment a) overall overview (1: system camera 2: headlights 3: light tent), b) detailed view (4: rotary drum 5: cross section internals 6: electric motor 7: frequency converter 8: stand)

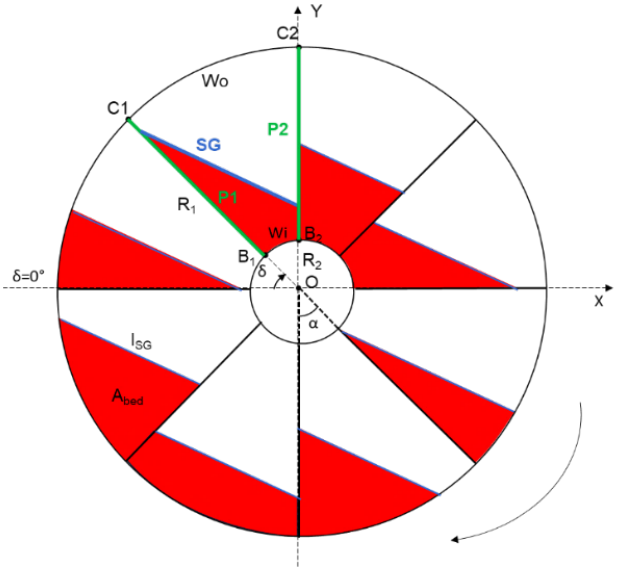

Figure 2. Schematic representation of the rotating drum with cross sectional internals and 30% filling degree made of monodisperse particles with a particle diameter of 2 mm

Results

To illustrate the significant impact of cross internals on particle motion, a comparison is made between the velocity profile of a system with cross internals and that of a conventional rotary drum. **Figure 3** displays the distribution of particle velocities in a rotary drum without internals, operating at a rotational speed of 8 rpm and a filling degree of 30%. **Figure 4** presents the corresponding velocity profile of the bulk material from **Figure 3** in a rotating drum with cross section internals.

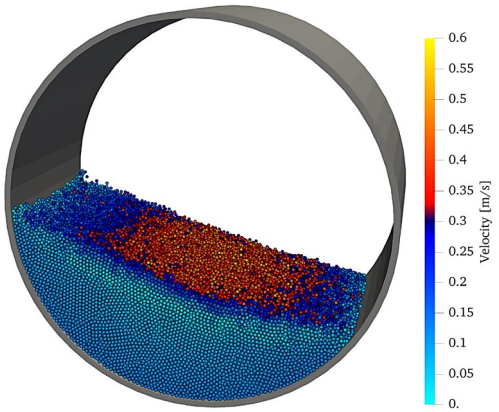

Figure 3. Velocity profile of 3 mm glass balls in a rotary drum

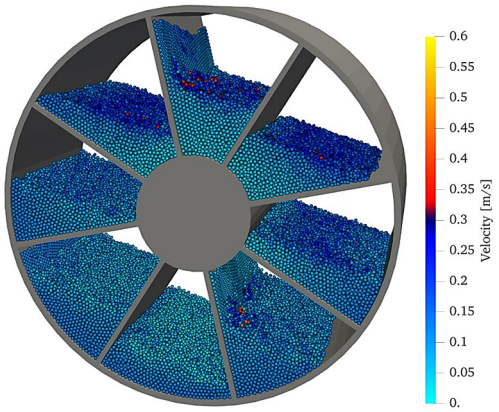

Figure 4. Velocity profile of 3 mm glass balls in a rotary drum with cross section internals

Significant differences in the distribution of particle velocities are evident. For instance, in **Figure 3**, the boundary layer separating the active and passive particle layers is discernible. These layers have a substantial influence on the mixing intensity of the bulk bed. In **Figure 4**, the cross internals eliminate the velocity gradients and enhance the mixing intensity at high filling degrees, compared to a rotary drum without internals. This improvement is attributable to the continuous reshuffling of the entire bulk bed within the individual segments.

Figure 5 depicts the progression of contact surface lengths for a bulk material of 2 mm glass spheres in a drum reactor with cross internals at a rotational speed of 1 rpm and a filling degree of 30 % (as shown in **Figure 2**). Over a complete rotation cycle (from $\delta = 0°$ to 360°), the experimentally determined contact surfaces between the particle bed and the gas or wall regions were recorded. The data indicate that, aside from the free surface SG, the contact surfaces P_1, P_2, W_o and W_i exhibit periodic behavior with equal rates of increase and decrease. It is important to note that the variance in diameter between the inner and outer walls of the rotary drum causes W_o to be larger than W_i. Cross section internals significantly enhance the particle-wall contact areas compared to a rotating drum without these structural installations. Consequently, this structural design in the area of rotary kilns can improve heat transfer since additional contact areas (W_i, P_1 and P_2) are available.

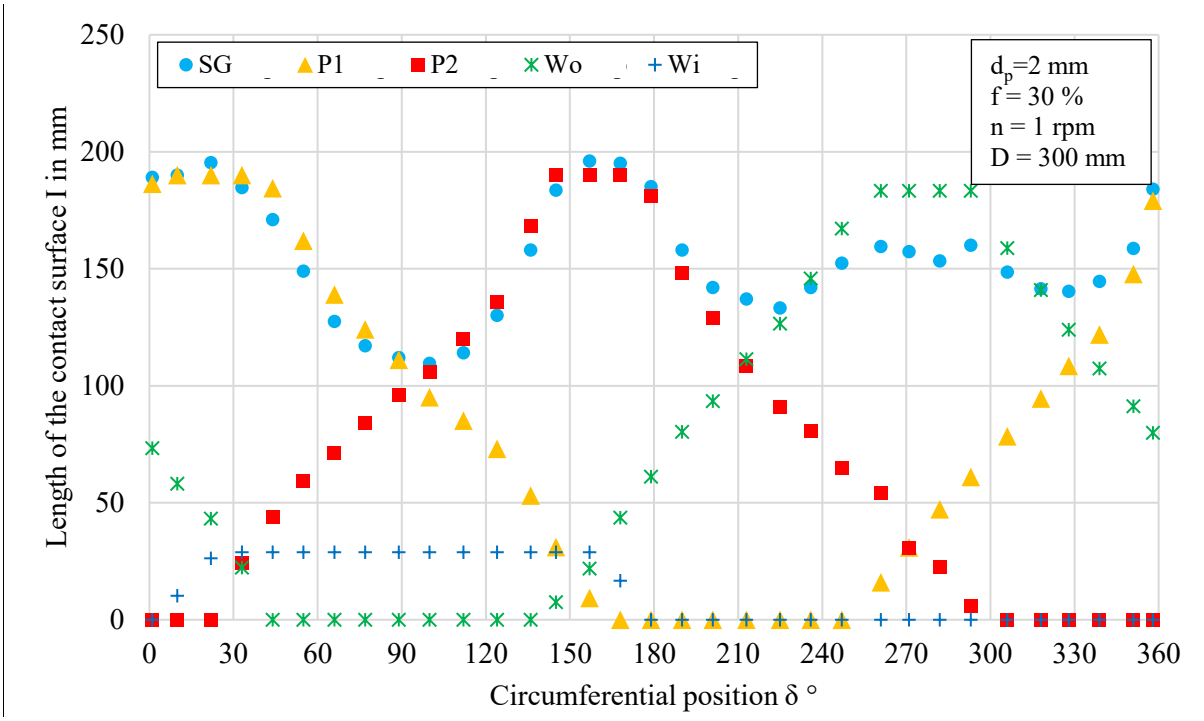

Figure 5. Lengths of the contact surface depending on the position δ ° in rotary drum with cross sectional internals

Outlook

This publication highlights the impact of cross internals on particle velocity and contact surfaces within the drum reactor. Further experimental and numerical studies will explore design variations, bulk material properties, and operating parameters. Special focus will be on the contact duration between particles, reactor walls, and gas, as these significantly affect heat transfer processes. With these findings, it will be possible to set up models, carry out optimizations and develop drum reactors with cross section internals that enable energy-efficient and gentle processing of bulk materials.

Acknowledgement

This publication has been funded by EU-EFRE Saxony-Anhalt in the project “Competence Network for Applied and Transfer-Oriented Research” (KAT) ZS/2023/12/182020 and the project “Development of

a reactor with cross section internals for energy-efficient and gentle thermal processing of biomass" ZS/2024/01/183851. The authors sincerely acknowledge this generous support.

References

[1] L. Zhang, "Experimental investigation and numerical simulation of the particle motion in flighted rotating drums," 2020. [Online]. Available: https://repo.bibliothek.uni-halle.de/handle/1981185920/36567

[2] L. Zhang, F. Herz, F. Weigler, E. Kleiber, X. Liu, and A. I. Nafsun, "DEM analysis of heat transfer in the bulk bed of rotary kilns," in *Proceeding of International Heat Transfer Conference 17*, Cape Town, South Africa, 2023, p. 12.

[3] Z. Zhang, N. Gui, L. Ge, and Z. Li, "Numerical study of mixing of binary-sized particles in rotating tumblers on the effects of end-walls and size ratios," *Powder Technology*, vol. 314, pp. 164–174, 2017, doi: 10.1016/j.powtec.2016.09.072.

Experimental Investigation of Thermal Mixing of Monodisperse Particles in a Rotary Drum

Wenjing Ma*, Nicole Vorhauer-Huget and Evangelos Tsotsas

*E-Mail: wenjing.ma@ovgu.de

Thermal Process Engineering, University of Magdeburg, Universitätsplatz 2, 39106 Magdeburg, Germany

Introduction and Research Need

The discrete element method (DEM) has evolved into a standard computational tool for analyzing particle flows driven by gravity or mechanical agitation. Within this framework, heat transfer problems are increasingly addressed, leading to the method being referred to as thermal DEM. For all problems requiring solutions via thermal DEM, a critical parameter is the particle-particle heat transfer coefficient, α_{pp} (the rate at which heat is transferred from one particle to another during contact), as it directly influences the predicted thermal behavior of granular systems. The ability to model and quantify heat transfer between particles is crucial for applications in industries for energy storage, chemical processing, and material manufacturing, where thermal transport within packed or mechanically agitated particle beds plays a fundamental role. For spherical particles, it is possible to a certain extend to compute α_{pp} by consideration of simple heat conduction rules on geometrical grounds. The same is though extremely difficult for particles of irregular shape, or for particles that differ in size, shape or material.

A New Approach to Particle-Particle Heat Transfer

To enable the computation of particle-particle heat transfer coefficient α_{pp} under any conditions, a new approach is followed. It is suggested to compute α_{pp} from the effective thermal conductivity of the corresponding particle system, typically a packed bed, denoted by λ_{bed}. Such derivation can be done either analytically [1] or by numerical calibration [2]. In this study, the former method is used, based on the fact that the homogenized heat conduction property of the packed bed, λ_{bed}, and the of the particle-particle heat transfer coefficient α_{pp} that can be used for DEM/CFD in packed, moving or mechanically agitated particle systems are directly proportional to each other. Moreover, the effective thermal conductivity, λ_{bed}, is much more easily accessible, either by measurement or by correlations. For example, enhanced methods for the prediction of the effective thermal conductivity with monodisperse particles of almost arbitrary polyhedral particle shape have recently been developed [3]. This has been done by expanding the Zehner-Bauer-Schlünder (ZBS) model for its reliable application to polyhedral particles by correlating crucial model parameters (bed porosity ε, the flattening coefficient φ, and form factor C_f) with quantities that can describe particle shape in a generalized way. The big data necessary to this purpose cannot be generated by measurements, so that the previous research has been mainly aiming at data on λ_{bed} from numerical simulations of heat conduction in virtual packed beds made of synthetic particles. And, this was accompanied by selected heat transfer experiments with real particles for combinations of particle shape and material that could be produced with reasonable accuracy, cost and effort, providing anchor points and validation for the envisaged development. Moreover, X-ray µ-CT measurements provided relevant morphological data.

While the above-mentioned concept makes sense, the proportionality factor (prefactor) of the linear equation that can be used to obtained α_{pp} from λ_{bed}, and vice-versa, needs to be known. To get this prefactor, both involved quantities must be known. Assuming that λ_{bed} is available from simulations, from measurements, or from correlations, this means that α_{pp} must also be retrieved experimentally. Respective experiments cannot be based on the heating of the particles from the gas phase, because then the particle-gas heat transfer mechanism prevails. They can also not be based on heating the particles from a hot wall, because then the wall-particle heat transfer mechanism prevails.

Consequently, other kinds of experiment, which are controlled by particle-particle heat transfer are necessary to this purpose, as further explained in the next section.

Novel Experiments for the Calibration of Thermal DEM

Experiments which are predominantly controlled by particle-particle heat transfer can be performed by the thermal equilibration or thermal mixing method in a simple rotary drum. In such experiments, hot and cold particles are initially separated, then respectively filled into the reactor, and then mixed (**Figure 1**). Immersed thermocouples are used to detect temperature transients. Measured temperature transients are then compared with respective thermal DEM simulations, in which the particle-particle heat transfer coefficient α_{pp} is adjusted until the experimental results can be accurately described. With α_{pp} defined in this way, and λ_{bed} obtained in some independent manner, the prefactor of the relationship between those two quantities can be evaluated, completing and fulfilling the thermal calibration of the DEM.

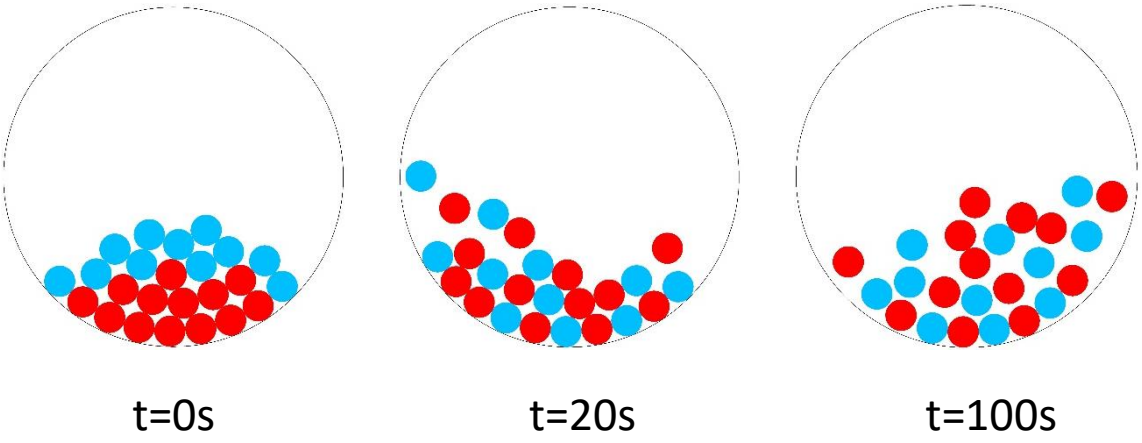

Figure 1. Schematic cross-sectional view of particle mixing in a rotary drum over time.

In the equipment that has been constructed to this purpose (see **Figure 2**), the rotary drum has an inner diameter of 60 mm and a length of 150 mm. The drum is light and thin, with a wall thickness of only 2 mm and small heat capacity. One face of the drum is transparent, providing optical access. This way, the movement of the particles can be observed by means of a camera from the transparent face, but also alongside of the drum with the help of an inclined mirror placed in it. The inner drum wall is roughened by glued sand-paper, so that rolling regime operation is obtained. Most important for the measurement is a central horizontal shaft with four vertical lances at different axial positions. In each lance, several thin thermocouples are placed at different radial positions. Shaft and lances are static, whereas the drum turns around with the help of a motor, and temperature evolution is monitored in different regions of the bed by the immersed thermocouples. The drum is placed in a plexiglass box with nearly stagnant air heated at the caloric mean temperature of the two initially segregated particle fractions at different temperatures. This insulates to a certain degree the drum from room conditions and also promotes the symmetry of the fractional thermal transients at both sides of the mean. Resulting in which is the declare goal of the equipment, namely to conduct thermal measurements which are primarily controlled by particle-particle heat transfer, and not by the thermal interaction with the environment.

A first series of investigations with the described equipment is conducted with monodisperse cubical particles made of PMMA (a low-conductivity polymer). Respective results will be presented, alongside with their evaluation and the resulting calibration of the thermal DEM.

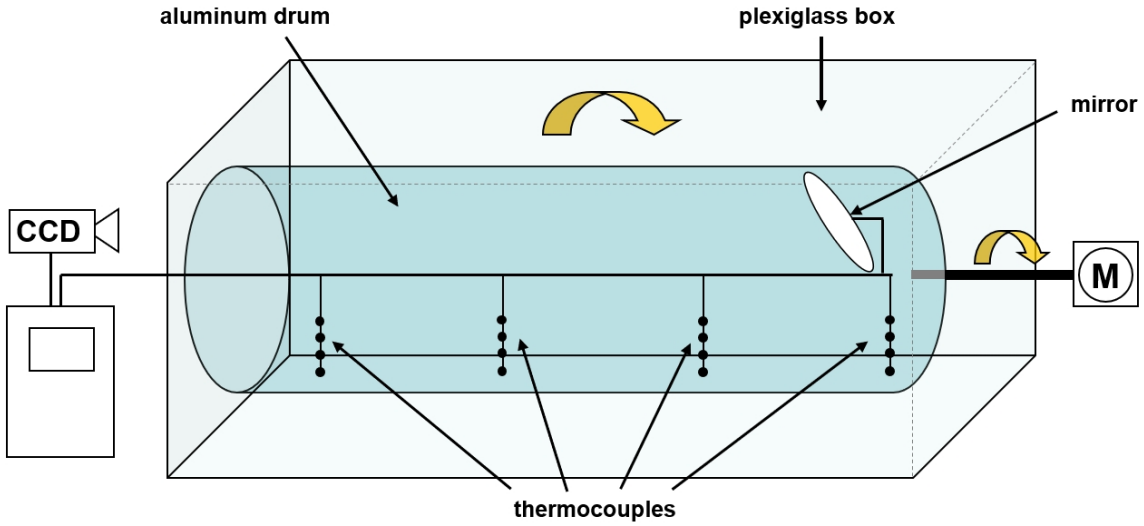

Figure 2. Scheme of rotary drum in tempered box for thermal equilibration experiments.

Acknowledgement
This work was funded by the Deutsche Forschungsgemeinschaft (DFG, German Research Foundation) – TRR 287 – 422037413.

References

[1] Tsotsas E.: *Particle-particle heat transfer in thermal DEM: Three competing models and a new equation*, International Journal of heat and mass transfer, 132, 939-943, 2019.
[2] Kwapinska M., Saage G., Tsotsas E.: *Continuous versus discrete modelling of heat transfer to agitated beds*, Powder Technology, 181(3), 331-342, 2008.
[3] Rodrigues S. J., Vorhauer-Huget N., Tsotsas E.: *Prediction of effective thermal conductivity of packed beds of polyhedral particles*, Powder Technology, 430, 118997, 2023.

Separation of micron-particle in rising Taylor bubbles

R. Maestri[1*], L. Büttner[2], J. Czarske[2], U. Hampel[1,3], and G. Lecrivain[1]
[*]E-Mail: r.maestri@hzdr.de

[1]Institute of Fluid Dynamics, Helmholtz-Zentrum Dresden-Rossendorf, Bautzner Landstraße 400, 01328 Dresden, Germany
[2]Laboratory of Measurement and Sensor System Techniques, Technische Universität Dresden, Helmholtzstraße 18, 01069 Dresden, Germany
[3]Chair of Imaging Techniques in Energy and Process Engineering, Technische Universität Dresden, Helmholtzstraße 18, 01069 Dresden, Germany

Abstract
Aerosol particle separation finds application in various industrial and medical systems. In the present context, the separation of particles in a rising Taylor bubble is investigated. A Taylor bubble is characterized by an elongated shape, a bullet-shaped nose, and a comparatively flat tail. The aerosols present in the gas Taylor bubble migrate to the water, where they are eventually trapped. With particles with diameters ranging from 1 to 5 μm, the separation takes place in the inertia-dominated regime, where the particle diffusion is strongly dependent on the air flow. In this study, we investigate, through experiments conducted in an 8 mm diameter channel, particle separation in a Taylor bubble.

Introduction

The transport of aerosol particles in gas flows and their transition to the liquid phase occurs when a gas loaded with pollutant particles is brought into contact with a scrubbing liquid. The dust particles bound in the liquid are thus separated, providing an efficient mechanism for air purification [1]. It is widely recognized that the accumulation of particles in the atmosphere can pose significant problems for human health and the operation of engineering systems. An essential element in that process is how particles are dispersed throughout the bulk of the gas under the action of different particle size-dependent forces. Although such motion for 'small' particles is stochastically equivalent to Brownian motion and, as such, is well understood [2] or for the 'big' particles will be subjected to the externally applied force, e.g., gravity [3], no straightforward approach exists to describe particle separation for intermediate-sized particles. This gap remains across the size scales of particle-fluid interaction, partly due to the lack of experimental evidence on particle separation in rising bubbles with a stable interface.

A primary question in the study of aerosol-particle motion in pool scrubbing is the effect of bubble interfacial shape on the average settling velocity of the inertia-dominated region of particle sizes [4,5,6]. The bubble shape affects the residence time of aerosol contaminants in the air bubble and its airflow velocity. It is relatively straightforward to determine the terminal particle settling speed in still fluid, with a perfectly spherical bubble shape under the assumption of Stokes flow, away from confining walls. Using a simplified assumption of spherical bubbles, the theoretical model of Fuchs et al.[7] for calculating particle separation shows a good agreement with the experimental values in the diffusion region; however, in the inertia-dominated region, where the flow field is of great importance, the separation rate shows an underprediction to the experimental values [8]. Extensive measurements have been made for bubbles with non-spherical shapes over a wide range of sizes, and these results are well summarized, for example, by Perez et al.[9].

We suggest using a Taylor bubble. It has a stable surface even in the millimetric size range [10], has high reproducibility of length during its flow, and is ideal for CFD validation. The Taylor bubbles can be an option as one can change the size by increasing its height. The Taylor flow features confined and elongated bubbles that almost occupy the entire cross-section of the channel. The liquid circulation flow pattern can suspend, transport, and mix solid particles in the liquid slugs, thus reducing the risk of clogging and agglomeration. Hence, new experimental validation in pool scrubbing with Taylor bubbles is crucial for developing physics-based correlations and simulation models for non-spherical characteristics. This paper investigates how the general separation ratio in air Taylor bubbles compares to that of spherical bubbles in still fluid, emphasizing the influence of particle inertia.

Methods

The apparatus consists of an aerosol generator, an aerosol size and concentration monitoring system, a circular milli-channel, and an exhaustion system. We use an aerosol generator (SLG-270, TOPAS, Germany) to generate monodisperse mist particles of Di-ethyl-hexyl-sebacate (DEHS) with diameters of 1.0 to 5.0 μm. The aerosol generation system includes a process aerosol monitor (PAM, Topas, Germany) to measure the particle sizes and concentration. The generated aerosol has a high particle number concentration of O(10^6) particles per cm^3 with spherical, electrically neutral particles of uniform diameter. In a dilution chamber with feedback control, we adjust the number concentration in the order of O($10^1 - 10^3$). The channel is a cylindrical tube with a diameter (D) of 8 mm. The tube, made of 1.5 mm thick borosilicate glass, is filled with deionized water at room temperature, that is, at T $\approx$ 20 °C. The tube was cleaned before each experiment to ensure particles did not accumulate on the tube walls. The viscosity and density of deionized water were measured. They are presently equal to μ_l = 1.06×10^{-3} kg $\cdot$ m$^{-1}\cdot$s^{-1} and ρ_l = 998.2 kg/m^3. The surface tension, taken from the literature, is estimated at σ = 0.072 N/m. The top of the tube is connected to a valve that is either open to the airflow meter or the particulate matter sensor, see Fig. 1. The membrane pump drives the low-pressure aerosol particles. Standard isokinetic measurements of upstream and downstream particle concentrations were carried out to monitor the particle concentration before and after passage through the channel. An Optical Particle Counter (SPS-30, Sensirion, Switzerland) was used for detecting and counting particles in size ranges between 0.1 and 10 μm.

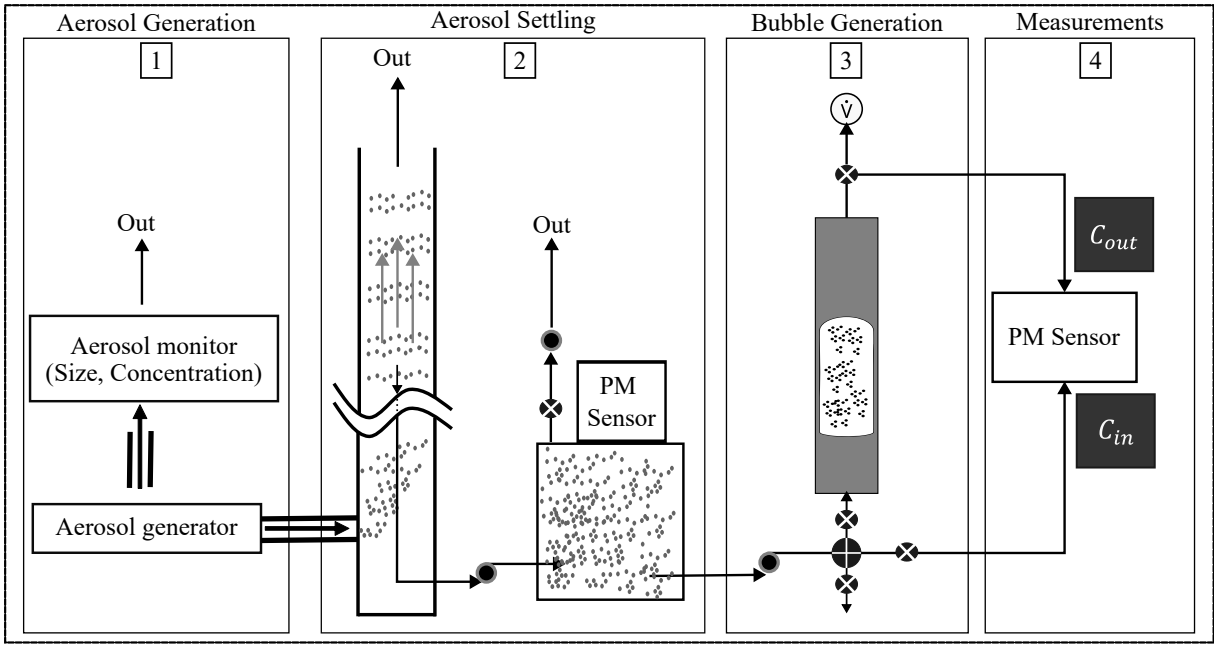

Figure 1. Schematic diagram of the experimental facility.

We conducted a series of experiments to measure the separation ratio under various operating conditions. The separation ratio η was calculated using the formula

$$\eta = \frac{\eta_2 - \eta_1}{1 - \eta_1}, \tag{1}$$

with

$$\eta_i = 1 - \frac{C_{in}}{C_{out_i}} \tag{2}$$

where C_{out} and C_{in} are the measured aerosol concentrations in the outflow and inflow, respectively. The location of sampling points before and after the filtering device is shown in Figure 1. These experiments included the separation ratio η_i in dry (η_1) and wet regimes (η_2), where the fluid was withheld on the channel with heights (h) of 0.1, 0.2, and 0.3 m. The temperature and humidity of the carrier gas were kept constant in an air-conditioned room.

Results

We performed experiments with Taylor bubbles of an average size of $\ell_a = 21.6$ mm or $\ell_a/(2R) = 2.7$, at different liquid heights. Figure 2 presents the measured separation efficiency η as a function of particle diameter d_p for three liquid heights h: 10, 20, and 30 cm, or equivalently $h/(2R) = 37.5$, 25.0, and 12.5, respectively. The results indicate particle separation efficiency increases with particle diameter and is consistently higher for greater liquid heights. To demonstrate the reproducibility of our results, three data points at each condition, collected on different days, are shown and exhibit excellent consistency.

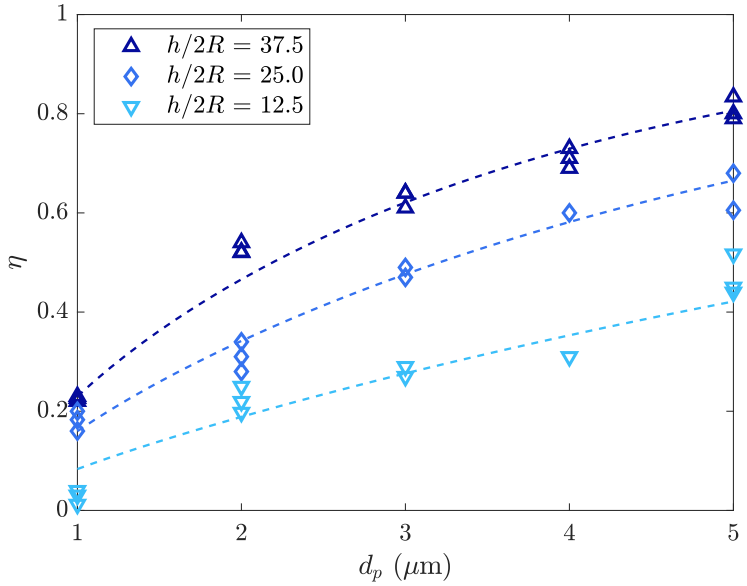

Figure 2. Particle separation efficiency (η) as a function of particle diameter (d_p). The plot presents three datasets corresponding to increasing liquid heights in the tube ($h/(2R)$).

References

[1] Sajeesh P., Sen A.K.: *Particle separation and sorting in microfluidic devices: a review*, Microfluidics and Nanofluidics, 17, 1–52, 2014, Springer.

[2] Charvet A., Bardin-Monnier N., Thomas D.: *Can bubble columns be an alternative to fibrous filters for nanoparticles collection?*, Journal of Hazardous Materials, 195, 432–439, 2011, Elsevier.

[3] Park S.-H., Lee B.-K.: *Development and application of a novel swirl cyclone scrubber: (2) Theoretical*, Journal of Hazardous Materials, 164(1), 315–321, 2009, Elsevier.

[4] Akbar M.K., Ghiaasiaan S.M.: *Monte Carlo simulation of aerosol transport in rising gas bubbles undergoing shape deformation*, Journal of Aerosol Science, 37(6), 735–749, 2006, Elsevier.

[5] Pan W., Chen X., Dai G., Wang F.: *Enhanced effect of bubble deformation on internal particle transport*, Industrial & Engineering Chemistry Research, 59(2), 905–918, 2019, ACS Publications.

[6] Fujiwara K., Yoshida K., Kaneko A., Abe Y.: *Experimental and numerical investigations of aerosol transportation phenomena from single bubbles*, International Journal of Heat and Mass Transfer, 195, 123160, 2022, Elsevier.

[7] Fuchs N.A., Daisley R.E., Fuchs M., Davies C.N., Straumanis M.E.: *The mechanics of aerosols*, American Institute of Physics, 1965.

[8] Cadavid-Rodriguez M.-C., Charvet A., Bemer D., Thomas D.: *Optimization of bubble column performance for nanoparticle collection*, Journal of Hazardous Materials, 271, 24–32, 2014, Elsevier.

[9] Perez A.R., Lind T., Petrov V., Manera A., Prasser H.-M.: *Two-phase hydrodynamics and aerosol mass transfer characterization in pool scrubbing: A simultaneous measurement technique*, Journal of Aerosol Science, 178, 106336, 2024, Elsevier.

[10] Maestri R., Radhakrishnakumar S., Bürkle F., Ding W., Büttner L., Czarske J., Hampel U., Lecrivain G.: *Equilibrium Taylor bubble in a narrow vertical tube with constriction*, Physics of Fluids, 36(3), 2024, AIP Publishing.

Acknowledgments

This work was supported by the German Research Foundation (Deutsche Forschungsgemeinschaft) under project number 459505672.

Dynamics of bubble interface during obstacle interaction

Masoud Outokesh[1*], Mahdi Saeedipour[1], and Mark W. Hlawitschka[2]

[*]E-Mail: masoud.outokesh@jku.at

[1]*Institute of Process Engineering, Johannes Kepler University, A-4040 Linz, Austria.*
[2]*Department of Particulate Flow Modelling, Johannes Kepler University, A-4040 Linz, Austria.*

Abstract
The interaction of bubbles with obstacles is widespread in bubbly systems, especially slurry bubble columns. It affects the performance of these columns by changing the size distribution of the bubble, consequently changing the nature of the column's behavior. As a result, in this study, a small-scale system of interaction of a single rising bubble and the static cylinder was utilized to investigate bubble-splitting behavior to provide an up-scale model in more complex systems. Three distinct regimes are defined based on the daughter bubble's cutting and volume: No-cutting, asymmetry cutting, and symmetry cutting. The result depicted that by shifting from No-cutting to symmetry-cutting cutting, the behavior of the bubble neck shifts from nonlinear to slightly linear. Additionally, the formation of a liquid film during the bubble-splitting cycle is observed in viscous fluid. This identification, alongside future investigation, provides a better understanding of the splitting regime's condition in the variation of the system parameters and the investigation of the behavior of the liquid film thickness.

Introduction

Interaction between bubble and obstacle is extensive and happens inside slurry systems. One of the practical systems in the industry is the Slurry Bubble Columns (SBCRs). These reactors are widely employed in chemical, biochemical, and petrochemical processes, where optimizing gas-liquid-solid interactions is crucial for improving efficiency and reducing environmental impact [1]. In some columns, the obstacle could be defined as a catalysis particle introduced to systems to improve the mass transfer and increase the gas transport by absorption and desorption [2]. Additionally, some internal equipment, like mesh sensors, is utilized to monitor the behavior of the columns and interact with the bubbles. These interactions can generate side effects on the column performance. As a result, identifying and investigating the bubble interaction is crucial.

Wang et al. identify the behavior of the bubbles in contact with the cylinder in highly viscous fluids and define the cutting behavior based on the volume of the bubbles [3]. In addition, the formation of a liquid film thickness is observed and identified by increasing the size of the bubble, which increases the thickness of this film. Jiang et al. also categorized the splitting behavior in the range of the bubble-to-cylinder diameter ratio and bubble Weber number [4]. The bubble Weber number represents the ratio between the bubble inertia and surface tension. The viscosity of the surrounding fluid should also be considered, as it can change the shape and velocity and experience drag force on the bubble. So, to provide better knowledge about the bubble splitting system, this study aims to better understand the geometrical identification of the bubble splitting regime, accomplish the hydrodynamic characterization of the interaction, and conduct a deep investigation of liquid film thickness behavior.

Experimental approach

A square cross-section Plexiglass column is used to analyze the interaction between the bubble and cylinder (Figure 1 (a)). Surrounding fluid properties significantly influence bubble behavior; therefore, different concentrations of Glycerine are mixed in water to produce various fluid specifications. The Morton number ($Mo = g\mu_l^4/\sigma^3\rho_l$) characterizes the surrounding fluid specification. A stainless-still cylinder is fixed above the bubble release point. Bubbles are generated by adjusting the input gas volume by using a precise syringe pump (MicroLab 1000, Hamilton company).

A high-speed camera (IDT high-speed camera, OS II—S8) captures bubble interface motion in 2500 frames per second. A Python script is used to identify the bubble's geometrical parameters, such as

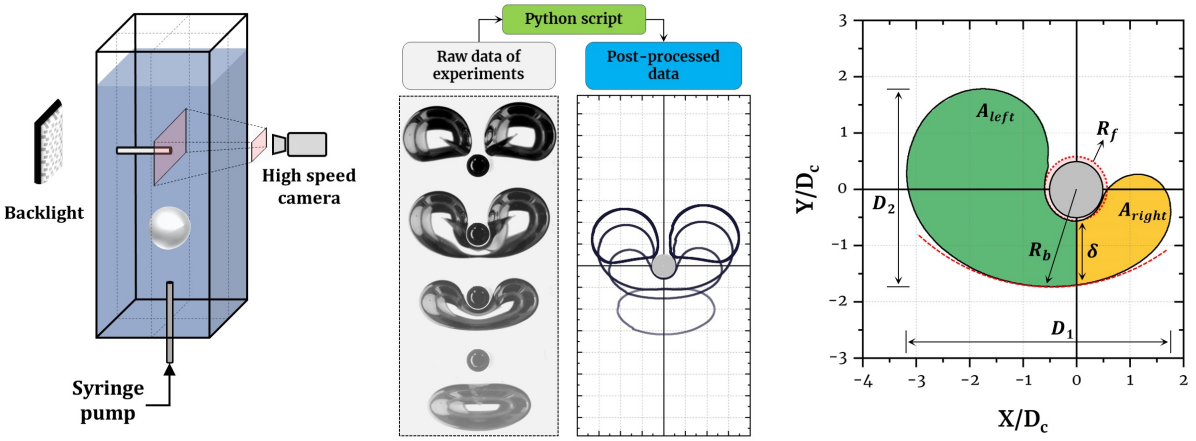

(a) (b) (c)

Figure 1: a) Schematic diagram of the experiment setup. b) Schematic demonstration of relation between raw image result and postprocessing data. c) Geometrical parameter of the system

interface curvature, bubble velocity, aspect ratio, symmetry index, etc (Figure 1 (b)). The bubble's interface is detected by the FIJI application [5] through binarization and edge detection, which creates a cloud of points, locating each pixel of the interface. This data set is filtered and sorted by utilizing a density-based KD-tree approach and DBSCAN algorithms for bubble detection.

As the image sequences are two-dimensional observations of the bubble motion, the aspect ratio of the bubble, $\chi = D_1/D_2$, can define it. Bubble velocity is also determined based on the bubble center velocity. In addition, the bubble neck behind the cylinder is characterized by a δ, ($\delta = R_b - R_f$). Furthermore, the symmetry index determined the area of the bubble in the two side of the cylinder vertical axis ($\xi = (A_{left} - A_{right})/(A_{left} + A_{right})$). All of these parameters are depicted in Figure 1 - c.

Result and discussion

As discussed, the bubble-splitting regimes identified three main regimes named "No-Cutting," in which bubble volume and inertial force are not sufficient to overcome the force balance dominance from surface tension force, and the bubble interface remains uncut. In this situation, bubbles turn around the cylinder and detach from the cylinder vicinity. On the other hand, in the higher bubble volume or velocity, the surface tension force is not sufficient to keep the interface of the bubble, and therefore, the breakup of the interface happens. "Symmetrical cutting" happens when the volume of two daughter bubbles is approximately equal ($\xi \approx 0$). While the difference between the volume of the two split bubbles is considerable, the "Asymmetrical cutting" regime occurs.

The shifting between these regimes also changes the behavior of the bubble neck, δ, from nonlinear in the No-Cutting regime to almost linear behavior in the Asymmetrical cutting, as shown in Figure 2 (a). The larger size of the bubble leads to more considerable lateral shrinkage of the bubble interface during the splitting process, and it can be proved by the increase in the aspect ratio during the bubble splitting cycle in Figure 2 (b). The formation of two equal volumes of the bubble before splitting behind the cylinder creates an equal buoyancy force that leads to stable and clean δ behavior. In contrast, the smaller bubble volume is not adequate to generate enough buoyancy force to deform the interface around the cylinder. As a result, the bubble experiences stagnation and then starts to bypass the obstacle. This behavior would be observed by monitoring the bubble aspect ratio, which increases at first while remaining constant, and when the bubble goes for bypassing, it decreases. The sudden increase in the symmetry index also indicates that the bubble shifted to one side of the cylinder (Figure 2 (c)). This rotation and stagnation leads to the nonlinear behavior of the δ.

In contrast, Asymmetric cutting is the intermediate case where the bubble interface, which is almost large, starts to shrink on both sides of the bubble, while this force is not sufficient to overcome the surface tension. As a result, the bubble experiences stagnation, and the balance between the volume of the two sides of the cylinder is destroyed. So, the instability causes the bubble to rotate partially, increasing the buoyancy force on one side of the bubble. Consequently, the symmetry index started to grow, but due

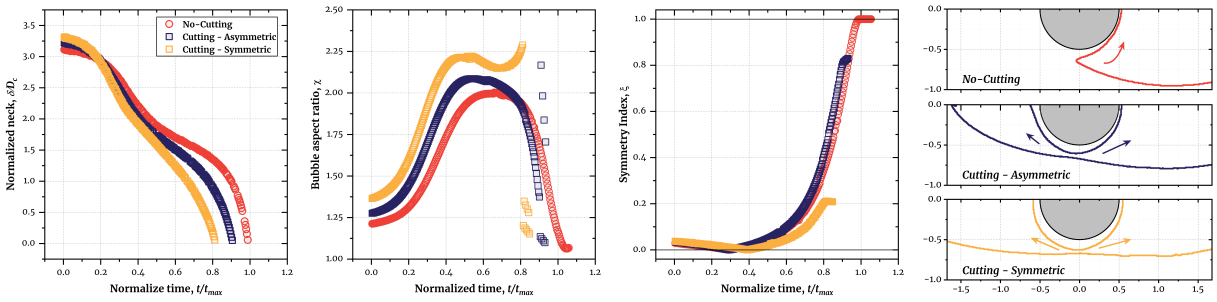

(a) (b) (c) (d)

Figure 2: a) The behavior of the bubble neck, δ, b) bubble aspect ratio, (χ), c) symmetry index, (ξ), and d) interface before splitting in three splitting regime in constant Morton number (Mo = 0.02 - D_c = 1470 μm).

to the larger size of the bubble, it could not find the opportunity to bypass the cylinder, and the bubble split. This partial rotation behavior leads to a shift in the bubble breakup point from the vertical axis in the Symmetry regime toward a smaller bubble in the Asymmetry regime, as depictedin Figure 2 (d). It should be mentioned that, all these cases are investigated in pretty high Morton number and the bubble interface in not in touch with the cylinder wall.

Conclusion

This study investigates the behavior of the bubble interface in the vicinity of an obstacle. These interactions are widespread inside slurry bubble columns, and understanding the bubble-splitting regimes leads to valuable information to categorize the dynamic behavior of such an up-scale and complex environment. Three distinct bubble-splitting regimes are identified and investigated based on the geometrical aspects in the small-scale model for single bubble and cylinder systems. Future studies about the hydrodynamics of this cycle using the Particle Image Velocimetry method (PIV) alongside with computational fluid dynamic (CFD) and the possibility of forming a liquid film and its behavior in different fluid properties can extend the knowledge about this phenomenon.

Acknowledgments

The authors gratefully acknowledge the financial support of the Austrian Science Fund (FWF) through the project PARBUIN (Grant No. P-37055)

References

[1] Mahmoudi S., Hlawitschka M. W.: *Effect of solid particles on the slurry bubble columns behavior–a review*, ChemBioEng Reviews, 9(1), 63–92, 2022.

[2] Alper E., Wichtendahl B., Deckwer W-D.: *Gas absorption mechanism in catalytic slurry reactors*, Chemical Engineering Science, 35(1-2), 217–222, 1980.

[3] Wang S., Rohlfs P., Börnhorst M., Schillaci A., Marschall H., Deutschmann O., Wörner M.: *Bubble cutting by cylinder–elimination of wettability effects by a separating liquid film*, Chemie Ingenieur Technik, 94(3), 385–392, 2022.

[4] Jiang W-T., Luo Q., Liao H-L., Luo Y., Qie F-X., Tan Q-F., Qian Z.: *Mechanism of bubble cutting by fibers: Experiment and simulation*, Chemical Engineering Journal, 478, 147225, 2023.

[5] Schindelin J., Arganda-Carreras I., Frise E., Kaynig V., Longair M., Pietzsch T., Preibisch S., Rueden C., Saalfeld S., Schmid B., et al.: *Fiji: an open-source platform for biological-image analysis*, Nature Methods, 9(7), 676–682, 2012.

Influence of the solvent hydrodynamics on the phase residence time distribution behaviour in a solid-liquid counter-current screw-extraction process

A. Lehr[1*], R. K. Bhuva[1], G. Janiga[1], A. Seidel-Morgenstern[2], D. Thévenin[1]

*E-Mail: annemarie.lehr@ovgu.de

[1] Laboratory of Fluid Dynamics and Technical Flows, University of Magdeburg, Universitätsplatz 2, 39106 Magdeburg, Germany

[2] Max Planck Institute for Dynamics of Complex Technical Systems, Sandtorstraße 1, 39106 Magdeburg, Germany

1. Introduction

A continuous solid-liquid counter-current extraction process was studied concerning the specific phase residence time behaviour (RTD) by Lehr et al. [1]. Experiments conducted in a glass extractor have been performed with water as solvent to investigate the extraction process of the valuable substance artemisinin from *Artemisia Annua L.* (ARTE) leaves, recommended as a standard anti-malaria treatment by the World Health Organisation [2]. However, water is not an appropriate solvent for extracting artemisinin. It was only used due to safety restrictions of the suitable solvent toluene [3]. To better capture during the RTD measurements the kinematic viscosities of the practically relevant solvent toluene pre-heated water in new experiments described here.

2. Materials and experimental setup

Dried ARTE leaves (Médiplant, Conthey, Switzerland) were pulverised into fine particles with an average diameter of 0.2 mm using a centrifugal grinder (ZM-200, Retsch, Haan, Germany). Concerning the solvent, the only hydrodynamical difference between water and toluene with constant reactor dimensions comes from their difference in kinematic viscosity (at 20°C: 32%, see **Table 1**). To overcome this limitation, the process was carried out at a temperature of 38°C, where the kinematic viscosity of water is similar with that of toluene (at 20°C), leading to identical Reynolds numbers.

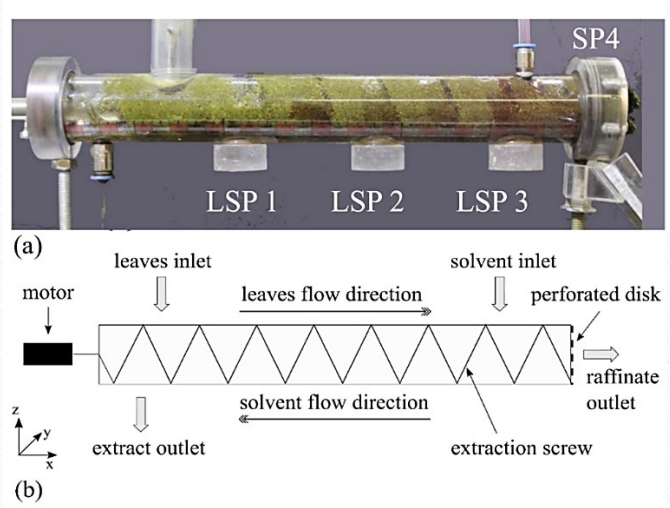

Figure 1. (a) Glass extractor with three lower sampling points (LSP) and the raffinate outlet (SP 4), (b) schematical representation of the process key features

Table 1. Adaption of kinematic viscosity of water to the efficient solvent toluene [4].

Parameter		Toluene	Water	Unit
kinematic viscosity	υ	0.68 (20°C)	1.002 (20°C)	$\cdot 10^{-6}$ m²/s
			0.683 (38°C)	$\cdot 10^{-6}$ m²/s

The experimental device was operated in a counter-current mode as reported in Lehr et al. [1]. As illustrated in **Figure 1 (a)**, the solid ARTE leaves were fed into the extractor using a screw feeder (DSR28, Brabender, Duisburg, Germany) at the left end of the extractor. The screw mechanism induced the movement of the leaves while they gradually absorb the employed solvent (water) along the entire length of the extractor. As the material approaches the perforated disk (PD) on the right, it forms a compressed cake. Close to this position the solvent water was introduced using a frequency-controlled peristaltic pump (PD-5201, Heidolph, Kelheim, Germany). The process temperature of water was regulated with a temperature control unit (93704220122 VT2, ANTON PARR GmbH, Graz, Austria), maintaining a stable temperature over time. Due to the compression cake at the perforated disk, the solvent flows in counter-current mode to the leaves, extracting the valuable component artemisinin until exiting at the extract outlet on the left. The process can be operated in steady state, ensuring continuous flow rates at both, extract and raffinate outlets.

3. Residence time distribution theory and measurement

The residence time distribution measurements in the extractor have been conducted using the stimulus-response method, introducing a pulse-wise input of tracer material. For constant mass flow rates of the involved phases, the recorded tracer concentration $c(t)$ at the four sampling points SP, as shown in **Figure 1 (a)**, are expressed as the normalised RTD function $E(t)$ which follows from Eq. (1) [5]:

$$E(t) = \frac{c(t)}{\int_0^\infty c(t)\,dt} \text{ with } \int_0^\infty E(t)dt = 1 \tag{1}$$

The mean residence time $\bar{\tau}$ and the variance σ^2 can be determined from $E(t)$ using Eqs. (2) and (3):

$$\bar{\tau} = \int_0^\infty t \cdot E(t)dt \tag{2}$$

$$\sigma^2 = \int_0^\infty (t-\tau)^2 \cdot E(t)dt \tag{3}$$

The standard deviation σ of the RTD curve is given by the square root of the variance σ^2. A number of theoretical stages N can be calculated using Eq. (4) [6]:

$$N = \left(\frac{\bar{\tau}^2}{\sigma^2}\right) \tag{4}$$

If N = 1 the flow behaviour corresponds to that of an ideal continuous stirred-tank reactor (CSTR). In contrast, a high N value represents the characteristics of an ideal plug-flow tubular reactor (PFTR), where $\sigma^2 = 0$ and $N \rightarrow \infty$ [5].

For the RTD measurements, the extractor was operated continuously for at least 30 min to ensure steady-state conditions, with all sampling ports sealed to prevent any disturbances. For solid-phase RTD measurements, spherical black mustard seeds (1.6 ± 0.4 mm) were used as tracers. A 1.5 g pulse was introduced at the leaves inlet where seeds immediately adhered to the solvent-soaked leaves. Three identical runs were conducted to assess the RTD behaviour at all sampling points. Samples were taken every minute from the three lower sampling points (LSP 1–3) and the raffinate outlet (SP 4). The solvent pump and screw motor were momentarily paused for each sampling. The collected mustard seeds were sieved, air-dried for one day, and weighed. For solvent RTD measurements, a 10 wt.% sodium chloride solution (99.5 % purity, Sigma-Aldrich, Merck, Darmstadt, Germany) was used. A 30 ml pulse was introduced and 10 ml samples were collected every minute at the extract outlet for three identical runs.

4. Results and discussion

4.1 RTD of the solvent (water)

The RTD of water as a solvent (indicated as l for liquid) was measured at 38°C and compared to the RTD at 20°C from Lehr et al. [1]. The resulting tracer concentration curve is used to calculate the RTD distribution (Eq. 1). As shown in **Figure 2** the RTD curve for 38°C is similar to the RTD curve for 20°C, with a slight peak shift to the right but no change in maximum intensity. Minimal deviations between the three repetitions, shown as error bars, indicate a high reproducibility. **Table 2** demonstrates that the standard deviation remains identical (20°C and 38°C: 2.5 min), while the mean residence time is decreased by only 3% (0.1 min = 6 s). The resulting stage number remains consistent at N_l = 3 for both setups, indicating a near-CSTR behaviour.

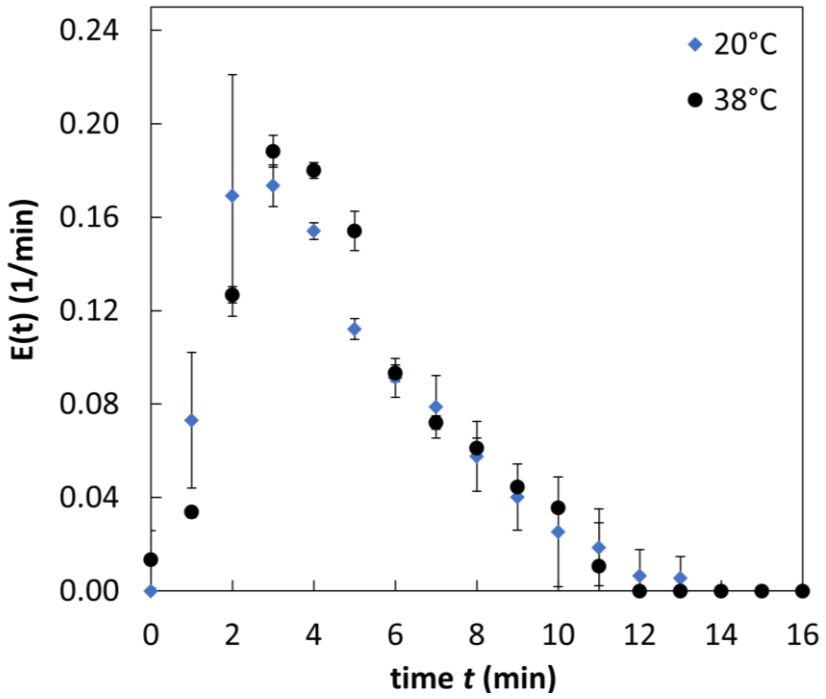

Figure 2. RTD curves of the solvent (water) at T = 20°C (blue) and at T = 38°C (black).

Table 2. Residence time distribution of the solvent water at T = 20°C or 38°C.

Parameter		T = 20°C	T = 38°C	Unit
mean residence time	$\bar{\tau}_l$ {Eq. (2)}	4.5	4.4	min
standard deviation	σ_l {Eq. (3)}	2.5	2.5	min
theoretical number of stages	N_l {Eq. (4)}	3	3	-

4.2 RTD of the solvent-soaked leaves

As depicted in **Figure 3**, the RTD of the solid leaves (indicated as s for solid) at LSP 1 and LSP 3 show a strong correlation between 20°C and 38°C, whereas deviations are noted at LSP 2 and SP 4, with the largest difference of 23% occurring at SP 4. This deviation is influenced by the compression cake at the PD, likely due to variations in cake humidity. Since the extraction process is expected to be finished in front of the PD, this deviation is not considered relevant for process characterisation. **Table 3** shows slight variations in the stage number N_s for 38°C, but with no noticeable change regarding flow characteristics.

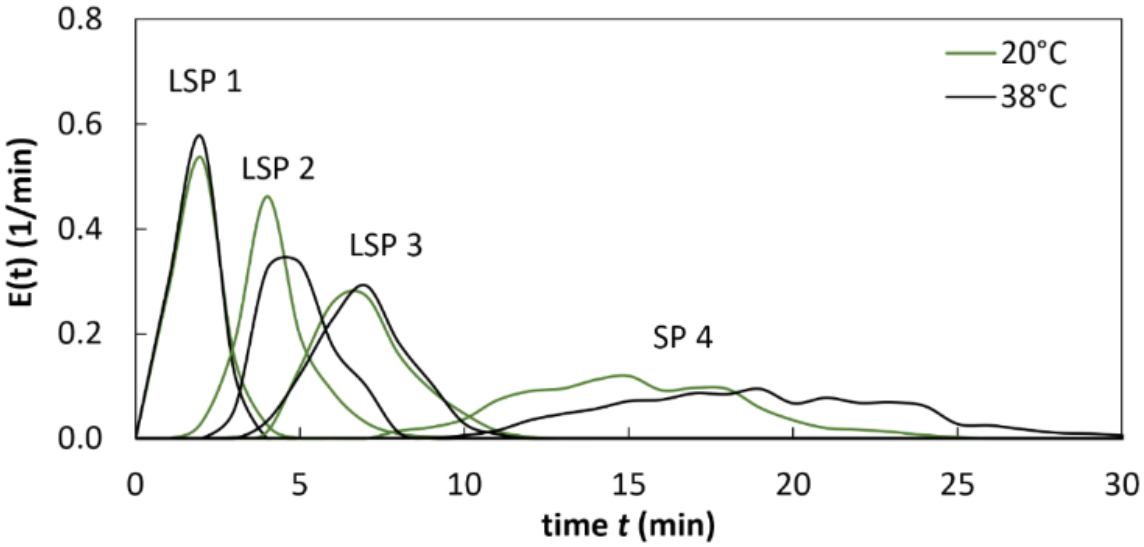

Figure 3. RTD curves for the solvent-soaked ARTE leaves at T = 20°C (green) and 38°C (black).

Table 3. RTD of the A. annua leaves with water as solvent at T = 20°C or 38°C.

T	Parameter	LSP 1	LSP 2	LSP 3	SP 4	Unit
20°C	$\overline{\tau_s} \pm \sigma_s$ {Eqs. (2), (3)}	1.6 ± 0.7	4.6 ± 1.0	7.3 ± 1.3	15.5 ± 3.2	min
	N_s {Eq. (4)}	5	21	33	23	
38°C	$\overline{\tau_s} \pm \sigma_s$ {Eqs. (2), (3)}	1.8 ± 0.6	5.0 ± 1.0	6.9 ± 1.3	18.9 ± 3.9	min
	N_s {Eq. (4)}	9	25	28	23	

5. Conclusion

The residence time distribution measurements of solvent and solvent-soaked leaves in a continuous counter-current extraction process reveal only minimal deviations between water at a process temperature of 20°C and 38°C. This confirms the transferability of hydrodynamic results conducted with water to the actual extraction process using toluene and validates water as a safe alternative for investigating certain sub-processes.

Acknowledgments

The authors gratefully acknowledge the funding by the European Regional Development Fund (ERDF) within the International Max Planck Research School for Advanced Methods in Process and Systems Engineering (IMPRS ProEng).

References

[1] Lehr, A., Vu, G. T., Janiga, G., Seidel-Morgenstern, A., Thévenin, D.*: Experimental investigation of the residence time distribution in a screw-type apparatus designated to extract artemisinin,* Chemical Engineering and Processing - Process Intensification 187, 109337, 2023.

[2] World Health Organisation: *World Malaria Report 2024*, Geneva, 2024.

[3] Liu, Y., Lü, H., Pang, F., *Solubility of Artemisinin in Seven Different Pure Solvents from (283.15 to 323.15) K,* Journal of Chemical & Engineering Data 3/54, pp. 762–764, 2009.

[4] Anton Paar GmbH: Anton Paar Wiki. https://wiki.anton-paar.com/en/tables/, accessed 4 Nov 2024.

[5] Levenspiel, O.: *Chemical Reaction Engineering,* John Wiley & Sons, New York, 1999.

[6] MacMullin, R., Weber, M.: *The theory of short-circuiting in continuous-flow mixing vessels in series and kinetics of chemical reactions in such systems,* Transactions of American Institute of Chemical Engineers 2/31, pp. 409–458, 1935.

Experimental approach for measuring aerosol inhalation dose in enclosed environments

Marco A. Cavagnola[1, 2*], Amar Aldnifat[1, 2], Holger Kryk[1], Uwe Hampel[1, 2] and Gregory Lecrivain[1]

*E-Mail: m.cavagnola@hzdr.de

[1] *Institute of Fluid Dynamics, Helmholtz-Zentrum Dresden-Rossendorf, Bautzner Landstraße 400, 01328 Dresden, Germany*

[2] *Chair of Imaging Techniques in Energy and Process Engineering, Technische Universität Dresden, 01062 Dresden, Germany*

Introduction

Inhalation of aerosols has proven to have a direct effect on health [1]. Inhalation of aerosols can be quantified by applying the inhalation dose concept. The inhalation dose D_i, can be simply defined as the amount of aerosols inhaled by an individual i in the exposure time interval t_e. Mathematically, it can be expressed as [2]

$$D_i = \int_{t_0}^{t_1} Q_i \cdot C(\boldsymbol{x}, t) \cdot dt, \tag{1}$$

where Q_i is the pulmonary ventilation rate of the individual i, $C(\boldsymbol{x}, t)$ the aerosol concentration at the inhalation point $\boldsymbol{x}$ at time t and $t_1 - t_0 = t_e$ is the exposure time. Experimental approaches to establishing the inhalation dose are limited not only by technical challenges but also by ethical and health concerns related to the involvement of human participants [3]. As a result, various alternatives have been developed to quantify the inhalation dose. The most common approach involves applying a simplification of Equation (1). Another alternative is the use of breathing thermal manikins (BTMs), which simulates human breathing and thermal plumes to assess inhaled aerosols. However, none of these methodologies fully capture human breathing dynamics: simplified equations overlook patterns and plumes, while BTMs fail to replicate physiological changes and fluctuations [4-5].

In this work, we aim to develop an experimental methodology for measuring the inhalation dose that addresses these limitations. The key innovation lies in its application to real human participants, allowing for the consideration of fluctuations in the breathing cycle and their effects on aerosol distribution. The methodology poses no health risks to participants and is suitable for measuring inhalation doses in everyday situations with varying air mixing conditions. Ethical and health concerns were thoroughly addressed. For validation, we constructed an experimental setup in a demonstrator room. The inhalation dose of an individual was measured in three scenarios with different airflow conditions. Additionally, the aerosol protection factor was calculated for each scenario to indicate the reduction in inhaled dose based on indoor airflow conditions.

Methodology

The methodology involves aerosolizing a known quantity of magnesium-water solution, where the water evaporates, leaving magnesium nuclei as tracers that follow the room's airflow. The magnesium aerosol is then collected through the inhaler's breathing action, with the inhaler positioned at known spatial locations (**Figure 1**). Collection is achieved using removable filters placed in the inhaler's breathing mask. The magnesium is extracted from the filters and quantified using inductively coupled plasma mass spectrometry (ICP-MS) for precise measurement of cations, including magnesium (Mg), sodium (Na), potassium (K), calcium (Ca), copper (Cu), and zinc (Zn), which also helps identify contaminants (**Figure 2**).

Three indoor airflow scenarios were implemented to measure inhalation dose: (1) No forced ventilation; (2) Forced ventilation, using an axial fan (VE-5931, Tristar) to generate turbulent mixing;

and (3) Forced ventilation with air filtration, using an air purifier (AirgoClean 350 E, Trotec) for aerosol removal. Each scenario involved five sets of four experiments (at 0.5, 1, 2, and 3 m) plus a control to measure background aerosol levels.

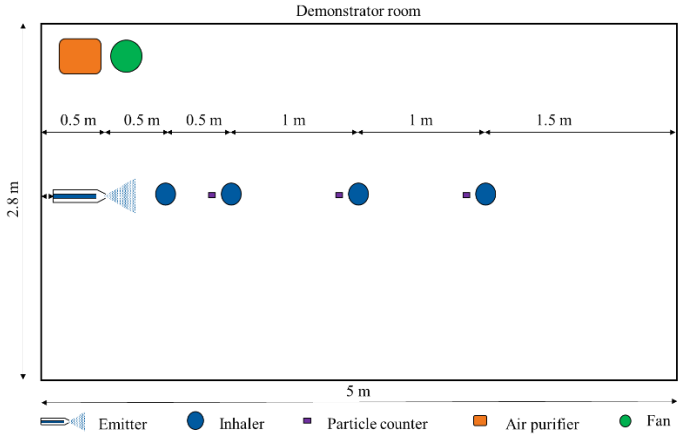

Figure 1. Diagram of the experimental setup. For every scenario the inhaler is located at 0.5, 1, 2 and 3 m from the aerosol generator.

Figure 2. **A**: Aerosol generator. **B**: Mask filter. **C**: Filter used for collecting the aerosols. Filters are placed in the breathing masks used by the individual (**E**) **D**: Demonstrator room. **F**: Magnesium extraction. **G**: ICP-MS.

Results

The inhalation dose results obtained by ICP-MS and the protection factor (PF), which compares aerosol exposure between two conditions [6], are here presented to evaluate dose variations across scenarios. The protection factor is calculated as [7]:

$$PF(x) = \frac{\int_{t_0}^{t_1} C(ref,t) \cdot dt}{\int_{t_0}^{t_1} C(x,t) \cdot dt}, \quad (2)$$

where the numerator represents the aerosol concentration over the exposure time in a reference scenario, and the denominator represents the aerosol concentration in a different scenario.

Figure 3 shows the inhalation dose (µg of magnesium) versus the inhaler's distance from the emitter across all scenarios. In Scenario 1 (**Figure 3A**), the dose decreases with distance, while in Scenarios 2 and 3 (**Figure 3B-C**), it is lower overall and less influenced by distance. **Figure 4A** shows that protection factors (PF) increase with distance, particularly in Scenario 1, where PF(3m) ≈ 6, meaning the inhalation dose at 3 m is six times lower than at 0.5 m. In Scenarios 2 and 3, PF peaks at ~1.5, indicating that forced ventilation minimizes the effect of distance. **Figure 4B** compares Scenarios 2 and 3 to Scenario 1, showing that forced ventilation is most effective at close range, with PF(0.5m) = 17.5 for Scenario 3 and PF(0.5m) = 7.5 for Scenario 2. This demonstrates that the air purifier offers strong protection at short distances but loses efficiency as distance increases.

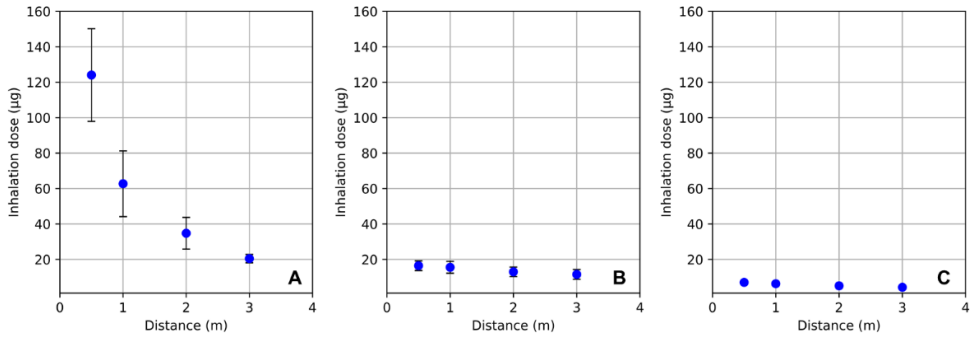

Figure 3. ICP-MS measurements with standard deviation indicated by error bars for scenarios 1 (**A**), 2 (**B**) and 3 (**C**).

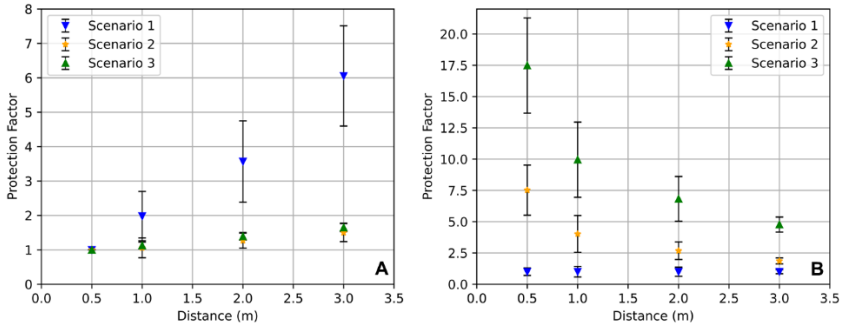

Figure 4. Protection factors within each scenario as a function of the distance (**A**) and protection factors across different scenarios evaluated at the same distance (**B**).

Conclusions

A methodology for measuring inhalation dose involving real people has been developed. This approach extends beyond lab conditions and can be applied in everyday situations. The inhalation dose was compared across scenarios with varying air mixing, emphasizing the impact of distance from emitter to receiver and differences in ventilation types.

References

[1] Arfin, T., Pillai, A. M., Mathew, N., Tirpude, A., Bang, R., & Mondal, P.: *An overview of atmospheric aerosol and their effects on human health*, Environmental Science and Pollution Research, 30(60), 125347–125369, 2023.

[2] Poon, C. K. M., & Lai, A. C. K.: *An experimental study quantifying pulmonary ventilation on inhalation of aerosol under steady and episodic emission*, Journal of Hazardous Materials, 192(3), 1299–1306, 2011.

[3] Rom, W. N., Boushey, H., & Caplan, A.: *Experimental human exposure to air pollutants is essential to understand adverse health effects*, American Journal of Respiratory Cell and Molecular Biology, 49(5), 691–696, 2013.

[4] Sun, S., Li, J., & Han, J.: *How human thermal plume influences near-human transport of respiratory droplets and airborne particles: A review*, Environmental Chemistry Letters, 19(3), 1971–1982, 2021.

[5] Van Den Bosch, O. F. C., Alvarez-Jimenez, R., De Grooth, H.-J., Girbes, A. R. J., & Loer, S. A.: *Breathing variability—Implications for anaesthesiology and intensive care*, Critical Care, 25(1), 280, 2021.

[6] Mittal, R., Meneveau, C., & Wu, W.: *A mathematical framework for estimating risk of airborne transmission of COVID-19 with application to face mask use and social distancing*, Physics of Fluids, 32(10), 101903, 2020.

[7] Lommel, M., Froese, V., Sieber, M., Jentzsch, M., Bierewirtz, T., Hasirci, Ü., Rese, T., Seefeldt, J., Schimek, S., Kertzscher, U., & Paschereit, C. O.: *Novel measurement system for respiratory aerosols and droplets in indoor environments*, Indoor Air, 31(6), 1860–1873, 2021.

Phase Tracking in Gas-Solid Fluidized Beds via Electrical Capacitance Volume Tomography and Borescopic High-Speed Camera Imaging

L. Lindmüller[1*], S. Heinrich[1], J. Theuerkauf[2], Y. Yao[3], Y. Fan[3]

*E-Mail: lennard.lindmueller@tuhh.de

[1] Hamburg University of Technology, Hamburg, Germany

[2] Engineering and Process Science, Core R&D, The Dow Chemical Company, Midland, MI, USA

[3] Engineering and Process Science, Core R&D, the Dow Chemical Company, Lake Jackson, TX, USA

Introduction

Fluidized bed systems have been used in industry for around 100 years. Bubbling fluidized beds (BFB) are well understood, however obtaining three-dimensional data of particle and bubble movements with methods like positron emission particle tracking (PEPT) [1] or magnetic resonance imaging (MRI) [2] is complex and very costly. In the case of circulating fluidized beds (CFB), the flow behavior of single particles and clusters in the riser section is still not fully understood. The reasons for this are complex and fast particle movements, which are hard to track with most sensors, especially for Geldart group A particles. For model development and improvement of existing processes, a better understanding of this topic is of great interest.

Methodology

For this work, electrical capacitance volume tomography (ECVT) is used in a BFB to evaluate bubble diameters, frequency, and rise velocity. The ECVT sensor (Model 4RD Cold Flow by Tech4Imaging) consists of 24 electrodes (divided into four axial levels), which generate a three-dimensional image of the solids concentration from capacitance data. This results in a 20x20x20 grid in a 10 cm wide bubbling bed, with a sensor height of 20 cm. Based on the reconstructed sensor data, a new phase detection method was developed, which more fully utilizes the three-dimensional potential of the sensor [3]. With this method, the bubble boundaries and velocities could be accurately detected. The obtained data was validated by comparisons with capacitance probes with synthetic data (virtual, rectangular bubbles). **Figure 1** shows two different virtual bubbles, which were identified regarding size, position and rise velocity.

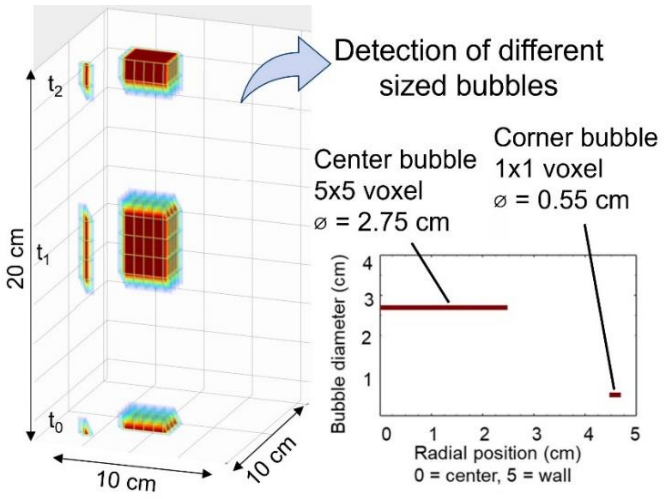

Figure 1. Left: Two detected virtual rising bubbles. Transparent voxels were not detected as bubbles. Colored voxels show bubble phase. The color scale is only used for motion visualization. Right: Bubble diameter and average radial position of virtual bubbles. Figure adapted from [3].

In the CFB system, the experiments focus on fluidization in the fully developed region of an 8 m high and 0.1 m diameter riser with Geldart group A particles. The ECVT and capacitance probe measurements had comparable radial and axial solids volume fraction trends. Variations in gas velocity, solid circulation rate, and total particle holdup result in different axial and radial concentrations in the riser. For the tracking of single particles, borescopic high-speed camera particle tracking velocimetry (PTV), as seen in **Figure 2, left** is used (Camera model: NX4-S2 by IDT). A light source is placed 4 mm in front of the borescope lens. The camera's focus is adjusted to 1 – 2 mm to the lens. At a used frame rate of 15600 fps, the image resolution is 192 x 128 px, which corresponds to an image of 1.2 x 0.8 mm.

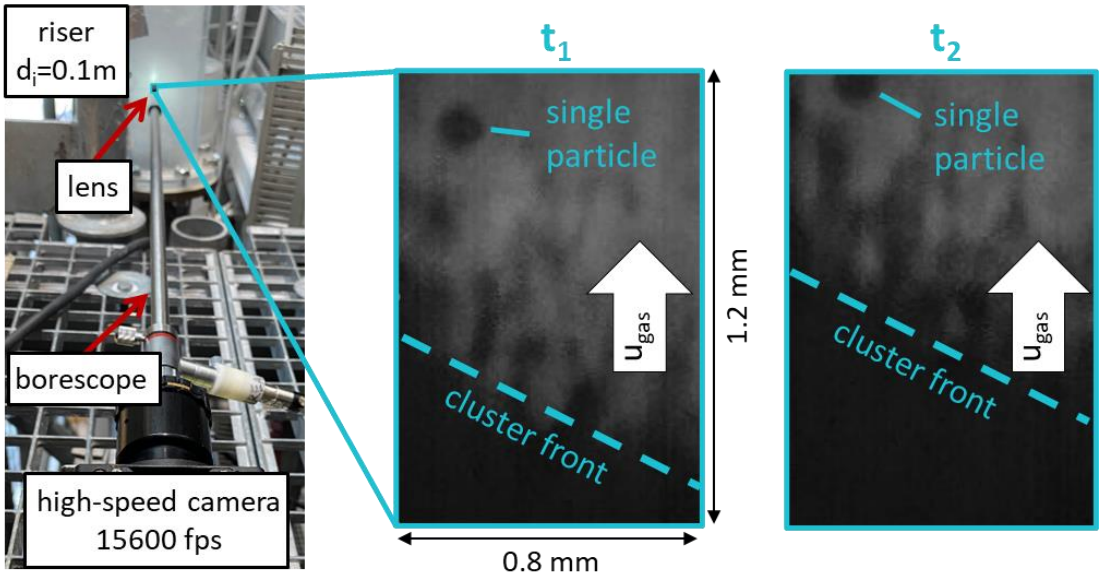

Figure 2. Left: High-speed camera with borescope connected to CFB riser. Right: Images of single particles and cluster captured by high-speed camera at radial center of riser, at two frames t_1 and t_2.

Results - Bubble Tracking

Due to the three-dimensional nature of the novel bubble detection technique, insight into the directional tendencies of detected bubbles can be gained. For example, bubble migration toward the radial center of the bed, as well as radial and axial bubble coalescence, and splitting, are more evident from the trends that are producible with this method [3]. Exemplarily, higher bubble diameters in **Figure 3** are seen in the reactor center since radial bubble coalescence yields wider bubbles in this area. Furthermore, the maximum diameter is not detected at the highest axial position (26 cm) but at a lower position (17 cm) due to bubble splitting. This effect was also observed with quartz sand and FCC.

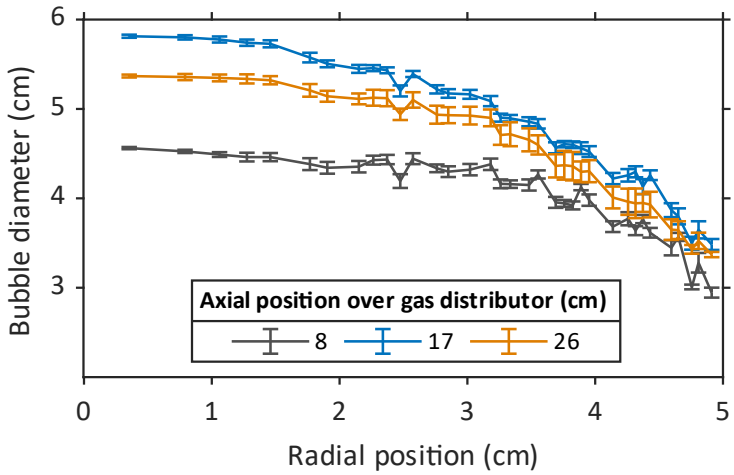

Figure 3. Bubble diameters over radial position in a BFB (bed material: glass beads, d_{Sauter} = 263 µm, resting bed height: 30 cm, u_g/u_{mf} = 3).

Results - Particle Tracking

With borescopic PTV, particle trajectories of Geldart group A particles (FCC) were evaluated at different radial positions in a CFB riser. Single particles and particle clusters were detected individually in each frame, as shown in **Figure 2**, **right**. As the first step of this PTV study, the focus is on upward particle movement, which predominantly occurs in the core zone. Upward trajectories with deviations up to a 20° angle were considered. Downward and sideward particle movements as seen in the wall zone were neglected. For each radial position, 1000 frames were evaluated. **Figure 4** shows particle velocities for three gas velocities (2.3, 3 and 4 m/s) at different radial positions. In the core flow (radial positions: 0 - 3 cm), $U_{particle}/U_{gas}$ was constant at around 0.7 for all three gas velocities.

At 4 cm, particle velocities decrease due to the wall effect. This corresponds to a typical core-annulus flow [4]. At the wall (radial position: 5 cm), partially particle downward movement, caused by wall friction was observed. Due to high solids concentration at the wall, PTV could not be conducted with the back light setup. In the core zone, the tracked particle clusters had comparable rise velocities to single particles.

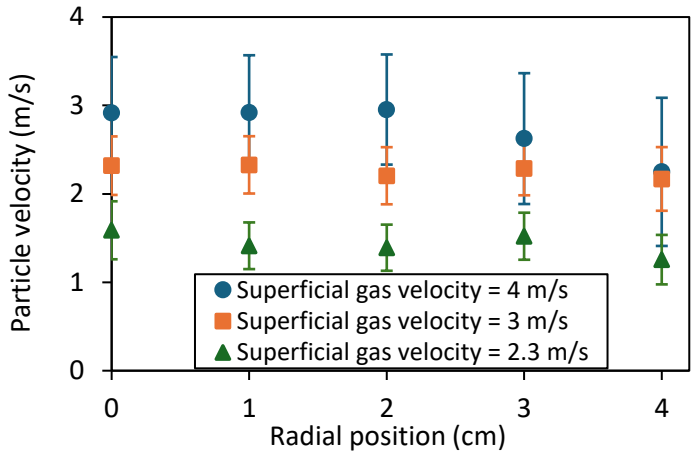

Figure 4. Particle velocities of Geldard A particles (FCC) at different gas velocities and radial positions in fully developed region of CFB riser (h = 8 m, d_i = 10 cm), measured with borescopic high-speed camera PTV. Only upward movement was evaluated.

Outlook

To validate the bubble tracking method for BFBs, a comparison of ECVT with magnetic resonance imaging (MRI) will be conducted at the Institute of Process Imaging at Hamburg University of Technology. For fast fluidization, the focus will be on the wall zone. Instead of a back light, a front light will be used for the high-speed camera imaging, to capture single particles and particle clusters. Further, PTV will be compared to particle image velocimetry (PIV). The particle and cluster movement data will then be used as validation for CFD-DEM simulations.

Funding: The Dow Chemical Company, Lake Jackson, TX, USA.
Project partner: University of Michigan, Ann Arbor, MI, USA.

References

[1] Stein, M., Ding, Y., Seville, J., Parker, D.: *Solids motion in bubbling gas fluidised beds.* Chemical Engineering Science, 55, 5291–5300, 2000.

[2] Penn, A., Boyce, C.M., Kovar, T., Tsuji, T., Pruessmann, K.P., Müller, C.R.: *Real-time magnetic resonance imaging of bubble behavior and Particle velocity in fluidized beds*, Industrial & Engineering Chemistry Research, 57, 2018.

[3] Watson, B., Lindmüller, L., Heinrich, S., Theuerkauf, J., Yao, Y., & Fan, Y.: *Dynamic bubble tracking in fluidized beds via electrical capacitance volume tomography*. Chemical Engineering Journal, 487, 150461, 2024.

[4] Shaffer, F., Gopalan, B., Breault, R. W., Cocco, R., Karri, S. R., Hays, R., Knowlton, T.: *High speed imaging of particle flow fields in CFB risers*. Powder Technology, 242, 86-99. 2013.

Millimeter-Wave FMCW Radar for Industrial Gas and Heating Process Monitoring

F. Schenkel[1*], J. Mahendran[1], J. Schorlemer[1], D. Tsukanova[1], T. Musch[2], A. Dieguez-Alonso[3], N. Vorhauer-Huget[4], C. Schulz[1], I. Rolfes[1], and I. Rolfes[2]

[*]E-Mail: francesca.schenkel@rub.de

[1]*Institute of Microwave Systems, Ruhr University Bochum, Universit¨ atsstraße 150, 44780 Bochum, Germany*
[2]*Institute of Electronic Circuits, Ruhr University Bochum, Universit¨ atsstraße 150, 44780 Bochum, Germany*
[3]*Laboratory of Transport Processes, TU Dortmund University, Emil-Figge-Straße 68, 44227 Dortmund, Germany*
[4]*Chair of Thermal Process Engineering , University of Magdeburg, Universit¨ atsplatz 2, 39106 Magdeburg, Germany*

Introduction

The adaptability of radar systems, attributable to their compact design and mobility, leads to an expansion of their applications across various industries. The impact of climatic conditions on radar signal behavior poses a central challenge in radar technology, given the significant alterations to the propagation characteristics of electromagnetic waves under different temperature and humidity conditions. This is particularly relevant in industrial and outdoor applications, where environments are often dynamic and demanding. In industries where gas leaks pose significant hazards, radar systems offer a non-invasive monitoring of gas fluctuations. Even small deviations in gas levels or structural integrity can lead to significant consequences, as changes in temperature and humidity can affect the accuracy of gas detection.The previously mentioned application scenarios employ millimeter wave approaches, as traditional techniques have limitations that are too high to adequately measure such phenomena, and therefore, they are not very effective in terms of resolution and sensitivity [1]. Millimeter-wave FMCW radar (68–92 GHz) [2] is well-suited for this task due to its high sensitivity and stability. The measurement concept enables a precise and contactless approach to characterize both the propagation properties of the electromagnetic wave and the dielectric behavior of the air. This study investigates the influence of environmental conditions on radar-based gas detection and process control. Controlled measurements characterize electromagnetic wave propagation and dielectric behavior under varying thermal and humidity conditions. Additionally, experimental data from heating processes demonstrate the radar system's potential for industrial drying and heating applications.

Measurement Procedure

In commercial FMCW radar applications, target distances are typically measured. However, this study focuses on fixed target measurements, where the distance is known, but the propagation speed may vary. The measurement process consists of four steps: First, a baseline measurement is taken with an unobstructed path, where the propagation speed is near the speed of light. The intermediate frequency signal is analyzed in both magnitude and phase. Next, the measurement is repeated with heating initiated between the radar and the target, altering the air's relative permittivity due to rising gases. The phase shift is then compared to the baseline, allowing visualization of these changes with high precision. We are using a noncommercial monostatic radar sensor from the Ruhr University Bochum. It operates in the frequency range of 68 GHz to 92 GHz. It can reach a measurement frequency of up to 140 Hz, with a chirp length of 4.1 ms. Each measurement contains 4096 samples and with a bandwidth of 24 GHz, a range resolution of 7.5 mm can be reached. More details about the radar sensor can be found in [2] and for the measurement procedure in [3].

Measurements in a controlled Environment

To investigate the impact of temperature and humidity on electromagnetic waves, measurements were conducted in a controlled environment. The radar transmits signals through a dielectric window into a climate chamber, where temperature and humidity are precisely regulated. The goal is to determine refractivity N as a key parameter for characterizing the interaction of electromagnetic waves with air. Refractivity is used because the change of the refractivity index n in gases is generally very small due

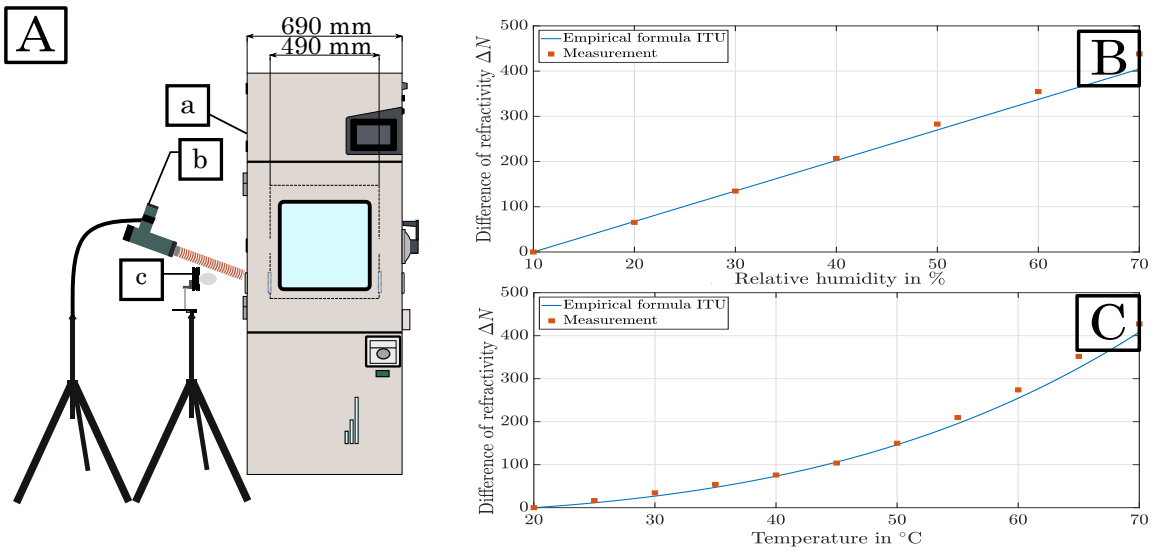

Figure 1: (A)- Measurement setup: (a) climate chamber, (b) hot air blower, (c) radar sensor. (B) Comparison of the refractivity curves at 60◦C as a function of relative humidity. (C)- Comparison of the refractivity curves at 50% relative humidity as a function of the temperature.

to the considerable separation between molecules. It is calculated using the formula $N = (n-1) \cdot 10^6$. For evaluating the refractivity N of radio waves across different atmospheric conditions, the International Telecommunication Union (ITU) has established a globally acknowledged standard formula, primarily focusing on weather-related atmospheric effects on signal propagation at lower frequencies. Valid for temperatures spanning from -40°C to 50°C, this formula takes into account the effects of temperature (T), pressure ($\rho_{\mathrm{x,partial}}$), and humidity on the refractive index.

$$N = 0.766 \cdot \frac{p_{\mathrm{dryAir,\ partial}}}{\mathrm{Pa}} \frac{K}{T} + 0.72 \cdot \frac{p_{\mathrm{waterVapor,\ partial}}}{\mathrm{Pa}} \frac{K}{T} + 3750 \cdot \frac{p_{\mathrm{waterVapor,\ partial}}}{\mathrm{Pa}} \frac{K^2}{T^2} \tag{1}$$

The measurements were conducted in two series. In the first series (Fig. 1 B), relative humidity was varied in steps of 10% from 10% to 70%, while the temperature was kept constant at 60°C (Fig. 1 C). In the second series, the temperature was increased step by step, while relative humidity was held constant at 50%. For each measurement, 1000 consecutive frequency ramps were recorded, and the phase values were averaged to minimize external influences. The results show that refractivity increases almost linearly with relative humidity. Up to 40% humidity, the values match the ITU model quantitatively, while at higher humidity, minor deviations occur. The investigation of temperature dependence revealed an exponential increase in refractivity. Up to 50°C, the measured values align well with the ITU model. Beyond that, slight deviations were observed. These results expanded the ITU model's validity from lower frequency ranges to millimeter-wave frequencies in the W-band. This successful extension allows for accurate compensation of climatic effects and significantly improves the reliability of radar measurements.

Heating Processes

The next step is to provide an outlook on how the sensitive measuring system can be used in industrial processes such as drying and heating. The sensor is fixed in a distance of 0.9 m to the target. The target is an anodized aluminium plate. Between the sensor and the fixed target a conventional hotplate and a cooking pot are placed. To evaluate the radar sensor's functionality for condition monitoring, two representative process conditions were selected, encompassing both conventional kitchen and industrial cooking scenarios. In Scenario I, the hotplate was activated without a cooking vessel and tested at four Heating Levels: Level 0 (inactive), Level 1 (low), Level 5 (medium), and Level 9 (high). Scenario II examined a pot of rapeseed oil, which was heated to a maximum of 220°C at Level 9, corresponding to its smoke point—a fire hazard in household settings. For each Heating Level, 10,000 measuring ramps were conducted. The FMCW radar is capable of transmitting and receiving 140 measuring ramps per second. A summary of all measurements is presented in Fig. 2, illustrating the two Scenarios (I-II). To mitigate

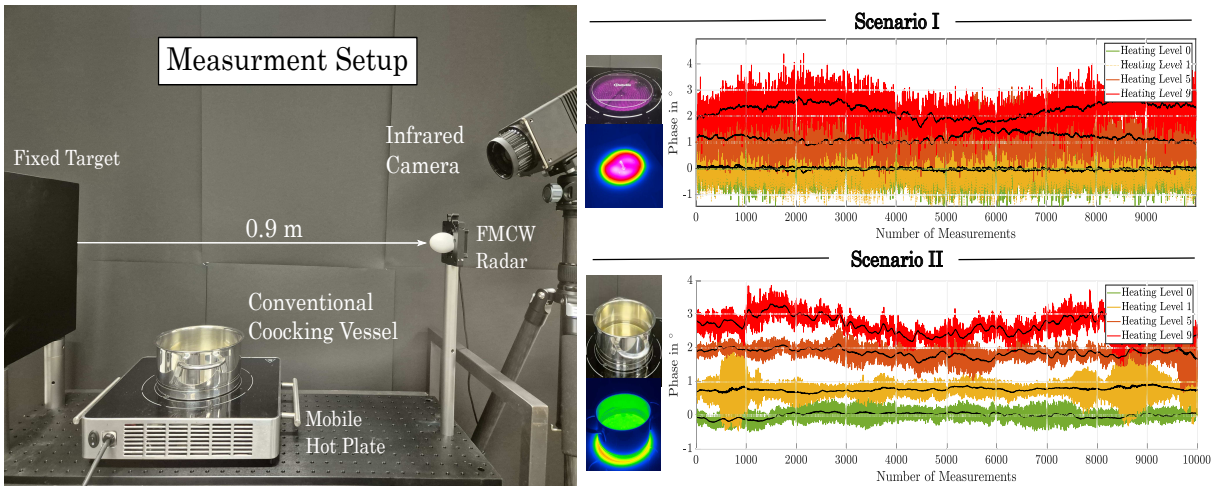

Figure 2: Measurement setup (left), with a fixed target (anodized aluminum plate), a conventional hotplate and cooking pot and FMCW radar. An infrared camera is used for contactless temperature control. Measurement results (right), with four levels: Heating Level 0 (green), Heating Level 1 (yellow), Heating Level 5 (orange) and Heating Level 9 (red).

variability in phase measurements, a moving average over 100 values was calculated and plotted as a black line. To ensure the comparability of the scenarios, the mean value of each baseline measurement was subtracted from all measurements. This approach ensures that the initial phase of the system is irrelevant. In Scenario I, the heating plate was set to Level 1. The maximum temperature reached by the hotplate was 142°C. A comparison of the measured phase with the baseline measurement reveals minimal discrepancy. The heat emitted by the plate is insufficient to alter the dielectric properties of the surrounding air. The measured phase exhibits an increase in both cases. However, what is particularly noteworthy in Scenario I is that a wave-like pattern of the phase can be observed over time at higher heat levels. This is attributed to the fact that the cooking zone of heating plates undergo a cycling process over time, alternating between active and inactive states. Scenario II involves the heating of rapeseed oil. Rapeseed oil begins to emit smoke at a temperature of 220°C. As the heat level rises, the absolute values of the phase increase. Upon reaching the smoke point, the pattern of the phase undergoes a gradual transformation, characterised by the emergence of light plumes of smoke. The measurement data illustrated clearly show a difference between the various scenarios. In the future, this data can be analyzed using various statistical analyses or data-driven algorithms to enable automated and contactless process control.

Conclusion

This study demonstrates the feasibility of using millimeter-wave FMCW radar for process control in industrial environments, particularly for gas monitoring and heating processes. Furthermore, the ability to detect phase variations in different heating scenarios underscores the potential of radar-based sensing for non-invasive and real-time process monitoring. By leveraging advanced signal processing and calibration techniques, these systems can enhance industrial safety, optimize process efficiency, and provide a reliable alternative to conventional gas detection methods. Future research should focus on refining environmental compensation models and integrating machine learning approaches for automated anomaly detection and predictive maintenance in industrial process control.

Acknowledgment

This research was funded by the Deutsche Forschungsgemeinschaft (DFG, German Research Foundation), grant number 422037413–CRC/TRR 287 ”BULK-REACTION”

References

[1] Baer C., Jaeschke T., Pohl N. and Musch T.: *Contactless Detection of State Parameter Fluctuations of Gaseous Media Based on an mm-Wave FMCW Radar*, in IEEE Transactionson Instrumentation

and Measurement, vol. 64, no. 4, pp. 865-872, April 2015.
[2] Pohl N., Jaeschke T. and Aufinger K.: *An Ultra-Wideband 80 GHz FMCW Radar System Using a SiGe Bipolar Transceiver Chip Stabilized by a Fractional-N PLL Synthesizer*, in IEEE Transactions on Microwave Theory and Techniques, vol. 60, no. 3, pp. 757-765, March 2012.
[3] Schenkel F., Schultze T., Baer C., Balzer J. C., Rolfes I. and Schulz C.: *Smoke Detection and Combustion Analysis Using Millimeter-Wave Radar Measurements*, in IEEE Transactions on Microwave Theory and Techniques, vol. 73, no. 1, pp. 361-372, Jan. 2025.
[4] Mahendran J., Schenkel F., Rolfes I. and Schulz C.: *Radar-based Investigation of Electromagnetic Waves Under Different Temperature and Humidity Conditions*, 2024 International Conference on Electromagnetics in Advanced Applications (ICEAA), Lisbon, Portugal, 2024, pp. 603-607.

A Radar Based System for Localizing Marker Particles in Bulk Materials

J. Schorlemer[1*], F. Schenkel[1], N. Karsch[2], E. Gramlich[2], J. Barowski[1], T. Musch[2], and I. Rolfes[1]

[*]E-Mail: Jonas.Schorlemer@rub.de

[1]Institute of Microwave Systems, Ruhr-University Bochum, Universitätsstraße 150, 44780 Bochum, Germany
[2]Institute of Electronic Circuit Technology, Ruhr-University Bochum, Universitätsstraße 150, 44780 Bochum, Germany

Introduction

Acquiring information about the internal kinetic behavior of particles in an industrial reactor is of central importance for optimal reactor design. However, measuring particle movement inside a reactor is a difficult task as it usually requires stopping the process or opening the entire system. A common solution to this problem is therefore, to create a miniaturized replica of the reactor. Particle tracking techniques such as tomography [1] can then be used on such a scaled system. The disadvantage of this approach is that the measurement methods are generally time-consuming, which means that they cannot be used in real-time applications. Furthermore, such methods cannot be scaled to large reactors due to the amount of measurements required. Other techniques such as magnetic particle tracking (MPT) [2] enable the tracking of marker particles in real time, but still suffer from the lack of scalability to larger reactors.
In this paper, we present a principle that relies on the use of radar sensors to solve both the problem of temporal resolution and scalability to large reactors. The aim is to show that radar sensors are capable of localizing a marker particle in a simplified reactor using only a very limited number of antennas. Limiting the number of antennas is of central importance in this context, as it ensures that the measurement principle can be transferred to much larger reactors. The approach presented makes use of the fact that electromagnetic waves are able to penetrate non-metallic materials at low frequencies. Thus, not only spatial information about the marker particles inside the granulate can be collected, but it is also possible to place the antennas at a certain distance from the reactor wall, which prevents possible heat coupling into the measurement electronics. In addition, the use of radar sensors allows the scaling of the penetration depth of the entire system by adjusting the transmission power. Here, the advantage of the radar approach is that the transmission power can be scaled to the reactor dimension by adjusting the external measurement electronics.

Measurement Setup

This section briefly describes the measurement setup used to evaluate the proposed method for particle localization. Figure 1 shows the setup from above in (a) and a three-dimensional sketch in (b). For a more detailed discussion of the signal processing and the measurement procedure, please refer to [3].
The measurement system consists of a rectangular reactor with a width of 30.2 cm or 32 cm, while the height is 30 cm. The reactor is filled with polyoxymethylene (POM) spheres with a diameter of 1 cm, which are used here as bulk material. The walls of the reactor are made of polycarbonate (PC), which is transparent and thus allows to use a camera to examine the first layer of spheres on the reactor wall. The radar system consists of 6 antennas arranged on a ring, with the antennas arranged in pairs on top of each other. The antennas are located at a distance of approximately 60 cm around the reactor. Cross-polarized antennas are used, i.e. each antenna can detect two polarizations, requiring two ports for each antenna. The system operates in a stepped frequency-modulated continuous wave (FMCW) mode, whereby the chirp signal required for this is generated by a two-port vector network analyzer in the frequency range from 1.7 GHz to 8.5 GHz. A switching matrix distributes the signal to the antennas in a time-division multiplexing process so that both, reflection measurements and transmission measurements from one antenna to the other can be recorded. A simple metal sphere with a diameter of 2 cm is used as a marker, which is located directly on the reactor wall in front of the camera system. This configuration allows the marker position calculated by the radar system to be evaluated with an accurate optical measurement system. It should be noted that although the position of the marker is fixed in the plane on the reactor wall, this measurement method can be generalized to any position in the entire reactor. As there is no direct

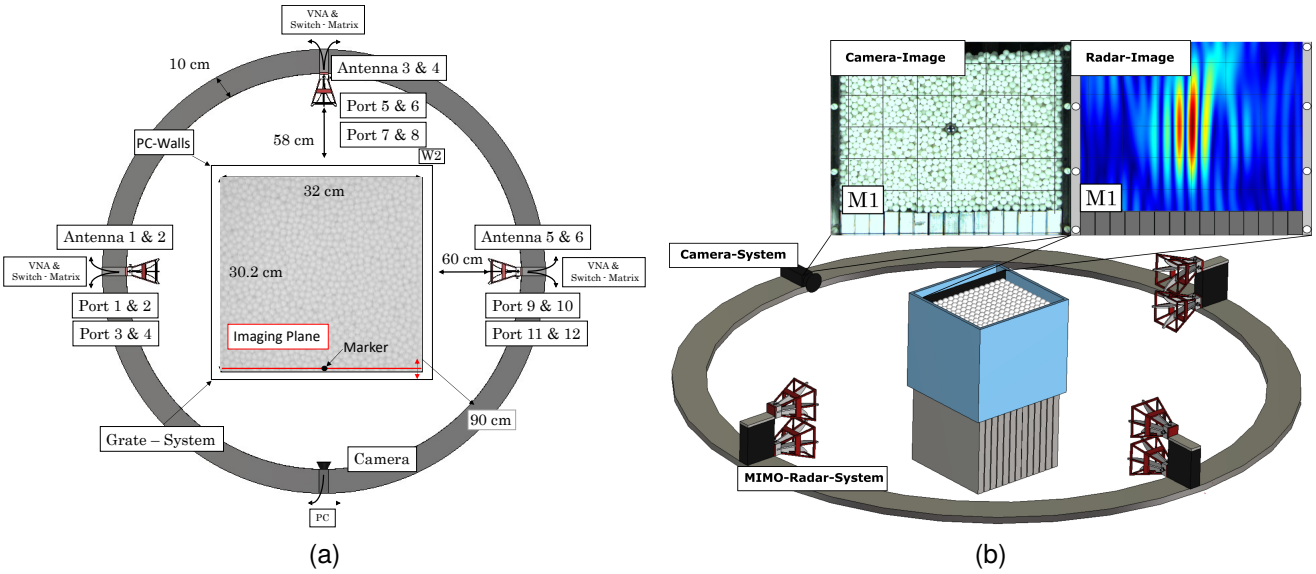

Figure 1: Measurement Setup (a) Top View (b) Three dimensional view with camera and radar image [3]

path for wave propagation between the antenna and the marker, the measurement scenario investigated is equivalent to a marker at any other position in the reactor.
Since this system, unlike conventional radar systems, does not operate in free space, additional effects such as refraction at material boundaries and varying transmission speeds must be taken into account. In this work, numerical methods were developed to take such effects into account during imaging. After the material boundaries have been compensated, the back-projection algorithm is applied to achieve pulse compression in all three spatial directions, allowing to localize the marker particle. This procedure can be applied to the entire reactor volume in three-dimensional space. However, in order to achieve a simpler presentation of the results, only two-dimensional images are shown here. This is possible because a coordinate of the particle is already known due to its placement at the reactor wall.

Measurement Results

Figure 2 shows the results of the two-dimensional imaging procedure. Here, the right side shows the image recorded by the camera, while the right side shows the according radar image. It is assumed, that the marker leads to the strongest reflection, since the surrounding bulk material can be approximated as homogeneous due to the low frequency components of the chirp signal. Thereby, the marker position is calculated from the radar image by taking the maximum value. The resulting localization result for the marker particle is indicated by a black circle in the processed image.
Comparing the camera images and the radar images, it shows that the radar system maps the marker on an extended pulse, which can be attributed to the limited resolution of the imaging system. It furthermore shows, that the marker particle can be better localized in horizontal direction than in vertical direction, as the pulse tends to expand more in height. This can be explained by the fact that the resolution of the system is significantly affected by the antenna distribution. While the localization in horizontal direction is achieved by a circular aperture, the localization in height is determined by a linear aperture. Overall, the proposed localization system reaches a localization accuracy with a standard deviation of $\sigma_{hor} = 0.17$ cm in horizontal direction and $\sigma_{ver} = 0.86$ cm in vertical direction. However, especially the accuracy in vertical direction can be improved significantly by mounting more antennas in height.
Regarding the radar images, it shows that there seem to be multiple disturbing reflections in the image, which can not be directly attributed to the position of the marker particle. These reflections can be explained by the undersampling of the aperture due to the low amount of antenna positions, leading to aliasing. Besides this, the surrounding bulk material is not perfectly homogeneous, leading to clutter in the received signals.

Conclusion

In this paper we demonstrated that imaging systems based on radar sensors are able to localize marker

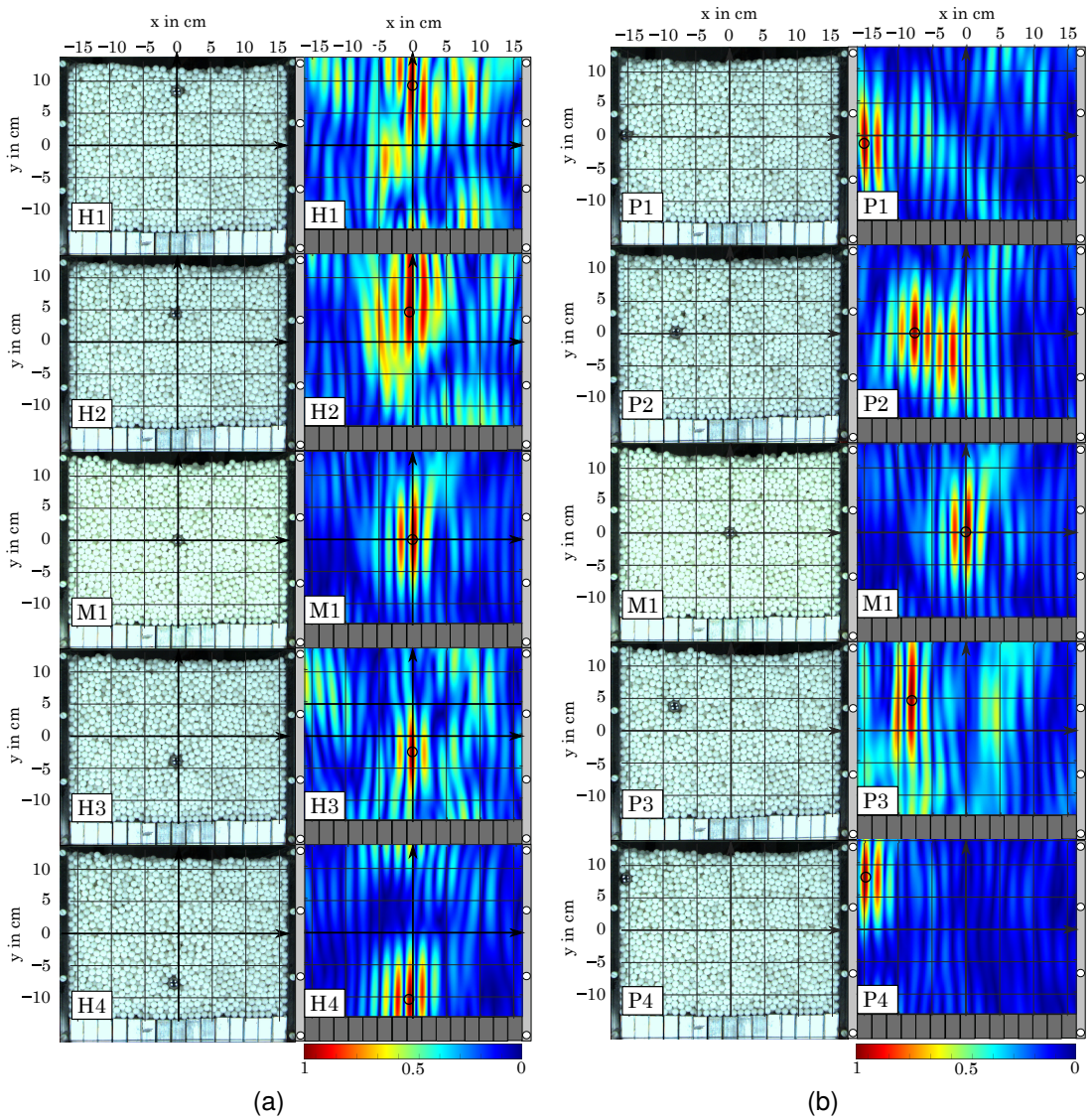

Figure 2: Camera image and radar imaging results for different marker positions [3]

particles in reactors filled with a bulk material by using only a very limited amount of antenna positions. For this, numerical algorithms were implemented to compensate for refraction effects at the reactor walls, before using the backprojection algorithm to achieve pulse compression. It shows, that radar sensors can be a reasonable approach to tackle the problem of particle tracking in large-scale reactors by using a minimal amount of measurements. To further improve the detection accuracy, further research should be carried out in improving the localization accuracy by exploiting the sparsity of the received signal. Furthermore, optimizing the marker particle can result in a specific reflection signature, allowing to further maximize the signal to noise ratio of the received signal after pule compression.

Acknowledgment

This research was funded by the Deutsche Forschungsgemeinschaft (DFG, German Research Foundation), grant number 422037413–CRC/TRR 287 "BULK-REACTION"

References

[1] J. -C. Bolomey and L. Jofre, "Three decades of active microwave imaging achievements, difficulties and future challenges," 2010 IEEE International Conference on Wireless Information Technology and Systems, Honolulu, HI, USA, 2010, pp. 1-4, doi: 10.1109/ICWITS.2010.5611904.

[2] Buist, K.A.; van Erdewijk, T.W.; Deen, N.G.; Kuipers, J.A.M. Determination and comparison of rotational velocity in a pseudo 2-D fluidized bed using magnetic particle tracking and discrete particle modeling. AIChE J. 2015, 61, 3198–3207.
[3] Schorlemer J, Schenkel F, Hilse N, Schulz C, Barowski J, Scherer V, Rolfes I. Radar-Based Particle Localization in Densely Packed Granular Assemblies. Processes. 2023; 11(11):3183. https://doi.org/10.3390/pr11113183

Flow field measurements in polyhedral packed beds – optical access to gas-solid systems

C. Velten[1*], K. Hülz[1] and K. Zähringer[1]

*E-Mail: christin.velten@ovgu.de

[1] Laboratory of Fluid Dynamics and Technical Flows, University of Magdeburg, Universitätsplatz 2, 39106 Magdeburg, Germany

Introduction

Many industrial processes, like drying, catalytic reactions or calcination, rely on packed bed reactors with gas flow. These processes involve high energy and resource consumption, which can be reduced through optimized heat and mass transfer. Therefore, the knowledge of the flow characteristics inside the bed is essential, but existing data is mostly limited to liquid flows.

To gain measurement data in packed beds with gas flow, optical techniques are generally restricted to flow regions where direct optical access is possible, e.g. at the bed surface or in well-defined positions in-between the pores [1]. In order to enable access to all void space inside a model packing with a minimum of optical distortion, in this study a configuration has been set up, which consists of several layers of parallel transparent bars. By using different rotation angles of each layer a complex regular or irregular structure can be generated inside the packing.

Here, we present a packed bed based on this approach which allows for the application of optical measurement techniques in the gas phase. PIV measurement results from flow fields inside a regular arrangement of the packed bed layers with airflow rates of particle Reynolds numbers from 100 to 1000 are presented.

Reactor concept and experimental setup

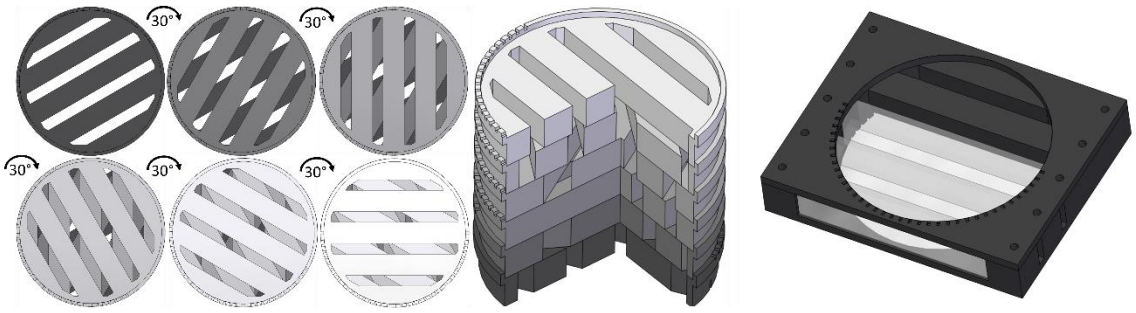

Figure 1. Concept of the packed bed reactor: Modules of five parallel rods are stacked onto each other with 30° rotation each (left). Six modules lead to a full rotation, the cutout shows the complex inner pore structure (center). One of the standard modules can be replaced by an optical module to generate optical access inside the packing (right).

The concept of the packed bed reactor is shown in **Figure 1** left. The packed bed consists of 3D printed modules of five parallel rods (10x10mm) and can be stacked onto each other. The cylindrical outer shape of the modules allows for different arrangements of the rotation angles to generate regular or irregular configurations with complex inner structures. Here, a rotation of 30° each will be presented and measurements in different arrangements (20 and 40°) are currently under investigation. For the 30° case, six layers are needed for one complete rotation. The considered total bed height is 18 layers and thus three rotations. In order to create optical access, one standard module can be replaced by an optical module (**Figure 1** right), that consists of the necessary number of high quality transparent parallel bars.

Figure 2 shows the reactor (R) included to the PIV setup. A Quantel Q-smart Twins 850 Nd:YAG PIV-laser (L) is used to create a light sheet and illuminate the region of interest. An Imager CX 12MP camera (C) from LaVision GmbH is used to record the Mie-scattering signal from Di-Ethyl-Hexyl-

Sebacat (DEHS) droplets in the flow. The volume flow rate of the air is controlled by a Bronkhorst mass steam controller to reach the required particle Reynolds number Re_p. Investigations were carried out for Re_P from 100 to 1000.

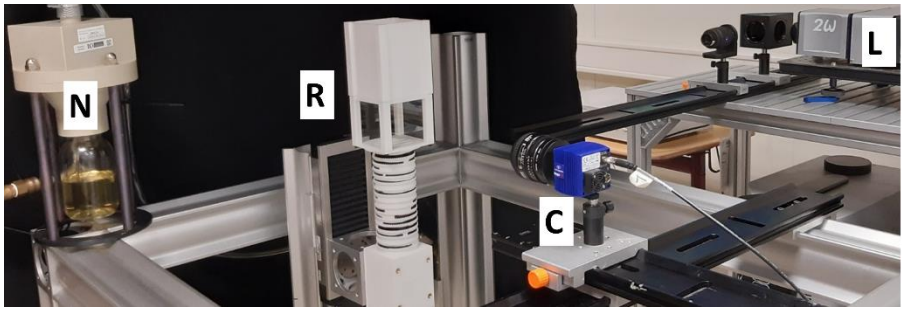

Figure 2. Experimental Setup with the bulk reactor (R), Imager CX 12MP camera (C), Quantel Q-smart Twins 850 Nd:YAG PIV-laser (L) and nebulizer (N).

Measurements can be performed in the inner of the packed bed by using the optical module (**Figure 1** right) and on the bed surface. Therefore, acrylic glass windows are integrated to the outlet box directly above the surface of the packed bed.

Results and discussion

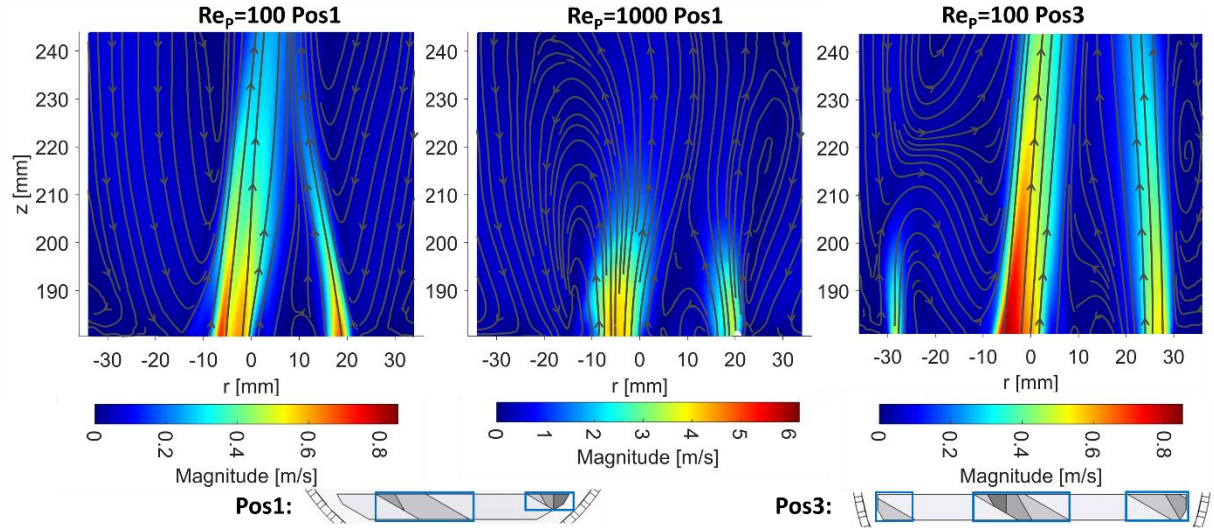

Figure 3. Averaged flow fields for Position 1 in the center between the first and second bar for Re_P=100 and 1000 (left and center) and for Position 3 (right) in the space between the second and third bar. The velocity magnitude is shown as color plot with streamlines as an overlay. A top view for both measurement positions is given below with the bars of the top layer given in light gray and darker gray for the underlying layers.

Measurements are carried out in the center of the slits in each layer inside the bed and also at the bed surface. The geometry of each layer is point symmetrical. Similar flow fields are expected for the first (Pos 1) and the fourth slit as well as for the second (Pos 3) and the third slit. In **Figure 3** the averaged flow fields for Re_P=100 (Pos 1 and 3) and 1000 (Pos 1) at the bed surface are presented. In Pos 1 two jets and in Pos 3 three jets appear with a width that matches well the pore openings from the underlying layers, as can be observed from the sketches of the pore structure in **Figure 3**. Due to the spiral like inner structure, pores from the underlying layers and their different depths contribute to the different aspects of the jets visible in the measurement positions. For higher Reynolds number, e.g. Re_P=1000, the jet height decreases due to the increased 3D movement and increased turbulence.

The inner structure of the packed bed is regular for each layer of the 30° arrangement. The averaged flow fields in **Figure 4** demonstrate that the same flow structures exist for different heights in the packed bed (top images for 17th layer compared to bottom images for 14th layer). For each depth position the

expected number of jets is visible: two for Position 1 and three for Position 3. The low velocity regions in blue show the influence of the underlying or overlaying bars which block the flow and force the jets to separate e.g. around an overlaying bar (Pos 1 at r= -5mm).

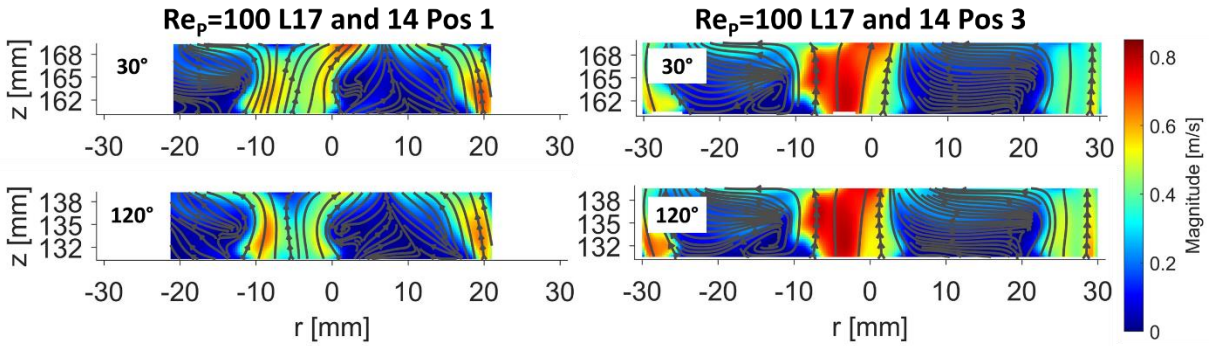

Figure 4. Averaged flow fields for Position 1 in the center of the first slit (left) and for Position 3 in the second slit (right) inside the 14th (bottom) and 17th layer (top) for Re$_P$=100. The velocity magnitude is shown as color plot with streamlines as an overlay.

Due to the high quality of the raw measurement data, which could be achieved by the special design of the packed bed system, also snapshot data is available for characterization of instabilities and turbulence in the flow. Some examples are given in **Figure 5** for the two measurement positions inside the packing for Re$_P$=200 and 1000. From Re$_P$=200 first instable vortical structures can be noticed.

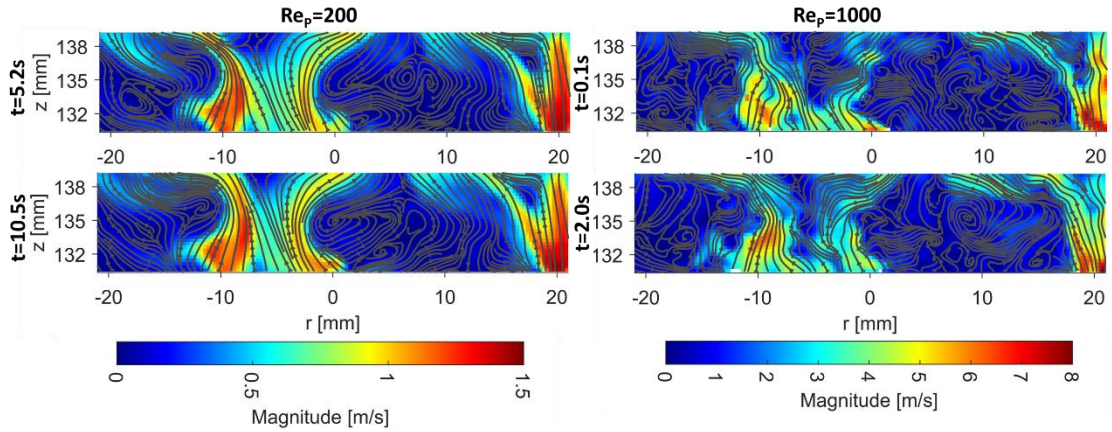

Figure 5: Snapshot data at Position 1 for different times *t* for Re$_P$=200 (left) and 1000 (right)

Conclusion

In this study a concept for a model packed bed reactor is presented which allows to generate optical access for PIV measurements in the interior of a packed bed by a special geometric design based on parallel bars. Thus a model packed bed with polyhedral inner structure can be achieved. The airflow through the packed bed for Re$_P$=100…1000 is characterized by PIV. The range covers the laminar to turbulent regime inside and above the packed bed. Averaged flow fields for specific positions show that the flow structures remain similar for different Re$_P$. The flow at different bed heights inside the bed shows the same behavior. Snapshot data for the characterization of turbulence is also available with this method.

References

[1] Velten C., Zähringer K.: *Flow Field Characterisation of Gaseous Flow in a Packed Bed by Particle Image Velocimetry*, Transp Porous Med 150, 307–326, 2023.

Funding

This work was funded by the Deutsche Forschungsgemeinschaft (DFG, German Research Foundation) – Project-ID 422037413 - TRR 287

Fluid flow velocity and temperature mapping in packed beds using phase contrast Magnetic Resonance Imaging

M. Sangal[1*], M. Anikeeva[2*], F. Godenschweger[1], J-B. Hövener[2], O. Speck[1,3,4,5]

*E-Mail: maitreyi.sangal@ovgu.de, maria.anikeeva@rad.uni-kiel.de

[1] *Department of Biomedical Magnetic Resonance, Otto-von-Guericke University, Magdeburg, Germany*

[2] *Section Biomedical Imaging, Molecular Imaging North Competence Center, Department of Radiology and Neurology University Medical Center Schleswig-Holstein, Kiel University, Kiel, Germany*

[3] *Center for Behavioral Brain Sciences, Magdeburg, Germany*

[4] *German Center for Neurodegenerative Diseases, Magdeburg, Germany*

[5] *Leibniz Institute for Neurobiology, Magdeburg, Germany*

Introduction

Mapping the flow of fluids and other physical parameters in opaque packed bed reactors remains a challenge. One approach is using Magnetic Resonance Imaging (MRI), which enables non-invasive investigation of optically opaque packed bed reactors in 3D [1-3]. Importantly, the MR signal's phase φ can be used to encode quantitative information about motion, temperature and magnetic susceptibility differences. Here, we utilized phase-contrast (PC) flow MRI to map the flow of liquid and gas around bulk particles in MR compatible fixed bed reactor-like setups (**Figure 1**), and the same PC sequence to demonstrate temperature mapping in water without flow.

Materials and Methods

Setups: Two equivalent MR-compatible setups were built for gas and water (Plexiglas tube, 7.4 cm inner diameter, 50 cm length). The inner packed bed, the honeycomb mesh, as well as the inlet (outlet) diffuser (nozzle) were 3D printed using a stereolithography (SLA) printer, Form 3, Formlabs, from Clear V4 resin. The packed bed consisted of 23 cylinders with 7.9 mm diameter and 5 mm gaps, yielding a porosity $\varepsilon = 0.68$. For water, the in- and outlets were fixed using screws and gaskets (**Figure 1 (a)**), for ethane flow, the diffuser and nozzles were glued (two-component hybrid adhesive, Loctite 3090, Henkel) (**Figure 1 (b)**). Temperature mapping was performed using a polypropylene bottle filled with water at room temperature (**Figure 1 (c))** containing a 3D printed, white ABS tube filled with (initially) ~80°C water and fibre optic thermometers in both compartments (FOTEMP OPTOCON).

Figure 1: Pictures of water flow (a), gas flow (b) and temperature setup (c). Note here the inner white tube filled initially with hot water is inserted in the plastic bottle filled with water at room temperature.

Ethane gas (99.95% purity, Linde plc) flow was controlled with a needle valve (SS-1RS10MM, Swagelok) and an electronic mass flow controller (MCP-50SLPM-TFT, Alicat) using a pump for explosive gases (EX-DE N630, KNF) regulated with frequency inverter (VersiDrive i PRO IP 20, Peter

Electronic). The volumetric flow rate was calculated from the nominal flow, actual pressure (1.1 - 1.2 bar) and temperature (21 - 23 °C) recorded with mass flow meter to Q = 9.8 - 10.1 L/min (pressure, 1.1 - 1.2 bar, and temperature.
Tap water was pumped through the setup (United Biologics pump, Flowtek 125) at Q = 1 L/min, as monitored with an ultrasonic inline flow meter (Sonotec Sonoflow IL5.2), to achieve equivalent flow conditions (Reynold number ≈ 60 - 100) within the packed bed.

Flow MRI: Water flow and temperature MRI was performed at 3 T (Skyra, Siemens) using the body transmitter, a flexible RF receive coil and a product 4D flow mapping sequence (BEAT_FQ, field of view (FOV) = 288 mm x 96 mm x 88 mm, isotropic resolution = 1 mm x 1 mm x 1 mm, velocity encoding V_{enc} = 3 cm/s, total acquisition time ≈ 5 min). Each measurement was repeated 3 times and then averaged.
Ethane flow MRI was performed at 7 T (70/30 BioSpec, Bruker, ParaVision 360 3.5) using a ^{1}H transmit-receive quadrature volume resonator (86 mm inner diameter, Bruker) and a product flow sequence (FLOWMAP, 2D multi-slice, FOV = 100 mm x 90 mm x 110 mm, voxel size = 1 mm x 1 mm x 10 mm, V_{enc} = 30 cm/s, 150 averages, total scan time = 40 min). The phase contrast images were initially post-processed in ParaVision and then colour-coded in MATLAB (R2023a, MathWorks).

MR Thermometry: The linear decrease of the MR signal frequency (ω) with temperature (T) was used to generate a phase shift Δφ using the flow compensated measurement with the same flow mapping sequence BEAT_FQ. $\omega(T) = \alpha(T)\cdot\gamma\cdot B_0$, where γ is the gyromagnetic ratio, B_0 is the magnetic field, and α = - 0.01ppm/°C (the frequency shift coefficient). By comparing Δφ at known (reference) and unknown temperature, the temperature difference (ΔT) and absolute value (T_{abs}) was calculated: $\Delta T = |\Delta\varphi - \Delta\varphi_{ref}|/(\alpha\cdot\gamma\cdot B_0\cdot TE)$, and $T_{i\_abs}^{MRI} = T_{ref} + \Delta T_i^{MRI}$ (where TE is the echo time and T_{ref} = 66.5°C, measured by the fibre optic thermometer in the inner tube at t = 0 (**Figure 3(b)**). A total of 10 MR measurements were done, resulting in 9 ΔT maps and $T_{i\_abs}^{MRI}$ values.

Results and discussion

Flow MRI was successfully acquired in the described reactors in gas and liquid phase. 3D flow maps were calculated (**Figure 2(a)-(b)**), showing velocities for water (ethane) of ~ 0.6 cm/s (~ 6 cm/s) before entering the packed bed, ~ 1.1 - 1.8 cm/s (~ 12 - 17 cm/s) in the central regions with a maximum of up to ~ 2.2 cm/s (~ 20-24 cm/s). The flow patterns were similar: laminar flow entering the packed bed was then divided into smaller jets converging after passing through the cylinders. The velocities, as expected, were about 10 times different. Notably, the signal to noise ratio of the gas MRI was lower, due to the lower density, and some signal voids around the cylinders were observed (the anisotropic voxel may induce partial volume effects). Likewise, high velocities were found at the outlet end of the field of view of the gas data, which may be attributed to field inhomogeneities (green arrows, **Figure 2(b)**).

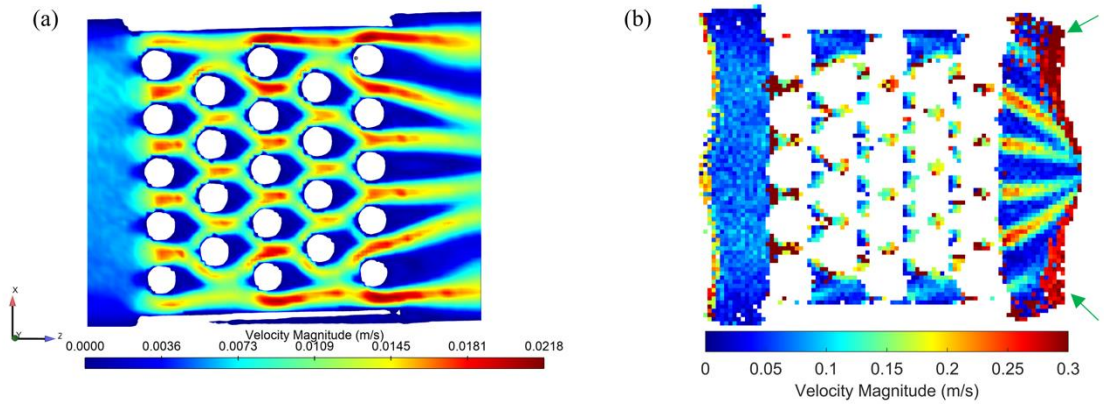

Figure 2: MRI velocity maps for water (a) and ethane (b) flowing through the packed bed reactor from left to right (once slice of 3D volume). Note the similar flow patterns, the expected, 10-fold difference in velocity, and the lower signal of the gas. The unexpected shape of the gas flow at the outlet maybe attributed to field inhomogeneities.

Temperature MRI in water was successfully conducted (**Figure 3**). Using the 1st measurement at t = 0 as reference T_{ref}^{MRI}, we calculated ΔT_i^{MRI} for the 9 subsequent measurements over a period of 17 min (every 1.54 min). **Figure 3(a)** shows $\Delta T_9^{MRI} = |\Delta\varphi_{10} - \Delta\varphi_{ref}|/(\alpha \cdot \gamma \cdot B_0 \cdot TE)$, where TE = 5.15 ms. **Figure 3(b)** shows the temperature evolution for all 9 $T_{i\_abs}^{MRI}$ (red) and fibre optic sensor measurements (blue). The average standard deviation of the MR measurements was 0.92 (1st red point) in the best case and 1.43 in the worst case (9th red point).

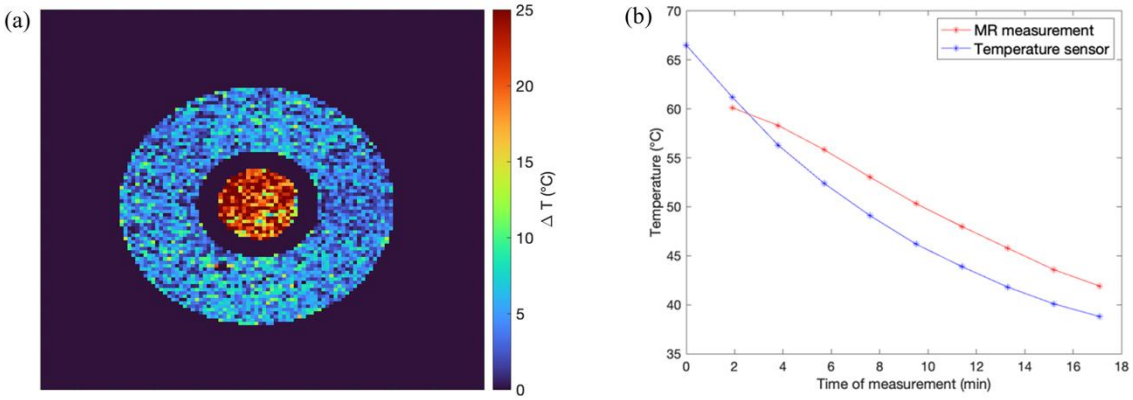

Figure 3 (a) The ΔT_9^{MRI} map between 10th and 1st measurement ($\Delta\varphi_{10} - \Delta\varphi_1$) for a central plane transverse to the tube's axis. (b) Temperature evolution, where x axis depicts each MR measurement's start time. Blue (red) curve depicts the fibre optic sensor (MRI, i.e. $T_{i\_abs}^{MRI}$) measurements. Each $T_{i\_abs}^{MRI}$ is the average over a region of 16 mm diameter in the inner tube over 8 planes.

Conclusions and Outlook

3D flow velocity fields of water and ethane gas were successfully measured with MRI in equivalent setups and showed similar flow patterns, the differences in which may be caused by magnetic field inhomogeneities, – this is particularly remarkable as it was unclear whether the low MR signal of ethane would be sufficient to achieve this. Improvements include isotropic voxels and possibly additional gas flow measurement of the outlet region of the packed bed. MRI temperature quantification was also successfully implemented and showed a difference of 1 °C (4 °C) in the best (worst) case to the reference. The quality of both flow and temperature maps are very much suitable for studying packed beds reactors and will be investigated further.

This work is supported by Sonderforschungsbereich/Transregio 287 BULK-REACTION (Projekt-ID 422037413) (DFG).

References

[1] Raquel Serial M., Benders S., Rotzetter P., Brummerloh D. L., Metzger J. P., Gross S.P., Nussbaum J., Müller C. R., Pruessmann K. P., Penn A.: *Temperature distribution in a gas-solid fixed bed probed by rapid magnetic resonance imaging*, Chemical Engineering Science, 269, 118457, 2023.

[2] Bruschewski, M.; Flint, S.; Becker, S.: *Magnetic Resonance Velocimetry Measurement of Viscous Flows through Porous Media: Comparison with Simulation and Voxel Size Study*, Physics, 3(4), 1254-1267, 2021.

[3] Buchenberg WB, Wassermann F, Grundmann S, Jung B, Simpson R.: *Acquisition of 3D temperature distributions in fluid flow using proton resonance frequency thermometry*, Magnetic Resonance in Medicine, 76:145–155, 2016.

[4] Anikeeva M.,Sangal M., Pravdivtsev A. N., Pravdivtseva M. S., Peschke E., Speck O., Hövener J-B.: *Magnetic Resonance Imaging and Velocimetry of Ethane*, Journal of Magnetic Resonance Open, 16-17, 100137, 2023.

Experimental investigation of the thermal radiation propagation in different bulk porosities

M.Tyslik[1*], B. Jaeger[1] and M. Schiemann[1]

*E-Mail: tyslik@leat.rub.de

[1] *Department of Energy Plant Technology, Ruhr-University Bochum, Universitätsstraße 150, 44780 Bochum, Germany*

General Information

Radiative heat transfer plays a major role in many technical applications. Most existing numerical methods reach their limits when the particle collective consists of independently moving particles. Furthermore, spectral redistribution is often not considered, especially for time-varying assemblies. The development of a model for radiative heat transfer in polydisperse beds with gaseous flow and a test rig are needed that allow to investigate the influence of surface properties, spectral redistribution and temperature gradients on radiative heat transfer. The experimental data obtained are used as a simplified validation test case for the developed DEM/CFD framework.

Experiments

The experimental setup to investigate complex radiative heat transfer consists of a quasi-2D arrangement in which hollow rods represent the particles. The measuring rods are made of high-temperature stainless steel and are 200 mm long with various diameters. The rods are positioned on a mounting plate, which is designed to realize different arrangements of the rods. The propagation of the thermal radiation is determined and characterized using an IR-camera (Infratec ImageIR® 8380, λ= 2-5.5 µm) and a Fourier Transform Infrared Spectrometer (FT-IR) (Shimadzu IR-Tracer). The IR-camera and the FT-IR are positioned to the left and right of the rods. In order to dampen the vibration-sensitive components such as the FT-IR from disturbances, the entire experimental setup is mounted on an optical table. The IR-camera, as well as the rods, can be moved by means of a linear unit in order to determine the radiation instants at several points with the FT-IR. The experimental setup including IR-camera, rod arrangement and FT-IR as well as a sectional view of a rod are shown in **Figure 1**.

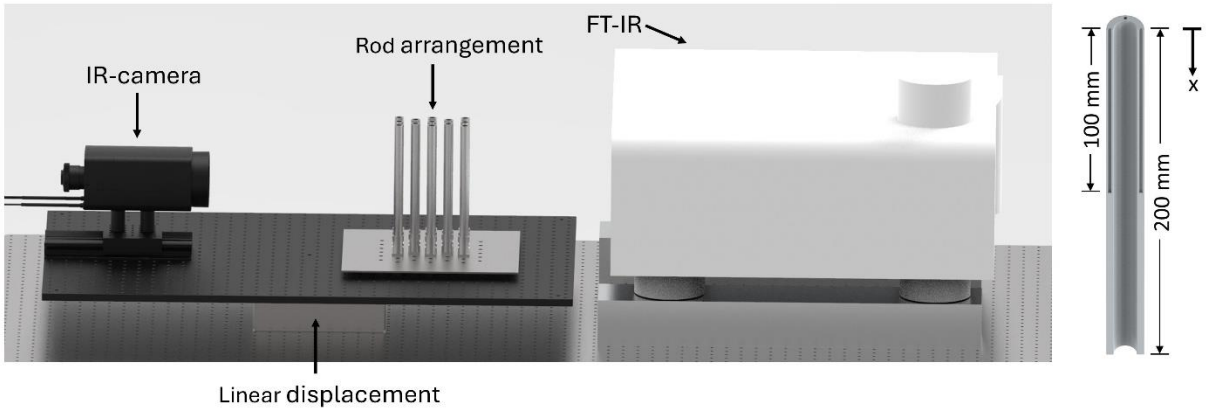

Figure 1. Left: Experimental setup including an IR-camera, a rod arrangement and a Fourier-transform infrared spectroscopy. Right: Sectional view of a rod sample.

As the surface temperature is an important parameter and the IR-camera can only measure this temperature for the visible rods, thermocouples are used to measure the temperature inside the rod walls. For this purpose, a total of four thermocouples are positioned at an angle of 90° around the circumference in the middle of each rod wall (drilling depth 100 mm). A total of 52 thermocouples are thus used for the 13 rods, enabling a detailed temperature field measurement. Depending on the experimental setup, 1 - 7 heated rods constitute the heat source (red rod in **Figure 2**). These are heated by an electric heating cartridge. In order to gain an understanding of the purely optical reflection profile of the geometries, a

high-power UV LED (Thorlabs M365LP1, λ= 365 nm) is also used instead of the heat source. Using a UV sensitive foil (Fujifilm UV scale LM), the incident UV radiation of the respective plane can be detected in different sectional planes. This allows the spatial intensity of the reflected radiation to be investigated in detail and the overlap of thermal radiation from a heat source and the intrinsic emission to be clearly quantified. The occurring overlap of reflected thermal radiation and intrinsic emission has already been shown in detail in previous studies [1].

The objective of this work is to investigate the influence of different bulk porosities on the transported and reflected thermal radiation. For this purpose, a total of 4 different rod arrangements, each with a different rod diameter *dp* (*dp* = 12 mm, 16 mm, 20 mm and 25 mm) are investigated. The different rod diameters allow different bulk porosities to be represented in a control volume V_c. The investigated rod arrangements are shown in **Figure 2**.

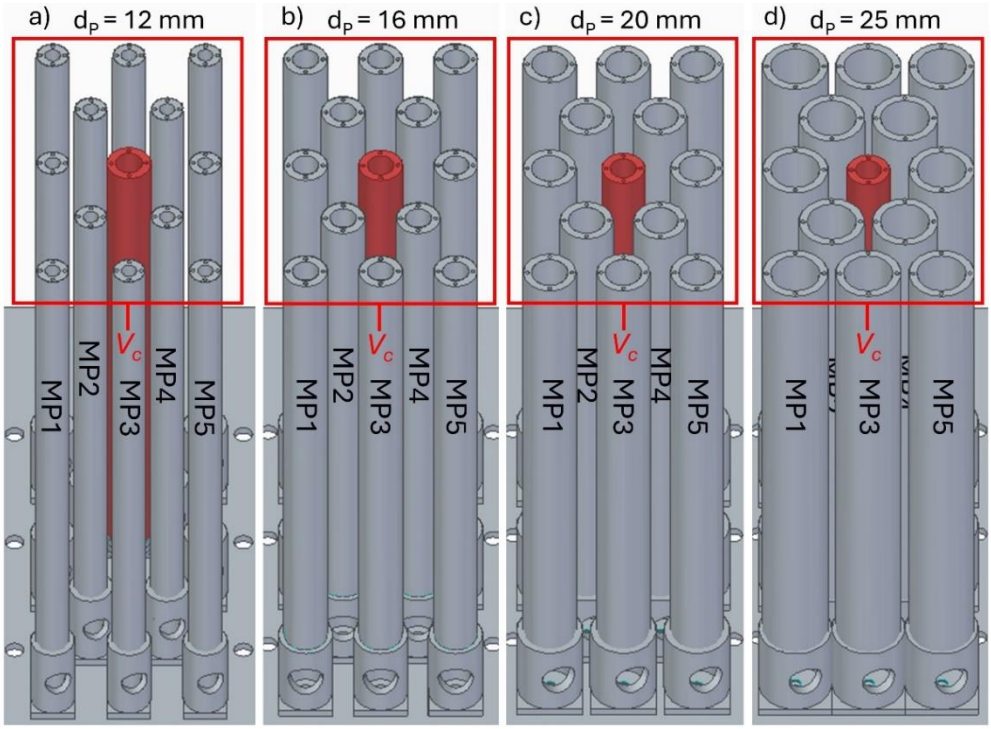

Figure 2. Investigated rod arrangements with a rod diameter of a) d_p = 12 mm; b) d_p = 16 mm; c) d_p = 20 mm and d) d_p = 25 mm.

For the comparison of different bulk porosities, only the middle rod is heated. This symmetrical arrangement enables simultaneous measurements with the IR-camera and the FT-IR from opposite sides. In each test case, three temperature levels of the heated rod, 200 °C, 400 °C and 600 °C are investigated. After reaching a thermal equilibrium, the radiation intensities and the surface temperatures are detected. In a further step, the same temperature levels are investigated, whereby the heating cartridge is replaced by the high-power UV LED and the UV sensitive foil is arranged at different positions within the rod arrangement.

The first results clearly show the influence of a highly reflective surface like stainless steel on the reflected heat radiation. On the rods that are closer to the heat source, MP2 and MP4, high surface temperatures are measured with the IR-camera. The temperature peaks are over 200 °C. Compared with the measured thermocouple temperature at the same position, which is only 67.60 °C, indicates that the measured surface temperature is clearly too high. The overlap between intrinsic emission and reflected thermal radiation from the heated middle rod becomes thus obvious. This effect is also evident in the measured radiation intensities with the FT-IR. The measured radiation intensity at MP2 is significantly higher than at MP3, which also indicates an overlap of intrinsic emission and reflected thermal radiation from the heated middle rod. **Figure 3** shows the infrared image of the rod arrangement with a rod diameter d_p of 16 mm (**Figure 3 a**) and the measured radiation intensities at MP2 and MP3 (**Figure 3 b**).

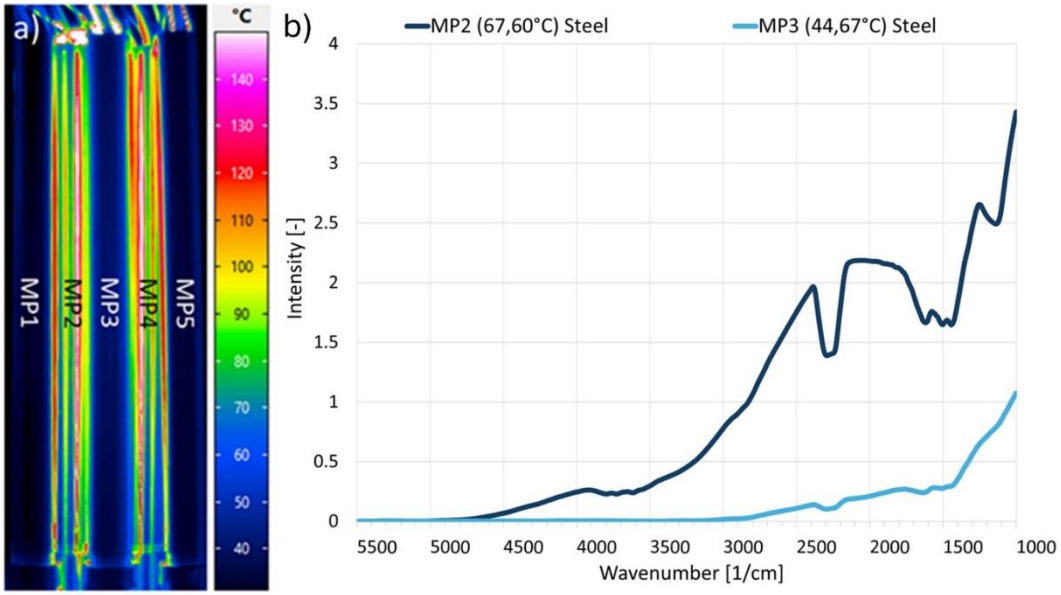

Figure 3. a) Infrared images for stainless steel at heating rod temperature of 600 °C; b) radiative intensities measured with the FT-IR at MP2 and MP3. The rod diameter d_p is 16 mm.

Outlook

The influence of different bulk porosities on thermal radiation transport in 2D particle beds is investigated in detail using various measuring devices. This enables to acquire unique experimental data on the thermal radiation transport within bulks of different porosities. The variation of particle sizes in the given domain will provide information on the influence of more densely packed particles on the propagation of thermal radiation.

The data for the spatially resolved radiative intensities will be further used for comparison with numerical simulations in a next step. The experimental setup will be modeled with the Blocked-Off & Discrete Ordinates (BO/DO) approach [2,3], enabling to capture the influence of different bulk porosities on radiative transfer numerically. Thereby the BO/DO approach provides the advantage of highly precise and computationally efficient numerical modeling. The detailed experimental data therefore provide a verification basis for the DEM/CFD framework developed in our group.

References

[1] Tyslik M., Pörtner L., Wirtz S., Schiemann M.: *Experimental investigation of radiative heat propagation in a simplified generic packed bed*, Particuology, vol. 88, doi: 10.1016/j.partic.2023.09.005, 2024.

[2] Jaeger B., Schlag M., Scherer V., Wirtz S., Schiemann M.: *Radiative heat transfer with a blocked-off approach for application in the discrete element method,"*, Powder Technology, vol. 392, doi: 10.1016/j.powtec.2021.07.010.

[3] Jaeger B., Tyslik M., Wirtz S., Schiemann M.: *Investigation of the radiative heating of cubic particles with DEM/CFD and the BO/DO approach*, Powder Technology, vol. 403, doi: 10.1016/j.powtec.2022.117424.

Acknowledgment

Funded by the Deutsche Forschungsgemeinschaft (DFG, German Research Foundation) – Project-ID 422037413 – TRR 287.

Gefördert durch die Deutsche Forschungsgemeinschaft (DFG) – Projektnummer 422037413 – TRR 287.

In-situ temperature monitoring during microwave heating using fiber-optic sensors

L. Briest[1*], R. Wagner[2], A. Tretau[2], M. Ganß[2] A. Narasimhaiah[1], E. Tsotsas[1] and N. Vorhauer-Huget[1]

*E-Mail: lucas.briest@ovgu.de

[1] Thermal Process Engineering, University of Magdeburg, Universitätsplatz 2, 39106 Magdeburg, Germany
2 Institute of Material Research and Testing at the Bauhaus-University Weimar (MFPA), Coudraystraße 9, 99423 Weimar, Germany

Introduction

Microwave drying has gained significant attention in the building material industry due to its potential for improving energy efficiency and reducing drying times [1]. However, the inhomogeneous temperature distribution caused by the interaction between microwave radiation (2.45 GHz) and the material structure presents a major challenge [2–4], especially for hollow clay bricks (HCB). Accurately capturing temperature profiles during the drying process is essential to understand heat distribution and optimize process parameters. In this study, fiber bragg grating and fiber optical sensors was employed to provide spatially resolved temperature data during the drying process [4]. The feasibility of these sensors for online monitoring is discussed, along with an analysis of temperature variations influenced by process conditions and brick geometry.

Material and Methods

The distributed fiber-optic temperature measurements were carried out using a single-channel coherent frequency domain reflectometer (ODiSI B from LUNA Innovations Inc., USA, distributed by Polytec GmbH, Germany) and a fiber bragg grating. This measurement system allows capturing measurement points with a resolution of approximately 0.65 mm along the sensor fiber over several meters. Optical glass fibers with polyimide coatings, each approximately 3 meters in length, were used as sensors. The fiber diameter was 150 µm. The sensor fibers were spliced and terminated using a three-axis splicing device (Fujikura 70S, Fujikura Ltd., Japan) [5].

Hollow clay bricks were used as test material in 3 different experiments. The HCB were freshly extruded from a factory and wrapped in foil to maintain a constant initial moisture content of approximately 27.5% (d.b.). The HCB had dimensions of 52 cm in width, 15 cm in depth and height of the bricks was approximately 20 cm. The wet mass of the samples ranged between 15.3 kg and 16.0 kg.

The drying process was conducted using a microwave apparatus from Püschner GmbH Germany, which is equipped with two magnetrons, each capable of generating up to 1000 W of power. The samples were rotated on a turntable, and the mass loss during the drying process was monitored using a scale. An inlet and exhaust fan, as well as an air humidifier, enabled controlled ventilation and conditioning of the samples. Additional temperature data was obtained from two commercial point fiber-optic sensors (Polytec) and an IR camera detecting the surface temperature.

For measuring the temperature profiles, the 3-meter-long fiber-optic sensors were routed through five measurement paths in all three experiments, as illustrated in Fig. 1. The fibers were applied in four horizontal profiles, each passing through a continuous bridge and adjacent chambers. A thin Teflon capillary (inner diameter = 1 mm) was used to guide and decouple mechanical influences. In Figure 1, an HCB sample from experiment 1 is shown with the numbered entry points for the measurement paths. Measurement paths 1 to 3 were used in all experiments. In experiment 2, an additional vertical measurement path was realized at the edge, chosen to intersect with the measurement path at a position 1 cm from the back of the sample. Table 1 lists the measurement paths used in each experiment.

Besides the fiber positions also three different experimental conditions were applied, as indicated in Table 1. All experiments began with a five-minute preheating phase at 1500 W (Phase I). Afterwards, the magnetron power was increased to 2000 W. The duration of each intermittent cycle was kept constant at 95 seconds. During the drying process, the microwave power was varied by adjusting the

pulse duration within the cycle. In experiments 1 and 2, temperature regulation was used to limit the sample temperature to 65°C, automatically shortening the pulse duration. In experiment 3, after preheating, the pulse duration was kept constant at 10 seconds. After 550 min, the temperature regulation and average power were reduced by switching off the magnetrons, and the drying process was completed after 840 min.

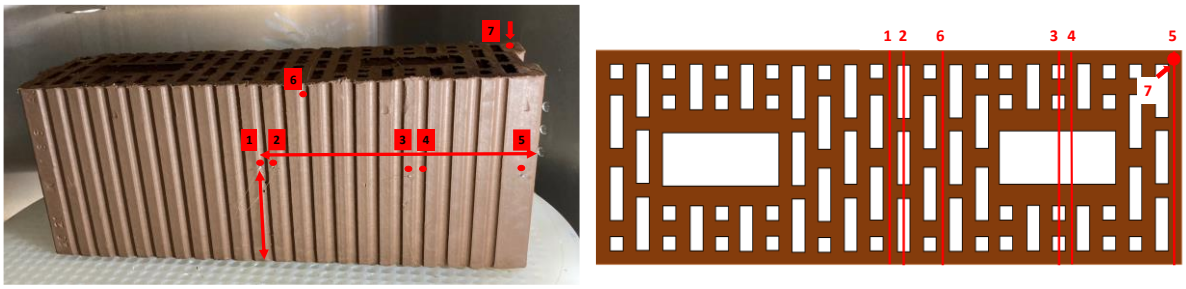

a) b)

Figure 1. a) The HCB sample from experiment 1 was placed in the microwave with the openings facing upwards. The numbers indicate the placement of the measurement paths. b) Sketch of the measurement paths as seen from top view.

Table 1. Position of the fiber optical sensors in the 3 different experiments. The "X" marks the different realizations in each experiment.

Measuring section	**1**	**2**	**3**	**4**	**5**	**6**	**7**
Vertical position [cm]	11.2	11.2	10.5	10.5	10.5	19.0	
Horizontal position [cm]	26.7	25.2	11.5	10.0	1.0	22.0	
Experiment 1 (constant intermittent power)	X	X	X	X	X	X	
Experiment 2 (stepwise increasing power)	X	X	X	X	X		
Experiment 3 (high constant power)	X	X	X	X			X

In experiment 2, the pulse duration was stepwise increased to raise the microwave power during drying. After 97 min, the pulse duration was increased from 10 seconds to 15 seconds (Phase II), and after 178 min, it was further increased to 30 seconds (Phase III). In Phases II and III, the temperature at the regulation sensor remained below 60°C. With the increase in average power per cycle to approximately 0.65 kW, the temperature in Phase III increased to 65°C, where it was maintained between 61°C and 65°C. From 195 min (Phase IV), the maximum power of 2000 W was used for drying, and the temperature regulation was increased to 90°C, which was reached rapidly due to a steep temperature rise. This phase was terminated after 212 min. For the final 30 min, drying continued at the maximum power. In experiment 3, there was no direct temperature regulation, and the pulse duration was set to 40 seconds. After 32 min, the exhaust fan was switched on. The process was stopped after 48 min when visible cracks appeared on the sample.

Results and Discussion

In the following, only experiment 1 with constant power is analysed. Figure 2 shows the spatially resolved temperature profiles for different process times at two measurement sections in this experiment. Up to an experimental duration of 150 min, the temperatures inside the sample after preheating are between 40 °C and 55 °C and remain nearly constant along the measurement section.

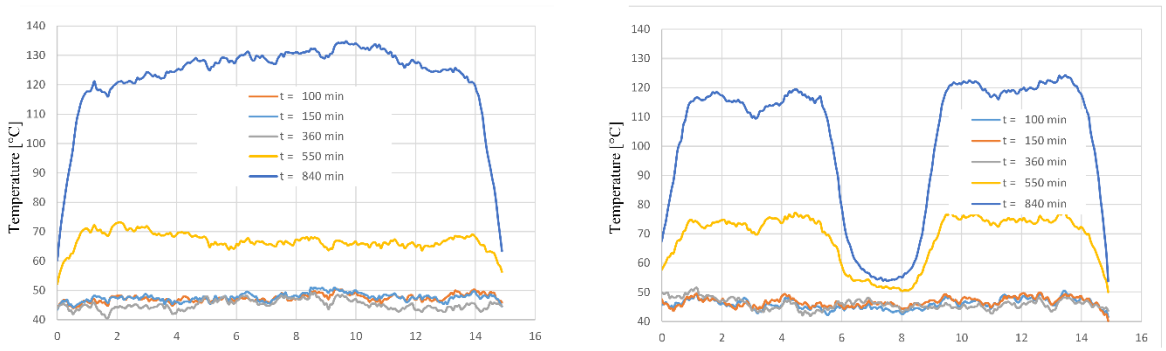

Figure 2. Different measurement sections at different times during experiment 1: a) Center section 1 and b) temperature profiles at section 4 at the sample boundary which shows a large hole in the HCB.

After 360 min, the temperatures near the edge rise to around 70 °C. Until just before the start of the power regulation (after 550 min), the temperatures in the center section are also around 70 °C. By the end of the experiment, despite power regulation, the temperatures in the measurement sections inside the HCB rise to over 100 °C. At this point, the holes inside of the HCB are clearly visible in the temperature curves, as they are filled with air at a much lower temperature level.

Conclusion

With the presented measurement technique, it is possible to resolve temperatures with high spatial and temporal accuracy, allowing monitoring of profiles along measurement paths. The measurements reflect temporal events and geometric specifications, such as the large holes inside the material. A gentle drying process with a constant, lower power input and longer equilibration phases, as in experiment 1, results in constant temperature profiles. The values are on the same level when comparing the center to the edge area. This reflects homogeneous heating.
The high energy input in experiments 2 and 3 instead yields much more heterogeneous conditions, which could be shown in an extended version of this work.

Acknowledgement

The authors N. Vorhauer-Huget and E. Tsotsas acknowledge the funding by the Deutsche Forschungsgemeinschaft (DFG, German Research Foundation) – Project-ID 422037413 – TRR 287 for their contributions to the study.

References

[1] L. Briest, R. Wagner, A. Tretau, E. Tsotsas, and N. Vorhauer-Huget, "Microwave-assisted drying of clay roof tiles," *Drying Technology*, 2021, doi: 10.1080/07373937.2021.1878369.
[2] Z. Y. Li, R. F. Wang, and T. Kudra, "Uniformity Issue in Microwave Drying," *Drying Technology*, vol. 29, no. 6, pp. 652–660, 2011, doi: 10.1080/07373937.2010.521963.
[3] P. Rattanadecho and N. Makul, "Microwave-Assisted Drying: A Review of the State-of-the-Art," *Drying Technology*, vol. 34, no. 1, pp. 1–38, 2016, doi: 10.1080/07373937.2014.957764.
[4] J. Juraszek and P. Antonik-Popiołek, "Fibre Optic FBG Sensors for Monitoring of the Temperature of the Building Envelope," *Materials (Basel, Switzerland)*, vol. 14, no. 5, 2021, doi: 10.3390/ma14051207.
[5] K. Schricker, M. Ganß, C. Könke, and J. P. Bergmann, "Feasibility study of using integrated fiber optical sensors to monitor laser-assisted metal–polymer joining," *Weld World*, vol. 64, no. 9, pp. 1565–1578, 2020, doi: 10.1007/s40194-020-00942-y.

A Comparison of Homogeneous 2-Dimensional Models and Resolved 3-Dimensional Models for Reactive Fixed Bed Systems

S.R. Srinivas[1*], F. An[1], M. Kropf and A. Richter[1]

*E-Mail: shreyas-rohit.srinivas@iec.tu-freiberg.de

[1] *Institute of Energy Process Engineering and Chemical Engineering, TU Bergakademie Freiberg, Fuchsmühlenweg 9, 09599 Freiberg, Germany*

Abstract

Fixed bed systems with low tube-to-particle diameter ratios are widely used in various industrial application for e.g., Synthesis processes. Due to their slender geometry, such geometries have high structural inhomogeneities. Nevertheless, homogeneous models are widely used for modeling slender reactive fixed beds. In this work we investigate in detail, the impact of the homogeneous assumptions on the modeling results and the extent to which these assumptions are valid. A packing with a very low tube-to-particle diameter ratio (N=3) particles is chosen as reference reactive system. The system is modeled with homogeneous porous-zone models and particle-resolved computational fluid dynamics (PRCFD) models which include the effects of local structural inhomogeneities. The results from both the models are compared and analyzed to assess the deviations in the porous-zone models due to the homogeneous assumptions.

Introduction

Quasi two-dimensional homogeneous models are quite popular for modeling industrial packed bed system with low tube-to-diameter particle ratios [1]. Such approaches model the effect of the packed bed on the fluid momentum, heat and mass transport with the help of additional source terms in the transport equations. In doing so, the local inhomogeneities are ignored. Although ignoring the inhomogeneities for beds with large tube-to-particle diameter ratios does not result in large modeling errors, the deviations become significant for lower ratios. Particle-resolved CFD on the other hand include the geometry of every particle in the packing and as a result are able to simulate the effects of local inhomogeneities. However, they are also computationally expensive and unsuitable for modeling industrial scale reactors.

Since homogeneous models have wide applications for modeling fixed bed systems, the modeling errors arising due to the homogeneous assumption must be investigated. In this work we compare the PRCFD approach with the 2D homogeneous approach, to investigate the deviation in results predicted by the two models for the same reactive reference system.

Numerical Setup

A small heterogeneous packing of 17 spherical particles inside a cylindrical reactor with a diameter of 36 mm was chosen for this study. The modeled particles represent iron ore pellets and have a diameter of 12 mm. The system was chosen to represent a boundary case with a tube-to-particle diameter ratio of 3. They are arranged in an ideal arrangement of three stacked particle layers as shown in **Figure 1**. The direct reduction of iron ore was modeled with a simplified single surface reaction:

$$3O_s + 3H_2 \rightarrow 3H_2O \quad (1)$$

The PRCFD model was meshed with a polyhedral mesh consisting of $1.6 \cdot 10^6$ cells where the boundary layer was resolved with two prism cells. The contacts between the particles and between the particles and the reactor wall were modified to generate a good mesh quality. The homogeneous model was created as a two-dimensional axisymmetric geometry of the reactor with the bed modelled as a porous zone with a porosity of 0.52. A structured computational grid with 98,000 cells was used for the

calculations. The porous zone model was also setup with surface reactions with available reactive particle surface area defined as a user input. A laminar reference case was defined to exclude additional complexities arising with turbulent chemistry. At the inlet velocity of the mixture was defined to be 0.6 m/s and the composition of the gas was set to 75 Vol.-% H_2 and 25 Vol.-% N_2. The reactor and the particle walls were modeled as no-slip boundaries. The temperature of the reactor walls and the inflowing gas were defined to be the same. Three different process temperatures of 900 °C, 1000 °C and 1100 °C were investigated.

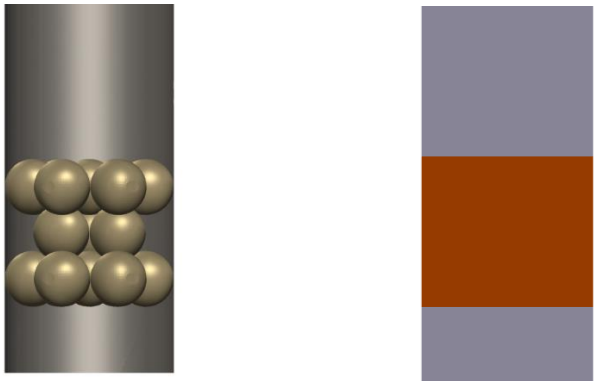

(a) (b)

Figure 1: Geometry of the reference case: (a) PRCFD and (b) Porous Zone

Results and Discussion

The distribution of H_2O mole fraction is shown in **Figure 2.** In the resolved model, a high concentration of H_2O can be seen in the middle of the bed around the second layer of particles, whereas the porous zone model predicts radially uniform concentration profiles which only vary in the axial directions. Due to the voids between particles a channeling effect of flow is seen in PRCFD results. In the voids between the particle, flow streams are separated from one another (see **Figure 3**(b)). Near the walls, where the voids are the largest, highest flow velocities can be seen whereas in the middle of the bed velocities are almost 0. This is depicted in **Figure 3**(a). As a result, streams passing through the middle of the bed have very low velocities and high residence times, resulting in greater concentration of H_2O in this region. Furthermore, due to the low gas velocities the produced H_2O remains in this region and does not mix with the rest of the streams. Near the walls the gas mixture does not have enough time to react with the surface oxygen and any H_2O produced is transported toward the reactor outlet. Since the porous zone model defines a uniform porosity for the entire bed, there is no channeling effects and the concentration field is also uniform without any visible radial profile.

Due to the large difference in velocities of gas streams, a recirculation zone is formed in PRCFD model at the bed exit. The recirculation zone results in mixing of different streams with different compositions.

Table 1: H_2 conversion at different operating temperatures

	Conversion of H_2	
	PRCFD	PZ
900 °C	0.268	0.264
1000 °C	0.327	0.324
1100 °C	0.384	0.384

Table 1 lists the conversion of H_2 calculated by the PRCFD model and the porous zone models for different operating temperature. This is calculated based on the gas outlet composition. It can be seen

that the influences of the local inhomogeneities are not observable at the outlet because of the mixing due to recirculation. In fact, both models yield same results for all cases.

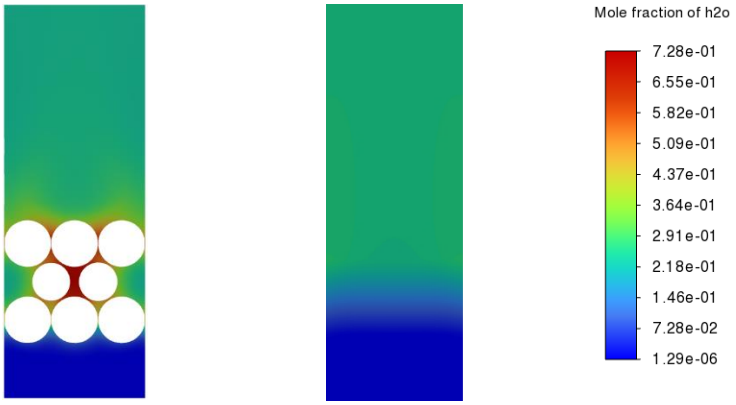

(a) (b)

Figure 2: Distribution of mole fraction of H_2O: (a) PRCFD (b) Porous Zone

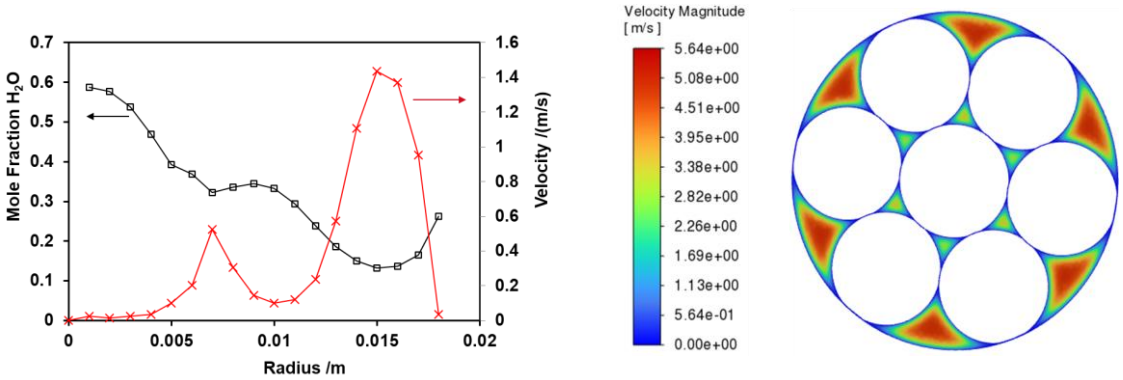

Figure 3: (a) Circumferentially averaged velocities and H_2O mole fraction at a cross sectional plane cutting the second particle layer. (b) Velocity distribution on a cross sectional plane cutting the first particle layer.

Summary and Conclusions

The influence of the local structural inhomogeneities on heat and mass transport are investigated with the help of resolved CFD model of low tube-to-particle diameter ratio. Comparing the results from PRCFD and the porous zone models, it was observed that even when the predicted global conversion by both models is same, there are significant local deviations. The channeling effects due to the void structure results in varying residence times for flows through different channels. It can be concluded that the structural inhomogeneities have a significant effect on the local concentration inside the bed. At the bed exit there is a recirculation zone which results mixing of different stream concentrations and homogenization of the outlet gas composition. However, because of the strong deviations within the bed more investigations are necessary for a wider range of operating conditions and bed structures.

References

[1] E. M. Moghaddam, E. A. Foumeny, A. I. Stankiewicz and J. T. Padding, "Multiscale modelling of wall-to-bed heat transfer in fixed beds with non-spherical pellets: From particle-resolved CFD to pseudo-homogenous models," *Chemical Engineering Science*, vol. 236, 2021.

Numerical Simulation of a Conical Spouted Fluidized Bed (CSFB)

F. Zhang[1*], X. Dai[1], S. Tavakkol[1], and D. Stapf[1]

[*]E-Mail: feichi.zhang@kit.edu

[1]*Institute for Technical Chemistry, Karlsruhe Institute of Technology, Kaiserstr. 12, 76131, Karlsruhe, Germany*

Introduction

A conical spouted fluidized bed (CSFB) is a specialized type of fluidized bed reactor widely used in various industrial applications, particularly for processing granular or particulate materials [1]. By combining the benefits of spouting and fluidization, CSFBs are highly effective for demanding processes such as drying, coating, granulation, pyrolysis, and chemical reactions. In a CSFB, a high-velocity gas jet is injected through a nozzle at the base of the conical chamber, creating a central spout that lifts particles upward. These particles are then carried to the top of the bed, where they fall back into the annular region of the chamber and are recirculated, establishing a continuous cycle. The conical geometry of the chamber enhances spout stability and prevents particle stagnation. This cyclic particle movement ensures thorough mixing, facilitating uniform heat and mass transfer. As a result, CSFBs can efficiently handle a broad range of particle sizes and types. Compared to conventional bubbling fluidized beds (BFBs), the high-velocity spout in CSFBs mitigates common issues such as defluidization, channeling, and dead zones, which are often encountered in BFBs. This makes CSFBs a more robust and versatile option for industrial applications.

The operational performance of CSFBs is heavily influenced by the hydrodynamics of gas-solid flow, which plays a critical role in heat and mass transfer, ultimately affecting chemical reactions and product yields. While extensive research and well-established guidelines exist for the design and operation of BFBs [2], the hydrodynamics of CSFBs remain relatively understudied and lack standardization. To address this gap, high-fidelity numerical simulations of a laboratory-scale CSFB were conducted to develop a comprehensive understanding of its hydrodynamics and to elucidate the fundamental physical mechanisms governing the formation of the spouted bed. Key hydrodynamic characteristics, such as bed height, pressure drop, and the kinetic energy of bed materials, were evaluated under various operating conditions and design parameters to identify optimal operating conditions. Additionally, a comparative analysis of the hydrodynamic performance of CSFBs and BFBs was carried out, highlighting the advantages and challenges of operating CSFBs over BFBs.

Simulation Setups

A hybrid Eulerian-Lagrangian approach is employed for modeling the gas-solid flow, combined with the multiphase particle-in-cell (MP-PIC) approach to address inter-particle collisions. The gas flow is regarded as a continuous phase, modeled using the Naiver-Stokes equations. The solid particles are treated dispersed, and their trajectories are calculated based on the balance of forces acting on the particles. Eulerian and Lagrangian equations for both the gas and solid phases are coupled via source terms that account for momentum exchange between the two phases.

Simulations were conducted for a generic laboratory-scale conical spouted fluidized bed (CSFB) studied in [3], featuring a gas nozzle inlet diameter of 1 cm and a cone angle of $\gamma = 36°$. As illustrated in Fig. 1 (a), the main components of the CSFB include (from bottom to top) the gas nozzle, the conical wall, and the cylindrical tube. A draft tube and fountain confiner are incorporated to stabilize the circulation of fine bed materials. Nitrogen serves as the fluidizing agent, entering the domain through the nozzle. The arrows in Fig. 1 (a) depict the circulation of solid particles and the direction of the gas flow. Sand particles, acting as the bed material, accumulate on the conical wall and slide downward until they entrain the high-speed gas jet near the nozzle outlet. The gas flow carries the solids upward through the central spout and draft

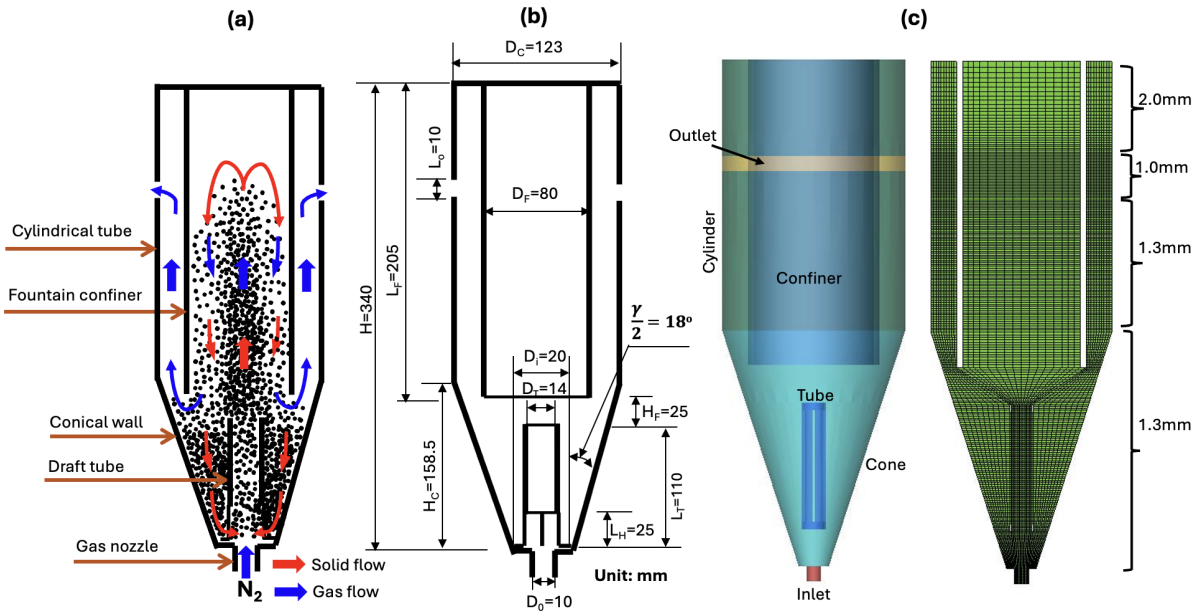

Figure 1: Work principle (a), dimensions (b), and computational grid (c) used for the simulation of a laboratory-scale, conical spouted fluidized bed (CSFB).

tube into the confiner, driven by aerodynamic drag forces. As the gas flow weakens within the confiner, the particles disengage and fall back along the sides of the cone, forming a fountain with outwardly spreading particles above the draft tube. The dimensions of the CSFB are detailed in Fig. 1 (b), with the corresponding computational domain and grid shown in Fig. 1 (c). The bulk gas flow velocity, u_G, ranges from 1 to 5 m/s, and the bed inventory, m_S, varies between 150 g and 390 g. A particle size distribution with a mean diameter of 0.23 mm was used for the sand particles. The grid resolution for the gaseous phase is set to 1 mm, and up to 5 million Lagrangian parcels are employed to track the motion of solids, depending on the bed inventory.

Results

Figure 2 (a) shows the particle distribution in a slice along the symmetry axis calculated for the case with $u_G = 3$ m/s and $m_S = 250$ g, which are colored by the moving velocity of the particle. As indicated in Fig.2 (a) by the arrows, the following four regions can be characterized for the solid distribution:

- **Annular bed** between the draft tube and conical chamber wall
- **Entrainment zone** between the annulus, nozzle exit and draft tube
- **Spout zone** with fast moving particles within the draft tube
- **Fountain zone** above exit of the draft tube and within the confiner

The solids in the annulus move downward along the conical wall due to gravitational force until they encounter the high-speed gas jet in the entrainment zone, where they are driven upward into the draft tube. Outside the draft tube, the axial gas velocity decreases significantly due to the expansion of the flow domain, causing a reduction in the aerodynamic drag forces acting on the particles. As a result, the particles descend within the confiner as the gravitational force overcomes the drag force, forming a fountain with sparsely distributed solids above the annular bed. This hydrodynamic behavior, which describes the solid circulation and spouting in CSFB, as well as the calculated pressure drop, aligns well with experimental observations. A similar behavior is illustrated in Fig. 2 (b), which shows contours of the instantaneous void fraction (ε) on a cutting plane passing through the centerline axis. Here, ε is relatively large in the fountain and spout zone, while it is smaller in the annular bed and entrainment zone. Figure 2 (c) depicts the streamlines from the calculated time-averaged, gas flow velocity. Two large, concentric, counter-rotating vortices are observed at the top of the draft tube. The upper vortex pair, which is larger, results from the outwardly recirculating gas flow within the confiner. In contrast, the

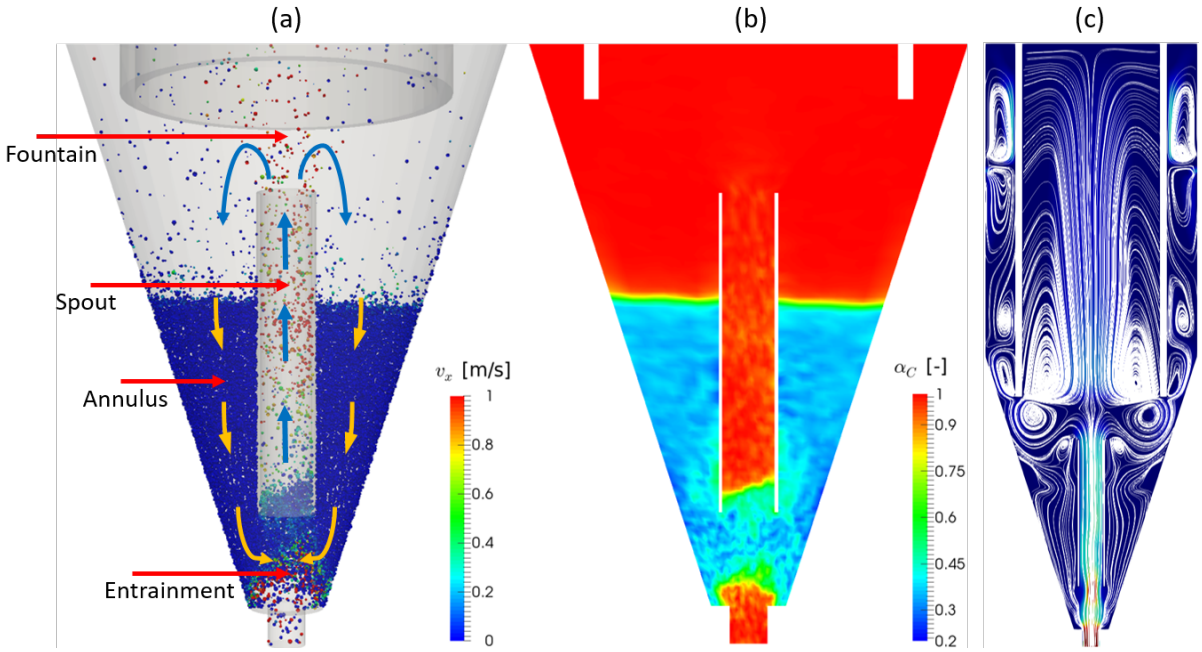

Figure 2: Particle distribution on a cutting plane passing through the centerline axis (a), instantaneous contours of void fraction (b), and streamlines based on time-averaged gas flow velocity (c) calculated from Eulerian-Lagrangian simulations of a laboratory-scale conicial spouted fluidized bed (CSFB).

lower vortices, located between the confiner and the sand bed, are caused by the expansion of the flow domain at the outlet plane of the draft tube toward the chamber wall.

To gain deeper insights into the hydrodynamics of CSFB, the specific kinetic energy of the bed materials, denoted as k_S is evaluated based on simulation results [4]. This parameter is defined as the kinetic energy of all particles normalized by the total mass of the bed material. In this way, k_S reflects the average velocity of the particles, which correlates with the efficiency of momentum transfer and mixing between the gas and solid phases. When the gas velocity u_G is varied from 1 to 5 m/s at a constant bed inventory m_S = 250 g, the bed height h_B remains nearly constant. However, k_S is at largest at 3 m/s, accompanied by the highest pressure drop Δp. This phenomenon can be explained by the fact that at low u_G, the gas jet from the nozzle lacks sufficient momentum to penetrate the entrained solids from the annulus, resulting in the fluidization of the entire bed. In contrast, at high u_G, only a small fraction of the bed material circulates through the central spout. Furthermore, increasing m_S at a constant u_G leads to an increase in h_B and Δp. However, k_S decreases with higher m_S, indicating a reduction in the efficiency of multiphase momentum exchange.

The previous simulations were conducted using a non-porous draft tube. Figure 3 (a) illustrates the particle distribution in a CSFB equipped with an open-sided draft tube featuring an aperture ratio of 60%, at m_S = 250 g and u_G = 5 m/s. The particles are color-coded according to their velocities. Compared to the case with the non-porous draft tube, the entrainment of solids from the annulus into the draft tube through its open side significantly reduces the gas phase velocity and void fraction within the draft tube for the CSFB using the porous tube, as shown by the contours of time-averaged axial flow velocity and void fraction in Fig.3 (b) and Fig.3 (c). As a result, the calculated k_S for the CSFB with the porous draft tube is approximately five times larger than that with the non-porous draft tube, indicating a substantial enhancement in gas-solid interactions. Additionally, the simulations reveal that the CSFB with the porous draft tube exhibits a significantly higher Δp compared to the configuration using the non-porous draft tube.

When comparing CSFBs with BFBs under identical bed inventory and gas flow rate conditions, the CSFB configuration demonstrates lower values of h_B and Δp compared to the BFB. This discrepancy can be attributed to the higher overall void fraction in the BFB, which results from the simultaneous fluidization

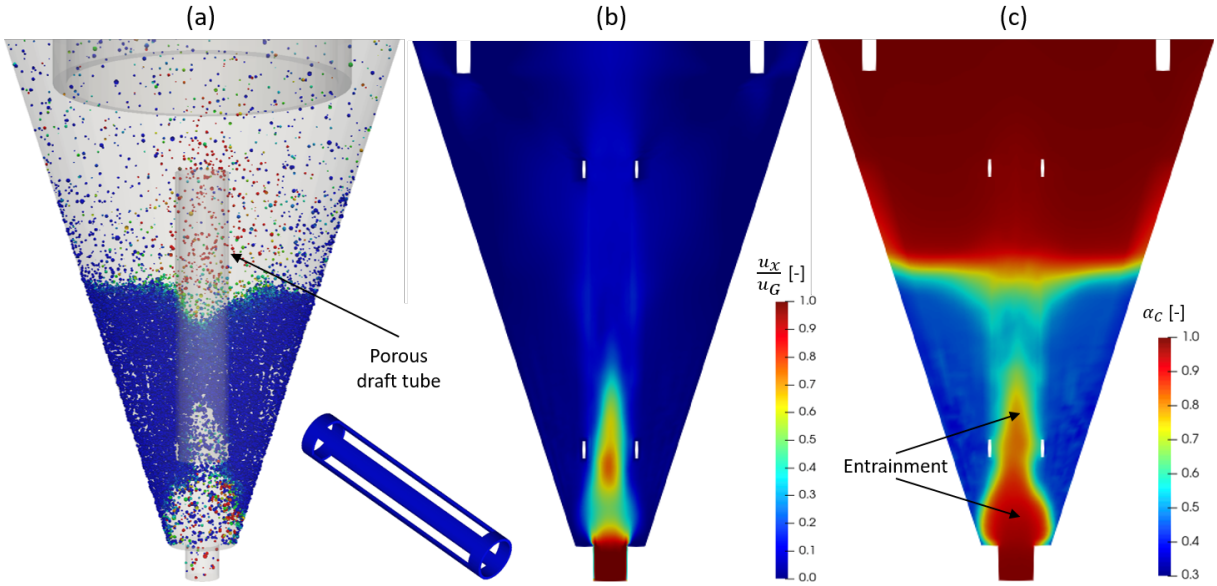

Figure 3: Results from Eulerian-Lagrangian simulations of a laboratory-scale conicial spouted fluidized bed (CSFB) using an open-sided draft tube: particle distribution on a cutting plane passing through the centerline axis (a), contours of time-averaged void fraction (b) and gas flow velocity (c).

of all bed materials. In contrast, the CSFB operates with only a portion of the bed material being spouted or circulated at any given time. Despite the lower h_B and Δp, the calculated k_S is higher for the CSFB. This is due to the significantly higher velocity of the circulated particles in the spout zone compared to those in the BFB.

The simulations provide valuable insights into the hydrodynamic behavior of CSFBs, highlighting operating conditions and design parameters that enhance the efficiency of momentum exchange between the gas and solid phases. In specific applications, such as handling coarse or sticky particles, CSFBs outperform conventional BFBs. This advantage is particularly evident in preventing issues like clogging of the perforated plate or defluidization in BFB, which can occur during processes like pyrolysis, especially when dealing with melting plastics. However, CSFBs also introduce greater complexity compared to BFBs. They require higher energy input for ventilation, leading to increased operational costs and more challenging system operation.

Acknowledgments
The authors gratefully acknowledge the financial support by the Helmholtz Association of German Research Centers (HGF), within the research program Materials and Technologies for the Energy Transition (MTET), topic Resource and Energy Efficiency. This work utilizes computing resources from the supercomputer HoreKa at the Scientific Centre for Computing (SCC) at KIT, Germany.

References

[1] Epstein N. and Grace J. (eds.): *Spouted and Spout-Fluid beds, Fundamentals and Applications*, Cambridge University Press, 2011.
[2] Alobaid F., Almohammed N., Farid M. M., May J., Rößger P., Richter A., Epple B.: *Progress in CFD Simulations of Fluidized Beds for Chemical and Energy Process Engineering*, Prog. Energy Combust. Sci. 91, 109930, 2022.
[3] Orozco S., Alvarez J., Lopez G., Artetxe M., Bilbao J., Olazar M.: *Pyrolysis of Plastic Wastes in a Fountain Confined Conical Spouted Bed Reactor: Determination of Stable Operating Conditions*, Energy Convers. Manage. 229, 113768, 2021.
[4] Zhang F., Tavakkol S., Dercho S., Zhou J., Zirwes T., Zeller M., Vogt J., Zhang R., Bockhorn H., Stapf D.: *Assessment of dynamic characteristics of fluidized beds via numerical simulations*, Phys. Fluids 36(2), 023348, 2024.

Accounting for small-scale thermochemistry in reacting granular assemblies: A PDF approach

D. Mapelli[1] and F. Sewerin[1*]

[*]E-Mail: fabian.sewerin@ovgu.de

[1]*Emmy Noether Group for Dispersed Multiphase Flows, Chair of Mechanical Process Engineering, Otto-von-Guericke-Universität Magdeburg, Universitätsplatz 2, 39106 Magdeburg, Germany*

Introduction

In the context of our transition to sustainability, it is becoming increasingly important to render industrial processes more energy- and resource-efficient and to limit greenhouse gas emissions. This particularly applies to high-temperature processes which account for a considerable amount of the total energy consumed by the industrial sector [1]. In the present contribution, we specifically consider industrial processes in which a granular assembly of particles is treated thermochemically by forcing a hot gas through the bulk. Examples include the calcination of limestone, the reduction of iron ore and the pyrolysis of biomass. In order to support a cost-efficient and timely revision or redesign of these processes, computer-based modeling and solution tools are currently being developed for reliable predictions and in-depth analyses.

In view of industrial-scale applicability, reacting granular assemblies with interstitial gas flows are commonly modeled based on an unresolved DEM-CFD approach [2]. Here, the flow field inside the inter-particle space is reduced to a volume-averaged or filtered velocity and a filtered pressure. Similarly, the reactive scalars that parameterize the gas' thermochemical state are replaced by volume averages. Concomitantly, the gas-particle interfaces are homogenized and the influence of the DEM particles on the gas-associated mass, momentum and scalar transport is referred to a void fraction, a surface density and volumetric sources. While this homogenization effectively eliminates small-scale variability and drastically reduces the spatial resolution requirements on part of a CFD-solver, it is accompanied by long-standing closure challenges. As intricate void spaces, unsteady particle wakes, chemical reactions and surface phenomena cause small-scale variability in the gas' velocity and thermochemical state, we encounter the question of how unresolved transport, localized chemistry and particle mass or heat effluxes influence the filtered descriptors. For chemical reactions and surface transfer, this closure problem is particularly grave because the corresponding rate expressions are commonly highly nonlinear.

While conventional DEM-CFD formulations are based on the assumption that the filtered gas composition is representative of the local composition [3], we propose a methodological enrichment which accommodates small-scale heterogeneity in the gas' thermochemical state and allows for the incorporation of detailed gas phase reaction mechanisms without intervening closure approximations. Following an idea that has originally been developed in the context of turbulent reacting flows [4–6], the thermochemical scalars inside the filter volume are conceived of as random variables whose values are governed by a probability density function (PDF). Since chemical reactions are spatially localized, this joint scalar PDF allows for the exact evaluation of the filtered gas phase reaction rates. Conversely, the effect of gas phase chemistry on the spatial and temporal evolution of the joint scalar PDF appears in closed form by construction.

By adapting the rationale underlying PDF methods to the DEM-CFD framework, we show how a transport equation for the joint scalar PDF may be derived while accounting for the presence of particles and accommodating gas-particle mass and heat exchanges. The scalars' distributions along the particle surfaces which occur here are approximated in terms of the joint scalar PDF. Upon integration over a single, finite-extent control volume, the PDF evolution equation is then reduced to the law governing a partially stirred reactor (PaSR) [7] that is coupled to an assembly of DEM particles. Finally, a closure for small-scale mixing is formulated and the PaSR is applied to model the heating of a particle assembly by interstitial combustion. This example serves as a testbed to gauge the influence of small-scale compositional heterogeneity on the gas-particle heat transfer, the average heating time and pollutant

emissions.

Modeling framework

A granular assembly is made from thermally thick, centimeter-sized particles that are distributed in physical space and undergo a thermochemical treatment mediated by a hot and often reactive gas. Within the scope of the discrete element method (DEM), each particle has a finite extent and its placement in relation to neighboring particles is determined by mechanical equilibrium. The state of each DEM particle is described in terms of a finite number of degrees of freedom $\mathbf{X}_p(t)$ that may change as the particle exchanges mass, momentum and heat with the surrounding gas or as intra-particle processes and contact interactions with other particles take place. For subsequent reference, we define $\mathbf{n}(\mathbf{x}, t)$ as the outward-pointing normal vector on the surface of any particle.

On part of the interstitial gas, a spatial filter with kernel $g(r)$, $r \geq 0$, is applied in order to reduce the spatial level of detail and permit a restriction of the velocity field $\mathbf{u}_g(\mathbf{x}, t)$, the pressure $p_g(\mathbf{x}, t)$ and the reactive scalars $\mathbf{\Phi}(\mathbf{x}, t)$ to scales that are comparable to the filter width [8]. In particular, the filtered counterpart $\langle Q(\mathbf{u}_g, \mathbf{\Phi})\rangle(\mathbf{x}, t)$ of an observable $Q(\mathbf{u}_g(\mathbf{x}, t), \mathbf{\Phi}(\mathbf{x}, t))$ is obtained from

$$\varepsilon_g(\mathbf{x}, t)\langle Q(\mathbf{u}_g, \mathbf{\Phi})\rangle(\mathbf{x}, t) = \int_{\Omega_g(t)} g(\|\mathbf{x} - \mathbf{y}\|) Q(\mathbf{u}_g(\mathbf{y}, t), \mathbf{\Phi}(\mathbf{y}, t))\, \mathrm{d}\mathbf{y}. \tag{1}$$

Here, $\varepsilon_g(\mathbf{x}, t)$ is the void fraction and $\Omega_g(t)$ represents the domain of the interstitial gas. For brevity, density-weighted averages are indicated by $\langle\cdot\rangle_\rho$ and defined according to $\langle Q(\mathbf{u}_g, \mathbf{\Phi})\rangle_\rho = \langle \rho_g(\mathbf{\Phi}) Q(\mathbf{u}_g, \mathbf{\Phi})\rangle / \langle \rho_g(\mathbf{\Phi})\rangle$, where $\langle \rho_g(\mathbf{\Phi})\rangle$ is the filtered gas density. Analogously to Eq. (1), we introduce the average $\{\cdot\}_p$ and its density-weighted counterpart $\{\cdot\}_p^\rho$ along the surface of particle p. The contribution by particle p to the surface density is denoted by $\xi_p(\mathbf{x}, t)$. Upon application of the filtering operation in Eq. (1), the evolution equations for the reactive scalars in the case of equal diffusivities $D(\mathbf{\Phi})$, a Lewis number of unity and a low Mach number [9, Chapter 1] turn into

$$\begin{aligned}\frac{\partial \varepsilon_g \langle\rho_g\rangle\langle\Phi_k\rangle_\rho}{\partial t} + \nabla_{\mathbf{x}} \cdot \left(\varepsilon_g \langle\rho_g\rangle \langle \mathbf{u}_g \Phi_k\rangle_\rho\right) &= \nabla_{\mathbf{x}} \cdot \left(\varepsilon_g \langle\rho_g\rangle \langle D(\mathbf{\Phi}) \nabla_{\mathbf{x}} \Phi_k\rangle_\rho\right) + \varepsilon_g \langle\rho_g\rangle \langle \dot{\omega}_k(\mathbf{\Phi})\rangle_\rho \\ &\quad + \sum_p \xi_p \{\rho_g\}_p \left\{\dot{s}_k(\mathbf{\Phi}, \mathbf{X}_p)\right\}_p^\rho .\end{aligned} \tag{2}$$

The evolution of $\langle\mathbf{\Phi}\rangle_\rho$ in Eq. (2) is driven not only by spatial transport, but also by gas phase chemistry at the rate $\dot{\boldsymbol{\omega}}(\mathbf{\Phi})$ and gas-particle mass and enthalpy transfer based on the surface fluxes $\rho_g(\mathbf{\Phi})\dot{\mathbf{s}}(\mathbf{\Phi}, \mathbf{X}_p)$. Note that, apart from scalar accumulation, all effects that influence $\langle\mathbf{\Phi}\rangle_\rho$ in Eq. (2) appear unclosed.

Drawing on the mature field of PDF methods [5, 6], the closure challenge associated with the gas phase chemical reactions is circumvented by considering, instead of $\langle\mathbf{\Phi}\rangle_\rho(\mathbf{x}, t)$, the density-weighted PDF $f^\rho(\boldsymbol{\phi}, \mathbf{x}, t) = \langle\delta(\boldsymbol{\phi} - \mathbf{\Phi})\rangle_\rho(\mathbf{x}, t)$ as large-scale descriptor of the gas phase composition. Correspondingly, the composition $\mathbf{\Phi}$ anywhere inside the filter volume may be considered as a random vector whose statistics are governed by the one-point, one-time PDF $f(\cdot, \mathbf{x}, t)$ with $f(\cdot, \mathbf{x}, t) = \langle\rho_g(\mathbf{\Phi})\rangle(\mathbf{x}, t) f^\rho(\cdot, \mathbf{x}, t)/\rho_g(\cdot)$. By time-differentiation of $\varepsilon_g(\mathbf{x}, t)\langle\rho_g(\mathbf{\Phi})\rangle(\mathbf{x}, t)\langle\delta(\boldsymbol{\phi} - \mathbf{\Phi})\rangle_\rho(\mathbf{x}, t)$ and substitution of the scalars' local balances on $\Omega_g(t)$, we obtain the following evolution equation for f^ρ,

$$\begin{aligned}&\frac{\partial \varepsilon_g \langle\rho_g\rangle f^\rho}{\partial t} + \nabla_{\mathbf{x}} \cdot \left(\varepsilon_g \langle\rho_g\rangle f^\rho \left\langle \mathbf{u}_g + \frac{\nabla_{\mathbf{x}}(\rho_g D)}{\rho_g} \middle| \boldsymbol{\phi} \right\rangle + \sum_p \xi_p \{\rho_g\}_p f_p^\rho D(\boldsymbol{\phi})\, \{\mathbf{n}|\, \boldsymbol{\phi}\}_p\right) \\ &= \nabla_{\mathbf{x}} \cdot \left[D(\boldsymbol{\phi}) \nabla_{\mathbf{x}} \left(\varepsilon_g \langle\rho_g\rangle f^\rho\right)\right] - \nabla_{\boldsymbol{\phi}} \cdot \left(\varepsilon_g \langle\rho_g\rangle f^\rho \dot{\boldsymbol{\omega}}(\boldsymbol{\phi})\right) + \mathcal{M} f^\rho + \sum_p \mathcal{S}_p f_p^\rho .\end{aligned} \tag{3}$$

This equation indicates that the temporal change of f^ρ (first term) at $\mathbf{x}$ is caused by large-scale advection (second term), large-scale diffusion (third term), gas phase chemistry (fourth term), molecular mixing (fifth term) as well as surface interactions (final term). The operators $\mathcal{S}_p$ that appear here involve the surface densities ξ_p as well as the surface fluxes $\{\rho_g\}_p \dot{s}_k(\boldsymbol{\phi}, \mathbf{X}_p)$. The particle surface contributions on either side of Eq. (3) rely on the surface distributions $f_p^\rho(\boldsymbol{\phi}, \mathbf{x}, t) = \{\delta(\boldsymbol{\phi} - \mathbf{\Phi})\}_p^\rho(\mathbf{x}, t)$ which we estimate in terms of the volume distribution f^ρ by setting $f_p^\rho = f^\rho$. Like the transport velocity in the large-scale advection term, the mixing operator $\mathcal{M}$ involves conditional expectations and is not closed in terms of

f^ρ. Indeed, our primary unknown f^ρ does not include any information on the spatial distribution of $\mathbf{\Phi}$ inside the filter volume or on $\mathbf{u}_g$-$\mathbf{\Phi}$-correlations. On the positive side, however, the influence of gas phase chemical reactions on the transport of f^ρ is naturally closed, permitting the inclusion of detailed reaction kinetics.

Upon incorporation into the DEM-CFD framework, the physically closed counterpart of Eq. (3) is combined with a modeled filtered momentum equation and the dynamic equations associated with the DEM particles. Since the DEM particles are exposed to a random gas phase composition, their associated mass and enthalpy balances include expectations with respect to $f(\cdot, \mathbf{x}, t)$. In order to be able to assess the ramifications of small-scale compositional heterogeneity without the closure challenges brought about by the second term on the left hand side of Eq. (3), the combined DEM-PDF formulation is reduced to the limiting case of large-scale homogeneity. This leads to the concept of a PaSR that interacts, through mass and heat exchanges, with a granular assembly.

Transition to the partially stirred reactor

Conceptually, the PaSR is akin to a single flow-through CFD cell that contains a reactive gas with a random thermochemical state $\mathbf{\Phi}(t)$. The randomness in $\mathbf{\Phi}(t)$ emulates small-scale variability and is governed by a time-dependent PDF $f(\cdot, t)$ [7, 10]. Based on Eq. (3), we may obtain a law for the temporal dynamics of the density-weighted PDF $f^\rho(\cdot, t) = \rho_g(\cdot) f(\cdot, t) / \langle \rho_g(\mathbf{\Phi}) \rangle(t)$ by integrating out the $\mathbf{x}$-dependency. The PaSR involves, as a parameter, the mean residence time τ_{res} and requires for closure a mixing model $\mathcal{M} f^\rho$. The mixing model that we consider here is based on an interaction-by-exchange-with-the-mean and involves the relaxation of $f^\rho(\boldsymbol{\phi}, t)$ to the completely mixed state $\delta(\boldsymbol{\phi} - \langle \mathbf{\Phi} \rangle_\rho(t))$ on the time scale τ_{mix} [7, 11].

A particular challenge associated with the solution of the modeled equation for f^ρ is its high dimensionality. Since the equation takes the form of the differential Chapman-Kolmogorov equation [12, Chapter 3], we follow a common strategy and circumvent the curse of dimensionality by constructing a statistically equivalent stochastic process as basis for a Monte Carlo solver. Algorithmically, this Monte Carlo scheme is coupled to a time integrator for the DEM particles' governing equations.

In order to estimate the influence of small-scale heterogeneity in the gas phase composition on global predictables, the PaSR is particularized to an assembly of particles that are heated by the combustion of a hydrocarbon fuel. In particular, we quantify the influence of the mixing over residence time ratio on the average heating rate, the propensity to quenching and pollutant emissions.

Summary

In classical DEM-CFD formulations, the velocity, pressure and scalar fields that characterize the interstitial gas phase are confined to large, resolvable scales with the aid of a filtering operation. Here, we augment the physical description of the gas' thermochemical state by, conceptually, replacing the filtered reactive scalars by the PDF associated with the reactive scalars inside the filter volume. This approach is gleaned from the field of turbulent reacting flows and has the advantage that the effects of homogeneous gas phase reactions are naturally closed. Additionally, gas-particle mass and heat exchanges may be accommodated by assuming that the joint scalar distribution along the surface of a particle coincides with the corresponding volume distribution. For the density-weighted joint scalar PDF, we obtain a transport equation that is linked to the DEM particles' degrees of freedom through the void fraction, the particle surface density as well as mass and heat exchange rates. Upon restriction to a finite-extent control volume and incorporation of a mixing closure, the augmented DEM-CFD formulation reduces to a PaSR model which is instrumented to assess the sensitivity of a realistic particle heat treatment to small-scale compositional heterogeneity.

Acknowledgments

This project was funded by the Deutsche Forschungsgemeinschaft (DFG, German Research Foundation) within the scope of the Collaborative Research Center/Transregio 287 (Project number 422037413).

References

[1] Hasanuzzaman M., Rahim N. A., Hosenuzzaman M., Saidur R., Mahbubul I. M., Rashid M. M.: *Energy savings in the combustion based process heating in industrial sector*, Renewable and Sustainable Energy Reviews, 16 (7), 4527–4536, 2012.

[2] Illana Mahiques E., Brömmer M., Wirtz S., van Wachem B., Scherer V.: *Simulation of reacting, moving granular assemblies of thermally thick particles by discrete element method/computational fluid dynamics*, Chemical Engineering & Technology, 46 (7), 1317–1332, 2023.

[3] Golshan S., Sotudeh-Gharebagh R., Zarghami R., Mostoufi N., Blais B., Kuipers J. A. M.: *Review and implementation of CFD-DEM applied to chemical process systems*, Chemical Engineering Science, 221, 115646, 2020.

[4] O'Brien E. E.: *The probability density function (pdf) approach to reacting turbulent flows*, Libby P. A., Williams F. A. (Eds.), Turbulent Reacting Flows, volume 44 of *Topics in Applied Physics*, Springer, Berlin, Heidelberg, ISBN: 3-540-10192-6, 185–218, 1980.

[5] Pope S. B.: *PDF methods for turbulent reactive flows*, Progress in Energy and Combustion Science, 11 (2), 119–192, 1985.

[6] Haworth D. C.: *Progress in probability density function methods for turbulent reacting flows*, Progress in Energy and Combustion Science, 36 (2), 168–259, 2010.

[7] Chen J.-Y.: *Stochastic modeling of partially stirred reactors*, Combustion Science and Technology, 122 (1–6), 63–94, 1997.

[8] Anderson T. B., Jackson R.: *A fluid mechanical description of fluidized beds. Equations of motion*, Industrial & Engineering Chemistry Fundamentals, 6 (4), 527–539, 1967.

[9] Poinsot T., Veynante D.: *Theoretical and Numerical Combustion*, 3rd ed., Aquaprint, Bordeaux, ISBN: 978-2-7466-3990-4, 2011.

[10] Finke J., Sewerin F.: *Combining a population balance approach with detailed chemistry to model the condensation of oxide smoke during aluminum combustion in spatially homogeneous reactors*, Combustion and Flame, 248, 112510, 2023.

[11] Jones W. P., Prasad V. N.: *Large eddy simulation of the Sandia flame series (D–F) using the Eulerian stochastic field method*, Combustion and Flame, 157 (9), 1621–1636, 2010.

[12] Gardiner C.: *Stochastic Methods: A Handbook for the Natural and Social Sciences*, 4th ed., Springer, Berlin, Heidelberg, ISBN: 978-3-642-08962-6, 2009.

Numerical study of reacting flows in particle beds using a hybrid lattice Boltzmann-Finite difference method under low Mach number conditions

R. Namdar[1], T. Neeraj[2], D. Thévenin[2], and F. Varnik[1*]

*E-Mail: fathollah.varnik@rub.de

[1]Department of Energy Plant Technology, Ruhr-University Bochum, Universitätsstraße 150, 44780 Bochum, Germany
[2]Laboratory of Fluid Dynamics and Technical Flows, University of Magdeburg, Universitätsplatz 2, 39106 Magdeburg, Germany

Abstract

The lattice Boltzmann method (LBM) has emerged as a powerful computational tool across diverse flow applications. While traditionally confined to incompressible flow regimes, recent advances have successfully extended its capabilities to compressible and dilatable flows. This study explores LBM's application in porous media through three comprehensive setups. First, we establish a reference configuration using cold flow conditions to validate our numerical framework. Subsequently, we investigate reactive flows within a packed bed configuration, examining the complex interplay between flow dynamics and chemical reactions. Finally, we present a detailed parametric study to assess the influence of key variables on flow characteristics and reaction kinetics. Our results demonstrate LBM's effectiveness in capturing both the hydrodynamics of porous media and the associated transport phenomena, providing valuable insights for engineering applications ranging from chemical reactors to energy systems.

Introduction

The lattice Boltzmann (LB) method has proven to be highly efficient for simulating incompressible flows. This efficiency has motivated many researchers to extend the applicability of these models to thermal compressible flows, where density variations go beyond the Boussinesq approximation. The boundary treatment proposed by LB methods allows for more effective handling of complex geometries compared to other numerical methods. Moreover, their compatibility with parallelization makes them particularly appealing for conducting simulations with high computational costs [1].

Given these advantages, we have adopted this model to study reactive flows interacting with an assembly of solid particles. Our primary objective is to understand the physicochemical phenomena occurring within such systems. Achieving this requires resolving all relevant processes at small scales. To this end, we developed a hybrid solver in which the flow field is solved using an LB approach, while the relevant transport equations regarding thermochemistry are computed using a finite-difference (FD) method. To study chemical kinetics in greater detail, we coupled our code with the open-source software CANTERA to obtain thermodynamic properties and kinetic data for our simulations.

As a validation step, we performed multiple tests and compared our results against known benchmarks as well as selected experimental studies. Moving forward, we aim to conduct a parametric study to identify key parameters that significantly influence reacting packed-bed systems.

Methodology

In this section, the governing equations of the model are briefly described. It is important to note that, although the flow consists of multiple species, the momentum balance equation is formulated for the flow as a single mixture, rather than for individual species. Thus, for a mixture of N species, the

governing equations are given as follows [2],

$$\partial_t \rho + \nabla \cdot (\rho u) = 0 \tag{1}$$

$$\partial_t (\rho u) + \nabla \cdot (\rho \vec{u}\vec{u}) = -\nabla p_{\mathrm{h}} + \nabla \cdot \tau + F_b \tag{2}$$

$$\partial_t (\rho Y_k) + \nabla \cdot (\rho u Y_k) = -\nabla \cdot j_k + \dot{\omega}_{\mathrm{k}} \tag{3}$$

$$\partial_t (\rho h) + \nabla \cdot (\rho u h) = -\nabla \cdot j_T + \partial_t p_t + \dot{\omega}_T \tag{4}$$

$$\rho(\vec{r}, t) = \frac{M_{\mathrm{w}}\, p_t(t)}{R\, T(\vec{r}, t)}. \tag{5}$$

where ρ, u, τ and F_b denote the fluid density, velocity, viscous stress tensor, and body force, respectively. The terms h, Y_k, j_k, j_T correspond to enthalpy, the mass fraction of species k, diffusion flux, and heat flux, respectively. Additionally, $\dot{\omega}_k$ and $\dot{\omega}_T$ represent the production rate of species k and the heat release rate due to chemical reactions. In this low-Mach formulation, pressure is decomposed into two components, hydrodynamic pressure p_{h} and thermodynamic pressure p_t. A detailed description of the methodology, lattice Boltzmann formulations, and implementation algorithm can be found in [2].

Results and Discussion

Cold flows

In this study we first investigate the characteristics of non-reacting air flow through structured packing composed of rotationally-aligned circular modules, with particular emphasis on the flow patterns above the packing surface in this work. Numerical simulations across a range of particle Reynolds numbers ($\mathrm{Re}_p = 100 - 1000$) are performed to reveal the distinct flow regimes, from laminar to turbulent. At lower Reynolds numbers ($\mathrm{Re}_p \leq 100$), the flow exhibits predominantly laminar behavior with well-defined secondary flow patterns induced by the spiral geometry. As Re_p exceeds 500, the flow transitions to more complex structures, characterized by enhanced mixing and the development of localized recirculation zones between the packing elements. The implemented 30° rotational offset between consecutive packing layers demonstrates significant enhancement in radial mixing, particularly prominent in the packing's middle section. Experimental validation of the numerical results provides a reliable foundation for future investigations of heat transfer in this configuration.

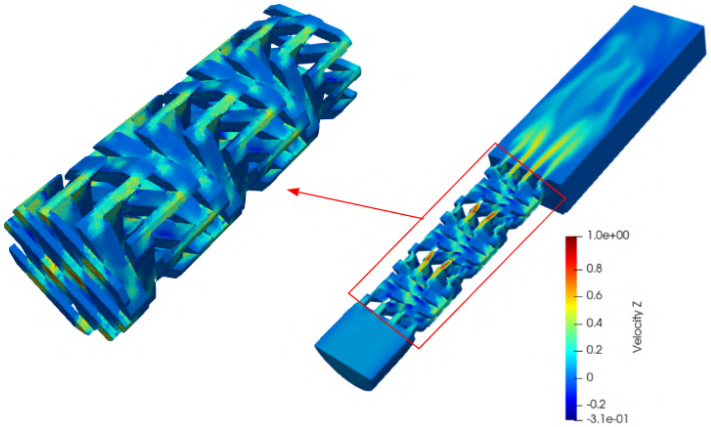

Figure 1. Visualization of axial velocity component in a structured packing: (left) details of packing structure; (right) flow field above and within the packing for particle Reynolds number of 100.

Reacting gas flows

As the next step, we investigate the interaction of premixed reactive flow gases with inert solid particles. As a case study, we chose an experimental setup consisting of an arrangement of cylindrical particles [2]. The schematic of the experimental setup is shown in Fig. 2(a). As can be observed, variations in the longitudinal direction can be neglected, allowing us to perform a two-dimensional simulation.

The bottom of the domain (inlet boundary) is divided into two parts (Fig. 2(b)): a central section responsible for injecting a premixed methane/air flow and side sections introducing air as a co-flow. This setup was designed to stabilize a flame between three cylinders positioned above the nozzle. Several controlling factors, such as inlet velocity, inlet temperature, cylinder temperature, and the equivalence ratio of the mixture, can significantly impact the flame structure.

As reported in [2], for the simulation, the inlet velocity, inlet temperature, cylinder temperature, and equivalence ratio were set to 0.3 m/s, 300 K, 373 K, and 1, respectively.

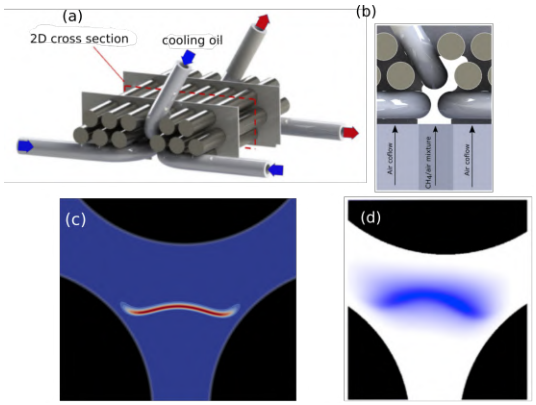

Figure 2. Panel (a) shows the configuration of the experimental setup (see [2] for details) to study flame stabilization within a packed bed. A stream of cooled oil is pumped into the cylinders surrounding the flame to maintain their temperatures at a constant value. Panel (b) displays the bottom section of the setup, where the fuel mixture and co-flow enter the bed. Panels (c) and (d) illustrate the flame position in simulation results and experiment, respectively.

Parametric study

The final study will rely on a systematic investigation of flame behavior in packed bed reactors through detailed numerical simulations, focusing on flame-packing interactions. A novel regime diagram shall be developed, analogous to classical combustion classifications, correlating temperature ratio and convective effects (Fig. 3). The preliminary analysis reveals three distinct operational regions: high convective terms leading to flame blockage and blow-off (Region I), stable flame anchoring between particles (Region II), and minimal flame-packing thermal interaction at high particle temperatures (Region III). The numerical framework incorporates detailed chemical kinetics and comprehensive heat transfer modeling for fixed, non-spherical particles. This classification system will provide a fundamental understanding of flame stabilization mechanisms in packed bed reactors and provides practical guidelines for their operational parameters.

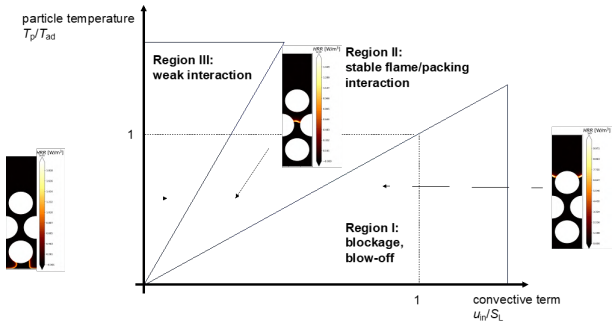

Figure 3. Exemplary interaction diagram between premixed flame and a bcc packed bed (color shows the rate of heat release at steady state). The vertical axis compares particle temperature to flame temperature, the horizontal axis flow velocity to laminar flame speed.

References

[1] Krüger T., Kusumaatmaja, H., Kuzmin, A., Shardt, O., Silva, G. and Viggen, E. M.: *The lattice Boltzmann method.*, Springer, 2017.

[2] Hosseini S. A., Safari H, Darabiha N and Thévenin D: *Hybrid lattice Boltzmann-finite difference model for low Mach number combustion simulation*, Combustion and Flame, 394–404, 209, 2019.

[3] Khodsiani M., Namdar R., Varnik F., Beyrau F. and Fond B.: *Spatially resolved investigation of flame particle interaction in a two dimensional model packed bed*, Particuology, 167-185, 85, 2024.

Acknowledgement

This work was funded by the Deutsche Forschungsgemeinschaft (DFG, German Research Foundation) – Project-ID 422037413 - TRR 287.

Combining LES with a population balance approach to model the dispersion of microcarriers in stirred bioreactors

K. Karimian[1] and F. Sewerin[1*]

[*]E-Mail: fabian.sewerin@ovgu.de

[1]*Emmy Noether Group for Dispersed Multiphase Flows, Chair of Mechanical Process Engineering, Otto-von-Guericke-Universität Magdeburg, Universitätsplatz 2, 39106 Magdeburg, Germany*

Introduction

Due to their ability to modulate the immune response, secrete trophic factors and differentiate into different cell types, human mesenchymal stem cells (hMSCs) are promising therapeutic agents that qualify for transplantation as part of regenerative therapies [1–3]. While biomedical investigations have traditionally focused on cell engraftment, for example, at the site of inflammatory or injured tissue [4], increasing attention has recently been paid to the cells' secretome [5]. Since hMSCs are isolated in small quantities, for example, from bone-marrow aspirates of healthy donors, there is a vast disparity between the initial cell count and the number of cells required for downstream clinical application, rendering the interposition of an *in vitro* cultivation process crucial [6, 7]. In particular, an industrial-scale deployment of hMSC-based therapies requires the intensification and scale-up of the cultivation, while maintaining both the cell quality and the composition of the cells' secretome [8, 9].

In this regard, the cultivation of hMSCs on microcarriers in stirred tank reactors (STRs) has shifted into focus. Here, the anchorage-dependent hMSCs are seeded onto small beads, so-called microcarriers, that are transported by the fluid flow [10]. Owing to the large surface-to-volume ratio, microcarrier suspensions allow many cells to be cultured in a single compact device that is both scalable and controllable [9, 11]. On the minus side, the transitional or turbulent flow in an STR causes elevated levels of mechanical stress which can promote spontaneous differentiation or be harmful and even lethal [12–14]. In the case of microcarrier-based hMSC cultivations, the STR is commonly operated at the just-suspended agitation rate, leading to transitional flow conditions at a modest Reynolds number [15, 16]. Although this choice minimizes the hydrodynamic stresses experienced by the cells on the microcarriers' surfaces and ensures a complete suspension, the microcarriers are inhomogeneously distributed in general and may be subject to collisions.

While the hydrodynamic stresses exerted on the microcarriers in an STR are difficult to access experimentally, they are readily available in simulations of the microcarrier-laden fluid flow. Here, however, two challenging aspects are the impeller-baffle interaction that induces continuous shape changes of the flow domain and the description of dispersed particles across a range of particle volume fractions. In particular, the particles may form a densely packed bed at start-up or at the STR's bottom with repeated or rapid particle collisions, while the fluid flow is dilute in the vicinity of the free surface [15, 16]. Previously, the particle-fluid interactions were modeled using Euler-Lagrange [14, 17] and two-fluid Euler-Euler formulations [16, 17]. While the former becomes computationally unfeasible for dense suspensions or industrial-scale reactors, the two-fluid approach involves closure assumptions that are unclear for rapidly changing and inhomogeneous flow regimes [18, Chapter 1] and was shown to overpredict the particle volume fraction at the STR's bottom [16].

In this contribution, we propose a combined modeling and solution strategy for the multiphase flow in an STR that accommodates both relative impeller-baffle motion and inhomogeneous particle concentrations. In the context of a large eddy simulation (LES), the spatially filtered carrier flow field is computed by applying the finite volume mesh-tying scheme that was recently reported by Karimian and Sewerin [19]. The dispersed microcarriers, moreover, are described statistically in terms of a velocity distribution whose spatial and temporal evolution is governed by a population balance equation (PBE). In order to estimate low-order velocity statistics while circumventing the common moment closure problem, the PBE is solved using a Eulerian Monte Carlo method [20]. The validity of our approach is assessed by

comparing model predictions with available experimental and numerical data from a transitional single phase flow [21] and existing experimental observations in a multiphase flow [15]. With regard to the optimization of the operating conditions for cell viability, predictions of the hydrodynamic forces acting on the microcarriers are obtained.

Physical description

In view of the transitional flow conditions in an STR for cell cultivation, we employ a wall-resolved large eddy simulation (LES) to describe the fluid phase. This choice represents a reasonable compromise between computational economy and physical level of detail as the temporal dynamics of the flow's resolved scales are accurately covered. The LES framework is based on the notion of a spatial filtering operation $\langle\cdot\rangle$ [22, Chapter 13] and involves the governing equations [23, 24]

$$\frac{\partial \varepsilon_f \rho_f}{\partial t} + \nabla_{\mathbf{x}} \cdot \left(\varepsilon_f \rho_f \langle \mathbf{u}_f \rangle\right) = 0, \tag{1}$$

$$\frac{\partial \varepsilon_f \rho_f \langle \mathbf{u}_f \rangle}{\partial t} + \nabla_{\mathbf{x}} \cdot \left(\varepsilon_f \rho_f \langle \mathbf{u}_f \rangle \otimes \langle \mathbf{u}_f \rangle\right) = \nabla_{\mathbf{x}} \cdot \left(\varepsilon_f \left(\langle \boldsymbol{\tau} \rangle - \langle p_f \rangle \mathbf{I} + \boldsymbol{\sigma}_r\right) + \boldsymbol{\sigma}_p\right) + \varepsilon_f \rho_f \mathbf{g} + \mathbf{F}. \tag{2}$$

Here, $\mathbf{g}$ denotes the gravitational acceleration, ρ_f is the constant fluid density and $\varepsilon_f(\mathbf{x}, t)$ represents the fluid volume fraction, while $\langle \mathbf{u}_f \rangle(\mathbf{x}, t)$ and $\langle p_f \rangle(\mathbf{x}, t)$ denote the filtered fluid velocity and pressure, respectively. Additionally, $\mathbf{I}$ is the identity tensor, $\boldsymbol{\sigma}_p(\mathbf{x}, t)$ corresponds to the particle-presence stress tensor and $\mathbf{F}(\mathbf{x}, t)$ represents the filtered force exerted by the dispersed particles on the carrier fluid per unit of volume. For simplicity, we employ an analytical expression for $\boldsymbol{\sigma}_p$ that has been obtained in the limiting case of Stokesian particles without fluid-mediated mutual interactions and is accurate to order $(1 - \varepsilon_f)$ [23, 24]. If the particles are rigid and the fluid viscosity μ_f is constant, then the filtered viscous stress tensor $\varepsilon_f(\mathbf{x}, t)\langle \boldsymbol{\tau} \rangle(\mathbf{x}, t)$ can be evaluated based on the dispersion velocity $\mathbf{v}(\mathbf{x}, t)$ and takes the form $\mu_f(\nabla_{\mathbf{x}}\mathbf{v} + (\nabla_{\mathbf{x}}\mathbf{v})^T)$ [23, 24]. Lastly, the deviatoric part of the residual stress tensor $\boldsymbol{\sigma}_r(\mathbf{x}, t)$ is closed in terms of the filtered velocity using a linear eddy viscosity model.

Microcarriers are spherical particles that typically possess a diameter of a few hundred micrometers and, hence, qualify as inertial particles. On an individual basis, the position and velocity of particle p at time t are denoted by $\mathbf{X}_p(t)$ and $\mathbf{U}_p(t)$, respectively. Since all microcarriers are identical, they share the same volume v and mass density ρ_p. In order to advance towards an economical descriptor of the dispersed phase that is compatible with a carrier phase LES and well suited for dense, many-particle dispersions, we introduce the filtered number density $N(\mathbf{u}, \mathbf{x}, t) = \langle \sum_p \delta(\mathbf{u} - \mathbf{U}_p(t)) \delta(\mathbf{x} - \mathbf{X}_p(t)) \rangle$ [25] with associated evolution law

$$\frac{\partial N}{\partial t} + \nabla_{\mathbf{x}} \cdot (\mathbf{u} N) + \nabla_{\mathbf{u}} \cdot \left(\left(\mathbf{A}(\mathbf{u}, \cdot_f) + \mathbf{g}\right) N\right) = 0. \tag{3}$$

The kinetic rate $\mathbf{A}(\mathbf{u}, \cdot_f)$ in this PBE corresponds to the average acceleration experienced by a particle with velocity $\mathbf{u}$ inside the filter volume about the location $\mathbf{x}$ owing to interactions with the fluid phase $\cdot_f$. The right hand side of Eq. (3) may further be amended by a source term $\dot{s}(\mathbf{u}, \mathbf{x}, t)$ for collisional particle-particle interactions [18, Chapter 6]. Collisions become prominent as microcarriers settle or are caught in recirculation zones, but are not yet included in our modeling framework. With the aid of the filtered number density N, the fluid volume fraction ε_f in Eqs. (1) and (2) and the dispersion velocity $\mathbf{v}$ that appears in the constitutive law for $\varepsilon_f \langle \boldsymbol{\tau} \rangle$ can be evaluated according to $\varepsilon_f = 1 - v \int N \, \mathrm{d}\mathbf{u}$ and $\mathbf{v} = \varepsilon_f \langle \mathbf{u}_f \rangle + v \int \mathbf{u} N \, \mathrm{d}\mathbf{u}$, respectively. Similarly, we obtain the expression $-\rho_p v \int \mathbf{A}(\mathbf{u}, \cdot_f) N \, \mathrm{d}\mathbf{u}$ for the contribution to $\mathbf{F}$ by the dispersed particles.

Numerical solution methods

In order to accommodate the continuous changes in shape of the flow domain in a baffled STR, the domain is decomposed into an inner and an outer subdomain. The motion of the fluid-particle dispersion on the inner subdomain is monitored from the perspective of a rotating observer that spins about the STR's axis at the same angular velocity as the impeller. The outer subdomain, by contrast, is associated with an inertial observer. At the common interface, the solutions of the filtered velocity and pressure are coupled in a mass and momentum conserving manner using a finite volume mesh-tying method [19].

The PBE for the microcarriers' velocity distribution, moreover, is solved with the aid of a Eulerian Monte Carlo scheme [20] that we extend to accommodate non-matching grids along the subdomains'

interface. Following a direct discretization in physical space, the velocity distribution inside a spatial grid cell is parameterized in terms of the total particle number density and an ensemble of velocity samples drawn from the distribution. Over the course of a time step, the ensembles in neighboring cells interact in such a way that the semi-discrete PBE is honored in a statistical sense.

Lastly, the walls of the impeller, the baffles and any additional obstructions are accounted for by a blocked-cell immersed boundary method [26, Section 7.3.2].

Validation

For a transitional single phase flow, the LES predictions are validated by comparison with the particle image velocimetry measurements and direct numerical simulations of Zhang et al. [21]. The flat-bottom STR investigated by Zhang et al. [21] features a six-blade Rushton turbine and four baffles and is operated at a Reynolds number of $Re = 1310$. Subsequently, the LES-PBE predictions of a particle-laden multiphase flow are compared with the experimental results of Collignon et al. [15]. Here, the setup consists of a 250 ml STR equipped with a four-blade Rushton turbine and cylindrical probe tubes that act as baffles. Specifically, measurements of the particle cloud height, the just-suspended agitation rate and the complete-dispersion agitation rate for a microcarrier volume fraction of 5 % are used to assess the validity of the multiphase flow model.

Summary

In the present contribution, we propose a novel modeling and solution approach for the numerical simulation of the transitional, dispersed multiphase flows in microcarrier-laden STRs. While the liquid phase is modeled by the spatially filtered continuity and momentum equations, a PBE is formulated for the velocity distribution of the microcarriers. A finite volume mesh-tying method is applied to compute the fluid flow driven by an impeller spinning past stationary baffles. Complementarily, the low-order velocity statistics of the microcarrier phase are estimated by a Eulerian Monte Carlo solver which is extended to non-matching grids. We examine the validity and accuracy of the proposed strategy by comparing model predictions of the velocity field in a single phase flow and the spatial microcarrier distribution in a multiphase flow with experimental and numerical reference data. From the multiphase flow calculation, the hydrodynamic forces acting on the microcarriers are obtained. The presented computational approach can be considered as a complementary tool for the development and calibration of a hMSC growth model [17] that accounts for the influence of the experienced mechanical stresses on the cells' fission and metabolism.

Acknowledgments

This project was funded by the Deutsche Forschungsgemeinschaft (DFG, German Research Foundation) within the scope of the Emmy Noether Program (Project number 443546539).

References

[1] Caplan A. I., Dennis J. E.: *Mesenchymal stem cells as trophic mediators*, Journal of Cellular Biochemistry, 98 (5), 1076–1084, 2006.

[2] Caplan A. I., Correa D.: *The MSC: An injury drugstore*, Cell Stem Cell, 9 (1), 11–15, 2011.

[3] Rodríguez-Fuentes D. E., Fernández-Garza L. E., Samia-Meza J. A., Barrera-Barrera S. A., Caplan A. I., Barrera-Saldaña H. A.: *Mesenchymal stem cells current clinical applications: A systematic review*, Archives of Medical Research, 52 (1), 93–101, 2021.

[4] Salazar-Noratto G. E., Luo G., Denoeud C., Padrona M., Moya A., Bensidhoum M., Bizios R., Potier E., Logeart-Avramoglou D., Petite H.: *Understanding and leveraging cell metabolism to enhance mesenchymal stem cell transplantation survival in tissue engineering and regenerative medicine applications*, Stem Cells, 38 (1), 22–33, 2020.

[5] Vizoso F., Eiro N., Cid S., Schneider J., Perez-Fernandez R.: *Mesenchymal stem cell secretome: Toward cell-free therapeutic strategies in regenerative medicine*, International Journal of Molecular Sciences, 18 (9), 1852, 2017.

[6] Jung S., Panchalingam K. M., Wuerth R. D., Rosenberg L., Behie L. A.: *Large-scale production of human mesenchymal stem cells for clinical applications*, Biotechnology and Applied Biochemistry, 59 (2), 106–120, 2012.

[7] Schnitzler A. C., Verma A., Kehoe D. E., Jing D., Murrell J. R., Der K. A., Aysola M., Rapiejko P. J., Punreddy S., Rook M. S.: *Bioprocessing of human mesenchymal stem/stromal cells for therapeutic use: Current technologies and challenges*, Biochemical Engineering Journal, 108, 3–13, 2016.

[8] Rafiq Q. A., Coopman K., Hewitt C. J.: *Scale-up of human mesenchymal stem cell culture: current technologies and future challenges*, Current Opinion in Chemical Engineering, 2 (1), 8–16, 2013.

[9] Silva Couto P., Rotondi M. C., Bersenev A., Hewitt C. J., Nienow A. W., Verter F., Rafiq Q. A.: *Expansion of human mesenchymal stem/stromal cells (hMSCs) in bioreactors using microcarriers: lessons learnt and what the future holds*, Biotechnology Advances, 45, 107636, 2020.

[10] Rafiq Q. A., Brosnan K. M., Coopman K., Nienow A. W., Hewitt C. J.: *Culture of human mesenchymal stem cells on microcarriers in a 5 l stirred-tank bioreactor*, Biotechnology Letters, 35 (8), 1233–1245, 2013.

[11] Justice C., Leber J., Freimark D., Pino Grace P., Kraume M., Czermak P.: *Online- and offline-monitoring of stem cell expansion on microcarrier*, Cytotechnology, 63 (4), 325–335, 2011.

[12] Yourek G., McCormick S. M., Mao J. J., Reilly G. C.: *Shear stress induces osteogenic differentiation of human mesenchymal stem cells*, Regenerative Medicine, 5 (5), 713–724, 2010.

[13] Jossen V., Schirmer C., Mostafa Sindi D., Eibl R., Kraume M., Pörtner R., Eibl D.: *Theoretical and practical issues that are relevant when scaling up hMSC microcarrier production processes*, Stem Cells International, 2016 (1), 4760414, 2016.

[14] Berry J. D., Liovic P., Šutalo I. D., Stewart R. L., Glattauer V., Meagher L.: *Characterisation of stresses on microcarriers in a stirred bioreactor*, Applied Mathematical Modelling, 40 (15–16), 6787–6804, 2016.

[15] Collignon M.-L., Delafosse A., Calvo S., Martin C., Marc A., Toye D., Olmos E.: *Large-eddy simulations of microcarrier exposure to potentially damaging eddies inside mini-bioreactors*, Biochemical Engineering Journal, 108, 30–43, 2016.

[16] Delafosse A., Loubière C., Calvo S., Toye D., Olmos E.: *Solid-liquid suspension of microcarriers in stirred tank bioreactor – Experimental and numerical analysis*, Chemical Engineering Science, 180, 52–63, 2018.

[17] Jossen V., Eibl R., Kraume M., Eibl D.: *Growth behavior of human adipose tissue-derived stromal/stem cells at small scale: Numerical and experimental investigations*, Bioengineering, 5 (4), 106, 2018.

[18] Marchisio D. L., Fox R. O.: *Computational Models for Polydisperse Particulate and Multiphase Systems*, Cambridge Series in Chemical Engineering, Cambridge University Press, Cambridge, New York, ISBN: 978-0-521-85848-9, 2013.

[19] Karimian K., Sewerin F.: *A finite volume mesh-tying method for computing flows in rotor-stator configurations*, Journal of Computational Physics, 531, 113863, 2025.

[20] Sewerin F.: *A Eulerian Monte Carlo method for the numerical solution of the multivariate population balance equation*, Journal of Computational Physics, 509, 113024, 2024.

[21] Zhang Y., Gao Z., Li Z., Derksen J. J.: *Transitional flow in a Rushton turbine stirred tank*, AIChE Journal, 63 (8), 3610–3623, 2017.

[22] Pope S. B.: *Turbulent Flows*, Cambridge University Press, Cambridge, New York, ISBN: 0-521-59886-9, 2000.

[23] Jackson R.: *Locally averaged equations of motion for a mixture of identical spherical particles and a Newtonian fluid*, Chemical Engineering Science, 52 (15), 2457–2469, 1997.

[24] Jamshidi R., Angeli P., Mazzei L.: *On the closure problem of the effective stress in the Eulerian-Eulerian and mixture modeling approaches for the simulation of liquid-particle suspensions*, Physics of Fluids, 31 (1), 013302, 2019.

[25] Minier J.-P.: *On Lagrangian stochastic methods for turbulent polydisperse two-phase reactive flows*, Progress in Energy and Combustion Science, 50, 1–62, 2015.

[26] Patankar S. V.: *Numerical Heat Transfer and Fluid Flow*, Hemisphere, New York, Washington, ISBN: 0-89116-522-3, 1980.

Carburization in Direct Reduction: Effects of Various CO-H_2 Gas Mixtures

S. Fong[1*], M.L. Ali[1], Q. Fradet[1], and U. Riedel[1]

*E-Mail: syafinah.bintimohdfawzifong@dlr.de

[1] *German Aerospace Center (DLR), Institute of Low-Carbon Industrial Processes, Äußere Oybiner Straße 14/16, 02763 Zittau, Germany*

Abstract

Carbon monoxide and hydrogen exhibit distinct reduction behaviors in ironmaking, impacting both the practical process operation and the resulting product. While hydrogen offers enhanced rates of reduction, its reactions with iron oxides are globally endothermic. In contrast, the reduction with carbon monoxide is not only exothermic, but is also accompanied by carburization, bringing the necessary carbon in steel. This raises questions about the optimal gas mixtures and the source of the carbon-containing gas, which should preferably come from renewable sources, such as biogenic wastes or residues. The availability of well-defined and comprehensive experimental data in the literature is currently limited. Direct reduction-grade iron-ore pellets have been reduced isothermally at temperatures from 973 to 1273 K in varying hydrogen/carbon monoxide gas mixtures. Weight changes were monitored using thermogravimetric analysis completed by analytical techniques allowing the further validation of the complex carbon deposition mechanism and the optimization of the direct reduction process.

Introduction

Hydrogen-based direct reduction (DR) followed by melting in electric arc furnace is the most promising path for decarbonization of the steelmaking industry. However, the use of carbon-containing gases is beneficial both for the ironmaking step in the shaft furnace by avoiding temperature drops from the endothermicity of hydrogen reduction, as well as for the steelmaking step in electric arc furnaces by incorporating carbon in direct reduced iron (DRI) [1]. In the mature natural gas-based direct reduction, synthesis gas from natural gas reforming is utilized and a cooling zone at the bottom of the shaft furnace permits the carburization of the pellets. To meet the decarbonization objectives and benefit from the above-mentioned advantages of carbon, the industry will gravitate towards H_2-based direct reduction enhanced by, for example, pyrolysis gases of biogenic materials. In DRI, carbon exists primarily in two forms: as iron carbide (in particular cementite Fe_3C), which is generally considered desirable, or as free carbon, which can in excess lead to operational challenges such as dusting. The investigation of carbon deposition and cementite formation for DRI is underexplored and calls for further exploration.

This study examines the effects of temperature and gas composition on the reduction of pellets and the deposition of carbon. Well-defined experimental conditions have been established to support the development of complex reduction and carburization mechanisms using a one-dimensional solid porous model [2]. This can ultimately be used to identify optimal operating conditions for industrial-scale processes, where complex temperature fields and gas mixtures, comprising CO, CO_2, CH_4, N_2, H_2, and H_2O, are encountered [3].

Experimental Method

DR-grade pellets were reduced and carburized in the experiments. The pellets contained roughly 66% (on weight basis) of iron (Fe), mostly present in the form of hematite (Fe_2O_3), and small amounts of nonferrous oxides such as Al_2O_3, SiO_2, and CaO. The pellets used in this study had a diameter ranging from 12 to 13 mm, with a mass ranging from 4.0 to 4.2 g, a porosity of approximately 29.5% and a true density of 5.06 g/cm^3.

Isothermal reduction experiments were carried out in a Linseis PT1600 thermogravimetric setup. Prior to the experiments, the sample chamber was purged with nitrogen. The sample was heated to the desired temperature in a nitrogen atmosphere. When the expected temperature was reached, a

dwell time of 20 minutes was imposed. The aim is to ensure a stable thermal equilibrium of the sample. After the dwelling, the nitrogen gas was replaced with a reducing gas mixture of a predetermined composition. All experiments were conducted using a consistent gas mixture flow rate of 300 mL/min. Variations in gas composition and reduction temperatures were introduced to study their effects. Upon completion of each experiment, photographs of each samples were taken and subjected to macroscopic analysis to evaluate the results.

Results and discussion

Figure 1 shows the conversion degree for a few of the tested conditions of the thermogravimetric test campaign. It should be noted that this so-called conversion degree is actually the pellet mass change divided by the theoretical mass after reduction of the hematite fraction to iron. As carburization results in a mass gain, it is not possible to discern it from an incomplete reduction of iron oxide. When carbon-containing gases are used, the conversion degree reaches a peak, followed by subsequent decrease due to excessive carbon deposition on the surface of the pellet. The results clearly show faster reduction with hydrogen compared to pure CO, and also higher extent of reduction. Interestingly, the rate of reduction with 50% CO is up to a certain extent very close to pure hydrogen reduction.

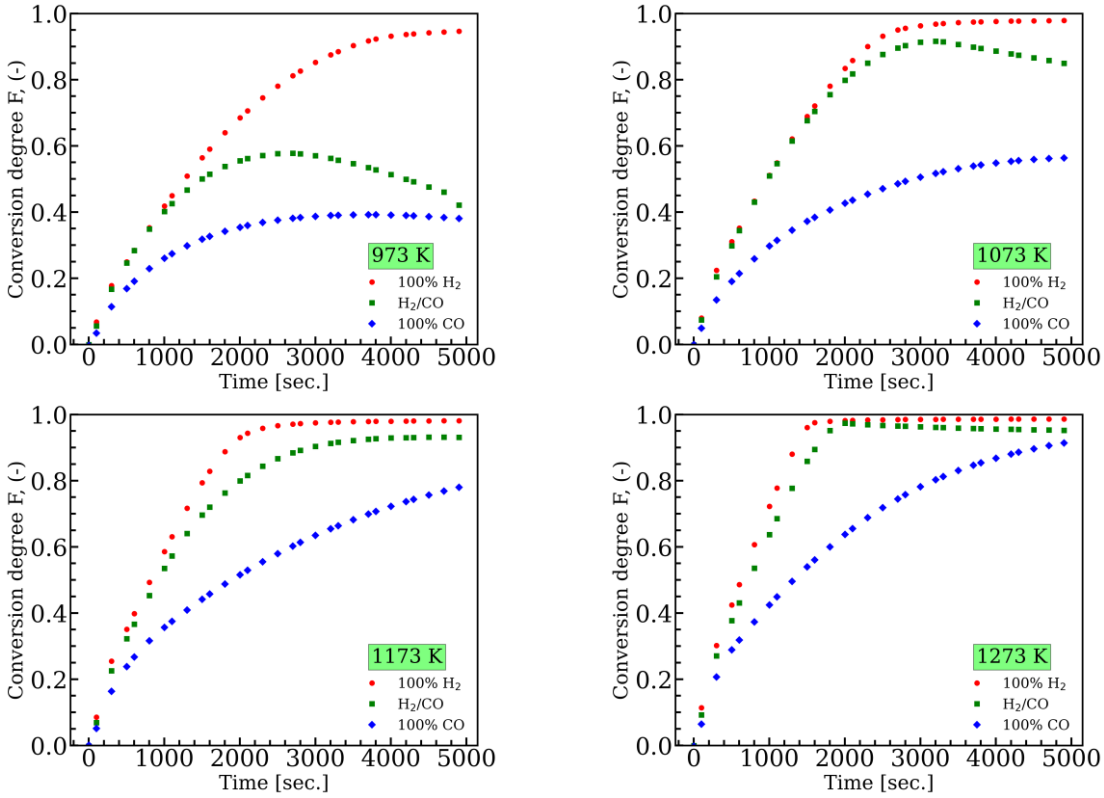

Figure 1. Conversion degree of iron ore pellets over time at 4 temperatures (973, 1073, 1173, and 1273 K). For each temperature, 3 gas compositions (100% H_2, 50/50% H_2/CO, 100% CO) were tested.

Post-reduction images of the pellets captured after 3-hour reduction time are visible in **Figure 2**. Carbon deposition is clearly promoted by lower temperatures. While the absence of carbon is obvious in the pure hydrogen cases, the much stronger carbon deposition with the H_2/CO mixture compared to pure CO shall be noted. At higher temperatures, irrespective of the gas composition, the pellets displayed visible cracks, thereby increasing the risk of pellet degradation. The experiment with the alumina ball demonstrates that iron (or iron carbides) does act as a catalyst on carbon deposition, as no carbon was found.

Figure 2. Post-reduction images of DR-grade pellets and, on the very left, alumina ball as comparison (T=973 K, 50/50% H_2/CO)

The higher reduction rate at elevated temperatures can be explained by the Arrhenius relationship of the reduction reactions. Carbon deposition, on the other hand, is favored at low temperatures due to thermodynamic considerations. In particular, the Boudouard equilibrium reaction ($2\ CO_{(g)} \rightleftharpoons C_{(s)} + CO_{2(g)}$) plays a role in the reduction process when using pure CO and is favored by lower temperatures and higher CO concentrations. But as the carbon deposition is much stronger for CO/H_2 mixtures, other pathways are at play. In particular, this effect might be attributed to the global reaction $CO_{(g)} + H_2 \rightleftharpoons C_{(s)} + H_2O_{(g)}$. An additional reason might be that H_2 promotes the reduction of iron oxide, and, as iron catalyzes carbon deposition, this further amplifies carbon deposition.

Outlook

To further validate and enhance our understanding of the reduction process, analytical techniques such as scanning electron microscopy (SEM), X-ray diffraction (XRD), and hardness testing will be employed. These analyses will provide elemental distribution across the pellet, experimental quantification of the phases present. Additionally, the TGA results will be integrated into our in-house 1D simulation model to support and validate its predictions. This combined experimental and modeling approach will offer deeper insights into the reduction mechanisms and will allow to optimize process parameters for industrial applications.

Acknowledgements

We acknowledge funding by the European Union and by tax revenues on the basis of the budget adopted by the Saxon State Parliament. European Regional Development Fund (EFRE) project "BioFe - Biomassenutzung in der Eisenerzeugung unter wirtschaftlichen und CO_2-mindernden Randbedingungen".

References

[1] Elkader M.A., Fathy A., Eissa M., et.al.: *Effect of Direct Reduced Iron Proportion in Metallic Charge on Technological Parameters of EAF Steelmaking Process*, International Journal of Science and Research (IJSR), 5(2), 2016.

[2] Ali M.L., Fradet Q., Riedel U.: *Kinetic Mechanism Development for the Direct Reduction of Single Hematite Pellets in H_2 /CO Atmospheres*, steel research int., 93(12), 2022.

[3] Kumar T.K.S., Ahmed H., Alatalo J., Björkman B.: *Carburization Behavior of Hydrogen-Reduced DRI Using Synthetic Bio-syngas Mixtures as Fossil-Free Carbon Sources*, J. Sustain. Metall., 8(4), 1546–60, 2022.

A reduced single particle model for biomass pyrolysis

L. Mieg[1*] and M. Mönnigmann[1]

[*]E-Mail: Lucas.Mieg@ruhr-uni-bochum.de

[1]*Chair of Automatic Control and System Theory, Ruhr University Bochum, Universitätsstraße 150, 44780 Bochum, Germany*

Introduction

Industrial-scale pyrolysis processes can be implemented with packed bed reactors. Packed bed reactors are often still designed based on experience, since simulations of industrial-scale reactors are challenging due to their computational cost. State-of-the-art simulation methods for this purpose couple the discrete element method (DEM) to computational fluid dynamics (CFD). The discrete element method is necessary whenever the motion of the particles in the reactor needs to be considered. The CFD simulation must describe both the flow of the surrounding fluid and needs to account for mass and energy transport between the solid and gaseous phase. In addition, the pyrolysis reaction that takes place inside the particles must be modeled. For reactions involving thermally thick particles, this necessitates models for single particles that describe the conservation of energy and mass with partial differential equations (PDEs).

Single particle models are established for thermally thick spherical particles (see e.g. [4]). A model with one spatial dimension suffices in this case to describe the progression of pyrolysis in radial direction. This is obviously no longer appropriate for non-spherical particles (see Figure 1a for an example indicative of the complexity of non-spherical particles). In general, models with three spatial dimensions are required, which are typically solved numerically with a finite-volume method. For simulations of industrial-scale reactors, solving such models for thousands of particles is not an option because of the excessive computational effort this number of particle models incurs.

The present paper investigates the use of projection-based model reduction methods for the generation of reduced particle models that can mitigate the excessive computational cost of single particle simulations for reactors that contain many particles. Specifically, we investigate whether the resulting reduced single particle model provides sufficient accuracy for packed bed simulations in spite of the computational simplicity of the reduced model. The proposed type of reduced model is chosen because it proved to be appropriate for single particle models for drying and calcination processes [3],[5], and because techniques are available to extend the resulting reduced model from a single particle to a parametrized family of particles [1].

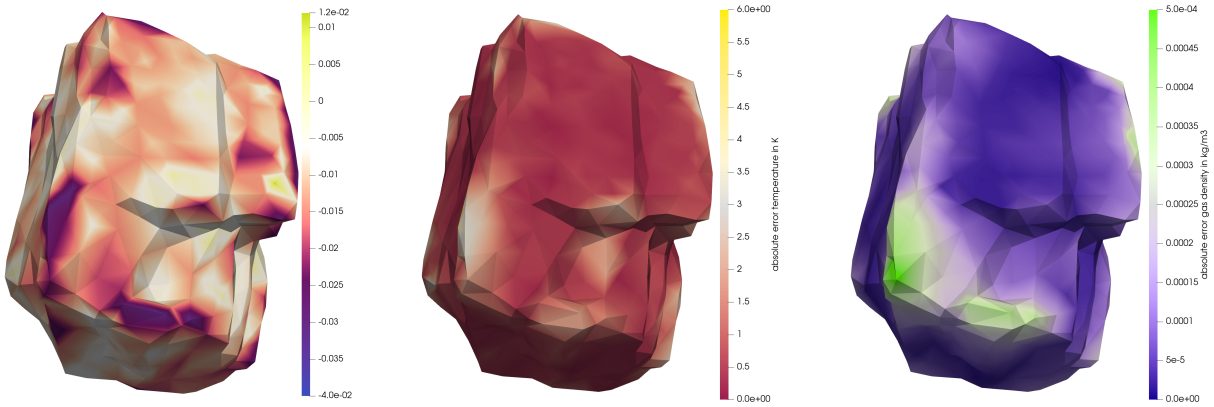

(a) dimensionless temperature mode $\varphi_5^{(T)}(x)$

(b) reconstruction error of temperature

(c) reconstruction error of gas density

Figure 1. Error measures defined in (7) for a representative thermally thick particle for an approximation with $r = 8$ modes

Continuum model for biomass pyrolysis

The reduced model is based on the particle model introduced in [2], which describes pyrolysis in terms of three lumped species: (i) biomass, here wood, (ii) a single gaseous species that lumps all volatile components and (iii) the solid reaction product, here char. While the reaction scheme is simplified, the model is no longer restricted to spherical particles but applies to arbitrary geometries. Let Ω denote the domain of the particle and let $x \in \Omega \subset \mathbb{R}^3$, t and T refer to a location inside the particle, time and temperature, respectively. Then, the conservation of biomass $m_{\text{bio}}(t)$ reads

$$\frac{\partial}{\partial t} m_{\text{bio}}(t) = -\sum_{X} \underbrace{m_{\text{bio}}(t)\, k_{\text{X}} \exp\left(\frac{-E_{a,\text{X}}}{RT}\right)}_{S_{\text{X}}(T)}, \quad X = \text{vol, char} \tag{1}$$

where the abbreviations for the source terms $S_{\text{vol}}(T)$ and $S_{\text{char}}(T)$ are introduced for use below. Since the biomass is modeled as a solid, there is no transport term in (1). To account for its porous structure, the particle is described as a volume-average continuum with porosity ε. The pyrolysis reaction is assumed to release volatiles into the pores of the particle, from where they are transported to the particle surface and released to the surrounding fluid due to pressure and concentration gradients according to

$$\frac{\partial}{\partial t}\big(\varepsilon \varrho_{\text{vol}}(x,t)\big) = \nabla \cdot \big(\varepsilon D_{\text{vol}} \cdot \nabla \varrho_{\text{vol}}(x,t)\big) + S_{\text{vol}}(T) \tag{2a}$$

$$\frac{\partial}{\partial t}\big(\rho c_p T(x,t)\big) = \nabla \cdot \big(\lambda \cdot \nabla T(x,t)\big), \tag{2b}$$

with density of volatiles $\varrho_{\text{vol}}(x,t)$, effective diffusion coefficient $D_{\text{vol}} \in \mathbb{R}^{3\times3}$, conductivity $\lambda \in \mathbb{R}^{3\times3}$, density ρ and heat capacity c_p. D_{vol} and λ are tensors to permit anisotropic materials, such as wood with its fibrous structure. The enthalpy of the pyrolysis reaction is neglected because it is small compared to the energy necessary to start the reaction.

Finally, the boundary conditions for mass and heat flux read

$$D_{\text{vol}} \cdot \frac{\partial}{\partial \vec{n}} \varrho_{\text{vol}}(x,t)|_{\partial\Omega} = \beta_{\text{eff}}\big(\varepsilon \varrho_{\text{vol}} \Delta V\big) \tag{3a}$$

$$\lambda \cdot \frac{\partial}{\partial \vec{n}} T(x,t)|_{\partial\Omega} = \epsilon_{\text{surf}}\big(T^4 - T_\infty^4\big). \tag{3b}$$

The release of the volatile surrogate species to the fluid is driven by advective transport, which is simplified in (3a) to be proportional to the mass of volatiles contained in a small volume layer ΔV at the particle surface by using an effective transfer coefficient β_{eff}. Pyrolysis takes place at comparably high temperature of 700 °C where radiation, rather than convection, dominantes heat transfer between particles and fluid, which is accounted for with (3b).

Projection-based reduced model in a nutshell

The reduced model is derived from the PDEs (2a) and (2b) analogously to the reduced model for calcination described in [3]. The key feature of the reduced model is the approximation of the PDEs by a system of r ordinary differential equations (ODEs), where the number of ODEs r is on the order of 10^1. These ODEs describe the temporal evolution of coefficients $a_j^{(T)}(t) \in \mathbb{R}$ and $a_j^{(\varrho)}(t) \in \mathbb{R}$, $j = 1, \ldots, r$, that yield $T(t)$ and $\varrho_{\text{vol}}(t)$, respectively, as linear combinations of r modes $\varphi_j^{(T)}(x)$ and $\varphi_j^{(\rho)}(x)$, $j = 1, \ldots, r$

$$T(x,t) \approx \sum_{j=1}^{r} \varphi_j^{(T)}(x)\, a_j^{(T)}(t), \qquad \varrho_{\text{vol}}(x,t) \approx \sum_{j=1}^{r} \varphi_j^{(\varrho)}(x)\, a_j^{(\varrho)}(t). \tag{4}$$

Essentially, the modes $\varphi_j^{(T)}(x)$ and $\varphi_j^{(\varrho)}(x)$ are particular spatial distributions of T and ϱ_{vol}. These particular spatial distributions are special in that they are independent of time (note that $\varphi_j^{(\cdot)}(x)$ do not depend on t) but have a particularly large contribution to $T(x,t)$ and $\varrho_{vol}(x,t)$ *at all times* considered in

the simulation. These modes can be determined systematically by finding a basis for the space spanned by the PDE simulation results, subsequently sorting the basis vectors according to the magnitude of their contributions to $T(x,t)$ and $\varrho_{\mathrm{vol}}(x,t)$ for all simulated time points t, and by disregarding all basis vectors that have a small contribution only. Technically, the modes can be found by solving a singular value decomposition of a time-series of $T(x,t)$ and $\varrho_{\mathrm{vol}}(x,t)$ obtained from a simulation of the original PDE model (see e.g. [3] for a more detailed explanation for a calcination model). The resulting modes $\varphi_j^{(T)}(x)$ and $\varphi_j^{(\varrho)}(x)$, $j = 1,\dots,r$, are defined at the same spatial locations x at which the simulation yields results, i.e. on the same spatial grid as the simulation of the PDE model is carried out on. The number r, referred to as the order of the reduced model, is equal to the number of retained basis vectors in the truncation step. The order r can be varied to control the approximation error of the reduced model. It can be expected to be on the order of 10^1 for the PDE model introduced in the previous subsection. The mode $\varphi_5^{(T)}(x)$ is shown in Figure 1a for illustration, where the domain Ω is the nonspherical particle that serves as the example in the present contribution.

After finding the modes $\varphi_j^{(T)}(x)$ and $\varphi_j^{(\varrho)}(x)$, the coefficients $a_j^{(T)}(t)$ and $a_j^{(\varrho)}(t)$ that determine the temporal evolution in (4) need to be described. These coefficients are governed by ODEs that are constructed by a projection of the PDEs onto the modes, which can be summarized as follows. By their construction via a singular value decomposition, the modes $\varphi_j^{(\cdot)}(x)$ are pairwise orthonormal with respect to the integral over the domain Ω

$$\int_\Omega \varphi_i^{(\cdot)}(x)\ \varphi_j^{(\cdot)}(x)\,\mathrm{d}v = \begin{cases} 1 & i = j \\ 0 & i \neq j \end{cases} \qquad i,j = 1,\dots,r \tag{5}$$

Substituting the linear combinations of $\varphi^{(\cdot)}$ from (4) into the PDEs, left-multiplying with $\varphi^{(\cdot)}(x)^T$ and integrating over Ω to carry out the scalar product (5) then yields the ODEs of the form

$$\sum_{j=1}^{r} M_{ij}^{(T)}\,\dot{a}_j^{(T)}(t) = J_i^{(T)} - \sum_{j=1}^{r} A_{ij}^{(T)}\,a_j^{(T)}(t), \tag{6a}$$

$$\sum_{j=1}^{r} M_{ij}^{(\varrho)}\,\dot{a}_j^{(\varrho)}(t) = J_i^{(\varrho)} - \sum_{j=1}^{r} A_{ij}^{(\varrho)}\,a_j^{(\varrho)}(t), \tag{6b}$$

where $J^{(\cdot)} \in \mathbb{R}^r$ and $M^{(\cdot)}, A^{(\cdot)} \in \mathbb{R}^{r\times r}$. The integration over Ω is converted to a surface integral with Gauss's divergence theorem such that the boundary conditions (3) are explicitly included in $J^{(\cdot)}$. The incorporation of the boundary conditions (3) is crucial since they are the connection of the single particles to the surrounding fluid and thus the whole reactor.

The reduction of the PDE model is achieved because the modes $\varphi_j^{(T)}(x)$ and $\varphi_j^{(\varrho)}(x)$, $j = 1,\dots,r$, while defined at the same spatial resolution as the PDE simulation results, need only be calculated once as a preparation, i.e. not at runtime of a full reactor simulation they are used in. At runtime, only the r ODEs (6) need to be solved, which invokes a computational effort that is smaller by an order of magnitude than that of the finite-volume method required for solving the original PDEs. It is eight times faster to solve the ODEs (6) than computing the finite-volume simulation. Figure 2 shows $a_i^{(T)}(t)$, $i = 1,\dots,4$ obtained from POD and the reduced model, respectively, for illustration. Note that it is evident from these time-series that the modes are ordered according to their contribution. The first coefficient $a_1^{(T)}(t)$, for example, indicates that the first mode contributes more strongly by at least one order of magnitude than mode 4 with $a_4^{(T)}(t)$. Furthermore, note that a steady state is attained around $t = 120s$ in Figure 2.This steady state corresponds to the pyrolyzed particle. Observe the reproduction of the this steady state by the reduced model.

In this contribution, we solve the PDEs (2) for a representative thermally thick particle with a finite-volume method. We then determine the modes $\varphi_j^{(T)}(x)$ and $\varphi_j^{(\varrho)}(x)$ introduced in (4) and the ODEs (6) to construct the desired reduced single particle model. We show that the approximation error of this reduced model can be controlled by choosing the number of modes r. To this end, we investigate the contributions of the reduction steps to this error. Figure 1, for example, illustrates the approximation

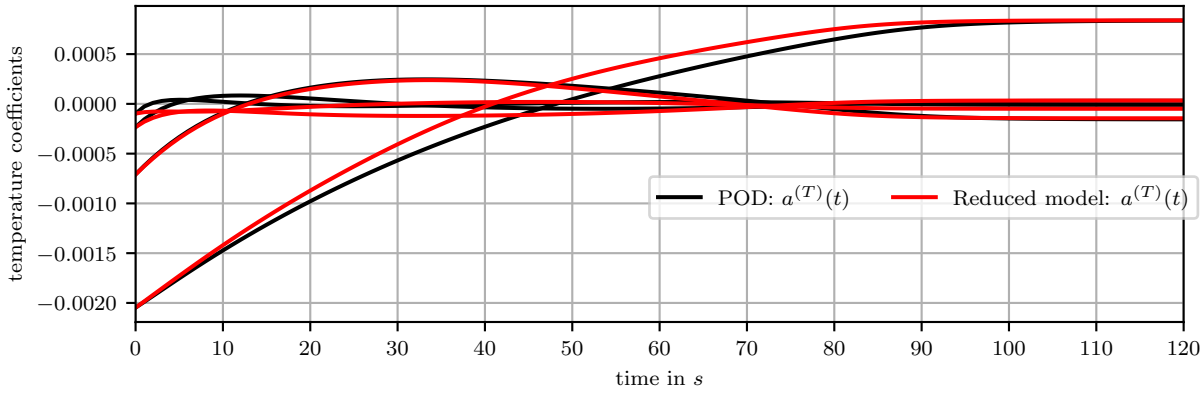

Figure 2. The temperature coefficients $a^{(T)}(t)$ for 120 s, capturing the whole pyrolysis of the wood particle shown in Figure 1a. Compare the coeficients obtained from POD (black) to the coeffcients obtained from the reduced model by integrating (6) (red).

errors in T and ρ with the quantities

$$e^{(T)}(x) = \max_t \left| T(x,t) - \sum_{j=1}^{r} \varphi_j^{(T)}(x) a_j^{(T)}(t) \right|, \quad e^{(\varrho)}(x) = \max_t \left| \varrho(x,t) - \sum_{j=1}^{r} \varphi_j^{(\varrho)}(x) a_j^{(\varrho)}(t) \right| \tag{7}$$

with reference values for the coefficients $a_j^{(T)}(t)$ and $a_j^{(\rho)}(t)$ extracted from the original PDE simulation, which essentially results in an error measure for the modes. Figure 1 shows that the error (7) is $e^{(T)}(x) < 5\,\mathrm{K}$ and $e^{(\varrho)}(x) < 6 \cdot 10^{-4}\ \frac{\mathrm{kg}}{m^3}$ for all times. Further, Figure 1 shows that the error is centered at narrow, sharp-edged elevations on particle surface.

In future work, we will extend the reduced single particle model to a parametrized reduced model that can describe the particles in a packed bed in spite of the varying boundary conditions from particle to particle. Ultimately, this parametrized reduced model will be used to speed up a DEM-CFD simulation of a packed bed containing non-spherical particles.

Acknowledgment - This work was funded by the Deutsche Forschungsgemeinschaft (DFG, German Research Foundation) - Project-ID 422037413 - TRR 287.

References

[1] Amsallem D., Farhat C.: *Interpolation method for adapting reduced-order models and application to aeroelasticity*, AIAA journal, 46(7):1803–1813, 2008.

[2] Jäger B., Illana Mahiques E., Wirtz S., Scherer V., Behling, J.: *Pyrolysis of complex-shaped single wood chips - 3D DEM simulation and a comparison with experiments*, 12th Mediterranean Combustion Symposium, Luxor, Egypt, 23rd - 26th January, 2023.

[3] Mieg L., Bergold T., Illana Mahiques E., Scherer V., Mönnigmann M.: *A reduced model for particle calcination for use in DEM/CFD simulations*, Particuology, 93:316-327, 2024.

[4] Peters B.: *Prediction of pyrolysis of pistachio shells based on its components hemicellulose, cellulose and lignin*, Fuel processing technology, 92(10):1993–1998, 2011.

[5] Reineking L., Fischer J., Mjalled A., Illana Mahiques E., Wirtz S., Scherer V., Mönnigmann M.: *Convective drying of wood chips: accelerating coupled DEM-CFD simulations with parametrized reduced single particle models*, Particuology, 84:158-167, 2023.

Advancing a Continuum Particle Model Through Pore-informed Transport Properties

F. Ryll[1], A. Dernbecher[1], N. Zhan[2,3], B. Fond[4], R. Kharaghani[2], and A. Dieguez-Alonso[1,*]

[*]E-Mail: alba.dieguez@tu-dortmund.de

[1]*Laboratory of Transport Processes, Faculty Biochemical and Chemical Engineering, TU Dortmund University, Emil-Figge-Str. 68, 44227 Dortmund, Germany*
[2]*Thermal Proccess Engineering, Otto von Guericke University Magdeburg, Universitätsplatz 2, 39106 Magdeburg, Germany*
[3]*School of Mechanical Engineering, Shanghai Jiao Tong University, Shanghai 200240, China*
[4]*Department of Aerodynamics, Aeroelasticity and Acoustics (DAAA), ONERA The French Aerospace Lab, Paris-Saclay University, Meudon, France*

1. Introduction

Research on chemical conversion in bulk solids under fluid flow has predominantly concentrated on reactor-scale models and subparticle-scale (mostly kinetic) models [1]. However, for many reactive systems, chemical reactions and transport processes in a multi-phase environment occur on comparable time scales at the particle level [1], impacting the fuel conversion rate and therefore the temperature, species, and porosity distributions [2]. The structure of the reacting particles is often complex and dynamic, particularly in biomass, which has a hierarchical structure from both physical and chemical perspectives [3]. Throughout the conversion process, both the chemical structure and physical morphology continuously evolve due to chemical reactions, directly influencing intra-particle transport and reactions, as well as the interaction of the particle with the surroundings [4,5,6]. Developing highly-resolved particle-scale models, that capture the evolution of particle morphology and its impact on intra-particle transport, chemical reactions, and particle-flow interactions to inform reactor-scale models, can greatly contribute to the development of more flexible and robust processes [1,2,3]. This advancement relies on detailed particle structure characterization through X-ray micro-computed tomography (μ-CT), supported by other techniques, which is then used to create structural geometries of varying realism [4,5,6,7]. Computational fluid dynamics (CFD) or pore network modeling (PNM) can simulate interactions at the pore level between microstructure, transport, and reaction. Despite their relevance, such highly-resolved particle-scale models cannot be directly implemented in reactor-scale models due to high computational costs. Scale-transition strategies that identify and transfer the governing physical and chemical phenomena to the next scale are therefore necessary [3].

This study explores the integration of intra-particle effective dynamic transport parameters, obtained from pore-resolved simulations, into a three-dimensional continuum particle model in the context of biomass thermochemical conversion. The predictive capability of the resulting advanced continuum particle model in reproducing the behavior of a reacting biomass particle is assessed by comparing it with experimental data. Existing data on conversion rates and major species production [8] are combined with new information on particle temperature evolution, obtained in the framework of this study.

2. Methods

The modeling and simulation part of this study builds upon an existing three-dimensional continuum particle model, which employs the uniform porous medium approach [9]. Effective dynamic transport parameters are derived from pore-resolved CFD [10] and PNM simulations performed on realistic structural geometries. These geometries have been obtained in a previous study [10] by freezing the pyrolysis reaction of a beech wood sphere at different conversion stages and characterizing the particle microstructure with X-ray micro-computed tomography.

To perform the required experiments for intra-particle and surface temperature evolution, a reactor with optical access is developed (**Figure 1**), able to reach temperatures up to 900 °C. The reacting particle is suspended in the center from a high-precision scale, providing information on reaction evolution. Type-K

thermocouples placed inside the particle enable simultaneous measurement of intra-particle temperature. However, surface temperature cannot be measured reliably with thermocouples. A thermocouple placed on the surface of the particle will not reflect the three-dimensional temperature distribution. Furthermore, due to particle shrinkage during reaction, the gas temperature in the close vicinity of the particle rather than the particle surface temperature will be monitored once the reaction becomes relevant. To characterize the particle surface temperature in the present study, phosphor thermometry has been selected as the optimal technique. The experimental setup (**Figure 1, (b)**) includes a Nd:YAG laser and a high-speed camera. A laser sheet with an excitation wavelength of 266 nm excites the $Mg_{3.5}FGeO_5$:Mn particles rubbed onto the surface of the reacting particle. The emitted phosphorescence lifetimes, directly related to the temperature, are recorded by the high-speed camera, similarly as done by Cai et al. [11].

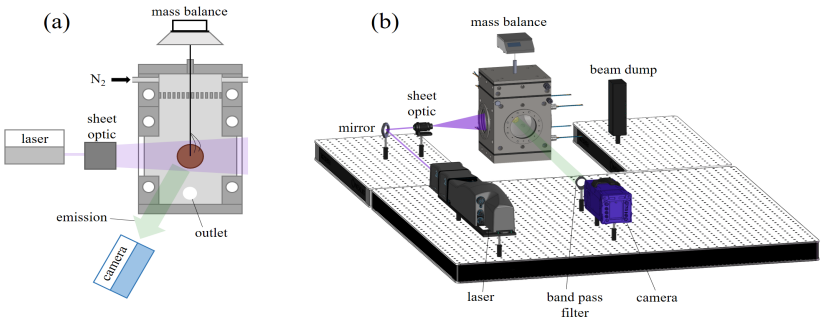

Figure 1. (a) Schematic representation of the single particle reactor. (b) Experimental arrangement.

3. Results and Conclusions

To elucidate the complex multi-phase and multi-scale processes in biomass thermochemical conversion, advanced particle models that incorporate the effects of biomass anisotropy and heterogeneous structure on intra-particle transport and reaction, alongside detailed experimental characterization, are essential. The proposed workflow for this task is shown in **Figure 2**, though this study addresses only specific aspects, as discussed below.

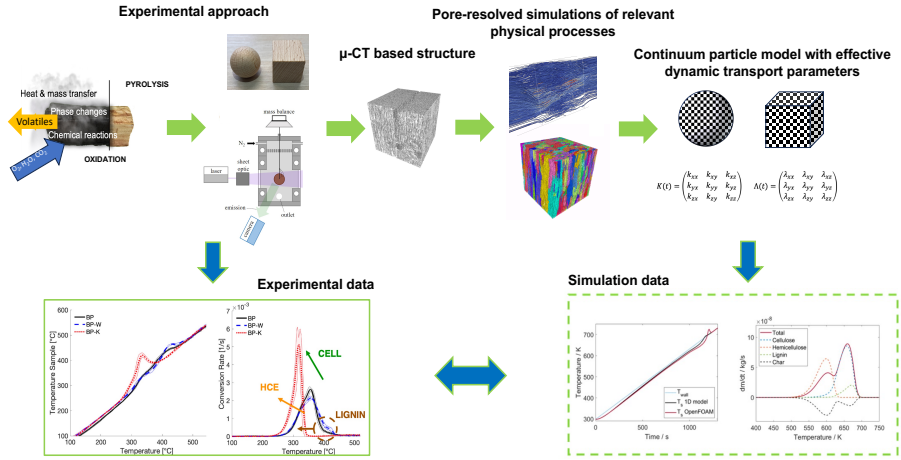

Figure 2. Proposed workflow. µ-CT based structure and pore-resolved CFD simulations on flow permeability [10], simulation results with conventional continuum particle model [12], and depicted experimental results [8] are not part of the present study.

Simpler but still representative biomass particle geometries are selected for thermochemical conversion processes. A combination of experimental techniques characterizes these processes from various perspectives. This study integrates new data on particle temperature evolution with existing data on conversion and major product species release (with ex-situ integral characterization) [8], in the framework of slow pyrolysis of beech wood particles. It particularly examines the non-homogeneous temperature gradients that arise during conversion, resulting from the non-homogeneous external reaction conditions and the particle anisotropic morphology and structure. Freezing the pyrolysis conversion at various stages allows access to the dynamic intra-particle pore microstructure. This was previously achieved using a

beech wood sphere [10]. The resulting µ-CT based structural geometries are used for pore-resolved simulations. Initial pore-resolved CFD simulations of flow permeability through selected subdomains of the aforementioned particle have shown strong anisotropic permeability, with non-monotonic increase with conversion [10]. This supports the need to implement pore-informed effective transport properties in particle-level models to properly address the intra-particle interaction between transport and chemistry,fab as well as the interaction of the particle with the surroundings. In the present study, the capabilities of CFD and PNM simulations are first assessed in terms of their ability to capture the impact of the dynamic and anisotropic intra-particle microstructure on permeability, effective conductivity, and diffusivity. Strategies for effective integration of these pore-resolved transport properties in the continuum particle model are evaluated and its performance is first assessed against the obtained experimental thermal behaviors. This comparison provides insights into the impact of intra-particle anisotropic transport on the particle behavior during reaction. Further comparison with conversion and major species production provides further information on the coupling between transport and chemistry in this complex conversion process.

Acknowledgements
This work was funded by the Deutsche Forschungsgemeinschaft (DFG, German Research Foundation) – Project-ID 422037413 - TRR 287.

References

[1] Ciesielski P. N., Pecha M. B., Thornburg N. E., Crowley M. D., Gao X., Oyedeji O., Sitaraman H., Brunhart-Lupo N.: *Bridging scales in bioenergy and catalysis: A review of mesoscale modeling applications, methods, and future directions*, Energy & Fuels, 35, 18, 2021.

[2] Fatehi H., Weng W., Li Z., Bai X.-S., Aldén M.: *Recent development in numerical simulations and experi mental studies of biomass thermochemical conversion*, Energy & Fuels, 35, 9, 2021.

[3] Ciesielski P. N., Pecha M. B., Lattanzi, A. M., Bharadwaj, V. S., Crowley, M. F., Bu, L., Vermass, J. V., Steirer, K. X., Crowley, M. F.: *Advances in Multiscale Modeling of Lignocellulosic Biomass*, ACS Sustainable Chemistry & Engineering, 8, 3512-3531, 2020.

[4] Crowley M. F., Sitaraman H., Klinger J., Usseglio-Viretta F., Thornburg N. E., Brunhart-Lupo N., Pecha M. B., Dooley J. H., Xia Y., Ciesielski P. N., *Measurement of Transport Properties of Woody Biomass Feedstock Particles Before and After Pyrolysis by Numerical Analysis of X-Ray Tomographic Reconstructions*, Frontiers in Energy Research, 10, 2022.

[5] Fong G. H., Jorgensen S., Singer S. L., *Pore-resolving simulation of char particle gasification using micro-CT*, Fuel, 224, 752-763, 2018.

[6] Pecha M. B., Garcia-Perez M., Foust T. D., Ciesielski P. N., *Estimation of Heat Transfer Coefficients for Biomass Particles by Direct Numerical Simulation Using Microstructured Particle Models in the Laminar Regime*, ACS Sustainable Chemistry & Engineering, 5, 1046-1053, 2017.

[7] Ciesielski P. N., Crowley M. F., Nimlos M. R., Sanders A. W., Wiggins G. M., Robichaud D., Donohoe B. S., Foust T. D., *Biomass Particle Models with Realistic Morphology and Resolved Microstructure for Simulations of Intraparticle Transport Phenomena*, Energy & Fuels, 29, 242-254, 2015.

[8] Almuina-Villar H., *Investigation of the pyrolysis mechanisms at particle level: insights into heterogeneous secondary reactions with the aid of in-situ laser-based spectroscopy*, PhD Thesis, Fakultät III Prozesswischenschaften, Teschnische Universität Berlin, 2022.

[9] Dernbecher A., Dieguez-Alonso A., *Advanced Porous Particle Model in Biomass Pyrolysis*, Chemical Engineering Transactions, 92, 2022.

[10] Dernbecher A., Bhaskaran S., Vorhauer-Huget N., Seidenbecher J., Gopalkrishna S., Briest L., Dieguez-Alonso A., *Investigation on the intra-particle anisotropic transport properties of a beech wood partiche during pyrolysis*, Particuology, In press, 2025.

[11] Cai T., Khodsiani M., Hallak B., Abram C., Beyrau F., Specht E., *Phosphor thermometry at the surface of single reacting large-diameter spherical coke particles to characterise combustion for packed-bed furnances*, Proceedings of the Combustion Institute, 38, 4225-4232, 2021.

[12] Dernbecher A., *Numerical Investigation of thermo-chemical conversion processes for small-scale biomass heating systems*, PhD Thesis, Fakultät III Prozesswischenschaften, Teschnische Universität Berlin, 2024.

Single Biomass Particle Pyrolysis - 2D Model Including Gas Pressure and Thermal Deformations

P. Hercel[1*] and D. Kardaś[1]

[*]E-Mail: phercel@imp.gda.pl

[1]*Institute of Fluid-Flow Machinery, Polish Academy of Sciences, Fiszera 14, 80-231 Gdańsk, Poland*

Introduction

The study presents a mathematical model describing thermal decomposition process of a single wood particle undergoing pyrolysis. The model incorporates fundamental conservation laws to predict temperature distributions, mass loss, gas pressure changes, and mechanical deformations due to thermal stresses. The governing equations are solved using the finite difference method with explicit numerical schemes. The applied numerical approach balances the simplicity of the model with computational efficiency and accuracy.

A precise description of a single shrinking particle is crucial for accurately simulating the behavior of particles within larger systems, such as packed or fluidized beds. The proposed model provides detailed insight into the evolution of particle size, internal stresses, and gas release, which are key factors in determining the overall efficiency of industrial processes involving particle beds. By capturing the complex interactions between thermal and mass transport phenomena at the particle level, this model contributes to improving the accuracy of large-scale simulations of particle beds in gas fluxes.

Geometry

The computational domain represents a wooden sample undergoing thermal decomposition. Initially, the domain is a two-dimensional quadrilateral shape with dimensions of 20×5 mm. The domain is divided into a structured Cartesian mesh composed of squared cells, each of equal dimensions. As the decomposition progresses, the integrity of the material changes. This includes non-uniform deformations in the structure. These deformations lead to modifications in the mesh, which will be updated dynamically to reflect the evolving geometry. The positions of the nodes will be adjusted on the basis of the computed displacements occurring due to thermal stresses.

Governing Equations

The model incorporates the coupled effects of heat transfer, mass transport, and thermal deformation within the particle. Two mass balance equations, solid phase energy equation, two pressure equations for pyrolysis gas and water vapour using Darcy's law, and a set of equations for mechanical deformations are solved.

The mass balance equations describe the production of pyrolysis gas due to solid mass loss and the dynamic changes in moisture content due to evaporation. The solid mass loss equation is:

$$\frac{\partial m_s}{\partial t} = -k\,(\alpha - \overline{\alpha}(T))\,m_{s,0}\,, \tag{1}$$

where m_s and $m_{s,0}$ are instantaneous and initial mass of solid fraction (kg). Parameter α is a ratio of total instantaneous mass and initial mass $m(T)/m_0$, while $\overline{\alpha}$ is a reference decomposition function measured for very low heating rate (1 K/min). It is assumed that, under conditions of a very low heating rate, all decomposition processes that can occur at a given temperature have sufficient time to take place. Introducing $\overline{\alpha}$ into the formula ensures that only the substrates that can actually decompose at a specific temperature are taken into account in the simulation. Similar approach was used previously by Postrzednik [1], Wardach-Święcicka [2], and Kardaś et al. [3].

The kinetic model uses a simple single-reaction approach. The pyrolysis reaction rate constant k is described by the Arrhenius equation:

$$k = A \exp\left(-\frac{E_a}{RT}\right) \tag{2}$$

where A is a pre-exponential factor (1/s), E_a is energy of activation (J/mol), R is the universal gas constant (J/(mol K)), and T is local temperature (K). For moisture mass balance the equation is:

$$\frac{\partial m_w}{\partial t} = -j_w A_i \ , \tag{3}$$

where m_w is instantaneous moisture mass, j_w is evaporation flux, and A_i is area of evaporation.

The energy equation describes the temperature distribution within the particle, considering conductive heat transfer, as well as heat effects resulting from the moisture phase change and the heat of pyrolysis reactions. The following form of equation is solved:

$$\frac{1}{V}\frac{\partial\left(m_s u_s + m_w u_w + m_g u_g\right)}{\partial t} = \lambda \nabla T + \frac{h_g}{V}\frac{\partial m_s}{\partial t} + \frac{h_{wv}}{V}\frac{\partial m_w}{\partial t}, \tag{4}$$

where u_s, u_w, u_g, and m_s, m_w, m_g are internal energies and mass of solid, water and gas, respectively. For simplicity, it is assumed in the mass balance that the mass of gaseous phase is negligibly small. On the right-hand side of the equation the first term describes conduction, where λ is thermal conductivity coefficient (W/(mK)), and T is temperature (K). The model takes into account different values of λ depending on the direction and the assumed structure of wood. The last two terms represent energy sources resulting from the released pyrolysis gases and the evaporating moisture.

Two pressure equations are used to calculate pyrolysis gas and steam pressure distribution in the porous medium of wood. The equations were derived based on the gas mass balance equation. The pyrolysis gas equation links the pressure to the flow of gases through the wooden sample. The steam pressure equation allows for a more accurate calculation of the moisture evaporation flux including the possible effects of condensation inside the particle, when the steam pressure is higher than the water vapor saturation pressure. The pressure equation for pyrolysis gasses is:

$$\frac{\partial p_g}{\partial t} = \frac{1}{V\frac{\partial \varrho_g}{\partial p_g}}\nabla\left(\varrho_g \cdot \vec{v}\right) + \frac{S_g}{V\frac{\partial \varrho_g}{\partial p_g}}, \tag{5}$$

where p is pressure (Pa), ϱ is gas density (kg/m^3), v is velocity (m/s). The pressure equation for steam is of the same form, but uses physico-chemical parameters for steam and the source term includes evaporated moisture mass (S_w) instead of solid mass loss term (S_g):

$$\frac{\partial p_w}{\partial t} = \frac{1}{V\frac{\partial \varrho_w}{\partial p_w}}\nabla\left(\varrho_w \cdot \vec{v}\right) + \frac{S_w}{V\frac{\partial \varrho_w}{\partial p_w}}, \tag{6}$$

The velocity vector in both equations is determined by Darcy's law:

$$u = -\frac{K}{\mu}\left(\frac{\partial p_g}{\partial x}\right), \tag{7}$$

and for the component in the direction of y axis:

$$v = -\frac{K}{\mu}\left(\frac{\partial p_g}{\partial y}\right), \tag{8}$$

where K is wood permeability (m^2), μ is dynamic viscosity ($Pa \cdot s$).

The motion equations used for calculating the thermal deformation are in the form:

$$\frac{\partial \sigma_x}{\partial x} + \frac{\partial \tau_{xy}}{\partial y} = \varrho\frac{\partial^2 u_x}{\partial t^2}, \tag{9}$$

$$\frac{\partial \tau_{xy}}{\partial x} + \frac{\partial \sigma_y}{\partial y} = \varrho\frac{\partial^2 u_y}{\partial t^2}, \tag{10}$$

where σ and τ are normal and shear stress, respectively (Pa), and u_x, u_y are displacement (m).

With the incorporation of appropriate constitutive relations for the wood model, the accurate computation of deformations is possible. At the current stage of this study, the relations have been implemented based on the work of Wilczyński and Gagolin [4], and the work is ongoing to obtain stable and high-quality results for thermal deformations.

Methods

The simulations were conducted using an in-house code written in Modern Fortran. All equations, except those for deformations, are solved using an explicit single-step finite difference scheme. This method ensures computational efficiency for transient heat and mass transfer calculations. However, for the thermal deformation equations, higher-order numerical methods will have to be employed to enhance accuracy.

The geometric change of the domain plays an important role in simulation of the coupled effects of temperature distribution, mass loss and gas pressure effects. Dynamically adapting non-orthogonal mesh allows for better reflection of the pyrolysis process. The governing equations are going to be solved on dynamically changing, non-orthogonal mesh. Therefore, special attention is required for the interpolation of field variables. Gradients of temperature and gas velocity (for pressure equation) are calculated on walls of each cell. In order to do this, in the first step, the interface areas between cells and normal vectors of these areas had to be calculated. The interface areas and normal vectors are calculated based on the coordinate points of the nodes.

Initial Results and Discussion

The current results focus on mass loss (α), temperature distribution, and pressure evolution within the particle. The results can be seen in **Figure 1** and **Figure 2**. The most interesting distributions were chosen for results presentation, therefore the time steps of the results are varying. Although the thermal deformation calculations are not yet completed, therefore the shrinking effect is not visible on the presented results at the moment, the model is designed and ready to accommodate dynamic mesh adaptation for planned simulations.

The most important and main conclusion from the results obtained so far is that thermal energy is crucial for the pyrolysis process. It can be observed that only after reaching the appropriate temperature, a reflection of the mass loss of the solid phase becomes visible. Then, a wave of increasing gas pressure can be noticed in the areas of the most intense decomposition. These processes occur one after another with a certain time gap, but not at the same moment. Similar behaviour can be observed in the case of steam pressure, which follows and reflects the moisture evaporation processes in the particle.

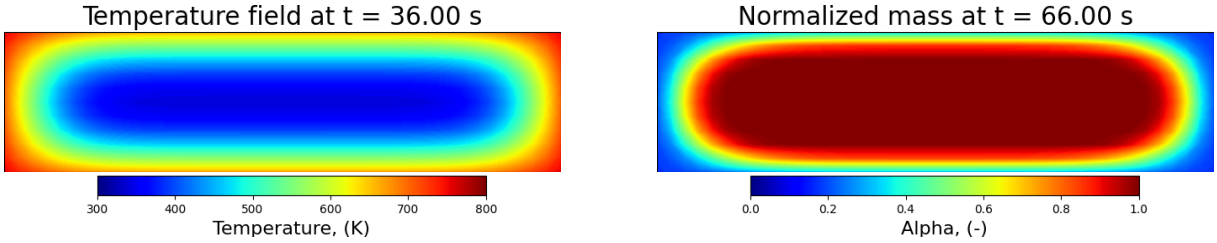

Figure 1. Temperature and decomposition stage (normalized mass, α) distribution.

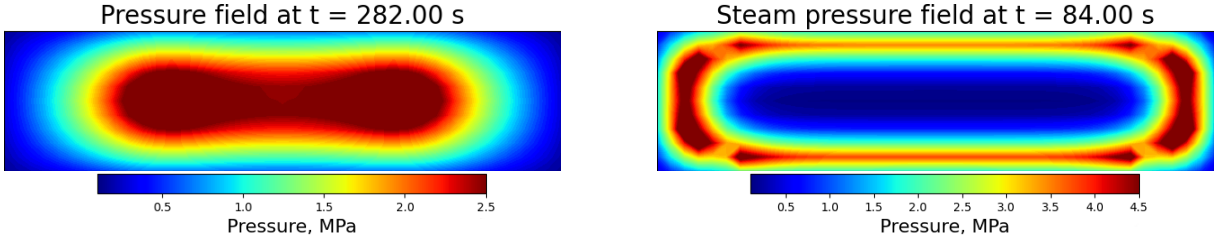

Figure 2. Gas pressure and steam pressure distribution for initial moisture mass fraction of 0.3.

Acknowledgment
This work was supported by the Horizon Europe research and innovation programme under the project ResMe2E, grant agreement No. 101172988.

References

[1] Postrzednik S.: *Heat of solid fuel pyrolysis - determination method, basic properties, in Polish*, Karbo-Energochemia-Ekologia, 9, 220-220, 1994.

[2] Wardach-Święcicka I.: *Modelling of physico-chemical processes in a single solid fuel particle in a stream of hot gases*, (in Polish), Ph.D. Thesis, Institute of Fluid-Flow Machinery, Polish Academy of Sciences, 2016.

[3] Kardaś D., Hercel P., Polesek-Karczewska S., Wardach-Święcicka I.: *A novel insight into biomass pyrolysis – The process analysis by identifying timescales of heat diffusion, heating rate and reaction rate*, Energy, 189, 116159, 2019, DOI: https://doi.org/10.1016/j.energy.2019.116159.

[4] Wilczyński A., Gagolin M.: *Badanie właściwości sprężystych drewna sosny, buka i dębu*, (in Polish), Zeszyty Naukowe Wyższej Szkoły Pedagogicznej w Bydgoszczy. Studia Techniczne, 15, 89-125, Wydawnictwo Wyższej Szkoły Pedagogicznej w Bydgoszczy, 1990.

Mixing behaviour of complex shaped particle assemblies on a generic grate

N. Hilse[1*], V. Scherer[1]

*E-Mail: hilse@leat.rub.de

[1] Department of Energy Plant Technology, Ruhr-University Bochum, Universitätsstraße 150, 44780 Bochum, Germany

Abstract

Building on previous studies that explored the mixing behaviour and the particle size segregation of polydisperse, spherical particle assemblies on a batch stoker grate, recent investigations have shifted towards complex shaped bulk materials. Under varying operational conditions, the mixing behaviour of monodisperse dodecahedra assemblies was examined and compared to bulks of spherical particles of similar size. The current contribution extends the data set by two regular polyhedra, which are further reduced in sphericity. Monodisperse and bidisperse octahedra and hexahedra assemblies are agitated on the generic grate to gain insight in their mixing behaviour and segregation effects. Results of Discrete Element Method Simulations are compared to experimental data to verify the numerical procedure and to gain knowledge about optical inaccessible processes insight the bulk.

In comparison, the octahedra and hexahedra assemblies show diverging behaviour in agitated monodisperse assemblies. For both geometries, the surrounding walls have a major influence on the particle arrangement.

For the bidisperse mixture, a clear segregation of the octahedra can be recognised. Here it also becomes clear that the main characteristics of the movement modes used, which have been observed in detail for spherical particles, also apply here.

Material and Methods

The experimental setup is modelled after industrial grate systems but does not include material feeding or discharge. Instead, the granular material is initially arranged manually in horizontal layers atop 15 individually movable stoking bars. Each aluminium bar is controlled by an independent stepper motor, enabling various movement modes. The rig is enclosed by polycarbonate walls, ensuring optical access to the particle bulk. The enclosed space measures 320 × 302 × 300 mm³. A detailed description of the set up and previous studies on mixing and segregation of spherical particles can be found in [1].

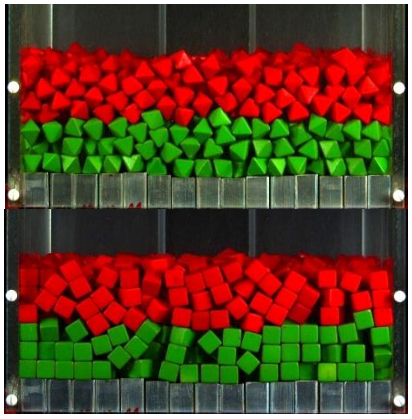

Figure 1. Initial monodisperse particle arrangement, top: octahedra, bottom: hexahedra

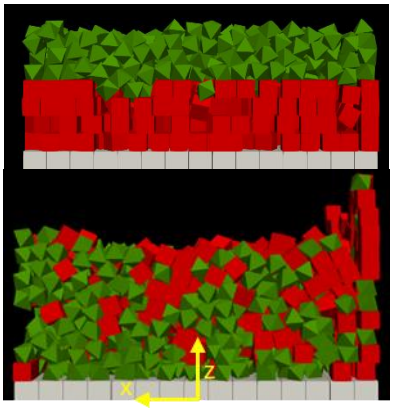

Figure 2. Bidisperse particle arrangement (DEM simulation), top: initial arrangement, bottom: final arrangement (410 s, three groups mode)

The particles used in the experiments consist of colored polymethylmethacrylate (PMMA) and are shown in figure 1. The octahedra consist of eight equilateral triangles with an edge length of 16.1 mm.

The hexahedra have an edge length of 15.5 mm. The number of particles used depends on an aimed bed height of 100 mm and is 882 particles for each hexahedra layer and 1180 particles for each octahedra layer. In each experiment, two layers of particles of different color are used to visualized particle movement. All experiments are recorded from the front view using a Basler acA2040-55uc camera with a resolution of 2048 × 1536 pixels. This study focusses on two movement modes. The wave mode (WM) and the three groups mode (3G) are described in detail in several studies, a. o. [2], [3] und were found to result in characteristic particle movement patterns in z- (height) and x- (width) direction when examining spherical particle bulks.

The Discrete Element Method (DEM) simulations are conducted using an in-house DEM code, developed as part of the ongoing research within the Collaborative Research Center Bulk-Reaction, funded by the German Research Foundation [4]. Particle interactions, including contacts between individual particles and the enclosure walls, are detected using the Gilbert–Johnson–Keerthi (GJK) algorithm, while forces are computed via a spring-dashpot model. The simulations not only allow direct comparison with experimental results from the front wall but also provide insight into the internal dynamics of the granular bulk. Figure 2 exemplarily shows images of the DEM simulation of the bidisperse particle assembly.

The visual comparison of the experiments and the DEM simulation shows good agreement. Figure 3 shows a selection of images that highlight the reproducibility of the characteristics of the particle movement. Due to the applied artificial illumination, the experimental results show the foremost layer of the particles, while the particles in areas behind are in shadow. In order to illustrate this effect in the simulation, only the foremost layer of the simulated particles is shown here. The original simulation consists of the entire particle bed and contains the particle quantities specified above.

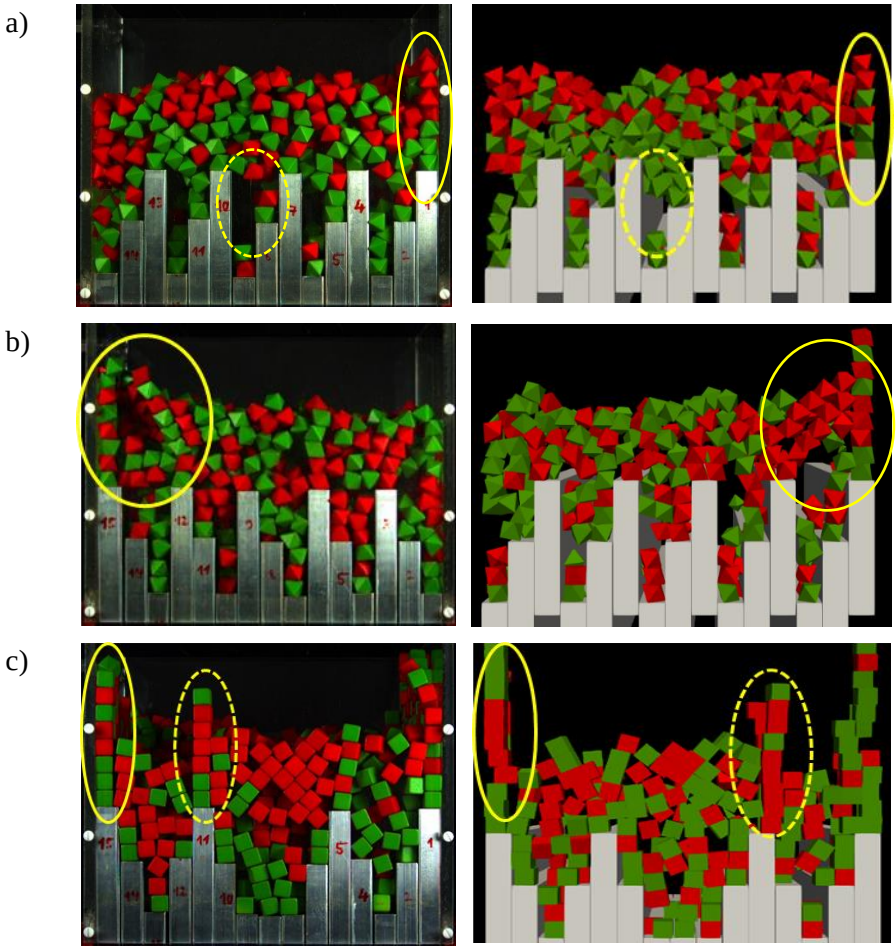

Figure 3. Comparison of experiments and simulation, 3a) and b): octahedra in 3G mode, c): hexahedra in WM mode

The octahedra assembly shows tendencies to build particle stacks which are mainly detected in the corners but also occur at plane walls. Between the bars gaps form due to bridgebuilding of the particles (figure 3a). This effect can also be seen on top of the particle bulk caused by diagonal stacking of the particles, shown in Figure 3b. The hexahedra assembly depicted in figure 3c shows a stronger stacking of the particles and less bridge building. It appears, that these effects are increased for the DEM simulation, resulting from the ideal geometry and mass distribution of the numerical geometries.

The particle positions received from the simulations are analyzed to investigate the influence of different movement modes on the distribution and segregation effects. The boxplots of the directional particle position in x-direction are shown in figure 4. For a simulation time of 410 seconds (3G), segregation effects can be visualized for the bidisperse particle bulk.

At the beginning the initial particle distribution is equal for both layers. The minimum and maximum values (-0.15 m and 0.15 m) correspond to the dimensions of the set up. The median for both geometries can be found in the center at 0.0 m. The continuous bar movement causes the octahedra to migrate towards positive values on the x-axis, while the hexahedrons tend to accumulate in the opposite direction. This behavior can also be observed in figure 2, where the octahedra accumulate in the lower left corner (positive x-values) of the grate.

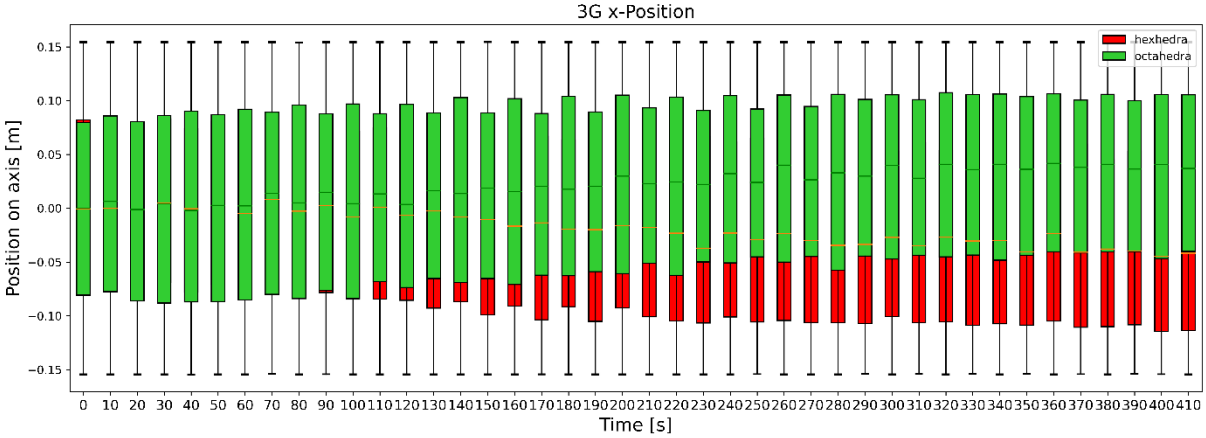

Figure 4. Development of particle position in x-direction for hexahedra and octahedra agitated by three groups mode

These findings are consistent with the observations that were made for spherical particles in mono- and polydisperse bulks. At the 2nd International Workshop on Reacting Particle-Gas Systems, the full set of results will be presented for homogeneous and heterogeneous particle assemblies of complex shape and particle segregation in z- and x-direction will be discussed.

Acknowledgement: This work has been funded by the Deutsche Forschungsgemeinschaft (DFG, German Research Foundation)-–422037413–CRC/TRR 287 "BULK-REACTION".

References

[1] N. Hilse, M. Kriegeskorte, E. Illana, S. Wirtz, and V. Scherer, ‘Mixing and segregation of spheres of three different sizes on a batch stoker grate: Experiments and discrete element simulation’, *Powder Technology*, vol. 400, p. 117258, Mar. 2022, doi: 10.1016/j.powtec.2022.117258.

[2] E. Simsek, F. Sudbrock, S. Wirtz, and V. Scherer, ‘Influence of particle diameter and material properties on mixing of monodisperse spheres on a grate: Experiments and discrete element simulation’, *Powder Technology*, vol. 221, pp. 144–154, May 2012, doi: 10.1016/j.powtec.2011.12.051.

[3] F. Sudbrock, E. Simsek, S. Wirtz, and V. Scherer, ‘An experimental analysis on mixing and stoking of monodisperse spheres on a grate’, *Powder Technology*, vol. 198, no. 1, pp. 29–37, Feb. 2010, doi: 10.1016/j.powtec.2009.10.011.

[4] ‘Bulk Reaction’. Accessed: May 02, 2024. [Online]. Available: https://bulk-reaction.de/

Refuse derived fuel classification by near-infrared spectroscopy and machine learning

J. Fischer[1*], T. Kunz[2], K. Treiber[2] and V. Scherer[1]

*E-Mail: fischer@leat.rub.de

[1] Department of Energy Plant Technology, Ruhr-University Bochum, Universitätsstraße 150, 44780 Bochum, Germany

[2] VDZ Technology gGmbH, Toulouser Allee 71, 40476 Düsseldorf, Germany

Introduction

In the cement clinker production, there has been a growing shift in the energy supply, moving from the traditional fuel, pulverized coal, to alternative fuels. In 2023, alternative fuel accounted for 73.4 % of the required 2807 MJ per ton of clinker [1]. One of the largest sources of alternative fuels is refused derived fuel (RDF) from industrial and municipal waste. RDF contains varying parts of foils, three dimensional plastics, paper and cardboard, textiles, rubber and foams. The transition to RDF is motivated not only by the significantly lower cost of RDF compared to coal but also by its lower carbon footprint. RDF emits roughly 50 g of CO_2 per megajoule of energy produced [2], compared to 94 g CO_2/MJ for hard coal and 111 g CO_2/MJ for lignite [3]. This lower emission is primarily attributed to RDF's lower carbon-to-hydrogen ratio and its partial biomass composition, which is considered carbon-neutral due to its renewable nature. Nevertheless, RDF presents operational challenges due to its highly variable composition, which can differ depending on the source, timing, and supplier of the waste stream. These fluctuations introduce complications in ensuring stable cement kiln operations and oppose a further increase of RDF usage in cement production. Despite regular increment sampling (at least every 62.5 t) [4], routine checks of the RDF composition by sorting are uncommon, since the required manual sorting is time and labor intensive. This results in a lack of real-time information for the kiln operation on quality limiting factors such as chlorine content (corrosion, chlorine cycle) or ratio of 3D plastics (these hit the clinker often not thermally converted, and, thereby, provide reducing conditions, which can harm cement quality). In order to meet climate targets, the introduction of carbon capture in cement production is necessary to capture raw material-related emissions; these technologies are inter alia sensitive in terms of process stability and, hence, require strict quality control of the fuel.

Near-infrared spectroscopy (NIRS) is a non-invasive analytical technique in which a sample is irradiated with light in the near-infrared wavelength range, typically between 800 nm and 2500 nm [5]. The reflected radiation by the sample is then detected using sensors, such as indium gallium arsenide (InGaAs) detectors [6]. Since the sample absorbs specific portions of the radiation, which correspond to anharmonic vibrations within the molecules, unique spectra are created. These contain detailed information about the molecular bonds and structural composition, allowing for a fast (<1 s) and comprehensive analysis without altering or damaging the sample. Since the absorbance spectra are hard to compare manually, NIRS needs to be coupled with statistical or machine learning methods.

Several machine learning approaches for classifying RDF using NIR have been proposed; however, proper validation remains limited. In [7], a classifier, initially trained on pure substances, such as PET, was applied to RDF to predict heating values. Due to the unsorted nature of the fuel, no true-value labels were available, preventing an assessment of classifier accuracy for RDF fractions. In [8], an FT-NIR was combined with a Support Vector Machine, though only a limited number of artificial model fuel samples (2-8 per fraction) were analyzed. A commercial product for real-time calorific analysis of RDF is mentioned in [9], yet its accuracy and algorithmic basis are not disclosed.

Experiment

This contribution aims to propose an automated method to classify refuse derived fuels into their contained fractions by a rapid NIRS at-line measurement and machine learning methods. As training data, RDFs from different German cement plants were manually sorted into one of six material fractions: foils, three dimensional plastics, paper and cardboard, textiles, rubber and foams. In total, 11526 different particles have been sorted. The sorted particles were introduced into the at-line (possible

sampling near the production line with rapid analysis) measurement setup, shown in **Figure 1**. By vibration, singular particles fall onto a conveyor belt, while dust and fine particle are sieved off by an 8 mm sieve. A Viavi 1700 ES NIR detector and an external halogen lamp (light in NIR region) are directed onto the conveyor belt. Automated particle detection (camera) triggers a measurement when a particle lays under the NIR detector, indicated by a change of pixel color values.
The measurement data were used to train a multi-layer perceptron classifier, here referred to as **MLP1**, which is a simple neural network. For the input data, the second derivative of the whole NIR spectra were calculated by a Savitzky-Golay finite filter and filtered by occurrence of peaks. After the input layer (125 nodes), 500 hidden nodes processed the signals. In the output layer, the final classification in one of the six fractions was determined. 80 % of the data were used for artificial neural network training, the remaining 20 % were used to test the network performance on unknown data.
In a second step, an artificial neural network with the same architecture, here referred to as **MLP2**, was trained by 3827 samples of sorted plastic types (PP, PE, PS, PET, PVC) NIR spectra provided by the measurement device manufacturer. This second neural network was first tested to determine if it can distinguish between different types of plastic. In the second step, the MLP2 network was used to predict the plastic types in both the foil and 3D plastic fractions.

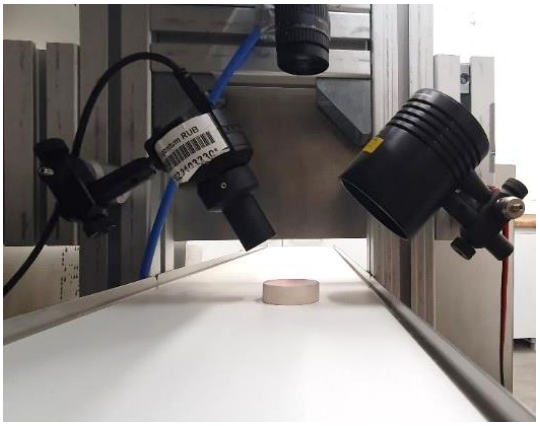

Figure 1: Measurement setup over a conveyor belt (middle, white). On the left, the NIRS Viavi 1700 ES measures NIR reflection of the light of the tungsten halogen lamp (right) from a sample. Mounted on top is a camera, which triggers a measurement when a sample particle is detected.

Results and discussion
With 90.3 % correct predictions on the test data set, the MLP1 neural network is able to distinguish the six main fractions of refuse derived fuels. Major mix-ups occur between textiles and paper / cardboard: 6 % of the textile particle in the test data set were predicted as paper / cardboard, and 5 % vice versa. Due to this, the accuracy for predicting textiles (88 %) was lowest. Foils are in some cases mixed up with 3D plastics (5 %) and paper / cardboard (4 %), leading to an accuracy of 86 %. Highest accuracies were observed for predicting rubber (95 %) and 3D plastics (94 %). Since artificial neural networks do not provide a discrete class, but rather probabilities for class membership, predictions can be filtered (threshold) such that only predictions with high probability are used to predict a refuse derived fuel composition. Here, the threshold was selected as 0.8. 90 % of all prediction are above this threshold. When only these predictions are considered, 94.0 % of all predictions on the test data set were correct. Not all parts (features) of the NIR spectra are equally important for the prediction quality. In **Figure 2**, the feature importance determined by permutation is shown for each wavelength. The most important features seem to be at 1200 nm, 1550 nm and 1676 nm. The absorbance at 1200 nm and 1676 nm can be due to the second and first overtone region for CH bonds [5]. The 1550 nm may correlate with NH bonds first overtone [5]. While CH bonds can clearly be found in all fractions, NH bonds are not. NH bonds may be present in both textiles (polyamide), foams (polyurethane) or rubber.
Before predicting the plastic types of RDF by MLP2, the performance of the second network was tested. The accuracy using the test data was 97.3 % with PVC as lowest (94 %) and PET as highest (99 %). Therefore, MLP2 was considered suitable to distinguish between the different plastic types.

Both plastic fractions, foils and 3D plastics were analyzed with MLP2. For the foils data, 67 % was classified as PE, followed by PET with 22 % and PVC with 6 %. The 3D plastic samples contrary were classified mainly as PET (61 %), followed by PE (23 %), PP (7 %) and PVC (5 %).

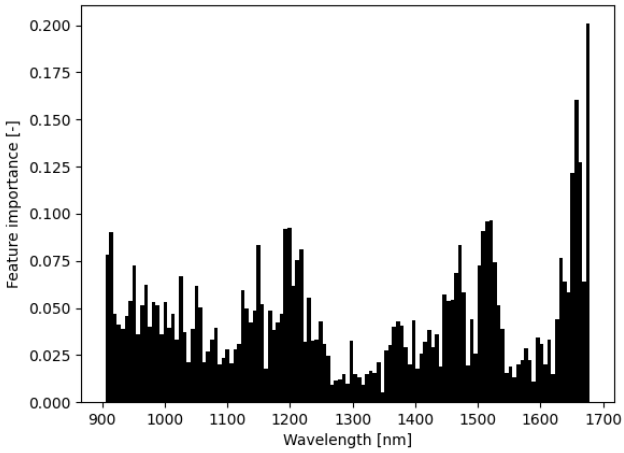

Figure 2: Feature importance of RDF classification for each wavelength, determined by permutation.

Conclusion and outlook

Refuse derived fuel samples were classified using an artificial neural network in six different fractions with an accuracy of 90.3 %. With thresholding, this accuracy could be improved to 94.0 %. The plastic containing fractions were analyzed by a second neural network to determine the composition in different plastic types. For the foils fraction mainly PE was predicted and for the 3D plastics fraction mainly PET. The classification into different plastic types was only conducted with ideal lab samples from the NIR manufacturer and could therefore not be tested further. For that, RDFs with known plastic type compositions would be needed. Although the considered plastic types represent 69.8 % of plastic in German production [10], the model should be extended to other plastic types such as PC, ABS or PU.

Acknowledgment

The IGF Project (01IF22676N) is supported within the program for promoting the Industrial Collective Research (IGF) of the German Ministry of Economic Affairs and Climate.

References

[1] Verein Deutscher Zementwerke e.V., Ed., "Umweltdaten der deutschen Zementindustrie 2023," Düsseldorf, 2024.
[2] M. Pohl, G. Becker, N. Heller, B. Birnstengel, and F. Zotz, "Auswirkungen des nationalen Brennstoffemissionshandels auf die Abfallwirtschaft," 2022.
[3] K. Juhrich, "CO2-Emissionsfaktoren für fossile Brennstoffe: CLIMATE CHANGE 27/2016," Dessau-Roßlau, 2016.
[4] *DIN EN ISO 21645:2021-09, Feste Sekundärbrennstoffe_- Verfahren zur Probenahme (ISO_21645:2021); Deutsche Fassung EN_ISO_21645:2021*, Berlin.
[5] H. W. Siesler, Ed., *Near-infrared spectroscopy: Principles, instruments, applications*, 2nd ed. Weinheim: Wiley-VCH, 2005.
[6] Y. Ozaki and Y. Morisawa, "Principles and Characteristics of NIR Spectroscopy," in *Near-Infrared Spectroscopy*, Y. Ozaki, C. Huck, S. Tsuchikawa, and S. B. Engelsen, Eds., Singapore: Springer Singapore, 2021, pp. 11–35.
[7] S. Verga *et al.*, "Estimation Of The Lower Heating Value Of Solid Recovered Fuel Based On Swir Hyper-Spectral Images And Machine Learning," in *2022 12th Workshop on Hyperspectral Imaging and Signal Processing: Evolution in Remote Sensing (WHISPERS)*, Rome, Italy, 2022.
[8] M. Ševcík, "Near-Infrared Spectroscopy for refuse derived fuel characterization: Classification of waste material components using hyperspectral imaging and feasibility study of inorganic

chlorine content quantification," Masterarbeit, School of Business, Society and Engineering, Mälardalen University, Eskilstuna, 2019.
[9] P. Krämer and S. Flamme, "Real-time Analysis of Solid Recovered Fuels using Sensor Technology," in 2015, pp. 339–348.
[10] C. Lindner, J. Schmitt, E. Fischer, and J. Hein, "Stoffstrombild Kunststoffe in Deutschland 2021: Zahlen und Fakten zum Lebensweg von Kunststoffen," Conversio Market & Strategy GmbH, Mainaschaff, 2022. [Online]. Available: https://www.bvse.de/dateien2020/2-PDF/01-Nachrichten/03-Kunststoff/2022/Kurzfassung_Stoffstrombild_2021_13102022_1_.pdf

Carbon Capture and Heating

Eva Klockow[1], Matthias Schmidt[2], Aldo Cosquillo[2], Venizelos Sourmelis[2], Viktor Kühl[2], Marie Gollsch[1], Marc Linder[1]*

*E-Mail: marc.linder@dlr.de

[1] *German Aerospace Center (DLR e.V.), Institute of Engineering Thermodynamics, Pfaffenwaldring 38-40, 70569 Stuttgart, Germany*

[2] *German Aerospace Center (DLR e.V.), Institute of Engineering Thermodynamics, Linder Höhe, 51147 Cologne, Germany*

Introduction and Background

The basic idea is a new concept for CO_2 removal (CDR) which utilizes synergies with renewable heat supply on a district level or individual houses. The process itself is based on the well-known lime cycle which consists of following steps, compare Fig. 1:

(1) The "limestone" ($CaCO_3$) is converted into "burnt lime" (CaO) using the electricity derived from renewable energy sources at low demand or periods of high supply. This calcination process could occur at a central location (e.g. a calcining facility serving a district). The released CO_2 represents a concentrated gas medium and can therefore be separated efficiently and cost-effectively.

(2) The “burnt lime” (CaO), as a heat carrier, is transported to the consumers or even industrial sites. There, the heat is released on demand by exothermal “lime slaking” with tap water resulting in the formation of $Ca(OH)_2$.

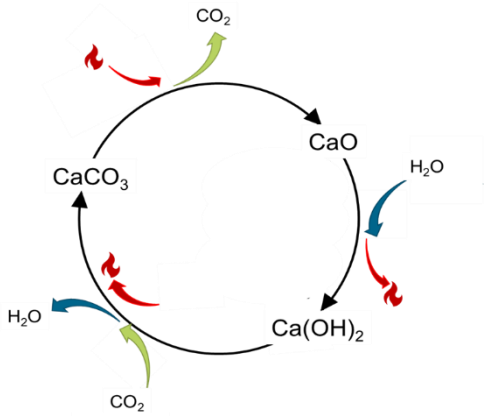

Figure 1. The closed lime cycle

(3) The slaked lime ($Ca(OH)_2$) is exposed to air where it is slowly converted to “limestone” ($CaCO_3$) again. As soon as the “limestone” ($CaCO_3$) is collected and transported back to the calcining facility serving the district, the lime cycle is closed. This transport consists of the initially delivered material (CaO), along with bound CO_2 captured from the atmosphere and basically represents the conversion of highly diluted CO_2 to a concentrated CO_2 point source (further described in [1, 2])

Due to its dual storage functionality (energy and CO_2), the individual steps can be operated independently from each other in terms of time and location, which could add an advanced flexibility for the electric grid (dynamic central calcination) and renewable local heat supply on demand.

The presentation will give an overview of the current state-of-the-art of this concept which includes a recently demonstrated thermochemical storage unit (compare Fig. 2) as well as recent results of the technical carbonation process and will discuss open questions of this concept in the context of Reacting Particle-Gas Systems.

Energy storage based on abundantly available materials

Whereas the decentralized production of renewable electricity has gained considerable progress in the years, the share of thermal energy supplied by renewable energy is lacking behind. This is on one hand surprising since it’s known for decades that more than 50 % of our total energy demand in Germany is actually spent for thermal needs. On the other hand, it’s again less surprising since a large fraction of this heat demand occurs only during winter which results in a fundamental challenge for the energy

transition: due to the consequently small amount of cycles, a storage material is most of the time passively waiting for its use.

In recent years, the German Aerospace Centre has developed an energy storage system that addresses this problem and can store large amounts of energy in inexpensive containers without losses. The basis for this storage system is the well-known reversible reaction of burnt lime and water, so that the storage materials are inexpensive, already available in industrial scale and, above all, can be provided and later disposed of in a resource-saving manner. The storage material is charged by electrical energy. Thereby water vapour is released and the remaining powder (CaO) is temporarily stored in containers at room temperature. The discharging process can take place on demand through the back reaction with liquid water, which releases around 300 kWh per t of CaO. In Figure 2, a first-of-its-kind heating unit which is based on this process, is shown. The research building D1244, shown on the right of Figure 2, has been developed within the framework of the CRC1244 at the University of Stuttgart. The lime-based test-facility is installed in the second floor and can be operated as stand-alone unit.

Figure 2. Thermochemical energy storage based on quicklime in the D1244 at the University of Stuttgart.

Decentral Carbonation

The challenge for the carbonation in technical scale lies in the dependence of the reaction on the local temperature, the local CO_2 concentration and humidity, the particle size, the material structure as well as the possibility to move the powder into and out of the capturing unit [3,4]. Since the required residence time of the material is related to the necessary volume of this carbonation unit, one major aspect is related to the question if a passive, mainly diffusion-controlled carbonation unit can offer sufficient conversion rates or if actively ventilated compartments, where temperature and humidity are controlled, are more effective in terms of residence time, required volume and overall energy consumption. In order to address this question, a specific test-rig has been built to measure the carbonation reaction under technically relevant boundary conditions (compare Figure 3).

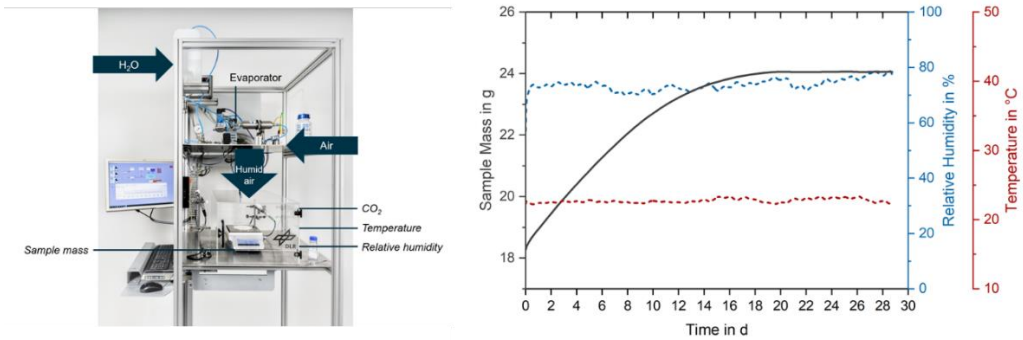

Figure 3. Left: Test-rig for technically relevant carbonation measurements; Right: One exemplary result to estimate the "cycle time" of one closed lime cycle and its feasible "conversion".

One exemplary result of these measurements is shown in Fig. 3, right. In this case the original sample mass was around 18.27 g, the CO_2 concentration in air around 350 ppm and the temperature and relative humidity were kept at around 22 °C and 75 %, respectively. It can be seen that the sample mass increases during the first two weeks and stabilizes at almost 24 g. After 28 days, the material was characterized and contained 86 % of $CaCO_3$.

Current status and Conclusion

Based on above given experimental results, the schematic shown in Fig. 4 can be drawn which visualizes the dual storage functionality of the concept and gives first numbers. The upper arrow corresponds to the distribution of stored energy, the right side shows the heat release on demand and the carbonation process and the lower arrow represents the collection and concentration of captured CO_2.

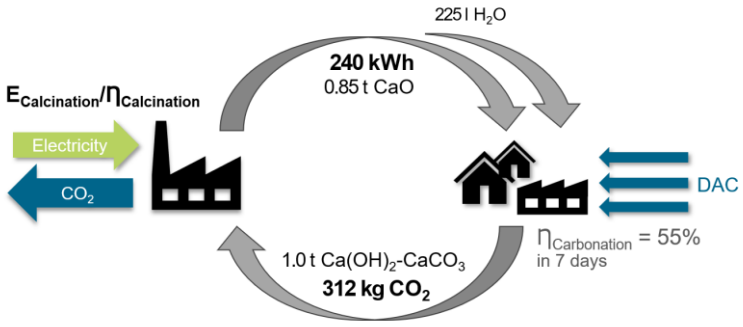

Figure 4. Schematic of the Carbon Capture and Heating concept based on experimental results (adapted from [1])

Even though, the transport of around 1 t of storage material per week seems a (too) large mass, Fig. 4 shows, that a continuous cycling during the heating period in Germany (around 20 weeks) would not only supply a substantial amount of the average heat demand (~ 4800 kWh) but also results in more than 6 tons of captured CO_2 – per capita!

One of the major technical challenges of this combined renewable heating and CDR concept is related to the powdery state of the cycled material. The renewable heating system (Fig. 2) has been developed for fine powder (d_{50} ~ 5µm) and the carbonation benefits from the large surface area, so the critical process step is the electric calcination of the cycled material. Research and development could therefore address the adaptation of electric calcination processes to fine powder or the modification of the material in such a way that it keeps certain properties during cycling.

References

[1] Eva Klockow, Nico Mader and Marc Linder: Combining Direct Air Capture and Long-term Energy Storage: An Approach for Renewable Heating With CO2 Capture; Proceedings of the 17th Greenhouse Gas Control Technologies Conference (GHGT-17) 20-24 October 2024

[2] Eva Klockow et al.: Could we change our perspective on lime: from CO2 emissions to carbon capture and renewable heating? , submitted

[3] Beruto, D. T. and R. Botter (1999). "Liquid-like H2O adsorption layers to catalyze the Ca(OH)2/CO2 solid-gas reaction and to form a non-protective solid product layer at 20°C." Journal of the European Ceramic Society 20: 497-503.

[4] Dheilly, R.-M., et al. (1998). "Influence of Climatic Conditions on the Carbonation of Quicklime." Journal of Materials Engineering and Performance 7: 789-795.

Modelling of packed bed biomass thermal conversion via CFD-DEM advanced approach

I. Wardach-Święcicka[1*]

*E-Mail: izabela.wardach@imp.gda.pl

[1]*Renewable Energy Department, Institute of Fluid-Flow Machinery of Polish Academy of Sciences, Fiszera 14 St., 80-231 Gdańsk, Poland*

Introduction

Numerous countries worldwide are engaged in ongoing efforts to identify novel and sustainable energy sources. This endeavour is driven by the desire for autonomy from external energy supplies and the aspiration to safeguard both the environment and human health. Direct combustion of solid fuels is a common method of rapid and cost-effective heat production; however, due to the non-uniform physical properties of biomass, it may encounter problems in the operation of heating units. The resultant instability can lead to inefficiencies in conversion, resulting in increased particulate matter in exhaust gases and subsequent air pollution. Consequently, there is a continued need for a detailed analysis of the combustion process of renewable solid fuels. The present work details the thermal conversion of biomass in a small-scale laboratory reactor using the XDEM method. The approach adopted is a mixed Eulerian-Lagrange method, which utilises a multiparticle system to predict the movement and conversion of each fuel particle. The integration of CFD with DEM has been shown to yield a reliable simulation tool, capable of providing detailed insights into complex multi-phase flows. The findings demonstrate that XDEM is a highly effective software for simulating the behaviour of moving thermally treated solid fuels. It provides detailed information about all the particles undergoing chemical reactions, which is very difficult to obtain from measurements.

XDEM Method

The XDEM method was developed by the team of prof. Peters for predicting the behaviour of moving particles during various thermochemical processes [1-3]. The main assumption of the model is that each particle moving in an external fluid field undergoes a sequence of thermodynamic processes described by a set of transient one-dimensional balance equations (mass, momentum, and energy). The proposed technique extends the dynamics of particles described by the classical DEM and is used with commonly applied CFD for simulating flow through porous media (granular material as a group of particles). While DEM predicts the position and orientation of each particle in space and time, the XDEM additionally estimates thermo-physical properties such as the internal temperature of a particle and its porosity and/or particle distribution or mechanical interaction with other bodies and shapes (walls, moving or stationary objects).

The translational and rotational motions of individual particles are predicted using the equations of classical mechanics. For each particle transition and rotational movement, the following equations in a Lagrangian approach are used [4]

$$m_p \frac{d\boldsymbol{v}_p}{dt} = \boldsymbol{F}_c + \boldsymbol{F}_g + \boldsymbol{F}_b + \boldsymbol{F}_D, \qquad I_p \frac{d\omega_p}{dt} = \sum_j \boldsymbol{M}_{p,j}, \tag{1}$$

where the following forces are considered: $\boldsymbol{F}_c$ - contact, $\boldsymbol{F}_g$ - gravitational, $\boldsymbol{F}_b$ - buoyancy, $\boldsymbol{F}_D$ drag. All particular pieces of information may be found in [4]. The second equation is the Newton's Second Law for rotation, where I_p is the particle moment of inertia, ω_p is the particle angular velocity, and $\boldsymbol{M}_{p,j}$ are the torques [4-5]

In a conversion module of XDEM, each particle is treated as a 1D porous medium, where one privileged direction is dominant, and through which a gas mixture of different chemical compositions can flow. The Eulerian approach for three-phase flow (gas, solid, water) in a porous material is used.

The mathematical form of the mass and energy balance equations depends on the considered shape of a particle. They obey transient cases with thermal equilibrium between the phases. Their detailed form is presented in [6]. The transport of gaseous species within the particle's pore space is considered to obey Darcy's law:

$$\frac{\partial p}{\partial r} = -\frac{\epsilon \mu_g}{K} v_g, \tag{2}$$

where p is the pressure, μ_g is the dynamic viscosity, and K is the permeability of the porous particle. Aditionally, the mass balance of an individual i-th specie within the pores of a given particle is considered. The chemistry is also taken into account by appropriate source terms in the balance equations.

The coupling of XDEM and CFD is performed within the OpenFOAM source.The granular bed is characterized as a porous zone in which gas flows inside the void space. The fluid flow is described by a three-dimensional Navier–Stokes equations, with energy equations for incompressible flow. The Brinkmann or Forchheimer relations are used to model the drag. Heat and mass transfer from particle to fluid is performed via the source terms of the corresponding conservation equations. Due to the character of the fuel thermal decomposition, chemical reactions are also considered in the CFD solver.

In this study, the presented coupled CFD-DEM approach is used to simulate the thermochemical conversion of biomass in the small-scale reactor.

Results

The XDEM method can be used for detailed analysis of the thermochemical processes taking place in biomass reactors during heating. The dynamic part of the software was used to fill the reactor with particles and to determine their initial positions. Two different cases were considered. In the first one, the container was filled with spherical particles of different sizes ranging from $d_1 = 0.006$ m to $d_2 = 0.01$ m. The second case involves cylindrical pellets with a diameter of $d = 0.006$ m and a length of $L = 0.02$ m. The reactor was filled with approximately 1650 spherical biomass particles and 460 cylindrical ones. The differences between the cases are shown in Figure 1.

The number of particles and their shape influence the overall conversion time, both in the case of individual particles and in the case of the whole bed. Figure 2 shows the biomass conversion and gas generation in the case of packed bed combustion. It displays the selected time step where the char is produced by devolatilisation in the central part of the reactor. Unconsumed air can be seen above the char production zone and CO2 is produced above the high temperature region. For this case, CFD-XDEM coupled calculations were used, i.e. dynamic and conversion part of XDEM and CFD (openFoam) for gas flow through the porous zone.

Figure 3 shows the CO_2 char gasification of different particle shapes. The results were obtained using only a conversion module of the XDEM software for single particle simulations. Here, it was assumed that each particle consists only of the char, whose mass reduces over time due to heterogeneous reaction with CO_2. The different Arrhenius equation constants were considered. The conversion time depends on the particle size and the kinetic reaction schemes used in the simulation. The cylindrical particles take longer to convert than the smaller spherical particles.

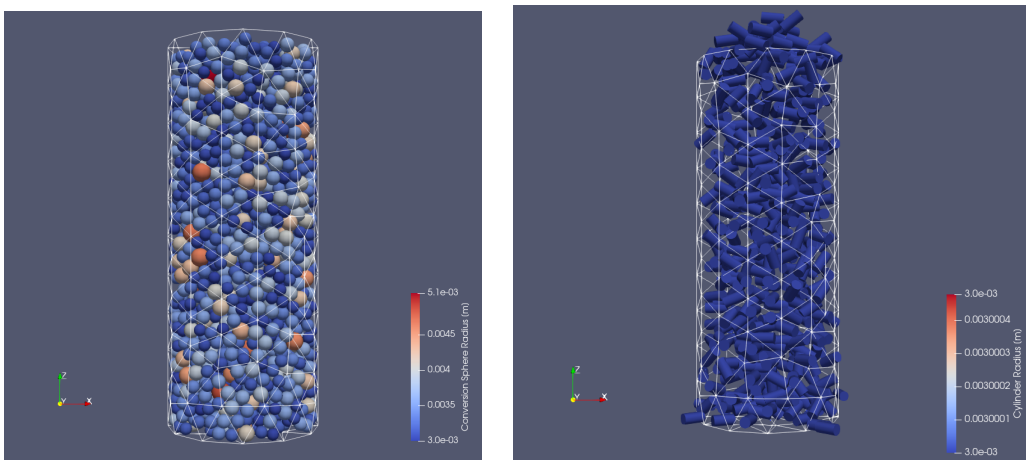

Figure 1. Filling the reactor with different types of particles: spheres (left) and cylinders (right).

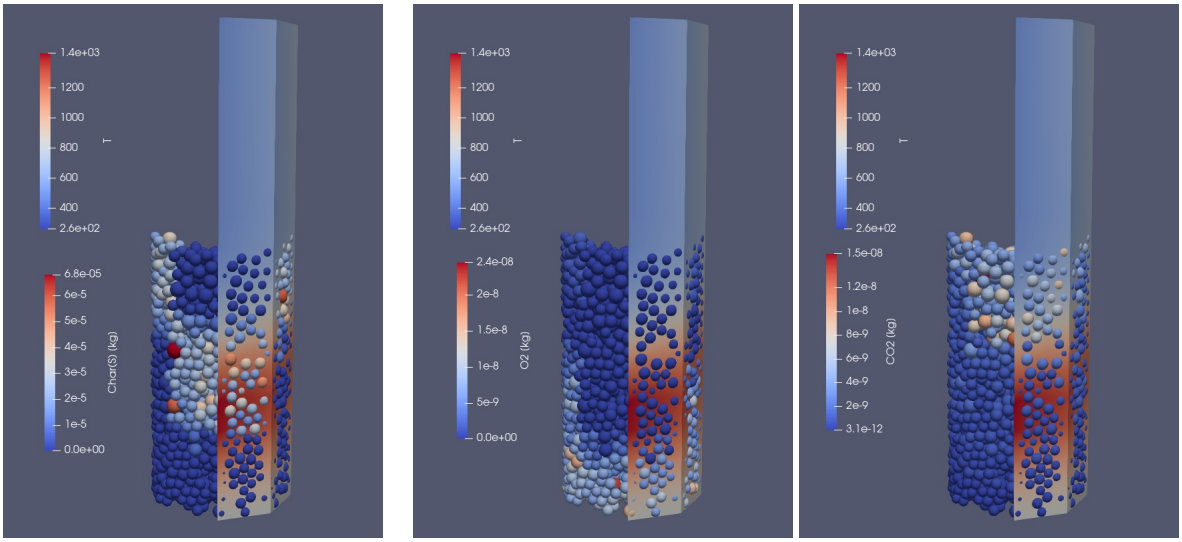

Figure 2. The conversion of biomass spherical particles during heating: amount of char (left), O_2 (centre), CO_2 (right) in each particle, with the corresponding gas temperature distribution (in K).

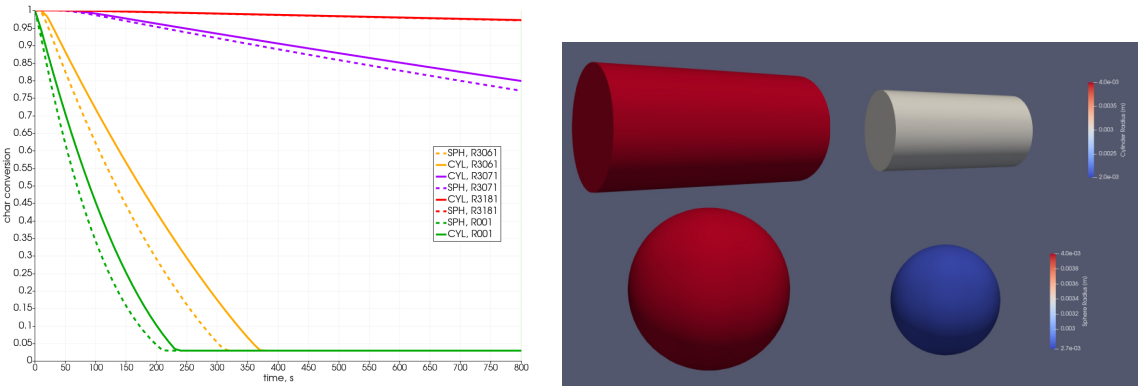

Figure 3. Char conversion (left) and change in the volume (right) of differently shaped particles due to char reduction - single particle simulations.

The XDEM is a useful tool for simulating complex multiphase systems with detailed particle interactions. In the case of a large number of different particle shapes, it is characterized by a high computational effort, due to the high complexity of the process. In addition, it needs to be validated by a large amount of data, which will be a significant challenge for its potential use in practical applications. Despite these limitations, XDEM remains a valuable tool for the design and optimization of small-scale applications and laboratory-scale thermal utilization and production of alternative fuels from various waste materials.

Acknowledgements

The author would like to thank Professor Bernhard Peters for the opportunity to use the XDEM software and for his valuable support, comments, and tricks. Without his invaluable help, this research would not have been possible.

References

[1] Peters B., Besseron X., Estupinan A., Hoffmann F., Michael M., Mahmoudi A. *Enhanced Thermal Process Engineering by the Extended Discrete Element Method (XDEM)*, Universal Journal of Engineering Science, 1, 139–145, 2013.

[2] Michael M., Vogel F., Peters B. *DEM–FEM coupling simulations of the interactions between a tire tread and granular terrain*, Computer Methods in Applied Mechanics and Engineering, 289, 227–248, 2015.

[3] Mahmoudi A. H., Markovic M., Peters B., Brem G. *An experimental and numerical study of wood combustion in a fixed bed using Euler–Lagrange approach (XDEM)*, Fuel, 150, 573–582, 2015.

[4] Baniasadi M., Baniasadi M., Peters B. *Coupled CFD-DEM with heat and mass transfer to investigate the melting of a granular packed bed*, Chemical Engineering Science, 178, 36–45, 2018.
[5] Peters B., Baniasadi M., Baniasadi M., Besseron X., Estupinan Donoso A., Mohseni M., Pozzetti G. *XDEM multi-physics and multi-scale simulation technology: Review of DEM–CFD coupling, methodology and engineering applications*, Particuology, 44, 176–193, 2019.
[6] Wardach-Święcicka I., Kardaś D. *Biomass Moving Bed Combustion Analysis via Two-Way Coupling of Solid–Fluid Interactions Using Discrete Element Method and Computational Fluid Dynamics Method*, Energies, 17, 3571, 2024.

Detailed characterisation of pore structure and transport properties of biomass particles during pyrolysis

N. Zhan[1,3], E. Liu[1], A. Dernbecher[2], N. Vorhauer-Huget[1], R. Wu[3], A. Dieguez-Alonso[2] and A. Kharaghani[1*]

*Email: reza.kharaghani@ovgu.de

[1]*Chair of Thermal Process Engineering, University Magdeburg, Universitätsplatz 2, 39106 Magdeburg, Germany*
[2]*Laboratory of Transport Processes, TU Dortmund University, Emil-Figge-Str. 68, 44227 Dortmund, Germany*
[3]*School of Mechanical Engineering, Shanghai Jiao Tong University, Shanghai 200240, China*

Introduction

Biomass- and waste-derived particulate materials offer great potential for reducing fossil fuel dependence and driving the circular economy forward [1]. This transition requires transforming these materials through thermochemical processes such as pyrolysis and char conversion, where complex physicochemical phenomena occur, both within the particles and between the particles and the surrounding medium. Often, the particles are thermally thick, meaning intra-particle transport phenomena play a crucial role and can significantly influence the overall conversion process. Transport phenomena themselves depend on the pore structure, which is not fixed during thermochemical processes, adding further complexity to the problem. This complexity is amplified when the pore structure is an-isotropic and also evolves non-isotopically, causing transport properties to change an-isotopically. Understanding the evolution of such complex structures and incorporating them properly into transport-reaction models remains inadequately understood [2]. Continuum models (CM) are commonly used to describe intra-particle and intra-bed transport by solving conservation equations for solids as composites of materials and pores [3]. These models are favoured for their high computational efficiency, as the governing equations are implemented using efficient algorithms. However, this efficiency comes at the cost of neglecting key pore-scale characteristics, such as pore size and shape distribution, hierarchy, connectivity, and dynamic pore evolution (e.g., expansion or shrinkage). These unresolved properties are critical for accurately modeling intra-particle transport, chemical reactions, and particle-environment interactions [4]. In contrast, discrete pore-scale models, such as pore network models (PNM), offer better resolution of pore structure details but come at a higher computational cost. While PNM can be applied at the representative elementary volume (REV) scale with manageable computational cost, this scale is insufficient for capturing the evolution of particle shape or the an-isotropic properties of transport parameters at the level of a single particle. Therefore, the objective of this study is to build upon our previously proposed extraction algorithm [5], incorporating domain decomposition and parallel computation to derive the equivalent pore network of an entire beech wood particle. Based on the extracted pore structure, we analyse how pyrolysis affects the structural evolution and transport properties of wood particles through detailed pore structure analysis.

Methods and Results

Pore network extraction is performed using the Omnidirectional Euclidean distance-based (OED-based) method, as described in our previous work [5]. Briefly, the process includes identifying anchored void voxels at boundary surfaces, computing OED values to establish a hierarchical structure (Fig. 1a), and applying the omnidirectional distance order homotopic thinning (ODOHT) algorithm to extract medial axes (MAs) and determine pore and throat locations. This approach ensures that the extracted pore network retains key topological and morphological characteristics, preserving pore connectivity, size distribution, and spatial arrangement. The extracted pore network, represented by nodes (pore and throat centres) connected by bonds, effectively captures the connectivity of the porous structure (Fig. 1b).

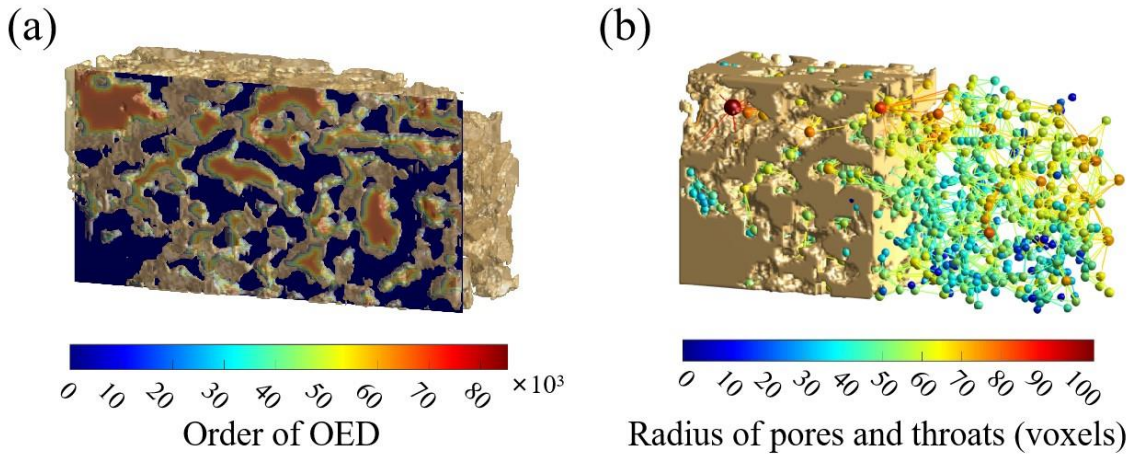

Figure 1. (a) Hierarchical structure of a wood particle with a domain size of 50×100×200 voxels, (b) extracted PNM showing pore and throat size distribution.

Figure 2 presents the extracted PNM of a beech wood particle. The CT images of the particle and the reconstructed 3D pore structure with a resolution of 1936×1936×1383 voxels are shown in Figs. 2a and 2b, respectively. Due to the large dataset size, domain decomposition and parallel extraction methods are employed to enhance computational efficiency. By partitioning the domain into smaller subdomains, parallel processing is enabled to significantly reduce memory and computational demands. Once the MAs are extracted from all subdomains, they are consolidated to reconstruct the full pore network, allowing the identification of pores and throats, as illustrated in Fig. 2c. This method ensures both computational efficiency and accuracy in large-scale pore network modelling.

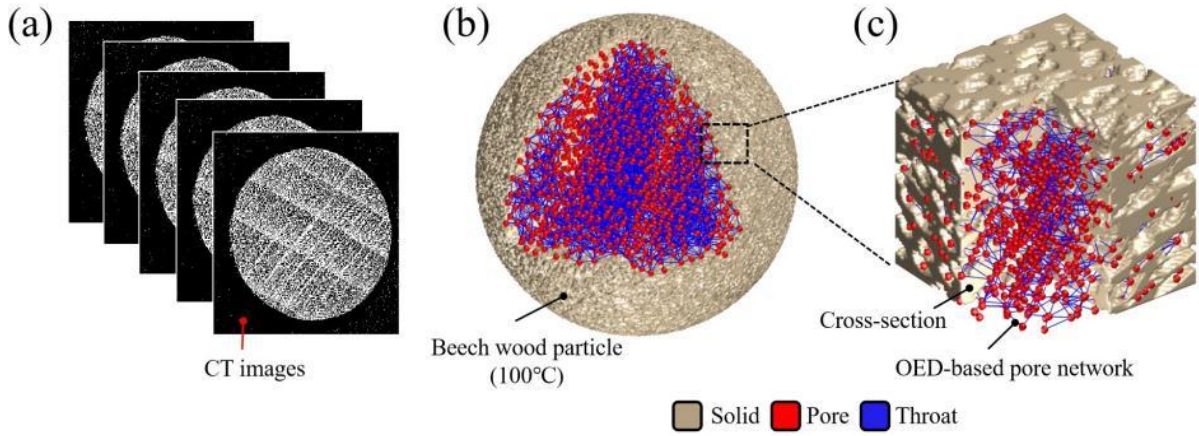

Figure 2. (a) CT slice images of the extracted structure of a beech wood particle, (b) reconstructed 3D pore structure, (c) extracted large-scale PNM.

Figure 3 illustrates the representation of an-isotropic pores using ellipsoids. Th orientation of each pore is defined by the direction vector of its semi-principal axes. Since visualizing the frequency of unit vectors in 3D is challenging, the semi-major axis direction vector of the fitted ellipsoid is converted into elevation (θ) and azimuth (φ) angles, as shown in Fig. 3a. The angles between the direction vectors and a given reference orientation are then calculated, and the number of vectors with an angle less than 10° is counted. On the left side of Fig. 3, an example is provided where an ellipsoid representing a pore has an orientation defined by $\theta = 16.5°$, $\varphi = 129.1°$.

The heterogeneity of porosity and permeability is analysed by dividing the wood particle into multiple REVs using a polar coordinate grid, as shown in Fig. 4a. The pore network of each REV is then extracted, and the single-phase pressure field is calculated to determine permeability, with results presented in the radial direction in Fig. 4b.

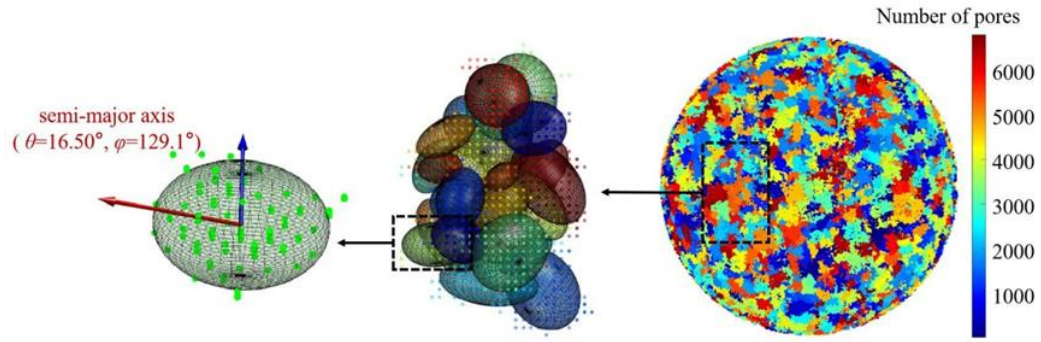

Figure 3. Discretization of pores with a set of point clouds superimposed by ellipsoids fitted to pores.

Finally, the distribution of local porosity and local permeability, reflecting the structural an-isotropy and heterogeneity, is derived from the results of different REVs, as illustrated in Fig. 4c. A more detailed analysis of the evolution of pore structure and transport parameters during the pyrolysis process, including particles pyrolysed at different temperatures, will be presented in the workshop.

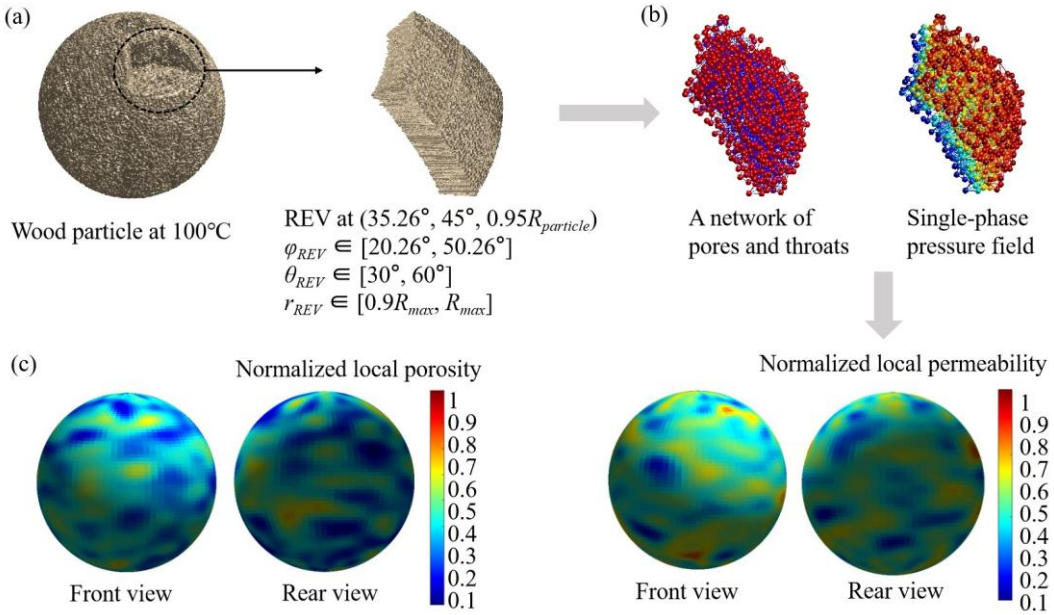

Figure 4. (a) A single wood particle segmented into multiple REVs using polar coordinates, (b) an REV located at (35.26°, 35.26°, 0.95$R_{particle}$), (c) distribution of local porosity and permeability.

References

[1] Lopez, G., Keiner, D., Fasihi, M., Koiranen, T., & Breyer, C. (2023): *From fossil to green chemicals: sustainable pathways and new carbon feedstocks for the global chemical industry*, Energy & Environmental Science, 16(7), 2879-2909.

[2] Ciesielski, P.N., Pecha, M.B., Thornburg, N.E., Crowley, M.F., Gao, X., Oyedeji, O., Sitaraman, H., & Brunhart-Lupo, N. (2021): *Bridging scales in bioenergy and catalysis: a review of mesoscale modeling applications, methods, and future directions*, Energy & Fuels, 35(18), 14382-14400.

[3] Gómez, M.A., Álvarez-Bermúdez, C., Chapela, S., Anca-Couce, A., & Porteiro, J. (2023): *Study of the effects of thermally thin and thermally thick particle approaches on the Eulerian modeling of a biomass combustor operating with wood chips*, Energy, 281, 128243.

[4] Dernbecher, A., & Dieguez-Alonso, A. (2022): *Advanced porous particle model in biomass pyrolysis*, Chemical Engineering Transactions, 92, 685-690.

[5] Zhan, N., Wu, R., Tsotsas, E., & Kharaghani, A. (2022): *Proposal for extraction of pore networks with pores of high aspect ratios*, Physical Review Fluids, 7(1), 014304.

Acknowledgment

Funded by the Deutsche Forschungsgemeinschaft (DFG, German Research Foundation) – Project-ID 422037413 – TRR 287.

Discovery of detailed kinetics for cellulose pyrolysis using an extended chemical reaction neural network

C. Chi[1*], A. Dernbecher[2], K.P.R. Subramanian[1], S. Adhikari[1], J.J. Rico[2], A. Dieguez-Alonso[2], S. Deng[3], and D. Thévenin[1]

[*]E-Mail: cheng.chi@ovgu.de (Cheng Chi)

[1]*Laboratory of Fluid Dynamics and Technical Flows, Otto-von-Guericke University Magdeburg, Universitätsplatz 2, D-39106, Magdeburg, Germany*
[2]*Laboratory of Transport Processes, TU Dortmund University, Emil-Figge-Str. 68, D-44227, Dortmund, Germany*
[3]*Department of Mechanical Engineering, Massachusetts Institute of Technology, MA 02139, Cambridge, USA*

Introduction

The future of energy is increasingly focused on clean vectors like hydrogen fuel, making sustainable production methods, such as biomass pyrolysis/gasification, highly attractive. However, a major hurdle in biomass pyrolysis research is the lack of detailed chemical kinetics that can fully capture the process's complexity. Traditional kinetic analyses, rooted in the seminal work of van Krevelen [1], have evolved over decades but often fall short, particularly when secondary and catalytic reactions are significant. This is where Chemical Reaction Neural Networks (CRNN) [2,3] come into play. CRNNs offer a data-driven, flexible alternative that embeds fundamental kinetic principles directly into their architecture. By incorporating the law of mass action and the Arrhenius law, CRNNs provide an interpretable framework that not only models primary reaction pathways but also adapts to the complexities of secondary and catalytic reactions. This integration allows for more accurate extraction of kinetic parameters from experimental data, enhancing our understanding of thermochemical processes [4].

In the present study, the CRNN approach is extended to encompass catalytic and secondary reactions. Thermogravimetric Analysis (TGA) experiments of cellulose pyrolysis were conducted using catalysts like potassium chloride, with varying conditions such as increased sample mass and closed lids to emphasize the effects of gas diffusion. Training the extended CRNN on this enriched dataset enables the discovery of a comprehensive kinetic model for cellulose pyrolysis, one major component in biomass.

Methodology

A total of 63 thermogravimetric analysis experiments were conducted to systematically explore the effects of various parameters on the biomass pyrolysis process. These experiments cover different initial sample mass (5 mg and 20 mg), different heating rates (2.5, 5 and 10 K/min), with/without catalyst, and with/without closed lid. All experiments were carried out with the device Linseis STA 1600 in nitrogen atmosphere, employing crucibles of the material Al_2O_3 as sample holders. These experimental data are divided into training and validation samples in the data-driven method.

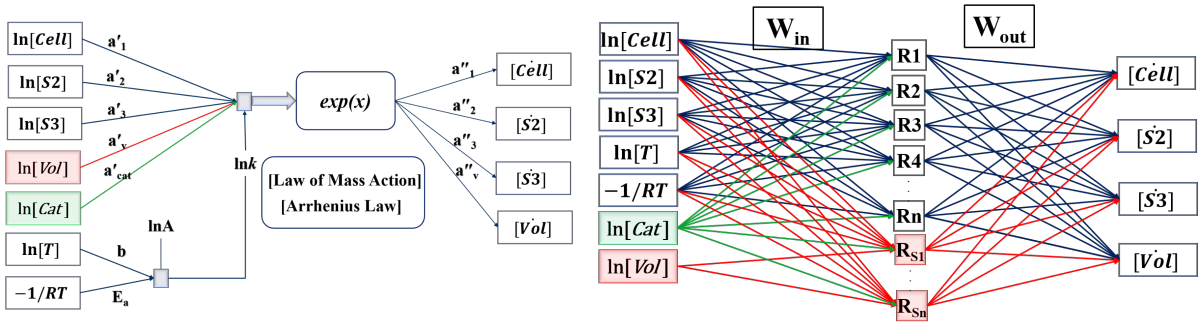

Figure 1. CRNN Structure with Single and Multi neurons in the hidden layer.

In this work, CRNN has been used and extended to explore the kinetics for cellulose pyrolysis, including catalytic and secondary reactions. CRNN is structured to satisfy the law of mass action and the Arrhenius law. The kinetic parameters A and E_a, along with stoichiometric coefficients a_i, are automatically obtained after training. More details about the state-of-art CRNN can be found in [2,3]. In

this study, catalyst species (KCl in the present study) is treated as an additional input in the CRNN. The corresponding weight for catalyst a'_{cat} determines whether the reaction is catalytic reaction ($a'_{cat} > 0$) or not ($a'_{cat} = 0$). A constraint is employed in the CRNN to make sure that $a'_{cat} \geq 0$. To check any secondary reactions, volatile gas could be considered as reactant. Only the additional secondary reactions (red color connections in Fig. 1) are trained, keeping weights and biases for all other reactions the same as the CRNN model without secondary reactions. A constraint is employed in the CRNN for a'_v and a''_v to make sure $a'_v > 0$ and $a''_v \leq 0$.

CRNN is trained using concentration $\boldsymbol{Y}$ and production rate $\dot{\boldsymbol{Y}}$ pairs:

$$\dot{\boldsymbol{Y}} = \mathrm{CRNN}(\boldsymbol{Y}, T). \tag{1}$$

However, practical experiments (e.g., TGA) typically lack intermediate species data, providing only residual mass evolution. To address this, CRNN is coupled with neural ordinary differential equations (ODEs) to predict residual mass:

$$\boldsymbol{Y}^{\mathrm{CRNN}}(t) = \mathrm{ODESolve}(CRNN(\boldsymbol{Y}, T), \boldsymbol{Y}_0, T_0, \beta). \tag{2}$$

where Y_0 and T_0 are initial conditions, and β is the heating rate. The loss function measures the deviation between the predicted and experimental residual mass and volatile gas mass:

$$\mathrm{Loss} = \mathrm{MAE}(m_{\mathrm{res}}^{\mathrm{CRNN}}(t), m_{\mathrm{res}}^{\mathrm{data}}(t)) + \mathrm{MAE}(m_{\mathrm{gas}}^{\mathrm{CRNN}}(t), m_{\mathrm{gas}}^{\mathrm{data}}(t)) \tag{3}$$

In this study, we employ the TRBDF2 integrator (Trapezoidal Rule + BDF2) for solving stiff ODE systems in chemical kinetics as it is highly efficient for extreme stiffness, minimizing re-evaluations and factorizations of the Jacobian.

Results and Discussion

Through CRNN training, a kinetic mechanism involving 8 reactions and 6 species is finally obtained, as shown in Table 1. R1 is the initial reaction decomposing cellulose (written Cell). R3, R4, R5 and R6 are catalytic reactions. R8 is the secondary reaction consuming the remaining volatile gas. The residual mass predictions using this mechanism match quite well with the experimental results under different conditions, as shown in Fig. 2.

Table 1. Kinetic mechanism discovered by CRNN with 6 species (including 1 catalyst species) and 8 reactions (including 1 secondary reaction) for cellulose pyrolysis.

	Reaction pathways	E_a (kJ/mol)	b	$\ln A$
R1	$1.08\,\mathrm{Cell} \longrightarrow 0.64\,\mathrm{S_4} + 0.44\,\mathrm{Vol}$	211.18	0.32	35.52
R2	$0.25\,\mathrm{S_4} \longrightarrow 0.2\,\mathrm{S_2} + 0.06\,\mathrm{S_3}$	142.17	0.07	19.03
R3	$0.14\,\mathrm{S_3} + 0.1\,\mathrm{Cat} \longrightarrow 0.16\,\mathrm{S_4} + 0.1\,\mathrm{Cat}$	237.41	0.04	21.29
R4	$0.05\,\mathrm{S_4} + 0.15\,\mathrm{Cat} \longrightarrow 0.05\,\mathrm{S_3} + 0.15\,\mathrm{Cat}$	244.46	0	20.16
R5	$0.73\,\mathrm{S_4} + 0.43\,\mathrm{Cat} \longrightarrow 0.49\,\mathrm{S_2} + 0.2\,\mathrm{S_3} + 0.43\,\mathrm{Cat}$	75.43	0	16.38
R6	$0.62\,\mathrm{S_2} + 0.22\,\mathrm{S_3} + 0.38\,\mathrm{Cat} \longrightarrow 0.83\,\mathrm{S_4} + 0.38\,\mathrm{Cat}$	152.43	0.04	28.1
R7	$0.98\,\mathrm{S_4} \longrightarrow 0.08\,\mathrm{S_3} + 0.88\,\mathrm{Vol}$	175.72	0.2	31.48
R8	$0.57\,\mathrm{Cell} + 1.42\,\mathrm{Vol} \longrightarrow 0.26\,\mathrm{S_2} + 0.57\,\mathrm{S_3} + 1.16\,\mathrm{S_4}$	73.61	0.03	7.73

Now by checking the time evolution of each species during the pyrolysis process, as shown in Fig. 3, it can be interpreted that S4 might be the active cellulose, S3 the solid char product, and S2 tar. Comparing Figs. 3(a) and (b), it is observed that S4 (active cellulose) is significantly reduced after the addition of catalyst. Catalytic reactions R4 and R5 help to consume S4 after its generation from R1. Comparing Fig. 3(b) with Fig. 3(c) or (d), it is observed that the volatile gas concentration is reduced after including the secondary reaction with a closed lid or larger initial mass (20 mg). These results demonstrate that data-driven mechanisms are useful to understand practical observations and optimize follow-up applications.

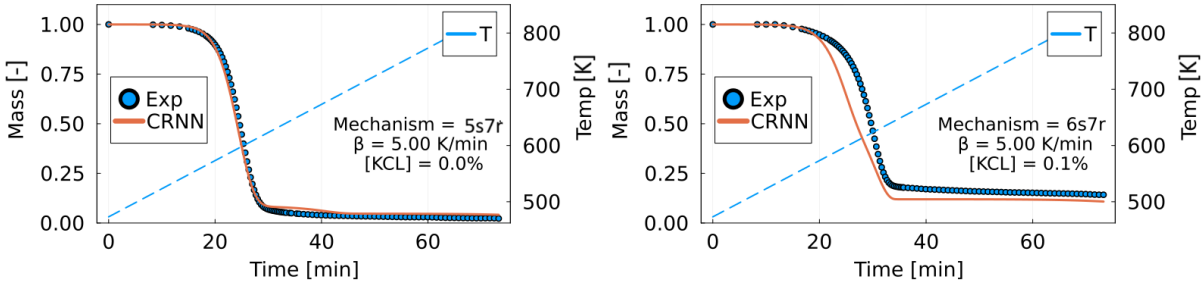

(a) 5s7r, β= 5 K/min (b) 6s7r, β= 5 K/min and [KCL]= 0.1%

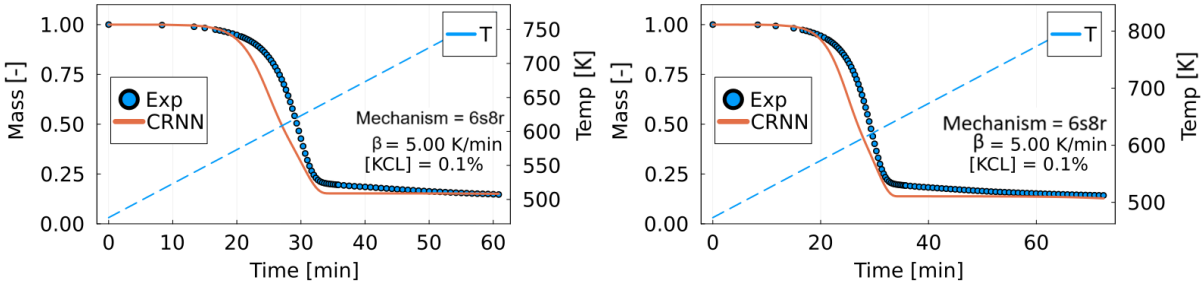

(c) 6s8r, β= 5 K/min, [KCL]= 0.1% and closed lid (d) 6s8r, β= 5 K/min, [KCL]= 0.1% and 20mg

Figure 2. Normalized residual mass predictions using CRNN models with different numbers of species (s) and reactions (r). Top: without (left) or with catalyst (right). Bottom: with closed lid (left), for 20 mg (right).

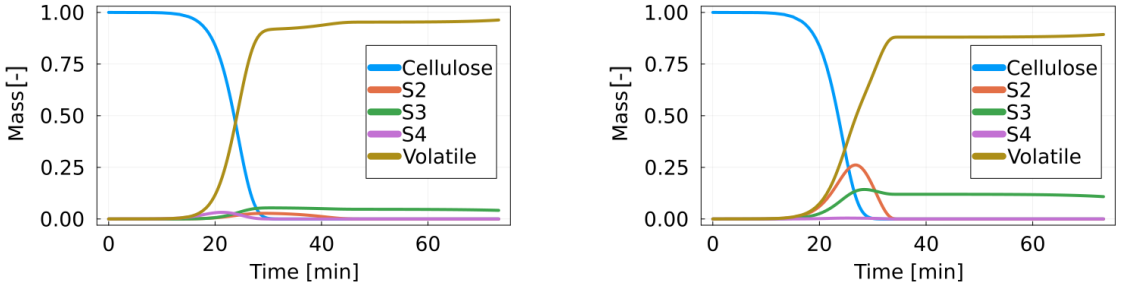

(a) 5s7r, β= 5 K/min (b) 6s7r, β= 5 K/min and [KCL]= 0.1%

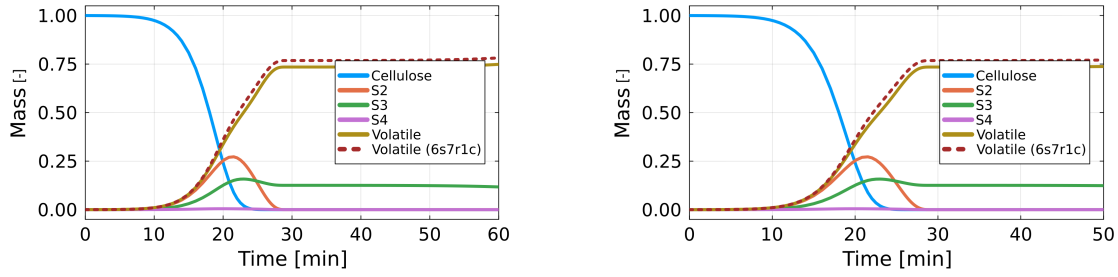

(c) 6s8r, β= 5 K/min, [KCL]= 0.1% and closed lid (d) 6s8r, β= 5 K/min, [KCL]= 0.1% and 20mg

Figure 3. Time evolution of each species (normalized) during the cellulose pyrolysis process using the mechanisms 6s7r without and with catalyst (a and b), or 6s8r with closed lid and 20 mg (c and d).

References

[1] van Krevelen, D.: *Micro- and macro-kinetics: General introduction to the symposium*, Chemical Engineering Science, 8, 5–17, 1958.

[2] Ji, W. and Deng, S.: *Autonomous Discovery of Unknown Reaction Pathways from Data by Chemical Reaction Neural Network*, The Journal of Physical Chemistry A, 125, 1082-1092, 2021.

[3] Ji, W., Richter, F., Gollner, M.J. and Deng, S. *Autonomous kinetic modeling of biomass pyrolysis using chemical reaction neural networks*, Combustion and Flame, 240, 111992, 2022.

[4] Kostetskyy, P., Broadbelt, L. J.: *Progress in modeling of biomass fast pyrolysis: a review.*, Energy & Fuels, 34(12), 15195-15216, 2020.